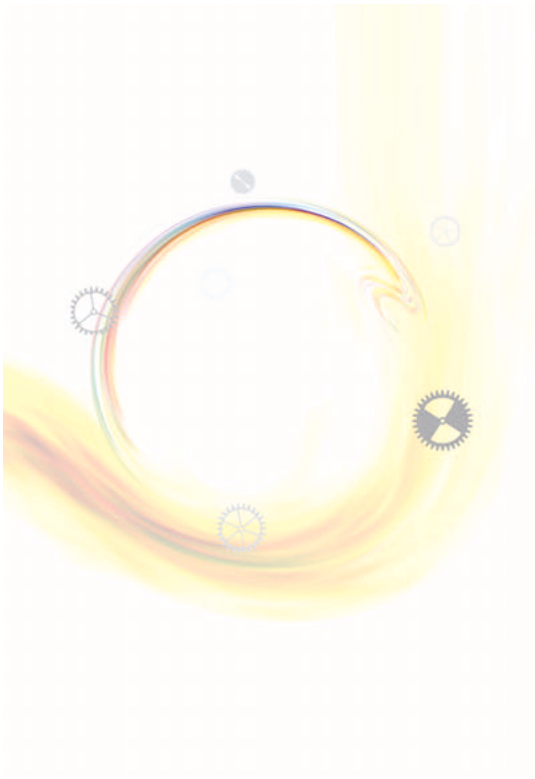
Honda R&D

Technical Review



October 2001





A Word About the Cover

New technology… produced as the result of painstaking research, repeated again and again. New technology… the outcome of cumulative failures. A relationship of deep mutual trust… a product born of communication between people. And new products… the final result of a skillful combination of the above elements.

By deepening our "connectedness," we attempt to gain something fresh, to make something new. No matter how small the "thing," no matter how tiny the event, every individual component is crucial; overlooking a single one will result in failure to achieve the best possible product.

We believe that good products contain a high degree of this "connectedness." The efforts of each one of us, something not easily seen on the surface, continue to live and breathe within each and every product we create.



Wako R&D Center
Takahiko Torii

Introduction of the Honda ASV-2, an Advanced Cruise-assist Highway System Test Vehicle (Passenger car)

Hiroshi MASHIMO* Yoshimi FURUKAWA* Nobuyoshi ASANUMA*
Tomoyuki FUKUMARU* Hideki KASEYAMA*

ABSTRACT

The Advanced Safety Vehicle phase 2 (ASV-2) proposed by the Road Transport Bureau, Ministry of Land, Infrastructure and Transport (formerly the Ministry of Transport) includes driver assistance services composed of 7 services or 8 systems that coordinate between the vehicle and the road infrastructure. The authors participated in proving tests that evaluated the basic functions of these driver assistance services. The following results were obtained:

- With respect to the "validity of road infrastructure functions," the services were verified to be effective in response to driver assistance conditions.
- With respect to "driver acceptance," we had braking driver assistance tests with haptic warning by brake actuation, and it was verified to be effective in reducing driver's emergency response time.

1. Introduction

The Advanced Safety Vehicle phase 2 (ASV*1-2) development program was proposed by the Road Transport Bureau, Ministry of Land, Infrastructure and Transportation (formerly the Ministry of Transportation). It was implemented as a 5-year project beginning in fiscal 1996 with the participation of 13 domestic Japanese automobile manufacturers.(1)

During this same period, the Road Bureau, Ministry of Land, Infrastructure and Transportation (formerly the Ministry of Construction) proposed the Advanced Cruise-assist Highway System (AHS*2) and established the Advanced Cruise-Assist Highway System Research Association (AHSRA) to develop systems that coordinate between the vehicle and the infrastructure. As part of this effort, studies(2) were conducted on the principal user services with the goal of reducing the amount of human loss and the number of fatalities resulting from accidents by a cumulative 90% or more.

In 2000, the National Institute for Land and Infrastructure Management (formerly the Public Works Research Institute) conducted the ASV/AHS Joint Proving Tests to evaluate the basic functions of the Smart Cruise Systems. The purpose of these systems is to coordinate the ASV-2 vehicle and the road-infrastructure to help prevent traffic accidents and reduce damages that occur during accidents. The objective of the tests was to evaluate the validity of the infrastructure and also driver acceptance by evaluating the basic system functions.

The Smart Cruise Systems that function through the cooperation of the vehicle and the infrastructure are able to provide drivers with information that is difficult for an autonomous system to detect. This includes short-range information on intersections with complex shapes, environments affected by dead angles, and so on, and long-range information on slippery road surface conditions due to snow and ice. It is therefore expected that these systems will reduce the impact of accidents that occur because of a lack of such information.

*Tochigi R&D Center

*1 ASV: Advanced Safety Vehicle promoted by the Road Transport Bureau, Ministry of Land, Infrastructure and Transportation

*2 AHS: Advanced Cruise-assist Highway System under the jurisdiction of the Road Bureau, Ministry of Land, Infrastructure and Transportation

Table 1 Services of joint proving test

No.	Service System	Partici-pation
1	Forward Obstacle Collision Prevention Support System	Yes
2	Curve Overshooting Prevention Support System	No
3	Lane Departure Prevention Support System	No
4-1	Intersection Stopping Support System	Yes
4-2	Crossing Collision Prevention Advisory System	Yes
5	Right Turn Collision Prevention Advisory System	Yes
6	Crossing Pedestrian Collision Prevention Advisory System	Yes
7	Road Surface Information System for ACC etc.	No



Fig. 1 Honda ASV/AHS

2. Overview of Services

The proving tests were conducted on the 7 services and 8 systems intended to help prevent traffic accidents and reduce damages that occur during accidents. Of these, the tests for the services and systems that Honda participated in are shown in Table 1.

The proving tests for road-to-vehicle cooperation involved the following:

- The road-infrastructure detected obstacles (fallen cargo, vehicles, pedestrians) and road surface information (slipperiness due to rain, snow, etc.) in poor-visibility road environments where it is difficult for the vehicle's sensor to detect such information.
- That detected information was transmitted to the vehicle by road-to-vehicle communication and used for information, warnings to the driver, and vehicle control.

Fig. 1 shows the test vehicle built for this project.

2.1 Systems to Reduce Damage by Prompting the Vehicle to Stop

2.1.1 Forward obstacle collision prevention support system

Aim: The objective of this system is to reduce accidents involving collisions with obstacles on roads with poor forward visibility.

Function: The system receives information from the road-infrastructure about such obstacles as fallen cargo and vehicles stopped due to traffic congestion in locations with poor forward visibility. The system calculates the distance from the subject car to the obstacle and when it judges that the driver maintains the velocity which may result in a collision, it provides the driver with voice guidance and visual displays urging caution and warnings prompting the driver to respond appropriately.

Target roads: Expressways, ordinary roads

Assistance level: Information, warning

2.1.2 Intersection stopping support system

Aim: The objective of this system is to reduce accidents caused by failure to stop at intersections without a traffic signal where stopping is required because of driver inattention and so on.

Function: The system receives information from the road-infrastructure about an intersection ahead that does not have a traffic signal but where stopping is required. The system urges caution about the approaching intersection with advance information in the form of voice guidance. The system further calculates the distance to the stopping point from that information and the subject vehicle's velocity, and if it judges that the vehicle will not be able to stop before the stop line, it provides warnings prompting the driver to stop.

Target roads: Intersections without a traffic signal where stopping is required

Assistance level: Information, warning

2.2 Systems for Reducing Damage by Controlling Vehicle Static Starts

2.2.1 Crossing collision prevention advisory system

Aim: The objective of this system is to reduce accidents at intersections without a traffic signal where stopping is required caused by improper movement into the intersection from a static start because of driver inattention, poor visibility, and so on.

Function: After the vehicle comes to a stop at the intersection stop line, the system receives information from the road-infrastructure about vehicles that will cross the intersection on the road that has the right-of-way. The system provides a warning to the driver with voice guidance and display messages urging caution.

Target roads: Intersections without a traffic signal where stopping is required

Assistance level: Information

2.2.2 Right turn (cross traffic) collision prevention advisory system

Aim: The objective of this system is to reduce accidents involving collisions with oncoming vehicles caused by driver miscalculation or poor visibility while turning right (in Japan, left in the U.S.) across traffic at an intersection with a signal.

Function: After the vehicle comes to a stop at the intersection stop line, the system receives information from the road-infrastructure about vehicles that will cross the intersection on the road that has the right-of-way. The system provides a warning to the driver with voice guidance and visual displays urging caution.

Target road: Intersections with traffic signal

Assistance level: Information

2.2.3 Crossing pedestrian collision prevention advisory system

Aim: The objective of this system is to reduce accidents with pedestrians in crosswalks caused by improper driving resulting from driver inattention, poor visibility, and so on.

Function: The system receives information from the road-infrastructure about pedestrians on the crosswalk ahead. Based on that information and the vehicle's current condition, the system provides a warning to the driver with voice guidance and visual displays urging caution.

Target road: Intersection

Assistance level: Information

3. Overview of Road-to-Vehicle Cooperation System Operation

An overview of system operation will be given using the Forward Obstacle Collision Prevention Support System as an example.

(1) Sensors installed on the road constantly monitor the road surface and obstacles on the road.

(2) The test vehicle recognizes the type of service being offered by passing the control detection marker that marks the location where the service begins. An overview of this operation is shown in Fig. 2.

(3) The test vehicle is successively sent the latest information on obstacles (the presence or absence of obstacles, the distance to obstacles, the road surface condition, etc.) by road-to-vehicle communication until it passes the control detection marker that marks the location where the service ends.

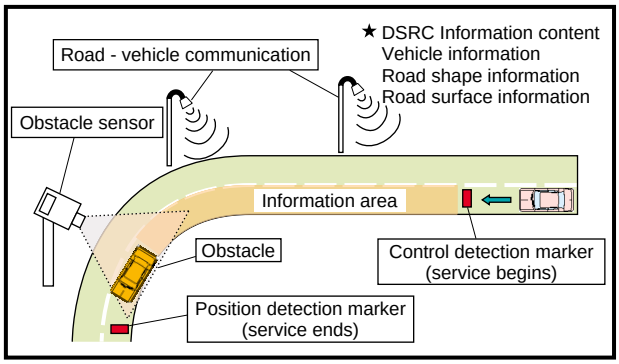


Fig. 2 Example of forward obstacle collision prevention support system (service begins)

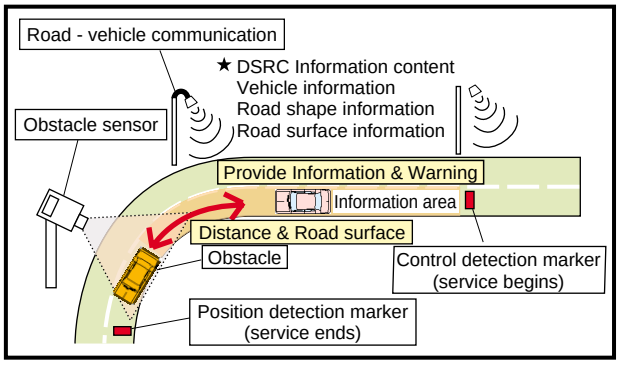


Fig.3 Example of forward obstacle collision prevention support system (information & warning)

(4) The test vehicle uses the distance to obstacles and the road surface condition to provide information on obstacles to the driver at an appropriate timing. When the driver does not stop or take other action with respect to the information provided, the system gives a warning. An overview of this operation is shown in Fig. 3.

4. System Configuration

4.1 Road-infrastructure System

The following facilities were installed on the road for the National Institute for Land and Infrastructure Management proving tests:

4.1.1 Control detection markers

These markers were installed where the Smart Cruise Services begin and end. They provide location information on lanes and so on in connection with the services.

- Information content: Road number, number of lanes, lane number, corresponding beacon number
- Radio mode: Active Modulated Radio Wave Type
- Radio frequency: 13.56 MHz

4.1.2 Road condition detection sensors

These sensors detect vehicles and other obstacles on the road and pedestrians on crosswalks and provide information about their position.

Information content: Obstacle type, position, and velocity of obstacle movement

4.1.3 Road surface condition detection sensors

These sensors classify the road surface condition in the service provision area into 5 categories: dry, wet, water-covered, snow-covered, and icy. It then provides this information to the vehicles.

4.1.4 Road-to-Vehicle communication system

This system transmits information detected by the roadside infrastructure to cruising vehicles.

- Radio mode: Dedicated Short Range Communication (DSRC)
- Radio frequency: 5.8 GHz band

4.2 Test Vehicle On-board Systems

The on-board configuration of the system that integrates the 5 Smart Cruise Systems subjected to functional testing in the proving tests is shown in Fig. 4. A block diagram of the system is shown in Fig. 5.

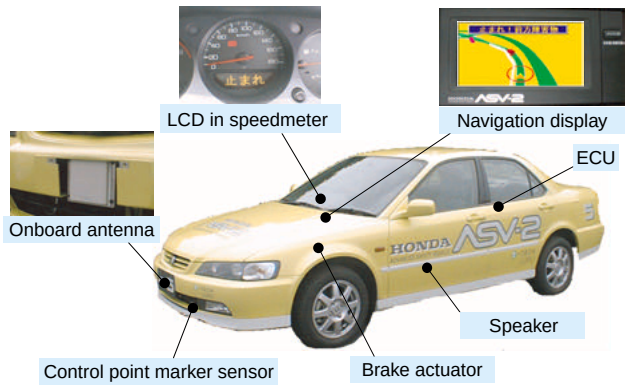


Fig. 4 Configuration of ASV/AHS

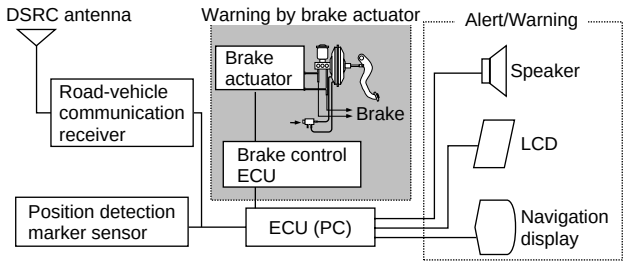


Fig. 5 Block diagram of the ASV/AHS

5. Features of the Test Vehicle Systems

5.1 High Accuracy Map Matching Navigation System

The road-to-vehicle cooperative system uses the control detection marker as the control point for distance in the service area. The on-board control detection marker sensor determines the control point according to the timing of the information received from the control detection marker when the vehicle passes by the control detection marker on the road. This method causes the distance control point to be displaced along the axis of movement because the timing for receiving the information is delayed due to the affects of vehicle velocity. The ASV/AHS Test Vehicle implemented the following processes to resolve this distance control point displacement.

(1) A digital map was created for navigation with control detection marker information added as node information.
(2) The vehicle position was determined using the digital map and control detection marker, map matching with the road configuration, and the Global Positioning System (GPS).
(3) Data on the location of obstacles sent by the roadside infrastructure was mapped onto the digital map.
(4) The information or warning timing was determined from the relative position of the subject vehicle and the obstacle on the digital map and the velocity of the subject vehicle.

As a result, it became possible to create a system in which the error in the distance to an obstacle consists only of the cumulative error in vehicle distance, thus enabling provision of highly accurate information or warnings to the driver. Fig. 6 presents an overview of the vehicle map matching for the AVS/AHS system.

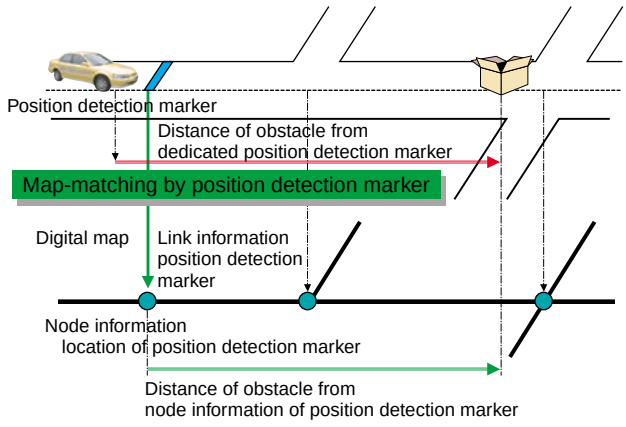


Fig. 6 Map-matching for the ASV/AHS

5.2 Haptic Warning by Brake Actuation

Appropriate information about potential dangers must be provided to drivers earlier in order to help prevent accidents from occurring. It has been reported[3] that using the sense of touch provides a faster driver response time than using either the sense of sight (visual display) or hearing (voice guidance) as have been conventionally used. Therefore, a system for haptic warning by brake actuation was installed in the vehicle and its function was verified. The haptic warning by brake actuation system is a system for warning the driver by applying brief, intermittent deceleration G-force along the axis of movement.

6. Validity of the Road-Infrastructure

The validity of the road-infrastructure was confirmed[4][5] to be effective in response to various driver assistance conditions.

7. Test Results for the Haptic Warning by Brake Actuation System

7.1 Evaluation of Response Time to Warning

A test vehicle equipped with the haptic warning by brake actuation system was used to compare driver response time with voice guidance alone and with a combination of voice guidance and the haptic warning system.

Test conditions:

Haptic warning by brake actuation consisted of a maximum deceleration of approximately 2.5 m/s^2 applied three times on a 300-ms cycle. Fig. 7 presents an overview of this operation. The voice guidance consisted of a buzzer sound.

The test was run by three male subjects who were provided with warnings by voice guidance alone and by voice guidance and haptic warning at velocity of 11 m/s (40 km/h) and 22m/s (80km/h), 10 times each.

Test results:

The results are shown in Fig. 8.

The sensory evaluation results were as follows:

For voice guidance alone:

• This method requires more time because the driver must first understand the warning and then apply the brake.

For haptic warning by brake actuation and voice guidance:

• The intention of prompting the driver to stop is felt directly by the body, which therefore leads to the action of applying the brake.

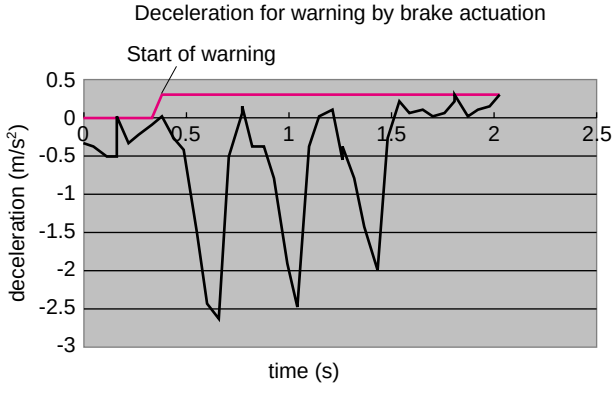


Fig. 7 Warning by brake actuation

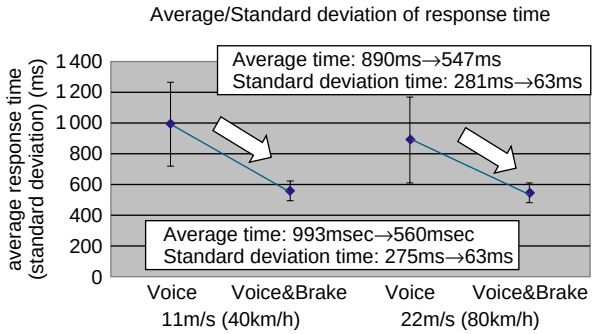


Fig. 8 Comparison of response times

(1) When voice guidance was combined with the haptic warning, 43% less time elapsed on average before the driver applied the brake than with voice guidance alone at 11 m/s (40 km/h) and 39% less time elapsed at 22 m/s (80 km/h). The results are shown in Table 2.

(2) When voice guidance was combined with the haptic warning, the standard deviation of the variations in time elapsed before applying the brake was reduced by 77% at 11 m/s (40 km/h) and by 78% at 22 m/s (80 km/h) relative to the use of voice guidance alone. The results are shown in Table 3.

Table 2 Average response time

Case \ Velocity	11m/s (40km/h)	22m/s (80km/h)
Voice guidance	990 ms	890 ms
Warning by brake actuation	560 ms	540 ms

Table 3 Standard deviation of response time

Case \ Velocity	11m/s (40km/h)	22m/s (80km/h)
Voice guidance	280 ms	280 ms
Warning by brake actuation	63 ms	63 ms

7.2 Evaluation of Driver Deceleration

A comparison was made of the amount of deceleration applied by the driver following haptic warning by brake actuation alone and warning by voice guidance alone.

Test conditions:

Haptic warning by brake actuation consisted of a maximum deceleration of approximately 2.5 m/s^2 applied three times on a 300-ms cycle. Fig. 7 presents an overview of this operation. The voice guidance consisted of a buzzer sound.

The test involved providing warning by voice guidance alone and™ by voice guidance and haptic warning by brake actuation at a velocity of 11 m/s (40 km/h).

The results showed that when voice guidance was combined with the haptic warning, the deceleration resulting from driver braking was approximately twice the deceleration that resulted with voice guidance alone. Fig. 9 shows deceleration after haptic warning when cruising at 11 m/s (40 km/h), and Fig. 10 shows the deceleration after warning by voice guidance.

7.3 Discussion

Fig. 11 shows driver brake timing after receiving a warning by voice guidance combined with the haptic warning by brake actuation when cruising at 40 km/h.

It is apparent from these results that the timing at which the driver begins to apply the brakes coincides closely with the second actuation of braking by the haptic warning system. The brake timing was more or less the same for all the drivers, suggesting that the response time with the haptic warning is unrelated to individual differences, that it shows a constant value, and that it reduces variation.

The above results confirmed that the haptic warning system is an effective means for providing warnings to the driver and that it provides the following benefits.

- The time that elapsed until the drivers applied the brake was reduced approximately 40%.
- The variation in the time elapsed until the drivers applied the brake was reduced approximately 80%.
- The drivers applied greater deceleration due to the haptic warning by brake actuation.

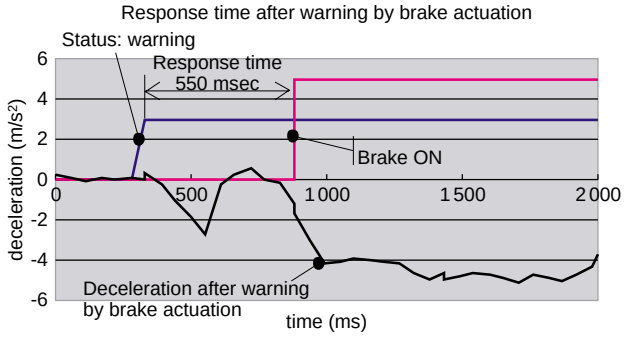


Fig. 9 Example of warning of brake actuator

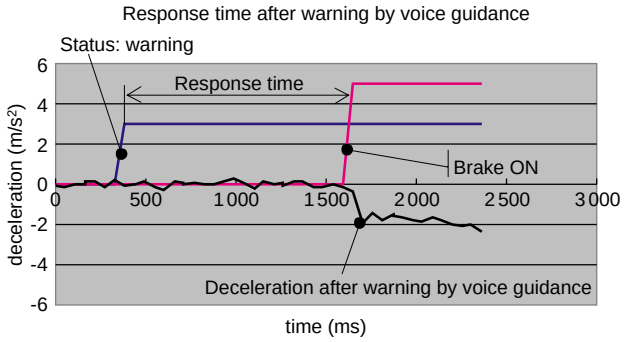


Fig. 10 Example of warning by voice guidance

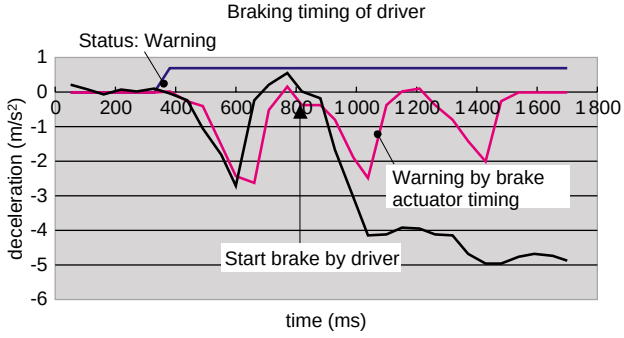


Fig. 11 Braking timing of driver

8. Conclusion

An AHS test vehicle was built in order to test and evaluate the Smart Cruise Systems at the National Institute for Land and Infrastructure Management, Ministry of Land, Infrastructure and Transportation. Participation by this test vehicle in the ASV/AHS joint proving tests allowed verification of the timing effective for providing information or warnings and verification of haptic warning by brake actuation.

9. Future Issues

Validity of the road-infrastructure and driver acceptance were evaluated during these proving tests. Although the effectiveness of warning by brake actuation was also evaluated, the limited time available for the proving tests meant that it was not possible to more thoroughly check the system with more test subjects, or to test the finer details of the magnitude, interval, and start of deceleration, and so on. Consequently, it is considered necessary to carry out verification of issues such as the following:

- Theoretical review and evaluation of the human-vehicle system.
- Verification of the effects of different road environment conditions, driver age, gender, and so on.

The 5-year Advanced Safety Vehicle phase 3 will begin this fiscal year, and again Honda will participate. It is hoped that the road-to-vehicle cooperative system will be brought to the point of practical application.

References

(1) Asanuma, N., et al., Introduction of Honda ASV-2 (Passenger Car), HONDA R&D Technical Review, Vol.12, No.2, p. 1–8 (2000)

(2) Kamata, G., Focusing on Principal User Service, Report of the Second AHSRA Research Seminar, Advanced Cruise-Assist Highway System Research Association (AHSRA), p. 106–109 (1998)

(3) Tsubouchi, K., Sense of Sight and Response Movement, Ergonomics, Tokyo: Nikkan Kogyo Shimbun, Ltd., p. 141–149 (1965)

(4) Furukawa, Y., Verification Tests of Vehicle/Road-infrastructure Cooperated System in ASV Phase 2 Project, ASV Phase 2 Promotion Project Conference Proceedings, The Way to a Safe Vehicular Society by ITS, p. 39–56 (2001)

(5) Study Group for Promotion of ASV, Road Transport Bureau, Ministry of Land, Infrastructure and Transportation, Coordination with Infrastructure, a Report on the Advanced Safety Vehicle (ASV) Promotion Project (Phase 2), p. 51–59 (2001)

■ Authors ■



Hiroshi MASHIMO



Yoshimi FURUKAWA



Nobuyoshi ASANUMA



Tomoyuki FUKUMARU



Hideki KASEYAMA

Introduction of the Honda ASV-2 Experimental Vehicle with a Road-vehicle Communication System (Motorcycles)

Kazumitsu KUSHIDA* Kazuhiro YAMAMOTO*
Norihiro KURATA* Kiyotaka SAKAI*

ABSTRACT

Joint proving tests of the Advanced Safety Vehicle (ASV) and Advanced Cruise-assist Highway Systems (AHS) were conducted by the Ministry of Land, Infrastructure and Transport (formerly the Ministry of Transport) for Smart Cruise systems. Thirteen domestic vehicle manufacturers participated in the tests on a proving test course set up at the National Institute for Land and Infrastructure Management of the Ministry of Land, Infrastructure and Transport. Seven services and eight test systems were tested. The objective of these systems is to receive information from the road infrastructure via Dedicated Short Range Communication (DSRC) concerning, for example, obstacles in the road ahead and the presence of oncoming vehicles; then, the systems provide warnings and information to motorcycle riders in order to reduce the occurrence of collisions. Honda provided a scooter, with an engine capacity of 250 cm^3, loaded with a road-vehicle communication receiver to receive the road information from the Dedicated Short Range Communication system, an information control ECU, and a newly developed Human Machine Interface (HMI) for motorcycles. The tests were conducted to confirm the effectiveness of the road-vehicle communication system from the viewpoint of driver acceptance.

The proving tests yielded the following findings:

(1) Information provided from the road infrastructure via DSRC for the purpose of enhancing active safety was confirmed to also be effective for motorcycles.
(2) An HMI system that combined sound information with visual information was confirmed to be capable of providing information appropriately for each driving assistance service.

1. Introduction

Honda designed two types of autonomous Advanced Safety Vehicle (ASV) motorcycles and carried out research on them as part of the activities promoted for the Advanced Safety Vehicle Phase 2 (ASV-2) activities proposed by the Road Transport Bureau of the Ministry of Land, Infrastructure and Transport (formerly the Ministry of Transportation)[(1)]. At the same time, work was underway on the Advanced Cruise-Assist Highway Systems (AHS) proposed by the Road Bureau of the Ministry of Land, Infrastructure and Transport (formerly the Ministry of Construction). As part of the ASV-2 project, 13 automobile and motorcycle manufacturers participated in joint proving tests held at the National Institute for Land and Infrastructure Management (previously the Public Works Research Institute of the former Ministry of Construction) of the Ministry of Land, Infrastructure and Transport. This article presents an overview of the proving tests and introduces an example of the results obtained.

* Asaka R&D Center

2. Overview of Services

The purpose of these proving tests was to verify the seven services and eight systems intended to help prevent traffic accidents and to reduce damage from accidents that do occur.

The road infrastructure sensors detect information about

Table 1 Services of joint proving test

Principal user services	Honda's motorcycle participated
Forward obstacle collision prevention support system	Yes
Curve overshooting prevention support system	Yes
Crossing collision prevention advisory system - Approaching support	Yes
Crossing collision prevention advisory system - Acceleration support	Yes
Right turn collision prevention advisory system	Yes
Crossing pedestrian collision prevention advisory system	Yes
Lane departure prevention support system	Automobile only
Road surface information system for ACC etc.	No

obstacles, other vehicles, pedestrians, the road surface, and other such information in areas with poor visibility that an autonomous system cannot detect. The road-vehicle communication system transmits this information to the cruising vehicle, where it is used for driver information and warning, for vehicle control, and so on. The services that Honda motorcycles participated in are shown in Table 1.

The content of each service is described in "Introduction of the Honda ASV-2, an Advanced Cruise-assist Highway System Test Vehicle (Passenger Car)."[(2)] It is difficult, for technical reasons, to create an autonomous system for a motorcycle that will prevent single vehicle accidents on curves. Therefore, Honda participated in testing of the Curve Overshooting Prevention Support System, which is anticipated to help reduce the number of this type of accident. An overview is presented in Fig. 1. In this system, information on the road surface condition, road shape, and so on is transmitted from DSRC antennas installed on the roadside.

- Name of service: Curve Overshooting Prevention Support System
- Purpose: Reduce the number of accidents in which vehicles enter curves without sufficiently reducing speed
- Functions: The system receives information about the curve shape and road surface condition for the road ahead from the road infrastructure via DSRC. Based on that information and the vehicle situation, it furnishes information to prompt caution and, when it is possible that deceleration will not take place in time, it warns the rider.
- Target road: Expressways, ordinary roads
- Caution level: Information, warning

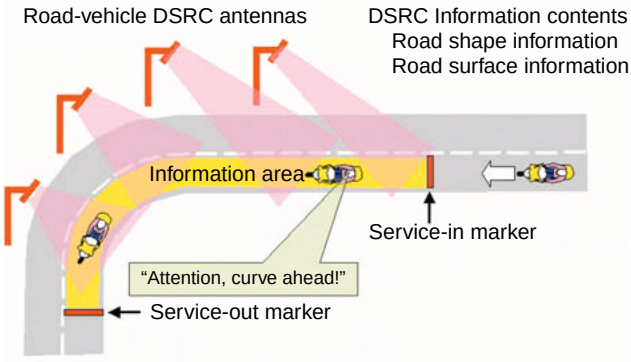


Fig. 1 Outline of curve overshooting prevention support system

3. Proving Test System

The Human Machine Interface (HMI) and the on-board equipment mounted on the experimental vehicle with road-vehicle communication system is explained below.

3.1 On-board Communication Equipment

Foresight scooters with a displacement of 250 cm^3 were used for the tests. Fig. 2 shows an external view of the Honda ASV-2 vehicle No. 6.

The on-board equipment included sensors to capture vehicle condition signals (for throttle, speed, brakes, turn indicators), an information control Electronic Control Unit (ECU) for communication control and HMI control processing, a wireless voice transmitter to send voice information to the communication helmet, a DSRC receiver and antenna for road-vehicle communication, a DSRC receiver and sensor for the Service-in marker, and so on (Fig. 3).

The DSRC antenna (Fig. 4) was built into the front fairing on the upper part of the headlight unit. It was attached at an elevation angle of approximately 10 degrees.

The proving tests for each support service required



Fig. 2 Honda ASV-2 vehicle No.6

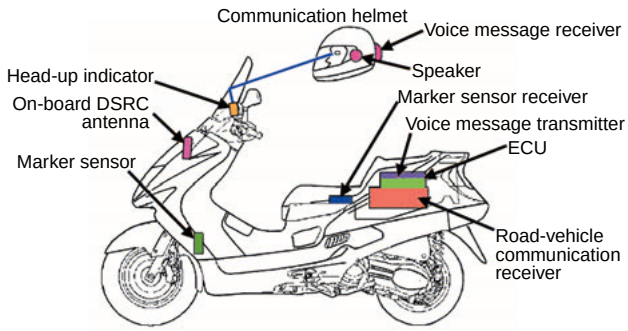


Fig. 3 Outline of prototype motorcycle system



Fig. 4 DSRC antenna

changing control parameters, revising algorithms, and conducting prompt data analysis within a limited test time. Consequently, the equipment was configured for operation in a seamless environment. To meet the requirement for real-time control of applications, the information control ECU configuration included a notebook computer (Toshiba Dynabook SS3380) and a signal processing controller. Microsoft Windows 2000[R] was used in order to realize a 50 ms sampling time for vehicle condition and sequence control every 100 ms. Fig. 5 presents a block diagram of the on-board system.

3.2 Human Machine Interface (HMI) Configuration

The HMI occupies a crucial position in safe driving support systems. However, HMI technology for motorcycles has not yet been established, and various methods are presently being explored. The performance and functions required are similar to those for automobiles, but the means for achieving them are limited by the differences in, for example, vehicle body design, audible sound range due to helmet use, driving posture, forms of steering control using steering and shifting body weight, vibration and defensive driving. The visual function, in particular, involves not only careful monitoring of the road ahead, but also of the subject motorcycle's behavior by means of the roll and yaw angles. Therefore, an HMI that is configured to change the rider's line of sight in order to receive information may end up having an effect significantly different from that originally intended. Taking these factors into consideration, the HMI concept for the present system was designed for the following:

- Active utilization of peripheral vision
- Information quantity should be kept to the required minimum in order to restrain eye movement
- Voice announcement as the principal means for presenting information

Information status is displayed visually, and the specific content of information is provided by voice announcement. Using the characteristics of visual and aural perception in this way allowed development of an HMI that can sustain the state of concentrated attention to the outside world.

3.2.1 Head-Up Indicator (HUI)

The HUI set into the upper face of the instrument panel uses a row of seven high-intensity LEDs to form a transverse band (Fig. 6).

It is important when making use of peripheral vision to provide the minimum quantity of information and to give it more than a certain fixed area of luminosity in order to prevent fixation of the rider's gaze.

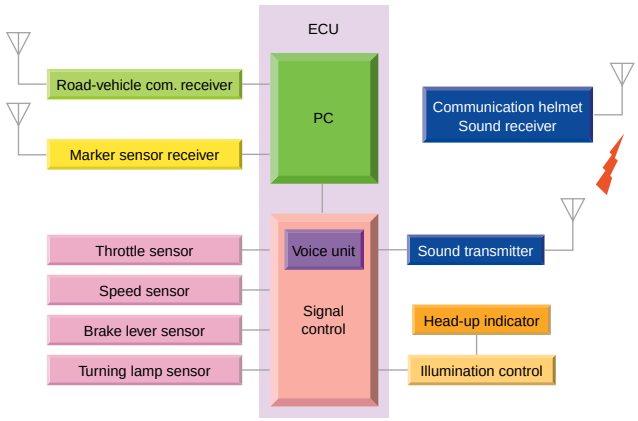


Fig. 5 On-board system block diagram



Fig. 6 Head-up indicator

The HUI illuminates an amber light that is reflected from the inside of the windscreen, where it creates a virtual image that is easily detected in the rider's peripheral vision. This location was also selected because it would not interfere with driving at night.

Information of the three kinds shown below is presented by the combination of LEDs that are turned on or off. This is intended to allow easy recognition of the current status of information provision.

- Service area
- Information to prompt caution
- Warning

It was decided to assign the seven LEDs to the three states of two left and right LEDs illuminated, central five LEDs illuminated, and central five LEDs blinking. Fig. 7 shows the HUI operating status and information content.

3.2.2 Communication helmet

Information provided by voice has the drawback that it cannot be understood without hearing the phrase to the very end. However, attention was paid to the selection of the wording, the length of the phrases, the use of distinct expressions, sound quality that enhances audibility, and so on. Thus, this method was found to be appropriate for accurately conveying information content.

A thin speaker is placed inside the helmet at the position of the outer ear. The system has several types of voice information recorded in advance, and the information control ECU activates these messages as necessary. Phrases were composed to convey voice information within three seconds. Table 2 shows examples of these voice messages.

High-quality wireless voice information is provided by the information control ECU using a voice transmitter with a built-in communication module and the communication helmet (Fig. 8).

4. Proving Test Results and Discussion

Analysis of motorcycle accident statistics shows that the greatest number of accidents involve automobiles, and the largest number of those are accidents involving vehicles turning right across traffic (a right turn as in Japan), and crossing accidents (accidents that occur at intersections)[(3)]. This article will use representative examples of test results to explain the Right Turn Collision Prevention Advisory System and the Crossing Collision Prevention Advisory System, which are intended to reduce the number of such

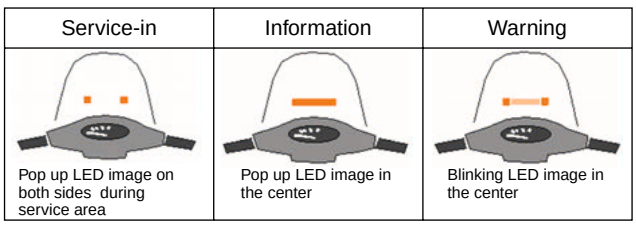


Fig. 7 Head-up indicator status

Table 2 Voice message examples

Services	Voice messages (Upper: Caution / Lower: Warning)
Forward obstacle collision prevention support system	Attention, obstacle 100 meters ahead
	Stop!
Curve overshooting prevention support system	Curve ahead
	———
Crossing collision prevention advisory system-Approaching support	Crossing 60m ahead
	Stop!
Crossing collision prevention advisory system-Accelerating support	Attention, vehicle from the right
	Stop!
Right turn collision prevention advisory system	Attention, approaching vehicle ahead
	Stop!
Crossing pedestrian collision prevention advisory system	Pedestrian at the right hand side
	Stop!

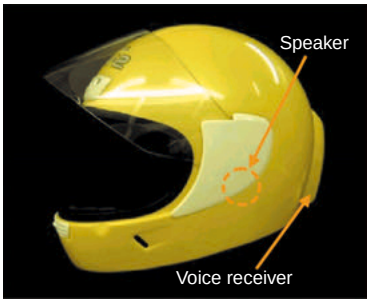


Fig. 8 Communication helmet

accidents, and the Curve Overshooting Prevention Support System, which is intended to reduce the number of accidents occurring on curves, which make up the largest number of single-vehicle accidents involving motorcycles. The effectiveness of these systems will be discussed from the perspective of driver acceptance.

All the proving tests were conducted on the proving test course of the National Institute for Land and Infrastructure Management of the Ministry of Land, Infrastructure and Transport. This proving test course was equipped with the test conditions and road environments envisioned for the various support services. For details regarding the test environment, please see “Introduction of the Honda ASV-2, an Advanced Cruise-assist Highway System Test Vehicle (Passenger Car)” in the Honda R&D Technical Review, Vol.13, No.2[(2)].

4.1 Right Turn Collision Prevention Advisory System

The test was conducted at an intersection equipped with a traffic signal and a dedicated right-turn lane. Fig. 9 shows an overview of the Right Turn Collision Prevention Advisory System for vehicles turning right across traffic. During the test, the HMI operated by turning on the LEDs on the two ends of the HUI to notify the rider of entry into the service zone at the point when the subject motorcycle approaching the intersection passed the Service-in marker. The vehicle receives information from the road infrastructure via DSRC concerning oncoming vehicles that are approaching the intersection. When there is a possibility that the subject motorcycle and an oncoming vehicle will collide or have a near miss, the central LED in the HUI is turned on, and a voice announcement conveys information to prompt caution with the message, “Approaching vehicle ahead.”

The test was conducted under two sets of conditions. In one, the status of the approaching vehicle can be seen from the subject motorcycle, while in the other, the view is

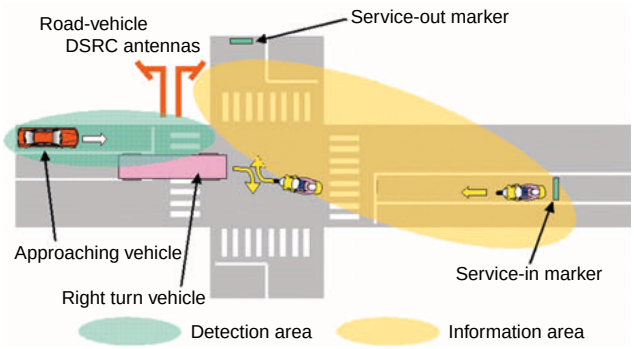


Fig. 9 Outline of right turn collision prevention advisory system

blocked by a large truck that is stopped in the right turn lane on the opposite side of the road.

The test results suggest that the rider can be prompted to caution regarding oncoming vehicles passing through the intersection and collisions can be prevented by setting the information timing to allow an appropriate time margin. Motorcycle rider evaluation comments also indicated that driver acceptance was significant. Some riders rated the system as effective, stating that it gave a strong sense of security when the view of the opposing lane from the subject motorcycle is blocked by a large vehicle stopped in the right turn lane on the opposite side of the road, making it difficult to see an oncoming approaching vehicle. Table 3 shows the results of driver acceptance evaluation.

Riders A and B are both test riders for Honda. The evaluation standards were set at the five levels of Excellent, Good, Fair, Poor, and Very poor.

4.2 Crossing Collision Prevention Advisory System – Applied When A Vehicle Is Approaching

The test location was a small intersection with a single lane for each direction and no traffic signal. Fig. 10 shows an overview of the Crossing Collision Prevention Advisory System.

The test determined whether the timing was appropriate for information notifying the rider of the need to make a

Table 3 Driver acceptance evaluation

Evaluation point of view		Rider A	Rider B
Safety	Visible condition without large vehicle	Fair	Fair
	Invisible condition with large vehicle	Excellent	Good
Rider's acceptance	Helpfulness	Good	Good
	Marketable	Good	Good

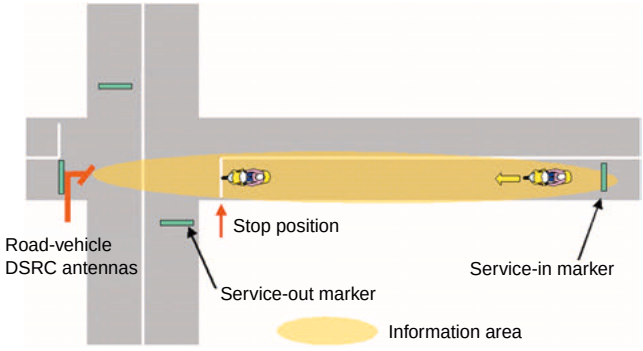


Fig. 10 Outline of crossing collision prevention advisory system - approaching service

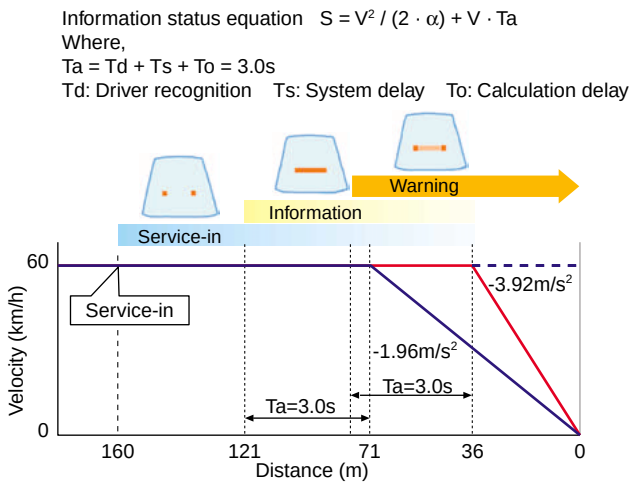


Fig. 11 Information status for crossing collision prevention advisory system - approaching service

complete stop when the subject vehicle is approaching a small intersection at a fixed speed on the non-right-of-way road. The effectiveness of the system was examined by comparing these results with the same setup without any information being provided. An example of information provision timing employed on the test course will be explained here. When the test vehicle passes the Service-in marker, the LEDs on both ends of the HUI light up to indicate that the vehicle has entered the information area. At this point, the vehicle receives data from the Service-in marker buried in the road surface concerning the distance (fixed value) to the intersection. The subject vehicle calculates its position in this area from the cumulative distance traveled. Then, as shown as an example in Fig. 11, the central LEDs in the HUI light up when the vehicle arrives at a point where, regardless of its speed, it will be able to stop at the stop line with a deceleration of 1.96 m/s^2 and a rider response time of 3 seconds. At this time, the rider is given information to prompt caution by means of the voice message, “Attention, crossing ahead”.

If the vehicle does not decelerate but further approaches the intersection, the system issues a warning to prompt it to stop. The central LEDS in the HUI blink and the voice message “Stop” is issued when the vehicle arrives at the point where it can stop with a deceleration of 3.92 m/s^2 and a rider response time of 3 seconds.

Typical examples of measurement data are shown in Fig. 12. The test series was set up so that the intersection location could be perceived 100 m or more in advance. Consequently, no conclusions were reached with regard to

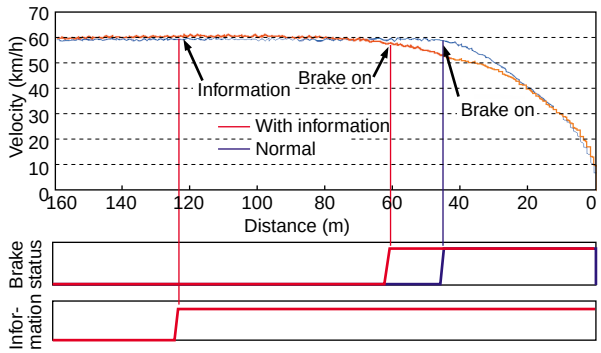


Fig. 12 Example of actual measured data - crossing-collision prevention advisory system (approaching service)

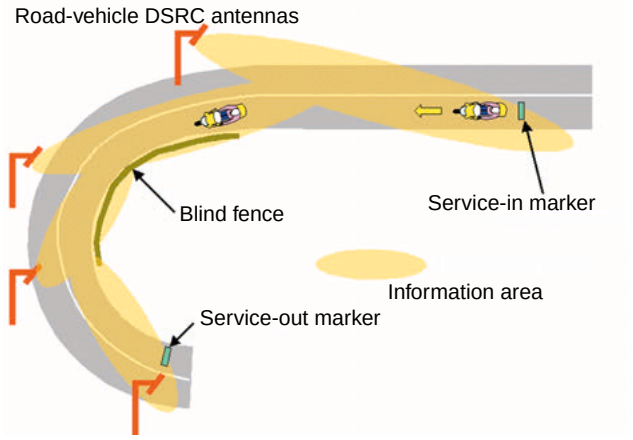


Fig. 13 Outline of curve overshooting prevention support system

driver acceptance or effectiveness of the service. As the data show, however, comparison of the test with and without information provision makes it clear that the point where deceleration begins comes earlier.

Therefore, it is thought that the service will be effective under conditions when the intersection location cannot be seen until the motorcycle is immediately before it, and when the rider has failed to notice the intersection due to oversight or absentmindedness.

4.3 Curve Overshooting Prevention Support System

The test location was a course set up to represent an ordinary road and an expressway. Fig. 13 shows an overview of the Curve Overshooting Prevention Support System.

The tests were conducted to provide information when the subject vehicle entered the curve at a set speed that exceeded the safe speed for the curve. The rider was presented with the information that there was a curve ahead and was urged to decelerate to a safe speed.

An example of the information timing employed on the test course will be explained here. When the test vehicle passes the Service-in marker, the LEDs on both ends of the HUI light up to indicate that the vehicle has entered the service area. At this point, the vehicle receives data from the Service-in marker buried in the road surface concerning the distance (fixed value) to the beginning of the curve. The subject vehicle calculates its position in this area from the cumulative distance traveled. Then, as shown in Fig. 14, the central LEDs in the HUI light up when the vehicle arrives at a point where, regardless of its speed, it will be able to slow down with a deceleration of 1.96 m/s^2 and a rider response time of 3 seconds. At this time, the rider is given information to prompt caution by means of the voice message, “Curve ahead.”

Representative examples of measurement data simulating an ordinary road are shown in Fig. 15. The ordinary road test course (V1: set service-in speed of 70 km/h; V2: safe curve speed of 40 km/h) is made up of a compound curve with two curvatures, the sharp curve (radius of 80 m) that is the target of this service, and before it a gentle curve (radius of 200 m). A fence is installed on the inside of the sharp curve to create an environment of poor visibility. As shown by the example in Fig. 14, when no information was provided, the test subject entered the gentle curve and predicted that the same curvature would be maintained. It is apparent that the sudden encounter with the sharp curve, however, caused the subject to decelerate rapidly. On the other hand, when information was provided,

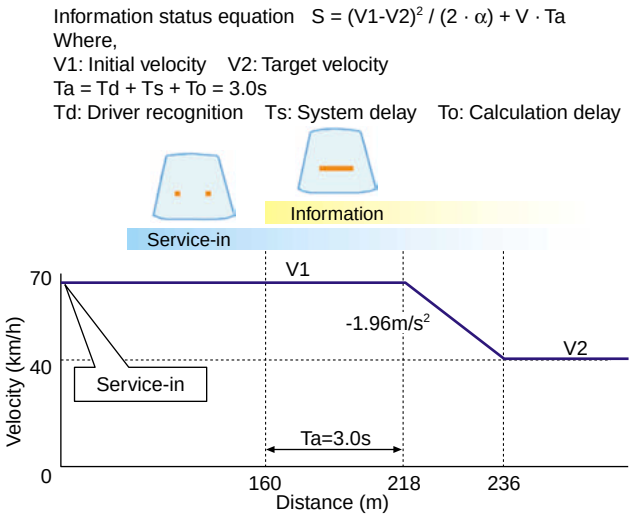


Fig. 14 Information status for curve overshoothing prevention support system

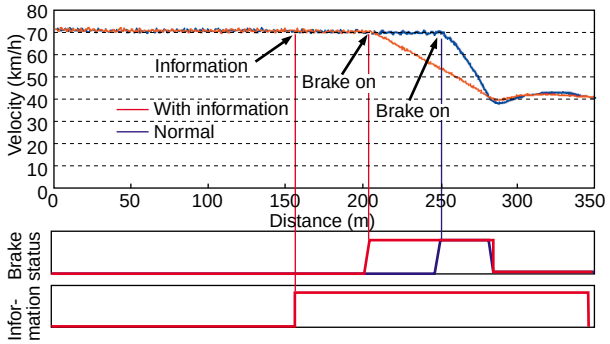


Fig. 15 Example of actual measured data- curve overshooting prevention support system -

it is evident that the subject decelerates with greater leeway.

On the expressway test course, however, the curve conditions were fully visible from a distance. The curve radius (148 m) was also larger. Consequently, there was only a slight difference between the initial speed and the target speed, and the deceleration could be accomplished by throttle operations. As a result, a significant difference between when the information was provided, and when it was not could not be found.

It will be necessary to conduct systematic tests in the future to determine rider acceptance and system effectiveness. The safe speed for a curve also varies with the type of vehicle and rider skills, and it is further thought to fluctuate with respect to the road design speed. Therefore, it is considered necessary to conduct a full study not only of safe speed but also of information timing and deceleration.

4.4 Issues for the Future

A variety of different disturbances and external factors are expected to affect operation in an actual traffic environment. Thus, it will be necessary to validate the overall effective function of the system under these types of conditions as well. At the same time, further effort will also be required to realize an HMI for the motorcycle that is effective and causes no discomfort from the perspective of driver acceptance. The creation of methods for evaluating the continuous flow that is composed of the accurate communication of information, correct judgement by the rider, and inducement of proper action, will also be an important issue.

5. Conclusion

It was confirmed that Smart Cruise systems with road-vehicle communication are capable of supporting driving for active safety in motorcycles as well as other vehicles. However, the proving tests were limited to facilities at the National Institute for Land and Infrastructure Management. It is considered necessary, therefore, to confirm the effectiveness of these systems in more realistic environments in order to work toward their practical application.

The HMI developed here was geared to the driving characteristics of the motorcycle. The HUI that makes use of peripheral vision can display three types of information, while the communication helmet can provide eleven types of information through voice messages. It was confirmed that an HMI combining voice and visual information constitutes a means of providing information that is capable of supporting various rider assistance services in the ways demonstrated in these proving tests.

6. Afterword

Starting in fiscal 2001, ASV, phase 3 proposed by the Ministry of Land, Infrastructure and Transport began as a five-year project. Honda is participating in this project along with other Japanese automobile manufacturers. In order to achieve practical application, it will be necessary to create a new framework that fuses together autonomous system and the road-vehicle infrastructure cooperation system.

References

(1) Yamamoto, K., et al., Introduction of Honda ASV-2 (Motorcycle), HONDA R&D Technical Review, Vol.12, NO.2, p.9-16 (2000)

(2) Mashimo, H., et al., Introduction of the Honda ASV-2, an Advanced Cruise-assist Highway System Test Vehicle (Passenger Car), Honda R&D Technical Review, Vol.13, NO.2, p.1-6 (2001)

(3) Statistical Annual Report of Traffic Accidents of 1998, Institute for Traffic Accident Research and Date Analysis, Japan (1999)

■ Authors ■



Kazumitsu KUSHIDA



Kazuhiro YAMAMOTO



Norihiro KURATA



Kiyotaka SAKAI

Introduction of the Gold Wing GL 1800

Masanori AOKI* Tetsuya TOSAKA* Hidemi MINAMI*
Hiroshi ISHIHARA* Koji KANO*

ABSTRACT

The Gold Wing GL 1800 was developed focusing on compatibility with the needs of riders and passengers. As a result, Honda succeeded in revolutionizing the luxury-touring category for motorcycles by combining the superior characteristics of long touring motorcycles with those of the sports type. This was made possible by making the engine more compact and moving it forward. In spite of heightened performance through increasing the engine displacement by 312 cm^3, the GL 1800 achieved both reduced weight and improvement of fuel economy. Through adopting numerous new technologies the GL 1800 was able to achieve superior environmental protection in exhaust emissions and was the first U.S.A. production model to apply an aluminum alloy frame.

1. Introduction

In 1975, Honda released the Gold Wing GL 1000, equipped with a horizontally opposed four-cylinder engine, as a super sports motorcycle. In the U.S., however, most customers used the GL 1000 as a touring motorcycle, not as a sports motorcycle. Equipping the motorcycle with a fairing, trunk, or saddlebags, couples would ride cross-country on the GL 1000. With the release of the 1980 Gold Wing model, the GL 1100, a fairing was made standard equipment, transforming the motorcycle into a true touring motorcycle. In 1984, the Gold Wing GL 1200 was even more fully equipped, and the 1988 model, the GL 1500, was upgraded to a horizontally opposed six-cylinder engine to again transform the motorcycle into a long touring motorcycle. These earlier versions of the Gold Wing are shown in Fig. 1.

The 2001 model, the Gold Wing GL 1800, is designed to provide not only the comfort that is expected in a long



Fig. 1 Appearances of GL1000, GL1100, GL1200 and GL1500

* Asaka R&D Center

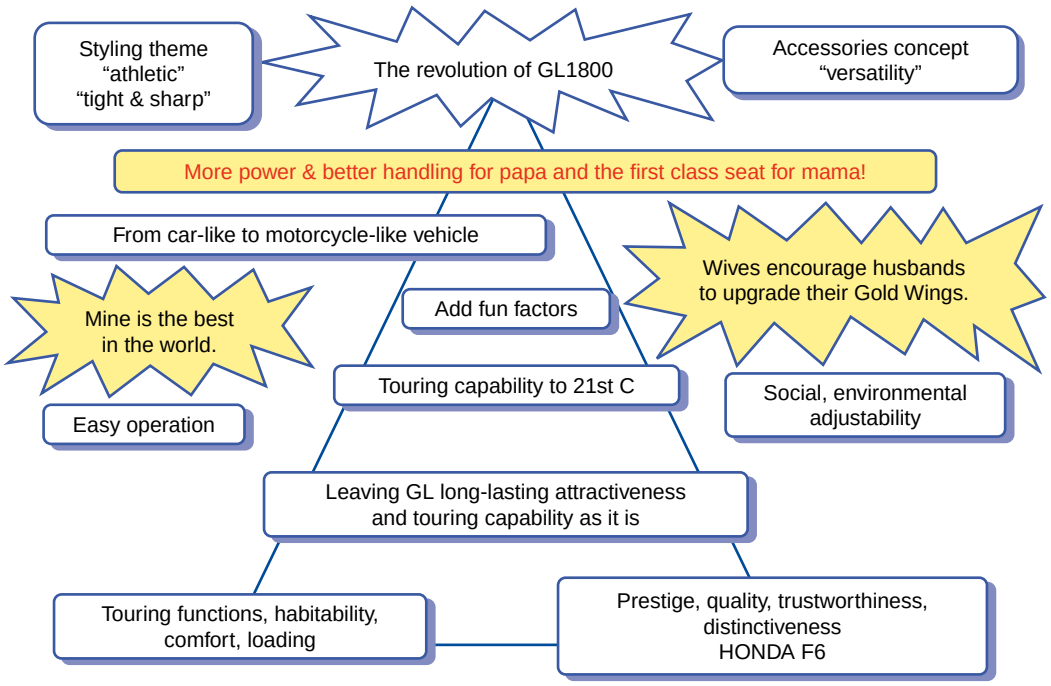


Fig. 2 Development concept

touring motorcycle, but also a sporty feel with well balanced driving, cornering and stopping performance. This maximum displacement motorcycle was also designed to be more environmentally friendly. Although this model was developed for the U.S., Japan, and Europe, this paper will describe the U.S. version which is the primary market, and also the version for Japan.

2. Development Concept

As shown in Fig. 2, the development team established “More power and better handling for the rider and first-class comfort for the passenger” as the development concept for the Gold Wing GL 1800, and commenced to study the technical elements that would be necessary in order to achieve this development concept.

If the riding position could be moved forward, it would be possible to provide the rider with the sporty handling expected of a motorcycle while also providing the passenger with more space. However, while the horizontally opposed six-cylinder engine does offer some benefits in terms of a low center of gravity and low vibration, it does restrict the foot space available to the rider. Therefore, it became important to be able to make the engine more compact and to move the engine forward; if these two aims could be met, it was felt that it would help improve fuel economy by reducing the frontal area. Fig. 3 shows a preliminary illustration of the concept, while Fig. 4 shows the final sketch.

3. Overview of the Gold Wing GL 1800

Table 1 lists the major specifications of the GL 1800, and Fig. 5 shows its appearance. Manufactured in the U.S.A., the GL 1800 features a 4-cycle OHC horizontally opposed 6-cylinder engine in a vertical configuration, and

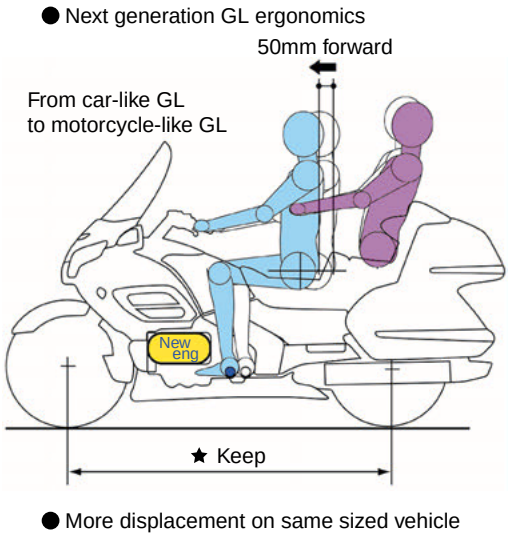


Fig. 3 Image diagram of the product concept

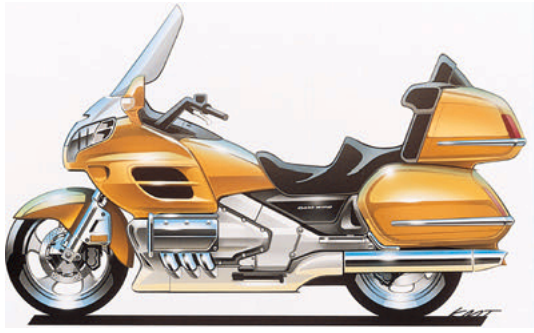


Fig. 4 Final styling design

Table 1 Specifications of GL 1800 and GL 1500 (for U.S.A.)

Item		Specifications	
Model		GL 1800	GL 1500
Cylinder arrangement		6-horizontally opposed	6-horizontally opposed
Cooling system		Liquid cooled	Liquid cooled
Valve train		OHC	OHC
Number of valves		IN: 1 EX: 1 per cylinder	IN: 1 EX: 1 per cylinder
Bore × Stroke (mm)		74 × 71	71 × 64
Engine displacement (cm^3)		1 832	1 520
Compression ratio		9.8 : 1	9.8 : 1
Fuel supply system		PGM-fuel injection	Carburetor
Max. power (kW/rpm)		88/5 500	71.6/5 000
Max. torque (N·m/rpm)		170.6/4 000	145/4 000
Transmission		5 speed constant mesh	5 speed constant mesh
Engine dimensions (L × W × H) (mm)		678 × 706 × 513	690 × 705 × 755
Engine mass (kg)		118.3	119.4
Vehicle dimensions (L × W × H) (mm)		2 635 × 945 × 1 455	2 615 × 955 × 1 495
Wheelbase (mm)		1 690	1 690
Vehicle dry mass (kg)		359 (Type-1), 362 (Type-2)	370 (SE), 364 (ASP)
Fuel capacity (L)		25 (6.6gallon)	23.8 (6.3gallon)
Tire size	Front	130/70R18 63H	130/70-18 63H
	Rear	180/60R16 74H	160/80-18 75H
Suspension	Front	Telescopic	Telescopic
	Rear	Single supported swing-arm (with PRO-LINK)	Conventional swing-arm
Brake system	Type-1	LBS (Linked Brake System) (both hand and foot operated)	Foot operated combined brake system Hand operated conventional brake system
	Type-2	LBS with ABS (both hand and foot operated)	———
Brake disk	Front	ϕ 296 floating double disc	ϕ 296 solid type double disc
	Rear	ϕ 316 ventilated single disc	ϕ 316 solid type single disc

an aluminum alloy dual-spar diamond type frame. Despite the fact that the engine displacement has been increased from 1520 cm^3 in the GL 1500 to 1832 cm^3 in the GL 1800, the engine weight has been decreased by approximately 1.1 kg and the vehicle dry weight has been decreased by approximately 11 kg. By optimizing the shape of the combustion chambers, reducing friction, optimizing the fuel injection timing, going to higher ratios in the transmission, various other engine improvements, and by reducing the frontal area in order to achieve approximately a 10% reduction in the drag coefficient (μaA), fuel economy at 75 mph (120 km/h) has been improved by 27% compared to the GL 1500. Furthermore, the improvement in fuel economy combined with a larger fuel tank capacity has increased the cruising range of the GL 1800 to 400 km compared with approximately 300 km for the GL 1500. Fig. 6 shows a comparison of the frontal area of the GL 1800 with that of the GL 1500.

Fig. 7 shows the engine performance curve. Due to the increase in engine displacement, the engine exhibits a 23% increase in maximum output, an 18% increase in maximum torque, and easy-to-handle output characteristics. Emission control devices include a three-way catalyst and an air-fuel mixture feedback control mechanism in the secondary air supplier as well as an electronic fuel injection system in the air intake system.



Fig. 5 Appearance of GL1800

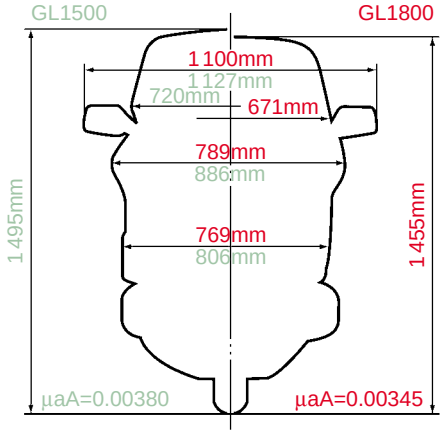


Fig. 6 Front view profile diagram

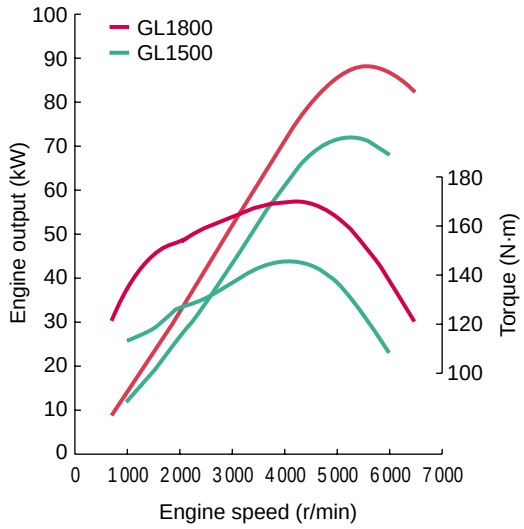


Fig. 7 Engine performance curve

4. Engine

4.1 Compact and Lightweight

Fig. 8 shows a perspective drawing of the engine. The valve mechanism was changed from the rocker arm type with HLA (Hydro Lash Adjuster) that was used in the GL 1500 to the direct acting parallel type using shim-under-bucket that is shown in Fig. 9. This change made it possible to reduce the number of parts and to save space and weight in the vicinity of the cylinder heads. Fig. 10 shows the components of the valve systems used in the GL 1500 and the GL 1800. The cam driving system was changed from belt drive to a silent camshaft chain driving system that uses an auto tensioner lifter. In addition to helping to make the engine more compact, this system is also maintenance free. In order to make it possible to mount the engine forward, the side-mounted radiators shown in Fig. 11 were adopted for the cooling system. In order to handle the heat load and improve the warm-up characteristics, the parallel coolant flow used in the GL 1500 was changed to series flow in the GL 1800.

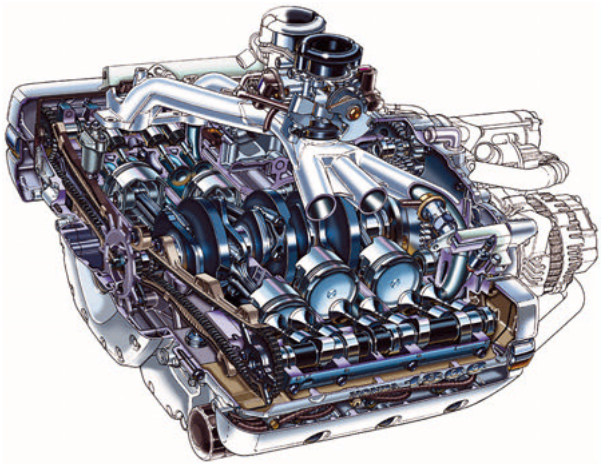


Fig. 8 Perspective drawing of engine

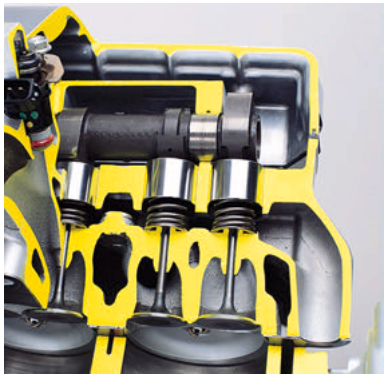


Fig. 9 Parallel two-valve train system

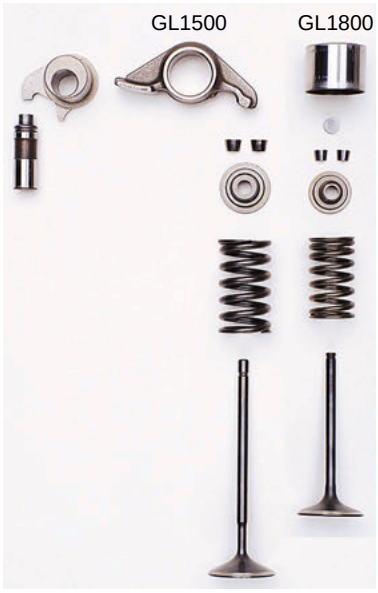


Fig. 10 Valve systems for GL1800 and GL1500

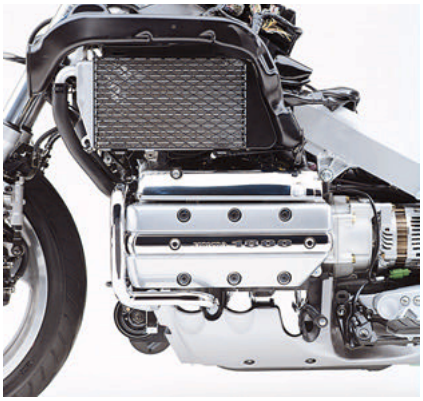


Fig. 11 Side-mounted radiators

As shown in Fig. 12, these changes made it possible to move the engine forward 25 mm in comparison to the GL 1500, and reducing the size of the components around the cylinder heads made it possible to secure even more

foot space for the rider.

The transmission was changed from a separate shifter type to a newly designed unibody shifter type in order to minimize the increase in weight. In order to minimize the increase in clearance while hot, a sintered bearing cap was adopted for the crank journal.

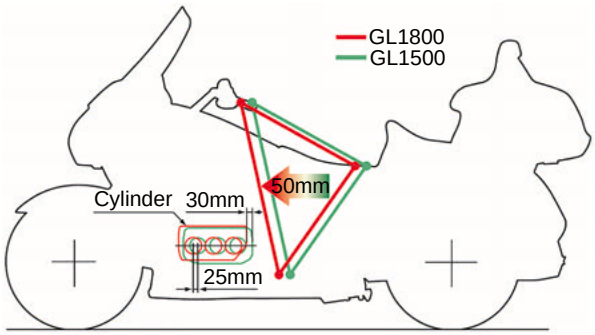


Fig. 12 Engine location and riding position

4.2 ACG Drive Damper System

In order to eliminate the reaction torque that is generated by the inertial force fluctuations of the crankshaft in a longitudinal mounted engine, speed increase and reverse drive is implemented in the ACG by means of gears. Furthermore, in order to handle the increased capacity of the ACG, two spring dampers are arranged in series as shown in Fig. 13, and a scissors gear is placed on the drive gear side.

4.3 Hydraulic-assist Clutch

The hydraulic-assist clutch uses hydraulic pressure in addition to the mechanical load to increase the clutch's

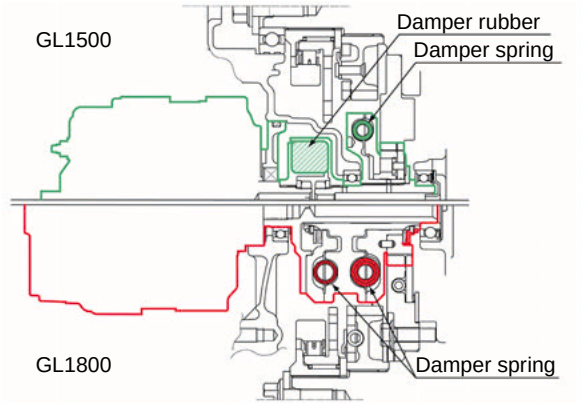


Fig. 13 ACG spring damper

engagement force, which made it possible to reduce the size and weight of the clutch and decrease the operating load of the clutch lever despite the increase in the engine displacement. Fig. 14 shows the clutch in the engaged and disengaged states.

When the clutch is engaged while the engine is running, the engine oil is controlled by the regulator valve through the hydraulic path. The high-pressure oil that is supplied to the clutch flows through the joint and main shaft oil path into the oil pressure chamber, moving the pressure plate towards the clutch center. Because the diaphragm spring is pressed against the pressure plate, the clutch plate and the friction disk are pressed together by the hydraulic pressure and the spring force. On the other hand, if the lifter plate is pressed by the clutch release rod, the spring pressure is released, the oil outlet that had been sealed opens, reducing the pressure in the oil pressure chamber and releasing the friction between the clutch plate and the friction disk.

5. Emissions Technologies

To address emissions requirements in the GL 1800, an

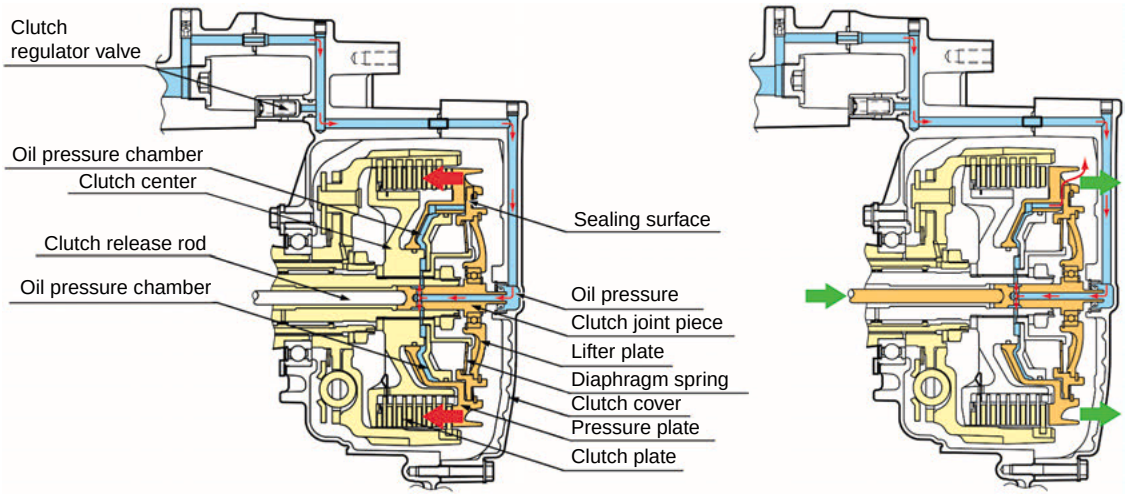
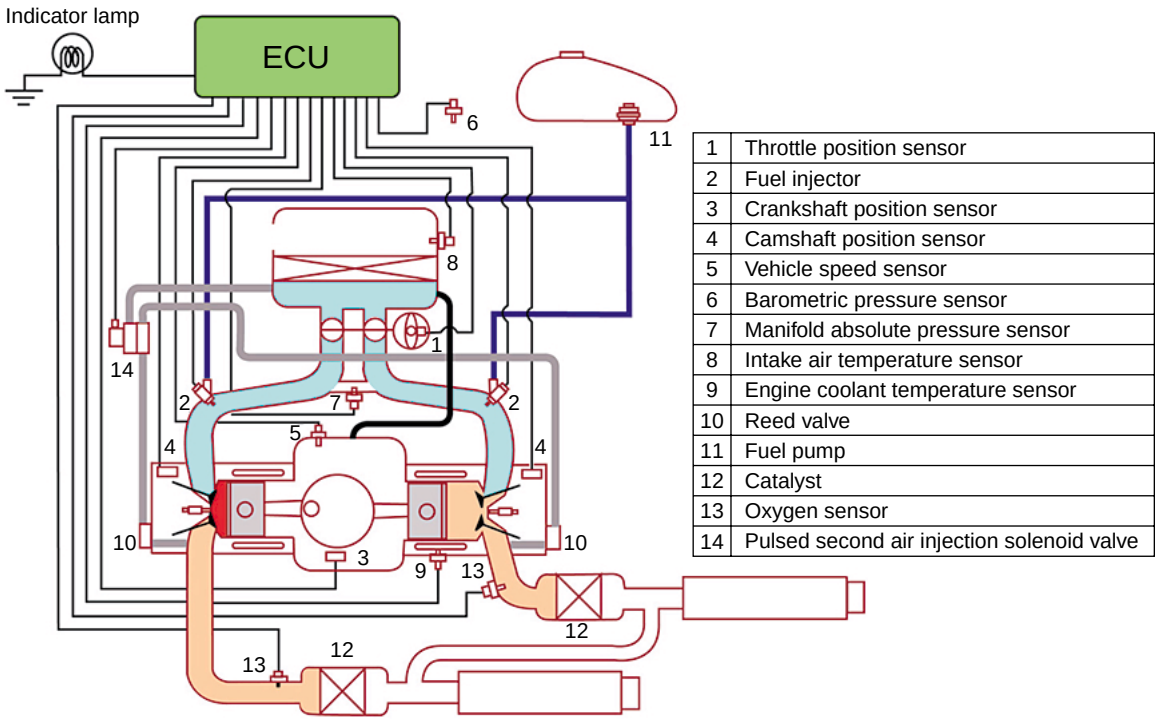


Fig. 14 Hydraulic-assist clutch



1	Throttle position sensor
2	Fuel injector
3	Crankshaft position sensor
4	Camshaft position sensor
5	Vehicle speed sensor
6	Barometric pressure sensor
7	Manifold absolute pressure sensor
8	Intake air temperature sensor
9	Engine coolant temperature sensor
10	Reed valve
11	Fuel pump
12	Catalyst
13	Oxygen sensor
14	Pulsed second air injection solenoid valve

Fig. 15 Emissions control system

electronic fuel injection system was included in the intake system; a system consisting of a secondary air supplier, a three-way catalyst, and an air-fuel ratio feedback control system was implemented; and the shield method was adopted for the crankcase emission control system. Fig. 15 shows the emissions control system.

In the electronic fuel injection system, the ECU (Electric Control Unit) calculates the fuel injection timing and amount on the basis of data such as the engine speed, throttle position, intake air pressure, intake temperature, barometric pressure and water temperature, and determines



Fig. 16 Fuel injector

the target air-fuel ratio according to the load. Fig. 16 shows the installation of the fuel injector.

In the spark timing control system, the ECU determines the optimal spark timing for the current operating status of the engine on the basis of data such as throttle position, engine speed, gear position, water temperature and the knock sensor.

Depending on the operating status, the secondary air supplier supplies secondary air from the air cleaner to the exhaust port through the reed valve. In addition to promoting oxidation of unburned gas, this also promotes reactions in the oxidation catalyst that is installed in the exhaust manifold.

Catalytic devices include a monolithic type three-way catalyst in the exhaust pipe and an air-fuel ratio feedback control system. These devices oxidize CO and HC in the emissions, and lower NOx emissions through a reducing process.

The air-fuel ratio feedback control system uses an O_2 sensor to detect oxygen levels in the emissions. The O_2 level signal is processed by the ECU, which then adjusts the fuel injection amount to roughly the stoichiometric air-fuel ratio in order to maximize the functioning of the three-way catalyst.

For the crankcase emission control system the shield system was adopted, in which blow-by gas is returned to the air cleaner from the top of the crankcase, and is then returned to the combustion chamber.

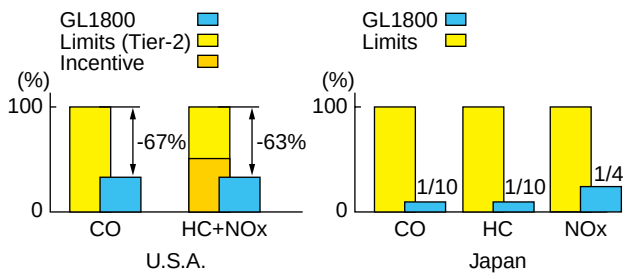


Fig. 17 Exhaust emission values

As shown in Fig. 17, the adoption of these emissions control technologies has resulted in a reduction of CO and HC emissions to 1/10 of Japanese requirements and a reduction of NOx to 1/4 of Japanese requirements. The GL 1800 also has reached the incentive level of 1/2 or lower of California's Tier-2 requirements for 2008 for HC + NOx emissions; these technologies will be used in motorcycles sold in all markets throughout the U.S.

6. Frame

The steel double-cradle frame used in the GL 1500 is being replaced with an aluminum alloy dual-spar diamond type frame, the first of its kind to be produced in the U.S. In addition, by using aluminum alloy for the trunk and saddlebag stays, the weight of this lightweight frame has been reduced by 35% to approximately 21 kg[(1)]. As shown in Fig. 18 and Fig. 19, the front frame consists of dual spars with a four-compartment section that offers high specific rigidity, a core box section type gravity casting head pipe, a pivot plate, stiffeners, and engine hangers. The rear frame consists of a circular section extrusion aluminum alloy seat rail pipe and an open section rear plate. The front and rear sections are welded together.

The engine is mounted with a fully rigid mount in order to use the engine crank case and the rear case as frame rigidity members. As a result, even though the frame is lighter than that used in the GL 1500, it offers 1.75 times greater torsional rigidity and 2.1 times greater lateral rigidity.

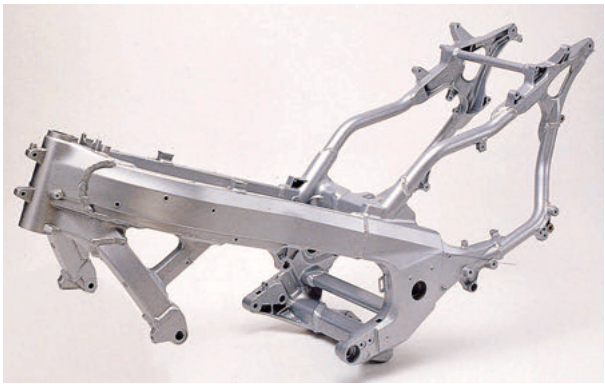


Fig. 18 Aluminum-alloy frame



Fig. 19 Spar section of frame

7. Riding Position and Seats

As shown in Fig. 12, making the engine more compact and positioning it farther forward made it possible to move the riding position 50 mm forward. This allows the rider to find a riding position that facilitates sporty handling. Although the wheelbase of the GL 1800 is the same as that of the GL 1500, passenger comfort has been enhanced by lengthening the passenger seat by 50 mm and widening it by 70 mm.

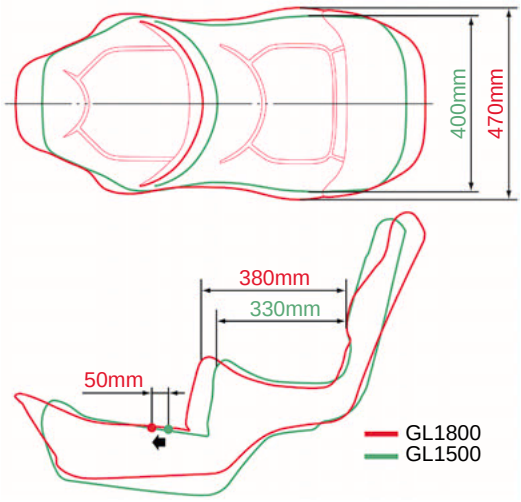


Fig. 20 Seat

8. Chassis

8.1 Electric Suspension Preload Adjustment System Equipped with Memory

Although the GL 1500 had a conventional suspension system equipped with twin rear shock absorbers, in order to achieve superior ride performance and driving performance, the Pro-Link construction was adopted for the rear suspension, and a motor-powered hydraulic jack type preload adjustment system suited for this suspension construction was also adopted. This system provided a comfortable ride, regardless of the weight of passengers and luggage. This system consists of an actuator that converts the rotational torque of the motor through a worm gear and trapezoidal screw into forward force on the leveling piston, and a piston mechanism on the reaction side that moves in proportion to the leveling piston of the actuator, pushing the shock absorber spring up. The actuator is also equipped with an adjustment position sensor that displays the adjustment status on the multi-display. Operability is also improved through the addition of a two-position memory.

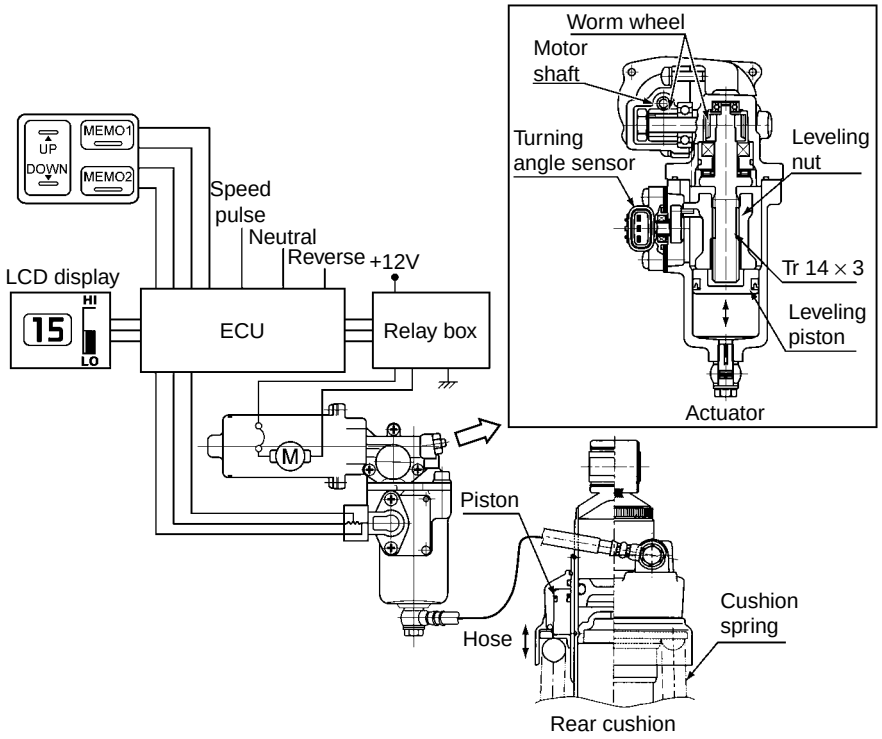


Fig. 21 Computer-controlled adjustable hydraulic rear suspension system

Fig. 21 shows the hydraulic jack type preload adjustment system.

8.2 Pro-Arm

The rear swing arm (Pro-Arm) construction has a simple torsion damper formed from two tubes joined by rubber built into the propeller shaft, and the wheel is fixed in place with the final gear on one side. Not only does the Pro-Arm enhance shift shock convergence characteristics due to differences in the hysteresis characteristics of the damper; it also makes serviceability easier when changing the tires, etc. Fig. 22 shows the drive shaft damper, while Fig. 23 shows the aluminum alloy swing arm.

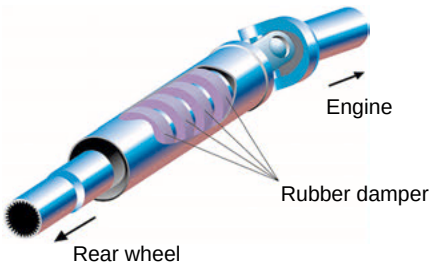


Fig. 22 Driveshaft-damper

8.3 Torque-reactive Combined Braking System with ABS

The Anti-lock Braking System (ABS)[2] for motorcycles prevents the wheels from locking up when the brakes are applied too hard in straight ahead braking, reducing rider concerns. On the other hand, the Linked Brake system (LBS, also known as "Dual CBS")[3] [4] makes high deceleration simpler by applying appropriate braking force distribution on the front and rear wheel. The basic system that combines these two functions simply, the torque-reactive combined braking system with ABS[5], is the same as that found in the ST 1100, but in the GL 1800, in which the foot brake is used frequently, the two pistons at both ends of the front three piston calipers on the left side function when the pedal brake is pressed, unlike the ST 1100, resulting in an increase in braking force when the pedal brake is applied. Fig. 24 shows the brake system.



Fig. 23 Single-supported swing-arm (Pro-arm)

8.4 Anti-dive Control System

The anti-dive control system controls any sudden dives forward by the vehicle while braking; this capability makes it possible to implement a shock absorber setting that emphasizes a suitable level of comfort during normal

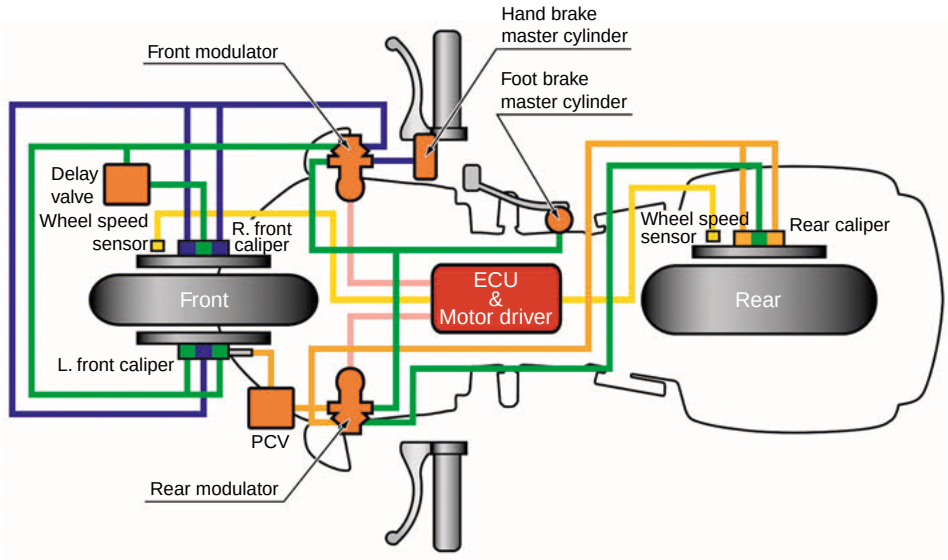


Fig. 24 LBS with ABS

driving. In the GL 1800, whether the hand brake is applied or the foot brake is applied, the hydraulic pressure in the LBS secondary master cylinder that is generated by the reverse torque of the left caliper on the front wheel is used to close off the hydraulic path to the front fork. Fig. 25 shows the anti-drive control systems for the GL 1500 and for the GL 1800. Ensuring an adequate anti-dive effect, the H.M.A.S. (Honda Multi-Action Suspension)[6], which used a cartridge valve, could be adopted on the right side of the front fork by installing the anti-dive control system on the left side of the front fork. Fig. 26 shows the damping characteristics of the front suspension.

9. Electronics

9.1 Motor Actuated Reverse System

In consideration of handling of the Gold Wing while parking, a motor actuated reverse system was adopted, starting with the GL 1500[7]. In the GL 1800, the positions

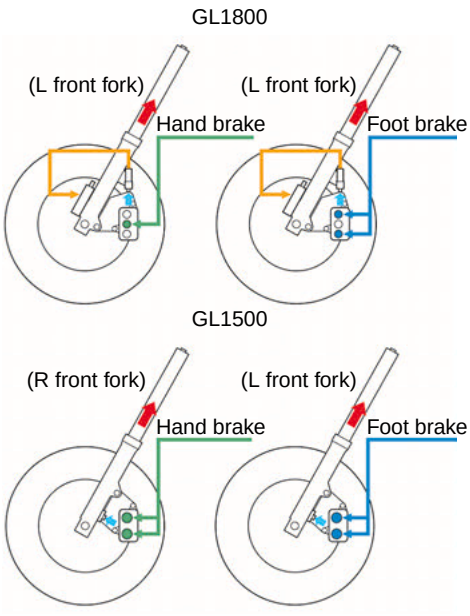


Fig. 25 Anti-dive systems for GL1800 and GL1500

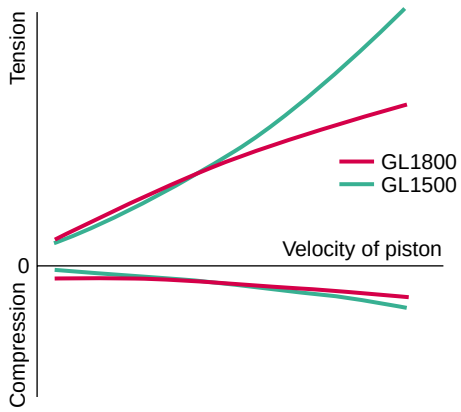


Fig. 26 Characteristics of damping force of front suspension

of the operation switches has been changed so that they can be operated by the thumb of the right hand without releasing the handlebar.

Fig. 27 shows the motor actuated reverse system. The system consists of a reverse shift switch, a reverse switch that is also used as the starter button, a reverse drive motor that is also used as the starter motor, a reverse shift actuator and an integrated ECU for cruise control.

When the reverse switch is turned on, the reverse shift actuator operates under ECU control so that the reverse gear on the engine side engages the driven gear on the final shaft side. The reverse drive motor operates under the control of the ECU powering the rear wheel through the final drive shaft. The ECU also handles speed control to ensure that a constant reverse speed is maintained. Note that shifting into reverse is possible when the engine is in neutral and the side stand is in the raised position; the motorcycle will then move backwards, if the engine is running.

9.2 Cruise Control System

A cruise control system is essential for a long-distance

touring motorcycle. While a negative pressure actuated type cruise control was used in the GL 1500, a motor actuated type was adopted in the GL 1800 in order to improve vehicle speed stability, to make the system lighter, and to save space.

Fig. 28 shows the cruise control system. This system controls the vehicle speed by trying to maintain a zero difference between the current vehicle speed and the vehicle speed at which the cruise control was set. The ECU controls the electromagnetic clutch and the control motor inside the actuator to adjust the opening of the throttle. Acceleration by manual means is still possible even while cruise control is on. Cruise control can be cancelled either by turning off the cruise control switch, using the front or rear wheel brakes, using the clutch, or closing the throttle.

9.3 Headlight

9.3.1 HID Headlight

Nighttime visibility has been enhanced by adopting, for the dipped-beam headlight used in Japan, the first HID (High Intensity Discharge) headlight to be mass-produced for motorcycles. In an HID headlight, high AC voltage is applied to electrodes at both ends of a sealed discharge tube (burner) containing xenon gas, mercury, and metal halide, which causes the lamp to shine as a result of sequential arc discharges. As a light source, the HID lamp is more efficient than a halogen lamp, producing 3,000 lm, or twice the approximately 1,500 lm that a halogen lamp produces. As shown in Fig. 29, the road surface illumination characteristics of the GL 1800 are superior to those of the GL 1500, illuminating a much larger area. Note that in conjunction with the adoption of the HID headlight, consideration is being given to the maximum luminosity and distribution of light so as to not create glare for oncoming vehicles.

9.3.2 Motorized Headlight Aiming System

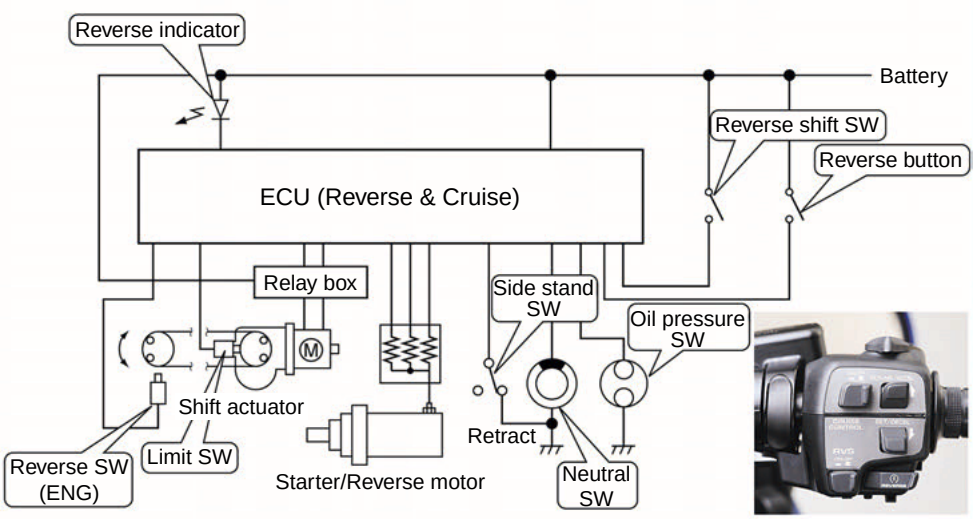


Fig. 27 Electric reverse system

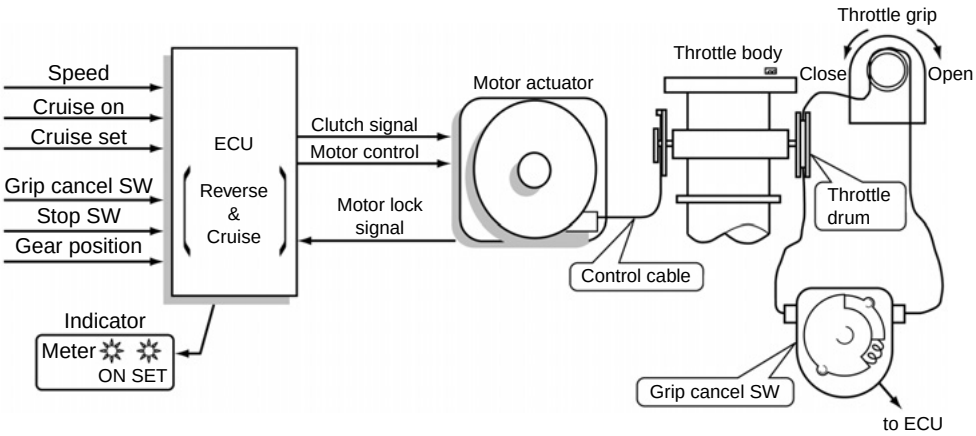


Fig. 28 Electronic cruise control system

Motorized control is used to adjust the axis of the headlight beam in the vertical direction so that the headlight can be aimed while sitting on the motorcycle. The aim can be easily adjusted to one of 11 positions simply by turning the dial on the left side panel. Fig. 30 shows the headlight aiming system.

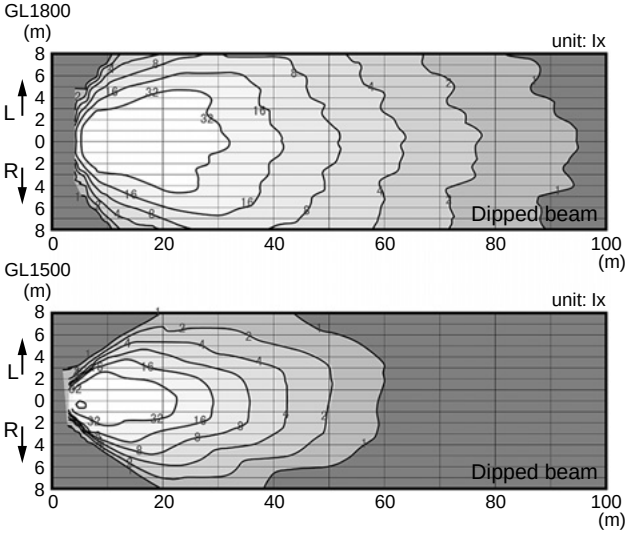


Fig. 29 Light distributions of GL1800 and GL1500

9.4 Audio System

The volume and sound quality of the GL 1800's audio system has been improved by increasing the amplifier output (25W × 4) and by changing the speaker specifications (with a new, specially designed speaker box), so that now the GL 1800 has one of the best audio systems found on a motorcycle. Furthermore, by placing the controls not only on the audio system itself but also on the left handle bar, the rider can now control the radio, CB, and CD without releasing the handle grip. The LCD multi-display in the meter has been designed so that the operating status of the audio system can be understood easily. In order to simplify the collection of useful information while touring, a weather band select button has been added in the design for the U.S., and a traffic information select button has been added in the design for Japan. Fig. 31 shows the audio system.

9.5 Trunk Lock Control System

A trunk lock control system has been adopted for the trunk and saddlebags in the GL 1800, with improved open/close and locking operability. Fig. 32 shows the trunk lock control system. By combining a transmitter, a receiver, a trunk open/close detection switch and an actuator, the system can lock and unlock the trunk and saddlebags, can detect whether they are open, and can pop open the trunk. When the remote control is used to lock or unlock the trunk, the turn signals flash to indicate that the action occurred. In addition, if any of the lids are open, the corresponding LCD indicator in the meter flashes as a warning. The system also includes other functions, such as a function in which the remote control can be used to make the horn sound in order to confirm the location of the vehicle (in the U.S. version), and a function that automatically locks the trunk and saddlebags after a certain period of time elapses in case the owner forgets to lock them.

10. Plastic Fuel Tank

Instead of the conventional steel fuel tank with welded seams, a fuel tank produced by high-density polyethylene blow molding was adopted for the GL 1800. Taking advantage of the high degree of design freedom that is made possible by blow molding, the battery, auxiliary parts, etc., are located under the seat while the capacity of the fuel tank

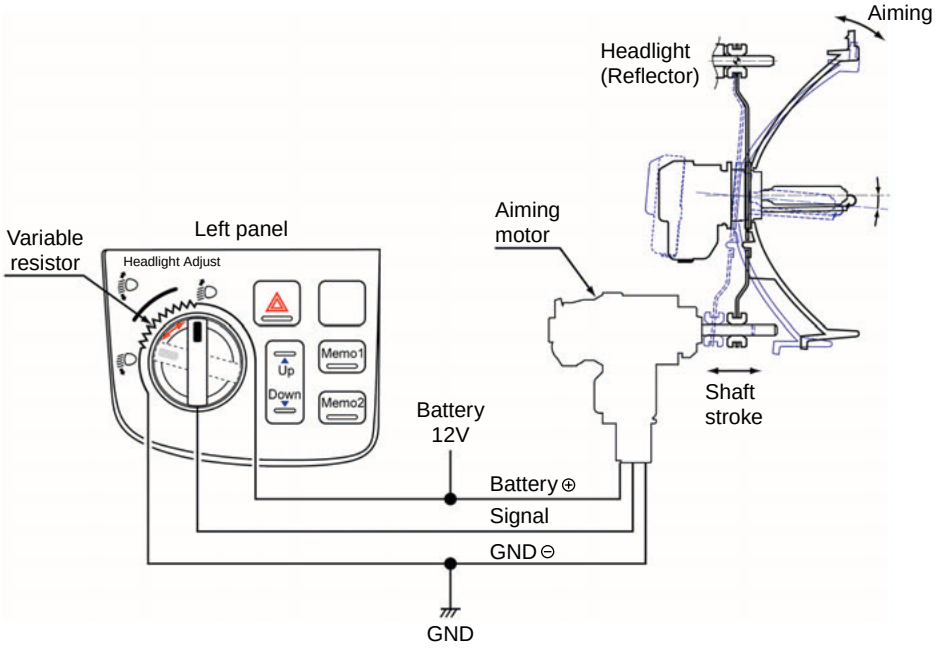


Fig. 30 Headlight aiming system

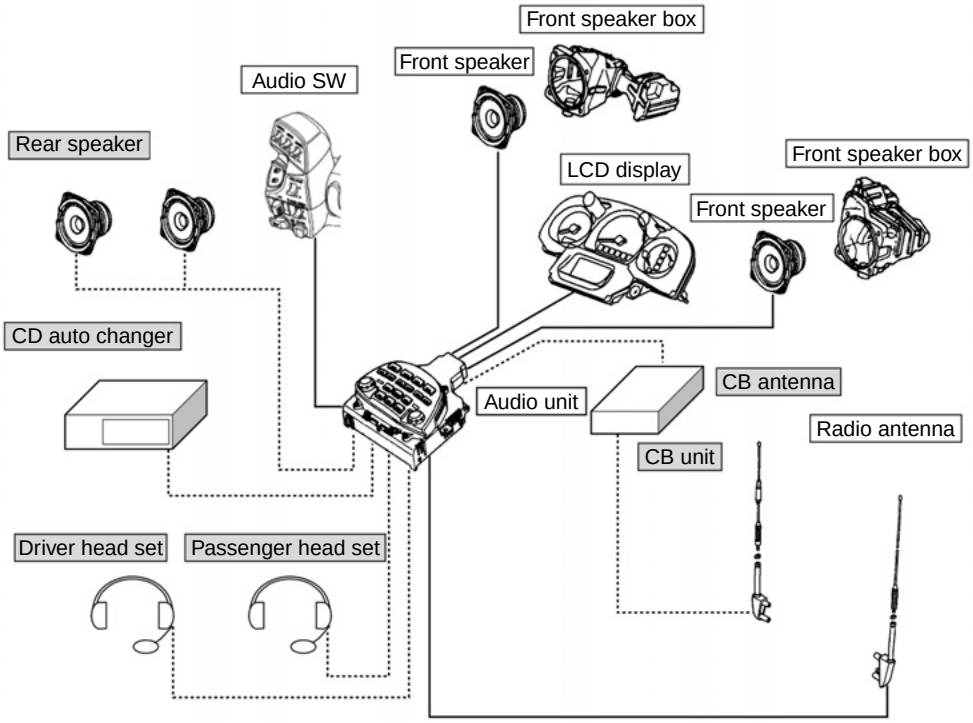


Fig. 31 Audio system

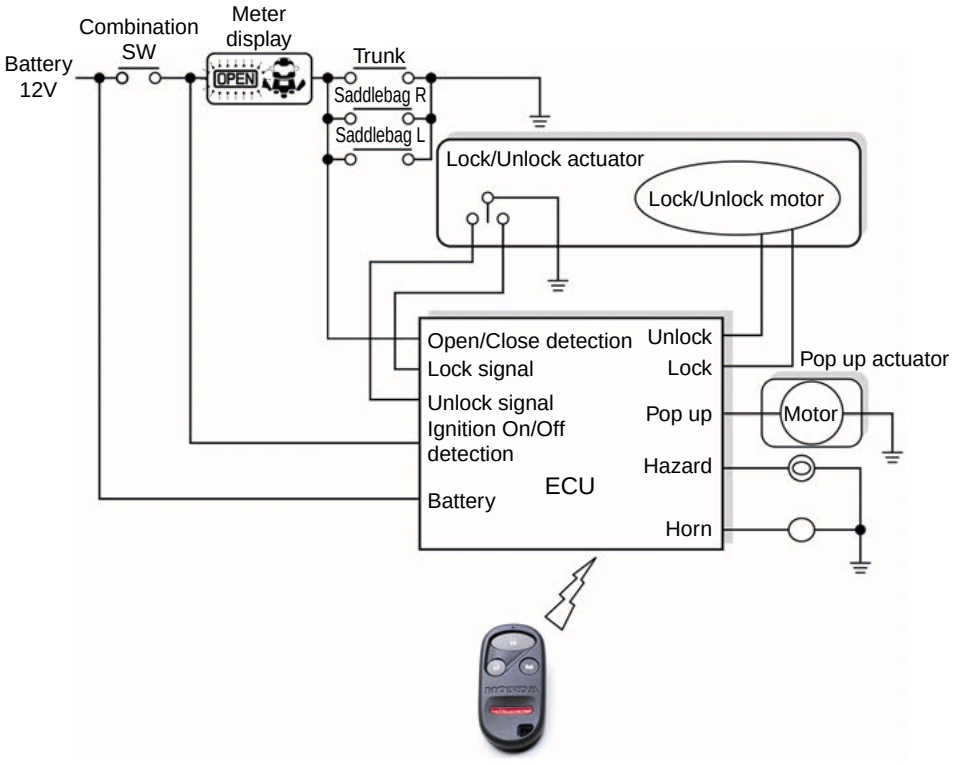


Fig. 32 Remote-control key-lock system

has been increased by 1.2 liters to 25 liters. Fig. 33 shows the external appearance of the fuel tank. As shown in Fig. 34, the fuel tank is formed of six layers of four different materials, with an EVOH barrier layer in the middle to prevent gasoline from penetrating. The fuel cap is air tight, and the evaporative emission canister system that is needed in order to comply with California Air Resources Board (CARB) evaporative emission requirements is provided in all markets throughout the U.S. Fig. 34 shows the evaporative emission canister system.

With the implementation of fuel injection, the pump unit is made of plastic and consists of a high-pressure pump and filter, and is built into the fuel tank as shown in Fig. 35. Gasoline is supplied to the injector through the fuel hose, and the gasoline that is returned through the return hose is returned at a higher flow rate through the orifice section of the pump unit intake. Since gasoline in the fuel tank is forcibly taken into the pump unit, the result is a stable fuel supply system that is not affected by changes in the fuel level.

11. Conclusion

The Gold Wing GL 1800 was developed with a twin focus on both the rider and the passenger. While offering further enhancements in the touring performance that has been developed over many years, the GL 1800 also provides excellent balance in terms of basic driving, cornering and stopping performance for a sporty feel that sets a new standard for the luxury touring category.



Fig. 33 External view of fuel tank

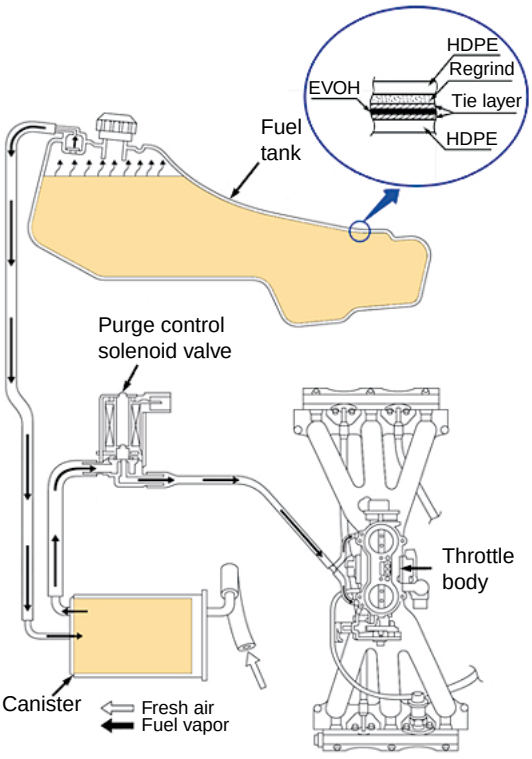


Fig. 34 Canister system for evaporative gas emission and plastic layer structure of fuel tank

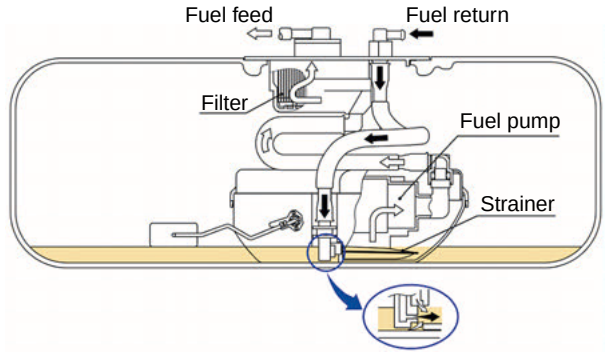


Fig. 35 Fuel pump system

References

(1) Rowdy, J., Ueda, J.: Development of 7003 Aluminum Extrusions for Motorcycle Frame Applications, Honda R&D Technical Review, Vol. 13 No. 1, p. 167 – 174 (2001)

(2) Hikichi, T., Tomari, T., Kato, M., Thiem, M.: Research on Anti-lock Brake System on Motorcycle Braking in Turns (in Japanese), HONDA R&D Technical Review, Vol. 4, p. 161 – 173 (1992)

(3) Nishimoto, Y., Iwashita, S., Tsuchida, T., Sawano, K.: Research on Dual Combined Brake System for Motorcycles (in Japanese), HONDA R&D Technical Review, Vol. 5, p. 100 – 108 (1993)

(4) Tsuchida, T., Iwashita, S., Sawano, K., Nishimoto, Y., Nakata, H.: Further Research on New Combined Brake System (Dual-CBS) for Motorcycles (in Japanese), HONDA R&D Technical Review, Vol. 6, p. 194 – 201 (1994)

(5) Tanaka, K., Matsuto, T., Kato, M., Hayashi, T., Ishihara, H.: Research on Combination of Combined Brake System and Anti-lock Brake System for Motorcycles (in Japanese), JSAE Proceedings 961, p. 279 – 282 (1996)

(6) Yamanaka.I, Kato.T, Hagiwara.S, Suzuki.T, Toyoda.H, Arakawa.K, Introduction of the CBR1100XX Super Blackbird (in Japanese), HONDA R&D Technical Review, Vol. 9, p. 33 – 43 (1997)

(7) Ota, J., Yamagata, T., Ito, T., Nebu, H., Uchibaba, K., Fujita, H.: Reverse System Design for a Motorcycle (in Japanese), HONDA R&D Technical Review, Vol. 2, p. 49 – 58 (1990)

■ Authors ■


Masanori AOKI


Tetsuya TOSAKA


Hidemi MINAMI


Hiroshi ISHIHARA


K o j i K A N O

Development of a Small Tiller: The New Komame F220

Masatoshi NAGAOKA* Hideaki KOBAYASHI*
Nobuchika KATAGIRI* Tatsuya TOKUDA*

ABSTRACT

The small tiller “Komame” has been used for various agricultural tasks ranging from cultivation of small vegetable gardens to more serious vegetable growing processes for the last 20 years. This tiller has gone through a full model change this year to become the “New Komame F220.” The New Komame’s engine now has a rounded full cover that helps even novice users feel at ease. Reduced emissions from its OHV engine and 5.5dB (A) less noise (obtained by utilizing a resin cam and larger muffler capacity) enable the “New Komame F220” to meet the requirements of both the CARB and EPA emission regulations as well as the EU Noise Directive. The machine weighs 9% less due to the smaller engine and resin parts. Changes to the tilling blades by simulation analysis have provided simple handling together with ample performance. The force required for the recoil starter has been cut by 30% through decreasing engine displacement. The force required to operate the clutch lever has also been reduced by 20% through the use of a different shoe clutch lining material. The new easier to use F220 delivers useful functions and high performance.

1. Introduction

In 1980, Honda introduced the small tiller “Komame F200” to the market. The small and light weight “Komame F200” was easy to operate and could be used for a wide range of jobs in vegetable gardening, from simple tilling to total soil management including forming ridges, cultivation, working humus into the soil and weeding. All these capabilities enabled the F200 to create a new market for small, easy to use tillers as a replacement for hoes on farms and in small vegetable gardens. The Komame F200 soon proved popular in Japan, Europe, and North America. Including the “Komame F210”, which was introduced in 1982 as the result of some minor changes made to the original model, the Komame tillers have become one of Honda’s best selling general-purpose products, with a total of more than 550,000 units shipped from the factory.

As public concern for the protection of the global environment has increased in recent years, Honda, which prides itself on its efforts to make its products even more environmentally friendly, undertook a comprehensive study of how to enhance the environmental friendliness of the “Komame” in regards to exhaust and noise. Furthermore, in the Japanese market, Honda found that the customer base for tillers contained fewer experienced farmers and more novices and elderly users every year, which meant that the market needed small tillers that were easier to use. To address these market trends, Honda developed the “New Komame F220” (“F220” hereafter), as described in this article.

2. Development Aims

The basic concept behind the development of the F220 was to produce a tiller that was easy to use and environmentally friendly. The development aims were:

* Asakahigashi R&D Center

(1) To meet lower fuel consumption and CARB and EPA emission requirements
  • CARB: California Air Resource Board
  • EPA: Environmental Protection Agency
(2) To reduce noise in order to meet the EU Noise Directive
(3) To produce a light machine that provides the desired tilling performance
(4) To make the operability of the machine easier and to reduce the operating load

3. Styling

With “user friendliness” as a key theme, the designers sought styling that would not be intimidating to first-time users of a tiller. Fig. 1 shows an external view of the F220, and Fig. 2 illustrates the design concepts.
The main styling points are:
(1) An overall rounded form that conveys a sense of compactness and lightness
(2) A full cover that conceals the mechanical components
(3) A symmetrical design that makes it easy to till in a straight line



Fig. 1 External view of F220

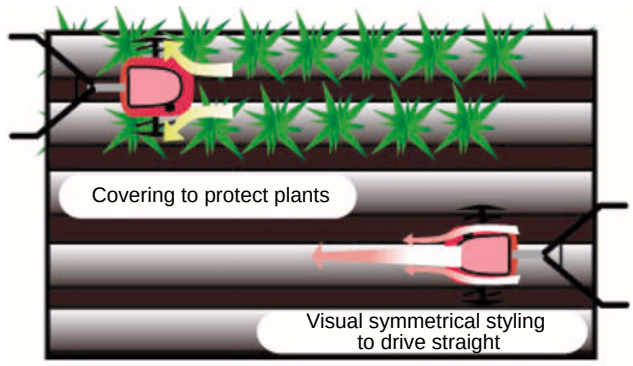


Fig. 2 Design concept

4. Basic Configuration and Main Specifications

Among walk-along plows, the F220 is classified as a tiller or soil management machine. Unlike motorized power tillers that have a drive section as well as a separate rotary tiller section that tills the soil, on the F220 the rotor is attached to the wheel shaft instead of the wheels so that the tiller moves forward as it tills[(1)]. The drag bar and the handle, which control the forward speed and tilling depth of the tiller, are mounted behind the rotor. The heavy engine is positioned directly above the rotor, allowing the tiller to effectively absorb the soil reaction force that is produced while tilling.

The engine is a vertical shaft type, in which the PTO (power train output shaft) is oriented downwards, and is directly linked to the transmission with a built-in shoe clutch system and planetary gear drive system. At the very bottom, beveled gears turn the rotating shaft 90° so that the tine shaft propels the tiller forward.

While tilling, the operator can adjust the tilling depth and the forward speed by moving the handle grips up or down. The braking force (Fb) is controlled by moving the handle in the direction indicated by (A), which increases or decreases the vertical load on the drag bar. The braking force can thus be balanced with the soil reaction force (Fa) of the rotor, which rotates in the forward direction. Fig. 3 shows the overall layout of the F220, and Table 1 shows a comparison of the main specifications of the F220 with those of the F210.

4.1 Engine

When making enhancements to a tiller, typical goals are to increase engine displacement in order to obtain better performance, and to increase output performance. In the case of the F220, however, in order to further enhance the small size and light weight that were features of the F210, the decision was made to reduce engine displacement while still maintaining the output performance. The reason behind this decision was that, given the market background described earlier, the designers were confident that ease of use was more important than enhanced performance in a tiller for family vegetable gardens.

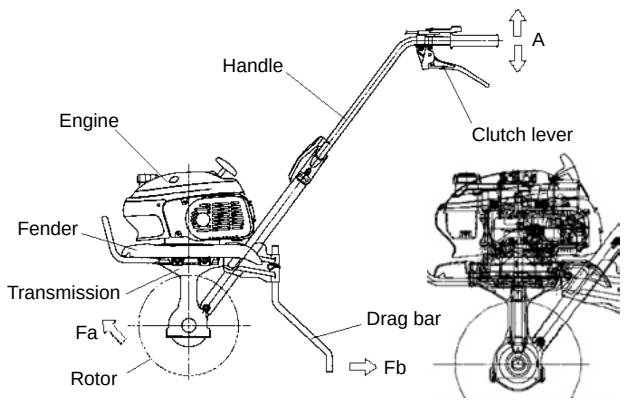


Fig. 3 Layout of F220

Table 1 Major specifications

Items		Specifications	
Model name		F210	F220
Engine model name		GV100	GXV57
Engine type		Air cooled 4-stroke SV single cylinder	Air cooled 4-stroke OHV single cylinder
Engine displacement	(cm^3)	90	57
Maximum power	(kW)	1.8	1.8
Rated power	(kW/rpm)	1.0/4 000	1.0/4 000
Maximum torque	(Nm/rpm)	3.0/3 000	3.0/4 000
Compression ratio		5.8 : 1	8.0 : 1
Minimum specific fuel consumption	(g/kwh)	476	354
Fuel tank capacity	(cm^3)	900	700
Overall length	(mm)	1 070	1 115
Overall width	(mm)	585	585
Overall height	(mm)	960	975
Dry weight	(kg)	27.5	25.0
Tine speed	(rpm)	117	130
Tilling width	(mm)	520	545
Tine diameter	(mm)	ϕ 280	
Starting system		Recoil starter	
Main clutch type		Shoe clutch	
Transmission speeds		1 Forward	

While a side valve (SV) engine had been used in the F210, an overhead valve (OHV) engine was adopted in the F220. Thermal efficiency was enhanced by seeking to achieve a high compression ratio by making the compression chamber more compact. These changes made it possible to maintain output performance that was equivalent to the F210 while reducing engine displacement by 33%, and also resulted in a 26% improvement in minimum specific fuel consumption.

While the engine displacement was reduced, the air cleaner and the muffler positioned on the left and right sides of the engine were made larger than in the F210. These changes reduced engine noise and greatly extended the maintenance interval for the air cleaner.

The reduction of engine displacement also made it possible to reduce the height by 15 mm and to reduce the weight by 1.9 kg, even with a full cover added to the engine. Fig. 4 shows the layout of the engine, which was a significant factor in making the F220 easier to use.

4.2 Transmission

The basic configuration of the power train has been retained since the F200. The transmission combines a planetary gear drive system, in which the tip of the PTO (power train output shaft) of the vertical shaft acts as the sun gear, with a shoe clutch system. The planetary gear drive system, which produces a large deceleration ratio (1/10) on this shaft, is a unique feature of the “Komame” and is a major factor in making the transmission small.

The clutch is constructed so that it is engaged and disengaged by the operation of an internal expanding brake on the clutch outer, which also serves as the planetary ring gear. Squeezing the clutch lever, which is mounted on the handle, moves the internal expanding brake. The clutch shoe stops the rotation of the planetary ring gear, and the three rotating planetary gears begin orbiting around the sun gear. This in turn causes the drive shaft that is splined to the planetary gear carrier to rotate. The beveled gears at the

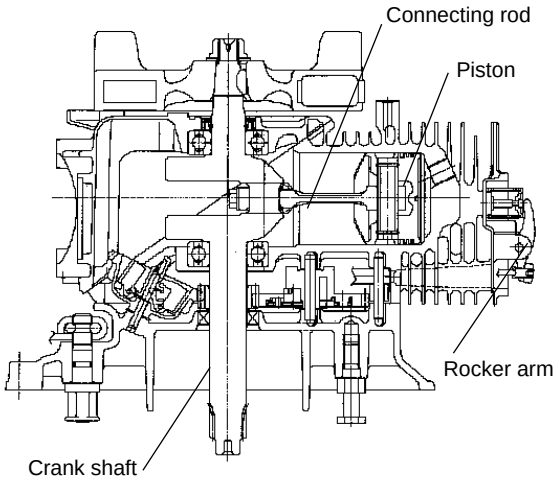


Fig. 4 Layout of GXV57 engine

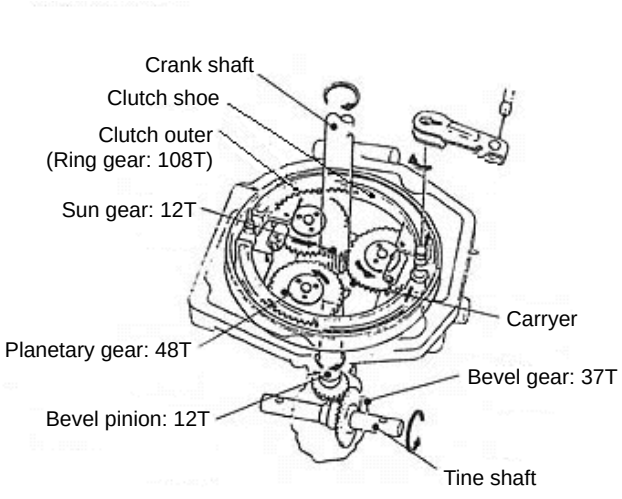


Fig. 5 F220 transmission layout

bottom of the transmission turn the axis of rotation 90°, and cause the tine shaft to turn in the forward direction. When the clutch lever is released, the planetary ring gear is again free to turn, causing the planetary gears to stop orbiting the sun gear and simply rotate. The planetary gear carrier, the drive shaft, and the tine shaft all stop rotating. Fig. 5 shows an illustration of the power train.

4.3 Handle Adjustment

The survey results of how tillers are used clearly showed the handle height that permits the easiest operation of the tiller also allows the operator to maintain an elbow angle ranging from 80° to 165° (120° being optimal) while gripping the handle. Users can set the height of the F220's handle at one of three positions ranging from 859 mm to 1003 mm and adjust the drag bar height to one of three positions. These adjustments allow users of various body sizes to work in a natural posture. Whether the tiller is being used for tilling, weeding, or working humus into the soil, the handle can be set so that the angle between the upper and lower arms can be kept between 118° and 139°. This holds true for users ranging from the 5th percentile among Japanese women (147 cm in height) to the 95th percentile among Japanese men (178 cm tall).

Furthermore, the overall length of the tiller can be reduced from 1115 mm to 690 mm and the overall height of the tiller can be reduced from 975 mm to 690 mm by folding the handle forward. This feature makes it easier to transport the tiller by car and reduces the amount of space taken up by the tiller in storage.

In addition, in order to make the tiller easier to use next to walls in a greenhouse or similarly confined area, the handle is designed to swing 22° to the left or right. This feature allows the user to use the tiller right against a wall without the handle getting in the way. Fig. 6 illustrates the above described handle adjustments.

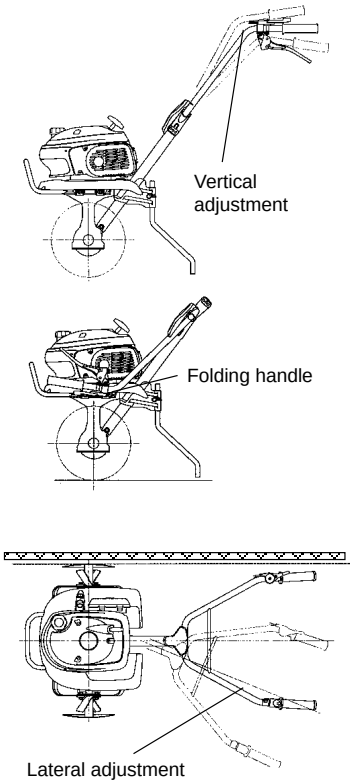


Fig. 6 Handle adjustment



Fig. 7 Attachments

4.4 Attachments

By maintaining the same dimensions for the tine shaft and the drag bar holder in the F220 as in the F210, the various soil management attachments that are available for the F210 for tilling, ridging, cultivation, working humus into the soil, and weeding can also be used with the F220. Fig. 7 shows some typical attachments. From top to bottom, these attachments are used in forming ridges, working humus into the soil, tilling hard soil, and for weeding work in orchards.

5. Features

5.1 Reduced Emissions and Fuel Consumption

The change to an OHV configuration (described above in section 4.1) improved combustion and enabled the F220 to meet the requirements of EPA Phase II and the CARB Tier II emission regulations, which will be implemented in 2002. The OHV engine consumes less oil than an SV engine, and the adoption of a uniblock cylinder[(2)] that suffers little cylinder distortion due to the effects of the joint axial force of the head bolt further reduces oil consumption. In addition, the amount of carbon that accumulates in the combustion chamber has been greatly reduced, which helps to minimize the increased emissions that occurs with the passage of time.

The decreased power required by the tines in comparison with the F210 (described later) has cut tilling fuel consumption roughly in half. The F210 had a range of 450 cm^3/h minimum to 540 cm^3/h maximum, whereas the F220 has a range of 225 cm^3/h minimum to 330 cm^3/h maximum. As a result, even though the fuel tank capacity was reduced from 900 cm^3 to 700 cm^3, the tilling time provided by a full tank has been extended from a range of 1.6 to 2.0 hours to a range of 2.1 to 3.1 hours. Furthermore, the amount of oil consumed while tilling has been reduced by 50%, from 5.5 cm^3/h to 2.7 cm^3/h.

5.2 Reduced Noise

As shown in Fig. 8, the noise experienced by an operator of the F220 compared with an operator of the F210 has been reduced by 4.5 dB(A) when the engine is running at maximum idling speed, and by 5.5 dB(A) while tilling.

The effects of the various noise reduction measures are described below.

(1) Adopting a large silent muffler
The muffler size was enlarged to 790 cm^3, or 1.6 times the size of the muffler applied to the F210.
This has the effect of reducing the noise experienced by the operator by 2.0 to 2.5 dB(A).

(2) Increasing the thickness of the engine oil pan
Increasing the thickness of the oil pan from 2.0 mm in the F210 to 3.5 mm in the F220 reduced the propagation of transmission gear noise.
This has the effect of reducing the noise experienced by the operator by 0.5 to 1.0 dB(A).

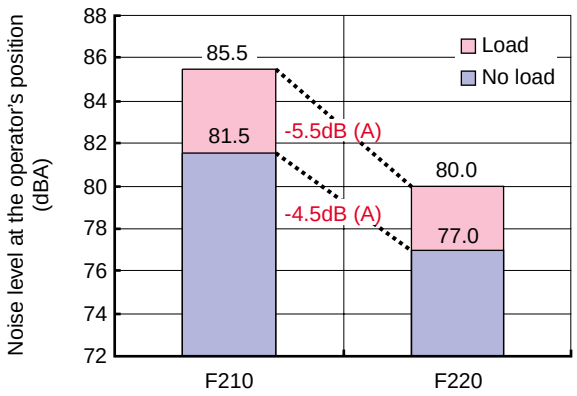


Fig. 8 Comparison of noise

(3) Adopting a noise-proof engine cover
The duplex construction of the fan cover and the recoil starter cover on top of the engine reduced the propagation of harsh engine noise and transmission gear noise.
This has the effect of reducing the noise experienced by the operator by 0.5 dB(A).

(4) Adopting a smaller engine displacement and plastic cams
The mechanical noise produced by the engine was decreased, by reducing the engine displacement by 37% compared to the F210, and by using plastic cams.
This has the effect of reducing the noise experienced by the operator by 1.5 dB(A).
These changes reduce psychological stress and fatigue in the user as a result of noise, and also make the tiller acceptable for use in a wider range of places and during a wider range of times during the day. Because they ensure a sound power level of 92 dB under EU Noise Directive regulations, these noise reduction measures also allow the F220 to satisfy the noise levels stipulated in the EU Noise Directive, namely 96 dB in 2002 and 93 dB by 2006.

5.3 Light Weight Without Sacrificing Tilling Performance

In order to ease the handling of the F220, the weight of the unit was reduced by 9% compared to the F210, or about 2.5 kg. This was accomplished primarily by replacing steel parts with plastic, and by using a lighter engine. A breakdown of the weight reductions achieved in individual components versus the F210 follows.

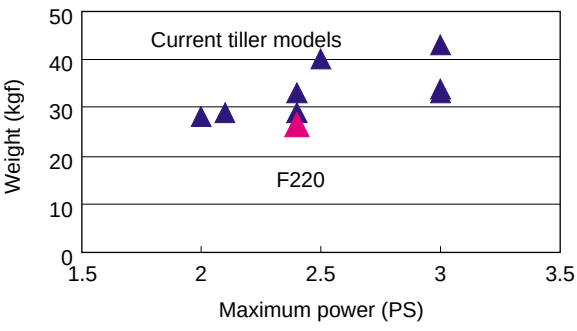


Fig. 9 Maximum power and weight

(1) Engine
A 1.9 kg weight reduction was achieved by reducing the engine displacement, reducing the number of components, and changing to plastic components.

(2) Fender
A 0.3 kg weight reduction was achieved by replacing steel with plastic.

(3) Rotor
A 0.3 kg weight reduction was achieved by changing the shape of the tilling blade in a way that reduced the amount of material used.

Typically, improving the working performance of a tiller in terms of tilling depth, for example, usually requires increasing the weight of the tiller. Fig. 9 shows that the more the engine output increases, the stronger the tendency for the tiller to be heavier. This is because increasing the working performance of the tiller causes an increase in the soil reaction force that pushes the tiller up and forwards, as described in Section 4. Accordingly, if the tiller is made lighter, the vertical load of the rotor may be inadequate compared to the size of the soil reaction force, preventing the tiller from tilling at an adequate depth.

A soil reaction force simulation[3] was used to analyze the effect that the shape of the F220's tilling blade had on the soil reaction force in order to produce a shape that would guarantee adequate working performance even with a lighter tiller. The effect that the changes in the angles of each part of the tilling blade (shown in Fig. 10) have on the soil reaction force was analyzed for the direction of rotation (shown in Fig. 11) and the component forces (shown in Fig. 12). Figs. 13 and 14 show the results of the analysis.

The results of this analysis are summarized below.

(1) By reducing the trailing angle (A), the average value of the soil reaction force FZ that pushes upwards on the tiller was reduced from 184.0 N to 116.1 N due to a multiplier effect with (4) described below.

(2) By increasing the cutting angle (B), the angle (E) is made smaller, reducing the time that the tilling blade is actually working in the soil; as a result, the average value of the torque MX required for tilling was reduced from 19.9 Nm to 14.6 Nm.

(3) By increasing the bending angle (C), the peak value of the soil reaction force FX that pushes sideways on the tiller was reduced from 49.1 N to 33.7 N for each individual blade.

(4) By increasing the trailing angle (D), the compression of the soil when the tilling blade cuts the soil is reduced, resulting in improved bite, and as a result of a multiplier effect with (1) above, the average value of FZ was reduced from 184.0 N to 116.1 N.

By reducing FZ, the lighter tiller is still able to achieve sufficient bite into the soil, maintaining a level of work performance equivalent to the F210. In addition, the tilling force was reduced by reducing MX. Because FX, which causes the tiller to vibrate from side to side, is cancelled out by the left and right placement of the tilling blades that comprise the rotor as a whole, the average value for FX obtained in simulations that assume a constant soil hardness was 0 N. However, by reducing the peak value, the vibration of the tiller when working with soil that is not of a uniform hardness was also lessened.

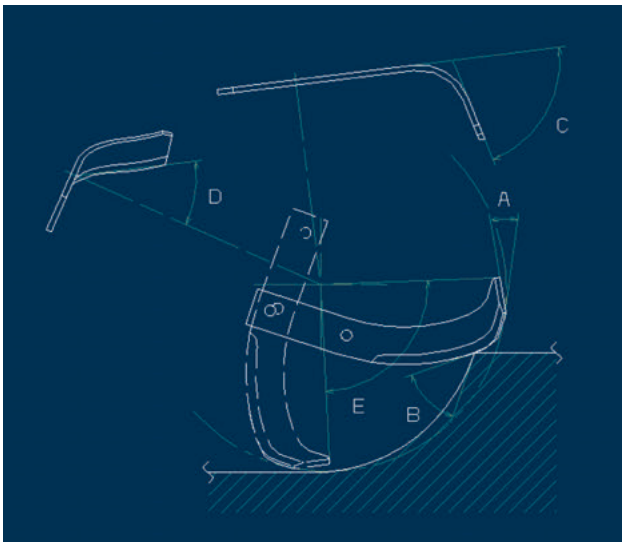


Fig. 10 Tilling blade

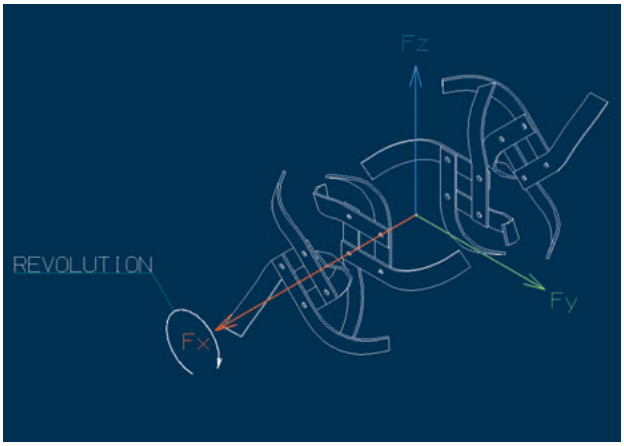


Fig. 11 Forces imposed on rotor shaft

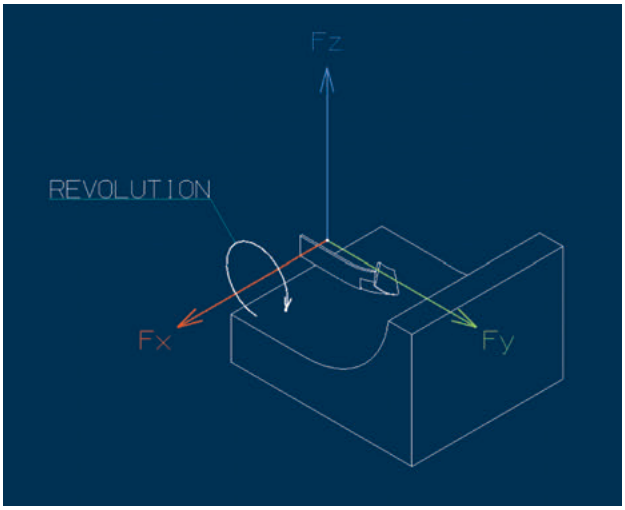


Fig. 12 Analytical model

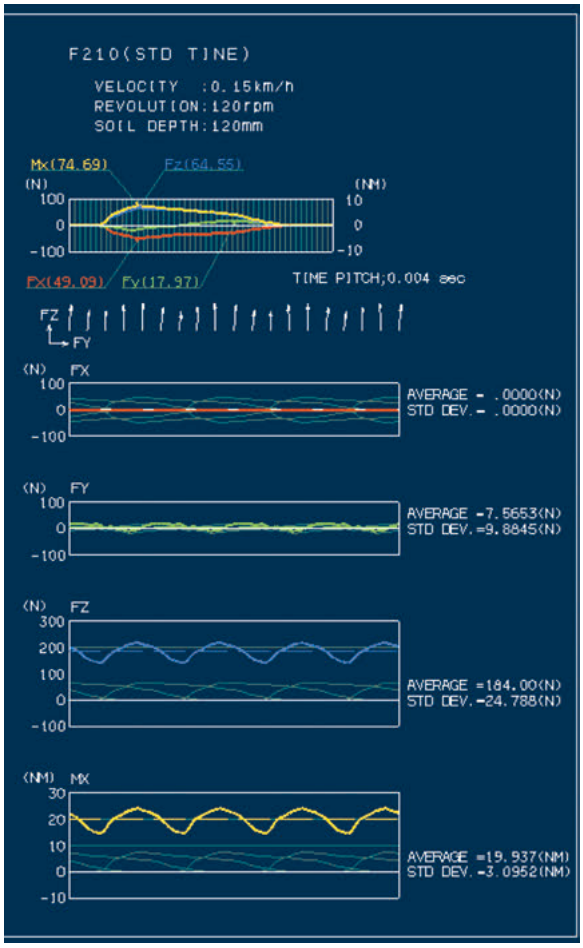


Fig. 13 Force and moment on rotor shaft of F210

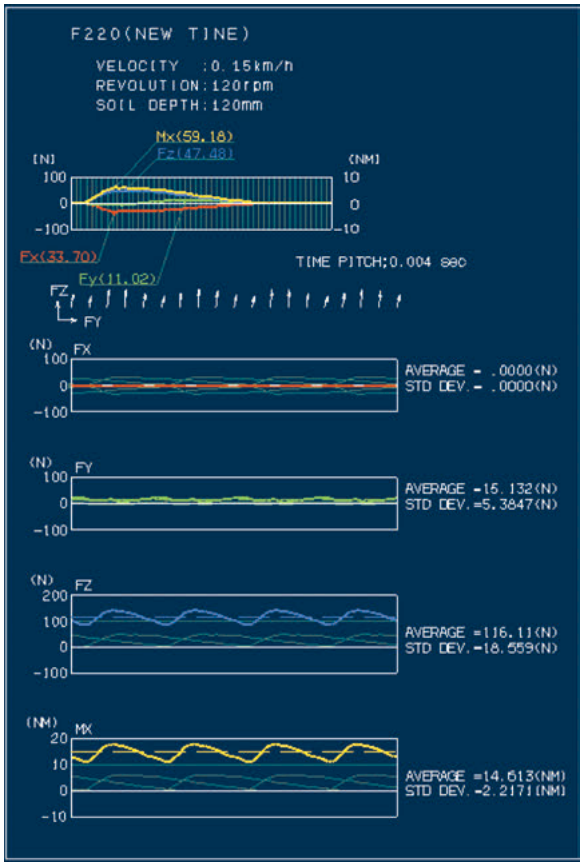


Fig. 14 Force and moment on rotor shaft of F220

5.4 Reduced Operating Load and Easier Operability

The reduction in engine displacement reduced the recoil starter pulling load needed to start the engine by 30%. Fig. 15 shows the relationship between engine displacement and the recoil starter pulling load.

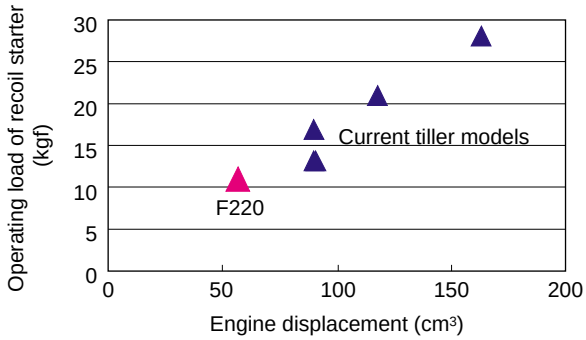


Fig. 15 Operating load of recoil starter

The clutch in the F210 had a lock mechanism for locking the clutch while tilling, but in the F220 a deadman's clutch mechanism was adopted because its simple operation is easier for novices to use. With this mechanism, squeezing the clutch lever causes the tiller to move forward and releasing the lever causes the tiller to stop. However, because the clutch lever is used more frequently and for a longer period of time with this mechanism than with a lock mechanism, a new clutch that can be operated with a low load was developed. Figs. 16 and 17 show the results of evaluations of the frictional properties of the clutch lining and the stroke characteristics.

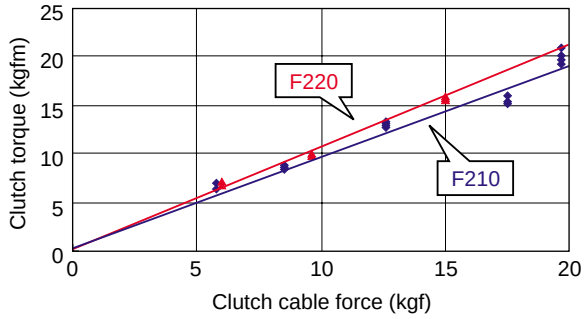


Fig. 16 Clutch capacity

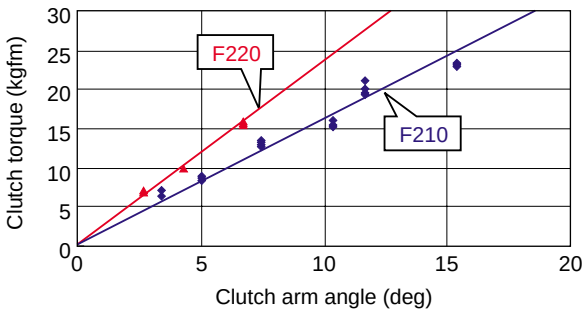


Fig. 17 Clutch capacity (Stroke)

The frictional properties were improved by changing the material used in the clutch lining, and the cable pulling load needed to obtain the clutch torque that is necessary in order to transmit the engine output was reduced. Furthermore, by improving the stiffness of the lining, the stroke characteristics were improved and the clutch arm angle needed to obtain the necessary clutch torque was reduced. The result of these changes was that the clutch lever operation load in the F220 was reduced by 20% with the same stroke as in the F210. These results are shown in Fig. 18. In addition, by changing the clutch lever from pressed steel to molded plastic, it was possible to reduce the coldness of the grip and to enhance the shape of the grip.

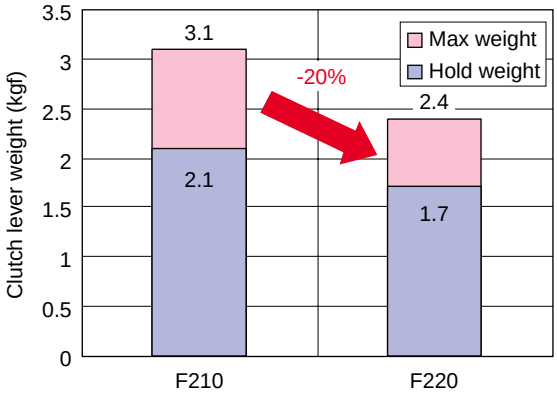


Fig. 18 Operating load of clutch lever

6. Conclusion

Based on past experience and common sense, it was believed that reducing the weight of the tiller and the engine displacement would make the tiller easier to handle, but would also cause a decline in work performance. By running simulations with new blade shapes and performing a variety of tests, it became apparent that the conflicting goals of a light weight, easy to use tiller and a tiller with good performance could all be achieved. Thus, the bold decision to use an engine with a smaller displacement was made.

This counterintuitive decision made it possible to retain the outstanding work performance of the "Komame F210" while further enhancing its characteristic compact size, light weight and ease of use, while also permitting the development of a product that addresses changes both in environmental awareness around the world as well as in the needs of the market.

The development team hopes that customers around the world will enjoy using the "New Komame F220". This development project was made possible with the cooperation of many people inside and outside Honda. Furthermore, much valuable advice was received from members of the editing staff in the writing of this article. The development team would like to express their thanks to all who helped in the course of this project and in the writing of this article.

References

(1) Masuda. S, et al., III. 4. Small Tractors, III. 5. Power Tillers, New Agricultural Mechanics, Tokyo, Asakura Book Co., 1975, P. 78 – 86

(2) Suzuki. S, et al., Development of General Purpose OHC Engines with Internal Timing Belts, HONDA R&D Technical Review, Vol. 10, P. 122 – 127 (1998)

(3) Kokuryou. T (MS Office), et al., Development of the Coaxial Counter-rotating Rotary System, HONDA R&D Technical Review, Vol. 6, P. 110 – 118 (1994)

■ Authors ■



Masatoshi NAGAOKA



Hideaki KOBAYASHI



Nobuchika KATAGIRI



Tatsuya TOKUDA

Development of the Lightweight, Compact Sine Wave Inverter-Equipped EU16i Generator

Toshifumi KOUCHI* Motohiro SHIMIZU*
Tadafumi HIROSE* Yukio SUGIMOTO*

ABSTRACT

The EU16i sine wave inverter-equipped generator was developed as the most lightweight and compact generator in the 1.6 kVA-rated output class. This generator has both superior portability and output capable of powering household appliances with their large power consumption. It also provides a low noise level, low fuel consumption, low exhaust emissions, and high-quality electrical performance with low waveform distortion and frequency variation. The efficient and lightweight high-speed multi-pole alternator and sine wave inverter system enables the engine to achieve higher speeds with a smaller displacement. With a frame that is fully covered with lightweight resin, this generator achieves a weight approximately one-half that of conventional generators. It also employs an electronic governor with automatic load-dependent speed control, together with an efficient generating system and a two-tiered noise dampening system. These allow this generator to achieve a reduction in noise level of 6 - 8 dB (A) over the practical load range and an improvement in fuel consumption of 20 - 40% compared to conventional generators. The EU16i generator meets the requirements of the EU Noise Directive, Stage II, as well as the CARB Tier II/EPA Phase II exhaust emission regulations. The EU16i is marketed worldwide though it is only marketed as the EU16i domestically. It is sold in North America as the EU2000i and as the EU20i when exported to other regions.

1. Introduction

Because they provide a convenient source of electricity, portable generators are becoming increasingly popular around the world for use by private individuals in leisure activities or as a backup power system for the home, and as a power supply for commercial and emergency applications.

In recent years, electrical equipment operating under advanced electronic control (microcomputer control), such as computers, has been coming into widespread use. In conjunction with this development, generators are now needed to provide quality electrical performance suitable for a wide variety of equipment.

Furthermore, due to society's continuing concern about the environment, demands for low noise levels, low fuel consumption and low exhaust emissions is being applied even to generators, with countries around the world enacting increasingly strict regulations designed to protect the environment. In regards to noise, the EU Noise Directive Stage I will go into effect in 2002, and Stage II will go into effect in 2006. In regards to emissions, following the

*Asaka Higashi R&D Center

EPA (Environmental Protection Agency) Phase II regulations that were implemented in 2001, the CARB (California Air Resource Board) Tier II regulations will go into effect in 2002.

Because conventional generators are equipped with a double-pole field rotational generating system, the engine speed is limited to 3000 rpm for a 50 Hz system and 3600 rpm for a 60 Hz system. This is due to the synchronous relationship that exists between the engine speed and the output alternating-current frequency. As a result, engines and generators both become larger in terms of volume and weight; in addition, the generated electrical output is approximately 15% lower in a 50 Hz system when compared with a 60 Hz system. Consequently, conventional generators, including those manufactured by other companies in the 1500 to 1800 VA output class that are capable of powering household appliances that consume large amounts of power, weigh as much as 30 or 40 kg, making them too heavy for one person to carry. Furthermore, Honda has offered no portable generators in this class.

This article introduces the EU16i Generator, a portable generator that is the lightest in its class due to the adoption of a lightweight, high efficiency inverter generating system and a full-cover and two-tiered noise dampening resin structure.

2. Development Concept

The development concept behind the EU16i was to produce a portable generator capable of generating enough output to power large electric appliances used in the typical home while still keeping the generator light and small enough to be portable by using the same sinusoidal inverter technology that was adopted in the EU9i (1)(2) (which has been in mass production since 1998). Furthermore, in order to enhance the competitive product strength of the generator, low noise level, low fuel consumption, low exhaust emission and quality electrical performance were also established as design goals.

The development targets were as follows:

(1) The generator must produce output capable of powering large electric appliances used in the typical home, while still being of a size and weight that allows it to be carried easily.
(2) The generator must offer quality electrical performance with minimal waveform distortion and frequency modulation so that it can also power electronic equipment such as computers.
(3) The generator must be made suitable for use in a variety of circumstances, such as at night or at a campground by reducing the noise produced by the generator and by reducing the fuel consumption of the generator in order to permit operation for extended periods.
(4) The generator must satisfy environmental regulations.
- CARB Tier II/EPA Phase II Emissions Regulations
- EU Noise Directive Stage II

3. Main Specifications and Basic Construction

The EM1500X, a conventional generator of the same class as the EU16i, had a pipe-frame construction that required two people, or one person using both hands, to



EU16i EM1500X

Fig. 1 External view of EU16i and EM1500X

Table 1 Comparison of specifications with EM1500X

Model			EU16i	EM1500X	
Engine	Type		4-stroke OHC	4-stroke OHV	
	Displacement (cm^3)		98	163	
	Speed (rpm)		∗ 3000-5000	3000	3600
			☆ 4300-5000		
	Operating noise level (dB (A) at 7m)		∗ 53-59	63	64
			☆ 59		
Generator	Type		Multi-pole field rotary	Double-pole field rotary	
	Excitation method		Magneto	Field current regulation	
	Voltage regulation method		※ PWM	# AVR	
	AC frequency (Hz)		50/60	50	60
	Max. AC output (VA)		2000	1500	1800
	Rated AC output (VA)		1600	1300	1500
	Voltage variation rate	Momentary	10% max.	15% max.	
		Stability	6% max.	7% max.	
	Frequency variation rate	Momentary	1% max.	15% max.	
		Stability	1% max.	7% max.	
	Waveform distortion	Linear load	5% max.	25% max.	
	Generating efficiency		81%	78%	
Dimensions	Dimensions L × W × H (mm)		510 × 290 × 425	505 × 420 × 420	
	Dry weight (kg)		21	41.5	

∗ : ECO-THROTTLE ON
☆ : ECO-THROTTLE OFF
※ PWM = Pulse width modulation
AVR = Auto voltage regulator

carry it. The EU16i, however, is fully covered with a plastic shell and has a narrow construction that allows it to be easily carried with one hand. Fig. 1 shows the appearances of the EU16i and the EM1500X, and Table 1 shows a comparison of the major specifications.

The EU16i employs an inverter system that does not cause the output alternating-current frequency to be limited by the engine speed. In addition, the engine itself was made smaller and lighter compared to conventional models by increasing the engine rpm, thus increasing the power output and reducing the required engine displacement. Further, in consideration of enhancements in cooling performance, noise insulating performance and the lighter weight of the engine, a cooling fan and an outer rotor-type high-speed multi-pole alternator that also serves as the flywheel are located in the position where a conventional flywheel would be located. The alternator and the fan are enclosed in an aluminum diecast fan cover and a plastic shroud. The engine unit is attached to the frame by vibration damping mounts at three points, one on the top of the engine unit and two on the bottom of the engine unit. The two-tier noise dampening structure is achieved by enclosing the unit in a plastic outer cover.

Each component (the power receptacle, the inverter unit, the alternator, the engine and the muffler) is arranged vertically in order, starting with the component that is coolest and radiates the least heat, which keeps the overall width of the unit to a minimum. This arrangement was designed to enhance cooling performance and portability. In addition, an effort was made to greatly reduce noise and fuel consumption by reducing the engine speed in the frequently used service load range, and a load-dependent speed control-type electronic governor that automatically controls the engine speed in accordance with the load of the electrical equipment being powered was adopted.

4. Component Technologies

4.1 High-speed Multi-pole Outer Rotor-type Alternator

As shown in Fig. 2, the alternator that is used in the EU16i is an outer rotor-type magnetic alternator with a three-phase multi-pole stator. This alternator generates three-phase high-frequency alternating current and supplies that current to the inverter. Commercially available strontium ferrite, a material with a very high magnetic flux density is used for the magnetic material, which further improved the high output/lightweight characteristics of the system.

Fig. 3 shows a comparison of the weight of the EU16i generating system (maximum output: 2 kVA), the weight of mass-produced (EU9i, EU24i, and EU28is) inverter generating systems (inverter unit + alternator) and the weight of conventional generating systems (alternator + flywheel). Table 2 shows a standalone performance comparison of the alternators.

As shown in the figure, the EU16i is less than 1/3 the weight of a conventional generating system, and approximately 20% less than a mass-produced inverter generating system (including the reduction in the weight of the inverter unit as described later).

4.2 32-bit CPU Control System Inverter Unit

Compared with the mass-produced EU9i (maximum output: 1 kVA), the output of the inverter unit that is incorporated in the EU16i (maximum output: 2 kVA) was doubled while minimizing any increase in weight and size by reviewing the system configuration in its entirety.

Fig. 4 shows a comparison of the inverter units in the EU16i, the EU9i, and the EU28is. 16-bit processors were

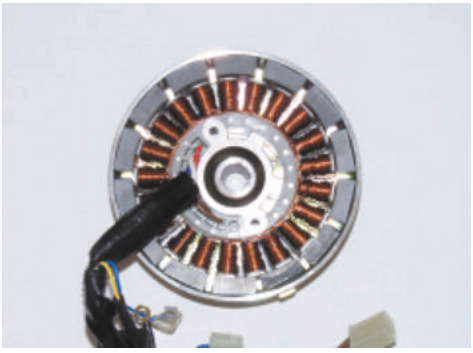


Fig. 2 Alternator

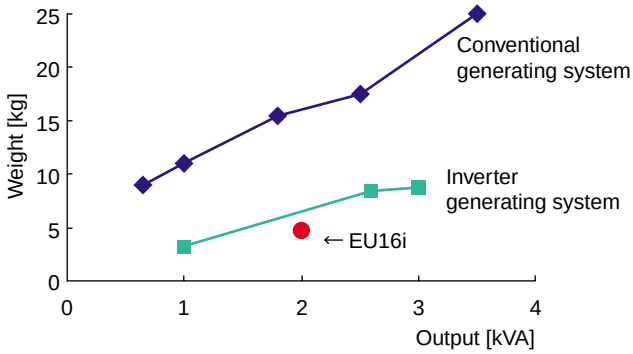


Fig. 3 Max. output and weight of the power-generating system

Table 2 Comparison of generation-system performance

Model			EU16i		EU9i		EU28is	
Alternator	Revolution	(rpm)	4300	5000	5500	6000	3500	3800
	Max. output	(W)	2500	3000	1350	1500	4100	4500
	Generating efficiency		88%	88%	88%	88%	87%	87%
	Weight	(kg)	2.8		1.8		5.4	
Inverter	Max. output	(VA)	2000		1000		3000	
	Rated output	(VA)	1600		900		2800	
	Efficiency		92%		90%		90%	
	Weight	(kg)	1.9		1.4		3.3	

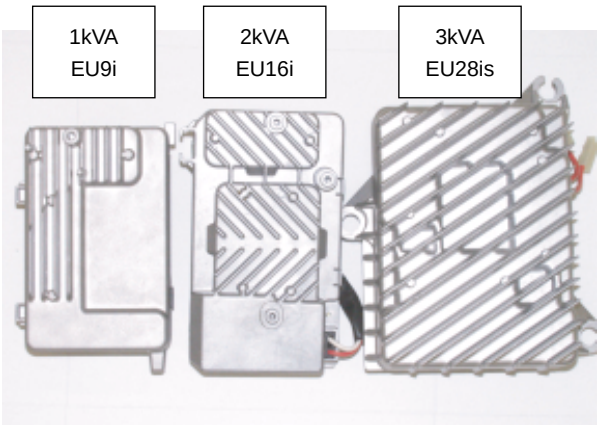


Fig. 4 Inverter unit

used for the CPUs in the EU9i and the EU28is, but a 32-bit processor is used in the EU16i to control the inverter section and the electronic governor section. By implementing most of the analog arithmetic circuitry that was used in the EU9i and the EU28 inverter through software in theEU16i's CPU, the number of control circuit components has been greatly reduced, which also contributes to keeping the system small and light. In addition, reducing the power loss in each section also results in enhanced conversion efficiency. Fig. 5 shows the block diagram for the system, and Table 2 shows a comparison of inverter performance.

4.2.1 Inverter section control

In the inverter section, the high frequency alternating-current from the alternator is rectified to a direct current, and is then converted into the sinusoidal alternating current that is output.

The control section can be broadly divided into the following four sections.

(1) Output waveform control

A precise 50Hz or 60Hz sine wave is created in the CPU as the basis for the output waveform. The inverter is driven by a PWM (Pulse Width Modulation) signal on a carrier wave of approximately 20 kHz. In addition, the output voltage and current waveforms are fed back to the CPU, which suppresses waveform distortion caused by the effects of the load equipment so that a precise sine wave and suitable voltage can be maintained.

(2) Protective function section

The inverter has functions that protect against overcurrent, overvoltage, and overheating. A breaker function protects against overcurrent by starting a timer and stopping output after a prescribed length of time has passed if the CPU determines that current above a prescribed level is being output. A peak current control function blocks overcurrent from being applied to ICs by means of an overcurrent protective circuit that protects against sudden overcurrent due to an output short, etc. Because the internal direct current voltage may increase under the effects of the load or during parallel operation, the CPU protects against overvoltage by suppressing voltage increases and by stopping output if the voltage is above a prescribed level. The overheating protection function stops output if the temperature of the power elements that make up the inverter rises above a prescribed value when operating under harsh environmental conditions.

(3) Rectification control

This section controls the continuity angle of the SCR (Silicon Controlled Rectifier) and converts the alternator output to a suitable direct current voltage. If the direct current voltage drops below a stipulated value due to a load that requires large starting power, for example, this section suppresses the inverter output and prevents an excessive

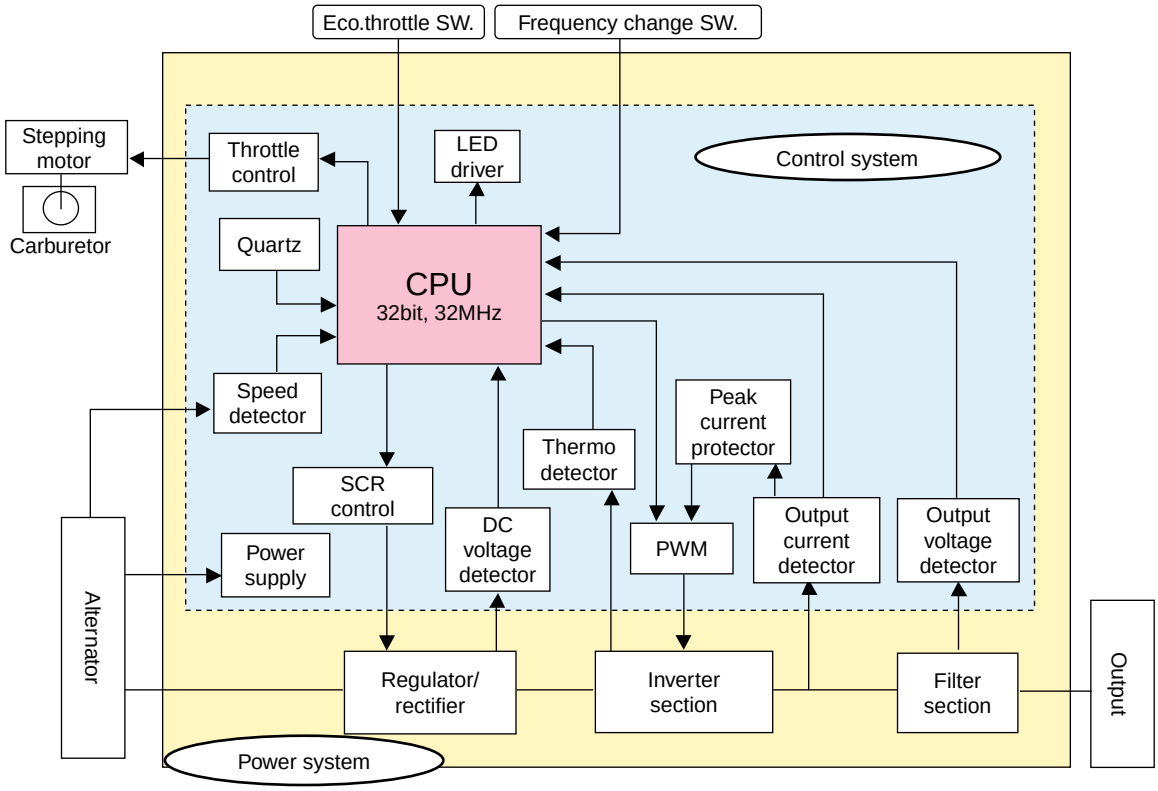


Fig. 5 Block diagram of inverter and speed-control system

drop in the direct current voltage, increasing the load starting capacity of the generator by always using a range where the alternator is efficient. This section also has a function that adjusts the direct current voltage up or down in accordance with the engine speed, which contributes to an expanded variable rotation speed range.

(4) Parallel operation control section

The generators in the Inverter Generator Series include a parallel operation function that allows the user to obtain twice the output simply by using a special cord to connect the outputs of two generators. In order to implement parallel operation, it is essential to match the phase and frequency of the two generators, as well as matching the voltage.

In order to match the phase and frequency, the CPU makes fine adjustments to the frequency in real time, based on the phase difference in the voltage and current. Next, in order to match the voltage, the CPU makes fine adjustments to the dropping characteristic and the voltage in order to prevent a load imbalance on the generators due to voltage differences.

4.2.2 Electronic governor section control

The electronic governor is of the load-dependent speed control-type, and it automatically controls the engine speed at a level suitable for the amount of power being used. The engine speed is kept at a level that matches the effective power by calculating the rotation speed on the basis of the load rate of the alternator. By enhancing the basic performance of the rotation speed control method and the rectification control, the variable range for the rotation speed has been increased by 15% compared with the mass-produced EU9i and EU28is. Incorporating this electronic governor made it possible to lower the engine rotation speed in the practical load range, reduce fuel consumption and reduce noise. Fig. 6 shows the effect on fuel consumption in comparison with conventional generating systems, while Fig. 7 shows the effect on noise. Note that the effect on noise also includes the effects of the two-tiered structure of the cover.

The electronic governor consists of the inverter unit, which handles throttle control, and a stepping motor positioned on the same shaft as the throttle.

(1) Determining the rotation speed

Fig. 8 shows the relationship between the engine speed and the generated output of EU16i. The SCR continuity angle is used as a parameter. The target speed is calculated such that the SCR continuity angle is maintained at a suitable value.

The SCR is an element that is used to rectify high-frequency alternating current from the alternator to a stipulated direct current voltage. If the load is large, the voltage drops and the SCR continuity angle widens; conversely, if the load is small, the SCR continuity angle closes. Therefore, it is possible to determine how much margin there is in the alternator output on the basis of the SCR continuity angle. Because the alternator output is proportional to the rotation speed, the SCR continuity angle can be increased to increase the rotation speed and maintain the alternator within the stipulated margin. Conversely, if the SCR continuity angle decreases and the alternator margin increases, the engine speed drops. This type of control is aimed at maintaining the alternator margin at a stipulated level to determine the optimal engine speed that is best suited to the power load that is being consumed.

(2) Rotation speed control

The engine speed is detected through the alternator subcoil. Because there are 14 magnetic poles in the

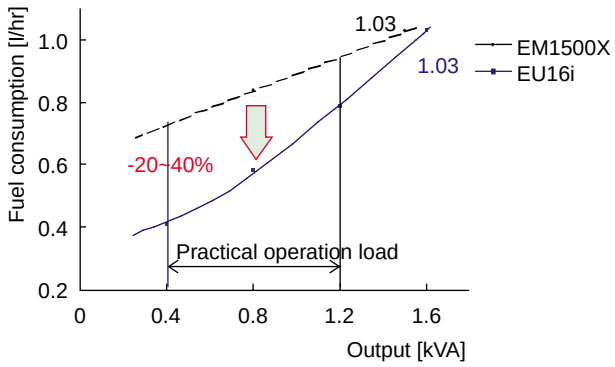


Fig. 6 Fuel consumption

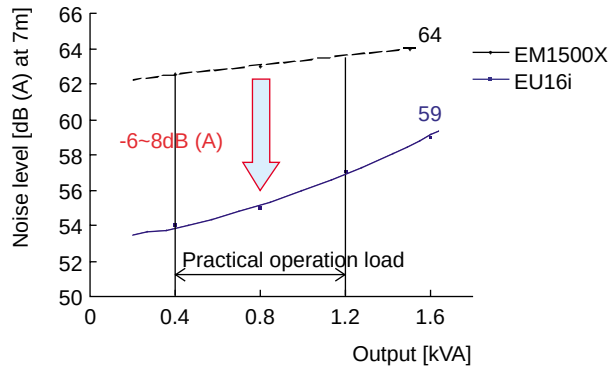


Fig. 7 Noise level

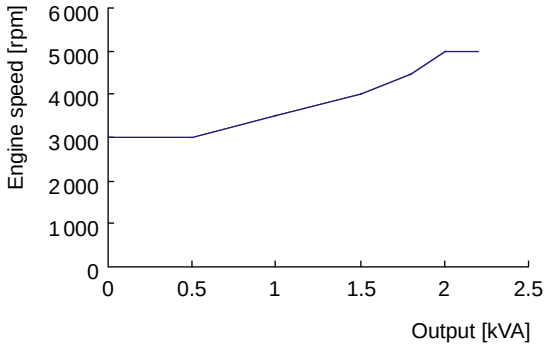


Fig. 8 Engine speed and output

alternator, the subcoil generates seven pulses per engine rotation. Because the combustion cycle occurs every two rotations in a single cylinder engine, an engine rotation is recognized every 14 pulses.

The rotation speed is determined at a prescribed interval, and the calculations are processed in order to derive the target speed which is then output to the stepping motor. The throttle position is recognized in the CPU at all times, and if a load that exceeds the capability of the engine is applied, the CPU suppresses the inverter output voltage to prevent the engine from stalling. This function makes it possible to use the engine to its maximum capacity for generating power, and contributes to increased output.

(3) Stepping motor

The EU16i uses the same stepping motor as in the mass-produced EU9i. The stepping motor is combined with the carburetor. Deceleration is achieved by means of a

reduction gear in the stepping motor, which is connected to the throttle shaft of the carburetor by means of a plastic linkage. The deceleration ratio is set to a value such that the throttle will be at the full extent of its stroke when motor operation is at 100 steps. The stepping motor is driven by the CPU through two-phase excitation via a motor driver. In order to enhance the following characteristics of the motor, the drive signal varies the rate of acceleration or deceleration. The value stored in the CPU after the throttle is set to wide open during the initial startup period is used for detecting the throttle position.

4.3 Engine

The engine used in the EU16i (the GX100) was developed by focusing on the following points to fully achieve the advantages of a portable inverter generator:

- Improved output at high engine speeds
- Smaller size, lighter weight
- Reduced noise
- Satisfaction of CARB/EPA emission requirements

The primary technologies that were adopted in order to meet these needs include: (1) uni-block cylinder, (2) built-in timing belt and high-speed valve system, and (3) emission reduction technologies.

4.3.1 Uni-block cylinder

In order to achieve a small size and light weight, a uni-block cylinder construction, in which the cylinder head and the cylinder block are one piece, was adopted for the GX100. Unlike the typical construction with a separate head, the uni-block cylinder does not require additional thickness at joints and does not require head bolts or gaskets. In conjunction with its higher rotation speed and lower displacement, the weight of the head and the cylinder block in the GX100 was reduced by approximately 40%. This construction eliminated the effects of forces along the tightening axis of the head bolt, which is one of the causes of cylinder distortion, and also produced benefits in terms of oil consumption and in degradation of emissions over time. Furthermore, while a sleeveless aluminum cylinder was used in the conventional uni-block cylinder[3], a cylinder cast in a thin cast iron sleeve is used in the GX100, which also reduces the degradation in emissions. The construction of the GX100's cylinder block is shown in Fig. 9.

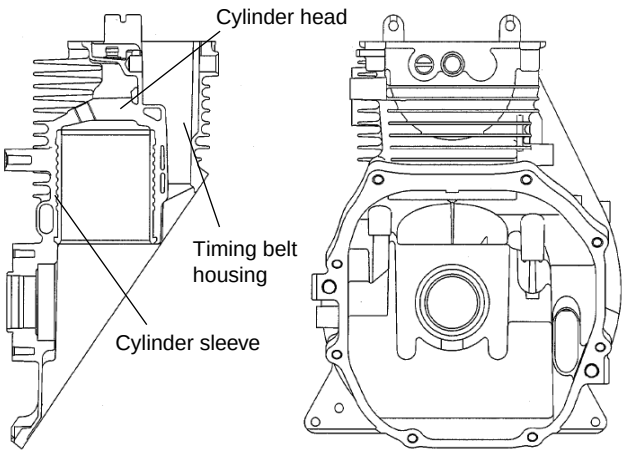


Fig. 9 Cylinder block section

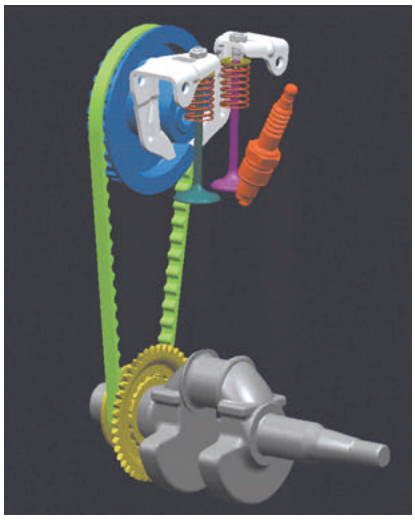


Fig. 10 Valve train

4.3.2 Built-in timing belt mechanism

The OHC construction that has been proven in the GC/GCV 135/160[3], shown in Fig. 10, was adopted in the GX100. By adopting a component configuration consisting of a built-in timing belt, a resin single cam pulley, and an L-shaped rocker arm, noise, size, weight, and cost could be reduced.

In addition to the OHC construction described above, the reduction in the equivalent valve weight by reducing the stem diameter of the intake and exhaust valves and the optimization of the rocker arm, the cam profile, and the belt size have realized a suitable valve system for engine speeds of up to 5000 rpm, a necessity in an inverter generator, as opposed to the 3600 rpm of a conventional generator.

4.3.3 Emission reduction technologies

The following technologies were adopted in order to satisfy the CARB Tier II/EPA Phase II emission regulations:

- Change to center plug by using a small spark plug
- Optimization of the shape of the combustion chamber, including minimization of the quenching area around the combustion chamber

Due to the effects of these technologies, the EU16i achieved the best emission values in its displacement class, as shown in Fig. 11.

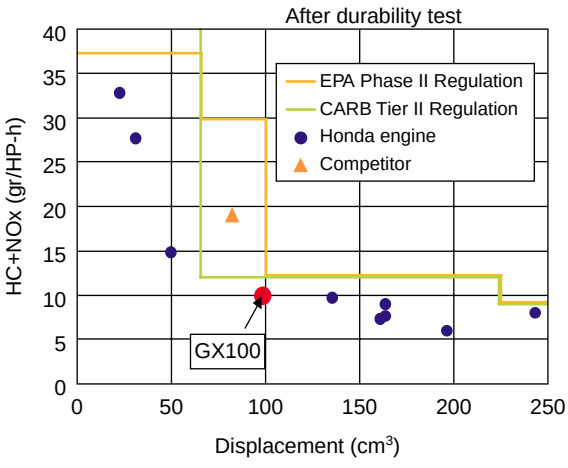


Fig. 11 Emission performance

4.4 Frame Construction

In order to attain the required cooling performance while remaining light and reducing noise in the EU16i, component placement was optimized and a full-cover, two-tiered noise dampening resin structure was adopted. Fig. 12 shows the construction of the EU16i's lightweight resin full-cover.

In the EU16i, an inverter system was adopted in which the output alternating-current frequency is not limited by the engine speed. A light multi-pole alternator that also serves as a flywheel was located at the position that would normally be occupied by a conventional flywheel. As a result, the weight of the components that are supported by the frame, including the engine and the alternator, was reduced by approximately 53% compared to earlier systems.

In addition, by using aluminum diecast components for not only the engine bracket but also the head cover and the fan cover, the engine itself could be used to support these components through their respective mounts on the rear portion of the carrying handle on the outer cover and a portion of the under cover. In addition, the high-strength plastic subframe that supports the large plastic fuel tank was connected to the front portion of the carrying handle on the outer cover and to the under frame. A feature of this construction is that the carrying handle directly bears the weight of the engine, the alternator and the fuel tank when the generator is being carried.

Reducing the weight of these components and adopting this support structure made it possible to switch to plastic while still retaining adequate strength and rigidity in the outer cover, the under frame, and joints between them, resulting in a large reduction in the weight of the generator as a whole.

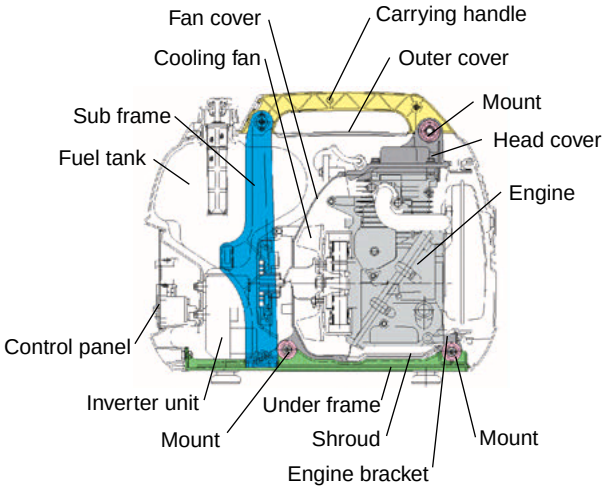


Fig. 12 Lightweight resin full-cover structure for EU16i

The under frame was created from plastic and its shape was optimized in order to ensure that it provided adequate strength and rigidity while the generator is in operation. The shape of the stress concentration areas was optimized by using simulation to analyze the distribution of stress in the under frame. Fig. 13 shows the results of this simulation and analysis.

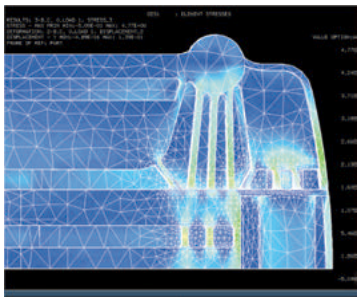


Fig. 13 Analysis of simulated under frame

Taking the cooling efficiency of each component into consideration, the alternator, the engine, the muffler and the inverter were arranged in a line, starting from the inverter unit, which produces little heat. The flow of cooling air was made unidirectional, and by causing the cooling air to flow over the components that produce the least heat first, the volume of cooling air needed was reduced. The alternator, the engine, and the muffler, which all produce significant heat, were enclosed by a sealed fan cover and a shroud in order to prevent warm air from recirculating over them. In addition, a two-tiered structure was adopted, with these components also covered by the outer cover. As a result, while conventional models had two fans, one to cool the engine and one to cool the alternator, the EU16i only needed one fan, contributing to the lighter weight and smaller sized generator. In addition, placing an intake opening in the rear of the outer cover creates a flow of cooling air from the rear portion inside the cover, which helps to prevent the temperature of the outer cover from rising due to heat radiated by the engine, and also serves to cool the carburetor. Fig. 14 shows the cooling system of the completed machine.

In order to reduce noise in the completed machine, fan noise was reduced by placing the inverter unit in front of the fan. In addition, a large air cleaner with a silencer nose, a large muffler, an electronic governor, and a variable pitch cooling fan were all adopted.

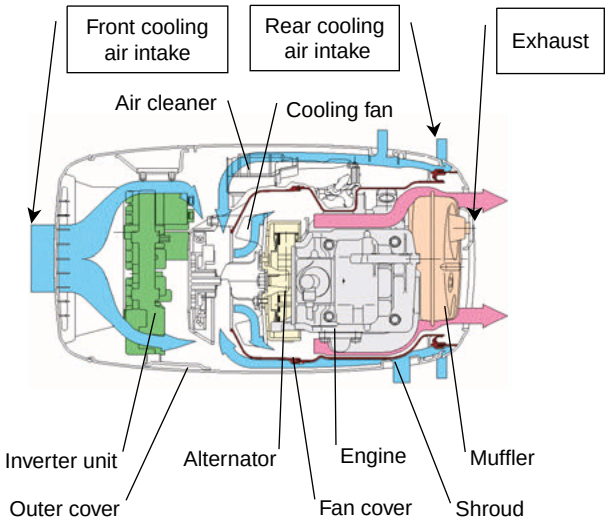


Fig. 14 Cooling system of the completed machine

The result of this structure was to reduce noise by 6 to 8 dB (A) under a practical load in comparison with the conventional EM1500X, which is sufficient to satisfy the EU Noise Directive Stage II scheduled to go into effect in 2006. This structure also resulted in approximately a 50% weight reduction. Fig. 15 shows a comparison of component weights between the EM1500X and the EU16i.

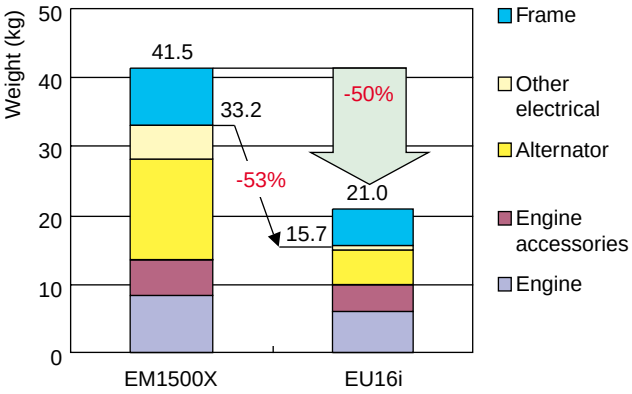


Fig. 15 Comparison of weight between EU16i and existing EM1500X

5. Conclusion

Rather than applying a conventional general-purpose engine, a small, high-speed, 4-stroke engine was combined with a high-speed multi-pole outer rotor-type alternator that also serves as a flywheel. Further, a sinusoidal inverter control and a lightweight plastic full-cover structure were adopted to develop the EU16i generator. This new EU16i generator is portable, produces output capable of powering large home appliances, and it provides quality electrical performance suitable for electronic equipment such as computers.

(1) Excellent portability was achieved with a dry weight of 21 kg, which is only half that of conventional models, and with a comparatively narrow suitcase style design.
(2) With waveform distortion of less than 2.5% and frequency fluctuation of less than 1%, electrical performance equivalent to that of commercial power supplies was achieved.
(3) Compared with conventional models, noise was reduced by 6 to 8 dB (A) and fuel consumption was reduced by 20 to 40% under practical loads.
(4) The EU16i satisfies EU Noise Directive Stage II (to be implemented in 2006) and CARB Tier II (2002)/EPA Phase II (2001) emission regulations.

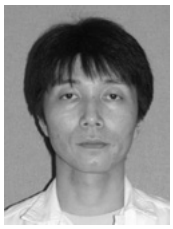
The EU16i is the version being marketed in Japan. The EU2000i is the version being marketed in North America, and the EU20i is the version being marketed in other export markets. The development team is confident that customers around the world will find all of these to be excellent products.

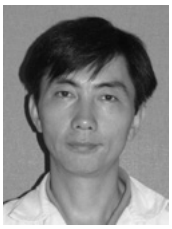
The development team would also like to express their thanks to all who helped in the course of the development of these products.

References

(1) Tanaka, Y., Kouchi, T., Ito, K., and Nakamura, M.: Development of the Lightweight and Compact Portable Generators-GENE21 Series, HONDA R&D Technical Review, Vol. 11 No. 2, p.15-22 (1999)
(2) Kouchi, T., Ito, K., and Nakamura, M.: Development of Lightweight and Compact 1kVA-class Portable Generator, SAE Paper 1999-01-3304
(3) Suzuki, T., Hojo, H., Inoue, S., Moriyama, H., Fujinaga, Y.: Development of General Purpose OHC Engine with Built-in Timing Belt, HONDA R&D Technical Review, Vol.10, p.122-127 (1998)

■ Authors ■


Toshifumi KOUCHI


Motohiro SHIMIZU


Tadafumi HIROSE


Yukio SUGIMOTO

Development of a 1.3L 2-Plug Engine for the 2002 Model 'Fit'

Yukio NAKAYAMA* Makoto SUZUKI*
Youichi IWATA* Junji YAMANO*

ABSTRACT

A lightweight and compact, 1.3L 4-cylinder engine was developed as the new-generation i-Series power train. This engine has twin plugs for each cylinder, and achieves rapid combustion by means of high-precision dual-point sequential ignition control that responds to the engine's operating conditions. In addition, reducing friction and using the newly developed CVT have yielded the low fuel consumption of 23 km/L in the Japanese 10-15 mode. The engine has achieved 'J-LEV' certification by reducing exhaust emissions to 50% of the fiscal year 2000 emissions standards.

1. Introduction

In response to demands for environmental protection and lower resource consumption, Honda has developed the 'i-series' – a lightweight, compact power train series – which improves environmental (exhaust gas), fuel economy, and drive performance. This 'i-VTEC' combines VTEC with continuously variable control camshaft phase [(1)] and is fitted to the 'Stream'. The 'i-series' is the general name for the latest generation of engines that carry out optimum fuel control in response to the engine speed and load conditions.

This report introduces the new 'i-DSI', an 'i-series' engine for use on sub-compact cars (DSI: Dual and Sequential Ignition). This new engine is a 1.3L, SOHC, two-plug, four-cylinder engine that is lightweight and compact, which has achieved both low fuel consumption and low emissions.

2. Aims of Development

The development concepts for the new small car 'Fit' to which this engine is fitted are 'spacious cabin' and 'best fuel economy performance in the world'. In order to achieve this concept, the aim was to develop a compact design that responds to the vehicle packaging and lower emissions, by focusing on engine fuel consumption improvements through friction reduction, adopting a rearward layout of the exhaust system and an exhaust gas oblique intake flow catalytic converter.

The detailed objectives for the development of the engine were as follows:

1) Highest fuel economy performance in the world (Japanese 10-15 mode fuel economy: 23 km/L)
2) High torque performance
3) 50% reduction over FY2000 emissions requirements ('J-LEV' certification)
4) Compact engine design that facilitates a roomy cabin

3. Outline and Main Specifications of the Engine

Fig. 1 shows the appearance of the engine, and Table 1 compares the specifications of the new engine (L13A) to those of the previous engine (D13B).

As shown in Fig. 2, the lightweight, compact design is achieved through the adoption of bracket-less accessories and a serpentine accessory belt, a long, plastic intake manifold and cam chain drive. In comparison with the existing 1.3L D13B engine, the new design is compact, being 118 mm shorter and 69 mm narrower, and lightweight, with a total engine weight reduction of 8%. Also, as shown in Fig. 1, the air cleaner and intake resonator chamber are placed above the transmission, to also contribute to a more compact power train overall.

The special features of this engine are a higher compression ratio (9.2 → 10.8) achieved through the placement of two spark plugs at opposite angles to each other in each of the cylinders (Fig. 3), and rapid combustion attained through dual-point sequential ignition

*Tochigi R&D Center

timing control. This provides both improved fuel consumption properties and output.

Fig. 4 shows cross sections of a conventional cylinder head and the type adopted in this engine. In the new head, there is a single rocker arm shaft supporting the inlet rocker arm and exhaust rocker arm, and the valve angle was narrowed from 46° to 30°. The adoption of these technologies results in a more compact combustion chamber. Also, to promote rapid combustion, a new intake port was adopted to strengthen mixture turbulence in the combustion chamber, as well as swirl and tumble. Furthermore, in order to decrease fuel consumption, friction was reduced through a full-scale review and revision of engine part shapes, changes to materials and improvements in machining and processing methods.

Fig. 5 shows the engine performance curve. Through the changes in the specifications in Table 1, improvements in volumetric efficiency through changes in valve lift characteristics, and tuning of the intake and exhausts, etc., the new engine achieves approximately 30% higher output than the previous engine (D13B).

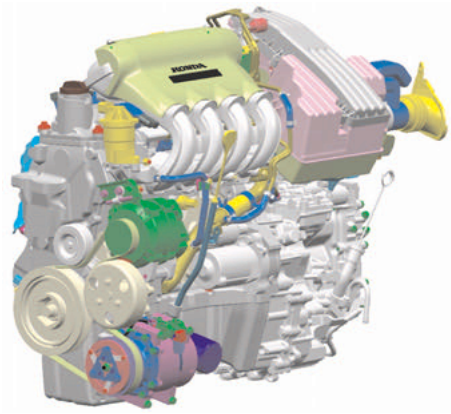


Fig. 1 View of 2002 model i-DSI engine

Table 1 Engine specification

Engine code	2002 model i-DSI L13A	1999 model Logo D13B
Cylinder configuration	In-line 4-cylinder	In-line 4-cylinder
Bore × stroke (mm)	73 × 80	75 × 76
Displacement (cm^3)	1 339	1 343
Compression ratio	10.8 : 1	9.2 : 1
Valve train	SOHC 2 Valves	SOHC 2 Valves
Number of valves	2 per cylinder	2 per cylinder
Valve diameter (mm) Inlet Exhaust	 32 28	 30 26
Fuel supply system	Programmed fuel injection	Programmed fuel injection
Ignition system	Dual point sequential ignition	Single point ignition
Max. power (kW/rpm)	63/5 700	49/5 500
Max. torque (N·m/rpm)	119/2 800	103/2 500

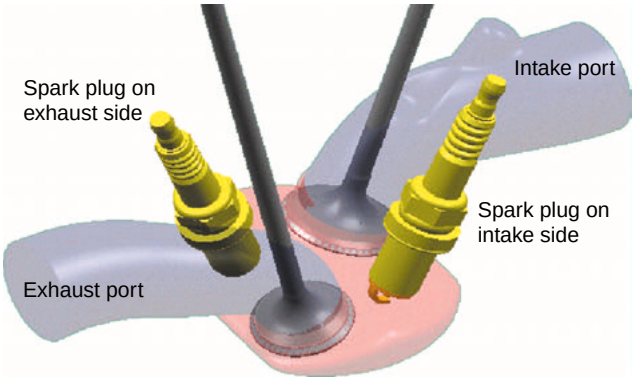


Fig. 3 Combustion chamber configuration

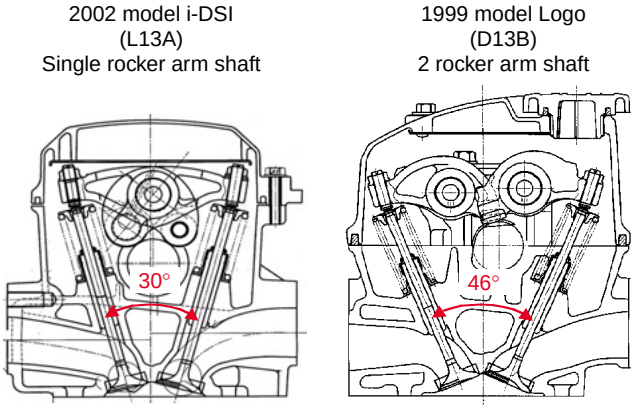


Fig. 4 Section view of cylinder head

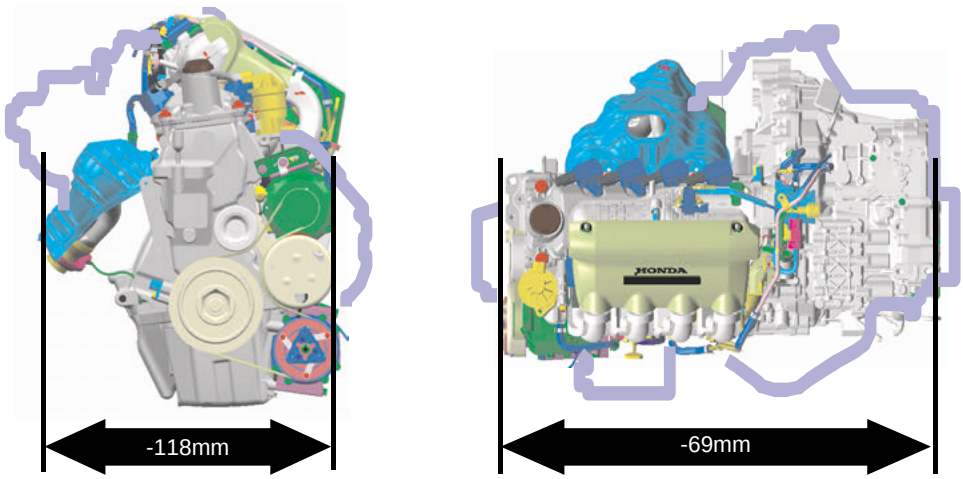


Fig. 2 Engine side and down views

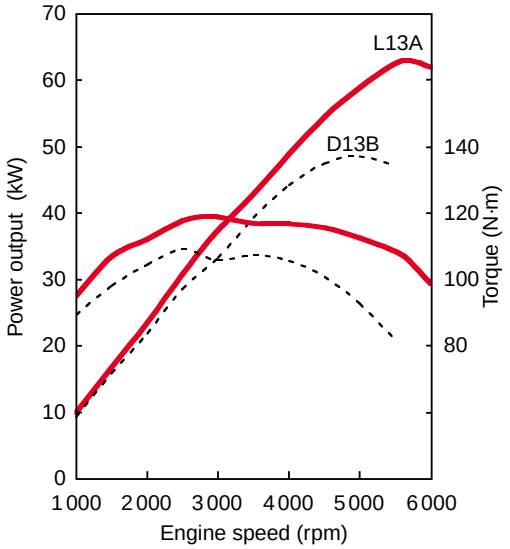


Fig. 5 Engine performance

4. Combustion of i-DSI

The i-DSI combustion concept is one of rapid combustion throughout all operating ranges, using optimal control in response to engine speed and load conditions at ignition timing, using a dual-point spark method. For better homogenization of air-fuel mixture formation, the flow pattern within the combustion chamber (kinetic energy, turbulent energy) is made uniform through the intake port and combustion chamber shapes. With high precision control of the dual-point sequential ignition timing, decreased fuel consumption, knock suppression, high torque and NV (noise and vibration) performance improvements were all achieved.

4.1 Modification of the Intake Port and Combustion Chamber

In order to raise the flame propagation speed, this engine's intake port is designed for higher swirl ratio (1.1 → 1.36) and tumble ratio (1.3 → 1.58) compared with a previous engine, and strengthens turbulent motion at the compression end (before ignition).

As well as the strength of in-cylinder turbulent motion, the air-fuel mixture homogeneity is an important factor in rapid combustion. Therefore, the combustion chamber is designed to attain the perfectly homogeneous air-fuel distribution. This distribution was studied by simulating the shape of the combustion chamber, with the focus on piston head shapes under the following conditions: Average air-fuel ratio A/F = 14.7 Fuel injection timing: 20 degrees after TDC (top dead center) of the intake stroke. The simulation showed the horizontal sectional views at the piston of the electrode in the center of the spark plug, and the vertical sectional views at the spark plugs positions on the intake side and exhaust side.

Fig. 6 shows the computed combustion chamber air-fuel distribution at 30 degrees before TDC of the compression stroke. Apparently, it is not homogenous with the conventional design. Fuel-rich mixture exists on the intake spark plug side and around the bottom area of the combustion chamber. By adjusting the swirl and tumble ratio balance and shaping the combustion chamber, it was made possible to homogenize the turbulent energy distribution thus realizing the totally homogeneous air-fuel mixture.

Fig. 7 shows co-variation of indicated mean effect

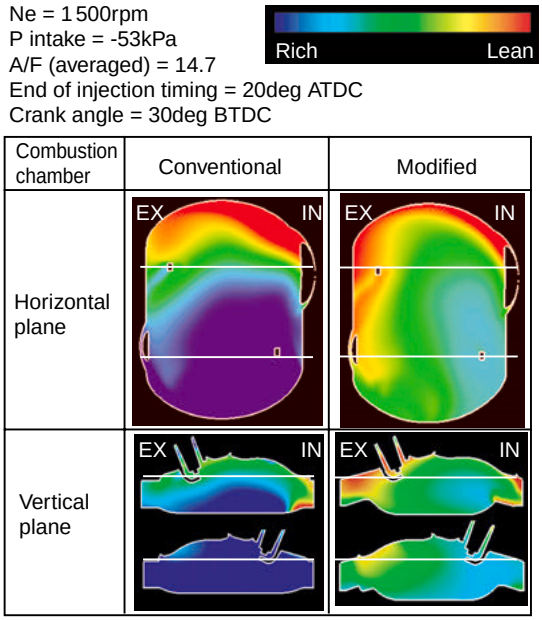


Fig. 6 Effect of combustion chamber shape modifications on in-cylinder A/F distribution

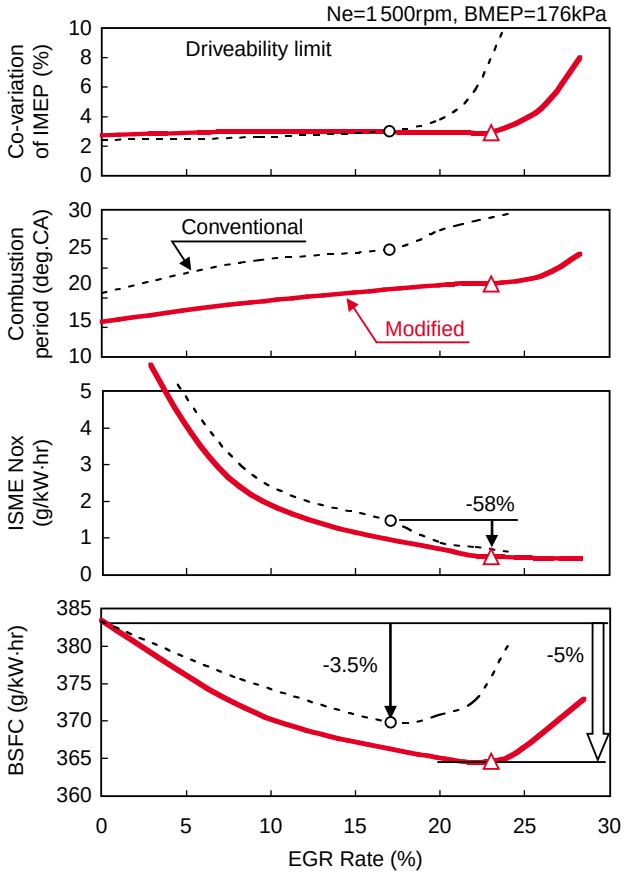


Fig. 7 Comparison of BSFC, NOx and combustion characteristics between the modified and conventional combustion chambers

pressure (IMEP), combustion period which means mass burned fraction (10%-90%), indication of specific mass emission–NOx (ISME-NOx) and BSFC in relation to the EGR (exhaust gas re-circulation) rate, both before and after the aforementioned in-cylinder air-fuel mixture formation modifications. By the rapid combustion with strengthened swirl and tumble as well as a more homogenous air-fuel

mixture, the stable combustion was achieved even with large-volume EGR rate of 23%. As a result, it is possible to reduce NOx emissions and to reduce fuel consumption by 5%.

4.2 Rapid Combustion Through Sequential Ignition

Fig. 8 shows a comparison of the various losses as determined from BSFC and pressure, in terms of ignition timing for an engine speed of 1500rpm under a partial load. With intake and exhaust side dual-point simultaneous ignition control, there is a point where BSFC is decreased if the ignition timing is advanced. Furthermore, by carrying out sequential ignition timing control that advances ignition timing on the intake side, a 1.3% reduction in BSFC can be achieved. This means by promoting ignition first on the intake side, which has a comparatively low temperature, more rapid combustion is achieved than with simultaneous ignition. As a result, there is tendency for an increased cooling loss (heat loss) but there is a larger reduction in time loss. Consequently, there is an improvement in efficiency due to a reduction in overall loss.

Fig. 9 shows the results of pressure analysis at BSFC minimum ignition timing with both simultaneous ignition and sequential ignition, as well as an image of the indicator diagram. Compared with simultaneous ignition, sequential ignition shows a faster pressure rise and the maximum pressure is higher. As a result, the combustion period, in which the mass-burned fraction increases from 10% to 90%, is shortened by 1.8 degrees, and through the above-described rapid combustion, time loss is reduced. Sequential ignition has, in comparison with simultaneous ignition,

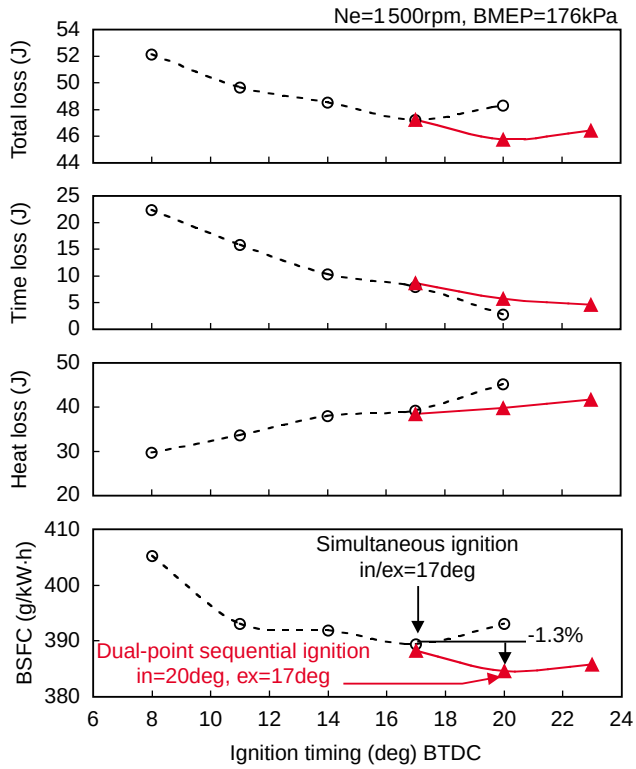


Fig. 8 Comparison of combustion characteristics

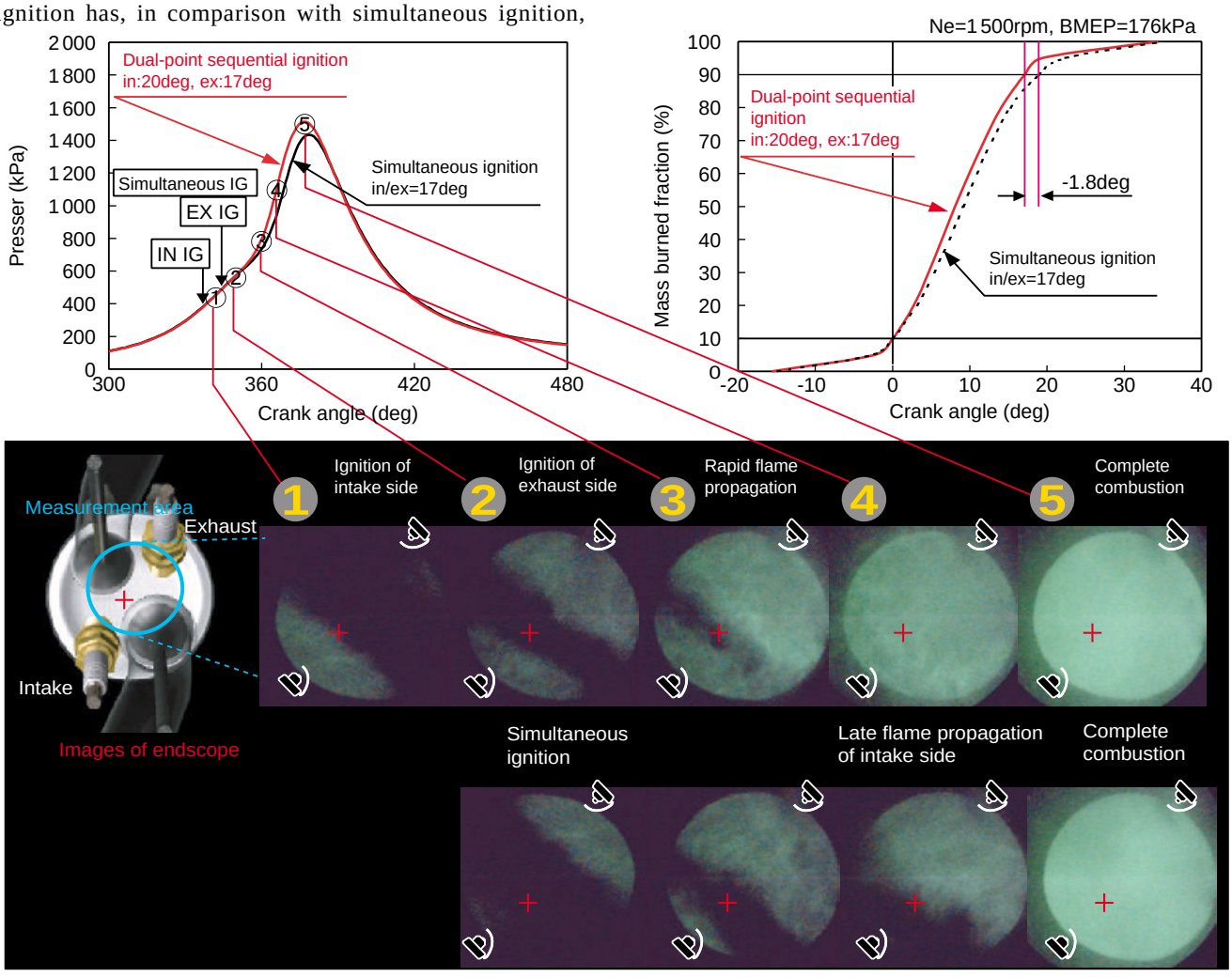


Fig. 9 Comparison of combustion characteristics

faster flame propagation, which is expressed in the image, and in the latter half of combustion, the flames on the intake and exhaust sides move to the center of the combustion chamber (in the visible range, offset to the lower left), which is an expression of the rapid combustion.

4.2.1 Knock suppression

Creating a high compression ratio is a major factor in improving thermal efficiency. However, knocking is a large obstacle. A study was made of the use of dual plugs and ignition timing control in order to overcome this problem and to achieve both torque at a low speed range and a high compression ratio.

Fig. 10 shows the schematic view and an image of knock suppression through dual-point sequential ignition. The plug on the intake side is ignited first, and it is clear from the image that the flame grows from the intake side at this time. Next, if the plug on the exhaust side does not ignite, the non-combusted fuel in the air on the exhaust side end part receives this flame growth from the intake side, increases in temperature and pressure, and then self-combusts, which causes knocking. In contrast, if ignition of the plug on the exhaust side is retarded, the end gas combusts normally before knocking occurs and knocking can be suppressed.

Fig. 11 shows one example of the effectiveness of knock suppression. This figure shows knocking points and torque characteristics at an engine speed of 2000rpm and under a full load condition when ignition timing is changed. A comparison of the following three ignition methods was made: (1) ignition of intake side plug only, (2) dual-point simultaneous ignition, and (3) dual-point sequential ignition. In contrast with ignition on the intake side only, dual-point simultaneous ignition makes possible rapid combustion and advanced ignition timing due to knock suppression, and, further, a 6% improvement in torque is achieved. In addition, using sequential ignition, knocking can be suppressed and sequential ignition's set ignition timing torque is improved by 1.5% compared with that for simultaneous ignition.

Fig. 12 shows torque characteristics when simultaneous ignition and sequential ignition timing control are carried out. In the low engine speed range of 2500rpm or less, there is a 2N·m torque improvement with dual-point sequential ignition timing control.

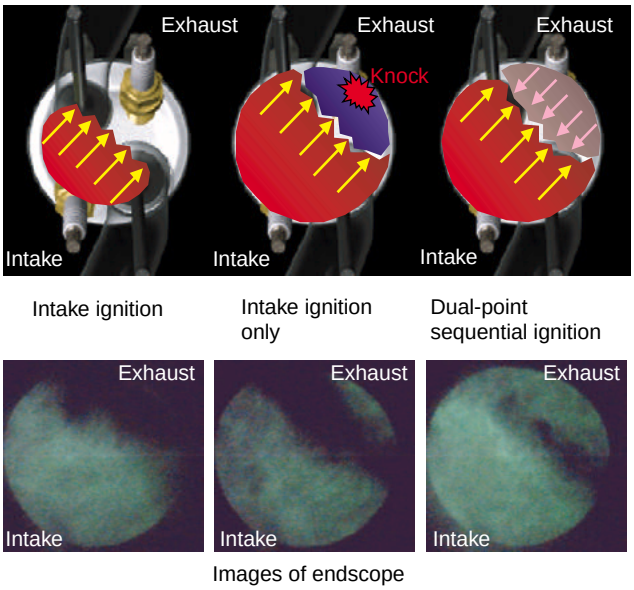


Fig. 10 Mechanisms of Improved knock suppression performance

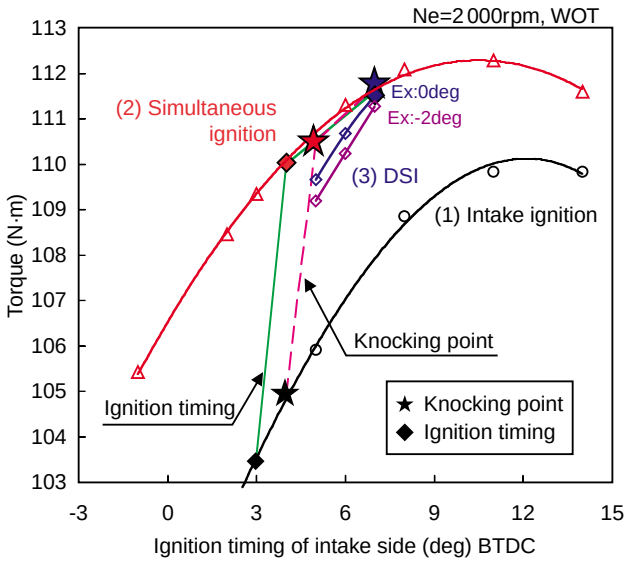


Fig. 11 Influence of ignition timing on engine torque

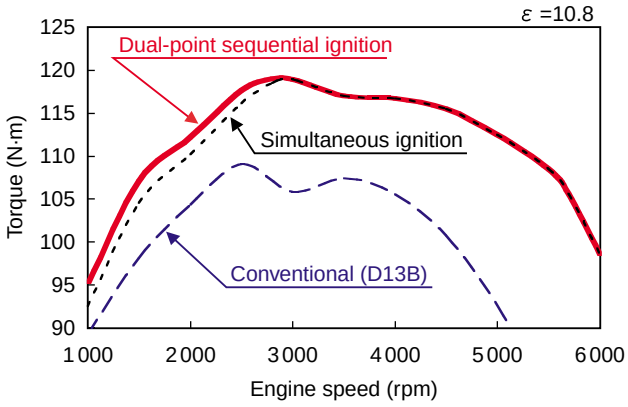


Fig. 12 Comparison of engine torque between dual-point sequential ignition and simultaneous ignition

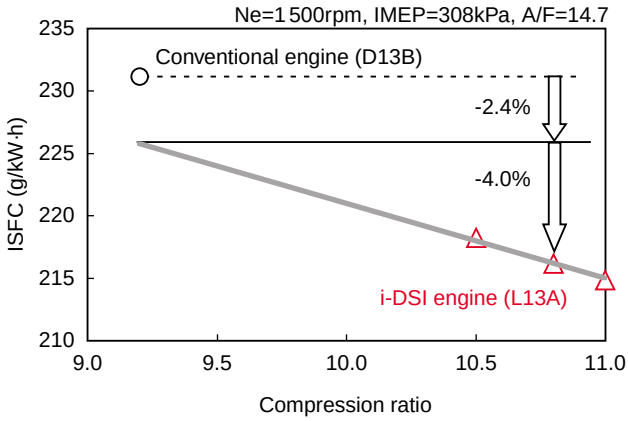


Fig. 13 Influence of compression ratio on ISFC

As a result of the knock suppression effect described above, it is possible to achieve both an improvement in torque at a low speed range, in comparison with existing engines, and the high compression ratio of 10.8. In combination with the rapid combustion gained due to the application of dual plugs and sequential ignition timing control, a 6.4% decrease in fuel consumption was achieved (Fig. 13).

4.2.2 High-precision ignition timing control

Thanks to the rapid combustion gained through sequential ignition timing control, improvements in knock suppression and fuel consumption performance were achieved. However, this rapid combustion leads to aggravation of engine vibration and noise, particularly crank rattle. Crank rattle has good correlation with the maximum combustion pressure (Pmax), and the maximum pressure rise rate (dP/dθq max.). Thus a study was carried out into reducing noise and vibration, as well as achieving good torque characteristics by suppressing combustion pressure. Fig. 14 compares engine radiation noise, combustion pressure and torque characteristics during simultaneous ignition and sequential ignition timing control. By retarding ignition timing on the exhaust side and reducing the maximum pressure rise rate, a 1 – 2 dB reduction in the medium engine speed range is achieved. Torque also drops as combustion pressure is reduced. However, by keeping the drop percentage to a minimum at 0.4%, noise performance can also be achieved.

Fig. 15 shows an ignition timing control map. The ECU (electronic control unit) controls ignition timing according to atmospheric and engine conditions based on the three ignition timing controls: the range where the intake side plug is ignited first and the exhaust side plug has a retarded ignition, the range where the exhaust side plug only has a retarded ignition, and the simultaneous ignition range.

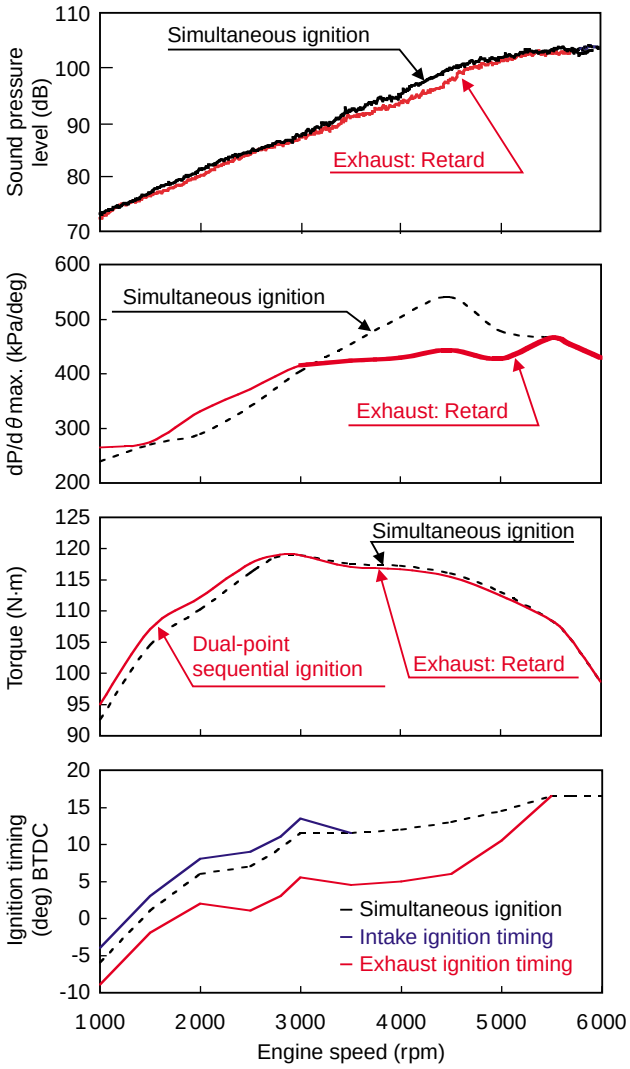


Fig. 14 Comparison of engine torque, combustion characteristic and radiation noise with control the ignition on consequential phase

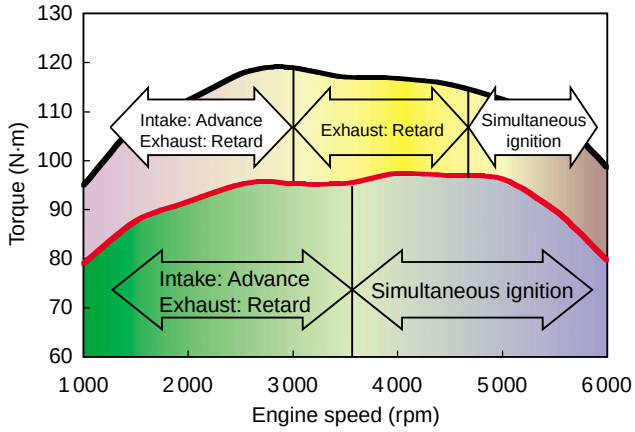


Fig. 15 Map of control the ignition on consequential phase

5. Reduction of Friction

In addition to the rapid combustion outlined above, a reduction in friction is an important factor in achieving decreased fuel consumption.

In addition to the offset cylinder structure, roller follower rocker arm, ion plated piston ring, striated crank journal and connecting rod bearing metal which were developed as friction reducing technology for the ECA1 engine applied to 'Insight', other new technologies were adopted. These technologies include molybdenum disulfide (MoS_2) shot peening of the piston skirt (first in the world), a two-mode cooling system, and a chain blade tensioner mechanism.

As for the piston skirt processing, there are the conventional molybdenum coating and the micro-dimple (MD) processing [3] adopted on the engine for 'Insight.' Here, a new friction reducing technology was developed which applies these process technologies. Fig. 16 shows the outline of piston skirt molybdenum disulfide (MoS_2) shot peening. In this process, a very fine powder (mean diameter 11μmm, measurement method: sensing zone method) of the solid lubricant MoS_2 is blown at the high pressure of 900kPa, and the heat thus generated causes the MoS_2 to penetrate the piston surface layer. Fig. 16 shows an example of a view with TEM (transparent electron microscope). Through surface changes, molybdenum

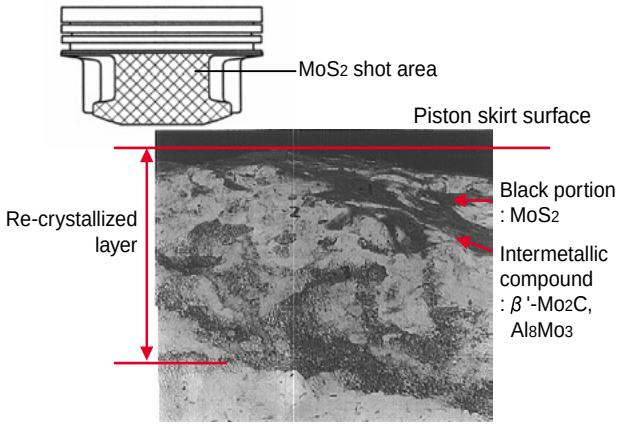


Fig. 16 Piston skirt surface treatnent

disulfide gets into the base material and a 6μmm re-crystallized layer is formed. In addition, an intermetallic compound, which is thought to be caused by the partial thermal expansion phenomena, can be found. Because with the conventional molybdenum coating process an adhesive component is necessary, it is difficult to raise the molybdenum purity level. In comparison, the newly developed MoS_2 shot does not have an adhesive component and is a highly pure MoS_2 shot. Thus, it serves to reduce friction loss and improve lubrication. Consequently, compared with the conventional molybdenum coating there is a friction reduction of 3.2%, and compared with the MD process there is a reduction of 2%. (Fig. 17)

A two-mode cooling system was adopted for the cooling method. Fig. 18 shows the coolant circulation condition when the engine is cold and after warming, according to different cooling methods. When the engine is cold, coolant flows to the cylinder head side, with the aim of increasing the block warm-up speed, in order to reduce friction through the rise in engine oil temperature. Also, after the engine is warm, the warm water that has cooled the cylinder head flows to the block side, maintaining its high temperature and thereby reducing friction. Cooling the cylinder head side first after the engine is warmed up also contributes to the suppression of knocking. Fig. 19 shows a comparison of engine oil temperatures from a cold engine through the warm-up process. Compared with conventional cooling systems, this two-mode cooling system provides a warm-up improvement of 4.2°C at 100 sec. after the start of driving. Fig. 20 shows the relationship between engine oil temperature and friction. The rise in engine oil temperature during the warm-up process gives a friction reduction of approximately 3%.

As for the chain blade tensioner, the structure is such that 5 layers of blades directly push on the chain to maintain tension. Compared with hydraulic tensioners, this system is characterized by there being no unnecessary tension applied to the chain thereby resulting in a reduction in friction.

In addition to these friction-reducing technologies, other technologies have been adopted, such as valve spring load reduction, piston ring tension reduction, and low viscosity engine oil (0W-20/SL/GF3).

Total engine friction is shown in Fig. 21. A 13%

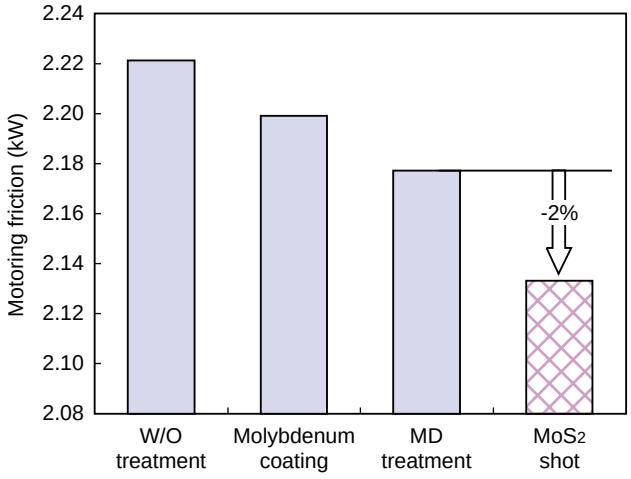


Fig. 17 Improvement of friction loss with piston skirt treatments

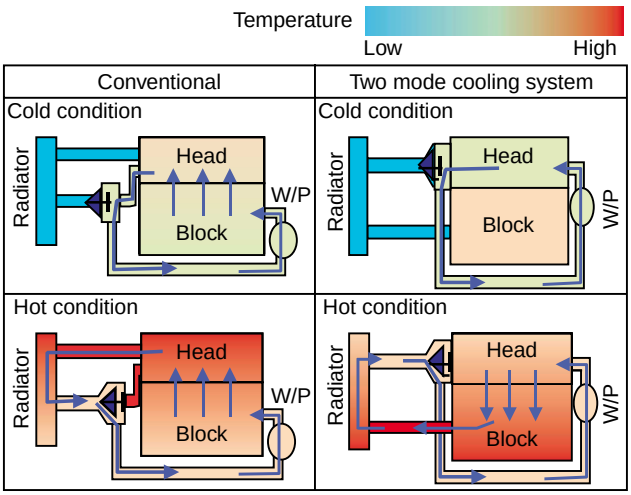


Fig. 18 Coolant of two mode cooling system

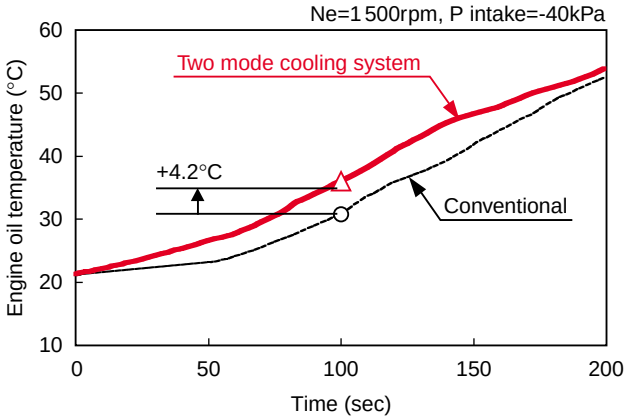


Fig. 19 Characteristics of engine oil temperature

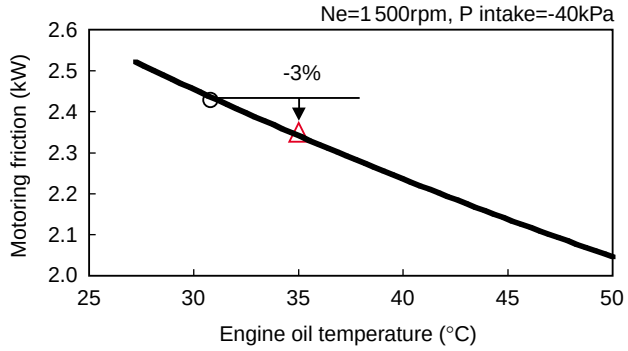


Fig. 20 Influence of engine oil temperature on motoring friction

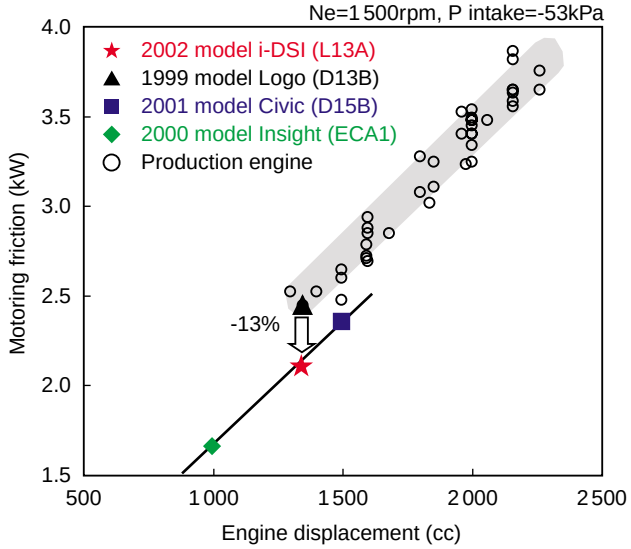


Fig. 21 Friction loss comparison

reduction in friction, as compared with previous engines, was achieved through the adoption of the above-described friction-reducing technologies.

6. Engine Fuel Consumption and Vehicle Fuel Economy

6.1 Engine Fuel Consumption

Fig. 22 shows the relationship between engine displacement and BSFC. By adopting the combustion improvement technologies of dual-point sequential ignition timing control and a higher compression ratio, as well as the friction-reducing technologies described above, this engine achieves an 11% BSFC reduction at stoichiometric combustion compared with previous engines, to thereby achieve a BSFC equivalent to existing lean burn engines. In addition, with combustion that introduces EGR (exhaust gas re-circulation), there is a further 5% BSFC reduction, so that a total BSFC reduction of 16% is provided.

6.2 Vehicle Fuel Economy

Fig. 23 shows the 10-15 mode fuel economy of the vehicle weight of Japanese domestic automobiles. 'Fit' has achieved a 28% improvement in fuel economy compared with the '99 model 'Logo' mounted with a previous engine. The improvement consists of the enhancement of the engine efficiency including control optimization (15%), the application of a newly developed CVT (10%), and the development of a lightweight and low friction body (3%). Achieving 23 km/L in the Japanese 10-15 mode that passes far beyond the 2010 fuel economy standard (17.9 km/L for vehicle weight of 828 to 1015 kg), the Fit deserves the category equivalent to the smallest size (Japanese K-class) vehicles.

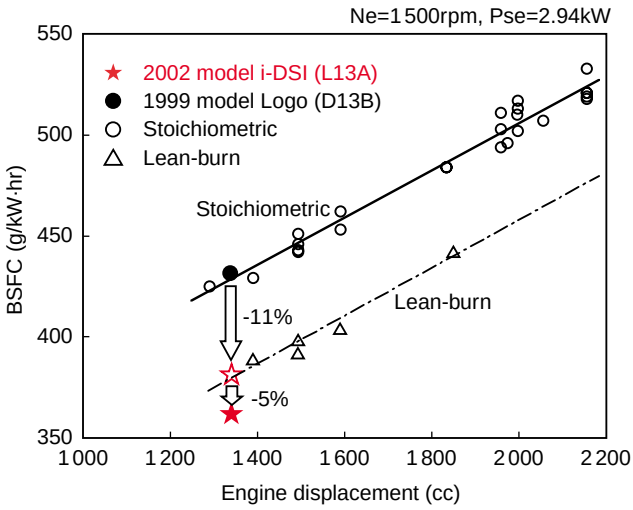


Fig. 22 Improvement of BSFC

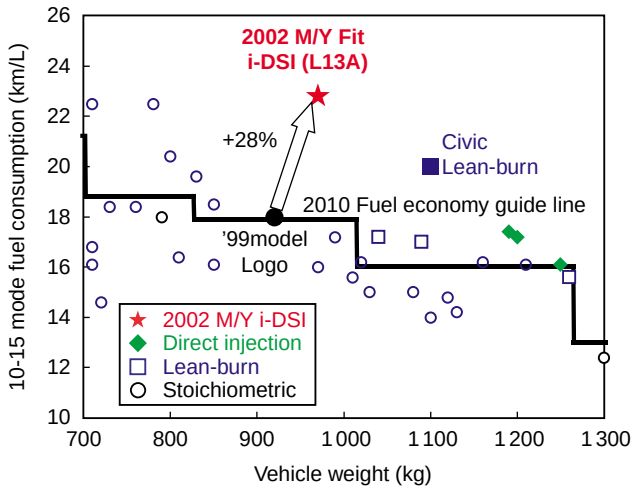


Fig. 23 Relationship between vehicle weight and 10·15mode fuel economy in production gasoline vehicles

7. Low Emissions Technology

7.1 Exhaust System

Fig. 24 shows the exhaust system. By making the exhaust manifold out of lightweight stainless steel tubes, heat mass is reduced. This, in combination with the rearward exhaust system, results in the early activation of the catalytic converter, thereby improving the catalyzing efficiency in the cold range. In the three-way catalytic converter placed under the floor, oblique introduction of exhaust gases is adopted. As the gases come into contact with the surface of the cells obliquely, the contact surface area is increased, and exhaust gas contact is more uniform, catalyzing efficiency is increased.

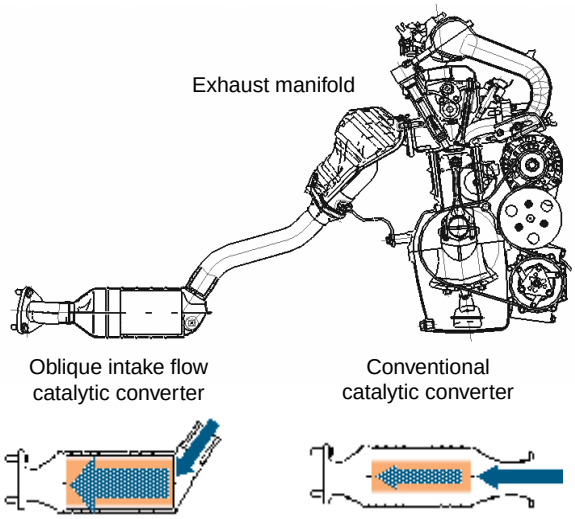


Fig. 24 Configuration of exhaust system

7.2 Multi-hole Injector

Fig. 25 shows the multi-hole injector adopted in this engine. This injector is 17% shorter in length and 58% wider than conventional injectors. In addition, in comparison with the conventional pintle type, a six-hole injection nozzle was adopted. As a result, spray atomization and the amount of gasoline adhesion to the intake port wall is reduced, so that a 5% reduction in HC emissions is achieved from a cold start in the 11 mode (Fig. 26).

7.3 Emissions Achievements

In addition to the emissions reducing technologies outlined above, the adoption of such measures as a reduction in feed gas through dual-point sequential ignition and high-precision electronic EGR valve control, it is possible to achieve the low fuel consumption of 23 km/L in the 10-15 mode, and a 50% reduction in emissions levels compared with the FY2000 regulations (Fig. 27).

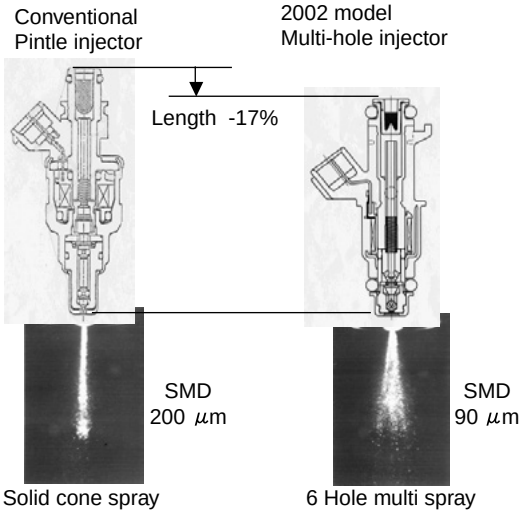


Fig. 25 Comparison of fuel injector between conventional and new one

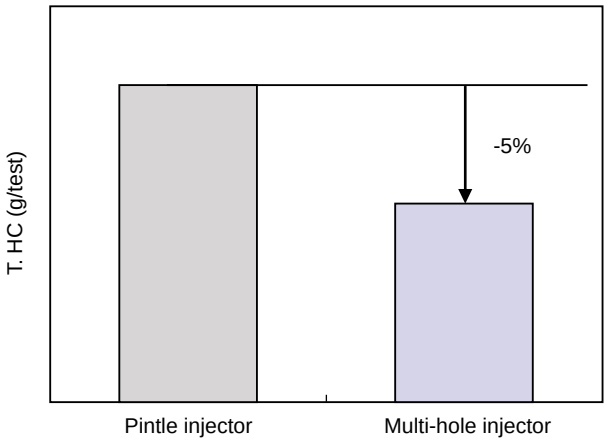


Fig. 26 Comparison of HC emissions in the 11mode between the multi-hole injector and the pintle injector

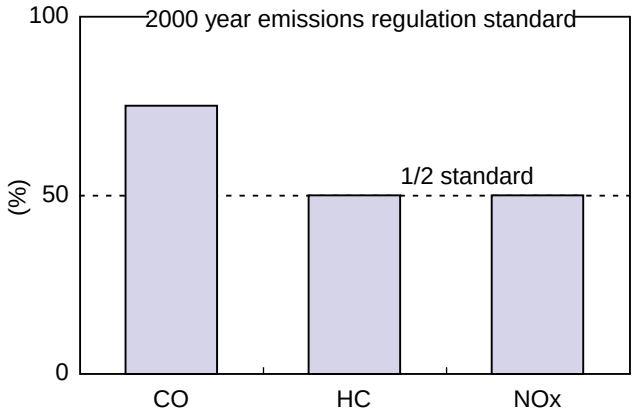


Fig. 27 10-15mode emission

8. Summary

Development of a lightweight compact engine with the i-DSI combustion improvement and the whole friction reduction leads to the followings.

1) Rapid combustion is made possible through the use of dual-point sequential ignition and uniform air-fuel mixture formation achieved with the new intake port and compact combustion chamber. It is also possible to achieve a compression ratio of 10.8 even with regular gasoline. These achievements, in combination with the new friction-reducing technologies, have resulted in the engine attaining a specific fuel consumption reduction of 16%.
2) Through high-precision control of dual-point sequential ignition in response to engine speed and load conditions, it is now possible to achieve good output, torque, and fuel economy as well as noise and vibration reductions.
3) With the adoption of the new L13A engine – with improved combustion and reduced friction– as well as the newly developed small size CVT and high efficient body technologies, a fuel economy level of 23 km/L in the 10-15 mode was achieved. In addition, with the adoption of the oblique exhaust gas intake flow three-way catalytic converter and the rearward exhaust system, a low emissions level, equivalent to a 50% reduction compared to the FY2000 regulations, was achieved (J-LEV certification).

9. Afterword

In order to respond to future environmental changes and customer needs, this newly developed L13A engine has a structure that can be used in derivative engines with larger or smaller capacities. It is firmly believed that this engine will be adopted as the core of our small vehicle strategy in Europe in the future, and that it will come to be widely used as our next generation power train, which has the potential to provide excellent fuel consumption properties and to meet EU2005 regulations.

It is not enough to be satisfied with the current level of refinement, but rather we plan to continue to make further enhancements, seeking to make technological improvements that will meet the demands of the coming era.

Finally, the authors would like to express their deepest appreciation and gratitude to those, both in the company and outside, who gave their cooperation in the development of this engine.

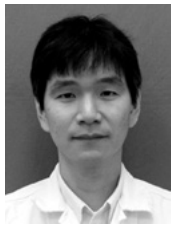
References

1) Niizato, T., Hayashi, A., Development of a New 2.0L Lean-burn Engine, HONDA R&D Technical Review, Vol.12, No.2, p.45-54 (2000)
2) Miura, K., Development of a Lean Burn Engine for Hybrid Vehicles, Journal of the Society of Automotive Engineers of Japan, Vol.54, No.9, p.36-41 (2000)
3) Ogihara, H., Technology for Reducing Engine Rubbing Resistance by Means of Surface Improvement, Society of Powder Impact Technology of Japan (1999)

■ Authors ■



Yukio NAKAYAMA



Makoto SUZUKI



Youichi IWATA



Junji YAMANO

Application of Stereolithography Apparatus to the Investment Casting of Prototype Parts

Sachio KAJIURA* Sadafumi YOSHINO*

ABSTRACT

Concerning investment casting, “decreased cost,” “reduced lead time” and “quick response to design changes,” are often required in the early stages of a project. Thus, stereolithography apparatus (SLA), a typical rapid prototyping technique, has been applied to the master pattern of investment casting prototype parts for our gas turbine engine. Accompanying this new application were problems peculiar to SLA, for example, adhesion of carbonized resin to the surface of the ceramic mold and SLA layer marks. The adhesion problem has been overcome by optimization of the burning conditions and the problem with the layer marks has been overcome with an improved surface finishing method. As a result, prototype parts, which satisfied the design dimension and configuration requirements, could be produced. At the same time, the cost and lead-time were reduced to 1/15 and 1/8, respectively, of those for the conventional method.

1. Introduction

Investment casting of prototype parts for gas turbine engines has traditionally been carried out using the lost wax method. This method requires a metal die to produce wax models through injection molding as a master pattern. This master pattern is used for making a ceramic shell mold to cast the required part. However, this method assumes the part will ultimately be mass produced, and both a significant amount of time and expense are required to produce the metal die. In addition, once the metal die has been produced, it is difficult to quickly respond to design changes.

Thus, there is a call to achieve lower costs, shorter lead-times and quicker response to design changes when producing prototype parts. Various methods have recently been studied in order to attain these three requirements without making a metal die. These methods include a prototype part production method utilizing a so-called “machinable wax,” in which a wax model is machined from a block of wax; and, a method in which prototype part production is carried out by forming the master pattern with a stereolithography apparatus (SLA), in which an ultraviolet-curable resin is cured with a laser[(1)].

Although a metal die is not produced with the method using machinable wax, time is required to create the machining program. In addition, measures need to be taken to handle the sag of wax during the machining of thin-walled portions. This makes it extremely difficult for some contours to be produced. However, once a proper model is made, parts can be cast by the conventional lost wax process.

Stereolithography enables a model represented by three-dimensional CAD data to be formed, regardless of the complexity of the shape. However, there are still problems that remain to be solved such as layer marks on the model surface and the post-molding process being different from that used in the lost wax process[(2) – (4)].

We have thus far attempted casting using a method that uses conventional wax models and a method that uses machinable wax. Moreover, in order to satisfy the three prototyping requirements mentioned above, prototyping of the functional parts of a gas turbine engine was carried out by applying SLA models as the master pattern. This process along with the problems that occurred and their solutions are reported here.

*Wako Research Center (HGF)

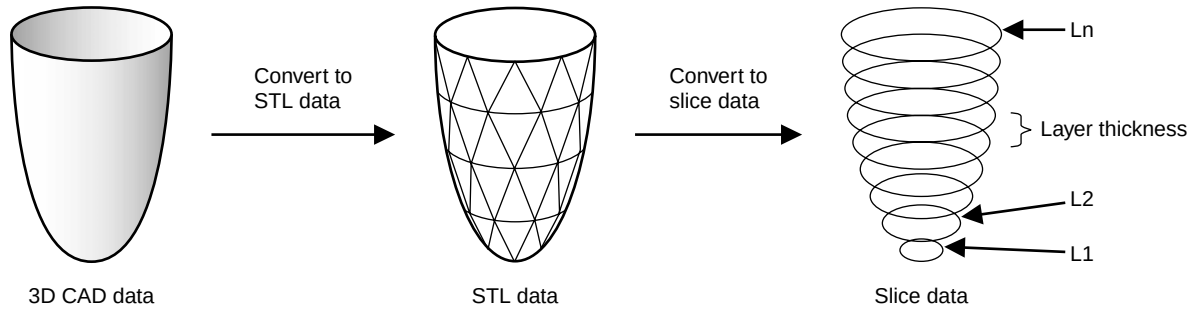


Fig. 1 Data conversion process

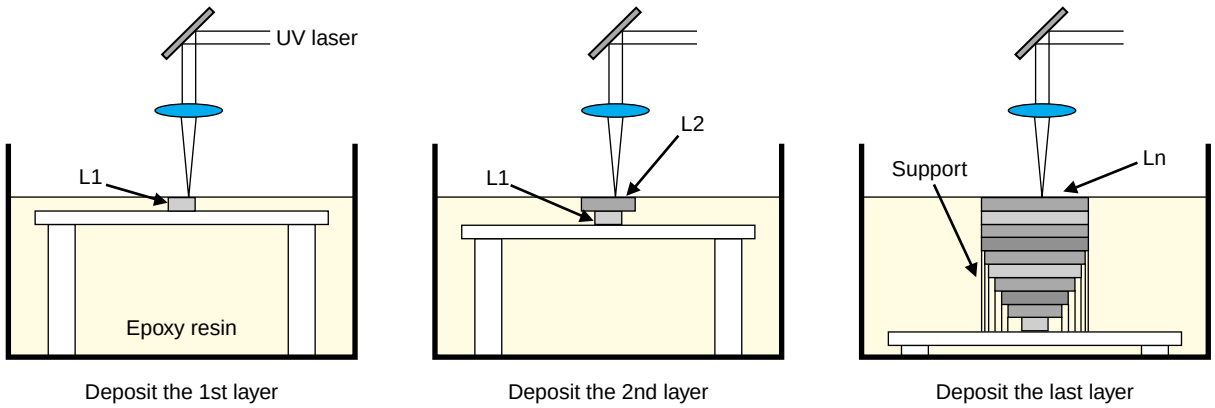


Fig. 2 SLA model deposition

2. The Stereolithography Apparatus (SLA) Forming Method

Rapid prototyping technology, which enables three-dimensional models to be formed directly from three-dimensional CAD data, has evolved rapidly in recent years[5]. Stereolithography apparatus (SLA) is one form of this rapid prototyping technology. SLA enables a model to be produced by irradiating a photocurable resin with an ultraviolet laser to cure the resin. An outline of the SLA forming method is shown in Figs. 1 and 2.

Three-dimensional CAD data is first converted to the stereo lithographic (STL) format, and additionally converted to slice data at the chosen deposition pitch. A table is next placed in a photocurable resin tank. The table is then submerged in a liquid epoxy resin to a depth equal to the deposition pitch, and an ultraviolet laser is used to irradiate the area within the slice data envelope to form the first layer (L1). After forming this first layer, the table is lowered by an amount equal to the deposition pitch, and the second layer (L2) is formed in a similar manner. This process is repeated until the final layer (Ln) is formed to create a three-dimensional model from the deposited layers. Supports are simultaneously formed between the table and any overhanging portions of the model. These supports are removed after the model is completely formed.

SLA models can be formed as solid or hollow models. Solid models have all of the resin cured inside the model and are mainly used for confirming the design and conducting wind tunnel experiments. Hollow models are formed with a thin skin to create a shell of about 0.4 – 1 mm in thickness that is supported by an internal honeycomb structure. When a solid model is used as the master pattern for investment casting, cracking of the ceramic shell mold can occur due to thermal expansion of the resin when the model is burned away. Consequently, hollow models are used for ordinary investment casting. A typical hollow model is shown in Fig. 3.

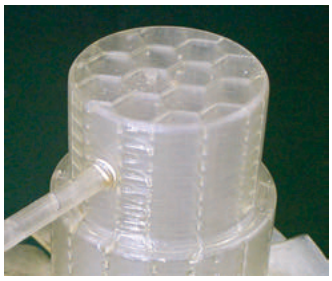


Fig. 3 Hollow model (SLA)

3. Prototyping of a Turbine Nozzle

Fig. 4 shows a turbine nozzle for a gas turbine engine produced by applying SLA to form the master pattern. The investment casting process is described below.

3.1 Component Process

Fig. 5 shows the SLA model of the turbine nozzle which would have been made entirely from wax in the past. SLA can be used to form only for the part itself, with wax being used to form the gating system, consisting of the sprues, runners and gates, used in directing molten metal to the actual part. In this example, the gating system was made with the part by SLA in order to reduce the man-hours required for making and assembling the gating system. The model deposition pitch was set at 0.1 mm, so the curved surfaces of the formed model consist of steps

with a pitch of 0.1 mm. This stepped profile is smoothed to a continuous curved surface by sanding or a similar polishing process. Although described later in detail, if this finishing procedure is inadequate, layer marks are transferred directly to the surface of the cast part resulting in surface defects.

A sprue cup is attached to the finished model and a shaft for molding the ceramic shell mold is positioned to give the complete master pattern of the component, as shown in Fig. 6.

3.2 Molding the Ceramic Shell Mold

The ceramic shell mold is molded around the master pattern. The pattern of the component is immersed in a liquid ceramic slurry to wet the model surface which is next sprinkled with ceramic powder (refractory material) to coat the surface. The model is then allowed to dry. This process is repeated about 10 times with a drying time of 3 – 4 hours between each coating. Ceramic powder with a fine particle size is used for the first layer of the refractory coating to ensure that fine surface details of the master pattern are faithfully reproduced on the surface of the casting. Subsequent layers through the backup layer use refractory material of progressively increasing particle size to ensure adequate strength of the ceramic shell mold. The final green ceramic shell mold has a wall thickness of about 8 – 10 mm.

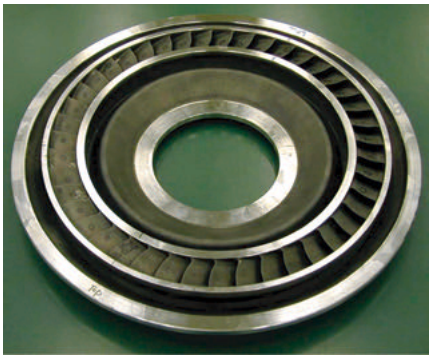


Fig. 4 Turbine nozzle

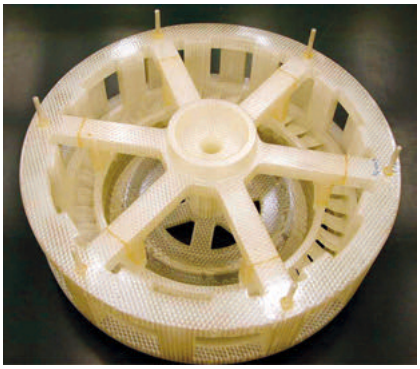


Fig. 5 SLA model of turbine nozzle

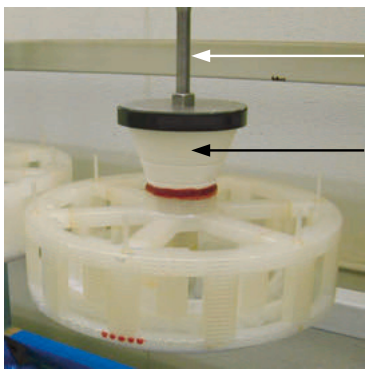


Fig. 6 Turbine nozzle components

3.3 Model Burnoff and Ceramic Shell Mold Sintering

The SLA model remains inside the green ceramic shell mold up to this point. In the next process, this ceramic shell mold is placed in a kiln, and the temperature inside the kiln is incrementally raised to the firing temperature of the epoxy resin (approximately 400°C) to burn off the material of the SLA model. The temperature is further raised to approximately 1000°C and then maintained for several hours to sinter the ceramic shell mold. Fig. 7 shows the finished ceramic shell mold.

If the resin has not been sufficiently burned off, a carbonized deposit remains inside the ceramic shell mold adhering to its internal surface. If the resulting profile of this deposit is transferred directly to the surface of the casting, it causes a surface defect known as "orange peel." The specific measures for the orange peel defect are described later.

3.4 Casting

The material used for casting was a Ni-based superalloy. A vacuum melting furnace was used for casting this superalloy to ensure that the mechanical properties of the material were satisfactorily obtained and to reduce misruns into portions having a complex shape. The ceramic shell mold is heated in the vacuum melting furnace to approximately 1000°C and, after being held at this temperature for about 1 hour, the molten material, with a temperature of approximately 1500°C, is poured into the mold and the mold is then allowed to cool. Fig. 8 shows the as-cast state of the turbine nozzle after the ceramic shell mold is taken apart and cleaned.

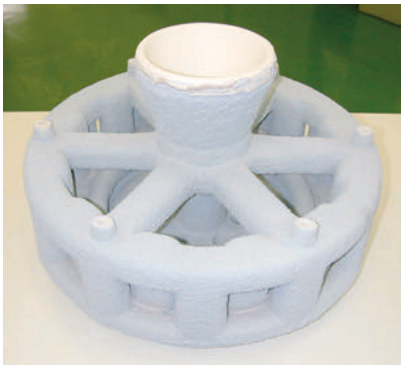


Fig. 7 Ceramic shell mold of a turbine nozzle



Fig. 8 As-cast turbine nozzle with gating system

3.5 Removing the Gating System and Machining

The gating system is removed from the resulting casting and, after undergoing a solution heat treatment and aging treatment, the casting is machined. A dimensional inspection confirmed that the finished dimensions of the cast component satisfied the dimensional tolerance for investment-casting standards as stipulated by JIS.

4. Problems and Solutions

4.1 Orange Peel Defect

The phenomenon by which carbonized resin adhering to the internal surface of the ceramic shell mold after burning off the SLA model is directly transferred to the casting surface is referred to as the "orange peel" defect. Fig. 9 shows the residual carbide adhering to the internal surface of the ceramic shell mold, while Fig. 10 shows the resulting orange peel defect on the surface of a casting.

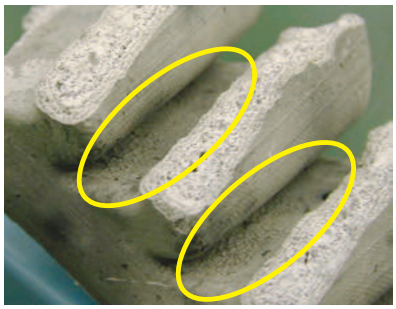


Fig. 9 Carbide adhesion (Mold)



Fig. 10 Orange peel (casting)

Orange peel is characterized by the formation of an infinite number of hairline cracks in close proximity to the surface of the casting, and results in a significant decrease in the mechanical strength of the component. A fluorescent dye penetrant inspection, which is one of the non-destructive inspections performed on cast parts, reveals the presence of such defects over the entire surface.

In order to solve this problem, the fan-shaped test piece shown in Fig. 11 was made by SLA and, after molding the ceramic shell mold, a combustion test was performed by three different methods. (The ceramic shell mold shown in Fig. 11 was molded to the second layer.)

(1) Conventional method: The ceramic shell mold was placed directly into a kiln.
(2) Air blowing method: Hot air was blown through an opening into the ceramic shell mold.
(3) Air blowing and air venting method: Air was blown through an opening into the ceramic shell mold and then vented through a hole created in the opposite side.

The heating conditions for the kiln were the same for all three methods.



Fig. 11 Test piece

The conventional method resulted in residual carbide adhering to the inside of the ceramic shell mold (Fig. 12). Hot air blown into the mold offered some improvement, although carbide was observed to be adhering to some areas inside of the mold since there was no air flow inside without venting (Fig. 13). When hot air was blown in and then vented, however, no adhesion of carbide whatsoever was apparent on the inside of the ceramic shell mold (Fig. 14).

For prototyping of turbine nozzles, hot air was supplied by placing a stainless steel tube inside the ceramic shell mold during model burnoff. By simultaneously discharging this air through a vent in the outer periphery of the ceramic shell mold, the resin was burned off completely, thereby inhibiting the orange peel defect.



Fig. 12 Carbide adhesion (Usual burning condition)



Fig. 13 Carbide adhesion (Air blowing)



Fig. 14 No adhesion (Air blowing and air vent)

4.2 Layer Marks and Support Marks

An SLA model is layered, so curved surfaces are formed in a series of steps, the height or each step being equal to the layer thickness. Normally, as shown in Fig. 15, slice data are offset outside the model profile. Consequently, after layering, it is necessary to remove the stepped surface to achieve the required surface profile of the model. In addition, supports may have been incorporated, depending on the shape, and those supports must also be removed.

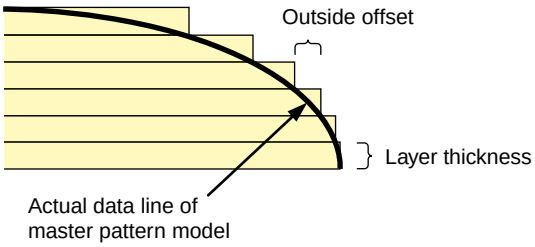


Fig. 15 Offset of slice data

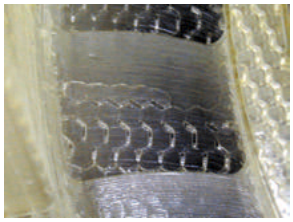


Fig. 16 Layer mark (SLA)

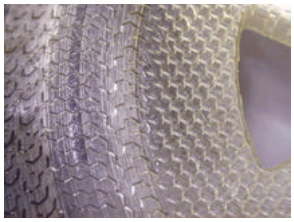


Fig. 17 Remains of support (SLA)

However, as shown in Figs. 16 and 17, since the SLA model is translucent, it is difficult to accurately determine the required finished profile by visual means alone.

When finished by simple visual observation, the layer marks and support marks shown in Fig. 18 and the presence of removed support debris shown in Fig. 19 were apparent on the surface of the casting, clearly indicating that the finished state of the model was inadequate.

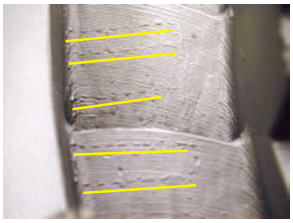


Fig. 18 Layer mark and remains of support (casting)

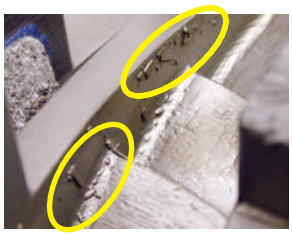


Fig. 19 Remnants of removed support (casting)

Although it is necessary to carefully finish the model to avoid these problems, it is difficult to determine the surface condition since the model is translucent. This problem was solved by applying a primer to the model surface to allow its surface condition to be visually confirmed. Figs. 20 and 21 show the primer-coated surface of the SLA model in the same finished state as that shown in Figs. 16 and 17. The color appeared closer to that of a casting, and the finished state of the surface was more easily apparent.

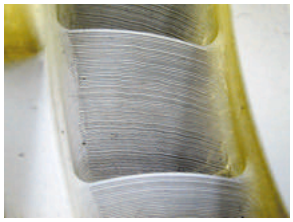


Fig. 20 Primer coated surface of SLA model (Layer mark)

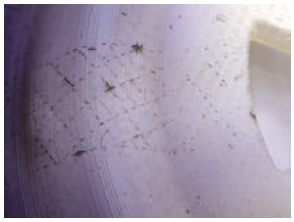


Fig. 21 Primer coated surface of SLA model (Remains of support)

A model finished after being coated with primer is shown in Fig. 22. The finished state obtained without the primer coating shown in Fig. 16 had a surface roughness of Rz = 70 to 100. On the other hand, the finished state obtained by coating with the primer shown in Fig. 22 demonstrated an improved surface roughness of Rz = 10 to 15.



Fig. 22 Finished surface of SLA model (Primer coated)

4.3 Wavy Lines on the Layered Surfaces

The SLA model is formed by converting three-dimensional CAD data into an STL format, generating slice data according to the defined layer thickness, and forming the model based on that data. Consequently, laser scanning is determined by the envelope defined by the slice data, resulting in the final shape of the model. A surface is represented in the STL format by the pitch of a series of interlinked triangles as shown in Fig. 23. Since the laser scans the sides of those triangles, rather than a smooth curve, a wavy line is generated as shown in Fig. 24. Fig. 25 shows these wavy lines reproduced on the casting surface, and Fig. 26 shows the laser scanning lines from the data. Even if the steps between layers of the model are removed by polishing in this state, the wavy lines remain and the skin thickness of the surface layer becomes inconsistent.

In order to correct this, the process called “Z smoothing” was performed on the STL data to obtain a smooth curve from the slice data as shown in Figs. 27 and 28. No wavy lines were apparent when the model was formed from data subjected to Z smoothing.

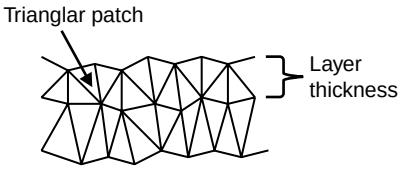


Fig. 23 Image of STL data model

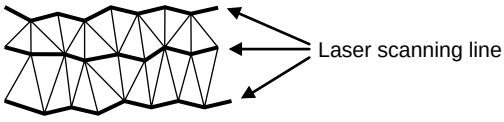


Fig. 24 Image of laser scanning line

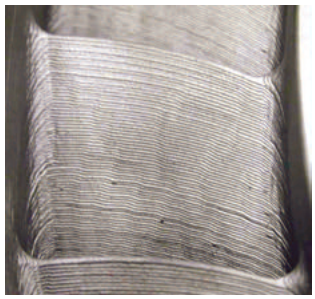


Fig. 25 Wavy lines on blade surface (casting)

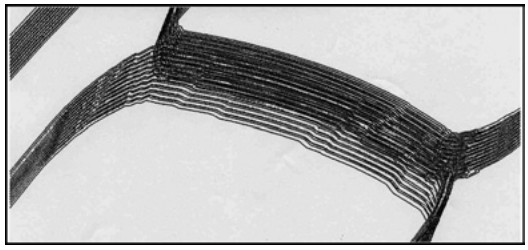


Fig. 26 Laser scanning line on data without Z smoothing

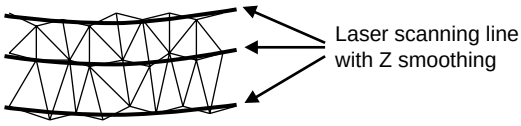


Fig. 27 Image of laser scanning line with Z smoothing

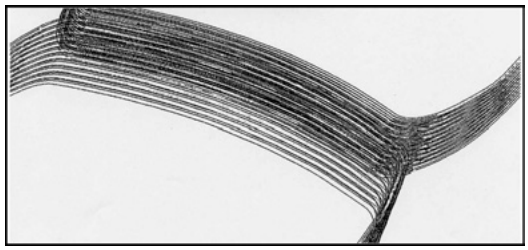


Fig. 28 Laser scanning line on data with Z smoothing

5. Comparison of Cost, Lead Time and Response to Design Changes

A comparison of cost, lead-time and response to design changes was made for the conventional lost wax method, the machinable wax method, and the SLA method. The comparison was based on the prototype turbine nozzle described in this paper. The comparison results are shown in Table 1. The cost indicated is for production of one model and is based on a value of 100% for the lost wax method; the lead time refers to the time required to complete the master pattern from three-dimensional CAD data.

The SLA method enabled the cost to be reduced to about 1/15 and lead time to about 1/8 compared with the conventional lost wax method. In addition, design changes could be accommodated more easily with the SLA method than with the conventional methods.

Table 1 Comparison of cost, lead-time, design change response

	Metal mold	Machinable wax	SLA
Cost (%)	100	13	7
Lead time (month)	4.0	1.5	0.5
Response to design revision	Difficult	Difficult	Easy

6. Summary

A turbine nozzle prototype was produced by applying stereolithography (SLA) to form the master pattern. Problems unique to the SLA method were revealed such as the adhesion of the resin, which remained after burning out the SLA model, to the inside of the ceramic shell mold, and the presence of layer marks on the surface of the SLA model. The problem of residual resin was solved by ensuring complete combustion of the resin by blowing hot air through the ceramic shell mold during burn out and discharging this hot air through a vent in the periphery of the mold. In addition, the problem of the layer marks was solved by coating the model surface with a primer to give better visualization of the surface to thereby enable finishing to a greater surface smoothness.

These actions enabled a turbine nozzle to be produced that satisfied the dimensional tolerance standards for investment casting as stipulated by JIS. At the same time, the master pattern production cost was reduced to about 1/15, and the lead-time decreased to about 1/8 of the figures for the conventional lost wax process.

We intend to proceed further with the application of stereolithography to cast parts, with the gating system, having different shapes from the turbine nozzle studied thus far.

Acknowledgments

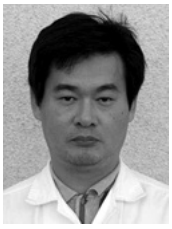
The authors express their appreciation to those at INCS INC. who cooperated in producing the SLA models.

References

(1) Imamura, M.: Application of RP Models to Investment Casting, JACT News, June 20, 1998, pp. 27 – 36 (1998).
(2) Arato, K., et al.: Development of Investment Casting Parts by Rapid Prototyping, Miyagi Prefecture Industrial Technology Center Research Report No. 27, pp. 49 – 51 (1996).
(3) Arato, K., et al.: Development of Investment Casting Parts by Rapid Prototyping, Miyagi Prefecture Industrial Technology Center Research Report No. 28, pp. 62 – 64 (1997).
(4) Arato, K., et al.: Development of Investment Casting Parts by Rapid Prototyping, Miyagi Prefecture Industrial Technology Center Research Report No. 29, pp. 34 – 38 (1998).
(5) Narahara, H.: Current Status of Rapid Prototyping Technology, Precision Engineering Journal, Vol. 67, No. 3, pp. 403 – 406 (2001).

■ Authors ■


Sachio KAJIURA


Sadafumi YOSHINO

Adaptive Sliding Mode Control for Secondary O_2 Feedback (Third Report)

—Improvement of Adaptability by Using Prediction and Identification Sliding Mode Control—

Yuji YASUI* Shusuke AKAZAKI*
Hiroshi KITAGAWA* Yoshihisa IWAKI*

ABSTRACT

Secondary O_2 feedback is one effective method for reducing vehicle emissions, and the improvement of this performance yields even greater emissions reductions. This report details a significant advance in the algorithm for the sliding mode controls that were described in our first and second reports, and the application of this newly designed algorithm to secondary O_2 feedback. The results show that feedback control performance was significantly improved under all engine loads and catalyst aging conditions. Moreover, the FTP mode emissions were reduced by 32 - 42%, and the emissions stability with respect to catalyst aging conditions was dramatically improved.

1. Introduction

The first[1] and second[2] reports explained secondary O_2 feedback[1] – [5] methods improved by modeling an exhaust system including a catalyst by the use of an auto-regressive exogenous model[6] and by applying an adaptive sliding mode control[1], [7] and prediction sliding mode control[2] which have high robust stability. However, the difficulties in improving the performance of secondary O_2 feedback remained. These include:

(1) Stability improvements relative to the nonlinear dynamic characteristic of the catalyst
(2) Stability improvements relative to the dead time characteristic of the catalyst
(3) Adaptability relative to changes in catalyst response characteristics due to catalyst aging conditions and engine load conditions.

However, the previous algorithm did not have sufficient stability with respect to item (3).

Therefore, a prediction and identification sliding mode control[8], [9] was designed by the addition of an identifier to the prediction sliding mode control explained in the second report. The identifier successively calculates (identifies) the parameters of the exhaust system model and resolves the outstanding difficulty outlined above.

This report describes the design method for the improved control algorithm and its effect on control performance and reducing emissions.

2. Background and Approach

2.1 Focus on Reducing Emissions

Fig. 1 shows the layout of the catalyst and sensors generally used in engines adopting secondary O_2 feedback. In this example, a linear air-fuel ratio sensor is positioned upstream of the catalyst (the diagram's Universal Air-Fuel Ratio Heated Exhaust Gas Oxygen sensor: UEGO sensor),

* Tochigi R&D Center

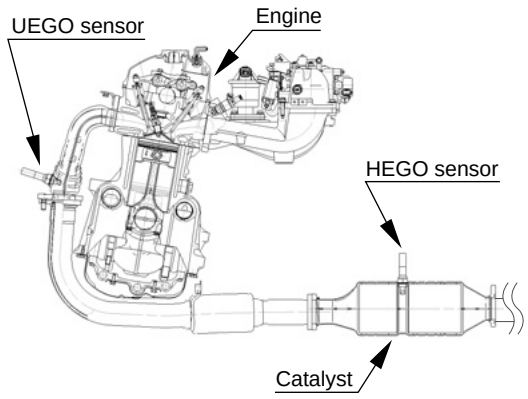


Fig. 1 Layout of sensors and the three-way catalyst

and a secondary O_2 sensor downstream (the diagram's Heated Exhaust Gas Oxygen sensor: HEGO sensor).

In the engine in the figure, the output of the linear air-fuel ratio sensor, according to the air-fuel ratio in the air-fuel mixture, is defined as ϕin. The output voltage of the secondary O_2 sensor, according to the exhaust gas composition after the catalyst, is defined as Vout. Furthermore, the CO, HC, and Nox concentrations upstream and downstream of the catalyst according to the engine operating air-fuel ratio were acquired by an exhaust gas analysis device; the catalyst conversion rates at each exhaust gas volume condition were calculated on the basis of those concentrations as shown in Fig.2. Fig.2 shows the relation between Vout and the exhaust gas volume when the catalyst conversion rates for the CO, HC, and NOx are each 90% or more. In the graph, when Vout indicates the optimum value around 0.6V (referred to as Vop hereafter), the catalyst conversion rate is optimized regardless of the exhaust gas volume conditions. However, this trend at exhaust gas volumes below 2000L/h is obscure due to the insufficient precision of the exhaust gas analysis device.

Therefore, regardless of the engine load conditions or the catalyst aging conditions, constantly controlling Vout to the fixed target Vop is the best way to optimize the catalyst conversion rate of the engine-exhaust system used in this system. In this report, controlling Vout at Vop is achieved by improving the controllability of the secondary O_2 feedback.

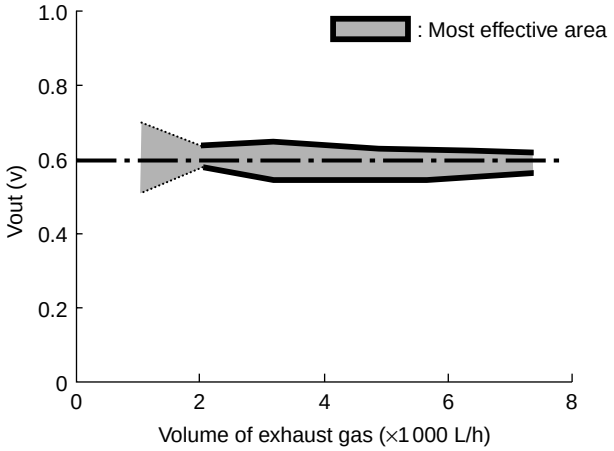


Fig. 2 Relation between the most effective catalyst conversion rate range and exhaust gas volume

2.2 Technical Issues Related to Secondary O_2 Feedback

As mentioned previously, in order to improve the controllability of the secondary O_2 feedback, it is necessary to improve the stability of the following catalyst characteristics.

1) Non-linear dynamic characteristics
2) Dead time characteristics
3) Change in dynamic characteristics due to engine load conditions and catalyst aging conditions.

Each of these will be discussed in detail below.

2.2.1 Non-linear dynamic characteristics of the catalyst

Fig. 3 shows the ϕin and Vout data when ϕin is oscillated in a sine wave pattern with a frequency of 0.2Hz and an amplitude of 0.2A/F under catalyst aging condition equivalent to 50,000 miles and under 50mph cruise condition. In the graph, the response of Vout according to the ϕin change from lean to rich is different from that of from rich to lean. This is the non-linear dynamic characteristic of the catalyst caused by the chemical reaction change of the catalyst according to the direction of ϕin change.

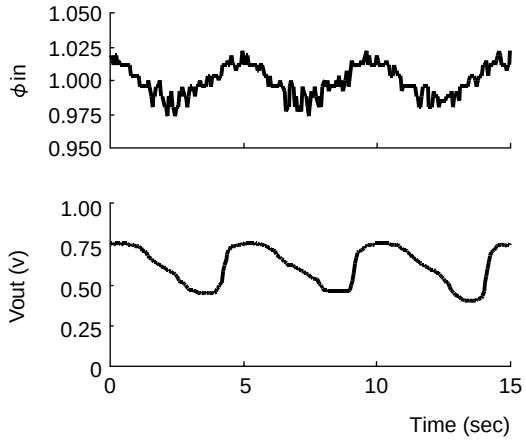


Fig. 3 Nonlinear characteristics of a catalyst

2.2.2 Dead time characteristics of the catalyst

Fig. 4 shows the ϕin and Vout data when ϕin is changed in a step pattern under catalyst aging condition equivalent to 120,000 miles. In the graph, corresponding to the ϕin lean to rich reversal, the Vout reversal has an ineffective period. This is the dead time characteristic of the catalyst, which mainly occurs due to the oxygen absorbing and storing characteristic of the catalyst.

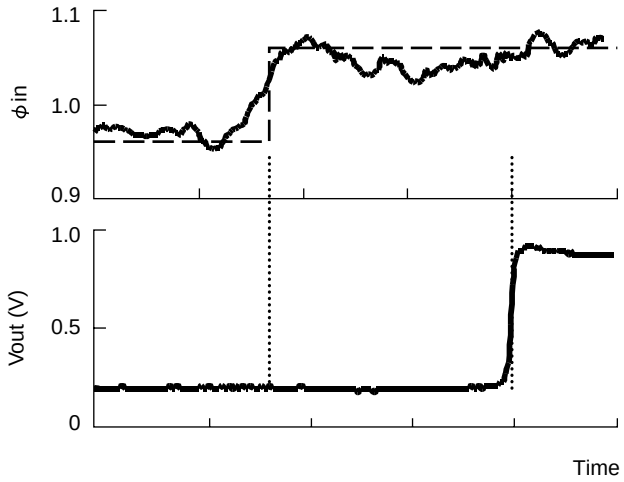


Fig. 4 Dead time characteristics of a catalyst

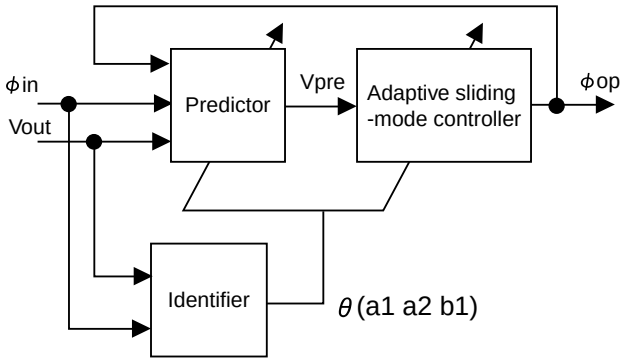


Fig. 6 Prediction and identification sliding mode control (PRISM)

2.2.3 Changes in the dynamic characteristics of the catalyst

Fig. 5 shows the power spectra from the Fourier transformation of the Vout measured when using catalysts aged to the equivalents of 50,000 miles and 200,000 miles under 50 mph cruise conditions. In the graph, as the deterioration proceeds, power spectra at each frequency increases. Furthermore, the trend rises, as the frequency becomes higher. This shows that the dynamic characteristics of the catalyst change according to catalyst aging conditions.

In addition, when engine load conditions change, the same dynamic characteristics change can be seen. In this case, when engine load conditions change to the high load direction, catalyst dynamic characteristics change in the same direction that they do in the catalyst aging process.

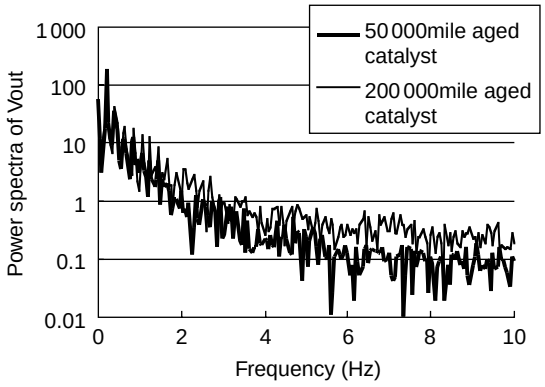


Fig. 5 Frequency characteristics of catalysts

2.3 Resolution Methods

In order to improve the stability of secondary O_2 feedback with respect to the three catalyst characteristics stated above, and to maximize the catalyst conversion rate, a new control algorithm, the Prediction and Identification Sliding Mode control (referred to as PRISM hereafter) was designed. As shown in Fig. 6, PRISM is composed of the following three elements.

1) An adaptive sliding-mode controller
2) A predictor
3) An identifier

The identifier determines model parameter θ (a1, a2, b1) of the exhaust system model explained below on the basis of the changes in catalyst dynamic characteristics. This adapts the sliding-mode controller and the predictor to those changes.

The predictor calculates Vpre, which is the prediction value of Vout, on the basis of θ, Vout, ϕin, and the target value for ϕin (referred to as ϕop hereafter) in order to compensate for the dead time characteristics of the catalyst.

The sliding-mode controller compensates for the modeling error in the exhaust system model described below and for the non-linear dynamic characteristics of the catalyst by using its robustness. Furthermore, it calculates ϕop in order to control Vout to Vop on the basis of θ and Vpre.

Consequently, PRISM resolves the three aforementioned issues by combining three elements, and it provides an accurate convergence of Vout to Vop.

Furthermore, Fig. 7 is a block diagram of the total fuel control system using PRISM. In the system, ϕop is calculated by PRISM and STR (Self-tuning Regulator) [10] is applied to the air-fuel ratio control upstream of the

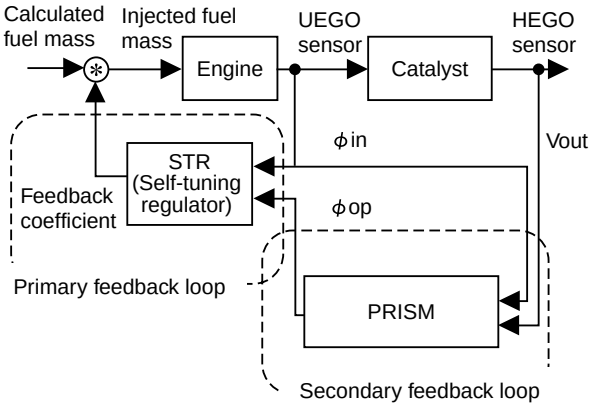


Fig. 7 Overall configuration of the double feedback loop

catalyst in order to control ϕin to ϕop. As a result, this double feedback loop composed of PRISM and STR achieves Vout convergence on converged Vop.

Details are provided below.

3. Modeling

In the air-fuel ratio control system shown in Fig. 7, the combination of STR, the engine, and the exhaust system up to the linear air-fuel ratio sensor is defined as the engine system, and the exhaust system, including the catalyst, from the linear air-fuel ratio sensor to the secondary O_2 sensor as the controlled object. Modeling for each of these systems is described below.

3.1 Engine System Modeling

The control system shown in Fig. 7 controls Vout by operating ϕin. Therefore, it is necessary to have ϕin follow ϕop in a highly accurate manner. However, the fuel transportation dynamics and combustion cycle of the engine cause dead time and lag characteristics between ϕop and ϕin. Therefore, it is necessary to compensate for these dynamic characteristics. However, as stated previously, the air-fuel ratio control system composed of PRISM and STR has a double feedback loop structure. Consequently, these two feedback loops overlap at the engine system, and cause interference.

Fig. 8 shows the ϕin response wave, when controlled by STR, for the rectangular wave ϕop. As can be seen from the graph, ϕin is the ϕop waveform shifted roughly with the de. This means that the lag characteristic of the engine system is sufficiently compensated for by STR. Therefore, the engine system can be thought to be a dead time element.

Consequently, in order to prevent interference of the double feedback loop, focus was placed on the relationship between ϕin and ϕop. As shown in Fig. 7, STR only compensates for engine system delay characteristics. Therefore, if PRISM does not carry out compensation for the lag characteristic of the engine system, the interference of the double feedback loops is prevented. Accordingly, in order to prevent interference, the roles of STR and PRISM are divided as follows. STR compensates for the lag characteristic of the engine system; and PRISM assumes that the engine system is the generator of ϕin, not one of its controlled objects, and it considers only the dead time characteristics of the engine system when controlling Vop.

Here, because the engine system does not have a lag characteristic, it is modeled as a dead time element as shown below.

$$\phi in(k) = \phi op(k\text{-}de) \quad (1)$$

k : control time
de : engine system dead time

3.2 Exhaust System Modeling

The exhaust system including the catalyst, which is the controlled object for PRISM, as shown in Fig. 4 and Fig. 5, has low pass characteristics. That is to say, it has a lag characteristic and a dead time characteristic.

Considering this and the ease of on-board identification of model parameters by the identifier, a controlled object model was created using a DARX model (Delayed Auto-regressive eXgeneous model, an auto-regressive model that has dead time in the input).

$$VO2(k+1) = a1\ VO2(k) + a2\ VO2(k-1) + b1\ KACT(k-d) \quad (2)$$

$$VO2(k) = Vout(k) - VO2_TARGET \quad (3)$$

$$KACT(k) = \phi in(k) - KACT_BASE \quad (4)$$

a1, a2, b1	: Model parameters
VO2(k)	: Deviation between Vout and Vop
VO2_TARGET	: Target value Vop
KACT(k)	: Deviation between ϕin and KACT_BASE
KACT_BASE	: Standard value for ϕin
d	: Dead time of the exhaust system

4. Control Algorithm

The equations for the identifier, the predictor, and the adaptive sliding-mode controller, which comprise PRISM, are described below.

4.1 Identifier

The Weighted Recursive Least Squares method (WRLS hereafter) is generally known as an identification algorithm for the model parameters in the DARX model given in Equation (2).

This algorithm can successively renew model parameters according to the change in dynamics of a controlled object. Therefore, it is useful for adaptive controls.

However, Fig. 9 shows the identification weight at each frequency of the identification algorithm. Here, it can be seen that when the model parameters of the controlled object having low pass characteristics, as shown in Fig. 5, are identified by the identifier, the higher the frequency, the higher the identification weight as shown by the broken line in the graph. That is to say, the gain characteristics of the controlled object at high frequencies are stressed, when the

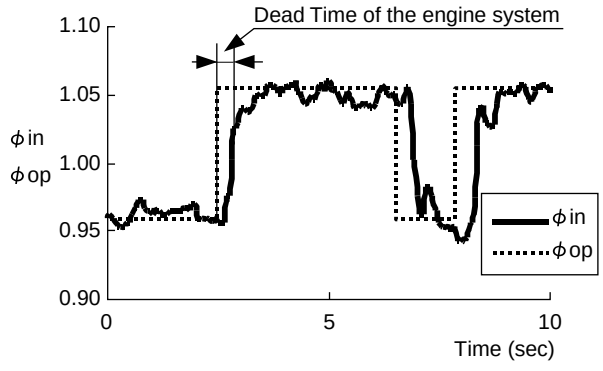


Fig. 8 Time series data of ϕin controlled by STR

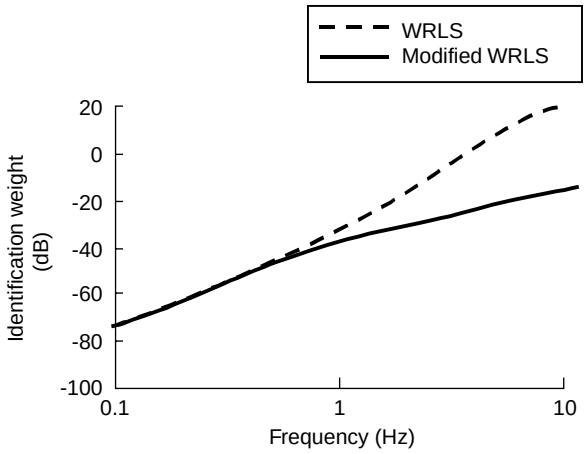


Fig. 9 Identification weight characteristics of basic and modified WRLS algorithms

controlled object model is identified[11]. Fig. 10 shows the gain characteristics of the controlled object and the model. In the graph, the gain of the model identified by WRLS is smaller than the actual object. This is because the identification weight of WRLS emphasizes the cut-off characteristics of the controlled object at high frequencies. Such gain characteristics of the model make the compensation by the adaptive sliding-mode controller larger than needed, and deteriorates Vout controllability.

Therefore, in order to improve the identification weight of WRLS, the identification algorithm was modified, as shown in Equations (5) – (12).

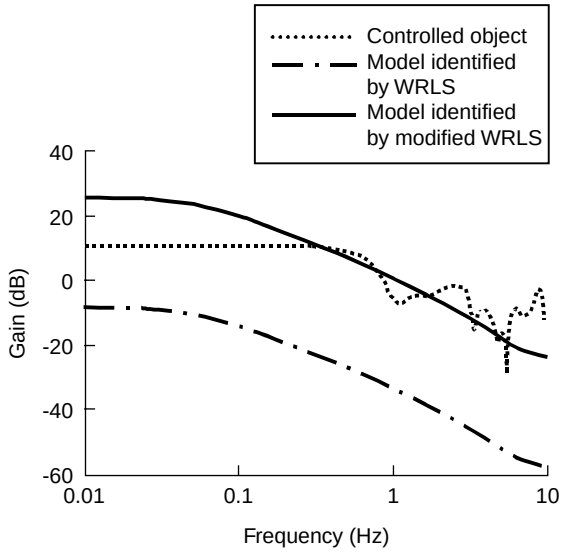


Fig. 10 Frequency characteristics comparison between the controlled and identified models

$$\theta(k+1) = \theta(k) + KP(k)\, e_id_f(k) \quad (5)$$

$$e_id_f(k) = Fid(e_id(k)) \quad (6)$$

$$e_id(k) = VO2(k) - VO2_hat(k) \quad (7)$$

$$VO2_hat(k) = \theta(k)^T \zeta(k-1) \quad (8)$$

$$KP(k) = \frac{P(k)\zeta(k-1)}{1 + \zeta^T(k-1)P(k)\zeta(k-1)} \quad (9)$$

$$P(k+1) = \frac{1}{\lambda}\left(I - \frac{P(k)\zeta(k-1)\zeta^T(k-1)}{\lambda + \zeta^T(k-1)P(k)\zeta(k-1)}\right)P(k) \quad (10)$$

$$\theta^T = [a1\ a2\ b1] \quad (11)$$

$$\zeta^T(k) = [VO2(k)\ \ VO2(k-1)\ \ KACT(k-d)] \quad (12)$$

Fid() : low pass filter
I : unit matrix
λ : Weighting parameter ($0<\lambda<1$)

In the above algorithm, Equation (5) calculating θ is altered by replacing the identification error e_id used by conventional WRLS with the low pass filtered e_id (e_id_f hereafter). This improves the identification weight as shown by the solid line in Fig. 9. The identification weight at high frequencies according to the above algorithm is lower than by conventional WRLS. Further, the gain characteristics of the model identified by the modified WRLS are improved by correcting the identification weight with the low pass filter Fid, as illustrated with the solid line in Fig. 10. Accordingly, the above-mentioned over-compensation by the controller is suppressed.

4.2 Predictor

In order to explain the prediction algorithm, the deviation value of ϕop from the standard value KACT_BASE for ϕin is defined.

$$KCMD(k) = \phi op(k) - KACT_BASE \quad (13)$$

KCMD(k): Deviation between ϕop and the standard value

Here, the engine system model expressed by Equation (1) becomes the equation below.

$$KACT(k) = KCMD(k-de) \quad (14)$$

In Section 3 it was explained that the engine system had lag and dead time characteristics, and that STR compensates for lag characteristics and PRISM assumes the system to be a dead time element in order to prevent interference between STR and PRISM.

The engine system is not the controlled object for PRISM, but rather it is an exhaust gas generator, which creates ϕin. That is to say, giving the example of a manipulator control, the engine system is equivalent to an actuator of a manipulator. However, because the engine system has dead time de, dead time exists until ϕop is reflected to ϕin. Therefore, this dead time deteriorates the stability and control performance of PRISM.

Accordingly, a total dead time dt is defined by PRISM by adding the dead time of the engine system, de, de to the dead time of the controlled object d, as shown below.

$$dt = d + de \quad (15)$$

Moreover, PRISM compensates for d by predicting VO2.

In order to accomplish this, a prediction algorithm[13] is applied. That is, the algorithm described by the equation below is used to calculate the prediction value VO2p(k) for VO2(k+dt).

$$VO2p(k) = \alpha 1\, VO2(k) + \alpha 2\, VO2(k-1) + \sum_{i=1}^{dt} \beta i\ KACT(k+de-i) \quad (16)$$

$$Vpre(k) = VO2p(k) + Vop \quad (17)$$

$$A = \begin{bmatrix} a1(k) & a2(k) \\ 1 & 0 \end{bmatrix} \quad (18)$$

$$B = \begin{bmatrix} b1(k) \\ 1 \end{bmatrix} \quad (19)$$

$\alpha 1$: A^{dt} first row, first column element
$\alpha 2$: A^{dt} first row, second column element
βj : $A^{dt-1}B$ first row element

However, because Equation (16) uses the unknown future values of KACT, KACT(k+de-1) ~ KACT(k+1), meaning ϕin, this equation is not possible to execute.

Thus, focusing on Equation (14), KCMD can be used as a substitute for the future values of KACT because STR sufficiently controls ϕin to ϕop.

$$KACT(k+de-1) \fallingdotseq KCMD(k-1) \quad (20)$$

Accordingly, the executable algorithm using KCMD is created as below.

$$VO2p(k) = \alpha 1\, VO2(k) + \alpha 2\, VO2(k-1) + \sum_{i=1}^{de-1} \beta i\, KCMD(k-i) + \sum_{j=de}^{dt} \beta j\, KACT(k+de-j) \quad (21)$$

4.3 Adaptive Sliding-Mode Controller

As stated above, the predictor compensates for dead time dt by calculating VO2p, and the identifier compensates for the dynamic characteristic change of the controlled object by identifying model parameters a1, a2 and b1. Therefore, in order to achieve superior control performance for VO2 while maintaining stability with respect to dead time and the dynamic characteristic changes of the controlled object, the adaptive sliding-mode controller should determine ϕop on the basis of VO2p and identified model parameters.

Accordingly, the adaptive sliding-mode controller should determine ϕop to meet the equation below.

$$Vop = Vpre(k) \fallingdotseq VO2''(k+dt) \quad (22)$$

In other words, the control subject of the controller is as follows.

$$VO2p(k) = 0 \quad (23)$$

At this time, the switching function σ to achieve Equation (23) is as follows.

$$\sigma(k) = VO2p(k) + S\, VO2p(k-1) \quad (24)$$

S: Switching function parameter

The equations for calculating ϕop on the basis of the switching function σ are as follows.

$$\phi_{op} = Ueq(k) + Urch(k) + Uadp(k) + KACT_BASE \quad (25)$$

$$Ueq(k) = \frac{-1}{b1}\{(a1-1) + S\}VO2p(k) + (a2-S)VO2p(k-1)\} \quad (26)$$

$$Urch(k) = \frac{-1}{b1} F\, \sigma(k) \quad (27)$$

$$Uadp(k) = \frac{-1}{b1} G \sum_{i=0}^{k} \sigma(i) \quad (28)$$

5. Test Results

5.1 Verification of Controllability

5.1.1 Verification of robustness with respect to engine load conditions

In order to evaluate control stability with respect to engine load conditions, Vout data controlled by a conventional control method and by PRISM in the FTP mode is acquired using a prototype vehicle with L4 2.3 L engine and a catalyst (600 cell/4.3 mil) aged to an equivalent of 50,000 miles. The data results are then compared.

Fig. 11 and Fig. 12 show histograms of Vout controlled by PRISM and a conventional control method. As shown in these graphs, the Vout probability by the conventional method in the Vop range of ±0.1V is 35.8%, and 74.3% by PRISM. Therefore it can be said that PRISM can double Vout controllability compared to the conventional method.

Fig. 13 shows the identified model parameters for the FTP mode. In the graph, model parameters change according to vehicle speed conditions – that is to say, according to engine load conditions. This reveals that the identifier continually adapts PRISM to the dynamic characteristic change of the controlled object according to engine load conditions.

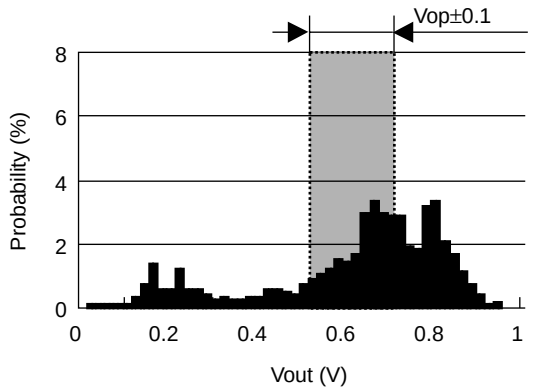


Fig. 11 Histogram of Vout controlled by conventional algorithm

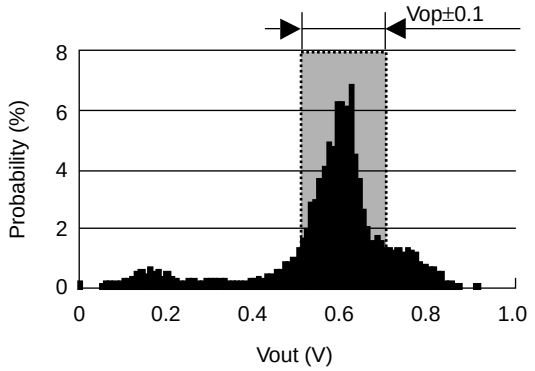


Fig. 12 Histogram of Vout controlled by PRISM

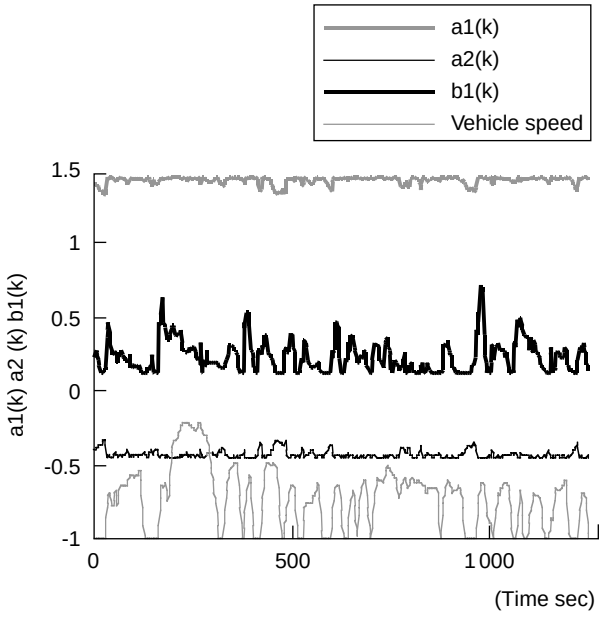


Fig. 13 Identification results for q in the FTP mode

5.1.2 Verification of adaptability with respect to catalyst aging conditions

In order to evaluate stability with respect to catalyst aging conditions, further Vout data is acquired using prototype vehicles with 0 mile and 100,000 mile equivalent aged catalysts. Table 1 is a comparison of the Vout probability in the range of Vop ±0.1V under the three catalyst aging conditions. The difference of Vout probability in Table1 is within 5%, which is a very small range. Therefore, it was verified that PRISM has superior adaptability with respect to catalyst aging conditions.

Table 1 Probability of Vout within the range of Vop±0.1V

Equivalent aging condition of catalyst	0	50 000	100 000
Probability	78.9%	74.3%	81.0%

5.2 Effect on Emissions Reduction

In order to evaluate the emissions reduction effects of PRISM, emissions in the FTP mode are measured using the above mentioned prototype vehicle with the catalyst aged to an equivalent of 100,000 miles. The emissions as controlled by PRISM and the conventional method are compared in Table 2.

In Table 2, compared to the conventional method, PRISM reduces CO, NMHC and NOx by 34%, 32% and 42% respectively. This confirms that PRISM has greatly improved the emissions reduction effect.

In order to evaluate emission stability with respect to catalyst aging conditions, further FTP mode emissions were measured under catalyst aging conditions equivalent to 50,000, 100,000 and 300,000 miles. Fig. 14 shows normalized emissions under each of the catalyst aging conditions based on the 100,000-miles emissions. In the graph, when comparing 100,000 mile and 400,000 mile equivalents, CO increases by 60%. However, HC increased

Table 2 Comparison of FTP mode emissions for PRISM and conventional control

	CO	NMHC	NOx
Conventional control	0.105	0.022	0.071
PRISM	0.069	0.015	0.041
Improved ratio	34%	32%	42%

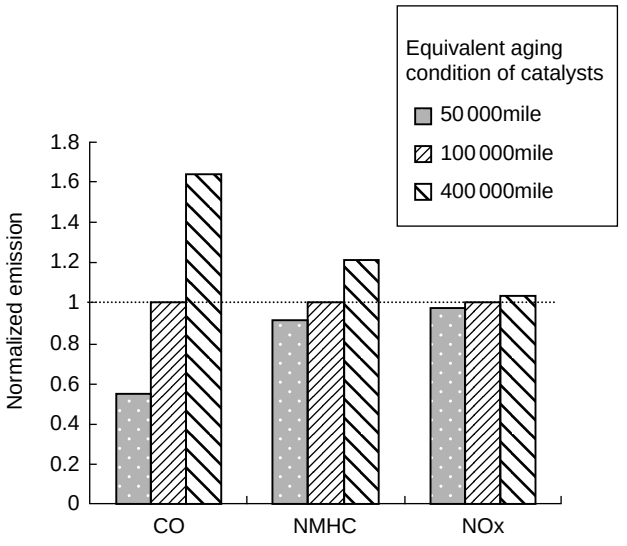


Fig. 14 PRISM emissions robustness

by approximately 20% and NOx by a mere 3%. This shows that PRISM has sufficient emissions stability with respect to catalyst aging and it verifies the use of PRISM as an appropriate emissions reduction concept.

6. Summary

By applying PRISM, which integrates an identifier, predictor, and adaptive sliding-mode controller to secondary O_2 feedback, Vout control was achieved as follows.

1) Compared with the conventional method, Vout to Vop controllability is doubled.
2) Regardless of catalyst aging conditions, Vout probability in the range of Vop ±0.1V was maintained at 74% or better.

These provide the following effects on emissions.

1) Compared with the conventional method, FTP mode emissions were reduced by approximately 32 – 42%.
2) The emission stability with respect to catalyst aging conditions was dramatically improved.

References

1) Yasui, Akazaki, Ueno, and Iwaki: Adaptive Sliding Mode Control For Secondary O_2 Feedback, HONDA R&D Technical Review Vol.11 No.1, p.65-71 (1999)
2) Yasui, Akazaki, Ueno, and Iwaki: Adaptive Sliding Mode Control For Secondary O_2 Feedback – A Second Report, HONDA R&D Technical Review Vol. 11 No. 2, p.51-56 (1999)
3) Ohata, A., Masu, M., and Inoue, T.: Model Based Air-Fuel Control for Reducing Exhaust Gas Emissions, SAE Paper 950075 (1995)
4) Yatabe, H., Tai, H., and Matsuura, M.: Air-to-Fuel Ratio of Gas Engines Using Response Characteristics of Three-Way Catalysts Under Dynamic Operation, SAE Paper 910083 (1991)
5) Harada: Automotive Control Technology, Tokyo, Asakura Publishing, 1997
6) Katayama: Introduction to System Identification, Tokyo, Asakura Publishing, 1994, p.196
7) Nonami, Den: Sliding Mode Control, Tokyo, Corona Ltd. 1994, p.263
8) Yasui, Y., Akazaki, S., Ueno, M., Iwaki, Y.: Secondary O_2 Feedback Using Prediction and Identification Sliding Control, SAE Paper, 2000-01-0936 (2000)
9) Yasui, Y., Akazaki, S., Ueno, M., Iwaki, Y.: Secondary O_2 Feedback Using Prediction and Identification Sliding Control – Second Report –, SAE Paper, 2001-01-0264 (2001)
10) Maki, H., Hasegawa, Y., Akazaki, S., Komoriya, I., Nishimura, Y., and Hirota, T.: Real Time Control Using STR in Feedback System, SAE Paper 950007 (1995)
11) Adachi: System Identification Theory for the User, Tokyo, Transactions of SICE, 1993, p.222
12) Watabe: Dead Time System Control, Tokyo, Transactions of SICE, 1993, p.206

■ Authors ■



Yuji YASUI



Shusuke AKAZAKI



Hiroshi KITAGAWA



Yoshihisa IWAKI

Development of a Magnetic Coupling Type Water Pump for 4-Stroke 50 cm³ Scooter Engines

Yutaka MIYAKE* Tadashi NIINO* Masatoshi FUKAMACHI*
Shin NABEYA* Osamu SATOU**

ABSTRACT

In the development of a magnetic coupling type water pump, the coupling pull-out phenomena, which leads to the impeller stopping, has been a concern. As a result of analysis of magnetic coupling behavior, two-types of pull-out were determined: pull-out due to insufficient transmission torque of the magnetic coupling in the high speed rotation range; and, pull-out due to the resonance of the inner and outer magnets. Major factors causing pull-out are the angular velocity input to the drive side, the inertia moment of the driven side, magnetic coupling characteristics, and the damping effect of coolant. Using the results of actual testing and a behavior simulation of a water pump, design specifications for a magnetic coupling were set within conditions that did not allow pull-out to occur. Consequently, the reliability of drive power transmission was assured. As a result, it was possible to decrease the size and weight of the water pump, and, at the same time, decrease engine friction.

1. Introduction

Water pumps in conventional internal combustion engines drive the impeller by a mechanical coupling, and thus it is necessary to have, on the drive shaft, a mechanical seal, an oil seal, and a shaft bearing. In comparison, with a magnetic coupling type water pump, the drive force is transmitted magnetically, and so the above-mentioned parts can be eliminated. This simplifies the structure, making it smaller and lighter, and also reduces engine friction.

The drawbacks of a magnetic coupling type pump are that due to sudden changes in rotational speed or at high rotational speeds, the driven side (impeller side) cannot follow the drive side, creating a pull-out phenomena (referred to as pull-out hereafter). When pull-out occurs, the impeller stops, and because the coolant ceases to circulate, there is a problem with engine cooling.

With a magnetic coupling type water pump, generally, in contrast with an electric motor driven pump, a shaft connected to the internal combustion engine's crankshaft drives the pump. Accordingly, it is used from low rotational speeds to high rotational speeds and there is large rotational speed fluctuation during a single revolution. These are severe conditions of use for the magnetic coupling, and it has been a big concern in guarantying the reliability of drive force transmission.

* Asaka R&D Center
** Yamada Seisakusho Co., Ltd.

This project has analyzed the pull-out mechanism, verified the effects of each factor, and established the appropriate specifications. This technology has been adopted for the 4-stroke 50 cm^3 scooter engine.

2. Structure

Fig. 1 shows the structural diagram of the magnetic coupling type water pump developed in this project. The special features are listed below.

- Because the water pump's impeller drive is carried out by the magnetic force of magnets, via a plastic pump case that separates water and oil, mechanical seals and oil seals are unnecessary.
- The impeller bearing structure eliminates the ball bearing, by using a slide bearing structure, of the type where the stainless steel shaft and the plastic bushing have direct contact.
- As for the magnets, as countermeasures to them breaking or to prevent them from flying off, the magnet on the camshaft side (the drive side, referred to hereafter as the outer magnet) is covered by a thin stainless steel wall, and the magnet on the impeller side (driven side, referred to hereafter as the inner magnet) is covered by plastic which integrates it into the impeller.
- As the camshaft drive, the outer magnet is fastened together with the cam sprocket.
- As the structure's water path is completely watertight, the seal performance is highly reliable, and the drain outlet structure, which conventionally was indispensable, is not necessary.

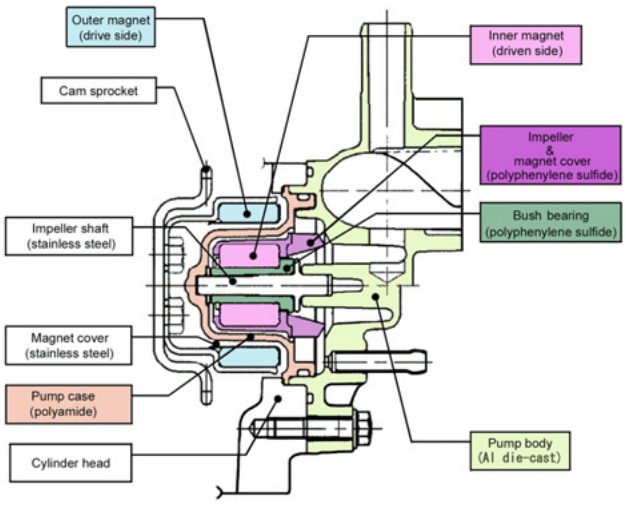


Fig. 1 Structure of magnetic coupling water pump

3. Pull-out Mechanism and Factors

In order to verify the pull-out phenomena, the behavior of the magnetic coupling's inner magnet and outer magnet were confirmed. The results of the behavior check showed that there are two types of pull-out: pull-out that occurs in high rotational speed range, and pull-out due to resonance of the inner magnet and outer magnet.

The pull-out in the high rotational speed range occurs because the water pump rotational torque exceeds the magnetic coupling's transmission torque.

The pull-out occurs due to resonance between the outer magnet's rotational speed fluctuation caused by fluctuation in engine speed and the inner magnet's rotational speed fluctuation caused by drive force transmitted by magnetic force. Due to the resonance, there is a large relative angle difference of the magnetic poles of the inner and outer magnets (referred to hereafter as phase difference), and if it exceeds the maximum pole phase difference where drive force transmission is possible, pull-out occurs.

The impeller behavior equation of motion is shown below[1].

$$I\ddot{\theta}in + C\dot{\theta}in - k(\theta in - \theta out) = 0 \quad (1)$$

I : Inner magnet inertia moment
C : Damping force of coolant
k : Magnetic coupling's torsion spring effect
θ in : Inner magnet displacement
θ out : Outer magnet displacement

Based on the equation of motion, factors thought to affect pull-out were studied. Those factors are shown in Fig. 2. Among the factors that affect pull-out, one having a large effect is the magnetic coupling transmission torque characteristics, which is the core of this mechanism.

Magnetic coupling transmission torque changes according to the following:

- magnetic force
- temperature
- gap between magnets (radial direction, thrust direction)
- phase difference
- number of poles

As for the magnetic force, the higher the magnetic flux density of the magnetic body used, the larger the transmission torque. However, in this new development, attention was focused on stable ferrite to inexpensively deal with reduced magnetism. Also, the larger the magnet's dimensions, the larger the transmission torque. However, the inertial moment also increases with magnet size. The magnet's dimensions, within the actual engine layout, were established for the minimum inertia moment for the required transmission torque.

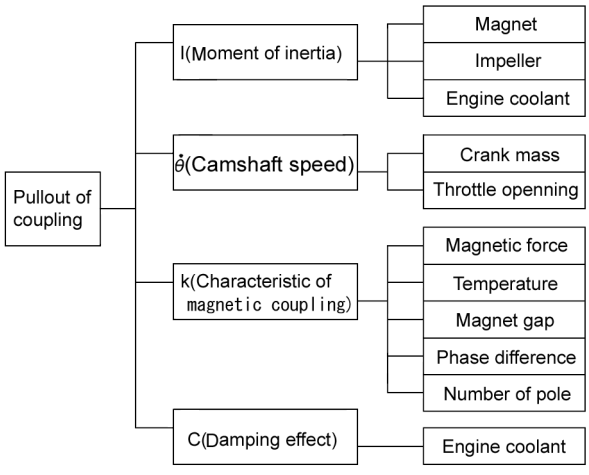


Fig. 2 Magnetic coupling pullout factor analysis chart

The relationship between transmission torque and temperature is shown in Fig. 3. With the ferrite magnet, the temperature coefficient of the magnetic force is large, and the characteristics are such that with a temperature rise, the magnetic force drops reversibly. When used in an internal combustion engine, the temperature range of use is broad, and so magnetic force changes due to temperature conditions have a large effect on transmission torque. The tests results show that the following equation is true.

$$T(t') = T(t) \cdot e^{k(t'-t)} \qquad (2)$$

T(t) : Static maximum transmission torque (measured when temperature is t°C)
T(t') : Static maximum transmission torque when temperature is t'°C
k : reversible temperature coefficient

If the gap between the magnets increases, magnetic flux density drops, and so transmission torque drops. Transmission torque also drops due to misalignment of the thrust direction of the outer and inner magnets.

In magnetic coupling, drive force is transmitted by restoration force generated when phase difference between opposing magnetic poles is applied. This restoration force is from the attraction and repulsion acting between opposing poles and poles adjacent to them, and so changes according to their positional relationship[2]. Fig. 4 shows the relationship between phase difference according to differences in number of poles and transmission torque. The phase difference and transmission torque characteristics occur under conditions when gap magnetic flux density distribution is a sine wave, and strictly speaking a 3D analysis is required. However, from the test results in this development project, the relationship approximates the following equation.

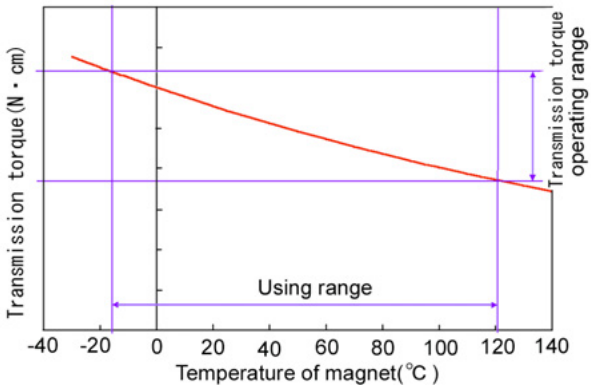


Fig. 3 Relationship between transmission torque and temperature of magnet

$$T = Tmax \cdot \sin\{(P/2) \cdot \theta\} \qquad (3)$$

T : Static transmission torque when the phase difference is θ
Tmax. : Maximum static transmission torque
P : Number of magnetic poles
θ : Phase difference

As shown in Fig. 4, the smaller the number of poles, the larger the angle range wherein torque transmission is possible (permissible phase difference until pull-out). However, as the maximum transmission torque changes according to the number of poles, it is necessary to study the optimum number of poles, while considering both transmission torque and angle range wherein torque transmission is possible.

4. Pull-out in the High Revolution Speed Range

Using a magnetic coupling with low transmission torque settings, confirmation tests were implemented of pull-out due to water pump unit motoring. Fig. 5 shows the water pump revolution torque characteristics used in the tests. The revolution speed when pull-out occurred was the point where the transmission torque of the magnetic coupling used in the test was the same as the pump revolution torque (see "a" in Fig. 5). The same results were also obtained in actual engine confirmation testing. From the above it was learned that, high revolution range pull-out occurs when pump revolution torque exceeds magnetic coupling transmission torque. Therefore, it is possible to avoid high revolution range pull-out by establishing pump revolution torque and magnetic coupling transmission torque while considering actual engine use conditions.

5. Resonance Pull-out

First, inner magnet and outer magnet revolution speeds were measured. Next, the inner magnet and outer magnet speed difference was integrated, and relative behavior was determined as the mutual angle difference from the position at the start of the measurement. As an example of measurement results, the left side of Fig. 6 shows the inner

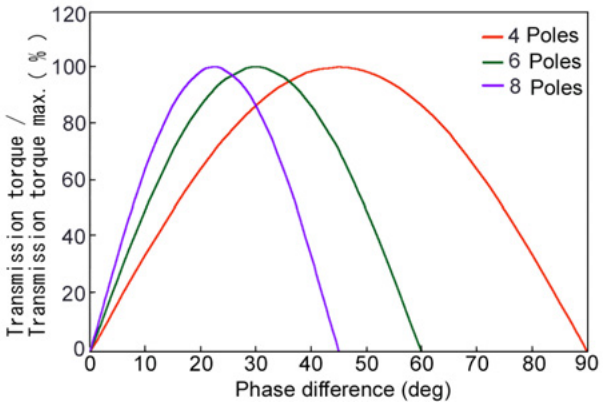


Fig. 4 Relationship between transmission torque and phase difference

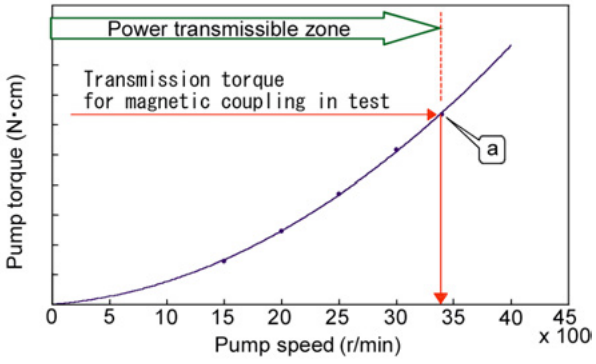


Fig. 5 Pullout point at high revolution speeds

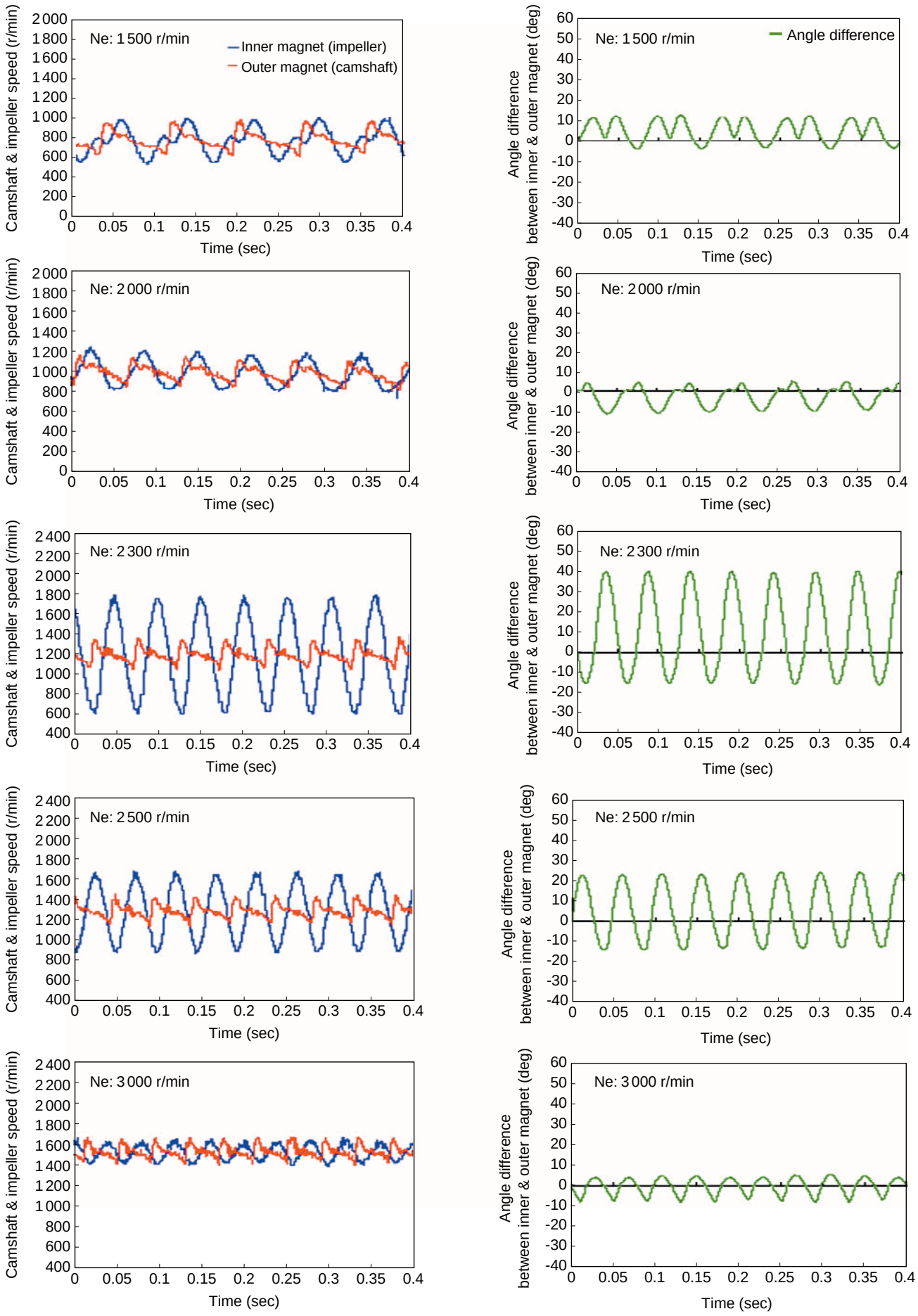


Fig. 6 Magnetic coupling behavior

magnet and outer magnet revolution speeds, and the right side of Fig. 6 shows the relative angle difference which is the result of integrated calculation. The total amplitude of the relative angle difference determined here is called the amplitude of phase difference. Next, the maximum amplitude of phase difference at each engine revolution speed was obtained, and was shown as the relationship between engine revolution speed and amplitude of phase difference. The data in Fig. 6, shown as the relationship between engine revolution speed and amplitude of phase difference, is Fig. 7's inertia moment 2.61×10^{-6} (kg·m^2) specification. The smaller this amplitude of phase difference, the greater the tolerance against pull-out. Also, when the amplitude of phase difference increases, if it exceeds the pole's maximum phase difference at which drive force transmission is possible, pull-out occurs. In this way, the effect of each factor on pull-out was compared.

5.1 The Effect of Inertia Moment

A comparison was made of three specifications wherein inertia moment was changed on the inner magnet side by using a dummy weight, without changing the magnet unit. The amplitude of phase difference for each engine speed was determined; the results are shown in Fig. 7. The greater the inertia moment, the greater the tendency for resonance revolution speed range to be in a low revolution range, and the results showed that the amplitude of phase difference also grew. The smaller the inertia moment, the greater the tolerance against pull-out.

5.2 The Effect of Angular Velocity Input on the Magnetic Coupling

The effects of angular velocity input on coupling according to differences in throttle opening were verified. Fig. 8 shows the engine speed fluctuation according to throttle opening differences and the amplitude of phase difference characteristics. As the throttle opening becomes larger, the amplitude of phase difference also grows; at a throttle opening of 40%, it is basically saturated. This trend corresponds to that of the engine speed fluctuation. Magnetic coupling behavior results show that the greater the engine speed fluctuation, the more the tendency for the resonance revolution range to be to the low revolution side. The amplitude of phase difference also increases towards the low revolution side. In addition, as shown in Fig. 9, the results when engine speed fluctuation is varied according to flywheel mass are the same as results when varied according to throttle opening differences. Concerning magnetic coupling input, the smaller the fluctuation of angular velocity, the better tolerance against pull-out.

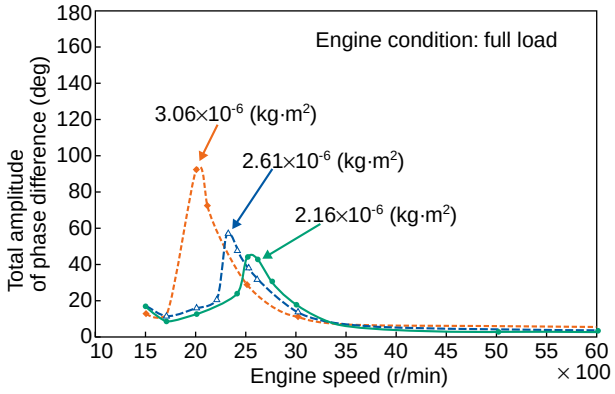


Fig. 7 Influence of inertial moment

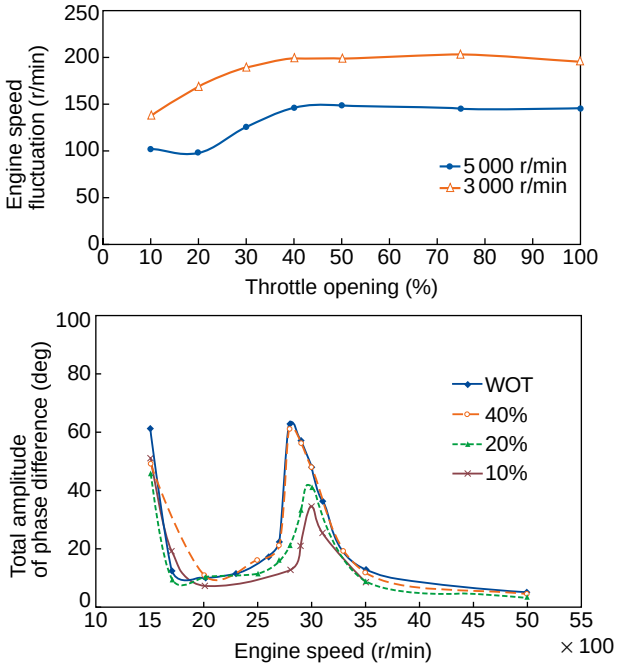


Fig. 8 Influence of throttle opening

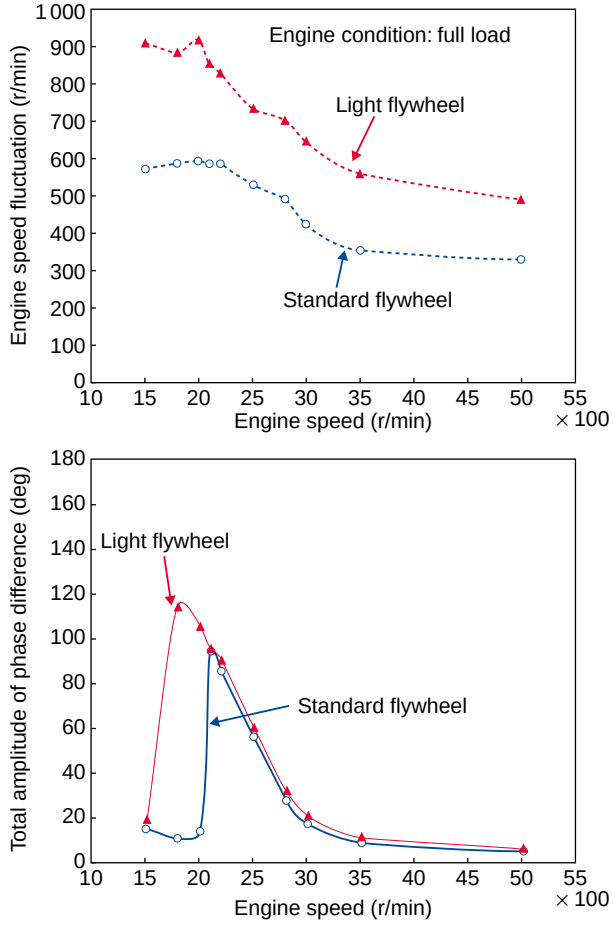


Fig. 9 Influence of flywheel inertial mass

5.3 The Effect of the Magnetic Coupling Characteristics

First, confirmation was made of the effects on pull-out of magnetic coupling magnetic force, temperature, and gap differences. As explained above, each of these factors affects transmission torque. The specifications used in the actual engine confirmation testing are given in Table 1. In addition, Fig. 10 shows the temperature characteristics for those specifications. Fig. 11 shows the results of confirmation of amplitude of phase differences at points A through D in Fig. 10. Measurement results at points A, B, and C show a resonance range whereby the smaller the transmission torque the larger the amplitude of phase difference on the low revolution speed side. As the transmission torque increases, the resonance range moves to the high revolution speed side, and amplitude becomes comparatively small.

Table 1 Magnet coupling specification for experiment

No.	1	2	3
Number of magnet poles	4	4	4
Driven magnet outer dia. (mm)	24	24	24
Drive magnet inner dia. (mm)	35	36	37
Gap (mm)	5.5	6	6.5

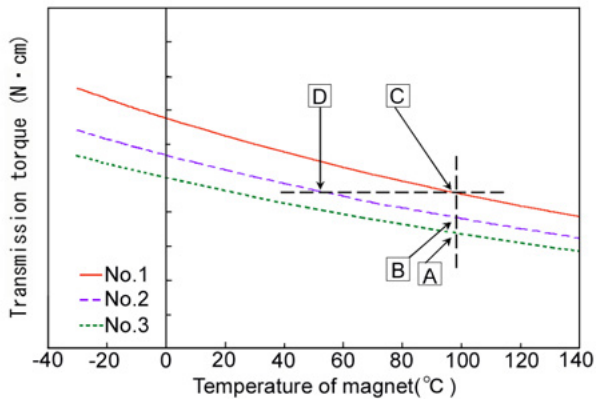


Fig. 10 Relationship between transmission torque and temperature for experiment

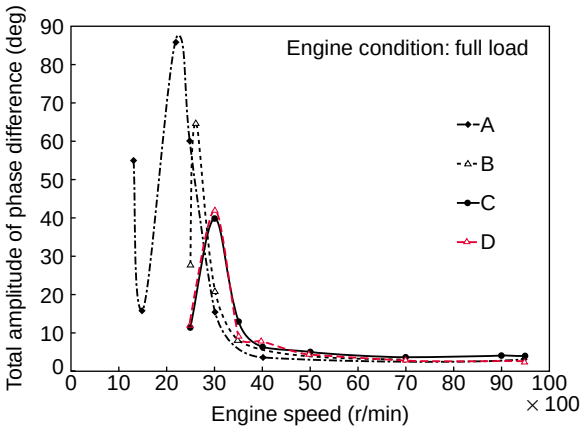


Fig. 11 Influence of magnet gap and temperature

Also, as a result of confirming that transmission torque is the same at points C and D, it was found that the characteristics where resonance occurs are also the same. From the above, it is known that it is possible to convert the factors of magnetic force, temperature, and gap with a transmission torque index.

The results of the next measurement of the effect of the number of poles are shown in Fig. 12. In order to eliminate the effects of a different maximum magnetic transmission torque due to a different number of magnetic poles, confirmations were carried out after adjusting transmission torque to be the same, using temperature settings. In comparison with the 6-pole spec, the 4-pole spec shows a large tolerance to pull-out angle and a resonance range on the low revolution speed side, even though the amplitude of phase difference is large. In addition, when there is a first order resonance range in the high revolution speed range around 4000 rpm and higher, it was found that there is a half order resonance range in the practical revolution speed range around 2000 rpm and higher.

5.4 The Effect of Coolant

First, assuming opening and closing of the thermostat, the effects of the amount of coolant flow were confirmed. The amplitude of phase difference was determined at a fixed revolution speed with varied flow. The measurement results are shown in Fig. 13. It was learned that differences in flow had no significant effect on amplitude of phase difference or resonance revolution range. Next, the effect of viscosity changes, due to coolant concentration,

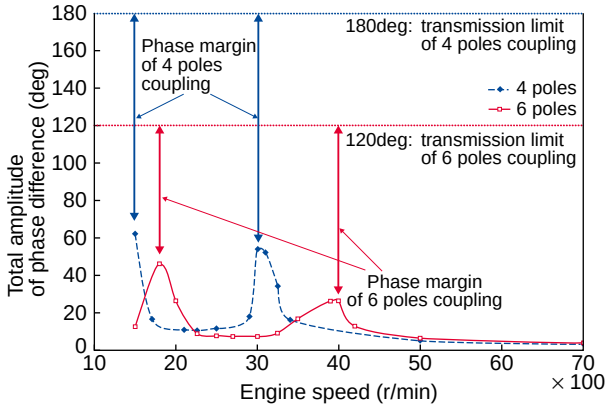


Fig. 12 Influence of number of magnet poles

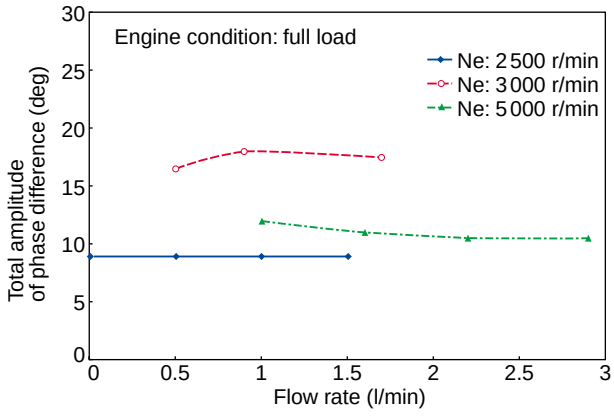


Fig. 13 Influence of flow rate

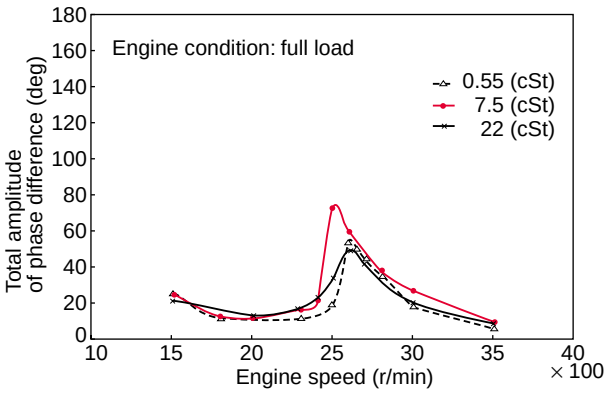


Fig. 14 Influence of viscosity

temperature, etc., was confirmed. The measurement results are given in Fig. 14. It was learned that viscosity differences had no significant effect on amplitude of phase difference and resonance revolution range.

6. Simulation

In order to learn the appropriateness of the resonance pull-out mechanism, a simulation was implemented. Fig. 15 shows the simulation model. A special feature of this system is that the equation of motion is non-linear, because magnetic force load acting between the inner magnet and outer magnet, that is to say the transmission torque, is not linear against displacement. The analysis method of this system uses the Newton-Raphson method of numerical integration. In comparison with the inner magnet side, the outer magnet side has sufficiently large mass, and so it was not modeled. Rather, the angular displacement of the outer magnet at each time obtained from the actual measurements was input into the calculation model. The calculation equation used in the simulation is shown below.

$$I\ddot{\theta}in + C\dot{\theta}in - k(\theta in - \theta out) = 0 \quad (4)$$

I : Inertia moment on the inner magnet side
C: Resistance due to the coolant (pump revolution torque)

$$k(\theta in - \theta out) = Tmax \cdot \sin\{P/2(\theta in - \theta out)\} \quad (5)$$

k (θ in – θ out) : Static transmission torque when the phase difference is θ
Tmax. : Maximum static transmission torque
P : Number of magnetic poles
θ in : Inner magnet displacement
θ out : Outer magnet displacement

$$\theta out = \int \omega(t)dt \quad (6)$$

ω (t) : Outer magnet angular velocity

Fig. 16 shows the actual measurement and simulation results of inner magnet angular velocity when the engine running condition is a sweeping engine speed. There is close agreement between the two sets of results, and thus the appropriateness of this system's equation of motion was confirmed. Further, theoretical evidence of the pull-out phenomena occurring in engines was obtained.

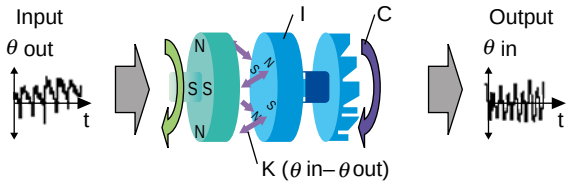


Fig. 15 Simulation model

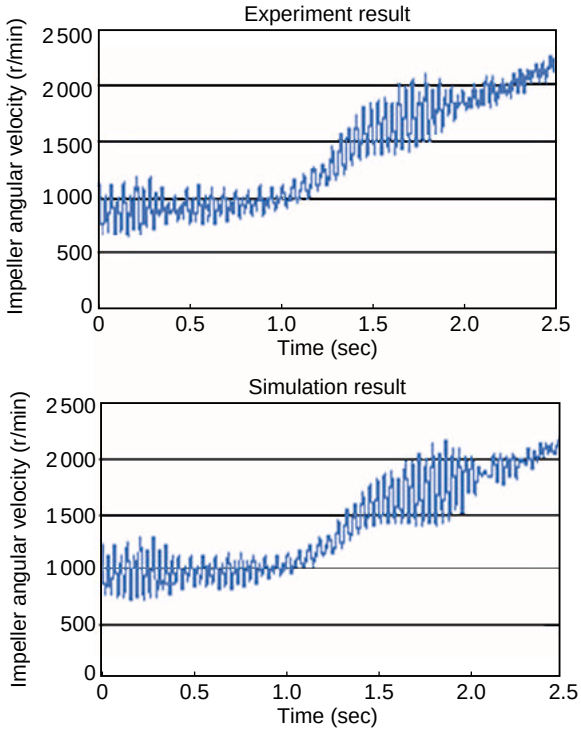


Fig. 16 Comparison between simulation and experiment results

7. Specification Settings and Benefits

In establishing specifications, the magnet temperature, angular velocity input to magnet coupling, and pump revolution torque are measured for the vehicle to which the system will be applied. A simulation is carried out whereby four specifications are varied to confirm the system. The four specification items are: number of magnetic poles, transmission torque, inertia moment, and angular velocity input. Fig. 17 provides an example of the results of simulation of a 4-pole spec, with fixed input, for the transmission torque and different inertia moments. Each specification was simulated and the results are provided in this graph, which shows the pull-out margin angle as an index. Specifications were selected based on the results of these simulations. Then, after confirmation testing with an actual engine, drive force transmission reliability under various conditions of use was guaranteed. By adopting this magnetic coupling water pump, pump unit friction was reduced to 1/5 (when Np = 4500 rpm) compared with conventional mechanical coupling water pumps. Further, the new pump is smaller and lighter, and the structure has been simplified.

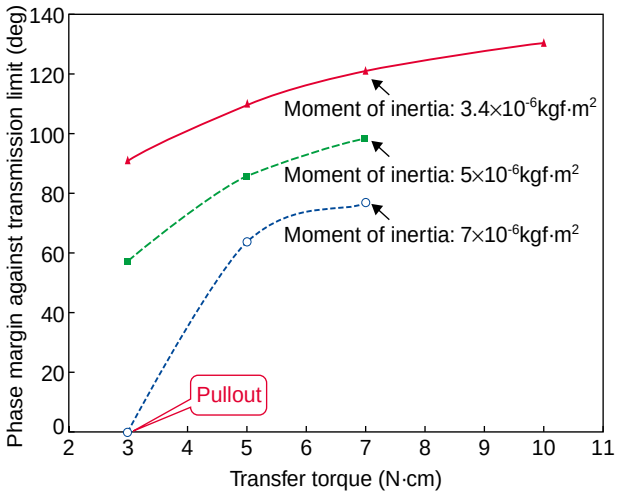


Fig. 17 Simulation results for transmission torque and inertia

8. Summary

In developing a magnetic coupling water pump for use in a 4 stroke 50 cm^3 scooter engine, the focus was on angular velocity input to drive side, driven side inertia moment, magnetic coupling characteristics, and coolant damping effect. The results of a behavior simulation for each factor and vehicle confirmation tests showed the following achievements.

(1) The pull-out mechanism has been clarified.
(2) Theoretical specification investigations are now possible due to this water pump behavior simulation program.
(3) Drive force transmission reliability is guarantied using vehicle confirmation tests and simulations.
(4) Engine friction reduction, smaller and lighter pumps, and a simplified structure have been achieved.

References

(1) Nagaya. K, et al., Feedforward Robust Velocity Control of a Magnet Coupling, Japan Society of Mechanical Engineers (No. 920 – 55) Mechanical Dynamics, Measurement Control Seminar Papers, 1992, B, p. 96 – 101 (1992)
(2) Tsurumoto. M, Magnetic Gear and Coupling Using Permanent Magnet, Japan Society for Industrial and Applied Magnetics Conference Papers, Vol. 11, No. 2, p. 391 – 394 (1987)

■ Authors ■


Yutaka MIYAKE


Tadashi NIINO


Masatoshi FUKAMACHI


Shin NABEYA


Osamu SATOU

Development of a 4WD System for SUVs

Koji KURODA* Kazuhiro NAKANO* Yoshikazu KONISHI*
Takeshi HORI* Kenzo NISHIDA* Kazunori KOBAYASHI*

ABSTRACT

Surveys of sports utility vehicle (SUV) use in the United States, where they are extremely popular, show that they are mostly driven on streets in urban areas. However, most SUVs are based on a truck chassis, and performance under adverse conditions is regarded as more important than on-road controllability and efficiency. Therefore, this system was created using an FF passenger car chassis with functions integrated in the rear final drive unit, clutch units installed on the axle for the left and right rear wheels, electronically controlled torque control, torque limit control, and so on. The result combines the rough road performance required for an SUV with the controllability of a passenger car, and achieves these goals in a system weighing only 97 kg, making it the lightest in its class.

1. Introduction

Sales of vehicles in the Sport Utility Vehicle category (SUV below) have shown a recent trend towards yearly increase in the US. Surveys have yielded various reasons for choosing an SUV, including the feeling of security from the greater visibility due to height and the ease of use for leisure activities.

In actual terms, SUVs are used almost exclusively for town driving and only rarely for off-road use. However, many present SUVs are based on a truck chassis, and many of them emphasize performance under adverse conditions over on-road controllability. This situation made it necessary to develop a 4WD system which corresponded to the pattern of actual use of SUVs.

2. Developmental Aim

Given the purpose of their use, various driving conditions are projected for SUVs. As a result of surveys on mode of use, we realized that in terms of drivability, ensuring traction to drive up gravel or snow-covered slopes or to tow a boat up a slope is sufficient for practical use, while it is also possible to provide users with easy-to-use SUVs which feature controllability performance equivalent to passenger vehicles on paved roads. On this basis, we established our developmental aim as ‘a balance between the necessary sufficient drivability as an SUV and controllability performance as a passenger vehicle’.

To ensure drivability, it is necessary to provide optimum control of driving force to the front and rear left and right wheels in response to vehicle conditions, while chassis performance equivalent to that of a passenger vehicle and weight savings are important to ensuring controllability performance. These were the considerations behind the development of the 4WD system introduced in this paper, Variable Torque Management-4 (VTM-4).

3. 4WD Systems

As a result of examination of the functions considered necessary to achieving SUV drivability and passenger vehicle controllability performance, we realized the importance of the following items (Fig. 1).

*Tochigi R&D Center

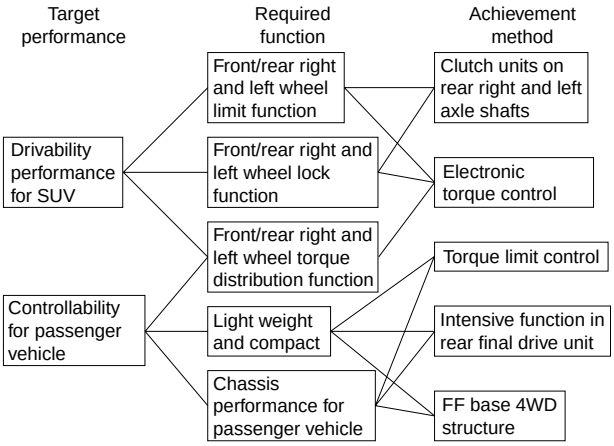


Fig. 1 Target performance and achievement method

There are various configurations among 4WD systems, including the full-time, direct type and center clutch type (Table 1).[1] [2] For the new development we examined methods of achieving weight savings and compactness by minimizing the number of elements involved in the necessary functions, and decided on the 4WD basic system shown below (Fig. 2).

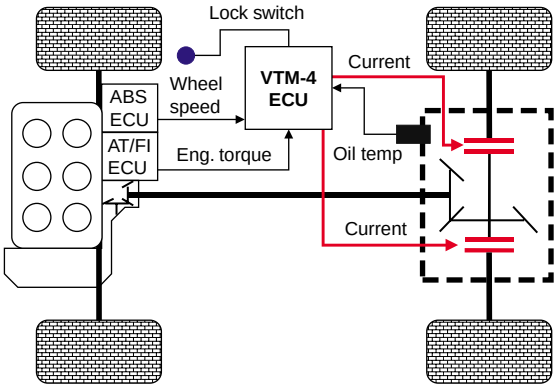


Fig. 2 VTM-4 system

3.1 Power Take Off (PTO)

Because of the adaptability of PTO, which receives traction from an automatic transmission (AT), to the engine room in an FF base, we were able to adopt a configuration in which hypoid gears change the direction of driving force after speed has been increased by helical gears on the differential. This has allowed us to lower the position of the section receiving driving force and to achieve weight savings. Fig. 3 shows a cross-section of PTO.

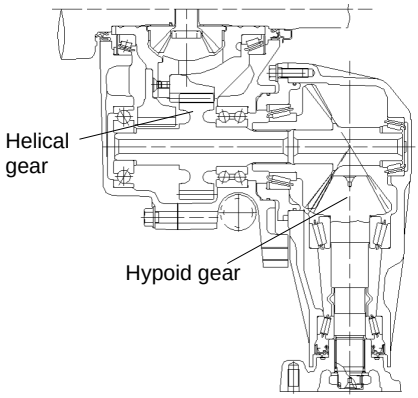
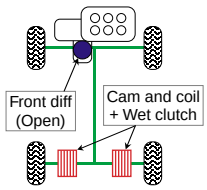
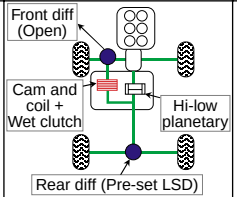
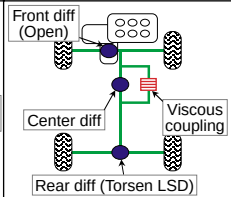
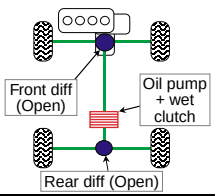


Fig. 3 PTO cross section

3.2 Propeller Shaft

Given the goal of weight savings, we adopted a two-piece type propeller shaft (Fig. 4). By regulating revolutions by means of PTO and the rear final drive unit gear ratio, we optimized joint size and pipe ratio. To suppress rotational vibration from the propeller shaft, we have maintained the rotational weight balance of the shaft below a fixed value, and adjusted it to be in locked phase with the rear final drive unit input flange. This has reduced noise and vibration during driving.[3]

Table 1 Respective functions of 4WD types and the number of elements

		VTM-4	Competitor A	Competitor B	Competitor C
					
Function	Driving force distribute Function (front to rear)	○	○	○	○
	Driving force distribute Function (rear left & right)	○	×	○	×
	Front and rear rock function	○	○	×	×
	Rear left and right lock function	○	×	×	×
Element	Differential	1	2	3	2
	Clutch	2	1	1	1

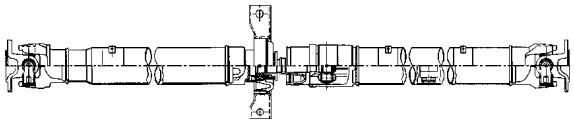


Fig. 4 Propeller shaft cross section

3.3 Rear Final Drive Unit

Given the goals of achieving weight savings and fitting the system in an FF base vehicle, we concentrated torque control functions in the rear final drive unit. We examined hydraulic, electromagnetic and other methods of torque control, but to achieve the target performance set for the new development, it was important to ensure controllability when rotational difference between the front and rear wheels is low. Hydraulic control of the clutch requires a separate oil pressure source, and the system becomes overly complex. Adoption of an electromagnetic coil-type clutch for torque control in the VTM-4 has ensured sufficient controllability with a simple structure.

The direction of torque input from the propeller shaft to the rear final drive unit is changed by the hypoid gears and transmitted to independently positioned electromagnetic coil-type clutches on the right and left. Fig. 5 shows a cross section of the rear final drive unit.

The electromagnetic coil-type clutches consist of a pilot clutch and a main clutch. When current flows to the electromagnetic coil, the armature is pressed against the rotor, producing friction torque. Friction torque is converted into thrust force by a ball cam inside the unit, and this becomes main clutch thrust force. Fig. 6 shows a cross section of the electromagnetic coil-type clutch.

The torque controlled by the main clutch is independently transmitted to the right and left axle shafts by the output shaft. As a result of investigating the relative effect of the various elements of the right and left clutches on the dispersion of torque transmission, we realized that pilot clutch clearance has the greatest effect on the amount of torque transmission. Fig. 7 shows the relationship between pilot clutch clearance and amount of torque transmission. In this system we have ensured right and left torque differentials and controllability by optimizing clearance of the rubbing surfaces of the armature and the rotor.

Lubrication is provided to the clutches by an oil pump positioned on the same axle as the hypoid gear. The oil pump is positioned almost exactly between the right and left clutches, and provides uniform lubrication to both, with lubricating oil conveyed and provided to the clutches from within the shaft. The oil used is specifically designed to stabilize clutch friction characteristics.

In addition to ensuring the necessary driving force for drivability, lock mode does not feature mechanical linkages but constantly provides the maximum current to the electromagnetic clutches, suppressing excess driving force and achieving weight savings.

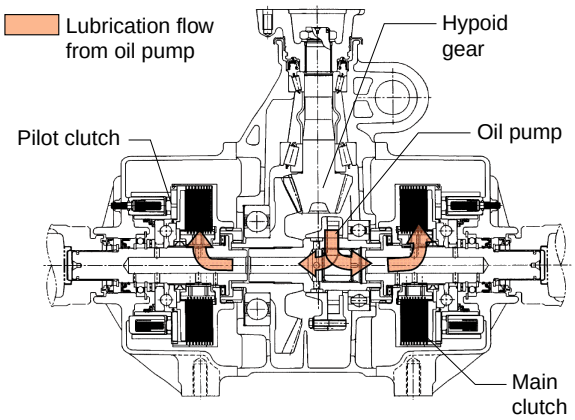


Fig. 5 Rear final drive unit cross section

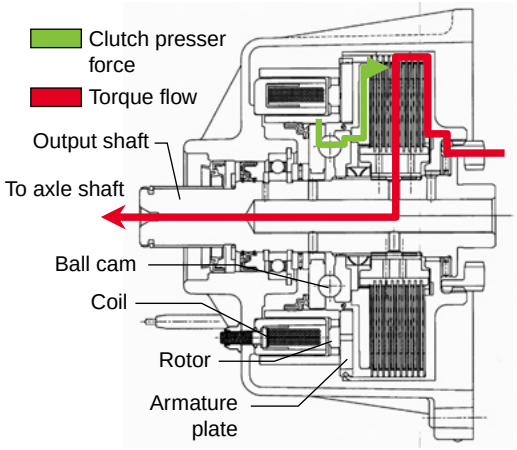


Fig. 6 Clutch unit Cross section

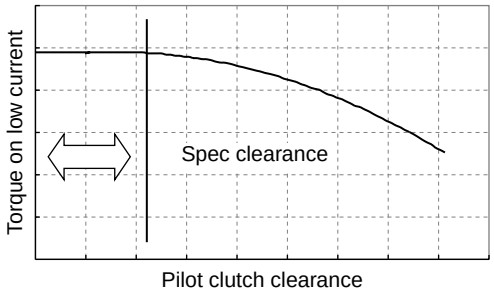


Fig. 7 Clearance and torque

4. System Control

The functions demanded of control to achieve the targets for the 4WD system were as follows:

(1) Allocate the optimum driving force to the rear wheels as necessary to improve both drivability and controllability.

(2) Do not transmit driving force when unnecessary, to achieve weight savings, compactness and fuel economy improvements.

We broadly set auto mode and lock mode to achieve these aims. Auto mode combines acceleration control, wheel speed control and hill climb control. Fig. 8 shows an outline of forms of control and their flow.

4.1 Auto Mode

1) Acceleration Control

The vehicle requires a large driving force during acceleration rather than when driving at a constant speed. We have therefore ensured drivability and controllability by optimal allocation of driving force to the rear wheels in response to acceleration. By not transmitting driving force to the rear wheels other than during acceleration, we have been able to make the system lighter, in addition to suppressing the tight corner braking phenomenon and improving fuel economy. This system calculates vehicle acceleration from engine torque, torque converter characteristics, vehicle speed, gear position, etc., and decides the amount of driving force to be allocated to the rear wheels. Fig. 9 shows the amount of driving force allocated against vehicle acceleration.

2) Differential Wheel Speed Control

Sometimes a large driving force must be provided from the rear wheels to ensure drivability on slippery road surfaces, such as found on bad or snow-covered roads. In addition to its utilization of acceleration control, this system ensures drivability by increasing rear wheel driving force in response to the front to rear wheel speed ratio. Fig. 10 shows rear wheel driving force against front to rear wheel slip ratio.

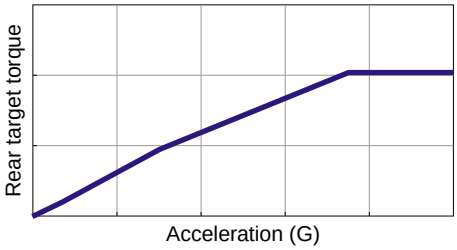


Fig. 9 Vehicle acceleration vs. rear wheel torque

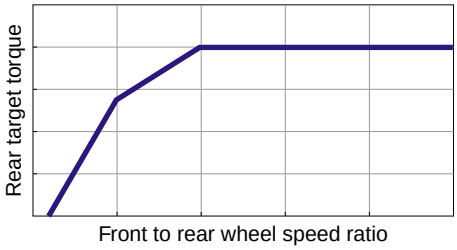


Fig. 10 Wheel speed ratio vs. rear wheel torque

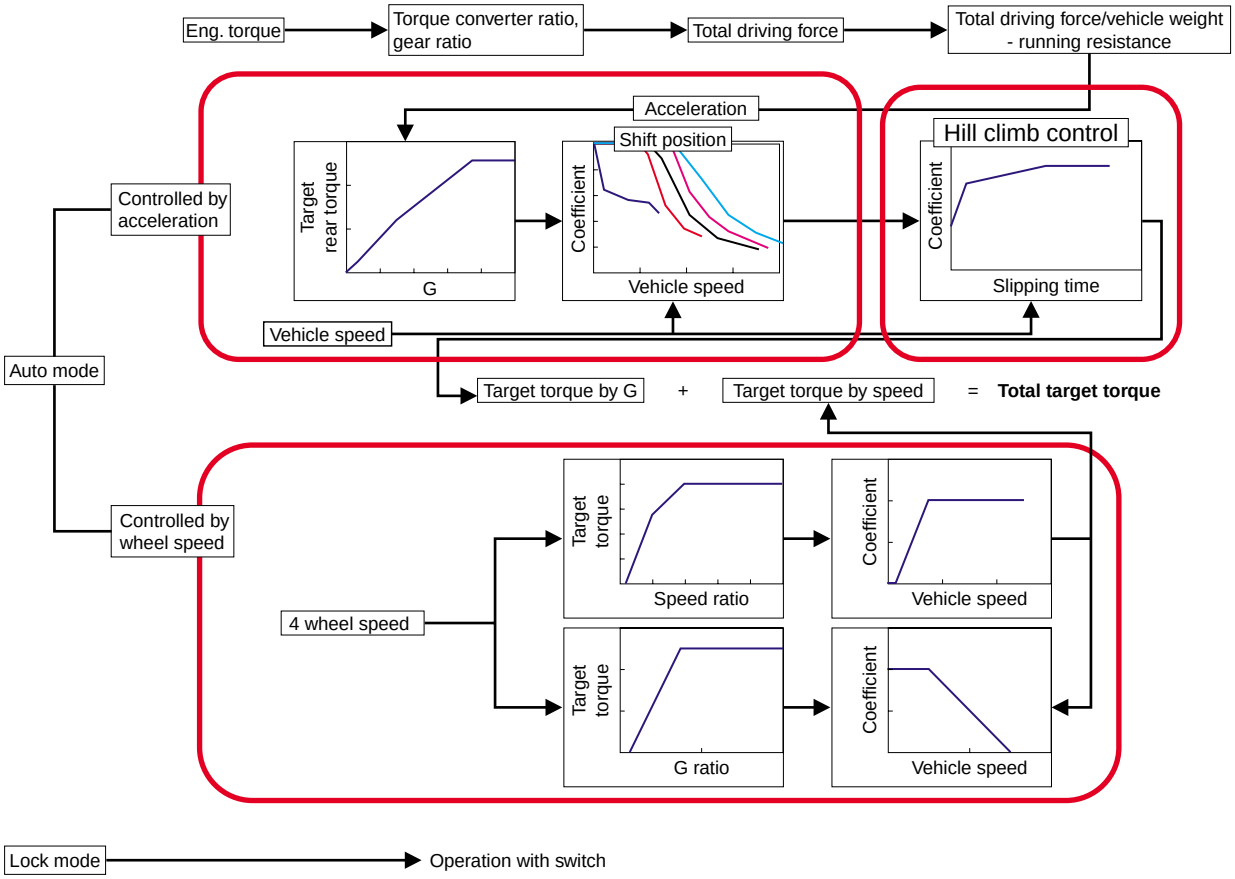


Fig. 8 Outline of control modes and flow

3) Hill Climb Control

When climbing extremely low μ gradients, there are cases in which the vehicle does not accelerate and front to rear wheel speed ratio does not greatly increase. To ensure drivability in such situations, when slight front wheel racing continues for a certain period, control is conducted to increase allocation of driving force to the rear wheels depending on the length of the period. Fig. 11 shows wheel racing time against the coefficient of increase of driving force.

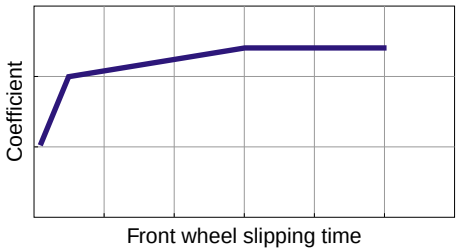


Fig. 11 Hill climb control

4.2 Lock Mode

When the vehicle is stuck or climbing a limit slope, it is possible to achieve greater drivability when the front and rear wheels and the rear right and left wheels are directly linked. However, this limits the differential between wheels, leading to strong braking when cornering, etc., and causing the vehicle to become unstable easily, and also puts more load on the drive system, increasing system weight. Because this type of drivability performance is required only at low vehicle speeds, this system gradually engages auto mode as vehicle speed increases, and limits use of lock mode to the low, 2nd and reverse positions on the AT shift lever. Fig. 12 shows vehicle speed against rear wheel torque.

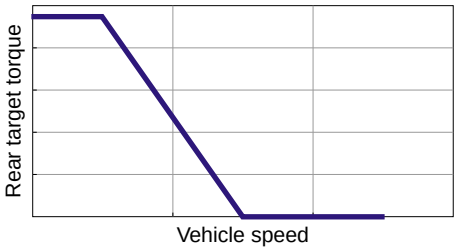


Fig. 12 Vehicle speed vs. rear wheel torque

5. System Weight

Fig. 13 shows a comparison between the weight of the VTM-4 used in the 2001 Acura MDX and the weights of the systems used in other models.

We have achieved the lowest system weight in the class (97 kg) through concentration of functions, the torque limit function, acceleration control, etc.

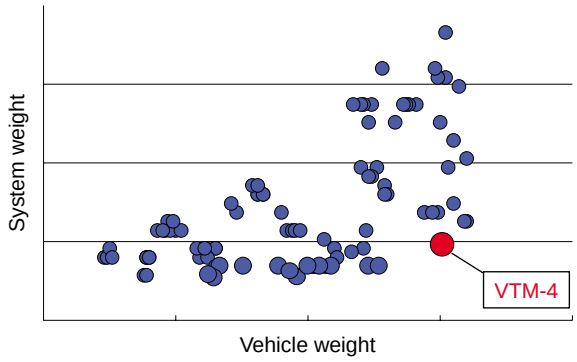


Fig. 13 System weight

6. Actual Vehicle Performance

The range of meanings covered by the term ‘actual SUV performance’ is broad and difficult to express quantitatively. Drivability and controllability performance must be evaluated with consideration of mode of use, road surface conditions, loading, etc. It has been normal to conduct relative evaluations of performance, utilizing subjective responses. For this paper, we have conducted a quantitative evaluation of basic performance in terms of drivability and controllability performance.

6.1 Drivability Performance

If the performance required to ensure drivability in a 4WD system is broadly divided, it is possible to generate the following broad categories:

- Absolute 4W driving force performance
- Front and rear driving force allocation performance
- Right and left driving force allocation performance

(1) Absolute 4W driving force is the necessary driving force for absolute hill climbing performance, hill climbing when towing a trailer, etc. It is one indicator in determining the absolute amount of maximum torque to be allocated to the rear wheels in front wheel drive based 4WD systems like the VTM-4. The torque must be transmitted with appropriate timing, before the rate of front wheel slip becomes excessive. We judged from market surveys that if the following two points were satisfied, the MDX would be able to ensure absolute driving force performance at a level which would be competitive in its target market.

- Acceleration uphill on dirt roads
- Acceleration uphill while towing a boat on a paved road

Results of measurements of necessary rear driving force under these conditions are shown in Figs. 14 and 15.

We have been able to achieve our target of necessary and sufficient hill climbing driving force and hill climbing performance. As can be seen from the rear wheel torque production characteristics, in auto mode it is possible to ensure the necessary sufficient hill climbing performance, while there is a moderate feeling of slip in the front wheels and road surface conditions are accurately transmitted to the user. In lock mode, the necessary driving force for hill climbing is instantaneously produced, and it is possible to show excellent hill climbing performance with a greater feeling of stability.

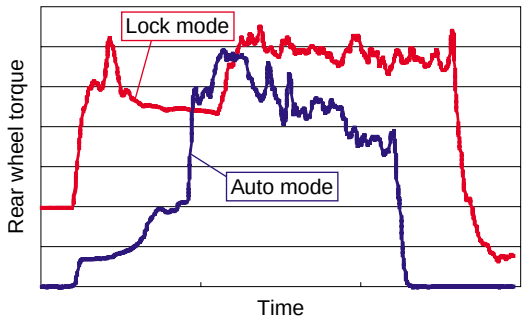


Fig. 14 Rear torque at hill climb on dirt

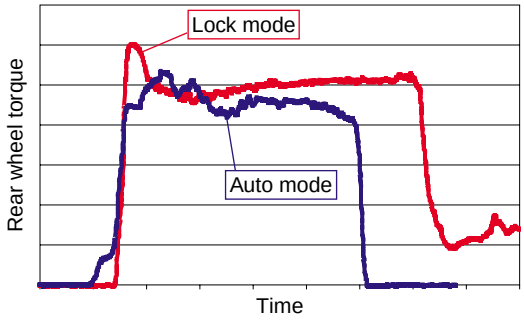


Fig. 15 Slope towing a boat on paved hill

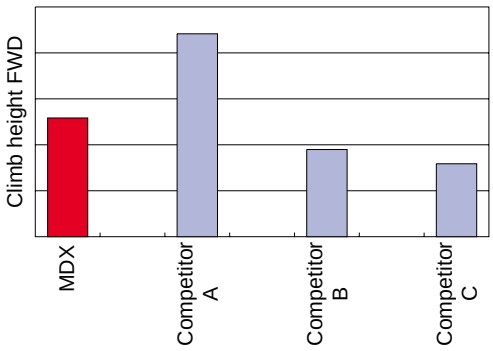


Fig. 17 Height difference for roller drive-over (Forward climb)

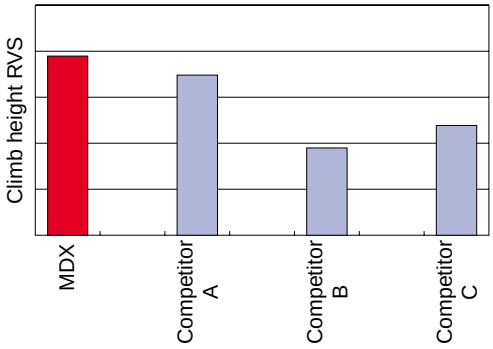


Fig. 18 Height difference for roller drive-over (Reverse climb)

(2) Front and rear driving force allocation performance is an indicator of drivability performance during driving on ordinary roads when there is snow cover, when there is a great difference between front and rear μ on the road surface, when traversing a difference in level, etc. To quantitatively evaluate this performance in an actual vehicle base, we conducted a test using a roller jig (Fig. 16) to determine the height up to which forward and reverse progress was possible. Comparative results from the same test for representative models using other systems are shown in Figs. 17 and 18.
These results indicate that we have achieved the target of necessary and sufficient driving performance in comparison with the other vehicles tested.

(3) Right and left driving force allocation performance is acceleration performance on an ordinary road in conditions such as occur on a sloping road with a split μ (e.g. the road shoulder is frozen) or performance in controlling a wheel which has left the road. To quantitatively evaluate these conditions, we used the same roller jigs as used in the previous tests. The front and rear wheels on one side of the car were placed on these (Fig. 19) and the towing force at that time measured. Fig. 20 shows comparative results with representative vehicles.
Under these conditions the MD-X could generate almost twice as much towing force as a normal preset-type LSD (competitor A), and could ensure the necessary and sufficient right and left driving force allocation performance for actual use.

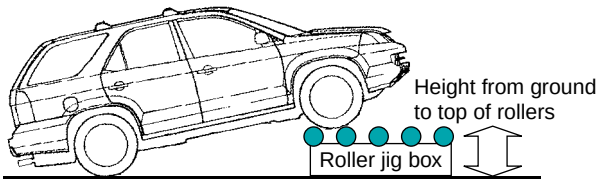


Fig. 16 The method for roller drive-over

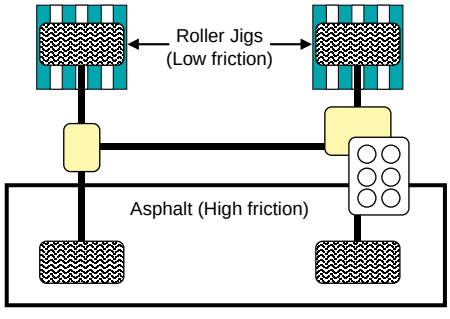


Fig. 19 The method for towing-strength measurement on split surface

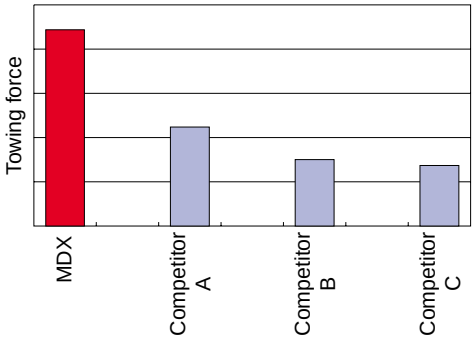


Fig. 20 Towing-strength measurement on split surface

6.2 Controllability Performance

Controllability performance is broadly divided into performance on wet and dry roads. Here, we conducted our evaluation by the standard method using circular acceleration characteristics.

We compared circular acceleration characteristics with those of representative passenger vehicles. As shown in Fig. 21, we have achieved controllability performance equivalent to that of a passenger vehicle, one of the targets set for this system.

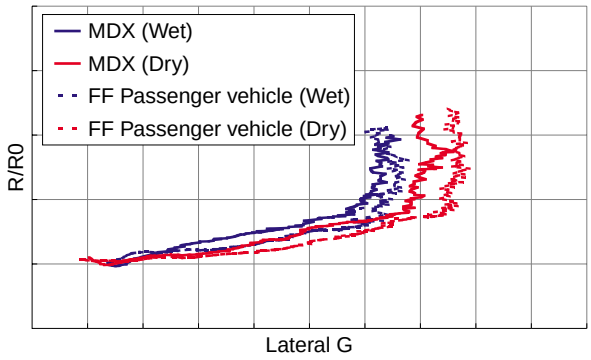


Fig. 21 US/OS Characteristics

7. Conclusion

These headings for comparative evaluation of 4WD drivability as an SUV and controllability as a passenger vehicle for the MDX and other vehicles are marked out as a radar chart in Fig. 22 below.

The target for this system was set as 'balancing necessary and sufficient drivability as an SUV with controllability as a passenger vehicle'. This target has been achieved at the lowest system weight in the class (97 kg), by the adoption of electronic torque control and a torque limit function, concentration of functions in the rear final drive unit, placement of clutch units on the right and left rear wheel axles and the use of a passenger vehicle chassis.

This system is being utilized in the 2001 Acura MDX, which has been well received by customers since being placed on the market in North America in September 2000.

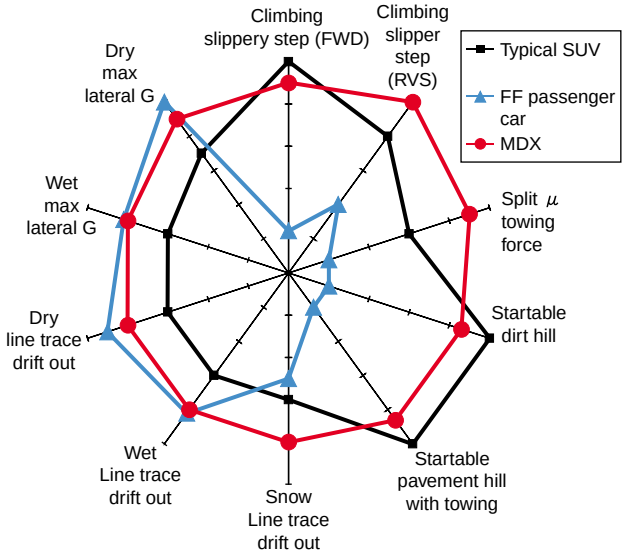


Fig. 22 Radar chart of 4WD performance

In conclusion, we wish to express our sincere gratitude to those at the R&D Center and elsewhere who provided significant support during the development of this system.

References

(1) Takuno, H., et al.: Development of New Electromagnetic Controlled Coupling for Four-wheel Drive Vehicles, Society of Automotive Engineers of Japan, Inc., PROCEEDINGS No. 75-99, p. 5-8 (1999)

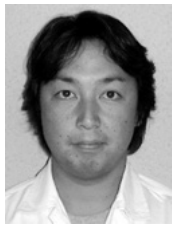
(2) Gotoh, A, et al.: Development of New 4WD System based on FF, Society of Automotive Engineers of Japan, Inc., PROCEEDINGS No. 97-99, p.1-4 (1999)

(3) Chulhee Lee: A Study of NVH Phenomenan in SUV Drivetrain caused by Propeller Shaft, JSAE Spring Convention Proceedings, No. 43 – 00, p. 17 – 20 (2000)

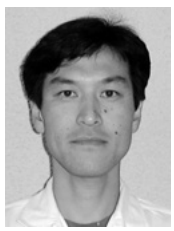
■ Authors ■


Koji KURODA


Kazuhiro NAKANO


Yoshikazu KONISHI


Takeshi HORI


Kenzo NISHIDA


Kazunori KOBAYASHI

Enhancements in Handling on Slippery Roads with VSA

Keiyu KIN* Tohru IKEDA* Osamu YANO*

ABSTRACT

The performance of Vehicle Stability Assist VSA was tested for reproducibility under various conditions encountered on slippery roads. The results showed that VSA enhances stability and steerability, that driver fatigue was reduced, and collision avoidance performance was enhanced. This thus demonstrated the effectiveness of VSA.

1. Introduction

The authors previously reported on enhancements to stability and steerability made through research into VSA with 4-wheel optimum slip control[(1)]. In this new research project they have performed vehicle handling verifications using VSA on ice- and snow-covered roads. The results confirm that there is an enhancement in vehicle stability and steerability under the snow and ice conditions encountered on these slippery road surfaces. Further, the authors confirmed that VSA with 4-wheel slip control is effective in reducing the likelihood of collisions where the vehicle over-steers or leaves the lane. The test vehicle used was an FF (front engine, front drive) vehicle with on-demand type 4-wheel-drive, and the test course was a snow- and ice-covered road surface.

*Tochigi R&D Center

2. Test Modes

In cold or snowy regions, one may encounter numerous situations where handling instability may occur. Examples of these situations include driving at an excessive speed leading to the vehicle being unable to trace a corner; seeing an obstacle and braking suddenly while turning; sudden steering to avoid something that jumps out onto the road; or, an operating error due to the fatigue and stress of driving on winding roads. From these scenarios, the following four test modes were established.

(1) J-turn (approaching a corner at excessive speeds)
(2) Braking in turn (sudden braking while turning)
(3) Double lane change (collision avoidance rapid steering)
(4) Continuous slalom (driving on winding roads)

VSA performance, in terms of both stability and

steerability, was evaluated in each of these situations.

That is, the purpose of this research project was to verify, using an actual vehicle, the achievement of both of the following:

(1) Reduction of driver fatigue due to stability enhancements: Stability (rear tire grip)
(2) Enhanced collision avoidance performance: Steerability (steering effectiveness)

3. Control Logic

VSA is composed of three basic control logics:

(1) Vehicle side slip angle estimation logic (β estimation logic)
(2) Tire and road friction coefficient estimation logic (μ estimation logic)
(3) Optimum 4-wheel slip control logic (λ control logic)

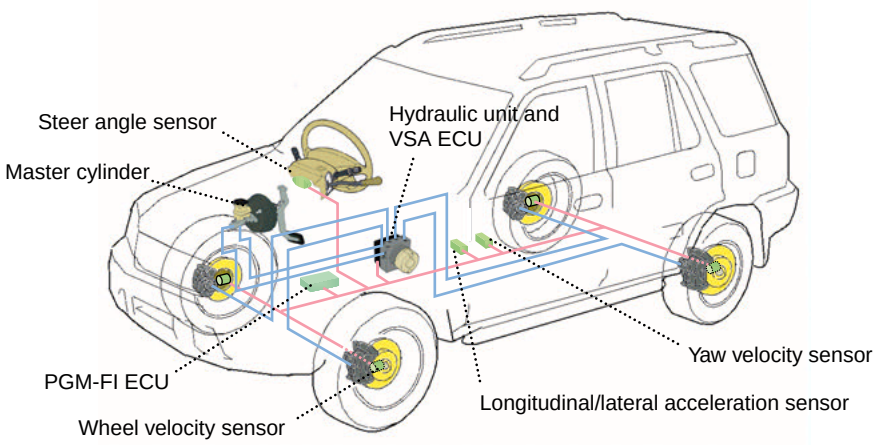


Fig. 1 System configuration

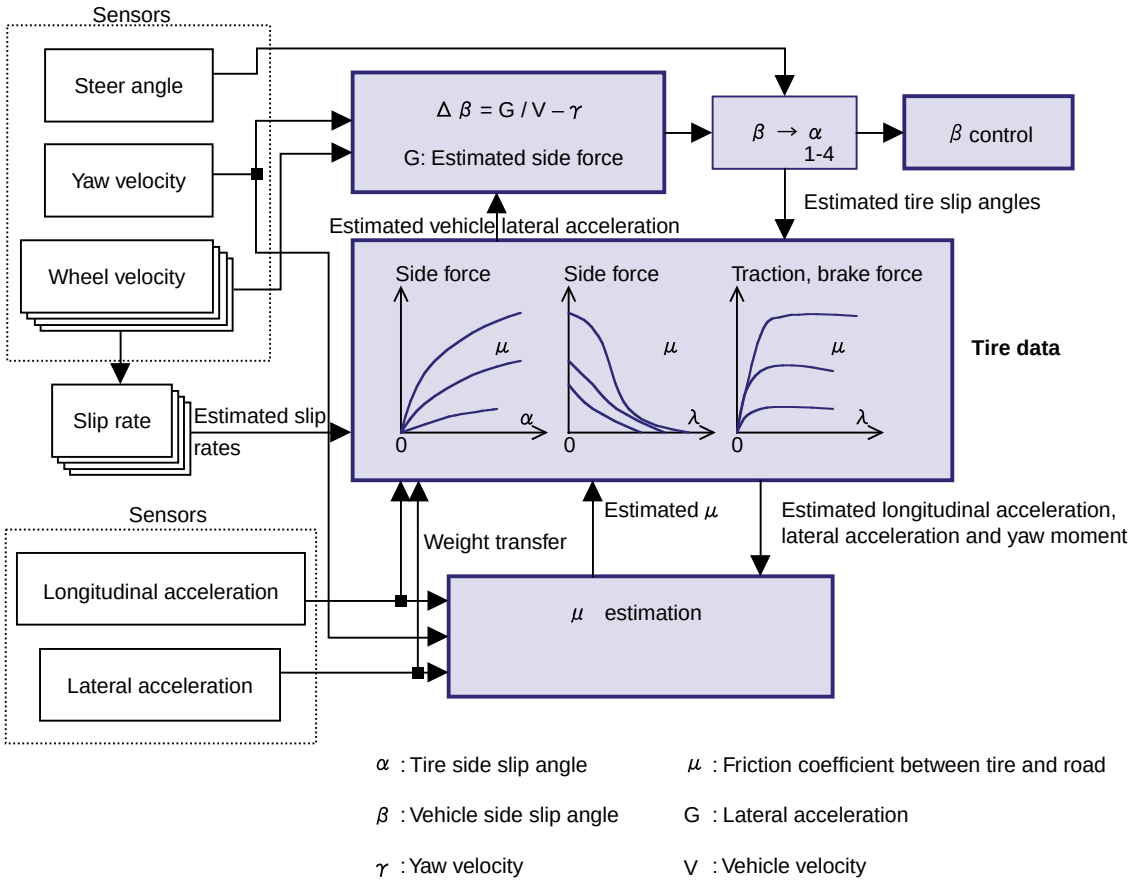


Fig. 2 Basic VSA logic

This project achieved enhanced performance on snow- and ice-covered roads by modifying the following three VSA control logics:
(1) Vehicle speed estimation logic
(2) Under-steer control logic
(3) Over-steer control logic

The basic configuration of the VSA control system is shown in Fig. 1. The basic control logics are shown in Fig. 2. The three control logics the team worked on to enhance performance on snow and ice are described below.

3.1 Vehicle Speed Estimation Logic

In order to increase vehicle speed estimation accuracy during start-slip control, low μ split driving, or slip control operation, vehicle speed is determined by converting total brake and traction forces for each tire, which is estimated from slip-μ characteristics (tire map data), into estimated longitudinal acceleration, as shown in Fig. 3. Also, tire characteristics are adapted to fit the μ estimation logic.

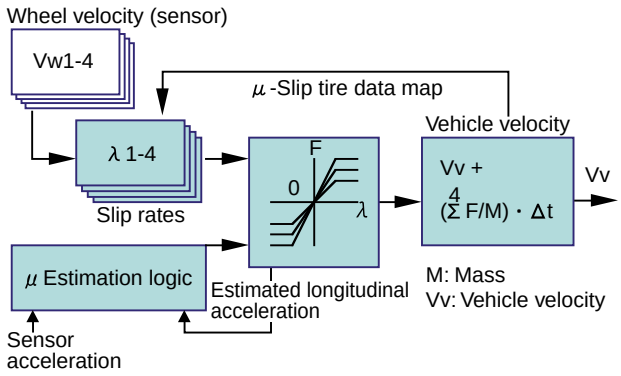


Fig. 3 Vehicle velocity estimation logic

3.2 Under-steer Control Logic

Under-steer (US) generally occurs when entering a corner at excessive speeds, as shown in Fig. 4. Thus, rear wheel brake control and front inner wheel moment control are activated simultaneously for 3-wheel control. In particular, as for rear tires, a brake force difference is applied to the left and right wheels after deceleration so that a proper moment is generated.

3.3 Over-steer Control Logic

A moment restricting control that operates at an earlier stage has been developed to help control over-steer (OS). This control works to help prevent the sudden yaw moment arising from rapid left and right continuous steering during an emergency avoidance maneuver, and also considers the comparatively heavy inertial moment of an SUV. In practical terms, as shown in Fig. 5, excess moment is estimated and controlled when (1) the vehicle side slip angle exceeds the threshold, and then (2) the yaw rate changes from a negative to a positive value, or vice versa.

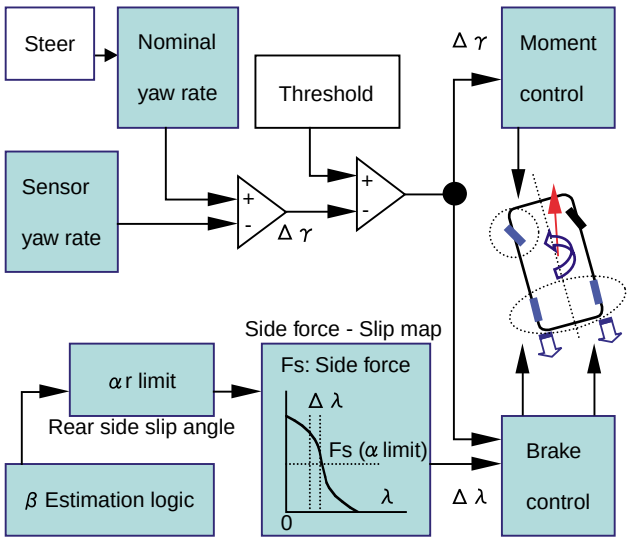


Fig. 4 Under-steer control logic

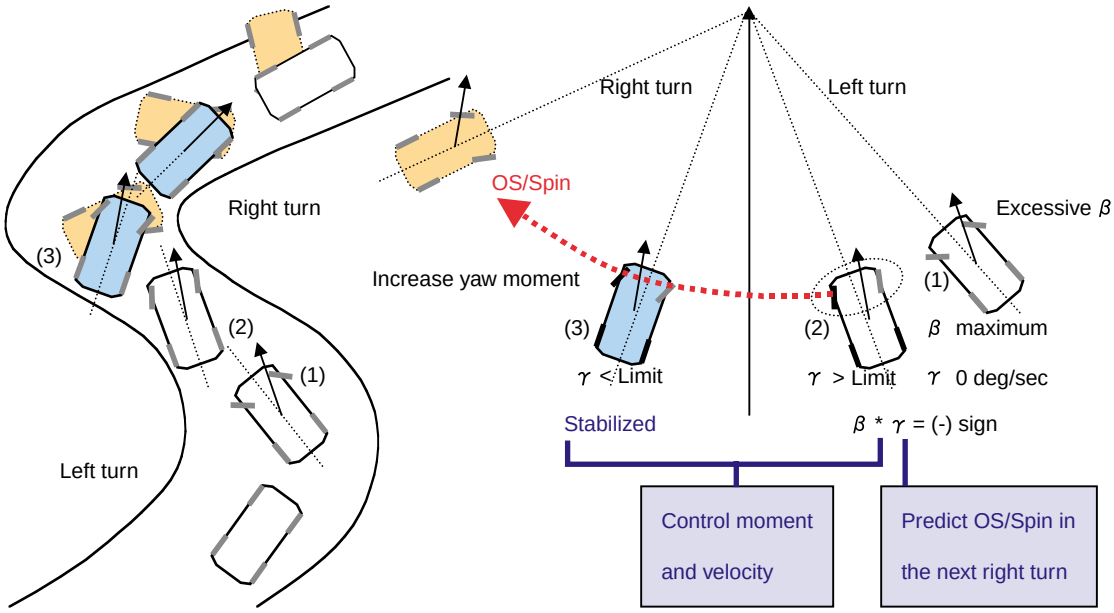


Fig. 5 Prediction and control for excessive yaw moment on the slalom course

4. Test Results

4.1 50R J-turn Test (entering corner at excessive speeds)

The test mode and images of a vehicle driving on the test course are shown in Fig. 6.

Fig. 7 shows the tire grip limits are exceeded, and the vehicle diverges outward from the target course when VSA is not in operation. In contrast, when VSA does operate, as shown in Fig. 8, the vehicle divergence from the target line is kept to a minimum, and stability and steerability are generally maintained. This is due to the operation of rear wheel deceleration control and front inner wheel moment control.

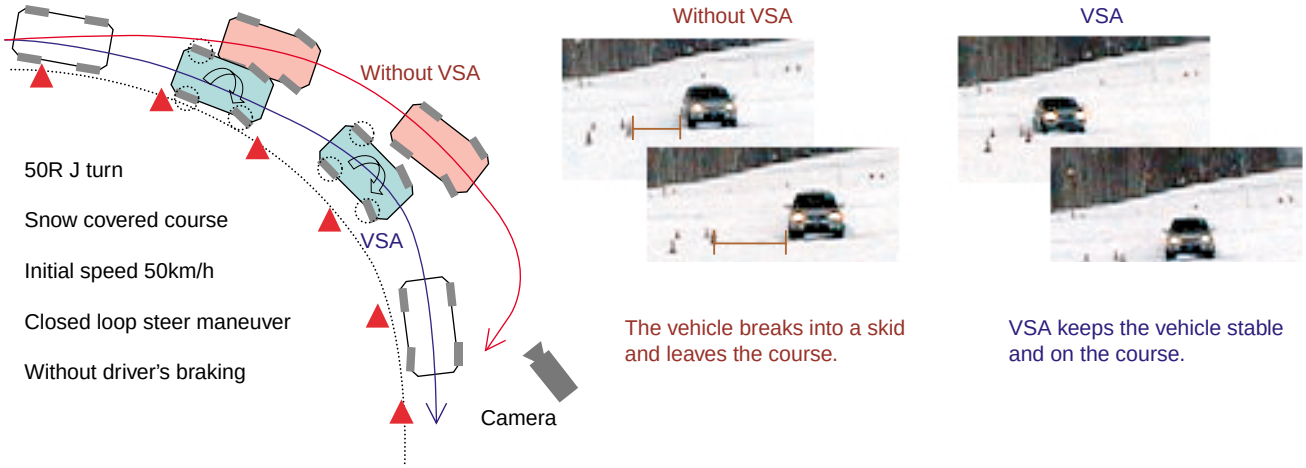


Fig. 6 50R J turn test

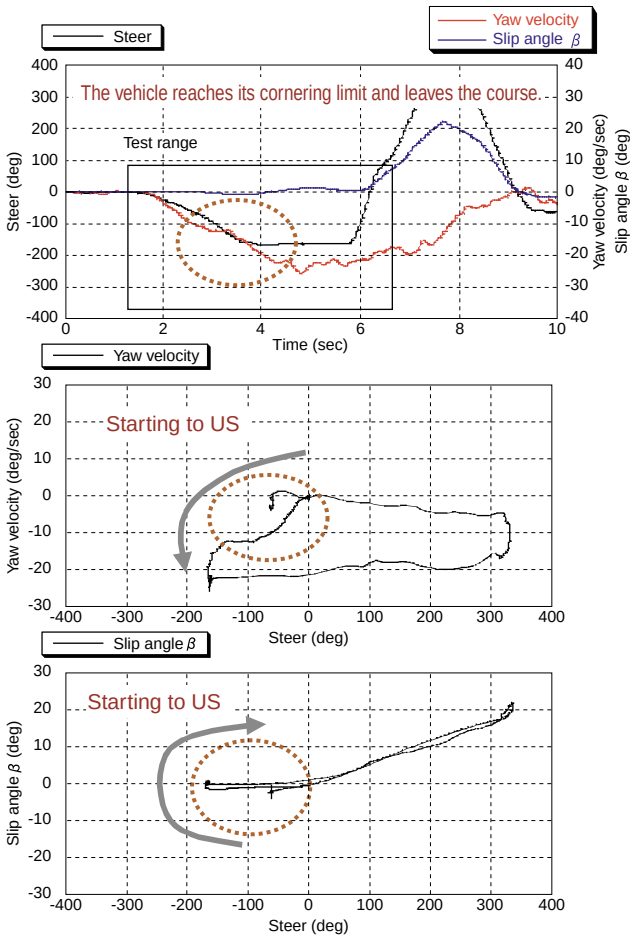


Fig. 7 50R J turn test on snow without VSA

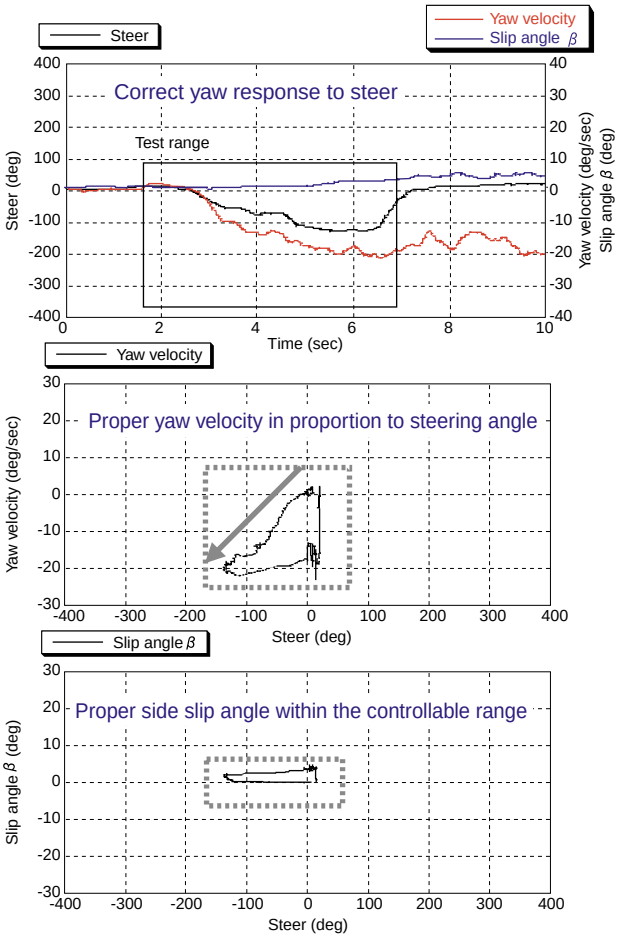


Fig. 8 50R J turn test on snow with VSA

4.2 50R Braking in Turn Test (sudden braking while turning)

The test mode and images of a vehicle driving on the test course are shown in Fig. 9.

Fig. 10 shows the tire grip limits are exceeded and the vehicle quickly diverges outward from the target line when VSA is not in operation. In contrast, as shown in Fig. 11, when VSA does operate, stopping distance is reduced 15%. This reduction is achieved due to the deceleration control of the two rear tires and the rear moment control which uses the left and right brake force difference, as well as front inner wheel moment control. This realizes the vehicle side slip angle and stability maintenance which subsequently results in the reduction in braking distance. Ideally, there should be more significant collision avoidance effects due to a further reduction in divergence from the driving lane.

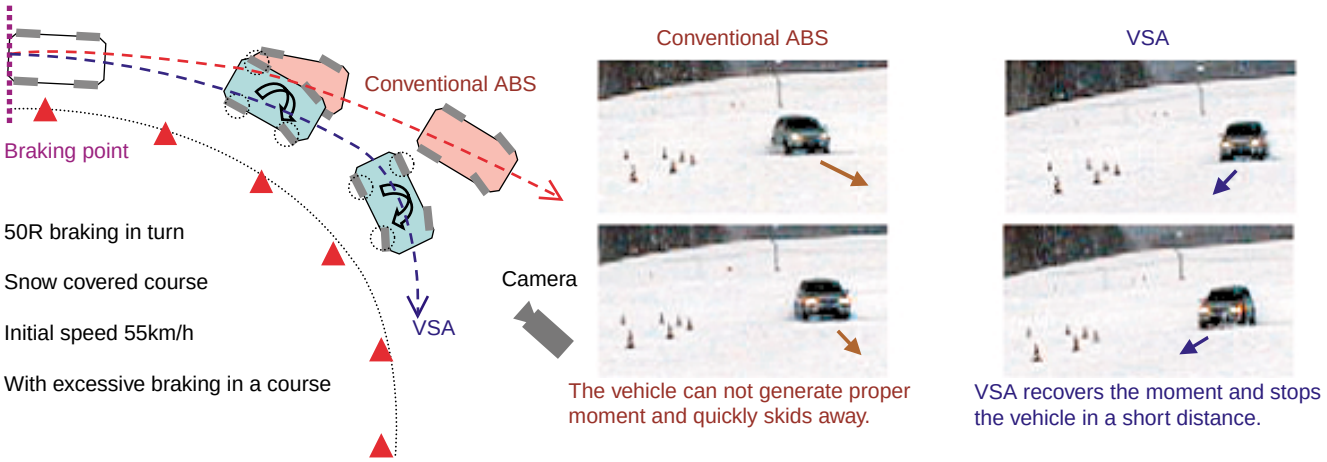


Fig. 9 50R braking in turn test

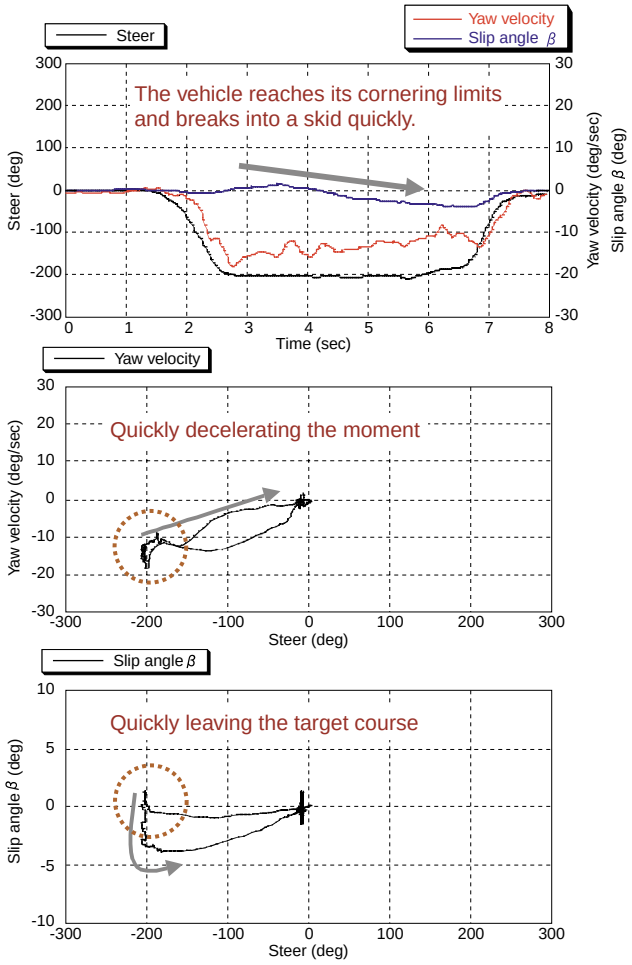


Fig. 10 50R brake in turn test on snow without VSA

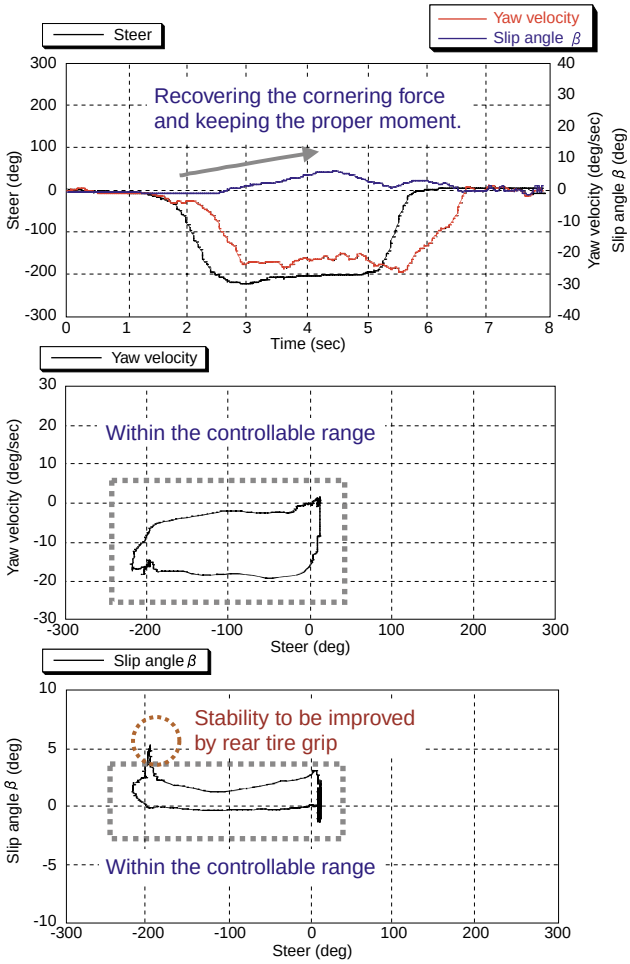


Fig. 11 50R brake in turn test on snow with VSA

4.3 Double Lane Change (collision avoidance steering)

The test mode and images of a vehicle driving on the test course are shown in Fig. 12.

Fig. 13 shows that there is a sudden increase in yaw moment when the vehicle returns to its original lane after an avoidance maneuver. It will enter into an over-steer condition if VSA does not operate. In contrast, as shown in Fig. 14, when VSA does operate, yaw moment and side slip angle restricting controls are quickly applied, so that stability is generally maintained and a more effective steering state is achieved to help prevent over-steer. This is realized with the control system predicting the excessive moment that will occur at the next turn based on the yaw movement in the initial avoidance steering.

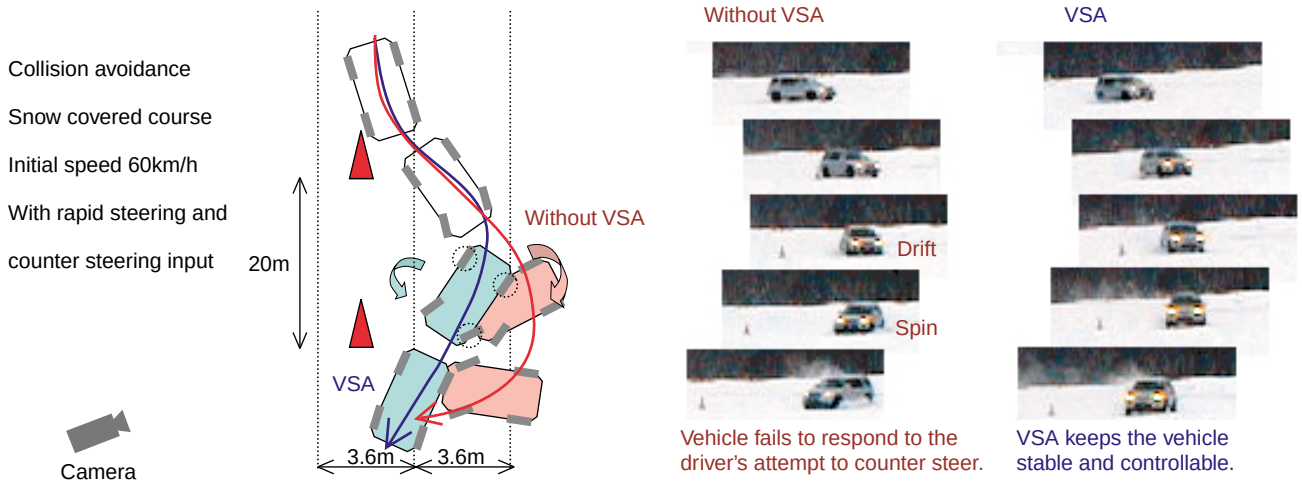


Fig. 12 Collision avoidance test

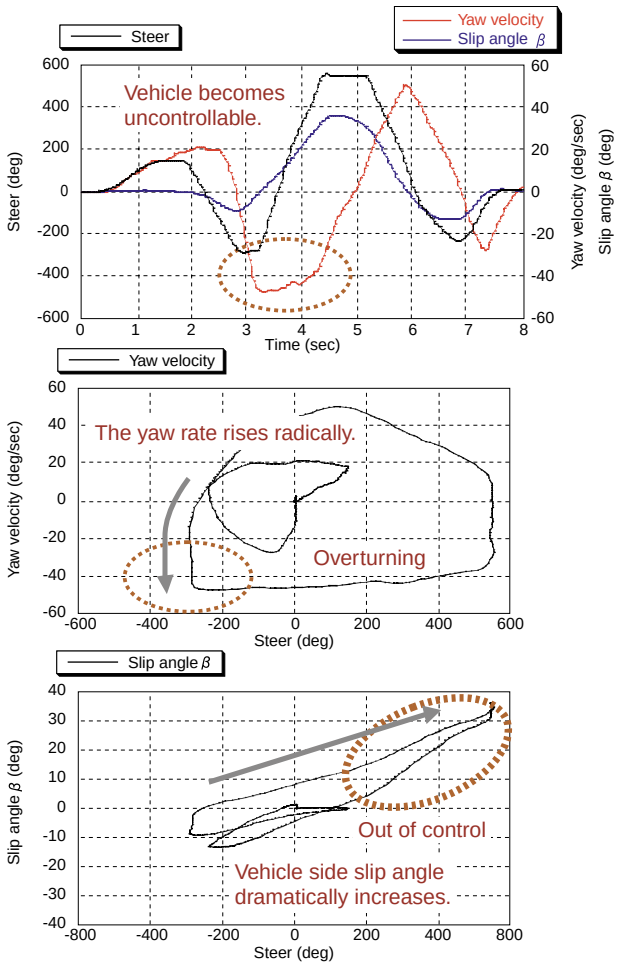


Fig. 13 Collision avoidance test on snow without VSA

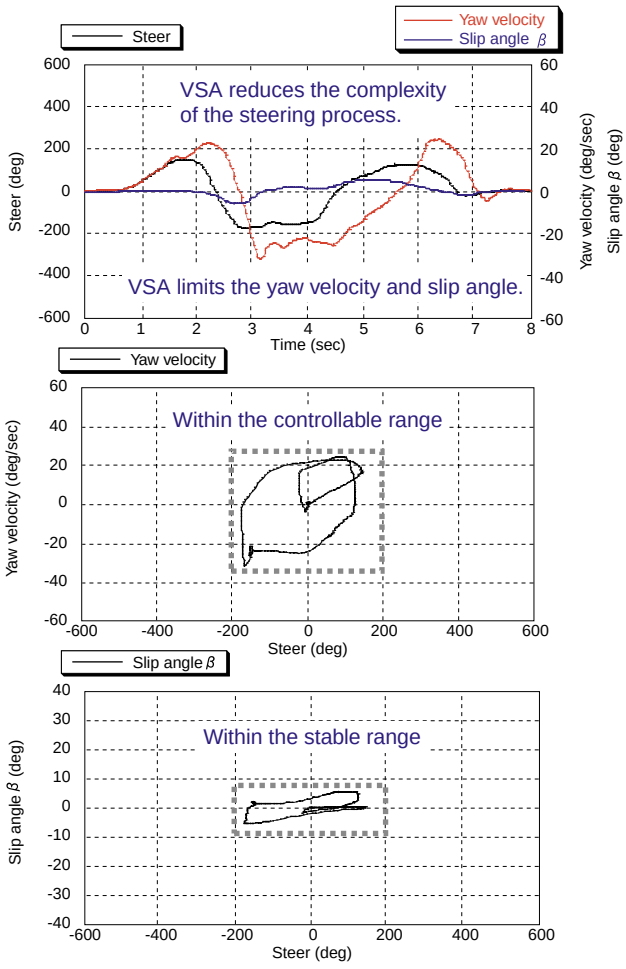


Fig. 14 Collision avoidance test on snow with VSA

4.4 Continuous Slalom (driving on winding roads)

Fig. 15 shows the test mode and photographic images of the actual vehicle while driving on the course.

As shown in Fig. 16, without VSA vehicle, behavior becomes increasingly unstable with each turn, so there is an increase in both steering and correction. In contrast, as shown in Fig. 17, both side slip angle and yaw moment are controlled more appropriately and quickly with VSA control. Thus, steering is more stable. This has the benefit of reducing driver stress and fatigue, and of helping reduce the frequency of operating errors.

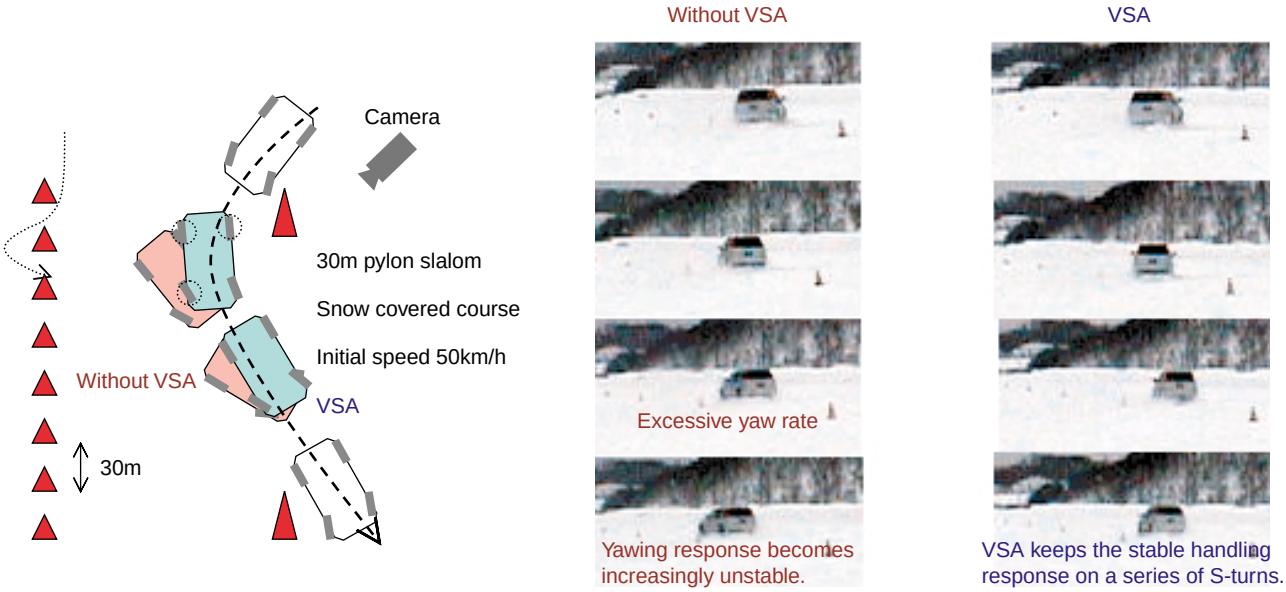


Fig. 15 Slalom test

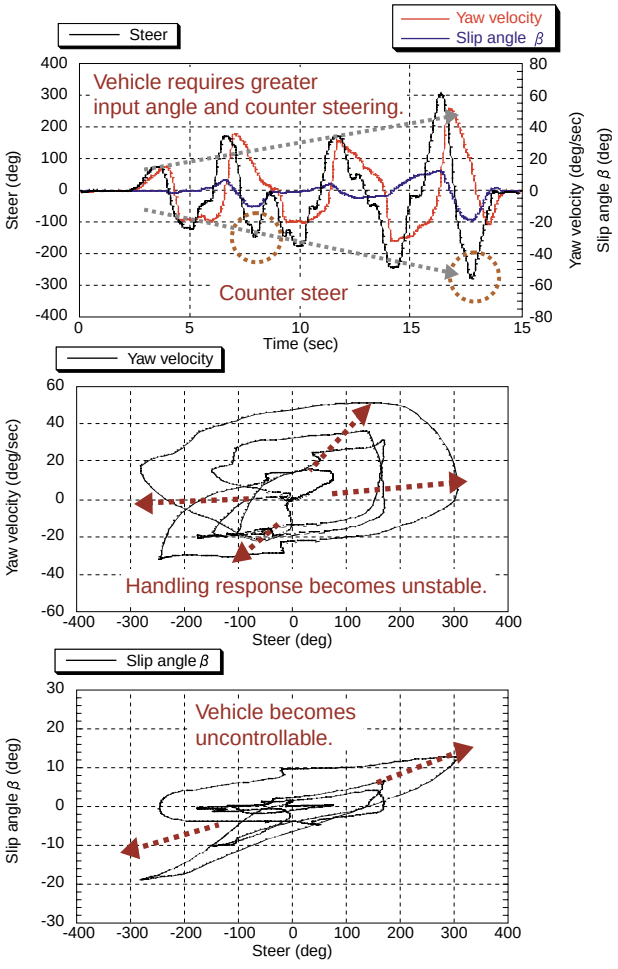


Fig. 16 Slalom test on snow without VSA

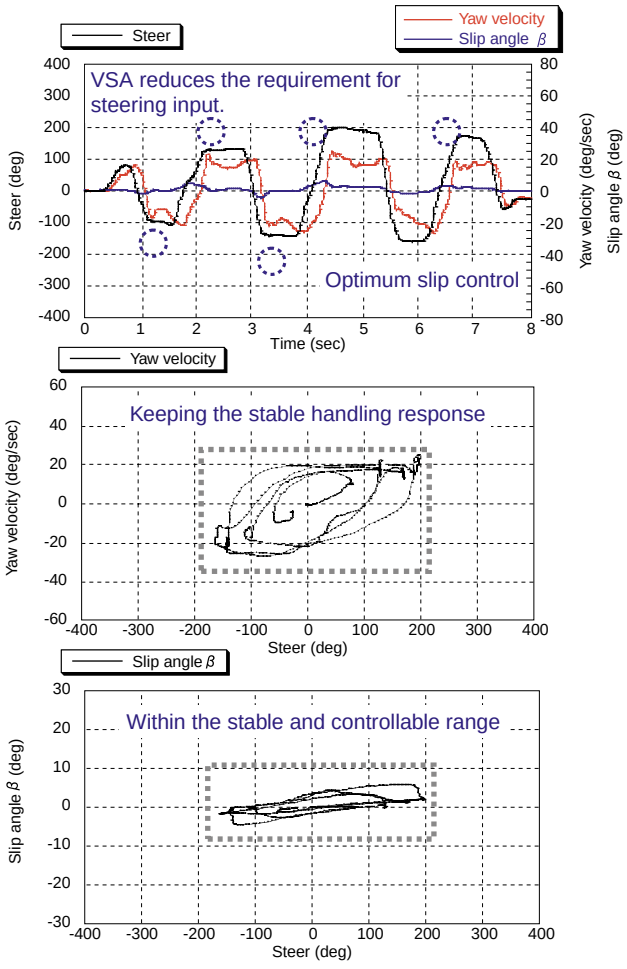


Fig. 17 Slalom test on snow with VSA

5. Observations

This paper will next discuss the effects of VSA on enhancing stability and steerability on ice- and snow-covered roads based on the results of the four tests outlined above.

(1) J-turn
Owing to the effects of deceleration control on the two rear wheels and under-steer control of the front inside wheel, it is possible to turn the vehicle while generally maintaining stability. In particular, yaw moment rises in proportion to the steering angle, thereby enhancing handling characteristics. However, it is necessary to further restrict drift-out from the point of view of potential collision avoidance.

(2) Braking in Turn
Stability has also been enhanced with a 15% reduction in stopping distance during turning while braking. However, the issue of divergence from the target line (caused by initial under-steer) remains, and further enhancement is necessary. In order to achieve this enhancement, it is necessary to develop predictive technology that, for example, anticipates not only the vehicle movement state in real-time but also the road situation ahead (for example, turning radius, etc.), to then apply advance speed control.

(3) Collision Avoidance Operation
Avoidance performance is enhanced even in situations where the vehicle sways widely due to rapid left and right steering, such as when avoiding an obstacle in the road. This performance is achieved through the stabilization of vehicle behavior resulting from the prediction of sudden increases in yaw rate and the early application of control.

(4) Slalom
The results of generally maintaining optimum steering characteristics during a continuous slalom are an enhancement in vehicle behavior stability and, consequently, allow for a reduction in fatigue.

6. Conclusions

The use of VSA control is beneficial in reducing driver fatigue when driving on ice- or snow-covered roads, and in reducing the likelihood of collisions.

(1) Over-steer caused by collision avoidance, a series of S-turns, winding roads, etc. can be effectively reduced with the control that predicts the related difficulties in advance and improves rear tire grip.

(2) Drift-out and under-steer caused by turning at excessive speeds or that occur during sudden braking can be effectively reduced, in comparison with conventional vehicles, due to a decrease in stopping distance and enhancements in handling characteristics. However, on ice- or snow-covered roads, where slightly excessive speeds or an operating error could lead to an accident, further enhancements are required in order to minimize divergence from the traffic lane.

7. Towards the Development of Active Safety Technology

Development has been proceeding with the goal of vehicle movement control that is highly effective in accident prevention. However, in order to make further improvements to safety, it will be necessary to develop the technology required to achieve a higher level of active safety, including technology that incorporates information surrounding the vehicle and new sensing technology.

Also, it is said that the leading cause of many collisions is driver error. Therefore, it is necessary to carry out investigative researches in external factors (vehicle behavior, road environment) and internal factors (drivers' state of mind) that compound to create conditions leading to operating errors as well as the estimation of vehicle behavior and road surface friction coefficients. In the future, in addition to analysis of vehicle dynamics and road conditions, analysis of human factor dynamics must be pursued in the development of accident prevention technology.

References

(1) Kin, K., Yano, O., and Urabe, H., Enhancements in Vehicle Stability and Steerability with Slip Control, Honda R&D Technical Review Vol. 13, No. 1, p. 91 – 98 (2001)

■ Authors ■



Keiyu KIN



Tohru IKEDA



Osamu YANO

Changes in Drivers' Heart Rates due to the Influence of Braking

Koji TANIDA*

ABSTRACT

This project focused on changes in drivers' heart rates while braking, as an approach to understanding driving behavior. Using tests designed to model a variety of braking conditions, it was observed that driver psychological states while braking are displayed in the form of changes in heart rate. In a test where an obstacle darts out from the side of the road, driver heart rates were observed to increase suddenly. On the other hand, a test where the vehicle comes to a halt at a stop line showed the heart rate gradually slowing before the vehicle stopped. It was thus inferred that changes in heart rate take on a distinctive pattern in response to braking behavior. In this light, an index formula was proposed that uses the magnitude of the response in heart rate acceleration during braking to determine whether an instance of braking behavior represented panic braking.

1. Introduction

A major goal of car development is to produce safe vehicles. While effort is naturally focused on safety technology designed to minimize the damage caused by collisions, a great deal of effort is also expended on the development of safety technology that can help to effectively prevent accidents from occurring in the first place. Examples of this type of technology that has been incorporated into cars include anti-lock braking systems and power-assisted braking systems. One means by which the effectiveness of both of these systems has been verified is through panic braking tests[1]. Such tests are set up so that the test subject is caused to panic in order to observe the braking behavior of a driver in an emergency situation. Ueno et al., presented a stress evaluation[2] focused on the driver's physiological state, and equated a state of excessive stress with panic. However, since there has been little research on physiological and psychological states during panic braking, it was felt that an attempt at a test that evaluates braking from the physiological standpoint of the driver would be useful in future automotive development.

This paper discusses methods for using changes in the driver's heart rate to identify panic braking when the driver is confronted with a vehicle that suddenly emerges from the side of the road.

2. Psychological State and Physiological Response

The autonomic nervous system, which is affected by emotions, consists of a sympathetic nervous system and a parasympathetic nervous system, and it is believed that psychological balance is maintained through an opposing relationship between these two systems[3]. When a person's psychological state is disturbed by stress or danger, a physiological response driven by the sympathetic nervous

* Tochigi R&D Center

system is observed. When the sympathetic nervous system takes precedence, the blood pressure rises due to constriction of the blood vessels in the extremities. In addition, the heart rate increases and variations in the intervals between heartbeats decrease. On the other hand, when the parasympathetic nervous system (the pneumogastric nerve) takes precedence, the heart works more calmly, the heart rate drops, and the intervals between heartbeats becomes more variable.[4] [5]

Therefore, this research tried to classify panic braking on the basis of differences in braking and changes in heart rate.

3. Classification of Braking Behavior

In order to compare and evaluate stress during braking, it is necessary to define braking behavior. Various types of braking behavior occur in real-world driving. Five basic modes of braking were established for this research. The first two modes are simple braking:

(1) "Signal mode", in which the driver brakes to stop the vehicle at a specific target position, such as at a red light
(2) "Curve mode", in which the driver brakes to slow the vehicle down to a suitable speed, such as when entering a curve

The remaining three modes concern more complex braking:

(3) "Escape mode", in which the driver brakes in order to secure sufficient time for steering avoidance such as when merging onto the expressway (when, for example, the merge lane is nearing an end) ,
(4) "Hard mode", in which the driver suddenly begins to brake hard at a known "brake start" position
(5) "Panic mode", in which the driver brakes suddenly because of the sudden emergence of an obstacle.

The "hard mode" is a special mode that was established for the purposes of our research as a comparison for "panic mode" in order to determine the differences in physiological response, depending on whether the driver knows the position at which to start braking beforehand.

4. Test Method

4.1 Test Overview

There were 39 test subjects (34 men, 5 women), with ages ranging from the 20s to the 50s. The test vehicle was a 1600 cc, 4-speed automatic transmission vehicle. The test subjects were instructed to drive normally, and were not informed that there would be a panic braking test. In a test such as this, controlling the vehicle speed is very important. Therefore, before commencing the tests, each subject was allowed to become comfortable with the vehicle, and was given adequate practice runs in which he or she was required to drive at a certain speed. When each subject was deemed able to control the vehicle speed adequately, the panic mode test was conducted during a practice run without warning. After the reason for the surprise test was explained to the subject, the subject's consent to proceed with the remainder of the testing was obtained. Subsequently, each braking mode was explained to the subject, and then a total of 13 braking tests were conducted: five signal mode tests, three curve mode tests, three escape mode tests, and two hard mode tests. The sequence in which the modes were tested varied from subject to subject.

4.2 Test Course Setup

Fig. 1 shows the test course for each braking mode. Fig. 2 shows the test scene for the panic mode test. In order to induce all test subjects to rapidly apply their brakes without

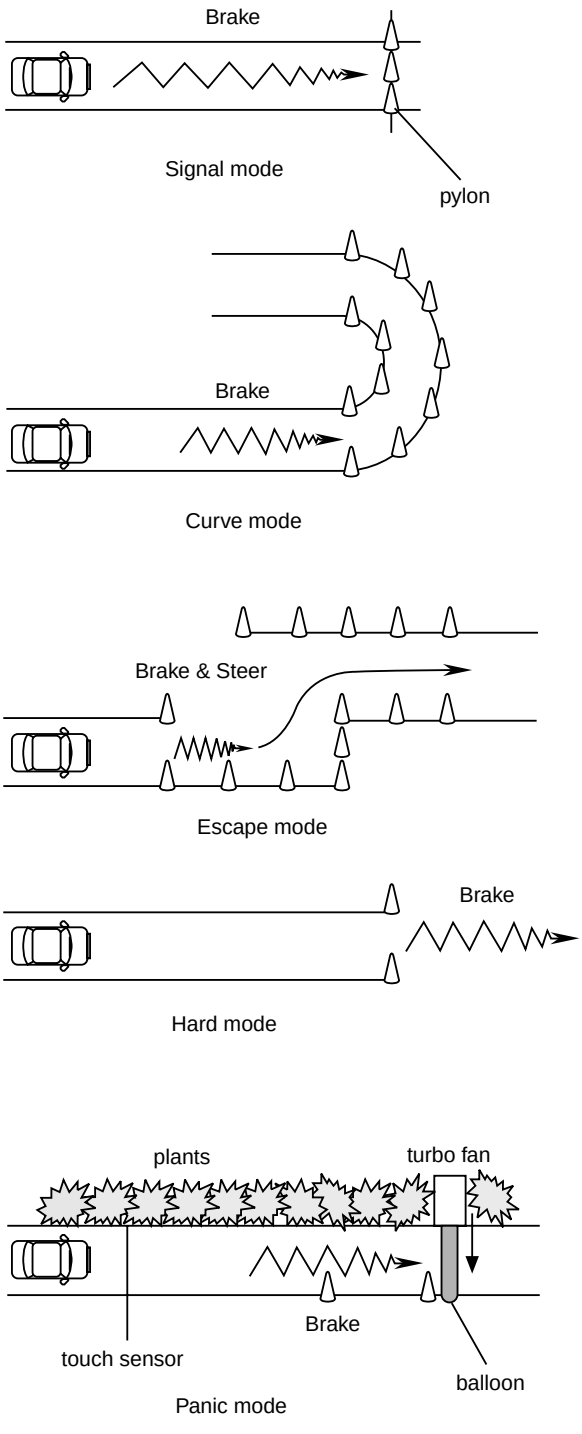


Fig. 1 Braking test modes



Fig. 2 Panic mode

steering avoidance, the test was set up so that a cylindrical balloon, inflated by a turbofan, would suddenly emerge from the left side of the road to fully block the driving lane in one second. In order to keep the timing of the balloon's emergence consistent for all of the test subjects, a touch sensor was placed on the road surface. When the front wheels of the vehicle passed over this sensor, the turbofan was activated.

A 200 m approach was set up for each mode. The braking tests were conducted from a constant vehicle speed of 50 km/h, with no other vehicles present. In addition, the road was defined by pylons, making it more difficult than it would be under actual driving conditions for the subjects to understand where the roadway was until they were in the proximity of that section of road. Therefore, it should be noted that the subjects paid more attention while driving than they normally would.

4.3 Heart Rate Measurement

To measure the heart rate, a ground electrode was attached to each subject's earlobe and an ECG (electrocardiogram) was taken from two electrodes attached to the chest. The ECG was recorded on a data recorder with a sampling frequency of 500 Hz. In addition, the level of physiological response in the autonomic nervous system is subject to cyclical fluctuation during the day, called the "circadian rhythm." [6] Therefore, it would be necessary for the measurements in each test to be taken at a consistent time of day. However, if the test looked only at changes that occur when the test subject is subjected to stress, it was felt that the direction of such changes would be constant regardless of the time of day. Therefore, the test focused only on changes in heart rate during braking, without relation to the circadian rhythm.

4.4 Scope of Analysis of Heart Rate Data

Because the sudden emergence of an obstacle is unforeseeable and induces a rapid psychological change, it is likely that the heart rate would change rapidly at that instant. On the other hand, the moment at which the subject recognized the emergence of the obstacle or the instant at which the subject decided to start braking reflect internal mental processes that are difficult for an external observer to define. However, in this test, behaviors that were common to all of the subjects were releasing the accelerator pedal and depressing the brake pedal. Therefore, a laser sensor that was capable of measuring the stroke of the accelerator pedal was attached to the accelerator pedal in the test vehicle in order to pinpoint the moment at which the subject began to release the accelerator pedal. This arrangement allowed the test to focus on changes in the heart rate before and after the accelerator pedal was released, even while braking was occurring. The scope of analysis, therefore, was defined as a certain period before and after the release of the accelerator pedal.

5. Test Results

In this test, 36 of the 39 test subjects provided valid results. Some of the subjects did not provide valid results due to problems such as the seat belt rubbing against and detaching some of the electrodes.

The test results are described below.

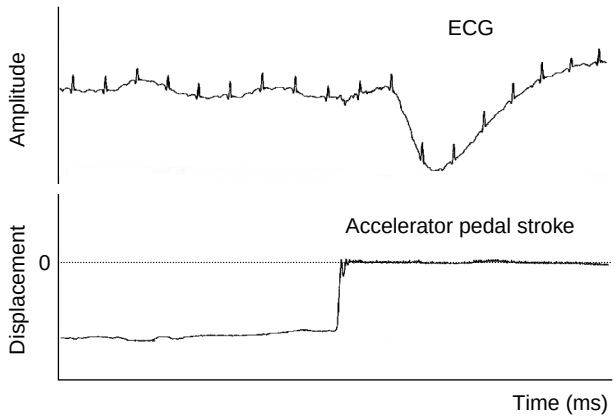


Fig. 3 Driver electrocardiogram (ECG) and accelerator pedal stroke displacement

5.1 Patterns of Change in Heart Rates for Each Mode

Fig. 3 shows an example of the data obtained from a single panic mode test. The graph shows the five second period before and after the accelerator pedal was released. (The five seconds after the pedal is released allows enough time for the vehicle to stop, whether in signal mode, hard mode or panic mode.) The upper portion of the graph shows the wave produced by the electrocardiogram; the fluctuation in the baseline is likely caused by the upper torso bending forward in response to the sudden and strong braking, or by perspiration produced in response to stress. The lower portion of the graph depicts the accelerator pedal stroke. In the graph, the negative direction represents the pedal being pressed. The graph clearly shows that the subject kept the accelerator pedal depressed by a nearly constant amount in order to maintain a constant speed up to the moment when he or she subject released the accelerator pedal. Time series data for the heart rate (Fig. 4) is obtained by calculating the instantaneous heart rate on the basis of the RRI, or the interval between peaks in the electrocardiogram. "AP-off" in the graph indicates the instant at which the accelerator pedal was released.

Once this conversion is made for all subjects and all tests, qualitative trends in changes in heart rate such as those indicated below can be determined. Fig. 5 shows the

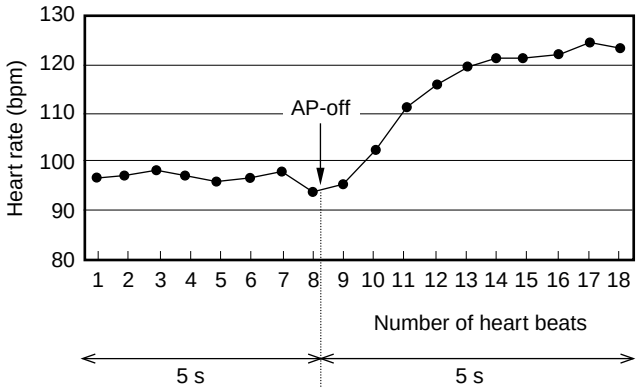


Fig. 4 Change in heart rate between 5 s before and after accelerator pedal release (AP-off)

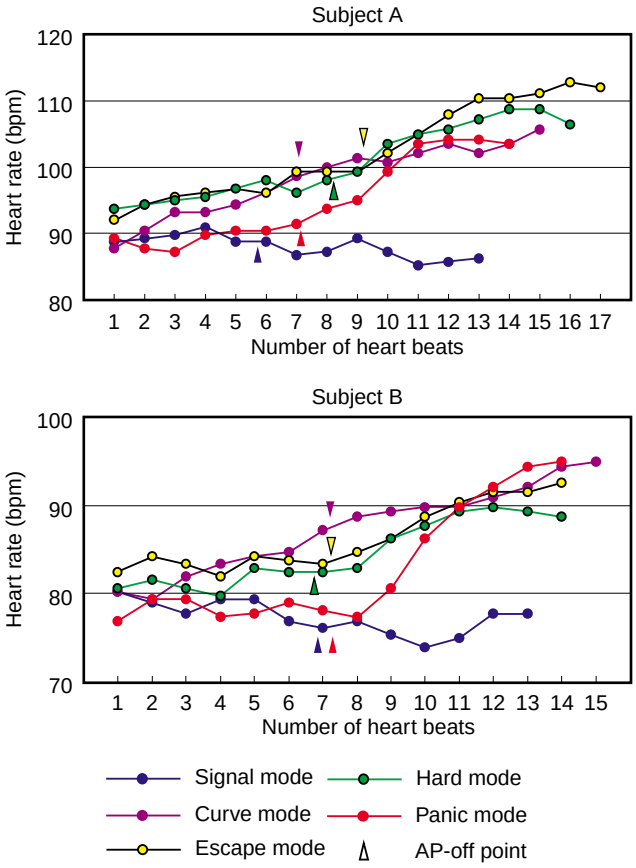


Fig. 5 Heart rate change pattern in each mode

data for two subjects.

In short, when braking in the signal mode, the heart rate begins to decline before the driver begins braking, and as the vehicle slows down the heart rate also slows down gradually with some fluctuation.

When braking in the curve mode, the heart rate increases as the vehicle approaches the curve, and continues to increase even as the subject enters the curve.

When braking in the escape mode, the heart rate increases as the vehicle approaches the point where braking begins. The heart rate increases further while the driver is performing steering avoidance maneuvers.

In the hard mode, the heart rate increases as the vehicle approaches the point at which the subject is supposed to begin braking. Subsequently, the heart rate continues to increase, but then it begins to decreases right before the vehicle stops.

In the panic mode, no change in heart rate is observed until immediately before braking. Once braking begins, the heart rate increases dramatically.

These results made it clear that there is a pattern to the change in heart rate in response to each mode. Next, an attempt was made to identify panic braking through a quantitative approach.

5.2 Quantification of Heart Rate Acceleration Response

First, a comment about terminology. “Heart rate acceleration response” in this text refers to a physiological condition in which the heart rate increases. This is

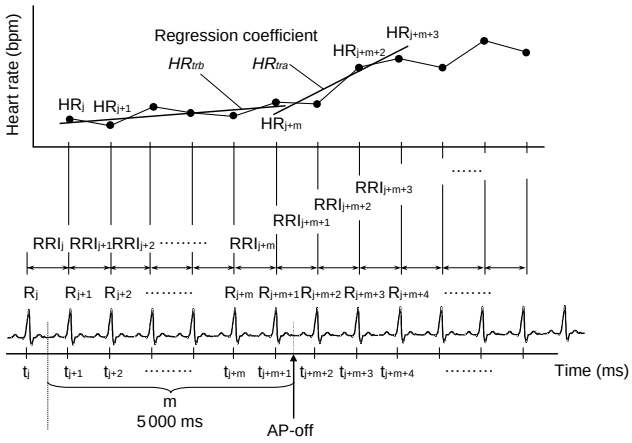


Fig. 6 Explanation for Eq.1

mathematically defined by Equation (1). V_{tr} is the difference between HR_{tra}, which is the slope of the regression line defined by one heart rate data point immediately preceding the release of the accelerator pedal and the next three subsequent heart rate data points, and HR_{trb}, which is the slope of the regression line defined by the heart rate data over the five second period immediately preceding the release of the accelerator pedal. This value represents the curve in the slope of the heart rate series arranged as a time series (Fig. 6), and it allows the consideration of the effects of both the gradual increase in heart rate before the pedal is released as well as the increase in heart rate that occurs subsequently while the subject is steering around the curve.[7]

$$V_{tr} = HR_{tra} - HR_{trb} \qquad (1)$$

here,

$$HR_{trb} = \frac{\sum_{i=j}^{j+m} \left(t_{i+1} - \frac{\sum_{i=j}^{j+m} t_{i+1}}{m}\right)\left(HR_i - \frac{\sum_{i=j}^{j+m} HR_i}{m}\right)}{\sum_{i=j}^{j+m} \left(t_{i+1} - \frac{\sum_{i=j}^{j+m} t_{i+1}}{m}\right)^2}$$

$$HR_{tra} = \frac{\sum_{i=j+m}^{j+m+3} \left(t_{i+1} - \frac{\sum_{i=j+m}^{j+m+3} t_{i+1}}{4}\right)\left(HR_i - \frac{\sum_{i=j+m}^{j+m+3} HR_i}{4}\right)}{\sum_{i=j+m}^{j+m+3} \left(t_{i+1} - \frac{\sum_{i=j+m}^{j+m+3} t_{i+1}}{4}\right)^2}$$

V_{tr} : difference between HR_{trb} and HR_{tra} (beats/min/s)
HR_i : heart rate (beats/min)
HR_{trb} : regression coefficient calculated from heart rate data before AP-off (beats/min/s)
HR_{tra} : regression coefficient calculated from heart rate data after AP-off (beats/min/s)

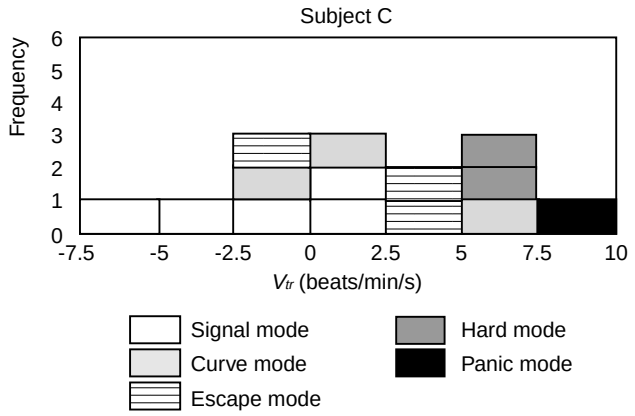


Fig. 7 V_{tr} frequency distribution (subject C) in each mode

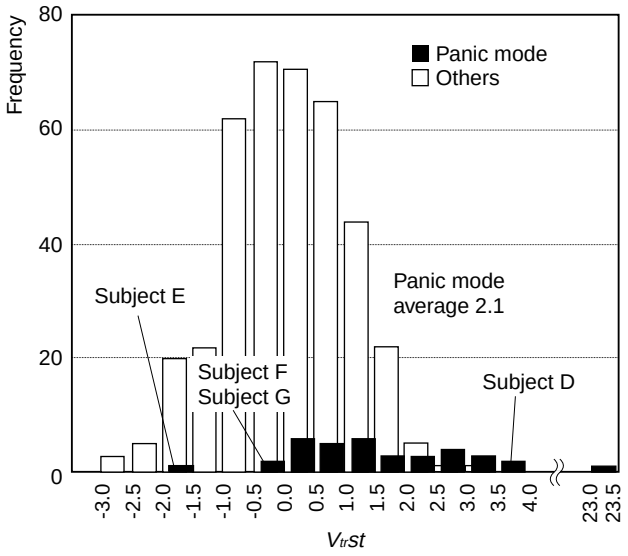


Fig. 8 $V_{tr}st$ frequency distribution

The V_{tr} frequency distribution shown in Fig. 7 is an example showing the results produced by processing the data for a given subject.

5.3 V_{tr} Standardization

Although this analysis focused on heart rate acceleration response, throughout all the tests some of the subjects demonstrated a small response while others demonstrated a large response. As a result, a simple comparison of the V_{tr} values among all of the subjects would not be useful. In order to compare the data among all subjects, an attempt was made to standardize the V_{tr} values for each subject. The standardization equation is defined in equation (2) below.

$$V_{tr}st = \frac{V_{tr} - AVV_{tr}}{\sigma} \qquad (2)$$

$V_{tr}st$: standardized V_{tr}
σ : standard deviation of V_{tr} without panic mode
AVV_{tr} : average value of V_{tr} without panic mode

Based on this equation, it becomes clear where V_{tr} in each mode for each subject falls in the frequency distribution graph for that subject. Because panic mode is not a phenomena that occurs frequently in normal braking behavior, the panic mode value cannot be included in calculations of σ and AVV_{tr} both of which presume normal driving. Fig. 8 shows the frequency distribution diagram that is obtained when $V_{tr}st$ is plotted for all subjects.

5.4 Subject Reaction

Immediately after the panic mode test, each subject was asked to fill out a questionnaire. Each subject was given four choices concerning their reaction to the panic mode test: "Did not notice", "Was not surprised", "Was surprised", and "Was very surprised". Of the 36 subjects, 34 indicated that they were surprised. (Fig. 9)

The subjects were also asked to select one of four choices that described their response during the test: "Could not do anything", "Braked instinctively", "Considered various factors and was barely able to brake in time", "Considered various factors, judged braking to be the optimal response and applied the brake". Fig. 10 shows the distribution of these results. According to these results, two of the 36 subjects answered that they "Could not do anything".

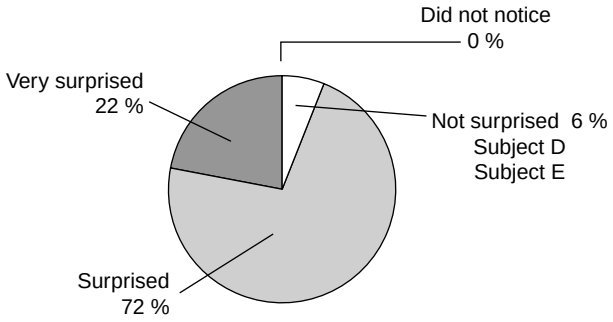


Fig. 9 Self-evaluation of feelings toward panic mode

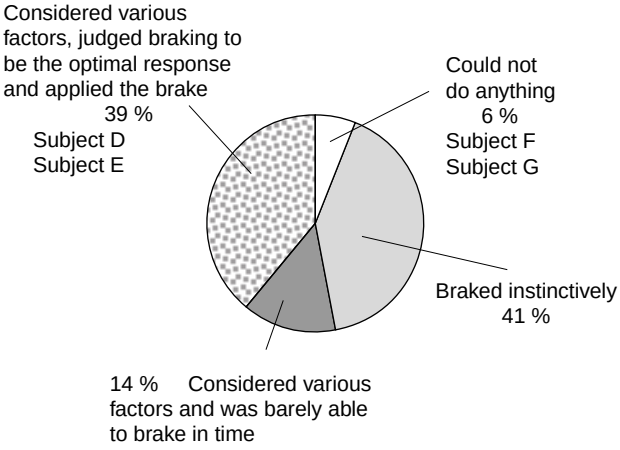


Fig. 10 Self-evaluation of behavior in panic mode

6. Observations and Conclusions

6.1 Patterns of Change in Heart Rate

Patterns of change in heart rate had certain special characteristics that corresponded to the braking behavior. In the case of the curve mode, escape mode and hard mode, it is likely that the increase in heart rate prior to removing the foot from the accelerator pedal was due to an increase in stress accompanying the vehicle's increasing proximity to the point where braking should start. In contrast to the prediction made by Ueno et al.,[8] it is likely that the increase was the result of stress produced by the mind preparing for an action, in the same manner as occurs when people get their heart rates checked. Each subject's mind, in these tests, was preparing for steering through a lane change, and rapid deceleration, respectively. In the case of the panic mode, however, the absence of an increase in the heart rate immediately prior to the release of the accelerator pedal confirms that the subjects were unaware of the impending need to brake suddenly and therefore did not undergo mental preparation prior to braking. Furthermore, the subsequent increase in heart rate in the curve mode and the escape mode indicates the continuation of stress due to the driving tasks of steering and lane changes, respectively, in addition to braking. On the other hand, the gradual decline in the heart rate in the signal mode and the decrease in the heart rate as braking ends in the hard mode likely reflect an easing of stress due to the decrease in vehicle speed caused by braking and the end of the driving task when the vehicle comes to a stop. Therefore, the gradual decrease in heart rate that occurs before the accelerator pedal is released in signal mode likely reflects that stress has begun to ease even before braking.

6.2 Relationship between Heart Rate Acceleration Response and Subject Reactions

Of the two subjects who were not surprised, subject D commented in regards to the emergence of the obstacle, "I was able to calmly react right away", and thus responded "Not surprised" on the questionnaire. When the obstacle emerged, subject D immediately "considered various factors", decided that applying the break was optimal, and began braking. The standardized value $V_{tr}st$ for the heart rate acceleration differential in this case is high, indicating that the heart rate increased instantaneously. (Fig. 8) In the case of subject E, a mistake by the tester allowed the subject to gain prior knowledge of the obstacle, resulting in subject E being "Not surprised", as this subject knew beforehand approximately where to brake for the suddenly emerging obstacle. In this case, $V_{tr}st$ does not reflect a sudden increase in the heart rate. Subjects F and G, however, answered on the questionnaire that they "Could not do anything," because they were so surprised, and the $V_{tr}st$ for the panic mode for both of these subjects was lower than the others even though they fell right in the middle of the distribution for the other modes. On the other hand, in terms of their actual behavior, both subjects stepped on the brake in panic mode, just like the other subjects.

Based on the above, it is possible that the heart rate acceleration response in the panic mode indicates whether stress emerged suddenly while the subject was braking in order to avoid the sudden obstacle, instead of merely being a response to the surprise caused by the sudden emergence of the obstacle. As indicated by the response, subject D calmly and quickly reacted to the sudden emergence of the obstacle, but the high $V_{tr}st$ value is likely to have been caused by stress that arose immediately after, while braking. Because subject E knew beforehand that braking would be necessary, it seems there was no sudden stress, resulting in a low $V_{tr}st$ value. The low $V_{tr}st$ values for subjects F and G is interpreted to be due to no stress developing while braking as a result of feeling that braking was hopeless and that they could not take any action in response to the sudden emergence of the obstacle. Therefore, the fluctuation in the heart rate of both of the subjects who answered "Could not do anything," even though they both applied the brakes was the result of physiological changes caused by subconscious behavior that is thought to be an automatic process[9].

The reason for the sudden increase in heart rate in the panic mode is likely to be the sudden stress caused by trying to brake in response to the sudden emergence of the obstacle. However, because this research focused only on heart rate as a physiological measure, it is not possible to clearly determine if a heart rate acceleration response occurred in subjects while braking because they gasped in surprise or because they held their breath for an extended period. Another possibility is that the subjects tensed their torsos when braking, which along with the seatbelt caused an increase of pressure on the heart and lungs, resulting in a heart rate acceleration response. In any case, the results of this experiment clearly indicate the occurrence of a major heart rate acceleration response when braking in conjunction with the stress of having to somehow stop the vehicle.

6.3 Detection of Panic Braking

It is possible to use a quantitative index to identify panic braking by focusing on differences in heart rate acceleration. The nature of the panic mode differs from the other modes in that braking occurs under unanticipated conditions. When a U-test was performed in order to determine whether there is a difference in the population of $V_{tr}st$ values between the panic mode and the other modes (excluding the results from subjects E, F, and G), it was found that the other modes are likely to have a distribution that is independent of that of population ($p = 1.18E\text{-}0.5 < 0.025$). When the panic mode results from this test are excluded, the distribution of $V_{tr}st$ is deemed to be a normal distribution ($p = 0.44 > 0.05$); therefore, assuming that the $V_{tr}st$ produced by braking has a normal distribution, and based on the 95% confidence interval of the $V_{tr}st$ distribution, the threshold value at which panic braking can be identified is believed to be around $V_{tr}st = 2$. However, because the test that was used for standardization was set up to be more difficult than normal driving conditions, it is believed that the distribution itself is formed by values that are high. Accordingly, given normal driving conditions, the distribution would move to a relatively lower position, which should result in making the distinction between panic braking and other types of braking even clearer. Furthermore, because the heart rate rapidly increases to around 100 to 120 beats per minute while braking after the sudden emergence of the obstacle, then using the definition proposed here makes it possible to identify the panic state within two seconds from the start of braking that induces a rapid change in heart rate in the driver.

7. Summary

This research focused on driver reactions, behavior, and physiological response while braking, and the following results were obtained from tests (conducted in actual automobiles) on the relationships among these elements.

(1) Patterns in the changes in heart rate were observed in relation to various braking modes. For example, as a vehicle approaches a curve, the heart rate increases, and the mental preparation made for entering the curve is reflected in a change in the heart rate. Research also clearly indicated that a large heart rate acceleration response occurs during panic braking.

(2) Next, a method of quantifying these trends was proposed. A relationship was established between non-ordinary braking behavior (such as panic braking) and physiological responses, suggesting that it may be possible to use the heart rate acceleration response to determine when panic braking is occurring.

References

(1) Yamamoto, A., et al., Development of Assistant System to Average Driver's Braking Operation in a Panic Situation, JASE Proceedings 973, p. 165 – 168 (1997)

(2) Ueno, K., et al., Evaluation of Vehicle Performance with Skin Impedance Level, Journal of Society of Automotive Engineers of Japan, Vol. 45, No. 10, p. 73 – 77 (1991)

(3) Ohsuga, M., et al., Development of an Apparatus for Monitoring Degree of Mental Tension, Transactions of SICE, 28 (8), p. 910 – 915 (1992)

(4) Sekine, T., et al., New Measuring Method of Mental Stress in Driving Situation, JASE Proceedings 946, p. 125 – 128 (1994)

(5) Atsumi, B., Evaluation of Mental Condition on Drivers by Analysis of Heart Rate Variability, JASE Proceedings 946, p. 133 – 136 (1994)

(6) Hashimoto.K, et al., The Meaning of Functional Measurements as Physiological Measurements, Methods for Examining Physiological Functions, Tokyo, Japan Publishing Services, 1973, p. 12 – 16

(7) Tanida, K., Attempt to Identify Panic in Terms of Heart Rate Acceleration Response during Braking, The Japanese Journal of Ergonomics, Vol. 37, No. 4, p. 159 – 168 (2001)

(8) Uno, H., et al., Heart Rate Changes in a Predicted Side Wind Condition, Automotive Technology, Vol. 17, No. 2, p. 55 – 58 (1995)

(9) Yagi, A., Perception and Recognition, Tokyo, Baifukan, 1997

■ Author ■



Koji TANIDA

Effects of Steering Torque Control Using a Driving Diagram

Shigeru YAMAWAKI* Yasuo SHIMIZU*

ABSTRACT

This paper proposes a driving diagram, sets out a new steering torque control method derived from the diagram, and explains the effectiveness of this method. The driving diagram uses the actual steering angle δ of the front road wheels and the difference between the front tire slip angle and the rear tire slip angle βfr to express the vehicle behavior resulting from driver operation. The new steering torque control applies steering reaction torque to the driver in order to elicit the actual steering angle of the front road wheel that will bring about the most stable state of the vehicle. In this way, when the vehicle enters a spinning state, the driver can know the direction in which to steer in order to help stabilize the vehicle.

Along with a discussion of the effectiveness of this driving diagram, the paper also provides the results of driving tests conducted using a vehicle equipped with Electric Power Steering (EPS) with steering torque control. These tests confirmed the effectiveness of this method for the vehicle in both under-steer and over-steer states.

1. Introduction

Steering reaction torque plays an important role in driver-vehicle systems. For example, if the self-aligning torque is increased with the vehicle in the over-steer state, the lag by which the driver returns the steering wheel can be reduced when recovering from spinning. In addition, there are also recent reports that the vehicle yaw response can be improved and vehicle fluctuation relative to disturbances can be suppressed by controlling the steering reaction torque according to the vehicle yaw rate, lateral acceleration and other factors[(1) – (3)]. On the other hand, it is also known that the vehicle under-steer and over-steer states can be described using the difference between the front tire slip angle and the rear tire slip angle (βf – βr), etc[(4)]. However, there are as yet no effective proposals for avoiding unexpected driver situations such as drift-out or spinning by applying steering reaction torque according to under-steer, over-steer or other driving conditions.

This paper proposes a driving diagram as a method for understanding the under-steer and over-steer states using the actual steering angle of the front road wheel and the difference between the front tire slip angle and the rear tire slip angle, and sets out steering reaction torque characteristics based on this diagram[(5)]. These characteristics are then used to derive a steering torque control method for recovering from drift-out in the under-steer state or spinning in the over-steer state. Tests were conducted under low road surface friction coefficient conditions using a vehicle equipped with an Electric Power Steering (EPS) system that uses this control method, and this paper reports the results of these tests which confirmed an improvement in performance.

* Tochigi R&D Center

2. Driving Diagram (δ – βfr diagram)

2.1 Driving Diagram

The vehicle conditions when a driver turns the steering wheel are expressed using the actual steering angle of the front road wheel δ and the difference between the front tire slip angle and the rear tire slip angle βfr (= βf – βr) as

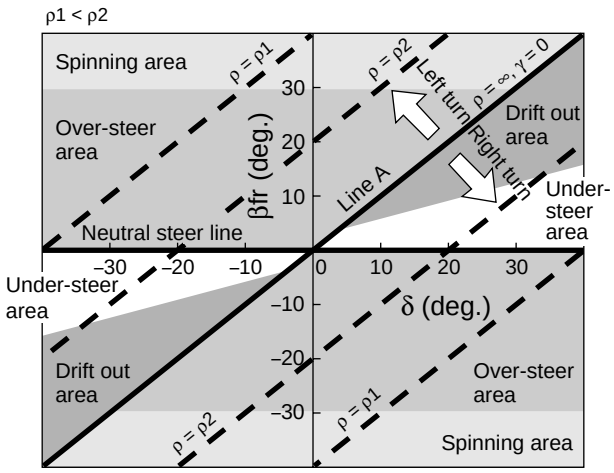
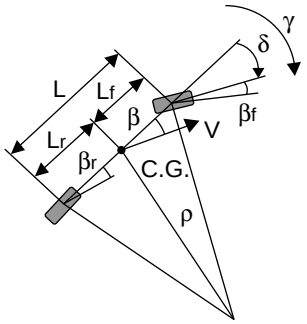


Fig. 1 Driving diagram



γ : Yaw rate
V : Vehicle speed
δ : Front wheel angle
β : Slip angle
βf : Front tire slip angle
βr : Rear tire slip angle
Lf : Distance between front axle and C.G.
Lr : Distance between rear axle and C.G.
L : Wheel base
ρ : Turning radius
C.G. : Center of gravity

Fig. 2 Vehicle model and nomenclature

shown in Fig. 1, and this is called the driving diagram. This diagram is explained using the bicycle model shown in Fig. 2. The tire slip angles βf and βr can be expressed by the following equations. Note that the slip angle is taken into account so that right turn is the first quadrant and left turn is the third quadrant in the driving diagram, and the opposite of the normal direction is positive.

$$\beta f = -\beta - Lf \cdot \gamma / V + \delta \quad (1)$$
$$\beta r = -\beta + Lr \cdot \gamma / V \quad (2)$$

Here, β is eliminated from equations (1) and (2) and βfr is obtained to express the vehicle steering characteristic conditions as follows.

$$\beta fr = \beta f - \beta r = -L \cdot \gamma / V + \delta \quad (3)$$

Also, ignoring β as a small value compared to γ at this condition and setting the turning radius to ρ = V/γ yields the following equations.

$$\beta fr = -L / \rho + \delta \quad (4)$$
$$\rho = L / (\delta - \beta fr) \quad (4')$$

Equation (4') indicates that for example when δ > 0 in steady state cornering, ρ becomes larger (under-steer area) when δ > βfr > 0, and ρ becomes smaller (over-steer area) when βfr < 0. In addition, even when δ < 0, ρ becomes even smaller when βfr < 0 and δ – βfr > 0, so this area is also the over-steer area.

Line A in Fig. 1 shows the relationship between δ and βfr in straight ahead driving (γ = 0). This indicates that βfr = δ when γ = 0 according to equation (3). In addition, line A shifts over the βfr axis with ρ as the parameter as shown by the dotted lines according to equation (4). This means that ρ can be obtained from δ and βfr.

2.2 Driving Locus by Actual Running Tests

Next, the driving locus was investigated to determine how best to express δ which shows the driver operation and βfr which shows the vehicle slip condition on the driving diagram. Figs. 3 to 6 show the driving diagrams when running in an actual vehicle. The vehicle used was an FF vehicle.

2.2.1 Under-steer area (Lane change)

When the vehicle speed is constant and assuming the yaw rate gain G_γ (= γ/δ) is fairly constant, equation (3) can be modified as follows.

$$\beta fr = \delta (1 - L \cdot G\gamma / V) \quad (5)$$

From this equation (5), βfr has the gradient (1 – L· G_γ/V) and is proportional to δ. However, in actual running a phase lag occurs when δ begins to turn, so the driving locus has hysteresis as shown in Fig. 3.

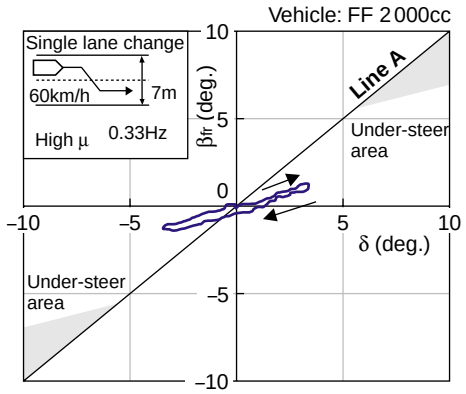


Fig. 3 Single lane change (Under-steer)

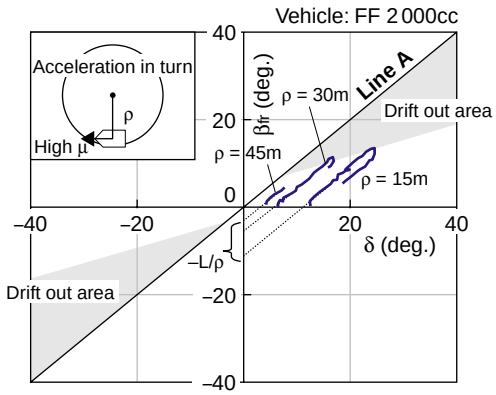


Fig. 4 Acceleration in turn (Under-steer)

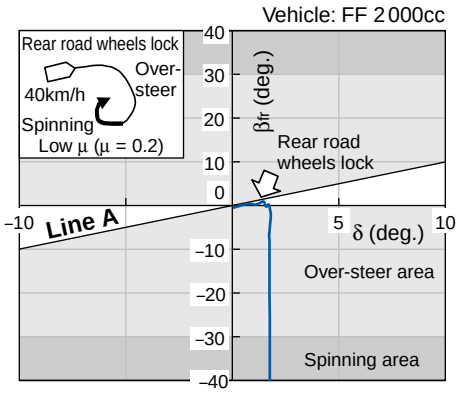


Fig. 5 Spinning (Over-steer)

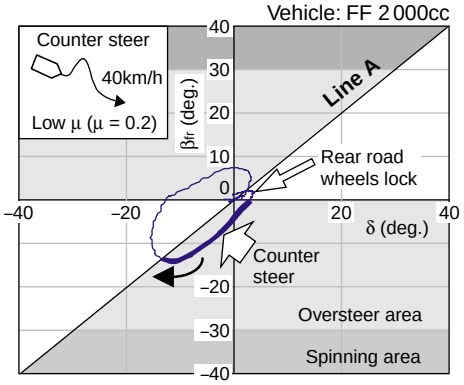


Fig. 6 Spinning recovery (Over-steer)

2.2.2 Drift-out area (Acceleration in turn)

As shown in Fig. 4, δ is turned at a constant angle to the right in the stopped condition so as to trace a circle, and then the vehicle starts to accelerate to make a circular turn while increasing δ. Here, ρ is a constant, so according to equation (4), the driving locus moves in a straight line parallel to line A which intersects the βfr axis at (–L/ρ). If δ or the vehicle speed V is increased further, βfr increases and reaches the drift-out area. The vehicle βfr has a limit, and due to the relationship with δ a drift-out area exists in which the turning radius does not decrease even if δ is increased. Fig. 4 shows the experimentally obtained drift-out area.

2.2.3 Over-steer area (Spinning)

When δ is fixed and the rear road wheels are forcibly locked using the brakes when starting to turn as shown in Fig. 5, the vehicle spins and |–βfr| increases rapidly. This occurs even at the same δ because equation (4) shows that ρ becomes smaller. The vehicle |–βfr| has a limit, and a spinning area exists in which the turning radius cannot be increased even if δ is returned. Fig. 5 shows the experimentally obtained spinning area.

Fig. 6 shows counter-steer when recovering from spinning. After entering the over-steer state, it was found that spinning can be avoided by turning δ in the opposite direction and performing operations that suppress the increase in |–βfr| and bring γ to 0 (approach line A).

3. Investigation of New Steering Torque Control

3.1 Steering Reaction Torque Characteristics

Fig. 4 shows that in order to avoid entering the drift-out area, steering torque control in the under-steer state should provide heavy steering controlled reaction torque which makes it difficult to increase δ so that βfr does not increase as it nears the drift-out area. In addition, Figs. 5 and 6 show that counter-steer in the over-steer state should be assisted by applying steering controlled reaction torque in the steering direction to return βfr and γ to zero. Therefore, equation (3) can be modified as follows.

$$\delta = \beta fr + L \cdot \gamma / V \qquad (3')$$

In order to reduce βfr and γ toward zero, the controlled reaction torque Tr1 can be obtained as follows from equation (3') as a steering reaction torque characteristic.

$$Tr1 = G1 \cdot \beta fr + G2 \cdot \gamma \qquad (6)$$

(G1 and G2 are coefficients.)

3.2 Control Method for Stabilizing the Vehicle

Specific control algorithms were investigated using Fig. 1 and equation (6). The vehicle under-steer and over-steer states can be determined as shown in the equations below from the sign of βfr and the sign of γ used when obtaining βfr. The under-steer state is given by equation (7), and the over-steer state by equation (9).

Note that the signs of G1 and G2 were given as follows in order to obtain the above-mentioned steering reaction torque.

$\beta fr \cdot \gamma > 0$ Under-steer
$G1 > 0,\ G2 = 0$ (7)

$\beta fr = 0$ Neutral steer (8)

$\beta fr \cdot \gamma < 0$ Over-steer
$G1 < 0,\ G2 > 0$ (9)

In addition, the steering rate generally tends to become higher in these areas, so the controlled reaction torque Tr2 is provided as a supplement to further increase the vehicle convergence.

$$Tr2 = C1 \cdot d\delta / dt \qquad (10)$$

(C1 is a coefficient.)

Therefore, the EPS control assist torque Tt is provided by subtracting equations (6) and (10) from the assist torque Th that is necessary to reduce the steering torque when stopped. Therefore, labeling the load torque as Tl, the steering torque Ts is obtained as follows.

$$Ts = Tl - Tt = Tl - (Th - Tr1 - Tr2) \qquad (11)$$

Equations (6), (7), (10) and (11) show that when the βfr is large during drift-out, Tr1 > 0 and the driver's steering torque Ts becomes heavier.

In addition, equations (6), (9), (10) and (11) show that γ and |–βfr| increase and Tr1 > 0 in the over-steer state. At this time the steering torque Ts returns in the Tl direction as it becomes heavier, so the amount by which the self- aligning torque is attenuated by the assist becomes smaller. Furthermore, when that γ and |–βfr| increase and Tr1 > Th, Tt acts in the direction to increase the self-aligning torque, so the driver's counter-steer is assisted.

4. Investigation when Applied to Under-steer

Vehicle drift-out occurring in the under-steer state was investigated. Bicycle model simulations were performed using nonlinear tire characteristics, and Fig. 7 shows the calculation results of the vehicle lateral distance when the amplitude θ (sine wave) is varied with the frequency of the input steering angle θ as the parameter while running at a constant vehicle speed (40 km/h) under low road surface friction coefficient conditions (friction coefficient μ = 0.2).

In Fig. 7, when the input frequency is changed from 0.2 to 0.25 Hz, the lateral distance decreases in the area where βfr exceeds 6 degrees, that is to say the area where the steering angle θ exceeds 130 degrees. Therefore, the driver performs operations to prevent βfr from increasing. This area is the drift-out area, and operations such as the following are necessary as methods to prevent βfr from increasing.

(1) Preventing the steering angle θ from increasing
(2) Preventing the acceleration force and braking force from increasing

In this study, the former method (1) was investigated.

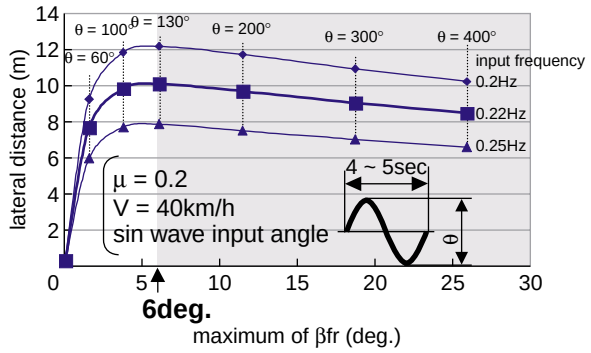


Fig. 7 Lateral distance in drift out area

4.1 Investigation of Controlled Reaction Torque Tr1 and Tr2 Using a Simple Simulator

As previously mentioned, investigations were conducted as to whether the driver could be prevented from increasing the steering angle by making the steering torque Ts heavier when βfr increases in order to prevent the vehicle from entering the drift-out area. The effects of steering torque control for tasks similar to low road surface friction coefficient conditions were estimated using the simulator[6] shown in Fig. 8 to investigate the minimum required controlled reaction torque Tr1 and Tr2.

This simulator is comprised of two horizontal rows of LED indicators (LED1, LED2) that indicate the target vehicle position used as the operation target and the current position of the driver's own vehicle, and a reaction component consisting of a steering wheel coupled to an EPS gear box that applies the actual reaction force. The actual vehicle position display (LED2) reflected the primary lag

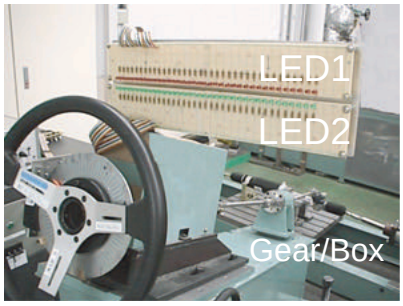
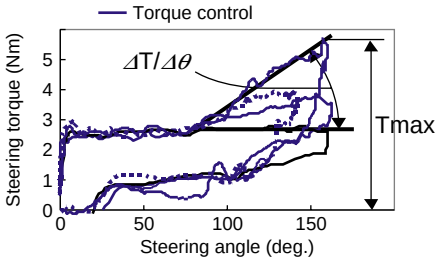


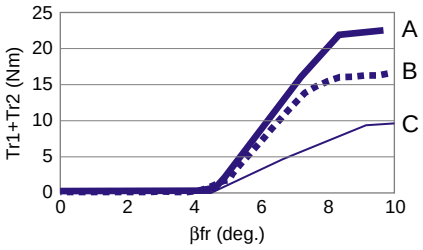
Fig. 8 Driving simulator

of the vehicle, and was set to move horizontally according to the steering operations of the test subject.

The test subjects were two normal drivers and one expert driver as the target. The controlled reaction torque (Tr1 + Tr2) was varied according to βfr as shown in Fig. 9 (b), and multiple controlled reaction torque gradients ($\Delta T/\Delta\theta$) were applied as shown in Fig. 9 (a). The maximum steering torque and maximum steering rate of the driver was surveyed at this time. This is because the steering rate generally tends to become faster under low road surface friction coefficient conditions, so it was thought that reducing the maximum steering rate would allow driving without increasing the steering angle. Fig. 10 shows the effects on the controlled reaction torque (Tr1 + Tr2). These results showed that at a controlled reaction torque gradient ($\Delta T/\Delta\theta$) of 0.25 Nm/deg. and a maximum steering torque (Tmax) of 8.3 Nm, the maximum steering rate could be reduced to the same level as an expert driver.



(a) Characteristics of torque



(b) (Tr1+Tr2) curves

Fig. 9 Steering torque on simulation

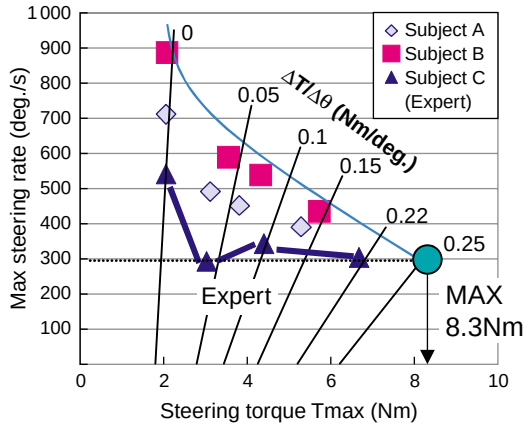


Fig. 10 Test result

4.2 Confirmation of Effects by Actual Running Tests

A test course was set as shown in Fig. 11 so that running was performed using the drift-out area under low road surface friction coefficient conditions in order to confirm the effects of steering torque control in the understeer state.

There were six test subjects including one woman, and the test results with and without steering torque control were compared. The controlled reaction torque (Tr1 + Tr2) used the value obtained using the above-mentioned simulator.

Fig. 12 shows the test results. In the vehicle with steering torque control, five of the six subjects (83%) successfully navigated the course. In contrast, only one of the six subjects (17%) successfully navigated the course in the vehicle without steering torque control.

At this point, the steering operations of subject *a* who was unable to successfully navigate the course in the vehicle with steering torque control were investigated by comparing with subject *b* who successfully navigated the course. Fig. 13 shows this comparison.

These results show that subject *a* who was unable to successfully navigate the course, continued the steering operation even when the steering torque increased due to steering torque control, and the torque produced by steering torque control was insufficient to suppress the steering operation. As shown in Fig. 13, subject *a* input a large steering angle (θ = 500 degrees, δ = 33 degrees) in order to avoid the pylon at the 40 m mark in the drift-out area,

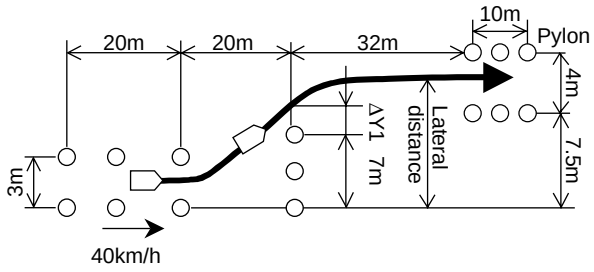


Fig. 11 Test course

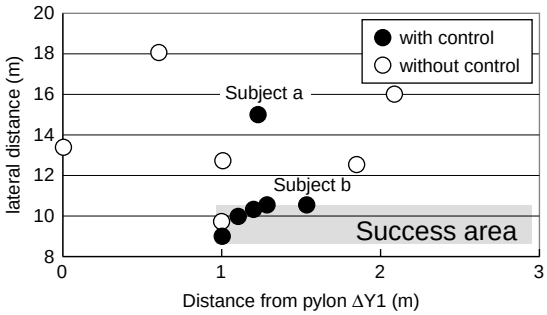
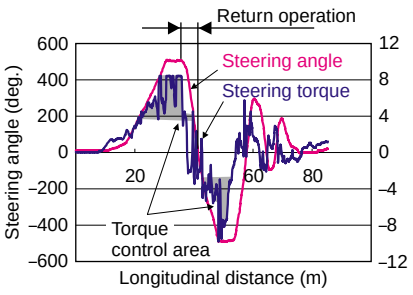
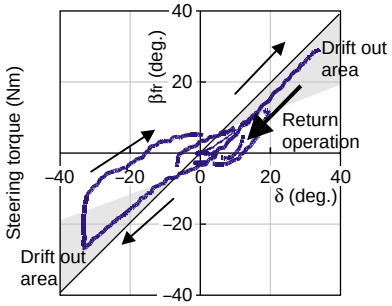


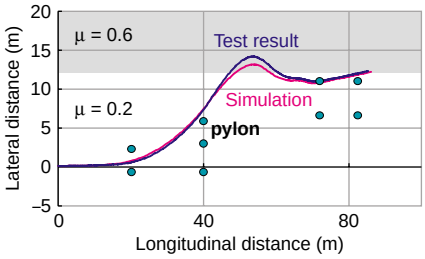
Fig. 12 Effect of steering torque control



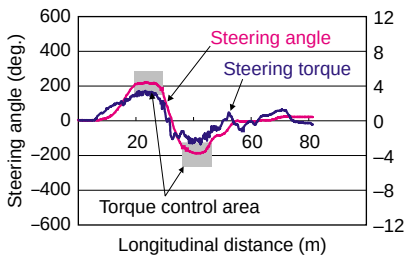
Steering operation (subject a)



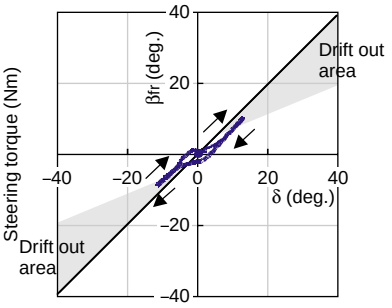
Driving diagram (subject a)



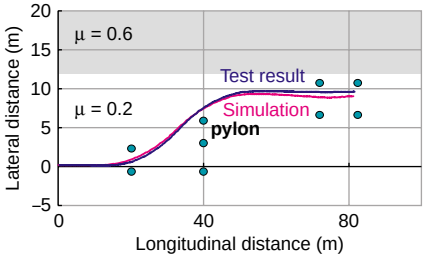
Locus of vehicle (subject a)



Steering operation (subject b)



Driving diagram (subject b)



Locus of vehicle (subject b)

Fig. 13 Test results

and as a result the steering return operation was delayed and the vehicle deviated from the course. On the other hand, subject *b* began to steer at approximately the same timing as subject *a*, but performed steering operations as shown in the driving diagram to prevent δ from increasing in the drift-out area, and thus successfully navigated the course. This confirmed the validity of steering control torque in the under-steer area. In addition, Fig. 13 shows both the results obtained using the above-mentioned bicycle model simulation and the actual running test results.

5. Investigation when Applied to Over-steer

The amount of control required to recover from spinning that occurs in the over-steer state was investigated.

5.1 Investigation of Controlled Reaction Torque Tr1 and Tr2

It has been reported that there is a relationship between the required steering rate and the reaction time lag of the driver after the vehicle γ increases until the start of steering operations when recovering from spinning.[7]

Therefore, actual running tests were conducted to investigate the degree of the actual driver steering lag in the over-steer area. The tests were conducted with four subjects as shown Table 1. The rear road wheels of the vehicle were locked during lane change under the low road surface friction coefficient conditions shown in Fig. 14 causing the over-steer state, and then the driver steering lag time, vehicle behavior and other factors were measured at that time.

The driver steering lag time (reaction time) was defined as shown in Fig. 15 as the response time from the point when the rear road wheels lock and γ starts to increase until counter-steer starts.

Fig. 16 shows the test results. Here, the vehicles driven by three of the four subjects spun. The driving diagrams in Fig. 16 show that subject D was unable to prevent γ from rising with respect to δ, and that while subjects A and C were able to prevent γ from rising, the βfr was too large so the spinning could not be stopped. Therefore, although there is some variance depending on the test conditions, vehicle conditions and other characteristics, a large steering rate must be input to avoid entering the spinning area.

Fig. 17 shows the steering lag time and steering rate obtained by the actual running tests in Fig. 16 plotted over the line L obtained by investigating spin recovery performance when spinning is produced by locking the rear road wheels in the bicycle model simulation. Here, the subjects indicated with an × could not avoid spinning, and the subject indicated with an O could avoid spinning. This shows that spinning occurs when steering input equal to or greater than the steering rate indicated by line L cannot be applied.

Here, it is thought that spin recovery can be improved if assistance can be provided to add controlled reaction torque so that the reaction time is shorter and the steering rate increases. As shown in Fig. 17, subjects A, C and D were able to input the steering rate indicated by line Lc or greater. Therefore, G1, G2 and C1 were set so that a steering rate of approximately 200 deg./s can be added by the above-mentioned controlled reaction torque (Tr1 + Tr2) to enable spin recovery.

Table 1 Subjects list

Classification		Numbers
age	sex	
20's ~ 30's	male	2
40's ~ 50's	male	2

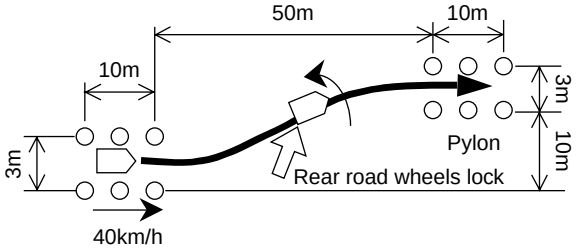


Fig. 14 Test course

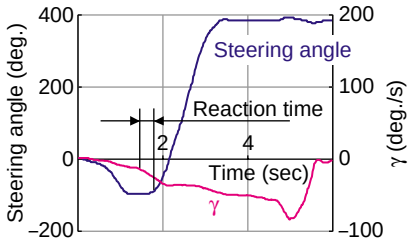


Fig. 15 Reaction time

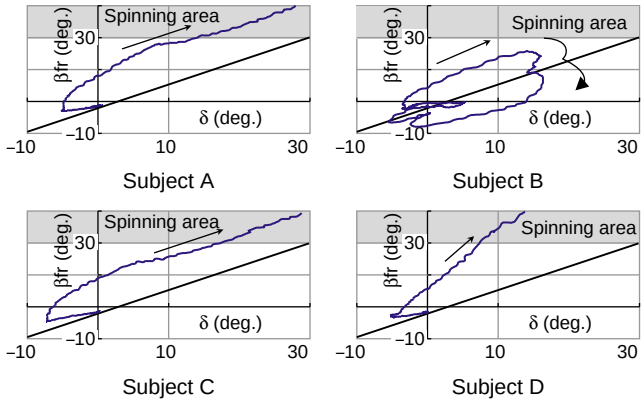


Fig. 16 Driving diagrams

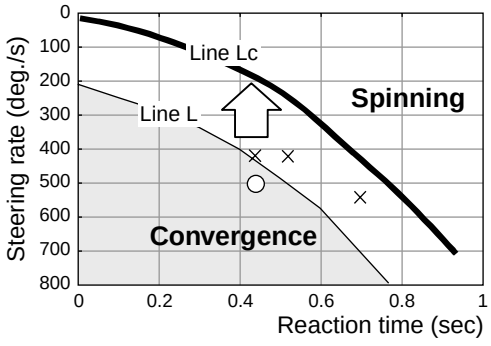


Fig. 17 Characteristics of steering wheel input to stop spinning

5.2 Confirmation of Effects by Actual Running Tests

The effects of steering torque control were confirmed on the test course shown in Fig. 14.

Four test subjects were selected from the same age group to prevent test experience from affecting the test results. As shown by the time series data in Figs. 18 to 20, controlled reaction torque was generated at the same time as over-steer occurred to assist the driver's steering operations. These results show that when γ increases, it is suppressed by the controlled reaction torque Tr1 (γ term), and when γ approaches 0, the control torque Tr1 (βfr term) assists in the direction to reduce βfr. Furthermore, Fig. 19 shows that convergence is improved by Tr2 which is a viscous term, and Fig. 20 shows the composite control torque amount.

Figs. 21 to 24 show the test results. None of the vehicles driven by the four subjects spun.

These results show that even subject H was able to suppress the rise in βfr from a δ of 12 degrees as shown in the Fig. 21 driving diagram.

In addition, Fig. 22 shows that compared to the results of subjects in vehicles without steering torque control indicated by the white circles, the controlled reaction torque increased the steering rate for vehicles with steering torque control indicated by the black circles. Furthermore, the steering lag time was also shortened as shown in Fig. 23.

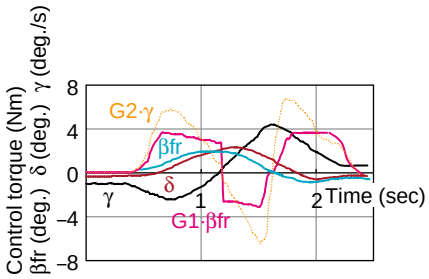


Fig. 18 Main control time chart

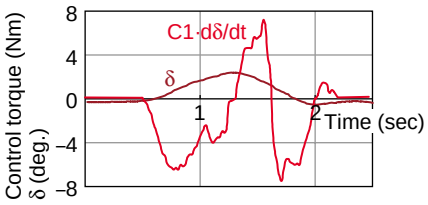


Fig. 19 Sub control time chart

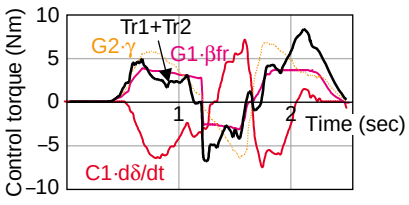


Fig. 20 (Tr1+Tr2) time chart

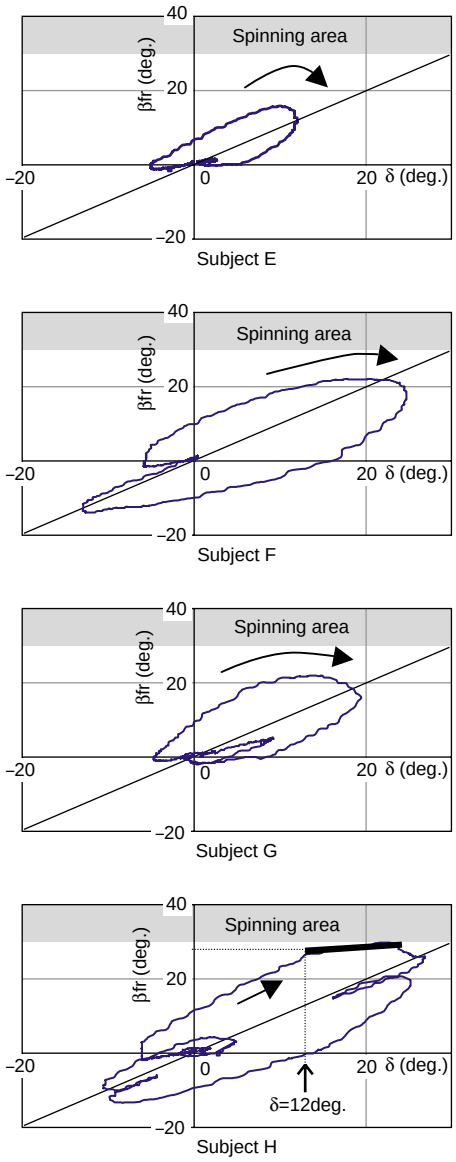


Fig. 21 Driving diagrams

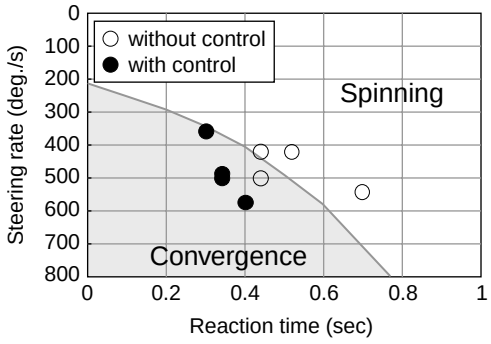


Fig. 22 Effect of steering torque control

Fig. 24 also shows that the yaw rate peak with respect to the steering lag time also decreased.

These results confirmed the developed method effectively improved recovery performance when spinning occurred.

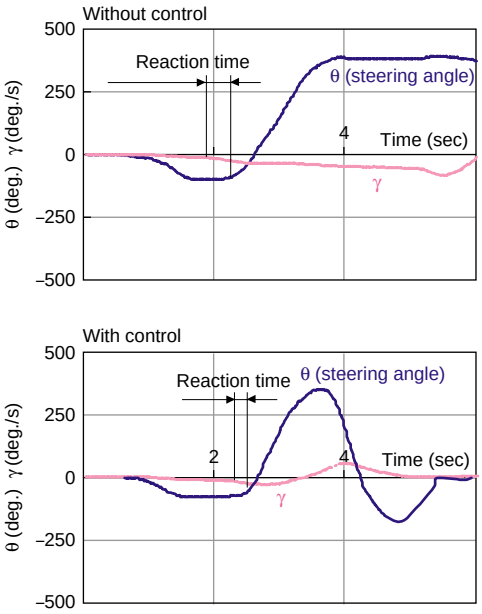


Fig. 23 Spinning recovery time chart

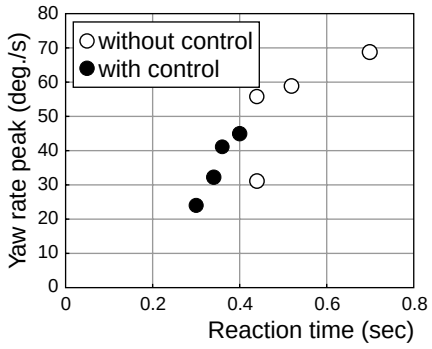


Fig. 24 Reaction time - yaw rate peak

6. Conclusion

This study proposed a driving diagram as a method for understanding the under-steer and over-steer states using the actual steering angle of the front road wheel and the difference between the front tire slip angle and the rear tire slip angle, and devises a steering torque control method based on this diagram. Tests were then conducted under low road surface friction coefficient conditions using a vehicle equipped with an Electric Power Steering (EPS) system that uses this steering torque control method, and the results confirmed the following.

(1) The under-steer and over-steer areas which are driving states when the driver is operating the vehicle can be described by a driving diagram using $\delta - \beta fr$.

(2) Based on this driving diagram, a new steering torque control was proposed which provides assistance to operate δ in the direction that βfr and γ approach zero.

(3) A method was established for detecting under-steer, over-steer and other driving states using the driving diagram.

(4) The following items were understood as a result of applying this method to the under-steer area.
   1) Drift-out tests were conducted using a vehicle with the controlled reaction torque gradient set to 0.25 Nm/deg. and the maximum torque set to 8.3 Nm based on the above-mentioned steering torque control. As a result, five of the six test subjects (83%) improved their test results.
   2) The one test subject whose test results did not improve was investigated, and the control torque set by this study was found to be insufficient.

(5) Spin recovery tests were conducted using a vehicle with the control torque set to allow addition of a steering rate of approximately 200 deg./s based on the above-mentioned steering torque control applied to the over-steer area. In this case as well, the control was confirmed to improve the test results.

These observations confirmed both the validity of the driving diagram and the effectiveness of steering torque control based on this driving diagram.

References

(1) M. Yamamoto, Active Control Strategies for Improved Handling and Stability, Automotive Technology, Vol. 45, No. 3, p. 43 – 51 (1991) (in Japanese)

(2) N. Yuhara, S. Horiuchi, N. Asanuma, Y. Nishi, T. Kohata: Improvement of Vehicle Handling Quality Through Active Control of Steering Reaction Torque, Proc. of International Symposium AVEC, Yokohama, Japan, p. 407 – 412 (1992)

(3) Y. Amano, S. Doi, H. Kawaguchi: Improvement of active safety by active front steering angle and torque control, JSAE Proceedings, Vol. 30, No. 3, p. 87 – 92 (1998)

(4) M. Abe: Vehicle Dynamics and Control, Tokyo, Sankaido, p. 249 (1992) (in Japanese)

(5) S. Yamawaki, Y. Shimizu: A Study on Steering Torque Control Using driving Diagram at the Oversteer, Japan Mechanical Association, Traffic Distribution Division Conference, No. 99 – 59, p. 144 – 158 (1999) (in Japanese)

(6) A. Yoneda, Y. Shimizu: A Study on Control Performance of the Quick Steering Vehicle, Japan Mechanical Association, Traffic Distribution Division Conference, No. 98 – 37, p. 239 – 242 (1998) (in Japanese)

(7) Y. Shimizu, T.Kawai, J. Yuzuriha, S. Takimoto: A Study of a New Steering System with Variable Gear-ratio According to Vehicle Speed and Steering Wheel Angle. HONDA R&D Technical Review, Vol. 11, No. 1, p. 107 – 118 (1999) (in Japanese)

■ Authors ■


Shigeru YAMAWAKI


Yasuo SHIMIZU

Development of a Real-time Analytical System for Motor Performance Measurement

Yoshinari MURAYAMA* Hirofumi ATARASHI*
Makoto KISHIDA* Kiyoshi ASAMI*

ABSTRACT

A method was devised for utilizing vector analysis to quantify inductance during switching, which is a major factor affecting such motor performances as maximum power and efficiency, and the appropriateness of this method was confirmed. The application of this method makes it possible to measure actual motor inductance during switching and to observe the magnetic saturation of the motor. By systematizing this analysis method, and representing measured values as a circle diagram, it is possible to evaluate motor operating conditions in real-time. This makes it possible for optimum motor control parameters, which are conventionally determined by analysis after testing, to be established during testing. This system reduces the overall manpower used in motor testing and data analysis by 30%. By incorporating the motor inductance value that is calculated with this method into the motor's digital control flow, the torque response is enhanced.

1. Introduction

With the continuing awareness of global environmental issues, there has been an increasing demand for low-pollution vehicles, including hybrid vehicles, fuel cell electric vehicles, etc. In creating the motors that are the source of the drive power of these new vehicles, there is a need to make them more efficient, smaller, and lighter weight. There has been a focus on higher speed motors as one means of making the motors smaller and lighter. Focus has also been placed on brushless DC motor weak field control as a method of creating a higher speed motor. Output limits in the high-speed range with weak field control is greatly affected by inductance during motor switching and the amount of weak field current[(1)]. Therefore, it can be said that the keys to creating more efficient high-output motors lie in optimizing inductance during switching and weak field current. This paper describes a method of calculating inductance during switching, which until now could not be quantitatively evaluated, and explains the benefits of application of this method as a new measurement system.

2. Aims of Development

Through recent academic papers [(1) – (3)] and actual current wave changes, it has become increasingly clear that changes to inductance, which greatly affects maximum motor output as well as responsiveness and efficiency, vary according to the amount of load. Inductance without switching can easily be measured by measurement devices commonly sold in the market, and so simulations can be carried out with good

* Tochigi R&D Center

accuracy. However, methods for measuring inductance during switching are complex, and those values cannot be evaluated or estimated quantitatively, due to such reasons as the values change according to the amount of switching. Because of this difficulty, there have been no tools to use during the design stage, and this has meant that designing the optimum motor involved repetitions of prototype building and modification, which took much time. Also, with the weak field control — widely used in motor control when aiming for smaller and lighter motors through higher motor speeds — in order to determine the weak field current's switching amount and timing, it is necessary to perform the vector analysis processing that accompanies d-q conversion. Therefore, establishing optimum parameters during testing is difficult, and a post-test process is required to determine the optimum values from the test data. This means much time is required, including the manpower required for re-testing.

Against this background, this research project has established a method for the accurate calculation of inductance during switching, and has made improvements to the efficiency of research and development by creating a system for this method. The goals of this research are:

(1) to quantitatively calculate inductance during switching, which greatly affects basic motor performance
(2) to improve the accuracy of, and shorten the time for setting optimum switching amount and timing by showing vector analysis in real-time.

3. Analysis Method

Torque current (Id), which determines the size of the torque generated by the motor, is driven by the electric potential difference between power-supply voltage (Vb) and motor phase voltage. The greatest phase voltage where it is possible for torque current to flow (maximum phase voltage) is when the motor permeable voltage waveform is the ideal sine wave, $Vb/\sqrt{6}$ (Vb: power-supply voltage). When motor speed and torque increase, motor phase voltage increases, and if the maximum phase voltage is exceeded, torque current is no longer able to flow. Regarding this, as shown in Fig. 1, canceling out the permeable voltage and the voltage rise due to the torque current to flow an electrical current (Iq) at a phase (q-axis) with an electrical angle which is advanced 90° from the torque axis (d-axis) is the method for passing torque current even at higher speeds. This is a widely known method of weak field control for brushless DC motors. In recent years, a major issue in the high speed motor research, which has been carried out in response to the increasing need for smaller and lighter, higher-speed motors, is the prediction of maximum output values in the high speed range.

Focus has been placed on the vector analysis method as a method for calculating maximum output in high-speed motors that adopt weak field control[(2)]. Fig. 2 shows an example of calculations using the vector analysis method, and Table 1 shows the list of symbols used in later calculations. The graph's horizontal axis and the letter d refer to the torque axis (d-axis), while the letter q refers to the flux field axis (q-axis). This method of vector analysis makes the motor drive state visible by separating motor drive parameters that change according to load state into d-axis and q-axis, and expressing them as vectors. Each motor parameter is expressed as a voltage vector, such as $I \cdot R$, $I \cdot \omega \cdot L$. By looking at the relationship between the phase voltage vector on the circle diagram and the circle of maximum phase voltage determined by the power-supply voltage, it is possible to make decisions about the possibility of output, and to calculate the size of the required weak field current. In this way, the method of vector analysis is an effective method for analysis concerning the verification of motor maximum output, particularly in the high speed range. As such, during motor design, it can be used to confirm whether or not output can be achieved with target motor speed and maximum current output using parameters such as Ke, R, Ld, and Lq that are determined in magnetic simulation.

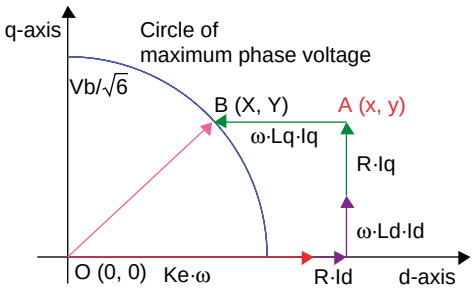


Fig. 2 Vector diagram of the brushless DC motor

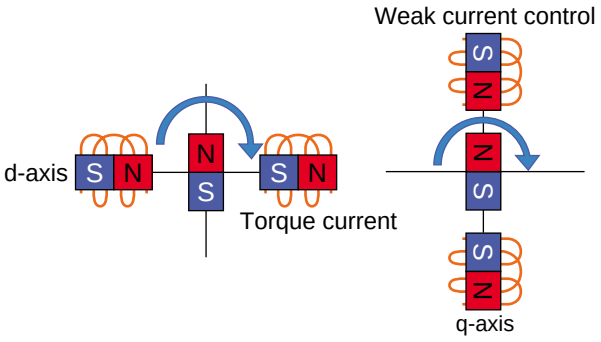


Fig. 1 d-axis and q-axis

Table 1 List of variables

Ke	[V/rpm]	back EMF constant
ω	[rad/s]	angular velocity
R	[Ω]	stator resistance
Id	[A]	d-axis current
Iq	[A]	q-axis current
Ld	[H]	d-axis inductance
Lq	[H]	q-axis inductance
Vd	[V]	d-axis voltage
Vq	[V]	q-axis voltage
V	[V]	phase voltage

The actual motor switching waveforms in the weak field control range for motors that are switching are waves composed of the electrical currents according to torque current Id and weak field current Iq, as shown in Fig. 3. Therefore, in a quantitative evaluation of each command value component, processing, such as d-q conversion, is required. Also, inductance, which greatly affects motor output characteristics, increases and decreases with changes in motor material permeability. For these reasons, it was very difficult to know the motor driving state during testing or to establish optimum control parameters. However, in recent years, thanks to the development of technology such as FFT analysis devices, it has become possible to elucidate basic phase current and phase voltage basic waves, and to carry out analysis of phases. Using this technology to calculate basic wave phase differences between the actual phase current and phase voltage waves and the poles, and to calculate the root mean square, a method has been devised to carry out vector analysis in the motor's actual load state[3]. Fig. 4 shows an example of vector analysis using this method. In the diagram, α is the phase difference between the d-axis and the phase current, and β is the phase difference between the phase current and the phase voltage, with $\alpha + \beta$ being the phase difference between the d-axis and the phase voltage. By comparing the equivalent A point coordinates in Fig. 2 and Fig. 4, drawn using different methods, under the same driving conditions (motor speed, torque), it is possible to calculate Ld and Lq in the actual load state.

$$Ke \cdot \omega + R \cdot Id = V \cdot \cos(\alpha + \beta) + \omega \cdot Lq \cdot I \cdot \sin\alpha$$

···A's X Coordinates

$$\omega \cdot Ld \cdot Id + R \cdot Iq = V \cdot \sin(\alpha + \beta)$$

···A's Y Coordinates

However,

$Id = I \cdot \cos\alpha$, $Iq = I \cdot \sin\alpha$

And from this,

$$Ld = (V \cdot \sin(\alpha + \beta) - R \cdot I \cdot \sin\alpha) / (\omega \cdot I \cdot \cos\alpha) \quad (1)$$

$$Lq = (Ke \cdot \omega + R \cdot I \cdot \cos\alpha - V \cdot \cos(\alpha + \beta)) / (\omega \cdot I \cdot \sin\alpha) \quad (2)$$

In this way, inductance of the d-axis and q-axis in the actual load state is expressed as the measured values of phase voltage, phase current, and phase difference between each component.

It is now possible to calculate inductance during motor switching using Equation (1) and (2), and confirmation was made of the fact that inductance drops according to increases in switching amount. However, inductance calculated according to this method includes a variety of error elements, and so, is insufficient in terms of reliable accuracy and the ability to be reproduced. The research here undertaken analyzes the elements causing the drop in calculation accuracy and reproducibility, correcting them and devising a method for calculating inductance with good accuracy and reproducibility. As can be seen in Equations (1) and (2), each inductance equation includes phase voltage as determined in each sample phase resistance in addition to motor speed, and a permeability voltage constant. As for

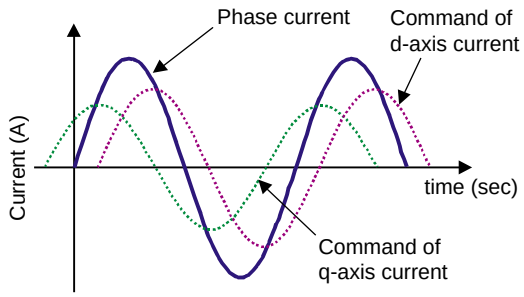


Fig. 3 Relationship between phase current and command current

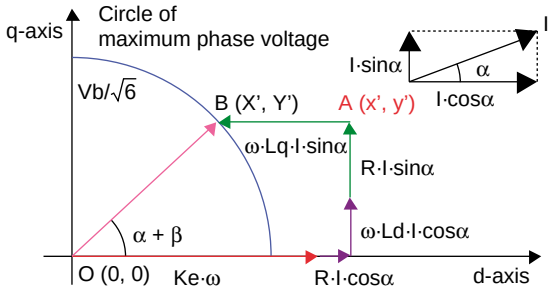


Fig. 4 Vector diagram drawn with measurement data

these values, because the values measured at normal temperatures are used in all driving states, they differ from the value at actual temperatures. In addition, things such as phase characteristics regarding motor speed of speed sensors for detecting pole locations, etc. can affect calculation accuracy. According to Equations (1) and (2), and Fig. 4, carrying out inductance calculations without considering resistance increase due to coil temperature increase gives values larger than the true values. Table 2 summarizes the factors and causes of these errors, and the methods for correcting them.

In preparatory tests prior to switching tests, no-load torque values, motor speed sensor, and magnetic pole location phase differences are obtained, and value corrections are made according to this advance information. Stator resistance correction is carried out according to actually measured coil temperature. Fig. 5 gives an example of analysis of inductance during switching and compares the results both with and without stator resistance temperature correction and no-load inductance. In this example, it is seen that there is a calculation error of about 3% due to

Table 2 Error factors and correction methods

Error factor	Cause	Correction
Torque value of no load	Torque meter hysteresis	Reference of hysteresis map
Phase difference between magnet and position sensor	Phase lag of position sensor	Reference of phase lag map
Stator resistance	Rise of stator resistance with coil temperature	Calculation of resistance

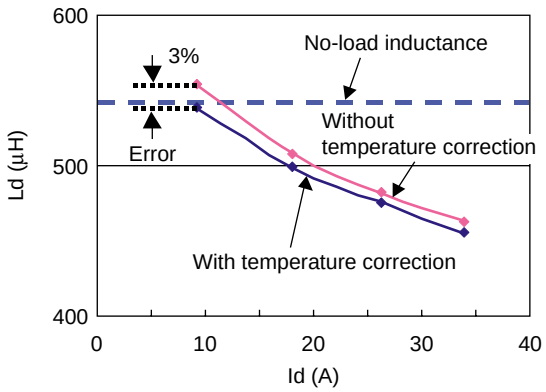


Fig. 5 Result of inductance analysis during switching

coil resistance increase. By correcting these, it is possible to make accurate calculations of motor inductance during switching that are not affected by changes in values due to such things as coil temperature fluctuations. It is also possible to make quantitative evaluations.

4. Creating the System

The following benefits are expected from the utilization of the system created from this analysis method.

- Centralized display of measured data, calculation results
- Automatic correction of measured data
- Real-time display of vector analysis

4.1 Centralized Display of Measured Data, Calculation Results

At present, there are eight types of measurement devices used in motor performance testing, with approximately 120 items measured using these devices. Conventionally, as the collection of this data is carried out separately for each device, much effort was needed, and there is a concern with data synchronization. Now it is possible to obtain data from all of the devices, carry out the aforementioned vector analysis and efficiency calculations, and save the measured values and analysis values with a single action. Further, it is possible to display the information required on the measurement software screen by selecting the information from among all the measured data and calculation results. Through this, data synchronization between measurement devices is improved, and the test period is shortened.

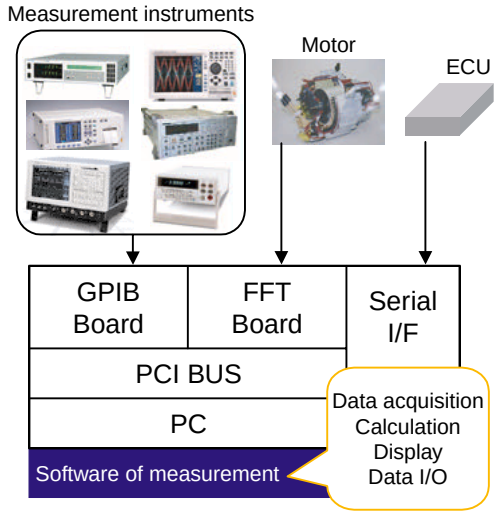


Fig. 6 Schematic diagram of measurement system

4.2 Automatic Correction of Measured Data

The error factors given in Table 2 also affect inductance during switching at times other than during calculations. Accordingly, a system to correct these items was created, wherein the data that has been corrected is visible in real-time. Thanks to this, improvements in analysis accuracy were achieved for each measured value and loss separation, etc. Fig. 7 provides the data correction flow for the system.

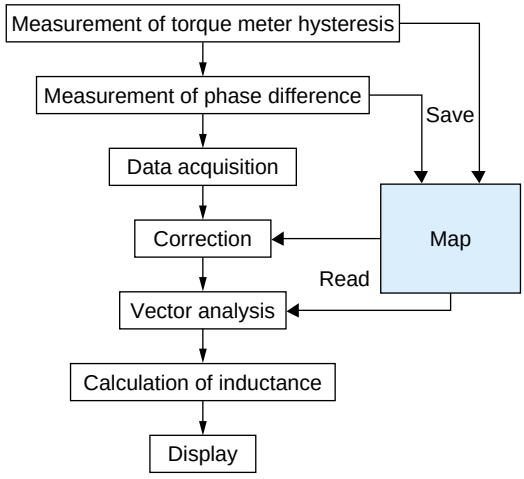


Fig. 7 Flowchart of correction process

4.3 Real-time Display of Vector Analysis

Conventionally, to understand the motor driving state during switching, complex processing, such as d-q conversion was required. Thus, in order to establish control parameters such as optimal switching amount, switching timing, etc., it was necessary to select various parameters from the test data after the test, which was quite time-consuming. By implementing the aforementioned vector analysis in real-time, and by displaying a circle diagram on the PC screen, it is now possible to make an immediate decision on optimum values. To carry out, vector analysis during switching in real-time, it is necessary to calculate motor speed pulse (magnetic pole location), phase voltage, phase current basic wave phase differences, and the root mean square. Also, with conventional measurement devices, concerns occurred with data synchronization, data processing and transmission speed. With this system, these concerns are resolved by fitting a multi-channel FFT board with an on-board DSP to a measurement PC's PCI bus. Fig. 8 shows the real-time vector analysis screens developed in this project. The left side of the screen is a circle diagram indicating the motor driving state, and the right side is a window providing a digital display of information relating

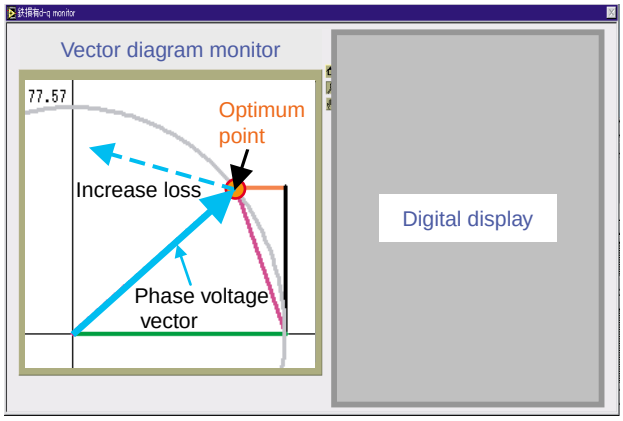


Fig. 8 Vector diagram monitor

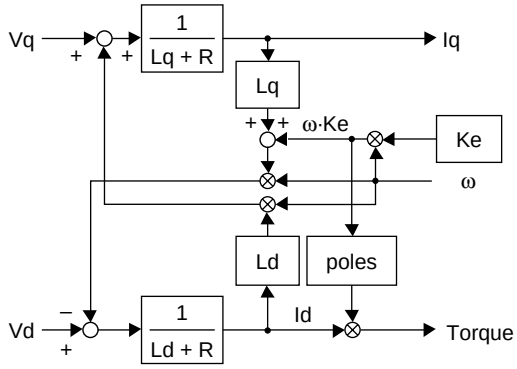


Fig. 10 Block diagram of brushless DC motor

to the state. On the circle diagram, the point where the tip of the phase voltage vector is the same as the circle of maximum phase voltage is the optimum driving state for maximum efficiency for a certain motor speed and output. In a driving state where the phase voltage vector shifts to the left of the optimum point, the weak field current is being excessively consumed, and motor efficiency suffers. In this way, it is possible to immediately judge optimum values for motor parameters with a given target motor speed and output by carrying out tests while monitoring the circle diagram. By systematizing this test flow and reducing the time spent in post-test data analysis, the test period is reduced by 30% (Fig. 9).

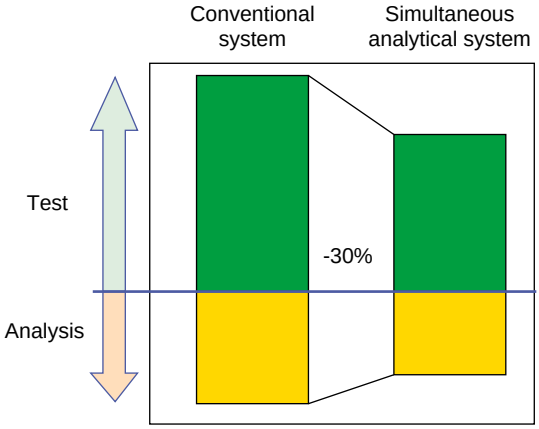


Fig. 9 Reduction of test time

from the true value, the mutual interference cannot be fully compensated for and torque responsiveness degrades. Fig. 11 gives an example of torque responsive-ness when operating a brushless DC motor, using a vector control controller that has an added mutual interference correction control. As shown in the diagram, when the inductance is not the same as the inductance during actual motor switching, there is a response delay in vehicle speed changes; in comparison, when the inductance is the same, there is good responsiveness. Accordingly, by carrying out real-time vector analysis and using the measured inductance during switching as the motor control's internal constant, it is possible to enhance torque responsiveness.

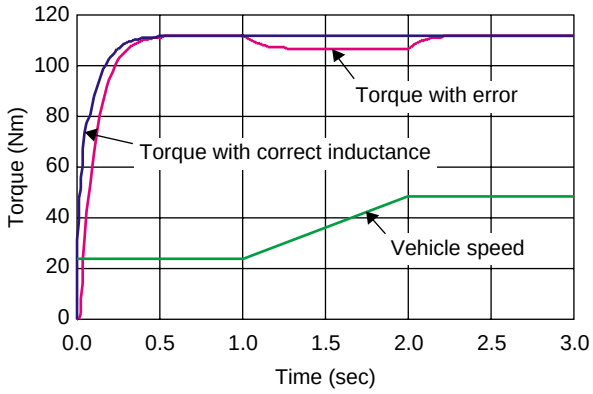


Fig. 11 Comparison result of torque response

5. Application Examples

5.1 Improved Torque Control Performance

In a motor for the hybrid electric vehicle (HEV) fitted to an Insight IMA, etc., high torque responsiveness is required in order to carry out engine vibration control. Fig. 10 shows a block diagram of an ordinary brushless DC motor[1]. As shown in the diagram, in the magnetic circuit there is mutual interference between the d-axis and the q-axis, and a discrepancy occurs between the actual torque and the command value. In order to compensate for this phenomena, it is necessary to add to control various correction items using motor parameters such as Ld, Lq, and R. When doing this, if the inductance value is different

5.2 Feedback into Motor Design

Fig. 12 takes the example of an ordinary brushless DC motor and shows the effect of inductance on motor performance. As shown in the diagram, if inductance is too small, the amount of weak field current needed to return the phase voltage vector to the circle of maximum phase voltage is large, and so efficiency drops. If inductance is too large, the voltage drop amount due to coil inductance exceeds the circle of maximum phase voltage so output is not possible in the high motor speed range. The motor inductance value is determined in close relationship with the permeable voltage constant and other magnetic circuits so it is not possible to freely choose this value. However, it

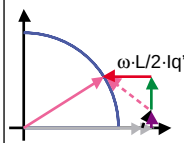
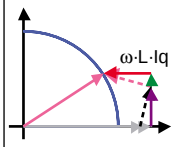
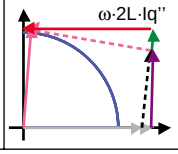
Inductance	Vector diagram	Flux weakening current	Performance
L1 = L/2		Iq' = 2Iq (big)	Low efficiency
L2 = L Optimum point		Iq (Optimum)	Optimum efficiency
L3 = 2L		Uncertainty	Low power

Fig. 12 Relationship between motor performance and inductance

is necessary to establish the optimum value, as it greatly affects motor maximum output and efficiency. By making it possible to accurately measure inductance during switching, which until now has not been quantitatively evaluated, inductance design targets at actual loads are now clear. This should contribute to the development of smaller and lighter motors. Also, it is possible to understand the situation of magnetic saturation in the magnetic circuits due to changes in inductance during switching according to load current (Fig. 13). Thanks to this, improvements to material selection can also be expected. In these ways, by making possible accurate measurements of inductance during switching, which has not been possible until now, optimum motor design is now possible.

Summary

By developing a system for immediate analysis of motor performance, the following are now possible.

(1) It is now possible to carry out immediate analysis of motor inductance during switching, which could not be calculated until now.
(2) It is now possible to obtain accurate measurements, thanks to the automatic test flow, which eliminates measurement errors.
(3) Test manpower has been reduced by 30% thanks to creating a test flow system, automating data processing, etc.

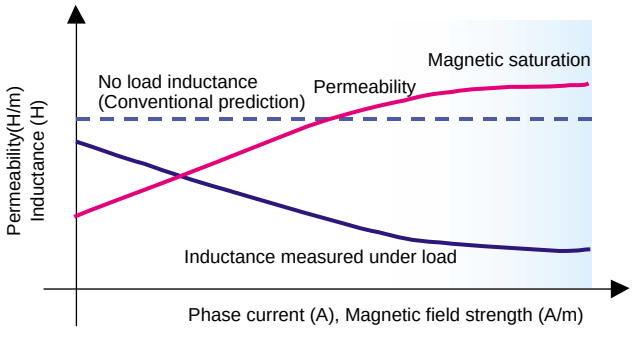


Fig. 13 Relationship between phase current and inductance

Acknowledgements

The authors would like to take this opportunity to thank in writing the many people, both with Honda and beyond, for their generous cooperation during this research project.

References

(1) Morimoto, S., Takeda , Y., and Hirasa, T., Comparison of Output Characteristics according to Current Control for PM Brushless DC Motors, The Institute of Electrical Engineers of Japan: Semiconductor Power Conversion Research Conference Material, SPC-89-3 (1989)

(2) Dote, Y. and Kinoshita T., Brushless Motor Basics, and their Use, Tokyo, Sogo Electric Publishing, 1985, p. 244

(3) Morimoto, S., Takeda, Y., and Hirasa, T., PM Motor dq Equivalent Circuit Constant Measurement Method, The Institute of Electrical Engineers of Japan: Industrial Application Division Newsletter, No. 113, Vol. 11, p. 1330 – 1331 (1993)

(4) Sugimoto, H., Koyama, M., and Tamai, S., AC Servo System Theory and Actual Design, Tokyo, Sogo Electric Publishing, 1990, p. 217

■ Authors ■


Yoshinari MURAYAMA


Hirofumi ATARASHI


Makoto KISHIDA


Kiyoshi ASAMI

Development of a Finite Element Model for the Pedestrian Lower Limb

– Development and Validation of Bone Models –

Yuji KIKUCHI* Yukou TAKAHASHI*
Atsuhiro KONOSU** Hirotoshi ISHIKAWA**

ABSTRACT

A finite element model for the long bones of the human lower limbs that accurately reflects their anatomical structure has been developed. The average values of the material properties of the bones as well as their strain rate dependency were determined from an extensive survey of the related literature and were reflected in the model. The model has been validated against published quasi-static and dynamic 3-point bending test results, confirming that it accurately predicts the peak impact force. In addition, it was found that the strain rate dependency of the material properties has a significant effect on the accuracy of peak force prediction.

1. Introduction

According to accident statistics, pedestrians account for a high proportion of traffic accident fatalities in Japan, at approximately 30%.(1) This accounts for the high priority placed on pedestrian protection together with occupant protection in the improvement of automobile safety. The Pedestrian Crash Data Study (PCDS), a database of pedestrian accident surveys in the United States, was used to examine distribution of the site of injuries with the Abbreviated Injury Scale (AIS) rating 2 or more. As shown in Fig. 1, the lower extremity area was found to be the most frequently injured body region. While not typically life-threatening, lower limb injury is becoming an increasingly important concern in terms of long recovery time and social cost.

Pedestrian lower limb injuries, as shown in Fig. 2, can be classified into two types: bone fracture and damage to knee ligament. Working Group 17 of the European Enhanced Vehicle-safety Committee (EEVC) has proposed a component test procedure using a legform impactor for evaluating these injuries.(2) However, recent studies have shown that the biofidelity of the impactor and validity of injury criteria should be further improved.(3) – (5) The test procedure will require further study for application to lower limb injury evaluation in car-pedestrian accidents. This paper reports on the development of a finite element model

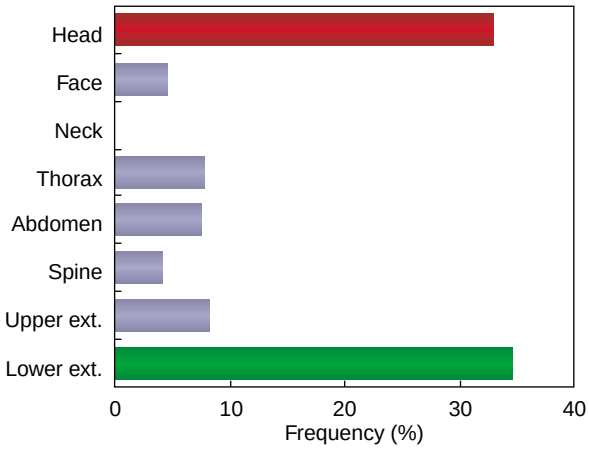
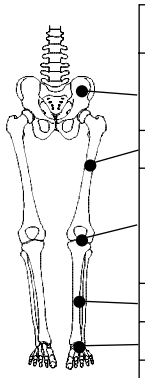


Fig. 1 Distribution of AIS2+ pedestrian injuries by body region (Source : PCDS database)

* Tochigi R&D Center
** Japan Automobile Research Institute



Region	Distribution (%)	Injury type
Pelvis	20.6	- Pelvis fracture - Sacroilium fracture
Femur	10.8	- Femoral shaft fracture
Knee	12.7	- Femoral supracondyle fracture - Tibial condyle fracture - Ligament rupture
Tibia/Fibula	31.9	- Tibial shaft fracture
Ankle/Foot	20.1	- Malleolus fracture
Whole	3.9	- Amputation above knee - Degloving injury

Fig. 2 Distribution of AIS2+ lower limb injuries by injury type (Source: PCDS database)

for the pedestrian lower limb with accurate anatomic structure. The purpose of this development was to identify the mechanism of injuries to the pedestrian lower limb and to establish an improved methodology for evaluating these injuries.

Large numbers of simulation models have been developed in the past in order to reproduce lower limb response in car-pedestrian accidents and identify the injury mechanism. Yang and Kajzer[6] used the MADYMO program to develop a three-dimensional multibody model of the pedestrian lower limb with a focus on the anatomic structure of the knee. Since the thigh and leg were each modeled as single rigid segments, it was not possible to simulate bone fracture. Yang et al.[7] [8] attempted to reproduce bone fracture by adding a joint element to this model in the upper part of the leg. The problem, however, was that this required the location of the bone fracture to be specified in advance. In these multibody models, the ability to simulate deflection of the bony structure and bone fracture is largely dependent on the modeling method, and it is difficult to construct a model that can be used under various different loading conditions.

Bermond et al.[9] [10] developed a three-dimensional finite element model of the knee joint, but this has not been validated for accuracy of dynamic response. Schuster et al.[11] developed a three-dimensional non-linear finite element model for the pedestrian lower limb. The response of the bony structure, however, has only been validated under quasi-static conditions. Tamura et al.[12] used a finite element model of the human body to study the tibial injury mechanism in passengers during a collision. However, quasi-static data were used for the material properties of bones, and the repeatability of the dynamic response has not been validated. Although the finite element models developed in the past studies had broader applicability than that of multibody models, no model has succeeded in simulating the dynamic response of the bony structure accurately.

This report describes the development and validation of a bone model produced in the course of development of a finite element model for the pedestrian lower limb. As noted above, lower limb injuries to pedestrians are generally categorized as bone fracture or ligament damage. Past experimental studies showed that ligament damage rarely occurs when bone fracture takes place.[13] A possible explanation for this is that a bone fracture interrupts the load path so that the force on the knee joint is reduced. In this study, the development of a bone model consequently incorporated a modeling method that was capable of simulating the interruption of the load path due to bone fracture. In order to accurately predict the dynamic response of the lower limb, the model also incorporated strain rate dependency of the material properties of bone that had not been taken into consideration in previous studies. Validation of this model was also carried out under dynamic conditions.

2. Structure and Material Properties of Bone

The structure of long bones is shown in Fig. 3. The surface of the epiphysis is covered by cortical bone, which has high stiffness, while the interior is filled with trabecular bone, which has a honeycomb-like structure and relatively low stiffness. The diaphysis forms a tubular structure of continuous cortical bone that grows progressively thicker toward the mid-section of the bone. There is no trabecular bone in the interior of the diaphysis, which is instead filled with yellow bone marrow. Consequently, prediction of the mechanical response of the bony structure requires the model to separately characterize and incorporate the

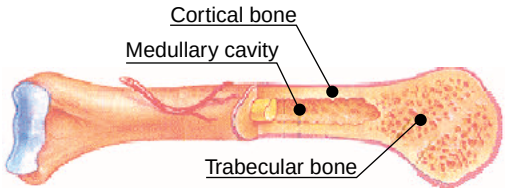


Fig. 3 Structure of long bones

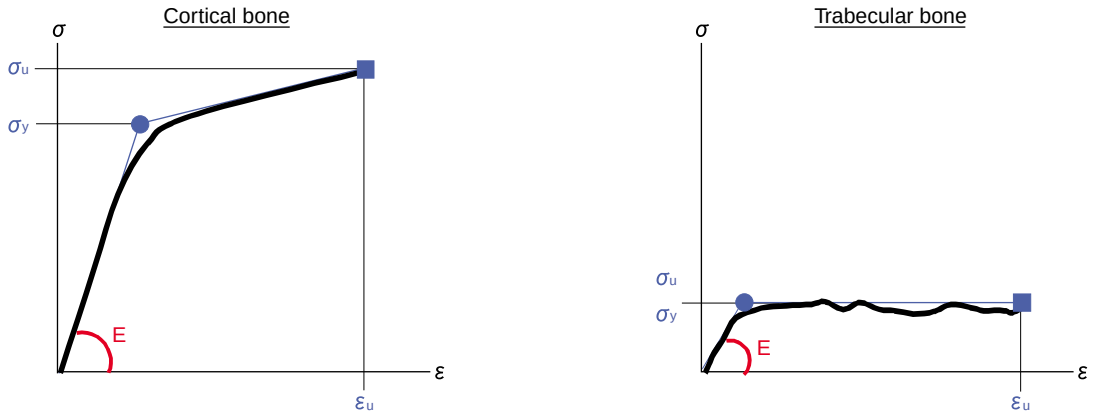


Fig. 4 Typical stress-strain curves for bone and parameters specified in the model

properties of the cortical bone and trabecular bone in order to take into account the difference in stiffness between these bone components.

The typical stress-strain curves for cortical bone and trabecular bone are shown in Fig. 4. To simplify modeling, the stress-strain relationships were approximated with the two phases shown by the blue lines, and the four parameters of the Young's modulus (E), the yield stress (σ_y), the ultimate stress (σ_u), and the ultimate strain (ε_u) were determined through extensive literature survey.[14) – 51)] For the trabecular bone, the properties of the plastic region were approximated by a constant stress ($\sigma_y=\sigma_u$). It was anticipated that the material properties of the bones would correlate with age when the survey results were compiled. Therefore the values for each property were plotted against age as the horizontal axis. The data set was not separated by gender, since past studies have shown no gender difference at the material property level.[52]

Fig. 5 shows the survey results for the Young's modulus and ultimate stress of femoral cortical bone. The data are presented under the categories of tension and compression. Clinical findings indicate that bone fracture is generally initiated in the portion subjected to tension. Consequently, these figures show that bone has less strength

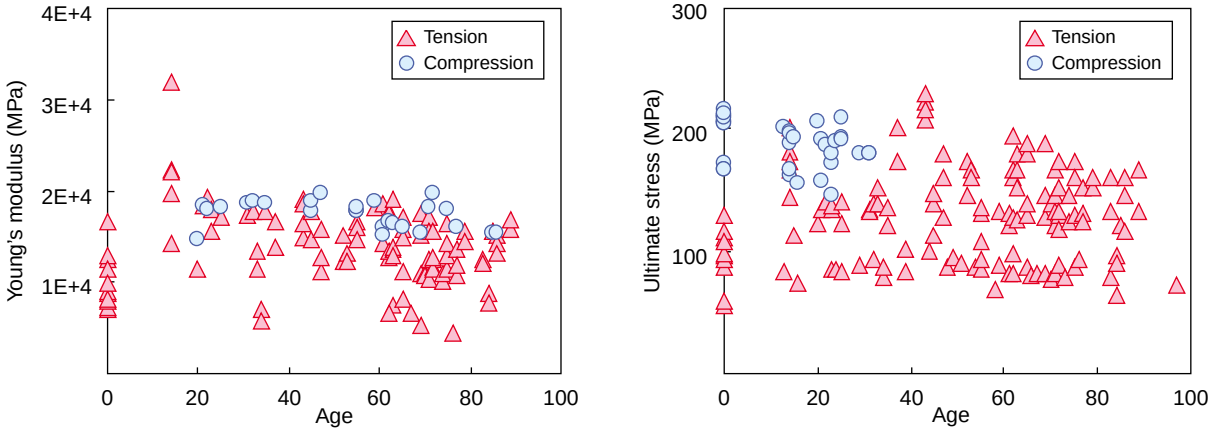


Fig. 5 Tensile and compressive properties of femoral cortical bone as a function of age

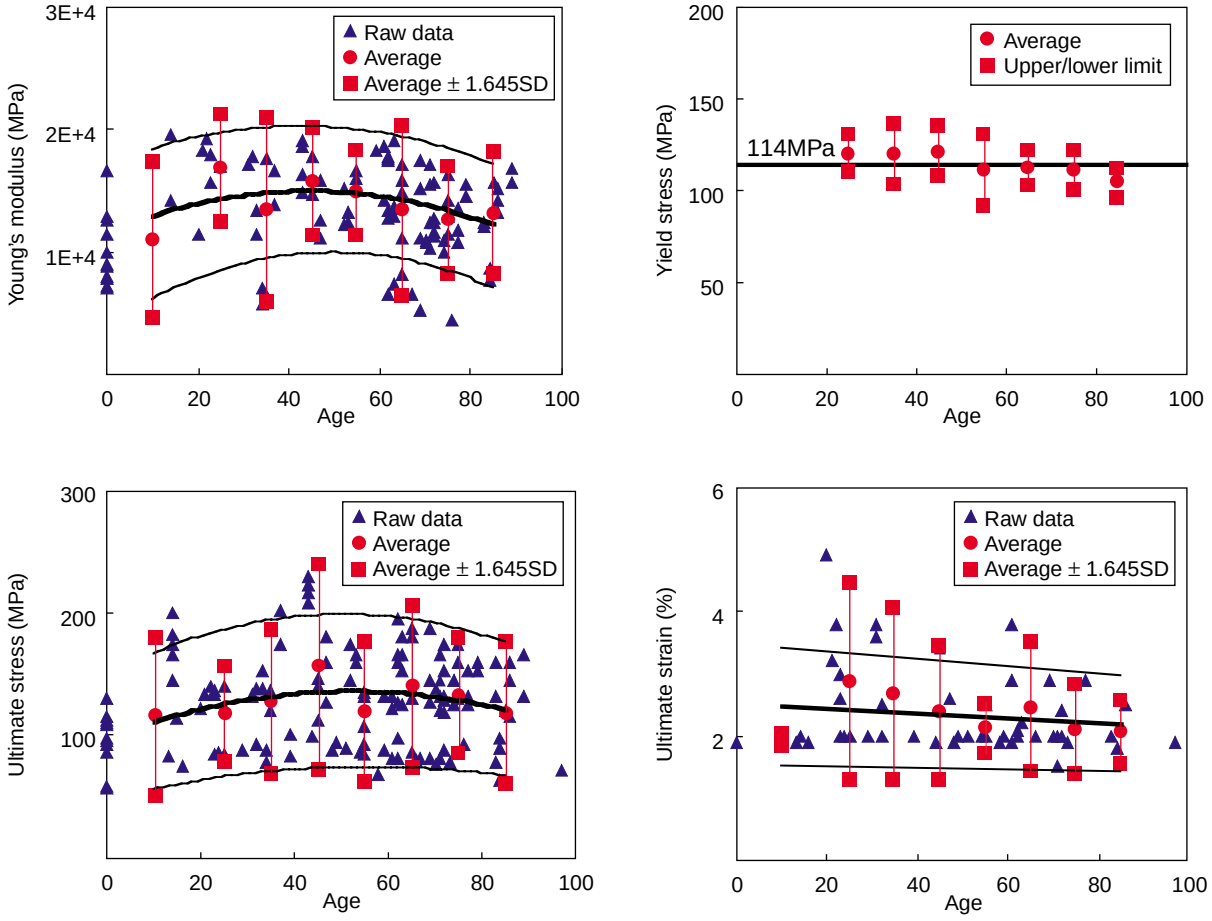


Fig. 6 Material property corridor of femoral cortical bone as a function of age

in tension than in compression, and the results are consistent with the clinical observations. In this research, therefore, the properties of bone in tension were used for the purposes of bone fracture prediction. Fig. 6 shows the survey results for the above four material properties with respect to femoral cortical bone. The values for properties other than the yield stress were divided into age groups at 10-year intervals and the averages were taken (red circles), and upper and lower limits were calculated (red squares) so as to include 90% of the data on the assumption of normal distribution. These were interpolated using a quadratic function to establish a corridor for the properties as shown in the graphs. For the ultimate strain, linear interpolation was chosen due to the relatively small amount of data and its wide variety. The only data obtained for the yield stress were the average values for the 10-year age groups (red circles) and the upper and lower limits (red squares). Therefore the correlation with age was not taken into account, and it was decided to use uniform averages instead.

Table 1 Differences in the material properties of the cortical bone in the femur and tibia (age 20 – 89, average)

Material property	Femur	Tibia	Ratio
Young's modulus (MPa)	16843	23843	1.42
Yield stress (MPa)	114	129	1.13
Ultimate stress (MPa)	132	157	1.19
Ultimate strain (%)	2.8	3.1	1.09

It is apparent from these graphs that the values for bone properties are affected even more by individual difference than by age. Use of these collected figures makes it possible to construct a model that incorporates the age and bone strength level of the pedestrian to be analyzed. The only data obtained for the tibial cortex were averages. Therefore, as shown in Table 1, the ratio of the average value for each property between the tibia and femur was used in order to obtain the corridor for the tibia by scaling that of the femur. No data at all were found for the fibula. The values for the properties of the femur were therefore used as initial estimates, and these were later adjusted to agree with test results during the process of validation, described below. Since there was also very little data on the properties of trabecular bone, it was not possible to determine material properties for each bone separately. The trabecular bone in the femoral head was found to have high stiffness compared to other regions, however, and this region was given different properties, as shown in Fig. 7. The stiffness of trabecular bone is about 1/10 that of cortical bone, and it was anticipated that the contribution of trabecular bone to the overall material properties of the bone is relatively small. Therefore, considering the small amount of data available, it was decided to use average values without defining the correlation with age. The ultimate strain for trabecular bone was set at 13.4%, using the only source that refers to this property.[53] A value of 0.315 was used as Poisson's ratio for cortical bone and trabecular bone in all the bones, taken from an average of the small amount of data available.[23] [27] [47]

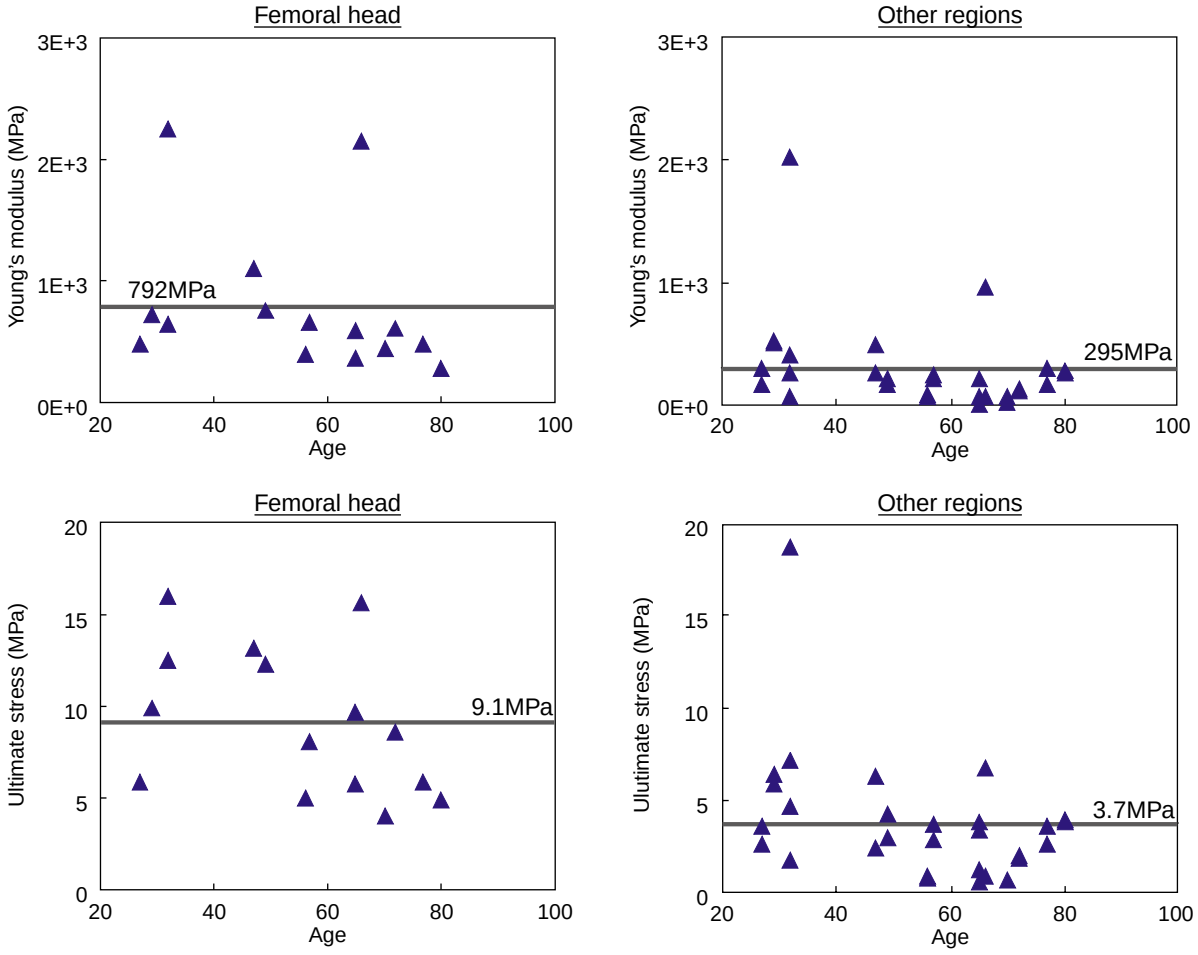


Fig. 7 Material properties of the trabecular bone for the femoral head and other regions

Carter and Hayes[54] [55] experimentally examined the effect of strain rate on the stiffness and strength in cortical bone and trabecular bone, and found that the stiffness and strength of bone are proportional to the strain rate raised to the power of 0.06 (Fig. 8). Based on these findings, the relationship between the strain rate and dynamic factor was defined as shown in Fig. 9. It is also apparent in Fig. 8 that a strain rate dependency exists with regard to the Young's modulus. Therefore, this relationship was applied to every region of the stress-strain curve, including the elastic region.

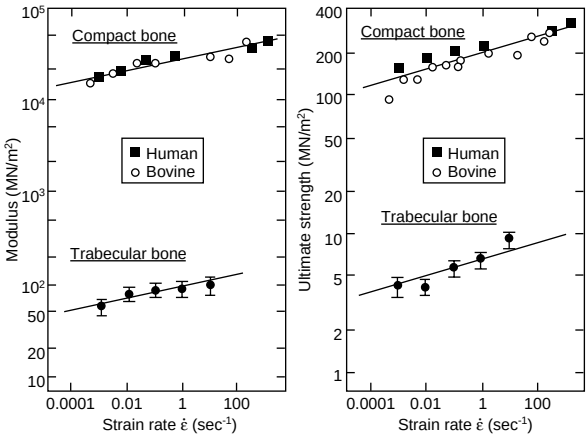


Fig. 8 Strain rate sensitivity of the material properties of bone

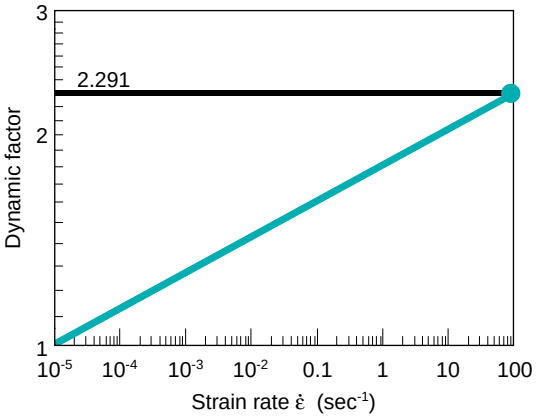


Fig. 9 Dynamic amplification factor versus strain rate specified in the model

3. Model Description

The external shape of the bone model was obtained from the H-Dummy™ [56] finite element model of the human lower limb developed by Nihon ESI. The shape of this model is anatomically accurate since it is based on the human bone model from the Viewpoint Datalab™ that was generated from scanned images of the human body.[57] The configuration of the bone model is consistent with that of human long bone shown in Fig. 3. As shown in Fig. 10, the epiphysis is modeled with a two-layered structure that uses shell elements for the surface cortical bone and solid elements for the internal trabecular bone. The diaphysis is modeled using solid elements for the cortical bone in order to simulate the internal cavity. A closer look inside cortical bone, as shown in Fig. 11, shows the existence of

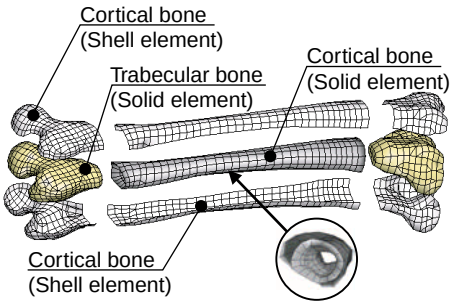


Fig. 10 Structure of femur model

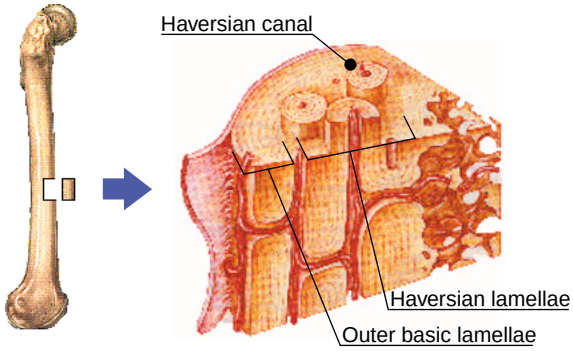


Fig. 11 Structure of cortical bone

Haversian lamellae enclosing large numbers of Haversian canals through which blood vessels pass. On the surface of the Haversian lamellae are outer basic lamellae that have even greater stiffness.[58] The material property of cortical bone found in the literature is related to these Haversian lamellae. Therefore, further shell elements were added to the outside of the diaphysis, where the cortex is thick and the outer circumferential lamellae are considered to have a significant effect. In this way the geometric moment of inertia of the diaphysis was corrected. As the literature did not contain quantitative data on the material properties of the outer circumferential lamellae, however, the data for the Haversian lamellae were used for this layer instead. The thickness of the lamellae was determined so that the geometric moment of inertia was identical to that calculated by applying beam theory to the published load-deflection curves from quasi-static 3-point bending tests conducted for each bone.

For the purpose of bone fracture modeling, material model Type 16 (solid element) and Type 105 (shell element) in PAM-CRASH™ were chosen for bones since they have fracture modeling functions. The Element Elimination option in these material models was applied in order to simulate bone fracture. This option steps the stiffness of certain elements down to zero when the elements reach the value set for the ultimate strain. For the strain rate dependency of material properties, the relationships in Fig. 9 were incorporated into the model using the PAM-CRASH™ logarithmic interpolation method.[59] [60]

4. Model Validation

The bone models were validated under quasi-static conditions against the results from quasi-static 3-point bending tests with human long bones conducted by Yamada

et al.[61] Though the test conditions are not described in detail in Yamada et al., they are assumed to have been as shown in Fig. 12. The literature contains load-deflection properties for human long bones, including such bones of the lower limb as the femur and tibia, in the form of average values. A model as shown in Fig. 14 was created and used for comparison of load-deflection curves. The computer simulations were run utilizing PAM-CRASH™. Since this computer program is for dynamic analysis, settings for the strain rate dependency of material property were excluded in order to simulate quasi-static conditions. The tests conducted by Yamada et al. used bones from persons aged 20 – 39 years. Therefore, average values calculated for the corresponding age group from the age corridor determined above were used. The material property values used in the computer simulation are shown in Table 2. A comparison of the simulation and test results for load-deflection properties of the femur, tibia, and fibula is shown in Fig. 15. The test results show slightly higher loads as compared to the simulation results when deflection is in the vicinity of approximately 5 – 10 mm, while the load and deflection at the point of bone fracture show excellent correlation for every bone.

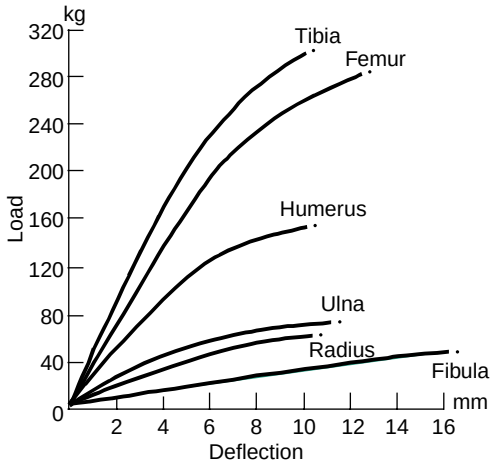


Fig. 13 Load-deflection curves for human long bones

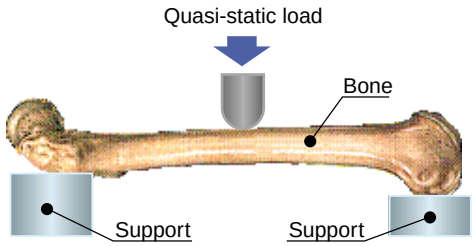


Fig. 12 Assumed quasi-static 3-point bending test setup for long bone

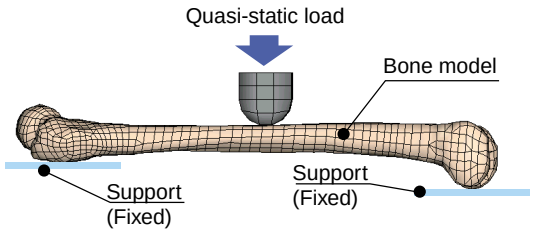


Fig. 14 Schematic diagram of femur model

Table 2 Material property of bones used in the model for quasi-static validation (for age 20 – 39, average)

Material Name	Density (kg/m³)	Young's modulus (MPa)	Yield stress (MPa)	Yield strain (%)	Poisson's ratio	Ultimate stress (MPa)	Ultimate strain (%)
Femur cortical	1850	14317	114.1	0.80	0.315	123.3	2.0
Tibia cortical	1850	20033	129.0	0.63	0.315	138.1	1.5
Fibula cortical	1850	17406	103.2	0.59	0.315	107.0	0.9
Trabecular	600	295	3.7	1.25	0.315	3.7	13.4
Femoral head trabecular	600	792	9.1	1.15	0.315	9.1	13.4

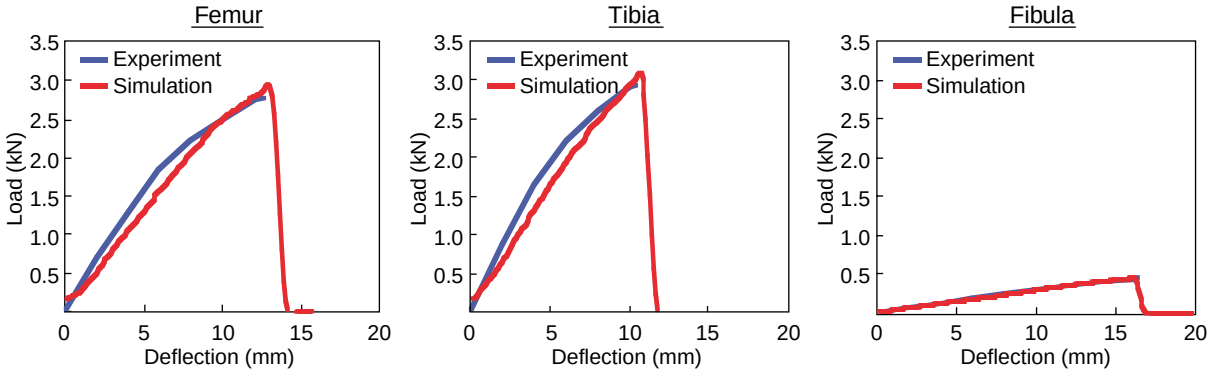


Fig. 15 Comparison of load-deflection response of bone in quasi-static 3-point bending

The bone model should also be validated under dynamic conditions since the impact between the pedestrian lower limb and the vehicle during an accident is a dynamic phenomenon. Dynamic validation of the bone model was carried out using the results from dynamic 3-point bending tests on many of the lower limb bones conducted by Kress et al.[62] Kress et al. used the test setup shown in Fig. 16 to obtain average peak forces occurring when an impactor weighing 50 kg is made to impact with the bone at a velocity of 7.5 m/s. Table 3 shows the test conditions and the average peak forces. The simulations employed the material properties corresponding to the average age for each set of conditions as calculated from the corridor. The tests applied impact to the femur and tibia from two directions, Lateral-Medial (L-M) and Anterior-Posterior (A-P), while the fibula only had L-M impact applied.

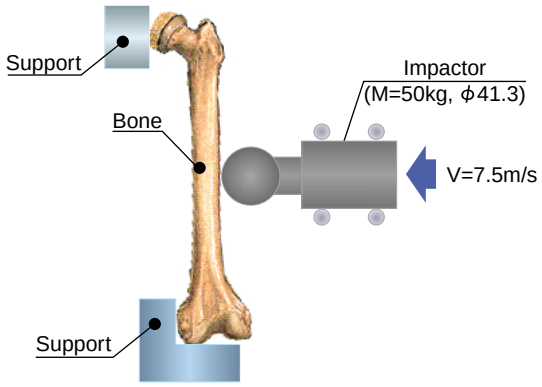


Fig. 16 Test setup for dynamic 3-point bending

Table 3 Test results of dynamic 3-point bending

Specimen	Impact plane	Age (Average)	n	Peak force (kN)
Femur	L-M	71.0yr	21	5.48 (SD 1.17)
	A-P	69.2yr	50	5.70 (SD 0.46)
Tibia	L-M	74.3yr	33	4.07 (SD 1.22)
	A-P	69.9yr	95	4.85 (SD 2.08)
Fibula	L-M	72.5yr	21	0.57 (SD 0.28)

* A-P : Anterior to Posterior / L-M : Lateral to Medial

Simulation models of the kind shown in Fig. 17 were created for all 5 of these cases and the peak forces were compared. The figure also shows deformation diagrams for the time of bone fracture, and the elements that exceed the ultimate strain threshold specified in the PAM-CRASH™ Element Elimination option are set not to be displayed. The mass of these elements is distributed in the surrounding nodes, and consequently they are conserved even after exceeding the threshold. The stiffness, however, diminishes to zero, so that load transmission does not take place in these elements to either side. In reality, butterfly-type fracture patterns are often observed in bone fractures caused by bending. However, in the simulation results in Fig. 17, the elements in the row immediately under the impactor are subject to Element Elimination. Therefore, this model is not capable of simulating the microscopic mechanism of actual bone fracture. This kind of model can, however, reproduce the interruption of the load path due to bone fracture, which is important for the analysis of pedestrian injury. A comparison of the peak forces between the simulation results and the test results is shown in Fig. 18. In the simulations, two models were employed: one with and one without strain rate dependency, in order to clarify the effect of the strain rate dependency of the material properties in dynamic loading conditions. It was found that the simulation results from the model without strain rate dependency showed a peak force of 1/2 of the test results

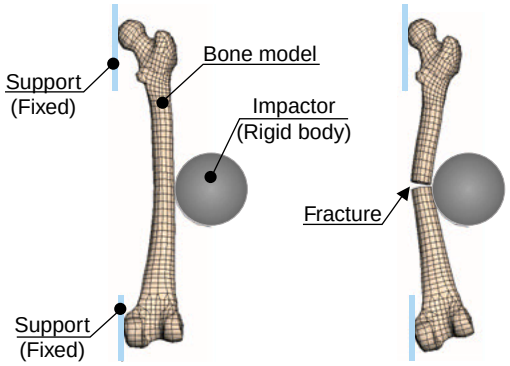


Fig. 17 Femur model setup for 3-point dynamic bending

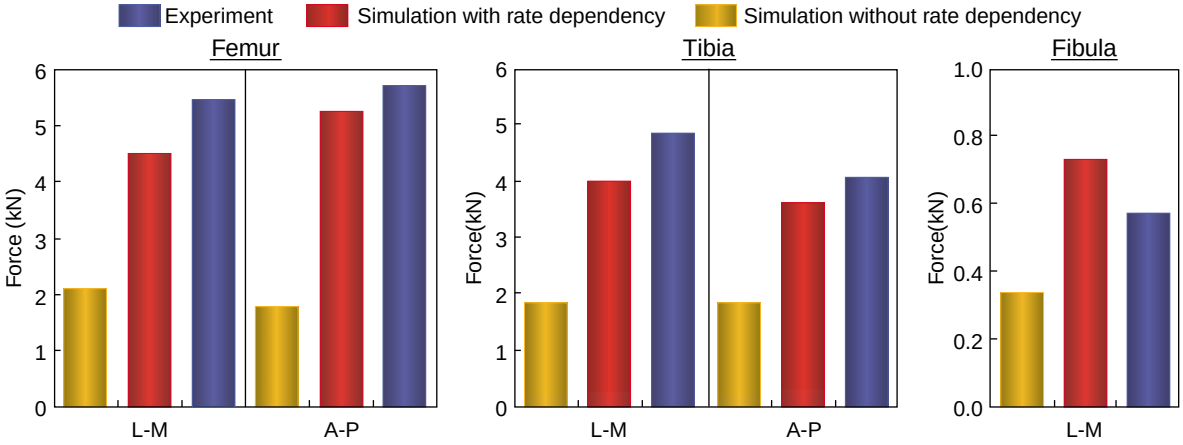


Fig. 18 Comparison of peak force between experiment and simulation

or less, while incorporation of strain rate dependency yielded results that were closer to the test results. This suggests that it is essential for the model to incorporate strain rate dependency of the material properties of bone in order to reproduce the injury mechanism of the pedestrian lower limb under dynamic conditions.

This research showed that the bone model developed was able to accurately predict the peak impact force in quasi-static and dynamic 3-point bending. In actual pedestrian accidents, however, the bumper frequently impacts the pedestrian lower limb immediately below the knee joint. Therefore, it is possible that the distribution of shear force and bending moment differs from 3-point bending. In addition, due to the microscopic internal structure of the long bone as illustrated in Fig. 11, the material properties are different in the axial and transverse directions.(63) A material model that simultaneously incorporates the anisotropy of a material, the strain rate dependency, and a fracture model is currently not available in PAM-CRASH™. Therefore, the model developed in this study focused on reproduction of bone fractures and assumed isotropic material properties. Future study should focus on the development of a material model that takes the above three elements into account simultaneously and the model validation should occur under conditions that more closely approximate actual pedestrian accidents.

5. Conclusion

A finite element model of the long bone of the human lower limb was developed that accurately represents the anatomic structure of the bone and incorporates material properties determined through extensive survey of the literature. The model was validated against test results from quasi-static and dynamic 3-point bending. The following conclusions were reached as a result:

(1) It was found through survey of the literature on material properties of bone that stiffness and strength are lower in tension than in compression. In relation to age, stiffness and strength tend to be at their peak around the age of 40, while individual difference has a greater effect even than age in terms of the amount of variation.

(2) The bone model developed in this study was found to correlate very well with test results in terms of the load and displacement magnitude at the time of bone fracture in quasi-static 3-point bending, and in terms of the load at the time of bone fracture in dynamic 3-point bending.

(3) It was found to be essential for the model to incorporate strain rate dependency of the material properties, which was not taken into consideration in previous research, in order for it to accurately simulate the dynamic response of bone.

(4) The reflection of anisotropy in the material properties of the bone model and the model validation under conditions more closely approximating actual accidents were identified as issues for the future.

References

(1) International Road Traffic and Accident Database (1995)

(2) European Enhanced Vehicle-safety Committee: “EEVC Working Group 17 Report – Improved test methods to evaluate pedestrian protection afforded by passenger cars” (1998)

(3) Matsui, Y., Ishikawa, H., Sasaki, A., Kajzer, J., Schroeder, G.: “Impact response and biofidelity of pedestrian legform impactors”, IRCOBI (1999)

(4) Konosu, A., Ishikawa, H., Tanahashi, M.: “Reconsideration of Injury Criteria for Pedestrian Subsystem Legform Test – Problems of RIGID Legform Impactor –”, 17th ESV Conference, Paper Number 263 (2001)

(5) Takahashi, Y., Kikuchi, Y.: “Biofidelity of Test Devices and Validity of Injury Criteria for Evaluating Knee Injuries to Pedestrians”, 17th ESV Conference, Paper Number 373 (2001)

(6) Yang, J.K., Kajzer, J.: “Computer simulation of impact response of the human knee joint in car-pedestrian accidents”, SAE paper 922525 (1992)

(7) Yang, J.K., Rzymkowski, C., Kajzer, J.: “Development and validation of a mathematical breakable leg model”, IRCOBI (1993)

(8) Yang, J.K., Kajzer, J.: “Mathematical model of pedestrian lower extremity”, 14th ESV Conference (1994)

(9) Bermond, F., Ramet, M., Bouquet, R., Cesari, D., “A finite element model of the pedestrian knee-joint in lateral impact”, IRCOBI (1993)

(10) Bermond, F., Ramet, M., Bouquet, R., Cesari, D.: “A finite element model of the pedestrian leg in lateral impact”, 14th ESV Conference (1994)

(11) Schuster, P. J., Chou, C. C., Prasad, P.: “Development and Validation of a Pedestrian Lower Limb Non-Linear 3-D Finite Element Model”, STAPP CAR CRASH JOURNAL, Vol.44 (2000)

(12) Tamura, A., Miki, K., Yang, K.: “A Tibial Mid-Shaft Injury Mechanism in Frontal Automotive Crashes”, 17th ESV Conference, Paper Number 355 (2001)

(13) Cesari, D., Cavallero, C., Roche, H.: “Mechanisms producing lower extremity injuries in pedestrian accident situations”, 33rd AAAM (1989)

(14) Goldstein, S., Frankenburg, E., Kuhn, J.: “Biomechanics of bone”, Accidental Injury (1993)

(15) Hirsch, C., Evans, F.G.: “Studies on some physical properties of infant compact bone”, Acta Orthop. Scand., 35 (1970)

(16) Sedlin, E.D., Hirsch, C.: “Factors affecting the determination of the physical properties of femoral cortical bone”, Acta Orthop. Scand., 37 (1966)

(17) Lindahl, O., Lindgren, A.G.H.: “Cortical bone in man. II. Variation in tensile strength with age and sex”, Acta Orthop. Scand., 38 (1967)

(18) Hirsch, C., Dasilva, O.: “The effect of orientation on some mechanical properties of femoral cortical specimens”, Acta Orthop. Scand., 38 (1967)

(19) Carter, D.R., Caler, W.E., Spengler, D.M., Frankel, V.H.: “Fatigue behaviour of adult cortical bone: the influence of mean strain and strain range”, Acta Orthop. Scand., 52 (1981)

(20) Evans, F.G., Bang, S.: “Differences and relationships between the physical properties and the microscopic structure of human femoral, tibial and fibular cortical bone”, Am. J. Anat., 120 (1967)

(21) Wall, J.C., Chatterji, S.K., Jeffery J.W.: “Age-related changes in the density and tensile strength of human femoral cortical bone”, Calcif. Tiss. Intl., 27 (1979)

(22) Carter, D.R., Spengler, D.M.: “Basic science and pathology - Mechanical properties and composition of cortical bone”, Clin. Orthop. Related Research, 163 (1982)

(23) Lappi, V.G., King, M.S., LeMay, I., “Determination of elastic constants for human femurs”, Journal of Biomechanical Engineering, 101 (1979)

(24) Hight, T.K., Brandeau, J.F.: “Mathematical modeling of the stress strain - strain rate behavior of bone using the Ramberg-Osgood Equation”, Journal of Biomechanics, 16 (1983)

(25) Cezayirlioglu, H., Bahniuk, E., Davy D.T., et al.: “Anisotropic yield behaviour of bone under combined axial force and torque”, Journal of Biomechanics, 18 (1985)

(26) Bonfield, W.: “Advances in the fracture mechanics of cortical bone”, Journal of Mechanics, 20 (1987)

(27) Katsamanis, F., Raftopoulos, D.D.: “Determination of mechanical properties of human femoral cortical bone by the Hopkinson bar stress technique”, Journal of Biomechanics, 23 (1990)

(28) Lotz, J.C., Gerhart, T.N., Hayes, W.C.: “Mechanical properties of metaphyseal bone in the proximal femur”, Journal of Biomechanics, 24 (1991)

(29) Saha, S., Hayes, W.C.: “Tensile impact properties of human compact bone”, Journal of Biomechanics, 9 (1976)

(30) Yoon, H.S., Katz, J.L.: “Ultrasonic wave propagation in human cortical bone-II, Measurements of elastic properties and microhardness”, Journal of Biomechanics, 9 (1976)

(31) Reilly, D.T., Burstein, A.H.: “The Mechanical properties of cortical bone”, Journal of Bone and Joint Surgery, 56-A (1974)

(32) Currey, J.D., Butler, G.: “The Mechanical properties of bone tissue in children”, Journal of Bone and Joint Surgery, 57-A (1975)

(33) Burstein, A.H., Reilly, D.T., Martens, M.: “Aging of bone tissue: Mechanical properties”, Journal of Bone and Surgery, 58A (1976)

(34) McCalden, R.W. et al.: “Age-related changes in the tensile properties of cortical bone”, Journal of Bone and Joint Surgery, 75-A (1993)

(35) Mather, B.S.: “The symmetry of the mechanical properties of the human femur”, J. Surg. Res., 7 (1967)

(36) Ruff, C.B., Hayes, W.C.: “Sex differences in age-related remodeling of the femur and tibia”, Journal of Orthopaedic Research, 6 (1988)

(37) Goldstein, S.A. et al.: “The mechanical properties of human tibial trabecular bone as a function of metaphyseal location”, Journal of Biomechanics, 16 (1983)

(38) Currey, J.D.: “The mechanical properties of bone”, Clin. Orthop. Related Research, 135 (1978)

(39) Leichter, I. et al.: “The relationship between bone density, mineral content and mechanical strength in the femoral neck”, Clin. Orthop. Related Research, 163 (1982)

(40) Parfitt, A.M. et al.: “Relationships between surface, volume, and thickness of iliac trabecular bone in aging and in osteoporosis”, J. Clin. Inverst., 72 (1983)

(41) Williams, J.L., Lewis, J.L.: “Properties and an anisotropic model of cancellous bone from the proximal tibia epiphysis”, Journal of Biomechanical Engineering, 104 (1982)

(42) Stone, J.L., Beaupre, G.S., Hayes, W.C.: “Multiaxial strength characteristics of trabecular bone”, Journal of Biomechanics, 16 (1983)

(43) Gibson, L.J.: “The Mechanical behavior of cancellous bone”, Journal of Biomechanics, 18 (1985)

(44) Linde, F., Hvid, I.: “Stiffness behaviour of trabecular bone specimens”, Journal of Biomechanics, 20 (1987)

(45) Rice, J.C., Cowin, S.C., Bowman, J.A.: “On the dependence of the elasticity and strength of cancellous bone on apparent density”, Journal of Biomechanics, 21 (1988)

(46) Pugh, J.W., Rose, R.M., Radin, E.L.: “Elastic and viscoelastic properties of trabecular bone, dependence on structure”, Journal of Biomechanics, 6 (1973)

(47) Behrens, J.C., Walker, P.S., Shoji, H.: “Variations in strength and structure of cancellous bone at the knee”, Journal of Biomechanics, 7 (1974)

(48) Ducheyne, P., Heymans, L., Martens, M., et al.: “The mechanical behavior of intercondylar cancellous bone of the femur at different loading rates”, Journal of Biomechanics, 10 (1977)

(49) Linde, F., Hvid, I.: “The effect of constraint on the mechanical behavior of trabecular bone specimens”, Journal of Biomechanics, 22 (1989)

(50) Courtney, A.C. et al.: “Age-related reductions in the strength of the femur tested in a fall-loading configuration”, Journal of Bone and Joint Surgery, A77 (1995)

(51) McElhaney, J.H.: “Dynamic response of bone and muscle tissue”, Journal of Applied Physiology, 21 (1966)

(52) An, Y.H., Draughn, R.A.: Mechanical Testing of Bone and the Bone-Implant Interface, CRC Press, 2000, p.68

(53) Lindahl, O.: “Mechanical properties of dried defatted spongy bone”, Acta Orthop. Scand., 47 (1976)

(54) Carter, D.R., Hayes, W.C.: “The compressive behaviour of bone as a two-phase porous structure”, Journal of Bone and Joint Surgery, 59-A (1977)

(55) Carter, D.R., Hayes, W.C.: “Bone compressive strength: The influence of density and strain rate”, Science, 194 (1976)

(56) H-Dummy™ Version 1.6 User’s Manual, Hankook ESI, Engineering Systems International, 1998

(57) Viewpoint Premier CATALOG, 10th Anniversary Edition, p. 81

(58) Mori, O., et al.: Anatomy 1, Tokyo, Kanehara & Co., LTD., 1998, p. 24

(59) Pam System International, PAM-CRASH™ PAM-SAFE™ Version 1998 Notes Manual, 1998

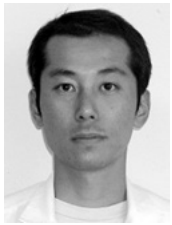
(60) Pam System International, PAM-CRASH™ PAM-SAFE™ Version 1998 Reference Manual, 1998

(61) Yamada, H.: Strength of biological materials, The Williams & Wilkins Company, 1970

(62) Kress, A. et al.: “Fracture patterns of human cadaver long bone”, IRCOBI (1990)

(63) Evans, F.G.: Mechanical properties of bone, Charles C Thomas Publisher

■ Authors ■



Yuji KIKUCHI



Yukou TAKAHASHI



Atsuhiro KONOSU



Hirotoshi ISHIKAWA

Development of a Finite Element Model for the Pedestrian Lower Limb

– Development and Validation of a Knee Joint Model –

Yukou TAKAHASHI* Yuji KIKUCHI*
Atsuhiro KONOSU** Hirotoshi ISHIKAWA**

ABSTRACT

A finite element model for a human lower limb in a standing position has been developed that connects long bone models of a lower limb at the knee with ligament models. The knee joint model incorporates both the articular cartilage and the meniscus, which are deemed to be important elements in the accurate prediction of ligament loading. The model has been validated against published lateral lower limb impact tests, and the results showed that the model can accurately reproduce the shearing displacement and bending angle of the knee joint. In addition, comparison of the model with test data on damage to four main knee ligaments showed that the model was able to simulate the ligamentous damage that had been observed in more than half of the test cases.

1. Introduction

The two main types of lower limb injury in car-pedestrian accidents are bone fractures and damage to knee ligaments. Consequently, investigative tools for identifying the mechanism of injury to the pedestrian lower limb need to be able to reproduce ligamentous damage of the knee in addition to bone fractures. This paper describes the development and validation of a pedestrian knee joint model constructed by combining lower limb bone models developed by the authors.

Damage to knee ligaments, unlike at the bony structure, is difficult to treat medically because ligaments have less capacity for self-repair, and this kind of damage has long been recognized as a serious injury. In addition, the knee joint does not experience the kind of constraint found in other joints, where the bones are fitted together. Instead, the stability of the knee joint is entirely dependent on ligaments. This special characteristic of the anatomic structure means that damage to knee ligaments can seriously affect walking function and often require a long time for recovery. Given this context, attention has been focused on damage to knee ligaments from pedestrian accidents. Working Group 17 of the European Enhanced Vehicle-safety Committee (EEVC) has proposed a test procedure using a legform impactor[1], where the shearing displacement and bending angle of the knee are used as injury criteria for knee ligament.

Past studies involved development of simulation models that focused on the anatomic structure of the knee in order to identify the mechanism of damage to knee ligaments. Yang and Kajzer[2] developed a knee joint model using the MADYMO program. This model represented the femoral condyle, tibial plateau, and tibial eminence with combinations of planes and ellipsoids, and modeled knee ligaments with spring elements. The damage to knee

* Tochigi R&D Center
** Japan Automobile Research Institute

ligaments was compared with test results, but the model could not represent either the contact between collateral ligament and the bony structure or the deflection of the bone. As a result, the model was unable to accurately predict the load on the ligaments. Yang et al.[3][4] attempted to predict bone fractures by adding a joint element to the bone in this model. However, this required determining the site of bone fractures in advance. Although these multibody models can simulate knee response to some extent by accurately representing the anatomic structure of the knee, their accuracy is limited by the significant effect of the bone deflection on the loading of the knee ligaments. Schuster et al.[5] developed a finite element model of the pedestrian lower limb. However, validation was only conducted with shearing displacement applied to the knee, and the loading rate was limited to a low speed (15 km/h).

In the present study, a lower limb model for pedestrians in a standing position was constructed by combining finite element models for bones in the lower limb that have been developed by the authors and validated for impact response. In order to accurately predict load on the knee ligaments, the articular cartilage and the meniscus were incorporated since these elements were deemed to have a significant effect on elongation of the ligaments. In addition, contact between the ligaments and bony structure was defined in order to accurately reproduce elongation of the ligaments due to knee joint deformation. The dynamic response of the knee was validated against published results of lower limb impact tests on impact force, shearing displacement, and bending angle. The injury description for ligamentous damage was also compared with the test results. Validation was carried out for a total of four conditions that combined two loading rates with two test conditions for knee shearing and bending.

2. The Structure and Material Properties of the Knee Joint

The structure of the human knee joint is shown in Fig. 1. The knee joint is the articulation between the tibia and femur, and is formed by the distal femur overlapping the flat portion of the proximal tibia. Consequently, there is no effective constraint among the bones of the knee joint, and the stability of the joint is maintained primarily by attachment of the ligaments. As shown in the figure, the knee is held together by four ligaments, the Anterior Cruciate Ligament (ACL), Posterior Cruciate Ligament (PCL), Lateral Collateral Ligament (LCL), and Medial Collateral Ligament (MCL). The cartilaginous meniscus is located around the tibial plateau, and the joint surfaces of the femur and tibia are covered with articular cartilage. These cartilaginous structures perform a buffer role when the knee deforms axially, suggesting that they affect the elongation of ligaments due to knee deformation by impact.

Fig. 2 shows a typical stress-strain curve for knee ligaments. The collagen fibers inside the ligament take a coiled form when they are not under load, and their orientation is chaotic. Application of tension, however, causes the coiled fibers to elongate until they become straight and their orientation also becomes aligned in the direction of the tension. This process corresponds to region I in Fig. 2. Under further loading, the tensile properties of the straightened collagen fibers causes them to show a more or less fixed modulus as in region II. Wismans[6] showed that since region I can be approximated accurately by a quadratic function, then taking the continuity of the first order derivative into account, the average modulus of region I can be approximated by 1/2 of the modulus of region II. The present study used this relationship and approximated the stress-strain curve by a three-stage straight line as in Fig. 2. The five parameters of region II were determined by a survey of the literature[7]–[11]: modulus (E), yield stress (σ_y), yield strain (ε_y), ultimate stress (σ_u), and ultimate strain (ε_u).

Fig. 3 shows the results of the survey for the ultimate stress. The horizontal axis shows the strain rate on a logarithmic scale, and data for the various ligaments are

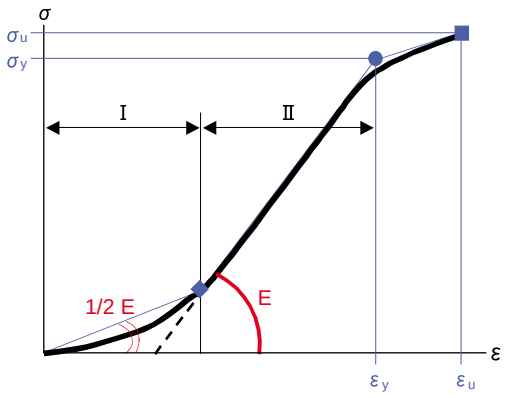


Fig. 2 Typical stress-strain curve for knee ligament

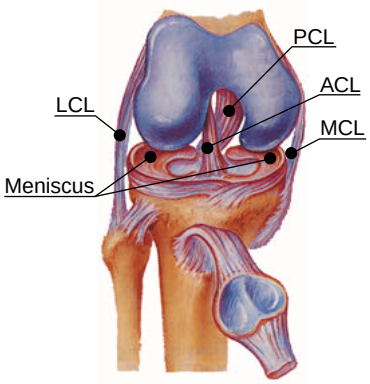


Fig. 1 Structure of knee joint

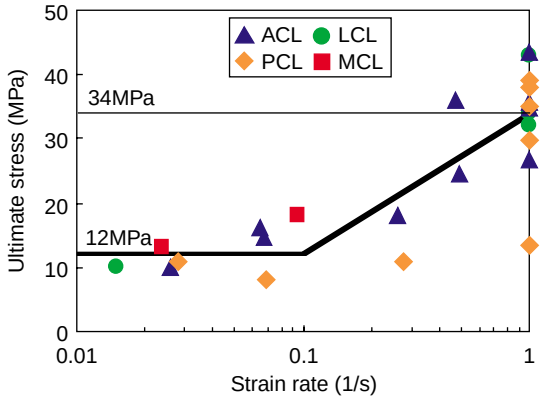


Fig. 3 Ultimate stress of knee ligaments as a function of strain rate

represented by different colors. As no significant differences in ligament properties were observed, the decision was made to assign the same properties to all ligaments. In the region where strain rate exceeds 0.1 /s, the ultimate stress was found to have a tendency to increase. Therefore, the relationship represented by a straight line in the figure was established as strain rate dependency. As no data were found for the region where the strain rate exceeds 1.0 /s, this was established by extrapolation. As shown in Fig. 4, no significant strain rate dependency was observed for the ultimate strain. Therefore, only average values were determined. As little data on the yield stress and yield strain were available in the literature, ratios between these and the ultimate stress and ultimate strain, respectively, were established as in Fig. 5. Although the modulus showed a tendency to increase with the strain rate, as shown in Fig. 6, there was a wide variety of data. It was assumed, therefore, that the strain rate dependency of the modulus was identical to that of the ultimate stress, and it was represented by a relationship depicted by the straight line shown in the graph. The skin was also assumed to have an effect on the mechanical properties of the knee joint, and its properties were established with reference to the literature.[12] [13] A search of the literature with reference to the cartilage and meniscus[14] did not yield data for the plastic region. Therefore these elements were modeled as linear elastic materials. The quasi-static stress-strain curve for the ligaments and skin determined in this way is shown in Fig. 7, and that for the cartilage and meniscus is shown in Fig. 8. As only quasi-static data could be obtained for the skin, cartilage and meniscus, it was assumed that they had a strain rate dependency identical to that of ligaments.

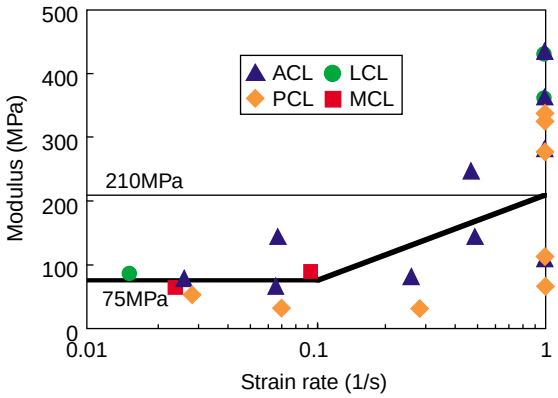


Fig. 6 Modulus of knee ligament

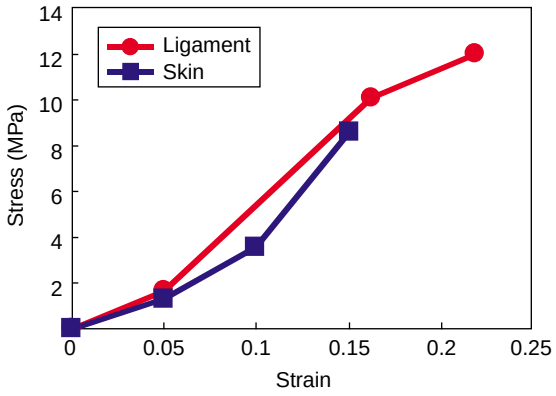


Fig. 7 Quasi-static stress-strain curve for knee ligaments and skin used in the model

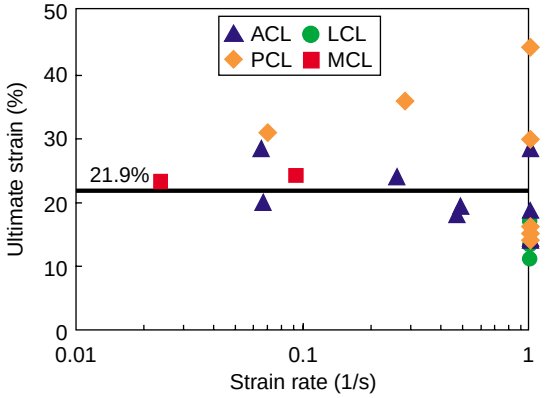


Fig. 4 Ultimate strain of knee ligaments

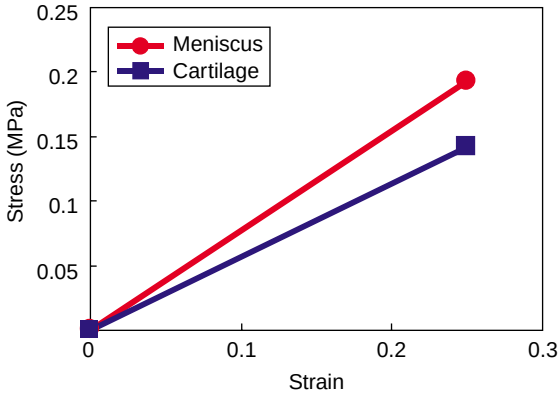


Fig. 8 Quasi-static property for meniscus and cartilage used in the model

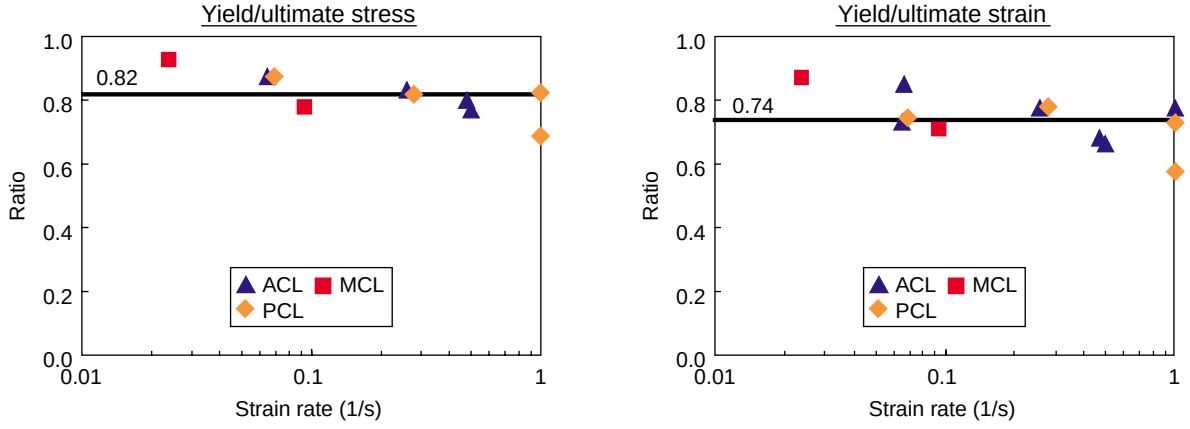


Fig. 5 Ratio between ultimate stress/strain and yield stress/strain

3. Model Description

In constructing a knee joint model by combining bone models, the lower limb was aligned with reference to the literature[15] so that the hip joint, knee joint, and ankle joint were located on a single straight line, as shown in Fig. 9. Knee ligaments were modeled with shell elements, as shown in Fig. 10. In order to accurately reproduce the elongation of ligaments due to joint deformation, a contact between the ligaments and bones was defined. Data was obtained from the Medical School of Hannover in Germany regarding the length and cross sectional area of each ligament, and these parameters were defined as shown in Table 1 and Table 2. The two ends of the ligament model were connected to the bone model by defining a rigid body in the area of the ligament attachment so that the ligament had an effective length consistent with the data in Table 1. All ligaments were given the same width (15 mm) for simplicity, and then a different thickness was set for each ligament according to its cross sectional area provided in Table 2. Ligament rupture was reproduced using the Element Elimination option[16][17] in PAM-CRASH™, which takes the stiffness of elements that reach the threshold set for the ultimate strain and steps them down to zero. Solid element models for the cartilage and meniscus were incorporated on the tibial plateau (Fig. 10) in order to reproduce the axial deformation of the knee joint. The soft tissue around the bony structure of the thigh and leg that consists mainly of the muscle and fat was modeled with solid elements, as shown in Fig. 11. A model for this part was taken from a finite element model of the human lower limb (H-Dummy™) developed by Nihon ESI. This model was validated against the results of dynamic indentation tests conducted from every direction using human volunteers.[18] The skin modeled with shell elements was added to the surface of this part, since it was deemed to have an effect on the knee response.

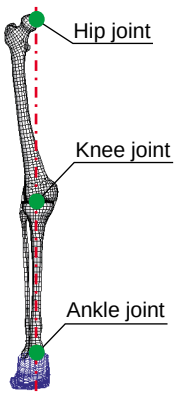


Fig. 9 Alignment of lower limb model

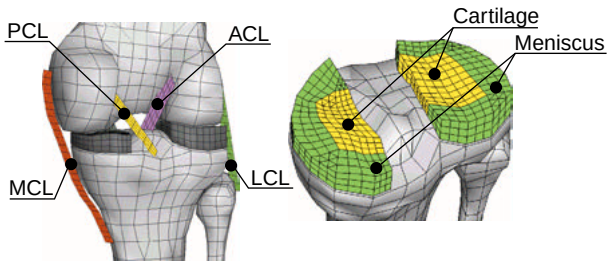


Fig. 10 Knee joint model

Table 1 Length of knee ligament used in the model

Ligament	ACL	PCL	LCL	MCL
Length (mm)	40	41	55	91

Table 2 Cross sectional area of knee ligament used in the model

Ligament	ACL	PCL	LCL	MCL
Area (mm^2)	46	77	29	37

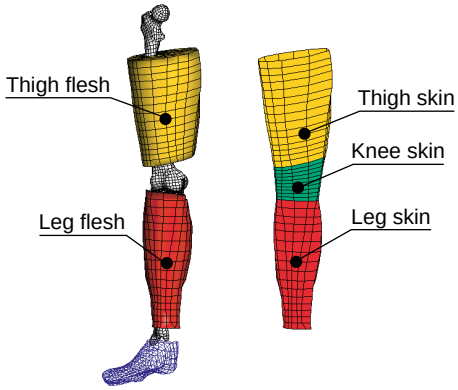


Fig. 11 Schematic diagram of lower limb model

4. Model Validation

The knee model was validated against the results of lower limb impact tests conducted by Kajzer et al.[19][20] The test conditions are shown in Fig. 12. Kajzer et al. used a jig to fix the femoral supracondyle and greater trochanter in place with a load cell interposed on each, and then propelled a 6.25 kg impactor into the leg laterally at velocities of 20 km/h and 40 km/h. The impactor was used with two impact conditions; one was a shearing setup to impact immediately below the knee joint to apply shearing deformation, and the other was a bending setup to impact against the ankle joint to apply bending deformation. A 400 N preload in the inferior direction was applied to the lower limb to simulate a walking condition, and a piece of foam was attached to the impactor head in order to prevent injury from direct impact.

The model shown in Fig. 13 was created to reproduce these tests. Kajzer et al. conducted their tests with the whole body of a human subject. In the experiments, no significant displacement of the upper body was observed during impact to the lower limb. Therefore, for simplicity, the model only represented the lower limb, and the femoral head that is the juncture with the upper body was fixed in inertial space. A boundary condition was applied to elements in the vicinity of the fixed parts of the greater trochanter and supracondyle of the femur to fix them in inertial space. The preload was applied to the lower limb by moving the surface corresponding to the ground in superior direction prior to the impact from the impactor. Only the foam material on the impactor head was modeled with solid elements, with the remaining impactor mass being applied to a single node so that the center of gravity would

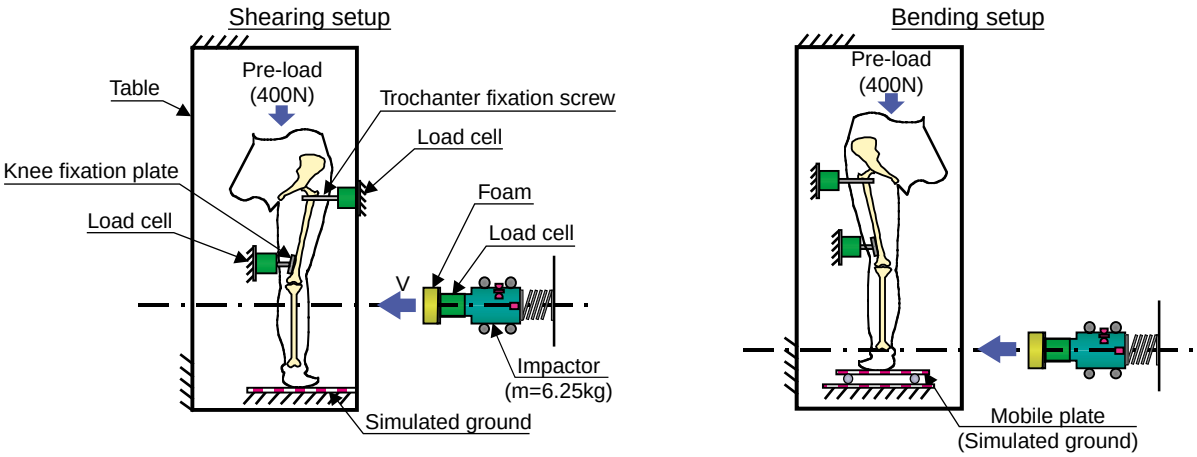


Fig. 12 Test setup for dynamic response of knee joint

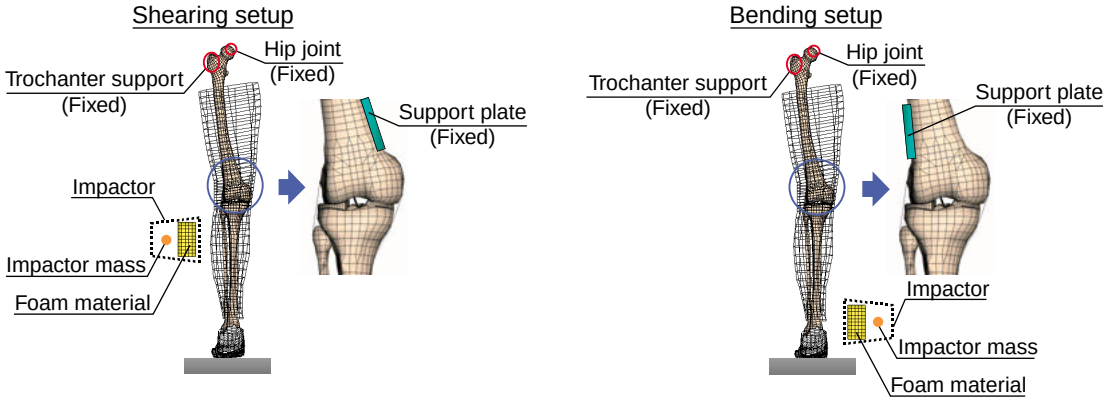


Fig. 13 Model setup for knee joint validation

correspond with that of the actual impactor. Since the foam material is the source for input to the lower limb, and therefore the accuracy of this part affects the accuracy of the knee response, validation of the foam material alone was performed in advance (Fig. 14).

Wittek et al.[21] analyzed the test results from Kajzer et al. and obtained a corridor from the average ± standard deviation for the impact force to the lower limb as well as the shearing displacement and bending angle of the knee

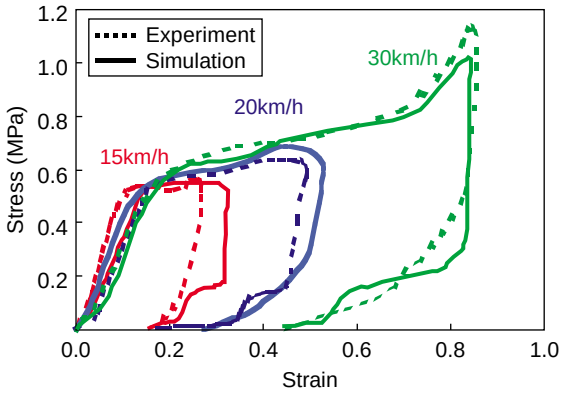


Fig. 14 Comparison of stress-strain curves of foam material between experiment and simulation (for 15, 20, 30 km/h of rate)

determined from high speed film analysis. This corridor was then used to compare the simulation results and test results. Fig. 15 shows the results from the shearing setup for an impact velocity of 20 km/h, and Fig. 16 shows the results from the bending setup for an impact velocity of 20 km/h. Fig. 17 and Fig. 18 show the shearing and bending setup results for an impact velocity of 40 km/h. With the shearing setup, the simulation results for the impact force were outside the corridor at both impact velocities. The simulation results for the shearing displacement fell almost within the corridor, while they tended to be somewhat smaller than the average response from the experiments. On the contrary, the simulation results for the bending angle were generally greater than the average response, and were even beyond the corridor in some parts. In tests with the shearing setup, in particular, many bone fractures due to stress concentration were observed in the vicinity of the jig fixation at the femoral supracondyle. As a result, the impact force is considered to have been lower than when there were no bone fractures. Target marks screwed in at the upper and lower part of the femur and tibia were traced in time series, and the straight line connecting the two points on each bone was used to determine the shearing displacement and bending angle. Therefore, when bone fractures of the kind noted above occurred, the shearing displacement was greater and the bending angle was smaller than when there were no bone fractures. As details of the jig fixation were not known, a simplified boundary

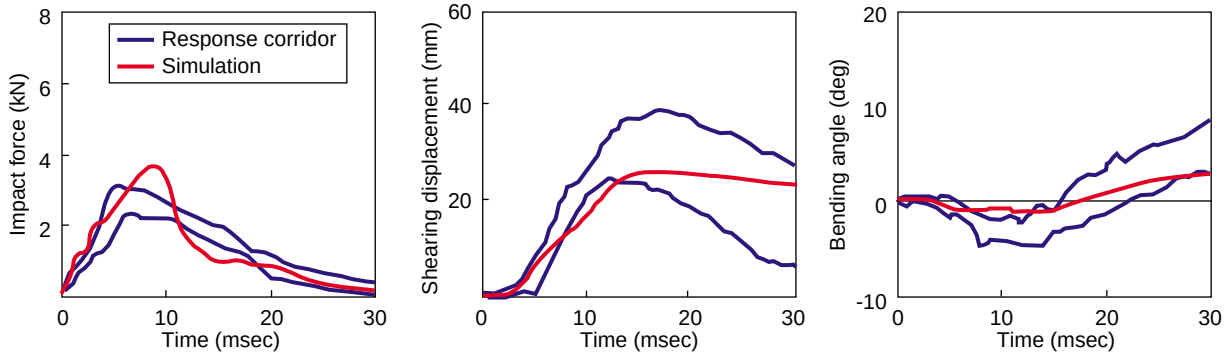


Fig. 15 Comparison between response corridor and simulation result in shearing setup at 20 km/h for impact force, shearing displacement and bending angle of the knee

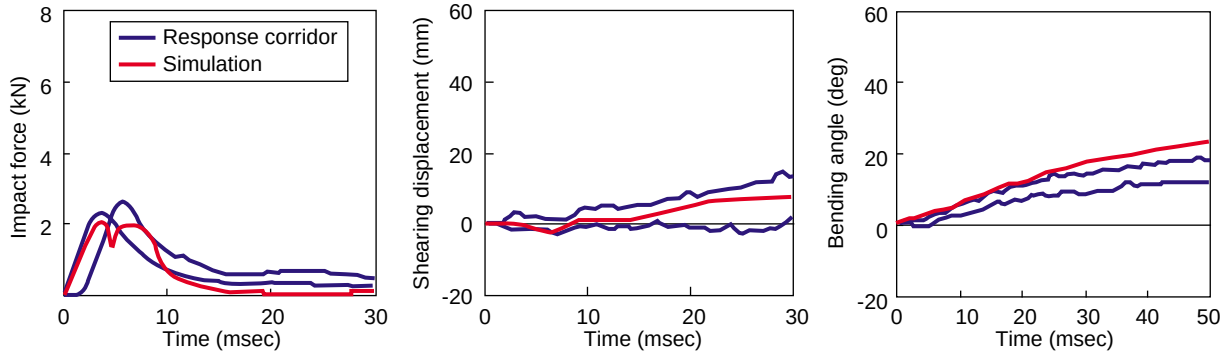


Fig. 16 Comparison between response corridor and simulation result in bending setup at 20 km/h for impact force, shearing displacement and bending angle of the knee

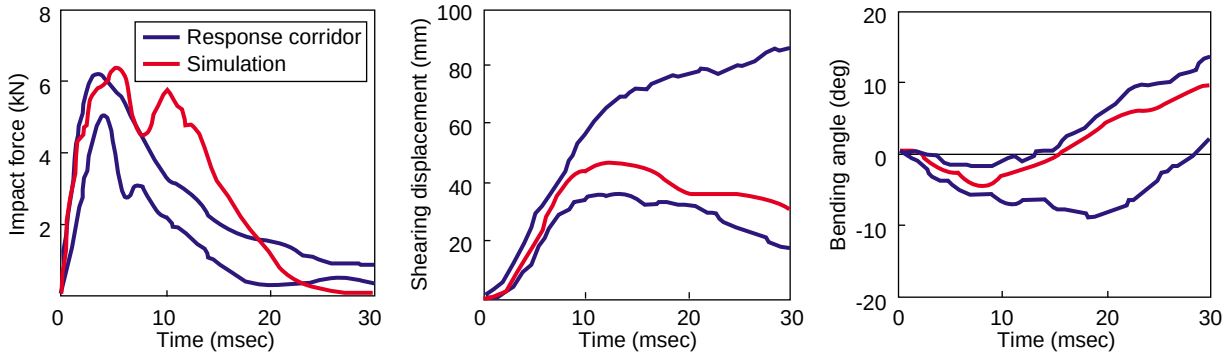


Fig. 17 Comparison between response corridor and simulation result in shearing setup at 40 km/h for impact force, shearing displacement and bending angle of the knee

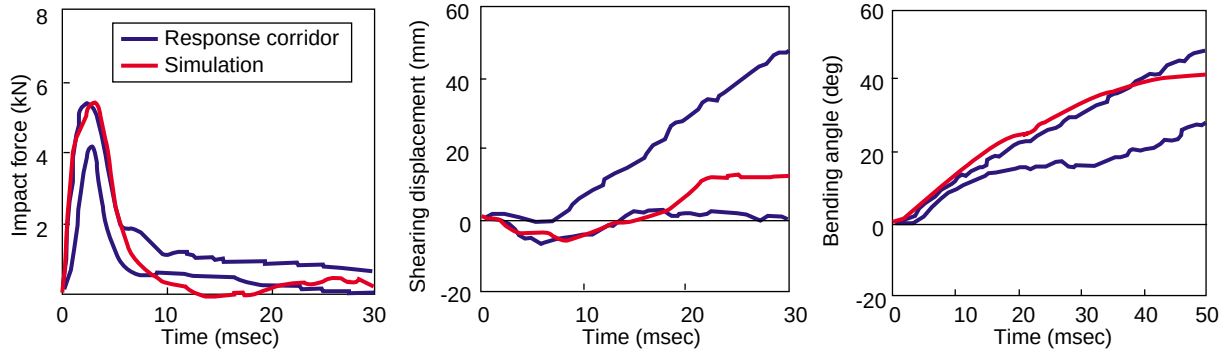


Fig. 18 Comparison between response corridor and simulation result in bending setup at 40 km/h for impact force, shearing displacement and bending angle of the knee

condition was used for the simulation, and therefore bone fractures of this kind were not reproduced. Although the simulation results for the impact force in the shearing setup, in particular, exceeded the corridor determined from the test results, when the above factors are taken into consideration, it can be concluded that the model can accurately predict the impact force and knee deformation.

The simulation results for knee deformation in the shearing and bending setups at an impact velocity of 40 km/h are shown in time series in Fig. 19 and Fig. 20, respectively. In the shearing setup, rupture of the ACL was observed approximately 6 msec after impact. In the bending setup, rupture of the MCL, ACL, and PCL takes place, in that order, during the first 20 msec after impact. The simulation results were compared with the test results for each ligament in terms of the description of damage under the various conditions (Table 3, Table 4). In order to compare the results between the experiment and simulation

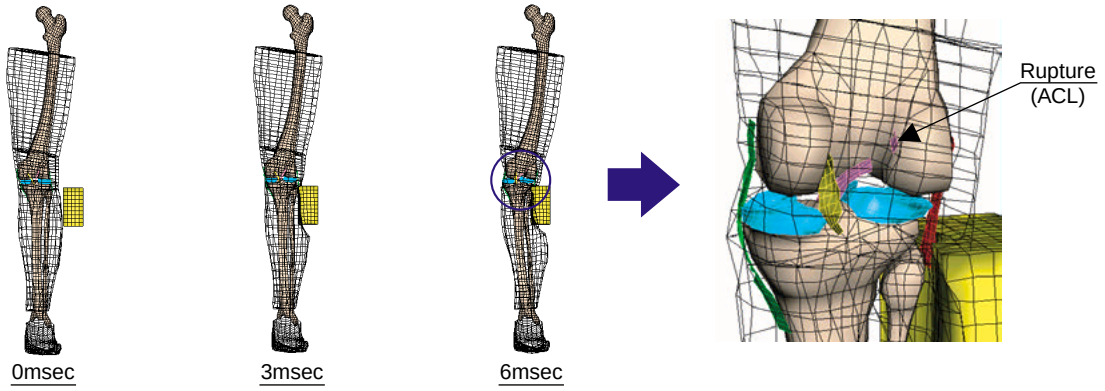


Fig. 19 Kinematics of the knee joint from FE simulation in shearing setup at 40 km/h

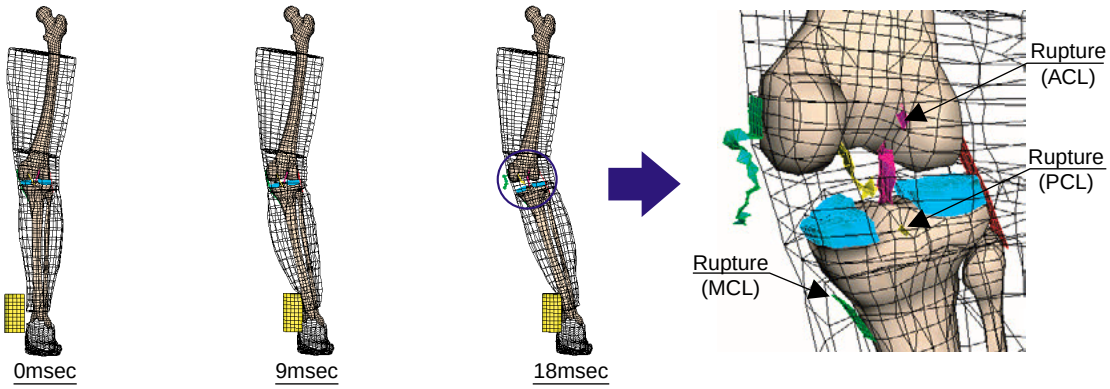


Fig. 20 Kinematics of the knee joint from FE simulation in bending setup at 40 km/h

Table 3 Injury description in shearing and bending setup at 20 km/h for both experiments and simulation

Shearing setup

Test case	Knee ligament			
	ACL	PCL	LCL	MCL
Simulation	■			
21S	■			
24S				
25S				
29S	■			

Bending setup

Test case	Knee ligament			
	ACL	PCL	LCL	MCL
Simulation				
23B				
26B				
27B				■
30B				■

* ■ : Ligament rupture, : Experiment, : Simulation

Table 4 Injury description in shearing and bending setup at 40 km/h for both experiments and simulation

Shearing setup

Test case	Knee ligament			
	ACL	PCL	LCL	MCL
Simulation	■			
1S				
8S	■			
16S	■			

Bending setup

Test case	Knee ligament			
	ACL	PCL	LCL	MCL
Simulation	■	■		■
3B		■		■
6B	■	■		■
19B	■			■

* ■ : Ligament rupture, : Experiment, : Simulation

under uniform conditions, only those test results in which there were no bone fractures due to the fixation of the femur were selected. The ligamentous damage observed in over half of the tests was also predicted by computer simulation, except for the bending setup with an impact velocity of 20 km/h. The ligaments in which no damage was observed in the tests were also undamaged in the prediction. These findings showed that this model was also highly accurate in predicting ligamentous damage of the knee.

These validation results confirmed the high accuracy of the model prediction for the deformation and ligamentous damage of the knee under impact loading. In car-pedestrian accidents, however, knee damage often include tibial plateau fractures in addition to ligamentous damage. Whereas ligamentous damage is determined only by ligament strain, bone fractures also depend upon force.[22] Consequently, prediction of tibial plateau fractures requires accurate prediction not only of deformation of the knee, but also of internal forces within the knee joint. Therefore, it will be necessary to validate the model against test results that reproduce tibial plateau fractures, after first validating the material properties of the ligament, cartilage, and meniscus at the high strain rate, for which extrapolation was used in the present study.

5. Conclusion

Bone models that had been validated for impact response were combined to develop a finite element model for the human knee joint in the standing position that includes the ligaments, articular cartilage, and meniscus. The model was validated through comparison with the results of lower limb impact tests, and the following conclusions were reached.

(1) The lower limb model developed in this study was found to accurately predict test results for the impact force as well as the shearing displacement and bending angle of the knee at a loading rate of both 20 km/h and 40 km/h.
(2) Comparison with test results in terms of the injury description for knee ligaments at a loading rate of both 20 km/h and 40 km/h showed that the simulation also generally predicted damage that occurred in one-half or more of the test cases.
(3) Issues for the future are validation of material properties of the knee ligaments, articular cartilage, and meniscus at high strain rates, and validation of the model for tibial plateau fractures frequently observed in car-pedestrian accidents.

References

(1) European Enhanced Vehicle-safety Committee: “EEVC Working Group 17 Report — Improved test methods to evaluate pedestrian protection afforded by passenger cars” (1998)

(2) Yang, J.K., Kajzer, J.: “Computer simulation of impact response of the human knee joint in car-pedestrian accidents”, SAE paper 922525 (1992)

(3) Yang, J.K., Rzymkowski, C., Kajzer, J.: “Development and validation of a mathematical breakable leg model”, IRCOBI (1993)

(4) Yang, J.K., Kajzer, J.: “Mathematical model of pedestrian lower extremity”, 14th ESV Conference (1994)

(5) Schuster, P. J., Chou, C. C., Prasad, P.: “Development and Validation of a Pedestrian Lower Limb Non-Linear 3-D Finite Element Model”, STAPP CAR CRASH JOURNAL, Vol. 44 (2000)

(6) Wismans, J.: “A three dimensional mathematical model of the human knee joint” (1980)

(7) Butler, D.L., Kay, M.D., Stouffer, D.C.: “Comparison of material properties in fascicle-bone units from human patellar tendon and knee ligaments”, J. Biomech., 19 (1986)

(8) Trent, P.S., Walker, P.S., Wolf, B.: “Ligament length patterns, strength and rotational axes of the knee joint”, Clinical Orthopaedics and Related Research, 117 (1976)

(9) Noyes, F.R., Grood, E.S.: “The strength of the anterior cruciate ligament in humans and rhesus monkeys”, Journal of Bone and Joint Surgery, 58-A (1976)

(10) Race, A., Amis, A.A.: “Mechanical properties of the two bundles of the human posterior crucial ligament”, Journal of Biomechanical Engineering, 27 (1994)

(11) Kennedy, J.C. et al.: “Tension studies of human knee joint ligaments”, Journal of Bone and Joint Surgery, 58-A (1976)

(12) Yamada, H.: “Strength and Aging of Human Body”, NHK Press

(13) Yamada, H.: “Strength of biological materials”, The Williams & Wilkins Company, 1970

(14) Mow, V.C., Ratcliffe, A.: “Structure and foundation of articular cartilage and meniscus”, in Basic Orthopaedic Biomechanics, Second Edition, Ed. Mow V.C., Hayes W.C., Lippincott-Raven, 1997, pp. 113 – 177

(15) Castaing, J., Burdin, P.H., Delplace, J.: Anatomie Fonctionnelle de l’Appareil Locomoteur

(16) Pam System International, PAM-CRASH™ PAM-SAFE™ Version 1998 Notes Manual, 1998

(17) Pam System International, PAM-CRASH™ PAM-SAFE™ Version 1998 Reference Manual, 1998

(18) H-Dummy™ Version 1.6 User’s Manual, Hankook ESI, Engineering Systems International, 1998

(19) Kajzer, J. et al.: “Shearing and bending effects at the knee joint at low speed lateral loading”, SAE paper 1999-01-0712 (1999)

(20) Kajzer, J. et al.: “Shearing and bending effects at the knee joint at high speed lateral loading”, SAE paper 973326 (1997)

(21) Wittek, A. et al.: “Validation and parameter study of a multi-body model for simulation of shearing and bending responses at the knee joint in lateral impacts at low and high speeds: Influences of ligament properties and boundary conditions on model responses”, IRCOBI (2000)

(22) Eppinger, R.H., Takhounts, E.G., “On the development of survival criteria for rate sensitive materials”, STAPP CAR CRASH JOURNAL, Vol. 44 (2000)

■ Authors ■


Yukou TAKAHASHI


Yuji KIKUCHI


Atsuhiro KONOSU


Hirotoshi ISHIKAWA

Development of a Finite Element Model for the Pedestrian Lower Limb

– Model validation for car-pedestrian impact –

Yukou TAKAHASHI* Yuji KIKUCHI*
Atsuhiro KONOSU** Hirotoshi ISHIKAWA**

ABSTRACT

A finite element model for a human lower limb in a standing position has been validated against published experiments simulating impact between a pedestrian lower limb and a car front. The results showed that the model can reproduce the peak linear acceleration during the impact at both the impact level and the knee joint. The comparison of injuries to leg bones and knee ligaments between the experiment and the computer simulation showed that the model can predict different injury patterns observed under different impact conditions. Further, in addition to reproducing the response of the lower limb, the upper half of the human body was modeled with rigid segments connected by joint elements in order to simulate the kinematics of the upper body. The neck model has been validated against published experiments that used human volunteers. While validating the full body model against published full-scale car-pedestrian impact tests, it was found that the full body model can simulate both injuries to the lower limbs and the kinematics of the human body.

1. Introduction

Bone fracture and damage to knee ligaments are the two typical lower limb injuries in car-pedestrian accidents. Past experimental studies have shown that bone fractures are rarely accompanied by damage to knee ligaments.(1) This suggests that the leg fracture reduced the load on the knee, and conversely, the damage to knee ligaments reduced the impact load on the bony structure. The question of whether bone fractures or ligamentous damage will occur also appears to depend upon the loading conditions on the lower limb. Consequently, validation of the damage predictions by the pedestrian lower limb model will require investigation of the prediction capabilities for various injury patterns under different loading conditions. It seems reasonable to suppose that differences in lower limb response have an effect on upper body behavior. Therefore, computer simulation models intended to be used for the enhancement of vehicle safety with regard to pedestrians should be capable of predicting the kinematics of the upper body as well as injuries to the lower limbs.

Schuster et al.(2) developed a finite element model for the pedestrian lower limb and they validated the model against the results of lower limb impact tests. The impact loading conditions, however, were limited to a single type, and the boundary conditions for the lower limb were also different from those in actual car-pedestrian accidents. Ishikawa et al.(3) developed a multibody model of the whole body of a pedestrian. Though this model accurately reproduced the kinematics of the whole body obtained experimentally, the prediction of lower limb injury was an issue. Likewise, pedestrian models developed in past studies have not been validated for prediction of lower limb injury

* Tochigi R&D Center
** Japan Automobile Research Institute

patterns under a variety of impact conditions. In addition, these models did not succeed in predicting both the kinematics of the upper body and the injuries to the lower limb.

This paper describes the validation results for injury prediction with the finite element model of the lower limb in a standing position that was developed by the authors. The validation results for the upper body kinematics of the whole body model, obtained by combining the lower limb model with an upper body component, are also presented. The lower limb injuries predicted by the model were validated against the published results of component lower limb impact tests performed under a boundary condition similar to actual car-pedestrian accidents, as well as a variety of different impact conditions. The upper body kinematics predicted by the whole body model were validated against the published results of full-scale tests, and a comparison of lower limb injuries was also carried out.

2. Model Validation of Lower Limb Injury Prediction

Previous studies utilized the results of lower limb impact tests[2), 5)] performed by Kajzer et al.[4), 5)] to verify lower limb models. However, the tests done by Kajzer et al. had the femur fixed in place with a jig, and consequently, the boundary condition was different from an actual car-pedestrian accident. Although the response of the knee joint could be verified with the test results, this could not be used for verification of injury prediction in car-pedestrian accidents. Bunketorp et al.[6)] added a mass equivalent to the upper body to the isolated lower limb, and applied an impact from a sled simulating a bumper and hood edge at a velocity of 32 km/h to the lower limb in a standing position. These tests were conducted under a total of four sets of test conditions, combining two bumper and hood edge heights with two bumper stiffness settings. Bone fracture and ligamentous damage were observed in different patterns with different impact conditions. In the present study, those tests were reconstructed using the finite element model of the human lower limb in a standing position developed by the authors, and the patterns of injury to the lower limb from the tests and computer simulations were compared for each set of test conditions.

Fig. 1 shows the model used for the simulation. The direction of impact was set, as in the tests, so that the sled would impact the lower limb at an angle of 15 degrees anteriorly from the pure lateromedial direction. In the tests, a block weighing 47 kg was affixed to a part of the pelvis to represent the upper body, while in the model, the block and the femoral head were connected by a spherical joint for simplicity. The joint was given the range of motion and other properties of the human hip joint. The ground was modeled with a rigid plane, and the entire model was given the downward linear acceleration field for gravity. The height of the bumper and hood edge was set to match the tests, with the bumper center at two heights, 325 mm (low) and 450 mm (high) above the ground. The tests used a sled with parts representing the bumper and hood edge attached. Information about the mass of this mechanism and the stiffness of the hood edge, however, was not available in the literature. Therefore, the model employed input force wave forms for the bumper and hood edge as they were described in the literature, and used them as prescribed external forces. For simplicity, input from the hood edge was applied as a distributed load in the area of contact between the surface of the thigh and the hood edge. However, it seemed necessary to replicate the external shape of the bumper, because the bumper was located close to the region where injury occurred. Consequently, a prescribed external force was applied to a rigid body bumper model such as shown in Fig. 1. The tests employed a total of four types of impact conditions derived from the combination of two different heights of the bumper and hood edge and two different degrees of stiffness for the bumper components (rigid , compliant). The wave forms for the input force from the bumper and hood edge that correspond to the respective test conditions are shown in Fig. 2.

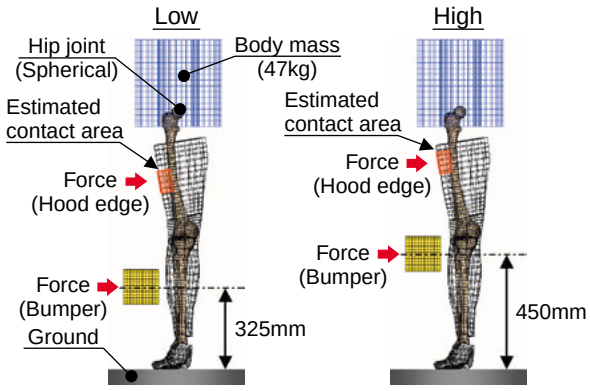


Fig. 1 Model setup for lateral impact validation

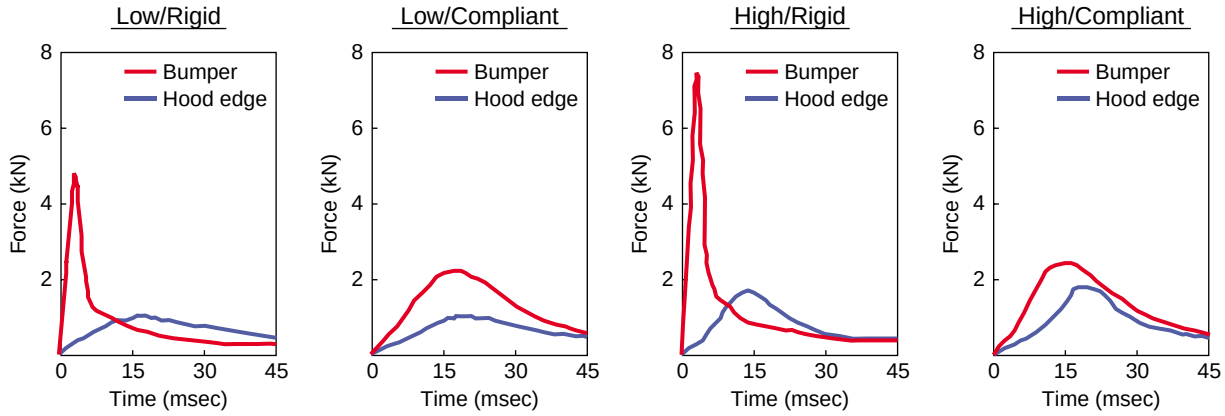


Fig. 2 External force applied to the lower limb

Simulations were performed for the four sets of test conditions described above, and comparisons were made for the peak linear acceleration in the lower limb and the patterns of damage to knee ligaments and leg fracture. Fig. 3 shows the results from comparison of the peak linear acceleration. The tests were conducted five times with each set of conditions, and the figure shows the resulting average as well as the upper and lower limits. The simulation results yielded values that were close to the test result averages for the linear acceleration at the impact level and the knee joint level. The simulation results fell almost completely between the upper and lower limits from the tests. The simulation results for linear acceleration at the ankle joint level, however, were higher than the test results. The simulation used an estimate for the coefficient of friction between the foot and the ground because the corresponding coefficient in the tests was not available. It seems that this led to the difference in the kinematics of the foot between the tests and simulations, and thus resulted in the difference in the linear acceleration at the ankle joint level. The injuries observed in the tests, however, were damage to knee ligaments and bone fractures near the impact level, and as the linear acceleration in these two regions was accurately predicted, it was determined that this did not significantly affect the accuracy of injury prediction.

Fig. 4 shows an example of the kinematics of the lower limb from the simulation with a low bumper. In the case of a rigid bumper, a comparatively large deflection of the leg, particularly conspicuous at 15 msec, can be seen, and a proximal fibula fracture is observed without any damage

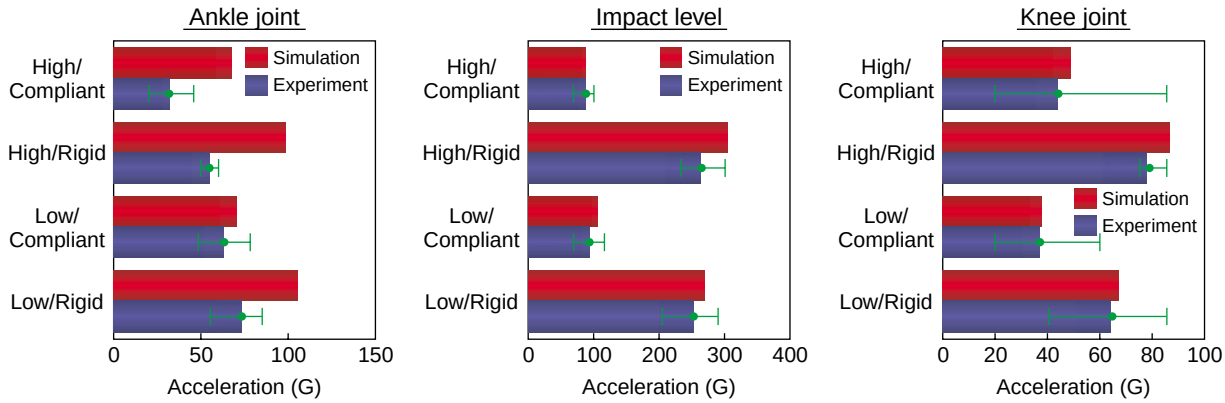


Fig. 3 Comparison of peak acceleration between experiment and simulation

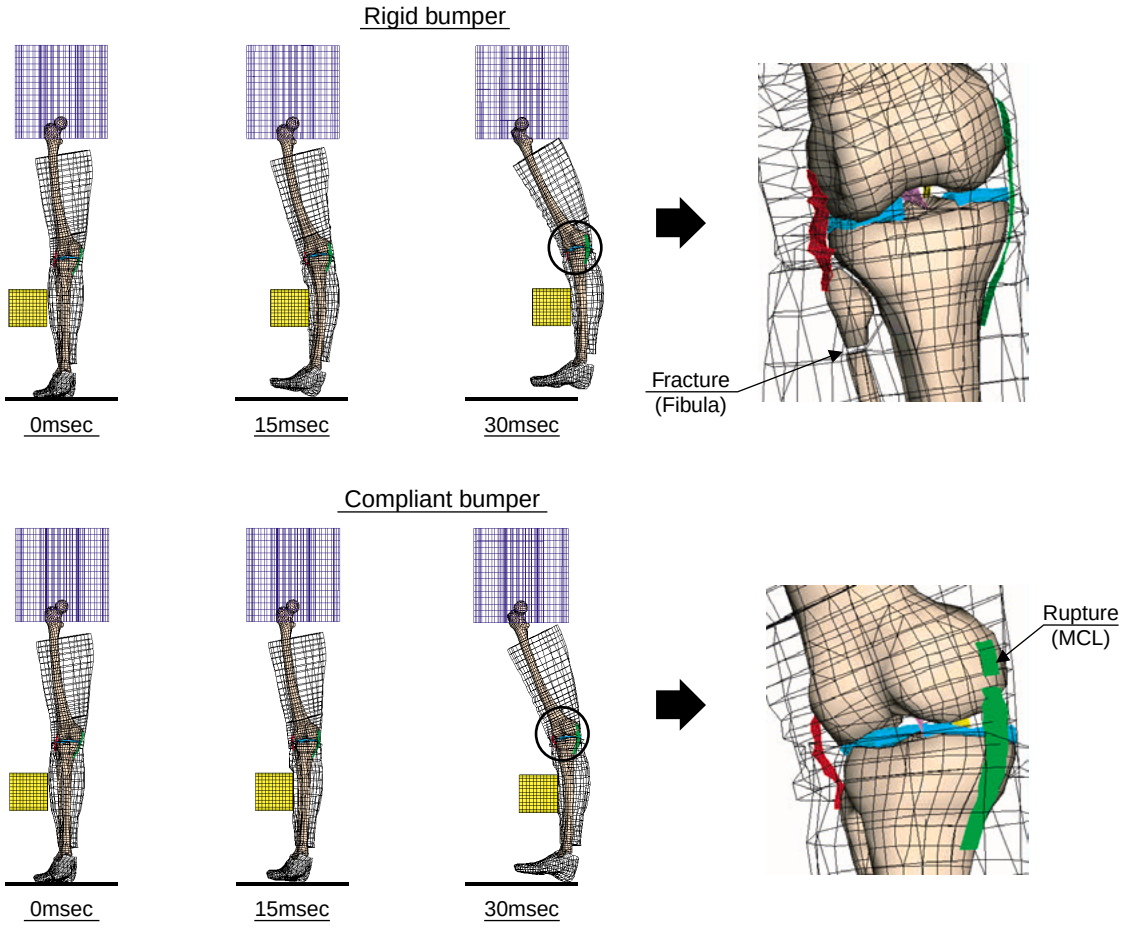


Fig. 4 Kinematics of the lower limb in low bumper configuration

to knee ligaments. Conversely, in the case of the compliant bumper, the deflection of the leg is slight, but a rupture of the medial collateral ligament is observed. Tables 1 and 2 present comparisons of the injury description including damage to knee ligaments and leg fracture for the case of the low bumper and high bumper, respectively. In the case of the low bumper (Table 1), fibula fracture was observed in all test cases where the bumper was rigid, while damage to knee ligaments occurred in only one of five cases. In cases where the bumper was compliant, rupture of the medial collateral ligament was observed in all test cases, while bone fracture occurred in only one case. In the simulation, only fibula fracture occurred with the rigid bumper, while only rupture of the medial collateral ligament occurred with the compliant bumper. It was found that the simulation predicts the difference in injury pattern in the tests due to the difference in stiffness of the bumper. Similarly, with a low bumper (Table 2), the injuries observed in more than half of the test cases were also predicted by the simulation. It was evident from these results that this model was able to predict the different injury patterns to the lower limb due to the difference in bumper height and stiffness.

3. Upper Body Modeling

In order to make a model capable of both analyzing the kinematics of the upper body and predicting lower limb injuries, a full body model for a pedestrian was constructed by incorporating a model of the pelvis and upper body into the validated finite element model for the lower limb. Fig. 5 shows the structure of the full body model. The model of the pelvis and surrounding soft tissue was taken from the finite element human model (H-Dummy™)[7] developed by Nihon ESI in order to enable the model to predict a wider range of injuries in the future including pelvic fractures. As the purpose of the upper body model was to predict kinematics, the model was constructed with rigid segments connected by joint elements so that the model would be comparatively simple and thus require less CPU time. It is crucial for the model to represent the flexibility

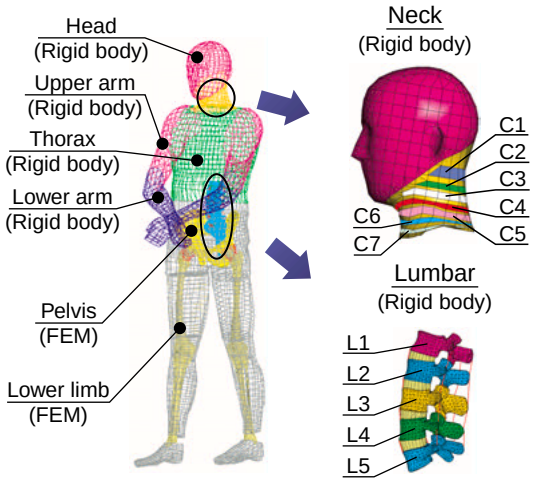


Fig. 5 Structure of full body model

Table 1 Comparison of injury description between experiment and simulation in low bumper setup

Rigid bumper							Compliant bumper						
Experiment No.	Ligament				Bone		Experiment No.	Ligament				Bone	
	ACL	PCL	LCL	MCL	Tibia	Fibula		ACL	PCL	LCL	MCL	Tibia	Fibula
Simulation						▲	Simulation				■		
11	■	■				▲	16				■		
12						▲	17				■		
13						▲	18				■		▲
14						▲	19				■		
15						▲	20				■		

* ■ : Ligament rupture, ▲ : Bone fracture, ▭ : Experiment, ▭ : Simulation
ACL : Anterior Cruciate Ligament, PCL : Posterior Cruciate Ligament, LCL : Lateral Collateral Ligament, MCL : Medial Collateral Ligament

Table 2 Comparison of injury description between experiment and simulation in high bumper setup

Rigid bumper							Compliant bumper						
Experiment No.	Ligament				Bone		Experiment No.	Ligament				Bone	
	ACL	PCL	LCL	MCL	Tibia	Fibula		ACL	PCL	LCL	MCL	Tibia	Fibula
Simulation	■			■			Simulation				■		
1	■			■			6					▲	▲
2	■			■			7						
3	■			■		▲	8		■		■		
4	■	■		■			9	■	■		■		
5	■			■			10				■		

* ■ : Ligament rupture, ▲ : Bone fracture, ▭ : Experiment, ▭ : Simulation
ACL : Anterior Cruciate Ligament, PCL : Posterior Cruciate Ligament, LCL : Lateral Collateral Ligament, MCL : Medial Collateral Ligament

of the spine in order for it to accurately predict the kinematics of the pedestrian upper body. The thoracic spine seems to be comparatively inflexible because this part of the spine, together with the ribs and sternum, forms the rib cage. However, the cervical spine and lumbar spine must be assigned the same degrees of freedom as the human body. Consequently, the thorax was modeled as a single segment for simplicity, while the cervical spine and lumbar spine were divided into seven segments and five segments, respectively, to match the number of vertebrae in each. The head, upper arm, and forearm were each modeled as a single segment.

Head injury is often the primary cause of death in fatal pedestrian accidents. Accurate prediction of the head motion is, therefore, particularly important in the prediction of the kinematics of the upper body. As the neck is considered to have a significant effect on kinematics of the head, the response of the head-neck model was subjected to validation separately from the upper body model. Thunnissen et al.[8] analyzed the results from impact tests in lateral bending and flexion conducted by Ewing and Thomas[9] using human volunteers to determine the corridor of the trajectory, linear acceleration, and rotational acceleration of the head relative to the first thoracic vertebra. In this study, the wave form of the average linear acceleration of the first thoracic vertebra shown in the literature by Thunnissen et al. (Fig. 6) was applied to the joint between the thorax and the seventh cervical vertebra in the head-neck model, and the resulting trajectory, linear acceleration, and rotational acceleration of the head were compared with the corridor determined from the test results. The simulation results for the head-neck kinematics in lateral bending and flexion are shown in Fig. 7. A coordinate system as shown in the figure was used for wave form comparison. Fig. 8 shows the results of the comparison for the head trajectory. The simulation results slightly exceed the corridor in the vicinity of the peak displacement in lateral bending. Otherwise, however, the results are within the corridor, and can be considered to display a trajectory generally equal to that of the human body. Fig. 9 and Fig. 10 show the results from comparison of the linear acceleration and rotational acceleration of the head for the lateral bending and flexion, respectively. Although the simulation results are not entirely within the corridor of the test results, they did yield wave form patterns and peak values that were close to the test results.

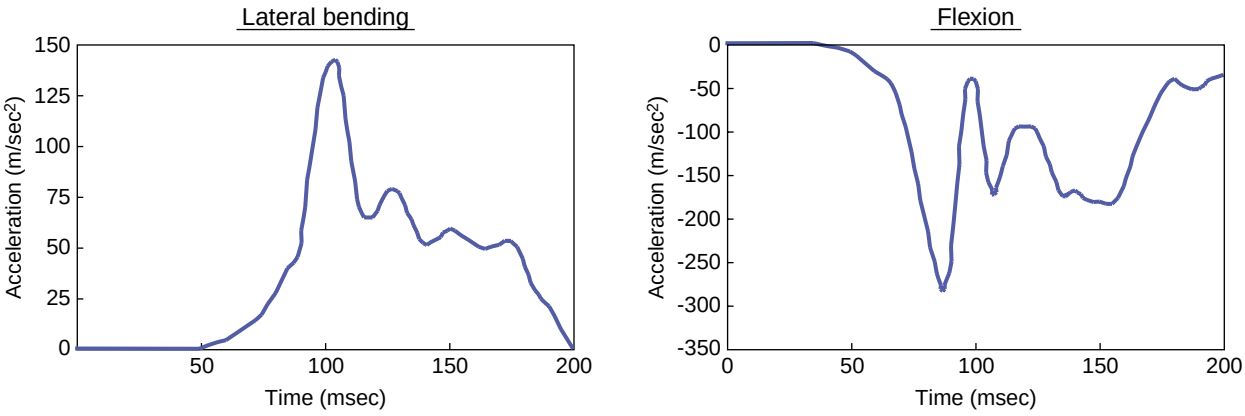


Fig. 6 Acceleration pulse applied to the first thoracic vertebra

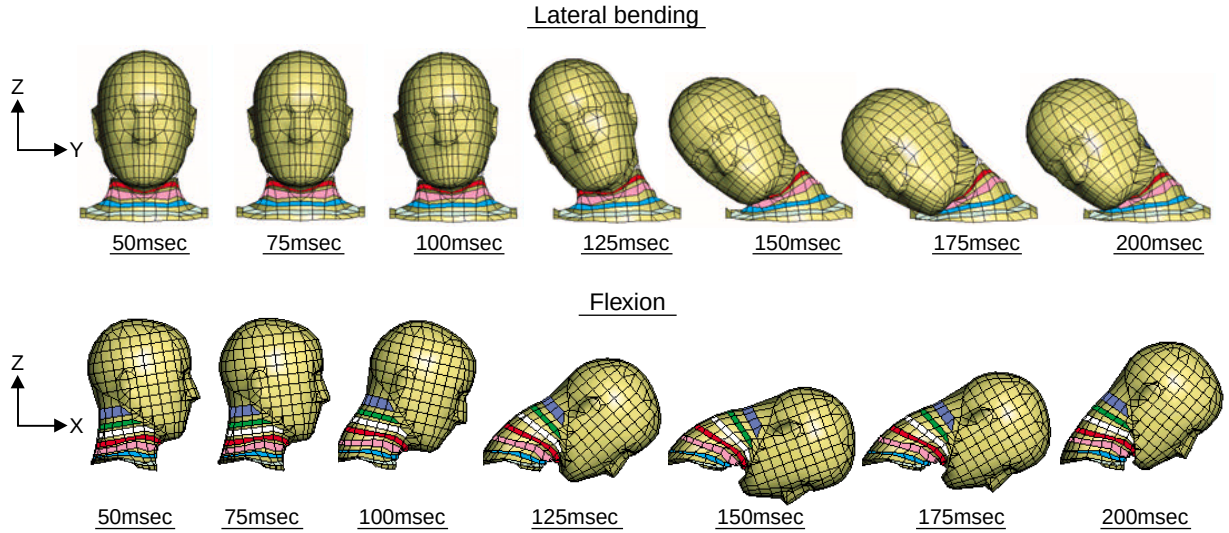


Fig. 7 Kinematics of the head-neck

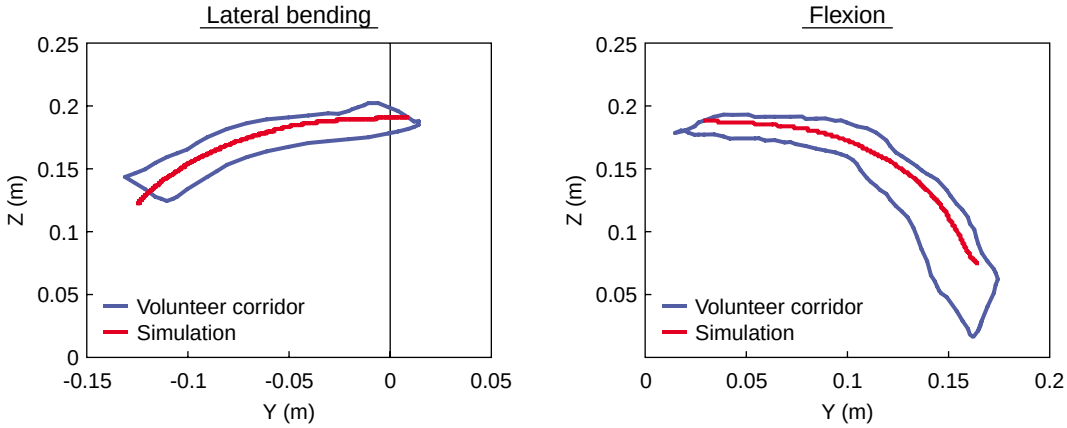


Fig. 8 Comparison of head trajectory between volunteer corridor and simulation results for lateral bending and flexion

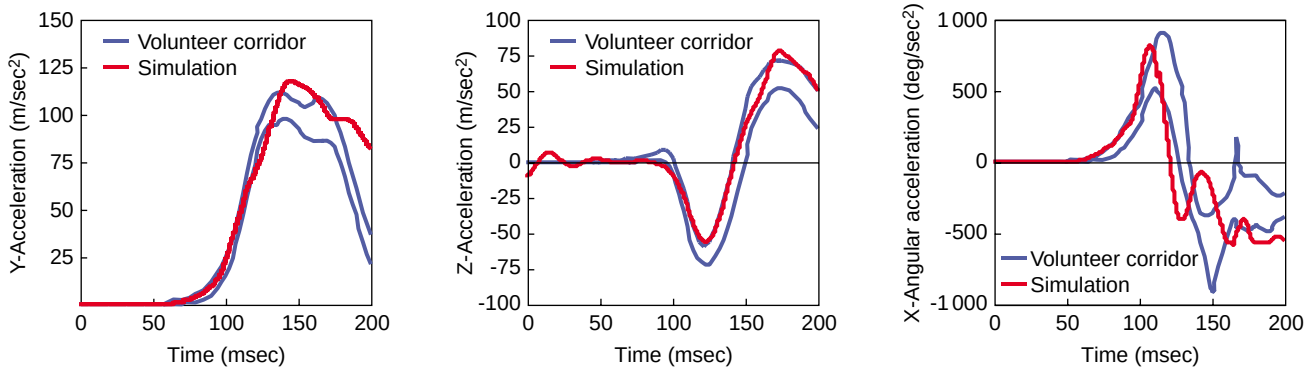


Fig. 9 Comparison of head linear and angular acceleration between volunteer corridor and simulation results for lateral bending

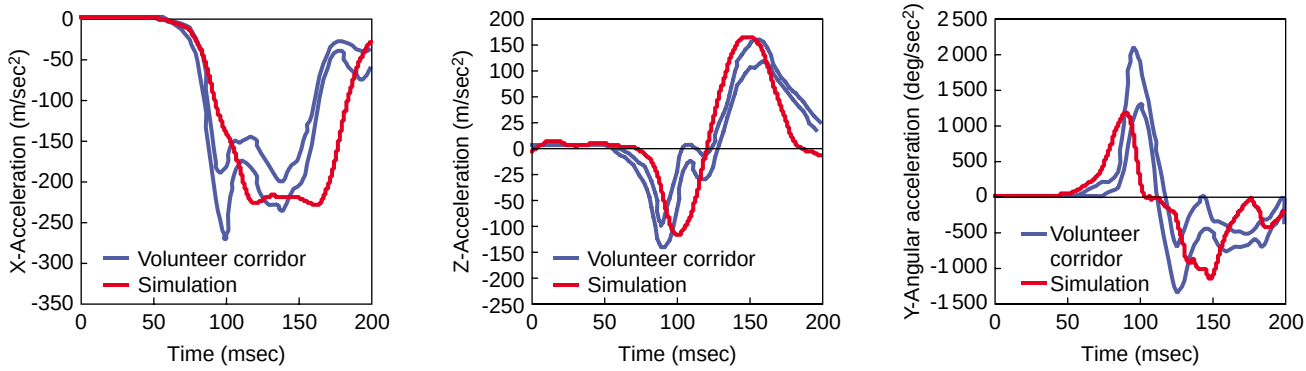


Fig. 10 Comparison of head linear and angular acceleration between volunteer corridor and simulation results for flexion

4. Model Validation for Upper Body Kinematics

Schroeder et al.[9] affixed a cutaway body of a relatively recent model vehicle to a sled in order to perform full body car-pedestrian impact tests at velocities of 30 km/h and 40 km/h. Three tests were conducted with different human subjects, and since the full body model had been developed to simulate the average anthropometry of an American adult male, the test case with the subject that most closely resembled this anthropometry was chosen for computational reconstruction. Table 3 shows the geometry data for the car front and anthropometry data for the human subject used in this test case. The impact velocity was 40 km/h. The simulation used a finite element model of a car with a front end geometry similar to this car. Fig. 11 shows the results from simulation for the kinematics of the lower limb. The lower limb injuries observed in the test were bone fractures of the tibia and fibula, and these injuries were similarly seen in the simulation. Knee ligaments were not damaged in either the test or simulation. The simulation results for the kinematics of the whole body in time series are shown in Fig. 12. Fig. 13 shows a comparison of the trajectory for the head, thorax, and pelvis. The kinematics of each region was predicted, and the full body model developed in this study was found to be very reliable with respect to the kinematics of the upper body as well as injuries to the lower limb.

Table 3 Test conditions (Schroeder et al., 2000)

Geometry of car front

Bumper height (mm)	446
Bumper protrusion (mm)	141
Hood leading edge (mm)	641
Hood length (mm)	1 110
Hood inclination (degree)	10
Windshield inclination (degree)	35

Anthropometry of human subject

Height (cm)	177
Weight (kg)	84
Gender	Male
Age (years)	66

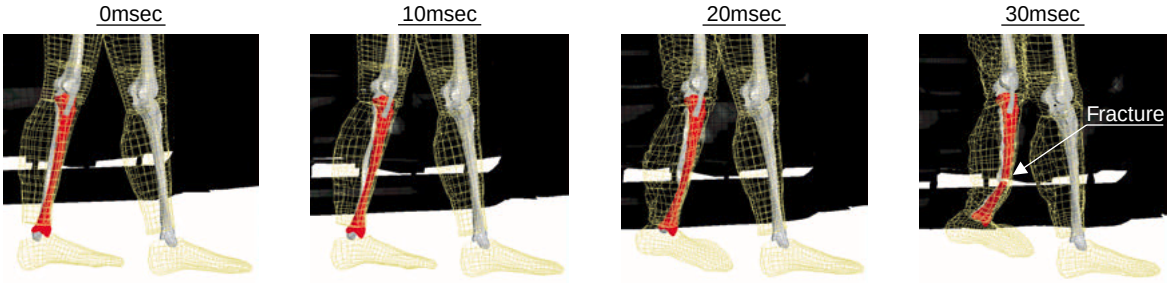


Fig. 11 Kinematics of the lower limb in car-pedestrian impact simulation

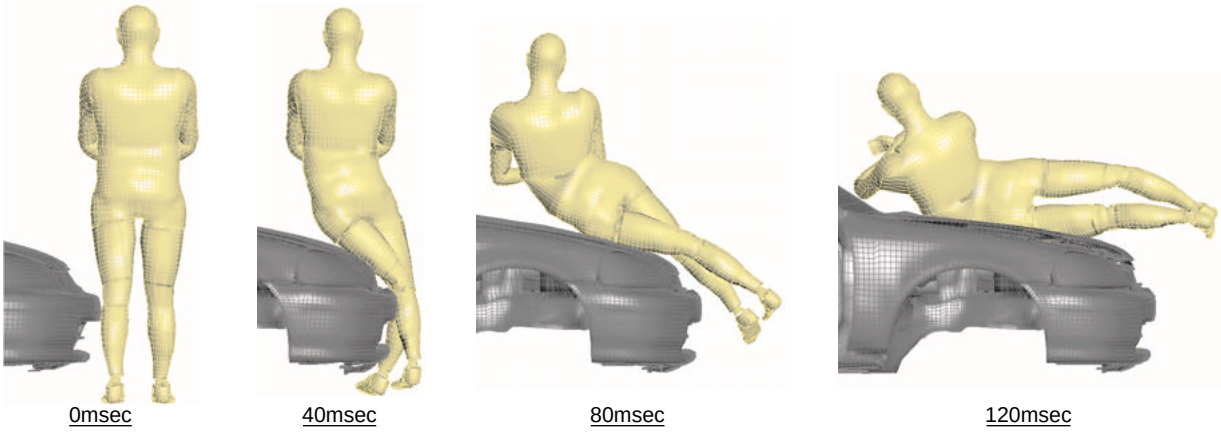


Fig. 12 Kinematics of the full body in car-pedestrian impact simulation (posterior view)

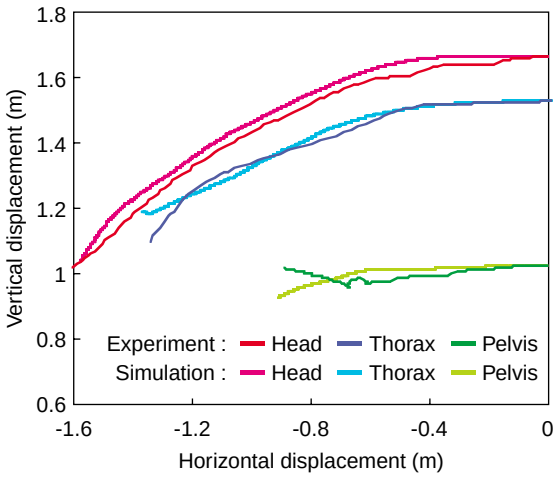


Fig. 13 Comparison of pelvis and upper body trajectories between experiment and simulation

5. Conclusion

A finite element model for the lower limb that had been validated for the response of the bony structure and knee joint was used to simulate experiments conducted under conditions similar to actual car-pedestrian accidents. A full body model constructed by combining this lower limb model with an upper body model was also used to simulate a full-scale car-pedestrian impact test. Comparison of the results of these simulations with the test results yielded the following conclusions:

(1) The lower limb model developed by the authors was found to be capable of predicting the different patterns of leg fractures and damage to knee ligaments that occurred due to the difference in impact conditions on the lower limb in situations close to an actual car-pedestrian accident.

(2) The head-neck model with rigid segments connected by joint elements was found to be capable of reproducing the dynamic response similar to that of the human body, when each vertebra of the cervical spine was modeled as a separate segment in order to provide the same degrees of freedom as the human body.

(3) It was found that the full body model developed in this study was capable of predicting the kinematics of the upper body as well as the injuries to the lower limb in car-pedestrian impact tests.

References

(1) Cesari, D., Cavallero, C., Roche, H.: "Mechanisms producing lower extremity injuries in pedestrian accident situations", 33rd AAAM (1989)

(2) Schuster, P. J., Chou, C. C., Prasad, P.: "Development and Validation of a Pedestrian Lower Limb Non-Linear 3-D Finite Element Model", STAPP CAR CRASH JOURNAL, Vol. 44 (2000)

(3) Ishikawa, H., Kajzer, J., Schroeder, G.: "Computer simulation of impact response of the human body in car-pedestrian accidents", 37th Stapp Conference Proceedings, SAE paper 933129 (1993)

(4) Kajzer, J., et al.: "Shearing and bending effects at the knee joint at low speed lateral loading", SAE paper 1999-01-0712 (1999)

(5) Kajzer, J., et al.: "Shearing and bending effects at the knee joint at high speed lateral loading", SAE paper 973326 (1997)

(6) Maeno, T., Hasegawa, J.: "Development of a finite element model of the Total Human Model for Safety (THUMS) and application to car-pedestrian impacts", 17th ESV Conference (2001)

(7) Bunketorp, O., et al.: "Experimental study of a compliant bumper system", SAE paper 831623 (1983)

(8) H-Dummy™ Version 1.6 User's Manual, Hankook ESI, Engineering Systems International, 1998

(9) Thunnissen, J., et al.: "Human volunteer head-neck response in frontal flexion: a new analysis", SAE paper 952721 (1995)

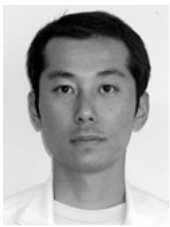
(10) Ewing, C. L., Thomas, D. J.: "Human head and neck response to impact acceleration", NAMRL Monograph 21 (1973)

(11) Schroeder, G., et al.: "Injury mechanism of pedestrians during a front-end collision with a late model car", JSAE Spring Convention (2000)

■ Authors ■



Yukou TAKAHASHI



Yuji KIKUCHI



Atsuhiro KONOSU



Hirotoshi ISHIKAWA

Research on Aluminum Structures for Crash Energy Absorption

Yuta URUSHIYAMA* Takayuki YAMADA*
Shunji SUZUKI* Toru KAWANO*

ABSTRACT

This research describes aluminum crash boxes for the purpose of absorbing crash energy. In this research, the load conditions of the boxes were calculated and the mechanisms of energy absorption were analyzed by experiment. This analysis achieved a crash box with a highly effective section shape. The research also achieved the additional goal of increasing the accuracy of crash simulation for evaluation of energy absorption by this crash box.

1. Introduction

The requirement for a vehicle with a lightweight body to absorb greater crash energy has become increasingly stringent. The use of extruded aluminum for the body frame structure offers one way of achieving this. Extrusion processing enables a variety of cross section shapes, thereby optimizing the advantages of aluminum as a material capable of absorbing crash energy.

A hexagonal beam with ribs which are located diagonally on a cross-section has been employed as an application example of an aluminum crash box[1](Fig. 1). There have been numerous research case studies in the past on determining the crash box cross section. Some research has looked at thin-walled structures, with a focus on the ratio of the thickness to width[2], and recently, simulations have been frequently employed. However, there have been few studies that attempted to take advantage of the characteristics of section shape when extruded aluminum was used.

This research focused on the characteristics of the cross section shape of ribbed aluminum beams by experimental investigation and the establishment of simulation technology for realizing both greater energy absorption and weight reduction. Described for the first time in this report is a method for determining the load in the axial direction of the beam and the bending moment in order to evaluate the strength performance required of the crash box. Experiments are then conducted on components of different cross-sectional shape to evaluate the energy absorption performance of each when installed at different angles in the frame structure. The experimental data are then used to increase the accuracy of crash simulation.

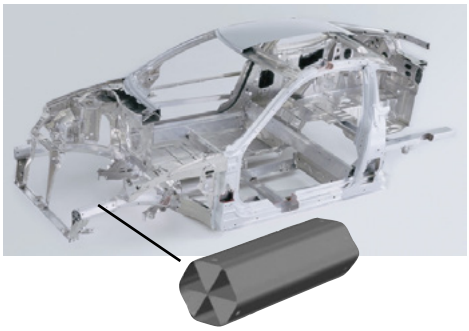


Fig. 1 Aluminum crash box

2. Load Applied to the Crash Box and Testing Apparatus

Generating a collapse mode in a frame involving continuous buckling from the end is effective for reducing weight and increasing the amount of energy absorbed[2] (Fig. 2). In addition, a shape that can realize a stable collapse mode with minimal load fluctuation during compression is preferable.

In practice, the front side frame that constitutes the crash box is installed at an angle as shown in Fig. 3 to provide

* Tochigi R&D Center

adequate space for both the engine and suspension. As the frame angle increases, the moment increases by the offset of the axial direction at the locations where the crash box is attached to the frame structure against the load input during a crash. If the maximum bending moment of the frame is exceeded, the bending mode shown in Fig. 4 occurs, and the amount of energy that can be absorbed decreases.

It is therefore important to determine the load applied to the frame. A crash test was conducted in the form of a sled test to experimentally confirm the relationship between the buckling mode of the front side frame and the frame installation angle, and to determine the load required to generate the buckling mode. The equipment used in the crash test is shown in Fig. 5.

Equation (1) represents the bending moment applied to the frame in this test as represented by Fig. 6.

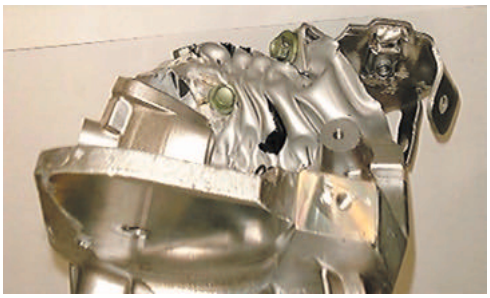


Fig. 2 Collapse mode of crash frame

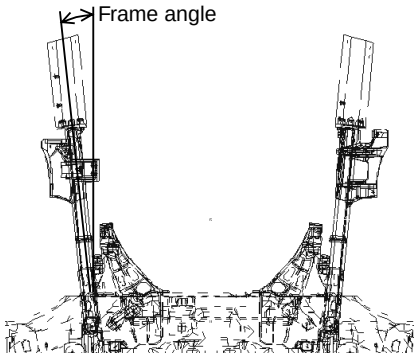


Fig. 3 Frame layout



Fig. 4 Bend mode of crash frame

$$M_z = F_{m2} \times (l_f \tan\theta) + F_y \times l_f + F_{m1}(l_m - l_{m1}) + \frac{F_{m1}(l_m^3 - l_{m1}^3)}{3l_m^2} + F_{ex} \times l_e \quad (1)$$

The symbols used have the following definitions:

θ : Frame angle
F_y : Horizontal force resulting from bumper beam
F_{m1}, F_{m2} : Barrier load
F_{ex} : Engine forward and backward inertia force
l_{m1} : Distance from bumper beam load point to bumper center
l_{m2} : Distance from bumper beam load point to frame load point
l_f : Distance from barrier to frame attachment point
l_e : Distance from frame attachment point to mount attachment point
M_z : Moment applied to frame attachment point (clockwise rotation is positive)

Engine inertia force can be calculated from experimental values.

$$F_{ex} = m_{ex} \cdot a_{ex} \quad (2)$$

m_{ex} : Engine mass
a_{ex} : Forward and backward direction engine acceleration

In addition, experiments on each part were conducted separately for horizontal force F_y of the bumper beam, and applied to equation (1) after obtaining the relationship between deformation and load.

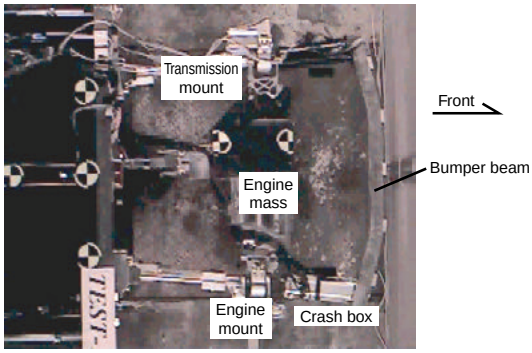


Fig. 5 Crash test equipment for frame resarch

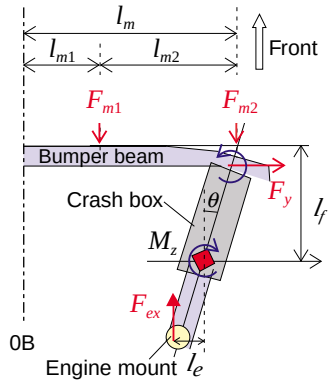


Fig. 6 Calculate moment for crash test

The results from the crash test indicated a collapse mode occurring at a frame angle of 5.6 degrees, and a bending mode occurred at a frame angle of 7 degrees. The following is the comparison of each mode.

Fig. 7 shows the energy absorption performance. The load in the axial direction is the sum of F_{m1} and F_{m2}, and differences due to the buckling mode became prominent at a post-crash deformation of 180 mm or more. Fig. 8 shows moment M_z. In the case of a frame angle of 7 degrees, moment M_z increased with a deformation of 180 mm, and the bending mode was initiated at 2.9KN·m.

Calculation of the load applied to the frame was made possible by equation (1) from the experimental values, and the relationship between the limiting load for onset of the collapse mode and the frame installation angle could therefore be determined from the crash test data.

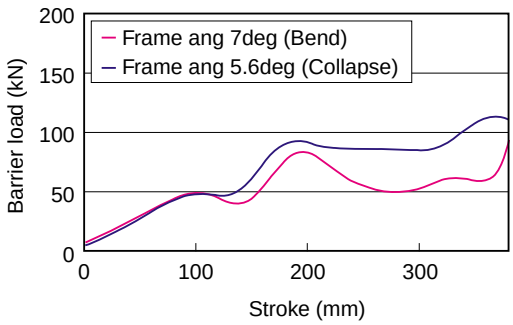


Fig. 7 Stroke-barrier load for crash test

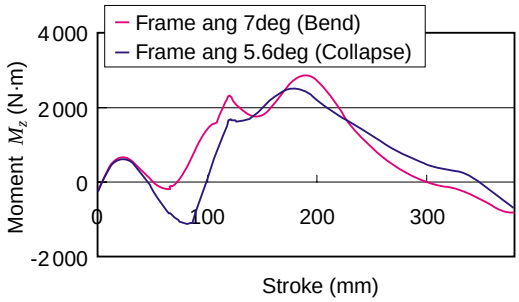


Fig. 8 Stroke-calculated monent M_z for crash test

3. Analysis of Frame Performance

3.1 Test Piece

A hexagonal cross section shape has been found suitable for achieving a stabilized collapse mode[1]. Previous studies on rectangular sections have indicated the effect of the corner radius on the collapse load.[3] An attempt was therefore made to evaluate the hexagonal cross section by focusing on the corner areas of the section while changing the shape.

Fig. 9 shows the cross section shape and corner area of the hexagonal section that were studied. R_1 and R_2 (Fig. 10) respectively indicate the internal and external radius in the three-legged corner area of the section. Table 1 shows the cases of radii tested, in which "*Area*" refers to the cross sectional area.

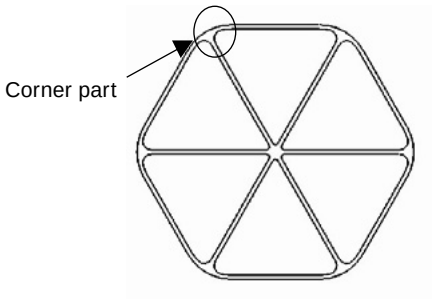


Fig. 9 Section view of hexagonal frame

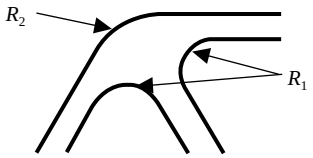


Fig. 10 Detail of corner part

Table 1 Scales of test-specimen

Case	R_1 (mm)	R_2 (mm)	*Area* (mm^2)
A	2	11	894
B	3	18	907
C	4.5	30	914

3.2 Compression Load

The collapse load was measured for each of the cases shown in Table 1. A summary of the test equipment is shown in Fig. 11. An AUTOGRAPH AG-10TD (Shimadzu Co., Ltd.) was used for the compression test. The compression load was measured with a load cell installed on the cross head, and the distance between the load face of the compression jig and the stage on which the test piece was mounted is designated as the compression stroke.

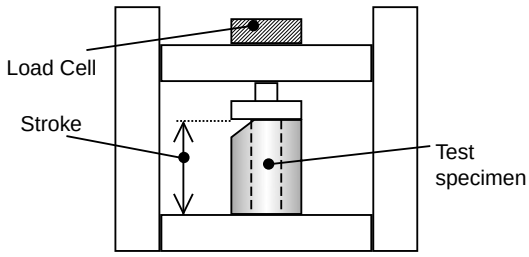


Fig. 11 Test equipment set-up

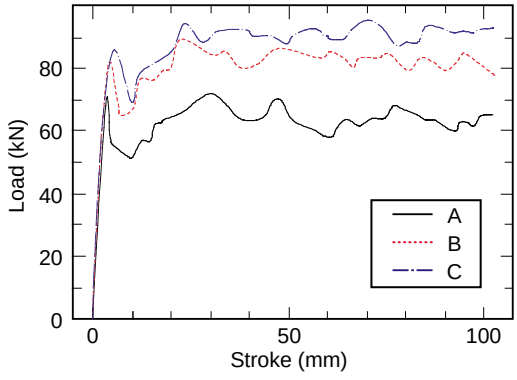


Fig. 12 Relationship between collapse (buckling) load and stroke

Fig. 12 shows the relationship between collapse load and stroke. In the figure, the solid line, dotted line and single dot broken line represent the test results of Case A, B and C, respectively. The collapse/buckling load can be seen to increase depending on the area between the inside corner part radius R_1 and outside corner part radius R_2.

3.3 Maximum Bending Moment

The maximum bending moment was measured next, a schematic illustration of the test being shown in Fig. 13. Three-point bending was used for the test, the bending load being measured by compression test equipment in a similar manner to that for measuring the collapse load. Equation (3) was used to calculate maximum bending moment M_{Smax} from the measured load.

$$M_{Smax} = W_{Smax}\, a(l-a)/l \qquad (3)$$

W_{smax} is the peak value for the bending load in equation (3). In order to prevent localized deformation at jig mount points due to the hollow structure of the test pieces, the test piece length was set at a = 2.5 m and l = 5.0 m to be sufficiently long in comparison with the strength of the shearing force. In addition, iron inserts were inserted at the load point and support points on both ends to prevent local cross sectional deformation.

Fig. 14 shows the results of the bending moment test. These lines represent the same design cases as in Fig. 12. Although stroke distance to buckling increased with increased corner radius (cases A to C) similar to correlation between stroke to collapse and corner radius, correlation between the maximum bending moment M_{Smax} and corner radius is low. Fig. 15 shows a comparison of the results for the maximum bending moment between the three-point bending and crash tests. The difference in shape of these two curves is believed to have been due to the crash test measurement of the bending strength being under an axial load, while the three-point bending test did not involve an axial load.

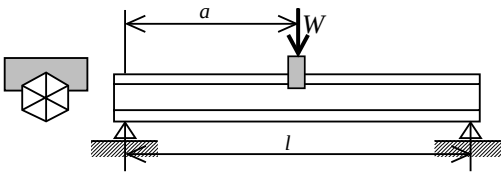


Fig. 13 Test set-up for bending frame

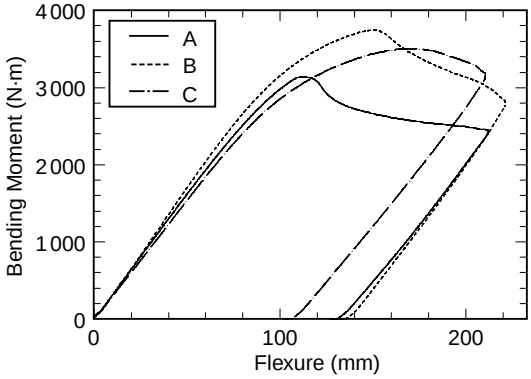


Fig. 14 Relationship between Bending moment and Flexure

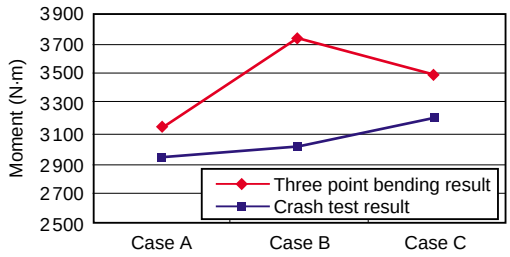


Fig. 15 Correlation between three point bending and crash test result

3.4 Mode Determination Conditions

This analysis focuses on the threshold value for the frame-buckling mode. This study evaluated the maximum moment arm, L_m, which was determined from the frame angle and frame length. L_m is defined by equation (4).

$$L_m = M_{max} / F_{ave} \qquad (4)$$

The symbols used have the following definitions:
M_{max}: Maximum bending moment obtained from the crash test
F_{ave} : Average compression load

The results of evaluation of results for the performance of the framelayout from the collapse load and bending moment are shown in Table 2. Although Case B demonstrated the largest value, there was only a very small difference compared to Case A, and conversely, the difference compared to Case C was only about 10%.

The foregoing results indicate little change in the moment arm due to changes in the shape of the corner part. One factor behind this is that, in the case of the collapse load of Case C relative to Case A, it increased just under 30% while the sectional area remained constant. While a change in the shape of the corner part had an effect on the collapse load, it had little effect on the installation angle that determines the bending mode. The following provides a discussion that focuses on this point.

Table 2 Result of lay out performance evaluation test

Case	F_{ave} (kN)	M_{max} (kN·m)	Moment arm length (m)
A	69	3.1	45×10^{-3}
B	80	3.7	46×10^{-3}
C	89	3.5	39×10^{-3}

4. Discussion and Theoretical Model

4.1 Examination of the Collapse Load

Fig. 16 shows a cross section of the corner part, while Fig. 17 shows the relationship between its sectional area and the collapse load. The results show a linear relationship between the sectional area of the corner part and the collapse load. Based on this, the cross section was divided into three parts, and the energy absorbed by each was measured in order to calculate to what extent the corner area was responsible for absorbing energy.

Fig. 18 shows how the section was divided into three parts comprising (1) the internal rib, (2) the external wall,



Fig. 16 Focused cross section of area corner

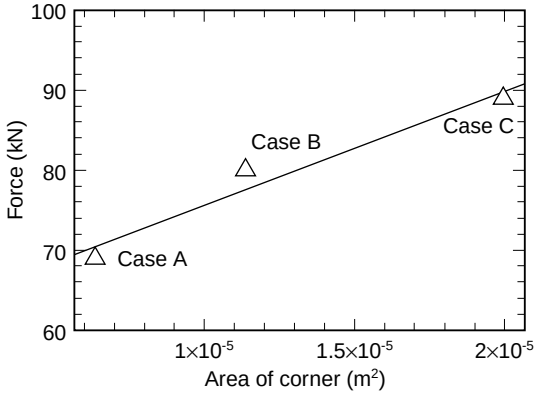


Fig. 17 Relationship between force and area of corner

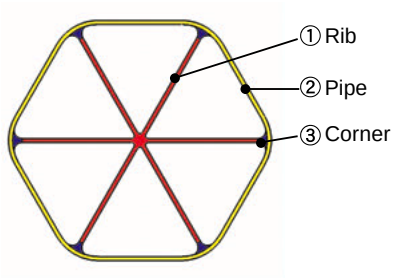


Fig. 18 Definition of divided parts

and (3) the corner area. Parts (1) and (2) were cut out for direct measurement. Each of these parts was cut to a length such that it would deform according to the buckling pitch of the collapse mode of the complete section. The amount of absorbed energy was calculated by multiplying the load and displacement. The contribution of part (3) was calculated by subtracting the amounts of energy absorbed by parts (1) and (2) from the total amount of energy absorbed by the complete section.

Fig. 19 shows the average amount of absorbed energy per unit of weight (referred to as the crash energy density) for Cases A, B and C of the cross section.

Equation (5) was empirically derived from the results of the experiment for estimating the sectional area and collapse load of each part.

$$F_{ave} = C\,(A_{rib} + 2A_{pipe} + 6A_{corner}) \qquad (5)$$

where,

A_{rib} : Rib sectional area
A_{pipe} : Pipe sectional area
A_{corner} : Corner part sectional area
C : Constant value, 4.72 x 10^7

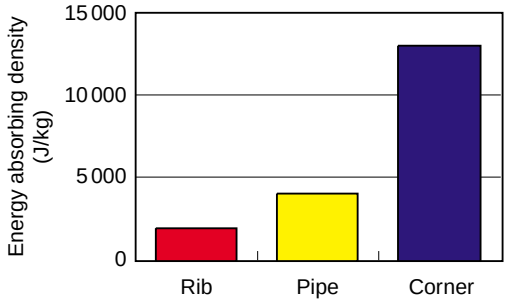


Fig. 19 Energy absorbing density of divided parts

The results of applying equation (5) to Cases A, B and C are shown in Fig. 20. The correlation plotted on the vertical axis uses the value obtained by dividing the calculated value with the experimental value. The error was 10% or less for all cases, thereby confirming the validity of equation (4) for calculating the collapse/buckling load of the aluminum crash boxes.

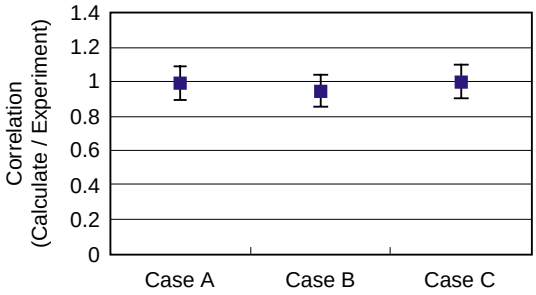


Fig. 20 Correlation of collapse load caluculation

4.2 Effect of Cross Section Shape on the Energy Absorption Density

The cross sectional area of the corner part made a considerable contribution to the collapse load. Therefore, a new shape was produced by maximizing inside radius R_1 and optimizing outside radius R_2 with the aim of achieving a collapse load of 150 kN with equation (5) (Fig. 21).

Fig. 22 shows the collapse loads for the new shape and

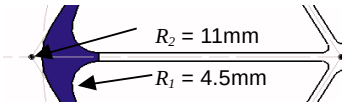


Fig. 21 Detail of new shape

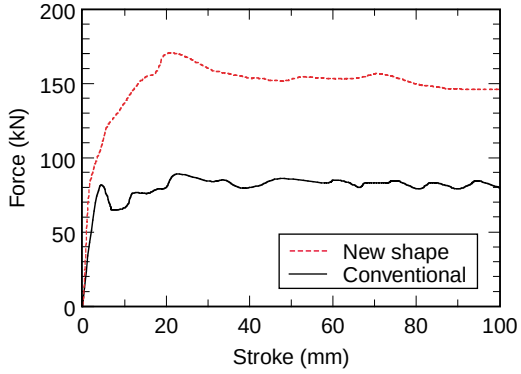


Fig. 22 Relationship between collapse load and stroke (Conventional and new shape)

for the Case B shape. The sectional area of the new shape was 1169 mm^2 due to the dimensional changes in the corner region. The collapse load for the new shape was an average of 150 kN, roughly double that for the Case B shape.

While the crash energy density was 3.1 x 10^4 (J/kg) for the Case B shape, it was 4.8 x 10^4 (J/kg) for the new shape, an improvement of 54%.

4.3 Maximum Bending Moment

A theoretical formula was also proposed for the maximum bending moment. Fig. 23 shows the test piece after the bending test. Measurements were taken for the cut-out parts above and below the neutral axis at the center of the test piece. A wall-buckling mode similar to collapse deformation caused by compression appeared in the region above the neutral axis, while plastic deformation caused by tension occurred below.

On the basis of these observations, an assumption of the compressive region plastic deformation by the collapse/buckling load, while the tensile region is defined as the moment resulting from fully plastic conditions as shown in Fig. 24. Their experimental values were then compared. The collapse load in the compressive region is thought to have acted on the centroid in the compressive half of the cross section. The maximum bending moment can be represented by equation (6). G and A_{all} represent the distance from the centroid to the center of the entire cross section and the total area of the hexagonal cross section.

$$M_{max} = \frac{A_{all}}{2} G\sigma_y + \frac{F_{ave}}{2} G \qquad (6)$$

Fig. 25 shows the correlation between the results calculated with equation 6 based on yield stress σ_y = 180 Mpa and the experimental values obtained from the crash test. The difference between the calculated values and experimental values was at the 7% level or less, indicating that it was possible to obtain satisfactory results by calculation.

The collapse load and bending strength could thus be suitably calculated by the equations, focusing on the area of the corner part.

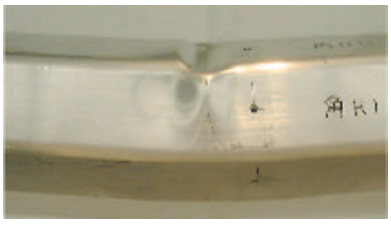


Fig. 23 Test specimen after bending test

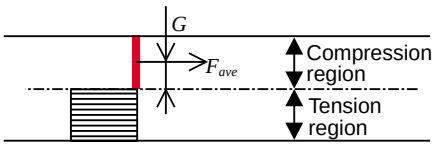


Fig. 24 Definition of bending moment calculation

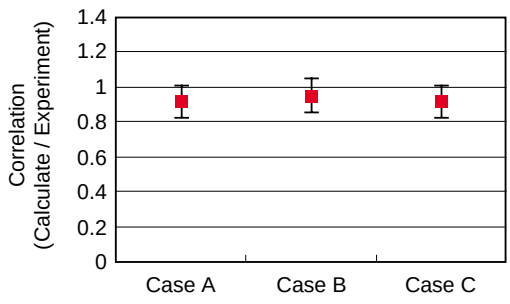


Fig. 25 Correlation of bending moment calculation

5. Establishment of a Predictive Simulation Model

The findings from the experimental analysis in section 4 indicated the desirability of a model that could accurately simulate the buckling of a strut with internal ribs in the corner region.

The stress distribution in the thickness direction of the strut corner part was analyzed with solid model in RADIOSS simulation software in order to establish a highly accurate predictive technique, while a study was also conducted on a simpler modeling method.

5.1 Solid Model Analysis

A model was produced from solid elements and then analyzed in detail in order to elucidate the stress distribution in the corner part. Calculations were first made for one, two, three and four plies each in the thickness direction by using the 1/6 model shown in Fig. 26 in order to determine the number of element plies that would be needed to provide sufficiently high accuracy.

Comparison between calculated results of each ply are shown in Fig. 26. The comparisons of the deformed shape and internal stress distribution indicated that the results of sufficient accuracy could be obtained with a minimum of three plies. A graph of the load versus deformation during compression with a minimum of three plies is shown in Fig. 27. Concerning the average values for the collapse load, the calculated values were 2% lower than the experimental results.

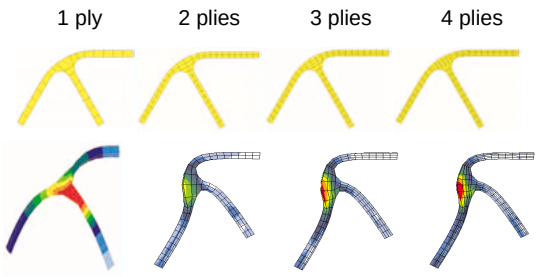


Fig. 26 Element plies of thickness and simulation results for deformation and stress

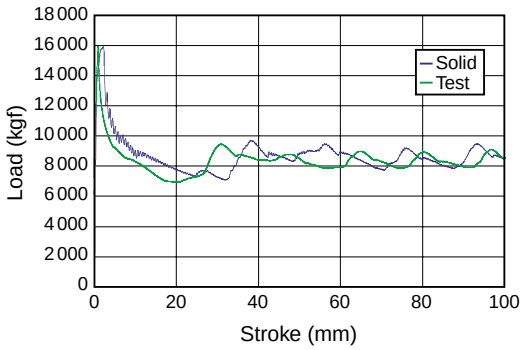


Fig. 27 Simulation result for solid model

The calculated stress distribution generated in the corner part is shown in Fig. 28. The stress was found to be greatest in the corner part and was generated in the thickness direction through the thickness, so the stress in the thickness direction had a significant effect on determining the collapse/buckling load.

Although the results calculated with the solid model were satisfactory in terms of their accuracy, there was the shortcoming of a single member requiring a considerable amount of calculation time. Therefore, two other methods were examined with the aim of reducing the calculation time. The first was a method for obtaining the equivalent load characteristics by using shell elements, and the other enabled increased accuracy of integration in the thickness direction, even with one ply, by tuning the solid model elements.

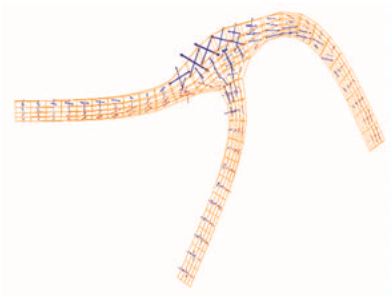


Fig. 28 Maxmum principal stress

5.2 Establishment of a Tuned Shell Model

In the case of an ordinary shell model, load is transmitted through a single node of the internal rib. Since the action of the load in the thickness direction was therefore considered to be different, modifications were made as shown in Fig. 29.

(1) Shell elements were added around the internal curve of the corner part to cause force to be transmitted in the thickness direction around the periphery of the corner part.
(2) The thickness of added shell elements were adjusted to give the same collapse/buckling load as that obtained in the experiments.

This thickness adjustment was based on the relationship between the sectional area of the corner part in the actual strut and that in the tuned shell model. As shown in Fig. 30, results were obtained for the relationship between A_0 and A_1 in the form of equation (7), with A_0 being the sectional area of the actual strut and A_1 being the sectional area of the additional parts and adjusted-thickness parts of the tuned shell model.

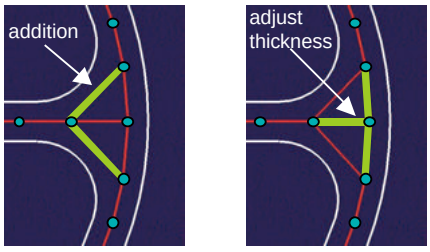


Fig. 29 Section shape of shell model

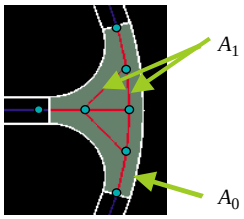


Fig. 30 Section shape of shell model

$$A_1 = 1.5 \times A_0 \qquad (7)$$

Fig. 31 shows the calculated results for Case B when A_0 was 25.9 mm^2 and A_1 was 40.0 mm^2. The difference between the calculated results and those of the individual frame compression test was within 8% in terms of the average compressive load.

Differences in the shape of the corner part (R_1 = 11 and 30 mm) can also be represented with the tuned shell model based on the same relationship (Fig. 32), and a comparison between the calculated and experimental values is shown in Table 3. The use of a tuned shell model focused on the corner part enabled highly accurate modeling with about the same calculation time as that required for a conventional shell model.

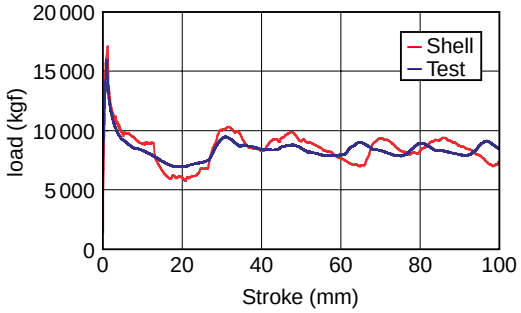


Fig. 31 Load and stroke result for the shell model modified

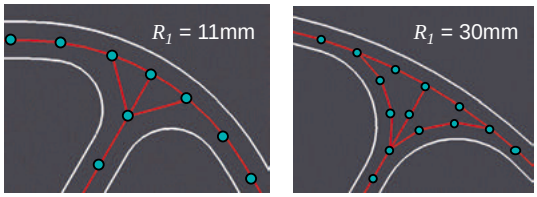


Fig. 32 Section shape of tuned shell model

Table 3 Result of loads

Case \ Load	Experiment F_{ave} (kN)	Calculate F_{ave} (kN)
A	69	69
B	80	78
C	89	92

5.3 Thick Shell Elements

Thick shell elements were examined in an attempt to modify the elements that would enable integration of the relationship between the stress and strain for changes in the thickness direction. Fig. 33 shows a model of the corner part with solid elements and thick shell elements. The thick shell elements represent thickness with a shape function in the same manner as solid elements.

However, in order to reduce the calculation time, a second-order shape function providing intermediate nodes was used in the width and length directions, while a first-

order shape function was used for the thickness direction. This was done to enlarge the shape that could be represented by a single element, while also enabling a model to be produced with a smaller number of elements even for the same shape.

Next, calculation of stress inside the elements is described. Fig. 34 shows a single thick shell element. Integration points were provided at 3 x 3 = 9 locations on the outer surface and setting of the direction through the thickness was made at maximum of 9 locations. The analytical results for the internal stress in a solid model indicated that three or more plies were necessary in the thickness direction in order to obtain adequate accuracy. Namely, it was considered that calculations could be made with sufficient accuracy if integration points were provided at six or more locations in the thickness direction in the case of thick shell elements.

Fig. 35 shows a comparison between the calculated results for thick shell elements and those for the solid model (three plies in the thickness direction). These two sets of calculated results can be seen to closely agree. In addition, the calculation time was only about 1/30 of that required for a conventional solid model.

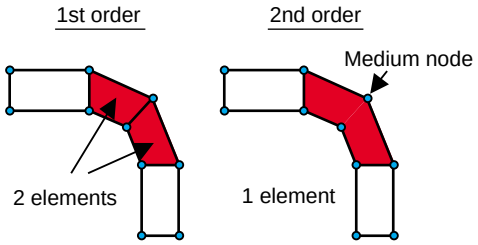


Fig. 33 Corner modelings

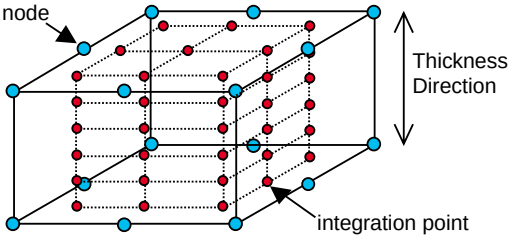


Fig. 34 Integration points

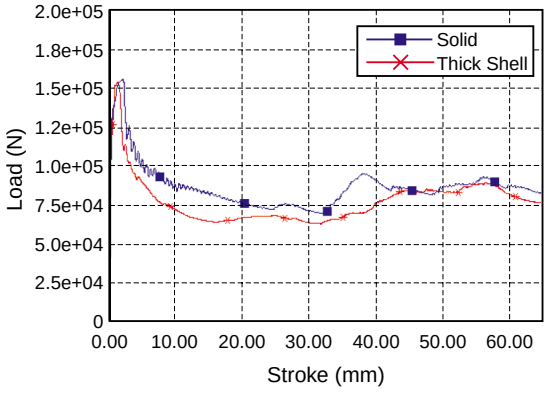


Fig. 35 Load and stroke result for thick shell model

6. Conclusion

A study was made by experimental tests and simulation methods on the energy-absorbing members of a ribbed aluminum crash box. The following results were obtained.

(1) Using a sled test, the bending moment of the compressive load applied to the box was calculated, and a method was established for calculating the moment at the time of bending mode of the box.

(2) An analysis of the energy-absorbing box determined the factors and locations of compressive load and bending strength in relation to the cross-sectional shape, and it was found that the corner part made a significant contribution. An empirical equation was established that made calculation within an error of 10% possible.

(3) Various simulation techniques were studied to identify the best match with the experimental results, and a suitable modeling method was then established.

References

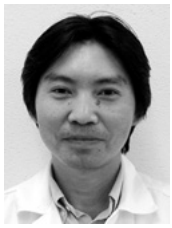
(1) Fukuo, K., Fujimura, A., Saitoh, M., Tsunoda, K., and Takiguchi, T.: Development of the “Insight” Ultra-low Fuel Consumption Hybrid Car, HONDA R & D Technical Review, Vol. 11, No. 2, pp. 1-8 (1999).(in Japanese)

(2) Satoh, T., and Takada, K.: Collapse and Energy Absorption of Thin-walled Frame with Polygonal Section, 96-S3-W-19, 15th International Technical Conference on Enhanced Safety of Vehicles, Melbourne, Australia, pp. 518-524, (1996).

(3) Integration of New Manufacturing for Body Longitudinals - Assessment of the Product Development Process and Implication on Passive Safety, Aachen Colloquium Automobile and Engine Technology (1999).

(4) Radioss Theory Manual, ver. 4.2 (1999).

■ Authors ■


Yuta URUSHIYAMA


Takayuki YAMADA


Shunji SUZUKI


Toru KAWANO

Research into the Reduction of Stick-Slip Noise in Exhaust System Joints

Masashi IWAI* Mototaka MAEDA* Etsuo TAKAKU*
Yasunori MURAKAMI* Masanobu MIKI* Takeshi FURUKIDO**

ABSTRACT

Ball joints, one type of joint applied as an automobile exhaust system joint, will often generate an abnormal noise upon oscillation. The noise generating mechanism of this phenomenon is explained using element analysis and friction characteristic analysis of the materials making up the surfaces of the joints. It was found that the roundness of the flare flange of ball joints which generate noise is imprecise. This causes the flange to come in partial contact with the spherical gasket eventually resulting in abnormal wear of the guard net in the gasket. The particles resulting from this wear accumulate on the gasket surface, where the stick-slip phenomenon then causes the noise. A study was also conducted to determine input frequency for oscillation angle and temperature of the ball joint during the use of an actual vehicle. The fabrication of a simple excitation device that could apply those input conditions made it possible to conduct a bench evaluation of the noise. This bench test method was used to conduct parameter studies of design variables that significantly affect the generation of the noise. The bench test was also used to determine the range of settings for set spring load and the flare roundness wherein the noise will not be generated.

1. Introduction

Currently, ball joints (referred to as joint hereafter) having an oscillation function are widely used in automobile exhaust systems. By locating these joints in the exhaust pipe, as shown in Fig. 1, the force applied to the exhaust pipe due to engine roll displacement is attenuated, making it possible to reduce vibration transmitted from the engine to the exhaust pipe. The basic structure, as shown in Fig. 2, is an exhaust pipe fitted with a spherical gasket (referred to as gasket hereafter) and an exhaust pipe with a flare-shaped flange (referred to as flare hereafter). These two parts are held together by a coil spring at a set load.

Ball joints often generate abnormal noise when they oscillate. However, this phenomenon is an early stage degradation phenomenon that occurs only in some vehicles after they have been driven several thousand kilometers under specific driving conditions. The cause and effect relationship between the factors has not been clearly understood. Therefore, many countermeasures have been found through post-build trial and error. Many examples of these measures eventually become examples of suppression of the essential oscillation function.

Therefore, this project carried out cause analysis in order to understand this phenomenon from both a macro- and micro-perspective. The macro-perspective was based on the relationship of the factors to such input characteristics as the oscillation angle and the temperature of the joints. The micro-perspective was based on the implementation of material element analysis of the oscillation surface material and friction characteristics analysis. Based on these analyses, a bench noise evaluation method was constructed. An "evaluation map" was created from the numerical values determined through tests using this method for joint design parameters. This paper reports on the above.

* Tochigi R&D Center
** OILES CORPORATION

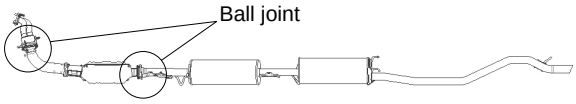


Fig. 1 Application example of a ball joint in an exhaust system

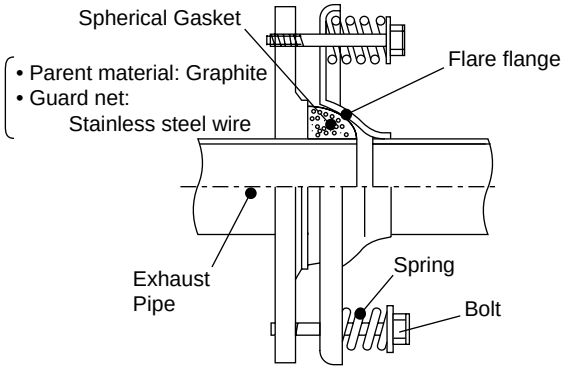


Fig. 2 Ball joint of an exhaust system

2. Noise Generation Factor Analysis

2.1 Noise Generation Condition in Vehicles

2.1.1 Measurement method

Measurements of noise generated by joints were made using actual vehicles. The measurement points, as shown in Fig. 3, were established in an adjacent area 100 mm below the joint. Driving conditions were fixed at a full load while idling after the engine is completely warmed up, the condition where the noise is most likely to occur. The oscillation angle and temperature were also simultaneously monitored at this time. Two sample joints were used for measurement: one normal part that does not generate noise, and one that does. Both joints were aged to an equivalent of the early stages of driving. The joints were not disassembled, but rather they were compared through use in the same vehicle, as assembled to the front and rear exhaust system components. This was done to reproduce, as closely as possible, the condition of the actual oscillation surface.

2.1.2 Measurement results

Fig. 4 shows the results of frequency analysis of noise near the joint, for both the normal parts and noise generating parts. The noise generating parts generated a metallic rubbing sound, "kyuru-kyuru", with the wide frequency range of 2 to 8 kHz.

Based on this data, the 2 to 8 kHz range was sampled, and Fig. 5 shows the noise level results in a time series graph. There was a clear difference between the two joints, and because there is a good correlation with the conventional feeling evaluation, this evaluation value will be used in the future as the noise level evaluation value.

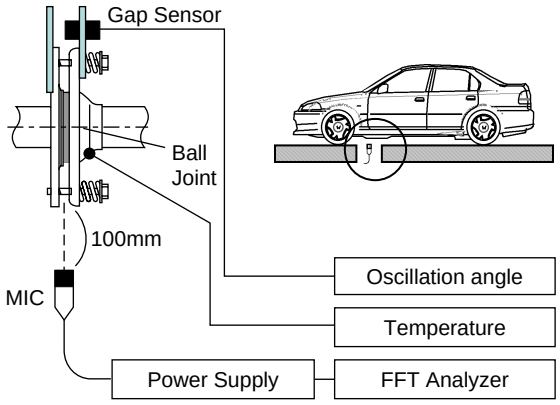


Fig. 3 Measurement system for noise in a vehicle

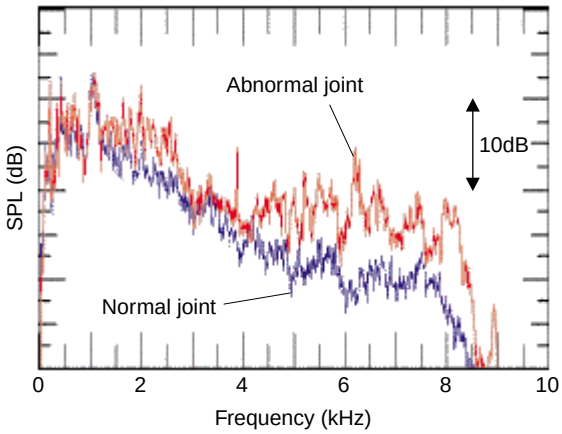


Fig. 4 Noise level frequency characteristics

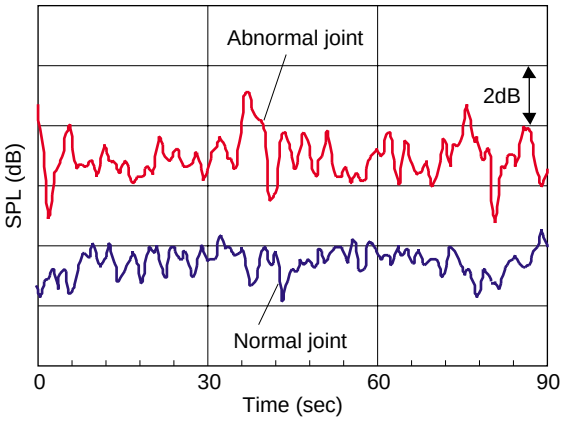


Fig. 5 Noise level time domain band pass data

2.2 Changes to Noise Level due to Differences in Driving Condition

2.2.1 Measurement method

In the previous section 2.1, the vehicle driving conditions were fixed at those where noise is generated most easily, but it is known that the noise level of noise generating parts changes according to differences in driving conditions. However, because it is difficult to take stable measurements when there are fine changes to driving

conditions, as shown in Fig. 6, confirmation was made using bench vibration tests. Under actual vehicle driving conditions, the joint oscillation angle and temperature fluctuate. Thus, the two parameters were changed slightly in the same way on the bench, and the relationship with surrounding noise levels was checked. The measurement method used was exactly the same as with the actual vehicle. In addition, the joints used were the same two samples as in the vehicle measurements, a normal part and an abnormal part. The joints were not disassembled, but rather vibrated together with the front and rear exhaust system components.

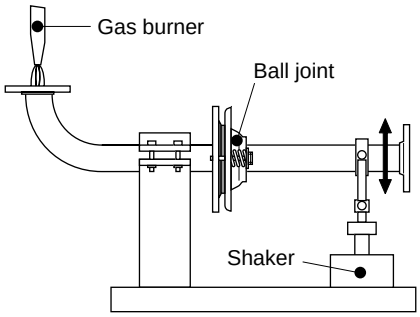


Fig. 6 Bench oscillation test (component parts of ball joint)

2.2.2 Measurement results

Fig. 7 shows the noise measurement results during the bench vibration test, when the oscillation angle and temperature are changed. With normal parts, there are no large changes to surrounding sound, even when the oscillation angle and temperature are changed, and no abnormal noise is generated. The maximum oscillation angle on the vehicle is 0.15° under full-load, idling conditions, but even if the oscillation angle is increased to 0.25°, no abnormal noise is generated. In comparison, surrounding noise tends to increase in noise-generating parts with greater oscillation angles and higher temperatures. The noise generation boundary line is at the point when the oscillation angle is 0.15° and temperature is 200°C. It was learned that when conditions are more severe than this, abnormal noise would, without fail, be generated.

From this, it was also confirmed through bench vibration tests that the conditions under which a vehicle generates the maximum abnormal noise levels, that is, with an oscillation angle of 0.15° and a temperature of 260°C, clearly fall within the noise generation range.

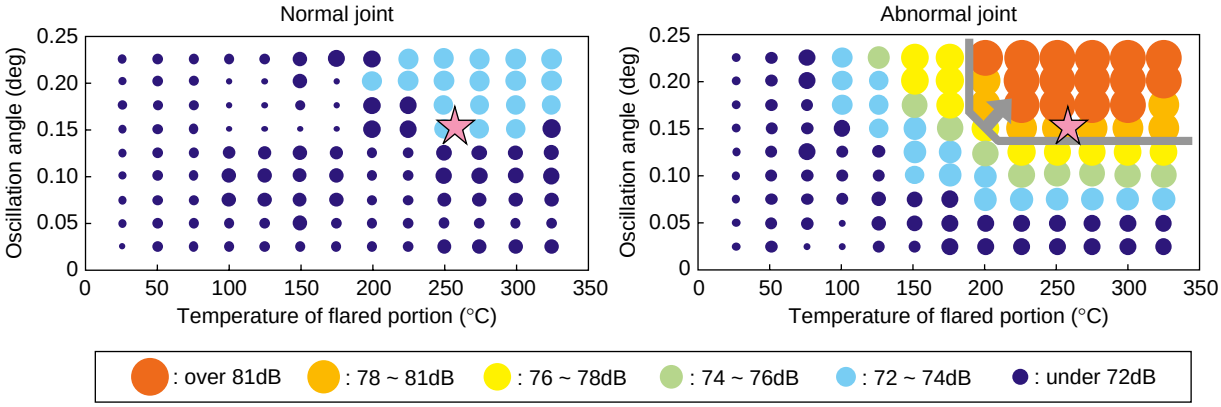


Fig. 7 Noise level during the bench oscillation test

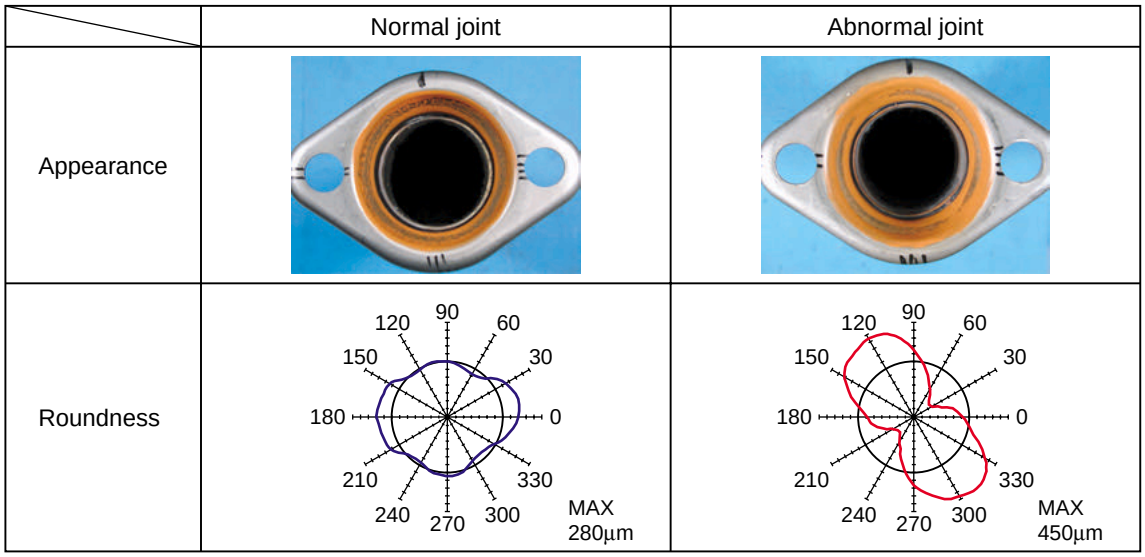


Fig. 8 Characteristics of the flare flange

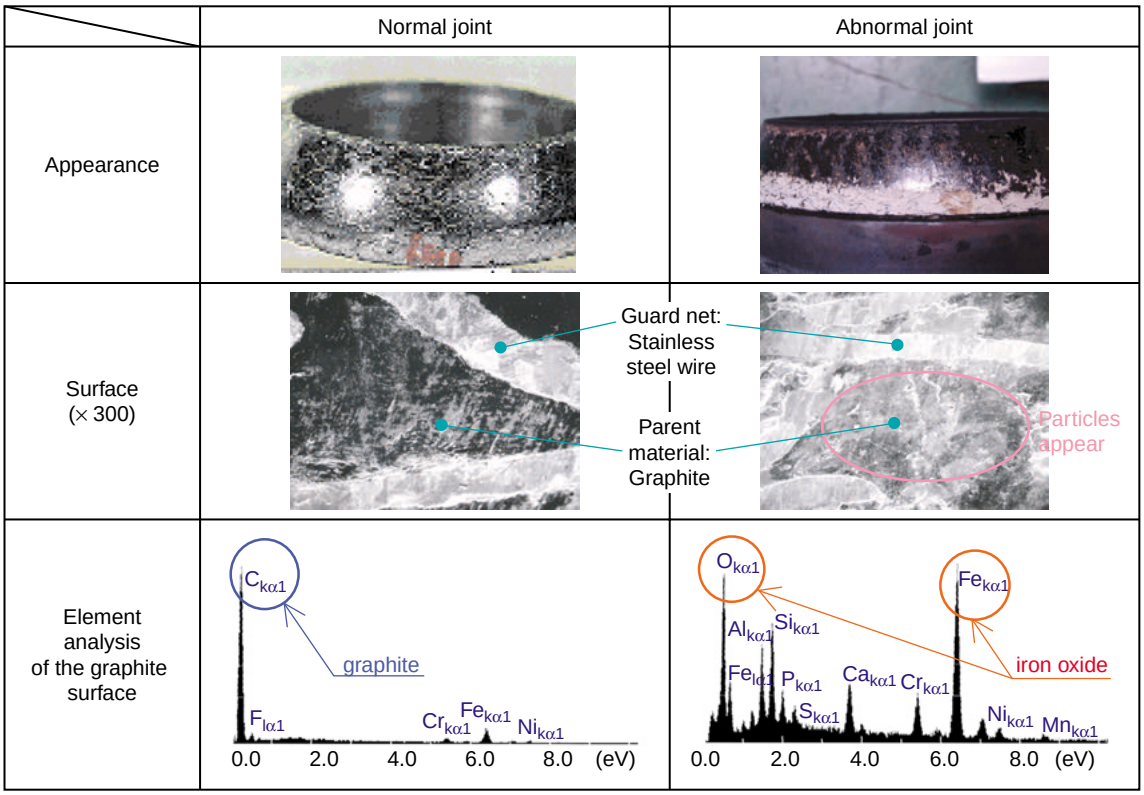


Fig. 9 Characteristics of the spherical gasket

2.3 Joint Contact Surface Investigation Results

2.3.1 Flare

A contact surface investigation was carried out for the two types of flare used in the noise confirmation tests. Those results are shown in Fig. 8. Looking at a photographic image of their appearances, it was learned that noise-generating parts have extremely uneven contact compared with normal parts. The results of flare roundness measurements show that normal parts have much better accuracy, 280 μm, than noise-generating parts, 450 μm.

2.3.2 Gasket

Next, an investigation was made of contact surface with the two types of spherical gaskets used in noise confirmation testing. The results are shown in Fig. 9.

With only photographic images of their appearances, no clear difference could be seen between them. Thus, the images were enlarged 300 times and reconfirmed. At this magnification a clear distinction could be made between the parent material graphite and the core stainless-steel wire. On the normal parts, the parent material was black, and the core material was white. However, with the noise-generating parts, there were many areas that gleam white on the parent material that originally looked black. It was confirmed that a contaminant had accumulated on the parent material.

Element analysis was carried out on the parent material surface for both parts. The major element of the normal parts was graphite. However, the major elements of the abnormal parts were iron and oxygen – that is, iron oxide. Therefore, it was learned that the accumulated contaminant is the powder generated by the core stainless-steel wire wear.

2.4 Joint Contact Surface Material Unit Analysis

2.4.1 Test method

From the results outlined in section 2.3 above, it is assumed that the core stainless-steel (JIS SUS310S-W1) powder (major element: iron oxide) that accumulates on the gasket parent material surface comes into partial contact with material equivalent to the flare material (JIS SUS304S-HP), and that the stick-slip phenomena during oscillation

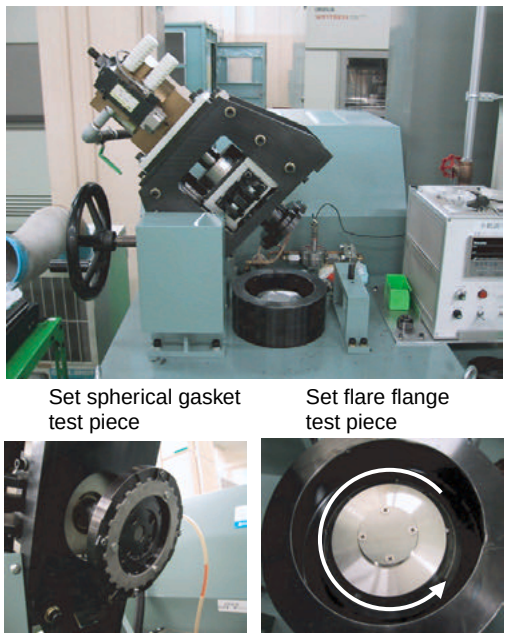


Fig. 10 Low velocity friction apparatus

is the origin of the abnormal noise. A friction test was implemented for each component material of the joint sliding surface to identify the causes of the noise generation.

As shown in Fig. 10, using a low velocity friction apparatus, the stainless-steel (JIS SUS304-HP) plate selected for the flare and the tip selected as the gasket raw material (core = JIS SUS310S-CB, parent material = graphite) were checked for friction behavior by sliding in the axial direction. Verifications were performed for the stick-slip phenomenon that occurs at high temperatures from the friction characteristics with combinations of these materials.

Also, test conditions were established based on conditions of actual vehicle use.

2.4.2 Test results

The results obtained with the low velocity friction apparatus are shown in Fig. 11.

First, a test was implemented with the combination of a stainless steel plate equivalent to the flare, and a graphite tip. The friction coefficient was in the 0.1 to 0.25 range, and even with a temperature rise the sliding state was stable in the normal wear range.

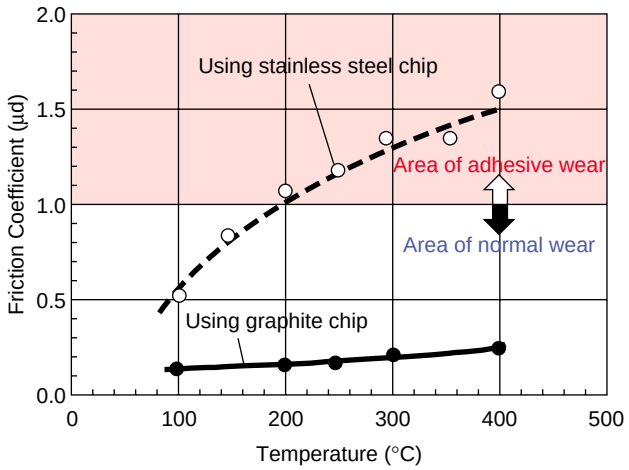


Fig. 11 Characteristics of the friction coefficient

Next, a test was implemented with a combination of stainless-steel plate equivalent to the flare and a stainless-steel tip equivalent to the gasket guard net. The friction coefficient was very high for the results using the graphite tip, and rose with a rise in temperature such that at a temperature of 200°C or more, it exceeds 1.0. That is to say, the shearing force of the sliding surface exceeds the contact load, and the sliding status is in the adhesive wear range.

Fig. 12 shows the results of a comparison of the friction coefficient change levels and the surface conditions of the core-equivalent stainless steel tip in the normal and adhesive wear ranges. The friction coefficient change level is small with normal wear, but it is extremely large with adhesive wear. Also, at this time, adhesion marks on the sliding surface were clear. That is, in the condition whereby the core stainless steel wire wear powder is accumulated on the graphite surface of the gasket material, there is partial contact with a material equivalent to that of the flare, creating an adhesive wear state, and causing the occurrence of the stick-slip phenomenon. The abnormal noise is generated from this phenomenon.

2.5 Abnormal Noise Generation Analysis during Vehicle Use

2.5.1 Test method

From the results of section 2.4 above, noise is generated when core material wear powder has accumulated on the gasket surface and the stick-slip phenomenon occurs. Next, an analysis was carried out for this phenomenon on how the gasket surface state changes from the new part state through use, and how it arrives at noise generation. First, giving full consideration to patterns of use, we looked into degradation input factors to the joint during operation, such as oscillation angle and temperature, in order to establish a vehicle verification mode. Next, the vehicle was driven in this verification mode in order to understand the relationship between the condition of the gasket surface changes and abnormal noise generation. The continuous verification flow is provided in Fig. 13.

First, data concerning oscillation angle and temperature applied to the joint was measured while driving for 500 km

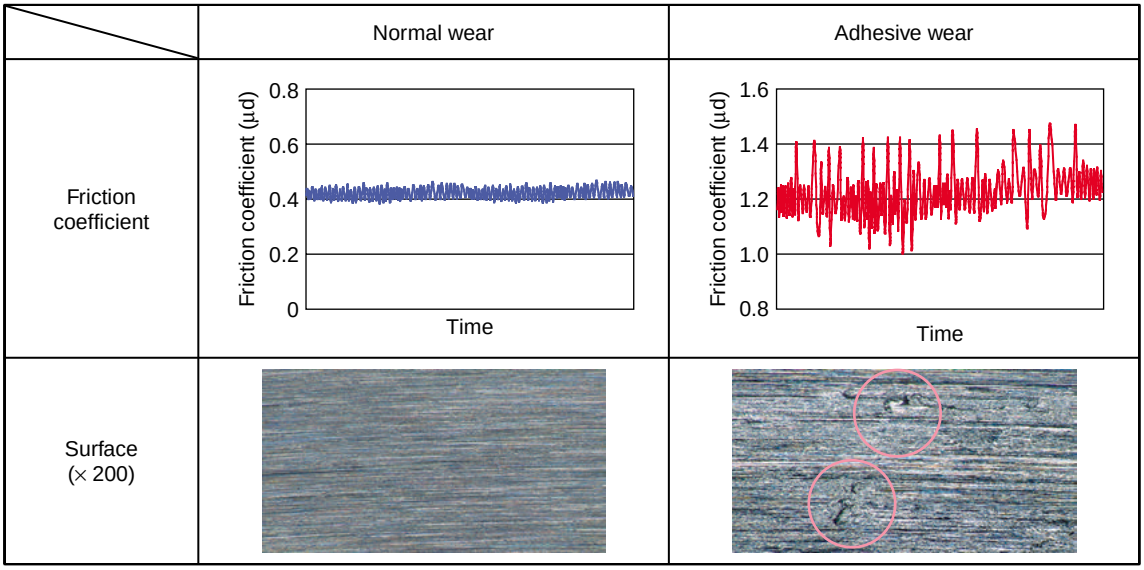


Fig. 12 Comparison between normal wear and adhesive wear

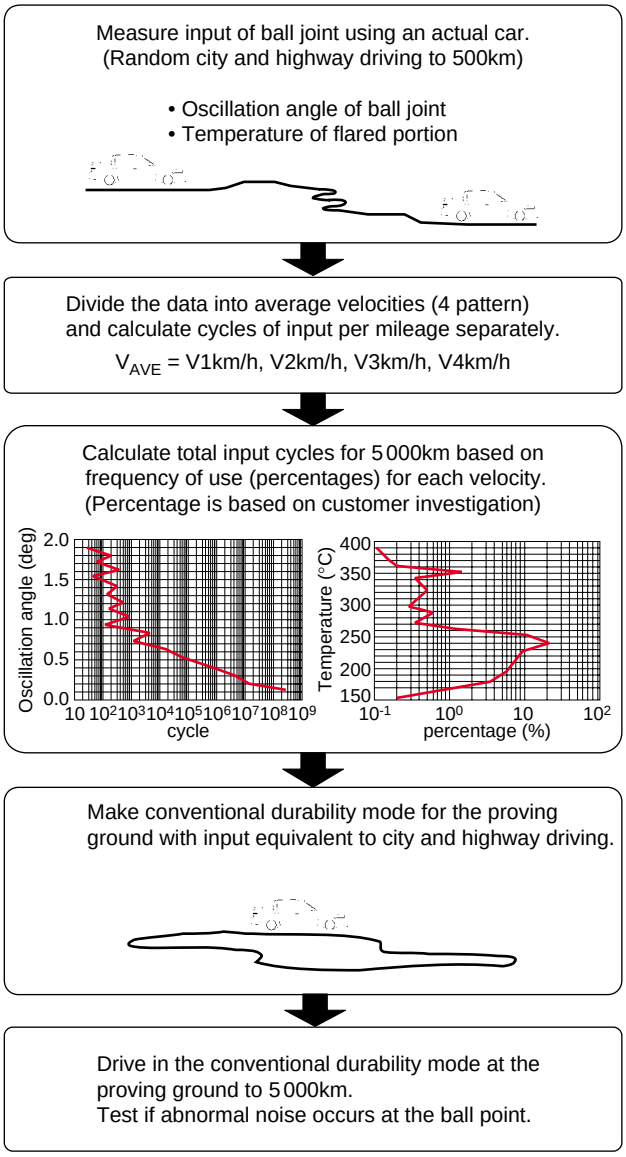


Fig. 13 Verification flow through noise occurrence

on a normal road. The measurement method used was the same as when performing the abnormal noise confirmation. Also, information on vehicle speed, engine speed, throttle angle, and gear position was gathered simultaneously, in order to understand the operating conditions. Next, the actual use vehicle speed range was divided into four patterns according to average vehicle speed, and input frequency data for each unit distance was calculated for each driving pattern.

Then, based on results of a user survey, wherein customers were asked how often they drove in each speed range, oscillation angle and temperature input frequencies were determined in proportion to frequency of use for each speed range for 5,000 km.

Further, based on results of input frequency obtained from driving on ordinary roads, a test course reproduction mode was created. This mode is a driving mode that provides input frequencies for oscillation angle and temperature that are equivalent to those on ordinary roads by having standardized the input levels for temperature and oscillation angle while driving on normal roads.

2.5.2 Driving results from the vehicle abnormal noise reproduction mode

A vehicle was driven 5,000 km in this mode. A new joint having the same flare roundness, 450 µm, as the part confirmed to produce the abnormal noise was used. Results of abnormal noise level changes in terms of driving distance are shown in Fig. 14. The abnormal noise was first confirmed at 2,950 km. The noise level reached its maximum at 3,700 km and it remained at approximately the same level until the 5,000 km. The gasket surface state changes that occurred at this time are shown in Fig. 15. With the new part (0 km) the gasket surface is covered with a layer of lubricant, and no noise is generated. According to the results of the element analysis of the parent material surface, the major element was iron, and the surface lubricant was PTFE.

After driving 1,700 km, contact occurred. The gasket surface lubricant was stripped, and the results of element analysis of the parent material surface show that the major element was carbon, which indicates that the parent material is graphite. Again, no abnormal noise is generated.

After driving 3,700 km, wear was more advanced, and looking at an enlarged photographic image, it was clear that the core stainless steel wire has been scraped.

According to the results of element analysis of parent material surface, the major elements were iron and oxygen – iron oxide – which indicated that the wear powder from the core stainless steel wire had accumulated on the surface. At this time, there was a noticeable abnormal noise. Also, it was confirmed that the state of the surface was the same as the noise-generating part described in section 2.3.

Based on the results above, because the flare roundness was poor (450 µm), partial contact occurred so that the core stainless steel wire was scraped. The resulting powder covered the parent material graphite surface. Consequently, the stick-slip phenomenon occurs and an abnormal noise was generated.

2.5.3 Comparison of the abnormal noise reproduction mode and conventional durability modes

As outlined above, abnormal noise generation was confirmed with the abnormal noise verification mode established with due consideration to the way users drive on an ordinary road. However, no abnormal noise occurred

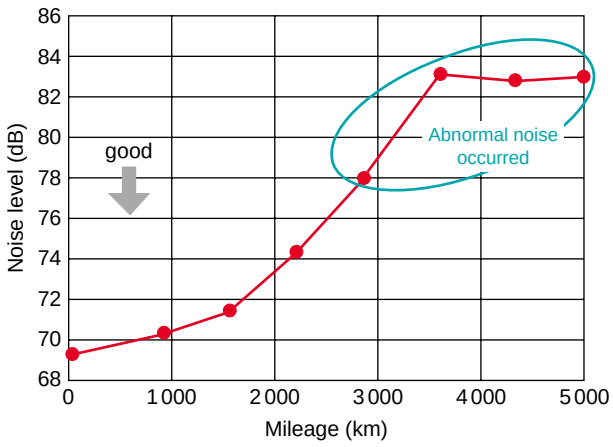


Fig. 14 Results of driving in the conventional durability mode at the proving ground

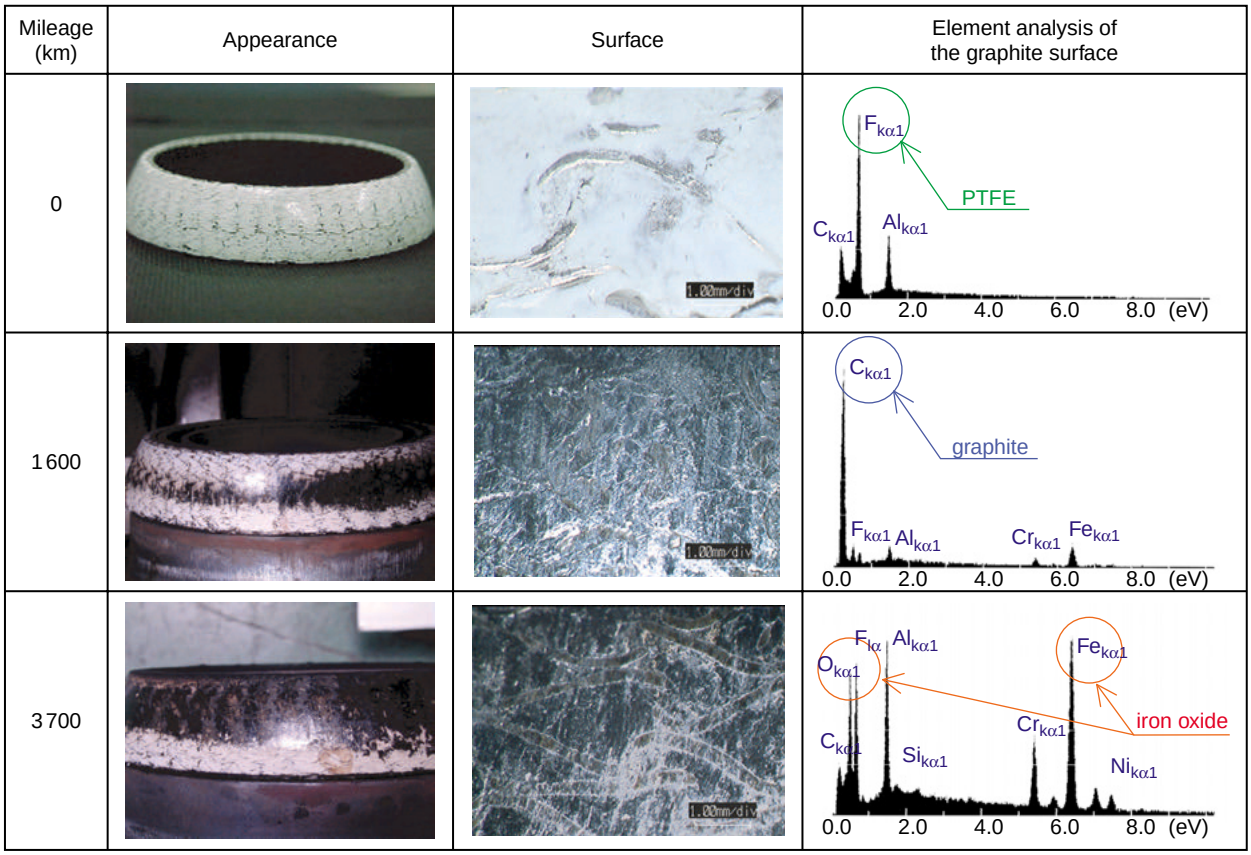


Fig. 15 Transition of the spherical gasket surface

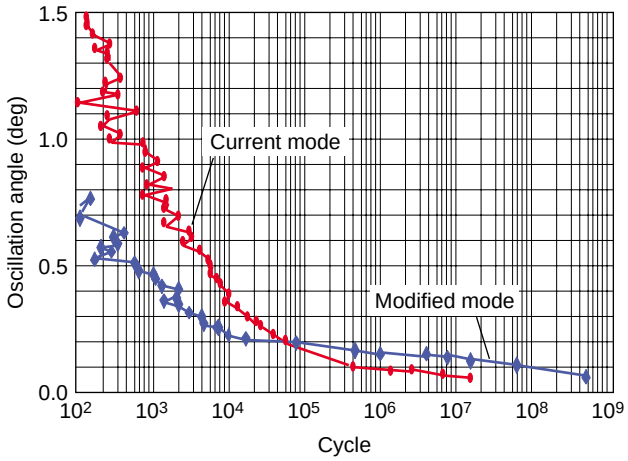


Fig. 16 Difference in oscillation angle for each driving mode

in the other durability modes implemented. These durability modes simulate driving situations where input is mainly concentrated on input to the chassis and body.

Therefore, joint input frequency was also measured in these conventional durability modes, and a comparative verification was made with this new abnormal reproduction mode. Oscillation angle input frequency measurement results are shown in Fig. 16.

From these results, we know that the abnormal noise reproduction mode is a low input, high frequency model, while conventional durability modes focus on high input. Comparing the range with an oscillation angle of approximately 0.1°, the abnormal noise reproduction mode shows a frequency approximately 10 times that of the conventional durability modes.

Because the cause of this phenomenon is the gasket guard net wear and the resulting wear contaminants accumulating on the surface, the abnormal noise reproduction mode (which has a high frequency with a fine amplitude) can be said to have more severe conditions than the conventional durability modes. Accordingly, when converting the actual driving abnormal noise reproduction mode to a bench test, the key points in setting the input conditions were low force input, high frequency conditions.

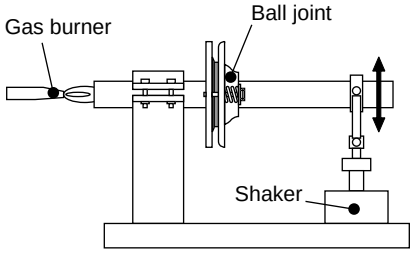


Fig. 17 Bench oscillation test (Ball joint test piece)

3. Creating a Bench Evaluation Method

An investigation was carried out for the conversion of the driving in the abnormal noise reproduction mode, which simulates input obtained from an ordinary road as obtained in section 2.5, into a bench test.

3.1 Bench Test Method

3.1.1 Shaker device

An outline of the bench shaker system is shown in Fig. 17. This system was constructed so that the oscillation angle and temperature inputs that are applied to the joint during actual driving can be set, facilitating verification of abnormal noise. In Fig. 3, the sample part joints are not disassembled but rather vibrated while connected to the front and rear exhaust system components in order to faithfully reproduce the abnormal noise of the recovered parts. However in this investigation, the tests were implemented with a test piece created by cutting out the joint and welding it to a pipe. This was done to prevent any constraints due to joint size or location, and to increase the versatility of the system.

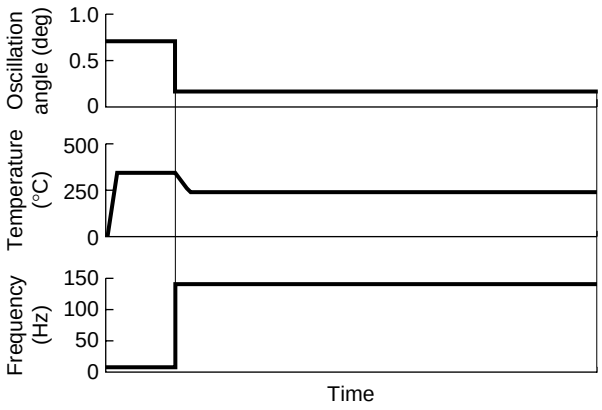


Fig. 18 Bench oscillation test conditions

3.1.2 Establishing oscillation input conditions

As explained in section 2.5.3, abnormal noise reproduction mode is a low input high frequency model. Thus, focus was placed on this point, and simplified input conditions were set. Fig. 18 shows these details. As for the input conditions, the focus was on low input with an oscillation angle of 0.10°, and temperature was set at the greatest temperature proportional to time. The oscillation frequency was set higher than with a vehicle, from the point of view of shortening the time period. Also, because the new gasket has a surface lubricant that includes PTFE, both the oscillation angle and temperature were set higher for the initial period only, with the idea of quickly removing the lubricant layer so that there is partial contact with the parent graphite material. In this investigation, the oscillation angle was set at the average value for the input in a vehicle, and the temperature was set at 300°C or more, a temperature which vaporizes PTFE. As the oscillation angle is large, the frequency is determined by the shaker capability.

Based on the above details, a bench mode equivalent to driving 5,000 km was established.

3.2 Results of Bench Evaluation Method Verification

In order to verify that this bench test method is appropriate, confirmation tests were carried out with new test pieces having an accuracy equivalent to the flare roundness of 450 μm used in the driving abnormal noise reproduction mode.

The test results are shown in Fig. 19. In the bench test, too, it was confirmed that abnormal noise occurs after 3,200 km of use. This is approximately an 8% difference from the 2,950 km at which noise occurred during driving, and is judged to be an adequate simulation of driving.

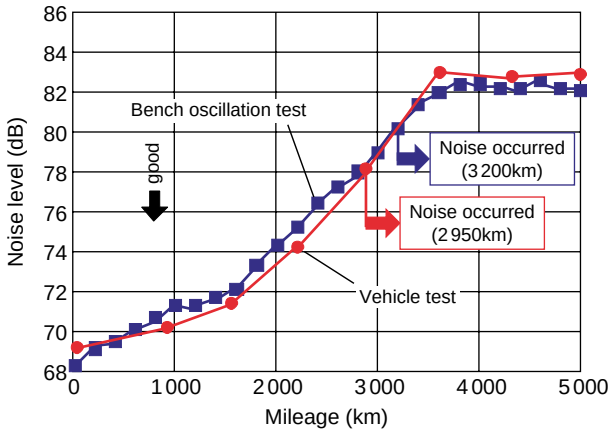


Fig. 19 Comparison between bench test and vehicle test

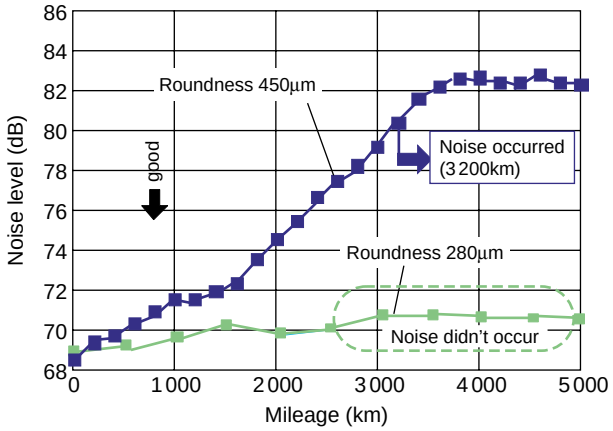


Fig. 20 Results of bench oscillation test

Next, verification was made of any abnormal noise generated by implementing testing on the bench using two types of new test pieces having different new part flare roundness.

According to the results in section 2.3.1, we know there is a clear difference in flare roundness accuracy for the normal part and noise-generating part. The flare roundness of the test pieces used in this case matched that of the test pieces used earlier, were 280 μm, equivalent to the normal part, and 450 µm, equivalent to the noise generating part.

The results of the above comparison are shown in Fig. 20. From these test results, we were able to confirm that the part specification with the poor flare roundness

accuracy of 450 μm resulted in the generation of abnormal noise at approximately 3,000 km. The flare with good roundness accuracy of 280 μm was confirmed to cause no abnormal noise even at 5,000 km.

From the results above, it can be said that the established bench test method can be applied to evaluate abnormal joint noise in vehicle driving.

4. Creation of Abnormal Noise Standards

Utilizing the bench evaluation method outlined above, the range of use wherein no abnormal noise is generated was investigated by looking into ball joint design variables. Because this phenomena is a problem of gasket guard net wear caused by gasket and flare partial contact, we limited our investigation to the main design variables that affect this contact, flare roundness and spring set load. Abnormal noise was judged with various combinations of oscillation angle, in a range of 0 to 0.50°, and temperature, in a range of 20 to 350°C, converting to driving distance, for every 1,000 km (up to 5,000 km), with the greatest noise levels plotted. Confirmation of noise levels was made according to the bench evaluation method when these parameters were changed, and the results mapped. These results are shown in Fig. 21.

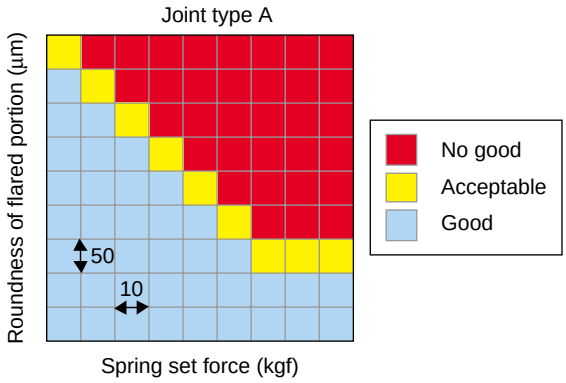


Fig. 21 Map of abnormal noise evaluation for ball joint

From this map it was learned that in order to restrict abnormal noise generation, it is most effective to have good roundness and a low spring set load. Also, even with the same spring set load, abnormal noise is generated in the range where flare roundness is large, shown in red, but no abnormal noise is generated in the low roundness range, shown in blue.

In the area of the map shown in blue, where abnormal noise is not generated, core wear powder contaminants have not accumulated on the surface and the normal surface state is maintained. That is to say, improving roundness accuracy and reducing spring set load actually reduces surface pressure on the contact surface, and is effective in restricting abnormal wear due to partial contact. Also, if roundness accuracy is established at a set value or less, abnormal noise will not be generated even if spring set load is increased. Thus, an improvement in roundness accuracy is thought to be effective at suppressing wear contaminant accumulation.

5. Summary

A detailed analysis of the causes of abnormal noise generation during ball joint oscillation was made, and the following results were attained.

(1) If the joint flare roundness accuracy is poor, there is abnormal wear due to partial contact between the gasket and the flare. This leads to powder formed from the wear of the thus exposed gasket guard net on the surface to adhere to the gasket surface. The gasket guard net is made of stainless steel, which means that when there is contact with the flare, which is also stainless steel, there is stainless-to-stainless contact. With oscillation, this results in an adhesion wear state, and when the parts slide, abnormal noise is generated due to the stick-slip phenomena.

(2) Based on the patterns of use on ordinary roads, data on the input frequency for the oscillation angle and temperature was simulated, and a simple bench test method was created. This makes it possible to evaluate abnormal noise.

(3) Using the bench evaluation method, a map was created from combinations of joint flare roundness and spring set load settings. This map can be used to judge abnormal noise.

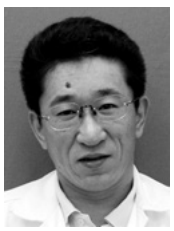
From the above, it is now possible to prevent abnormal noise, by determining the appropriate joint flare roundness accuracy and spring set load in the early design stage of development.

■ Authors ■


Masashi IWAI


Mototaka MAEDA


Etsuo TAKAKU


Yasunori MURAKAMI


Masanobu MIKI


Takeshi FURUKIDO

A New Analysis Approach for Motorcycle Brake Squeal Noise and Its Adaptation

Hiroyuki NAKATA* Kiyoshi KOBAYASHI** Masashi KAJITA*

ABSTRACT

Concerning the potential for low frequency brake squeal noises from motorcycles, the issue of the noise caused by the structural instability of the system was addressed with mode-coupling mechanism analysis utilizing complex eigenvalue analysis. The equation of motion of the brake system was simplified by converting it from the physical domain to the modal domain. The parameters required for the stability analysis were obtained from the normal mode solution of the system model. Moreover, it was possible to decrease the time required for repeat calculations with different friction coefficients and to complete instability-cause analysis in a mode by 70% or more by using a numerical-analysis solver. A highly accurate analysis model was established and applied in the new approach to specify the modes affecting squeal noises and to study countermeasures. From the test results for the subsequently modified brake system, it was verified that the new method is effective for quickly predicting and making countermeasures for brake squeal noises in the design stage.

1. Introduction

Brake noise adversely affects customer satisfaction, and, further, a number of man-hours are required to resolve the problem of brake noise. Thus, it is an important technical issue in the development of motorcycles. Squeal noise is one of the harshest of all brake noises to the ear. It is hypothesized that there are two generating mechanisms for squeal noise. The first mechanism is a phenomenon resulting from “stick-slip” on the friction side. The second mechanism is a phenomenon resulting from geometric instabilities of the brake assembly. One recent approach to the squeal noise caused by geometric instability of the system is the application of mode-coupling analysis of the mechanism using complex eigenvalues analysis. However, in the current complex eigenvalue method, complex eigenvalues are merely plotted on a complex plane. Thus, when the density of the mode is high, the identification of unstable modes is very difficult. Furthermore, complex eigenvalues are generally solved using MSC-NASTRAN. Since system model computation is only possible with one condition at a time, much time is needed in order to obtain a root locus by numerous calculations with different coefficients of friction. Therefore, phenomenon analysis and design change analysis are difficult. The authors have developed a new modeling and numerical analytical method, which makes it possible to obtain a root locus in a short time. At the same time, a new evaluation scale was developed to express the coupling strength of an unstably coupled mode[(1)].

Generally, squeal noise is defined to be in the range from 1 kHz to about 15 kHz. The range is divided into a low frequency domain (1 to 3 kHz) and a high frequency domain (5 kHz and above). In this research, the new

* Asaka R&D Center
**Tochigi R&D Center

analytical method concerning the geometric instability of the brake system was applied to the low-frequency squeal noise (1 kHz level) of motorcycle brakes to prove the appropriateness of the method.

2. New Analysis Approach

2.1. Simplification of the Equation of System Motion

The equation of system motion was greatly simplified by shifting the analysis of stability from physical to modal domains. The general equation of system motion can be expressed, in matrix form, as shown in equation (1).

$$[M]\{\ddot{u}\} + [C]\{\dot{u}\} + [K]\{u\} = \{F_f\} \tag{1}$$

where, M, C, and K are the mass, viscous damping, and stiffness matrices respectively for the non-friction system, u is the displacement vector of the system, F_f is the friction force applied to the system. A dot over the displacement denotes differentiation with respect to time. The stability evaluation model represents the contact surface between the disc and pads in the direction normal to the surface only. The friction force is derived by the following equation.

$$F_f = \mu N \tag{2}$$

N is the force between the pad and disc normal to the contact surface. μ is the coefficient of friction. Brake system instabilities can result if either the coefficient of friction or the normal force vary. The theory of brake squeal stability used here is such that the coefficient of friction is constant and the normal force varies as a function of the vibration of the pad and disc. The friction equation is then modified as follows.

$$\{F_f\} = \mu(\{N_{static}\} + \{N_{dynamic}\}) \tag{3}$$

While solving for eigenvalue, the static term will be dropped from the dynamic equations. The dynamic normal force is caused by the vibration of the pad and disc. The contact points are connected with a simple spring Ks. Dynamic friction force is modeled by the following equation.

$$\{N_{dynamic}\} = Ks\,(\{u_{N.disk}\} - \{u_{N.pad}\}) \tag{4}$$

where $u_{N,pad}$ denotes the displacement of the pad in the normal direction. The resulting friction force, F_f, is applied to degree of freedom (DOF) $u_{T,pad}$ and - F_f is applied to DOF $u_{T,disc}$, where T denotes the tangential direction.

The normal force is determined by the relative displacement (*rel*) between node pairs as using equation (5).

$$F_{T.rel} = -\mu \times K_s \times u_{N.rel} \tag{5}$$

Based on equations (2) – (5), the equation of motion (1) becomes

$$[M_g]\{\ddot{v}\} + [C_g]\{\dot{v}\} + [K_g]\{v\} = -\mu[K_f]\{v\} \tag{6}$$

where M_g, C_g and K_g are mass, damping and stiffness matrices, which includes the generalized DOF. The vector of the DOF is then as indiated in equation (7).

$$\{v\} = \begin{Bmatrix} u \\ \cdot\cdot \\ u_{N.rel} \\ u_{T.rel} \end{Bmatrix} \tag{7}$$

and the friction force term is as indicated in equation (8).

$$[K_f] = \begin{bmatrix} [0] & [0] & [0] \\ [0] & [0] & [0] \\ [0] & [K_{T.N}] & [0] \end{bmatrix} \tag{8}$$

By using Laplace conversion on equation (6), we arrive at system equation (9). For the stability analysis, we omit the viscous damping term $[C_g]$ from the system equation of motion, the purpose being to simplify the equation. The damping curve will be defined in the final stability analysis.

$$s^2[M]\{\bar{v}\} + [K]\{\bar{v}\} = -\mu[K_f]\{\bar{v}\} \tag{9}$$

where $\{\bar{v}\} = Laplace\{v\}$.

In order to convert equation (9) to a modal domain, equation (10) is utilized.

$$\{\bar{v}\} = [\psi]\{\bar{\gamma}\} \tag{10}$$

where $[\psi]$ is the mode shape and $\{\bar{\gamma}\}$ is the modal displacement.

By substituting equation (10) into a pre-multiplied equation (9) by $[\psi]^T$ the final system equation of motion in the modal domain is obtained (equation 11).

$$\left(s^2 + \begin{bmatrix} \omega_1^2 & 0 & \cdots & 0 \\ 0 & \omega_2^2 & \cdots & 0 \\ \vdots & \vdots & \ddots & \vdots \\ 0 & 0 & \cdots & \omega_n^2 \end{bmatrix} + \mu[\Lambda_f] \right) \{\bar{\gamma}\} = \{0\} \tag{11}$$

where the ω_i is the i -th natural frequency of the non-friction system.

From the definition of friction term $[\Lambda_f]$ in equation (8),

$$[\Lambda_f] = [\psi]^T[K_f][\psi] = Ks \cdot f([\psi_{T.rel}], [\psi_{N.rel}]) \tag{12}$$

$\psi_{T.rel}$ is the mode shape of contact point in the tangential direction.

$\psi_{N.rel}$ is the mode shape of contact point in the normal direction.

All parameters of the equation of motion (11) can be obtained from the normal mode analysis of a non-friction system. The necessary parameters are natural frequencies and the mode shapes of the contact points. All parameters represent real values and the results are all highly accurate. The complex eigenvalue in equation (11) can then be computed in a numerical analysis solver such as Matlab of The MathWorks Inc. Even when evaluating the complex eigenvalues with different coefficients of friction, there is

no need to change the model set up, and thus the results can be obtained immediately. It is possible to significantly decrease the amount of time required for computations by 70% compared to the conventional method.

2.2. New Evaluation Scale for the Instability Mode

Complex eigenvalue analysis of the actual part size can provide us with information about the probability of a squeal noise occurring. However, it does not provide us with any information regarding the magnitude of that noise.

Further, model accuracy, connecting conditions, boundary conditions, and natural frequency variations due to the tolerance of components in the analytic model are sometimes larger than the gap between the two modes, and may significantly affect the prediction of the complex eigenvalues. Thus, it is necessary to have evaluation criteria to determine the degree that the system is latently unstable as a portion of the squeal stability evaluation method. When the coupling strength is strong, the brake system possesses characteristics which can lead to squeal. The physical meaning of coupling strength is how quickly the eigenvalues converge when the coefficients of friction increase from zero.

Therefore, we define the new Evaluation Scale for the Instability Mode. It expresses qualitatively the coupling strength of the coupling mode.

The coupling strength between the two unstable modes which converge and split when the coefficient of friction increases can be expressed by Cs_{il} in equation (13)[1].

$$CS_{il} = \frac{[\Lambda_f]_{il} \cdot [\Lambda_f]_{li}}{(\omega_l^2 - \omega_i^2)} \qquad (13)$$

We use the complex eigenvalue and the coupling strength (CS) to evaluate the probability of brake squeal.

3. Examples of Brake Squeal Analysis in Motorcycles

3.1. Construction of Motorcycle Brake Systems

The brake system for motorcycles as used in the present study consists of twin piston floating-type calipers as shown in Fig. 1. The calipers are fastened to the front fork by bolts through the support. The brake discs are fastened to the wheel by bolts.



Fig. 1 Front brake system of test motorcycle

3.2. Understanding the Squeal Noise Phenomenon

Brake squeal noise was verified with a brake noise tester using an actual motorcycle. The characteristics of squeal noise were judged in a matrix mode simulating the conditions of users applying the brake with speed, extent of deceleration, temperature and applied pressure as parameters. The test results reveal that squeal noise is generated in the low deceleration zone of about 1.2 kHz as shown in Fig. 2.

3.3. Preparation of Analysis Model and Correlation

3.3.1. Component models for analysis

FE models were made for the disc, calipers, friction pads, support and the wheel. In order to ultimately obtain a reliable brake-system model, a high correlation between the FEM frequency-response function (FRF) and the impact excitation test are required for every component. Therefore, the model geometry and the physical property values are adjusted to exact values. The measurement points on the disc are shown in Fig. 3. The correlation of the impact excitation test and the FEM results is shown in Fig. 4.

The correlation was similar for the component parts. Another example is provided below. The measurement points on the caliper are shown in Fig. 5. The correlation of the impact excitation test and the FEM results is shown in Fig. 6.

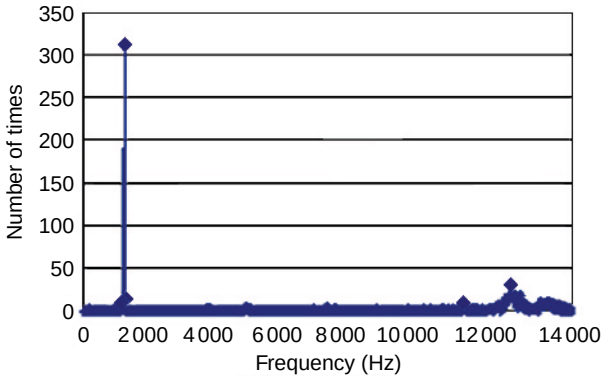


Fig. 2 Histogram of squeal noises

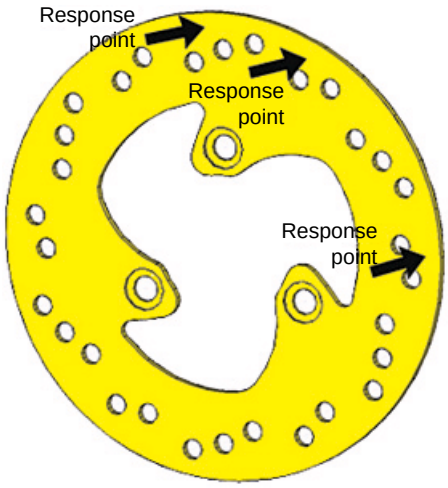


Fig. 3 FRF measurement points

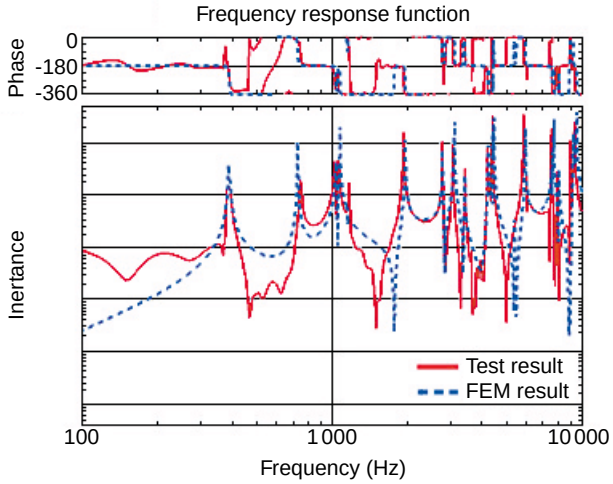


Fig. 4 Correlation sample of disc

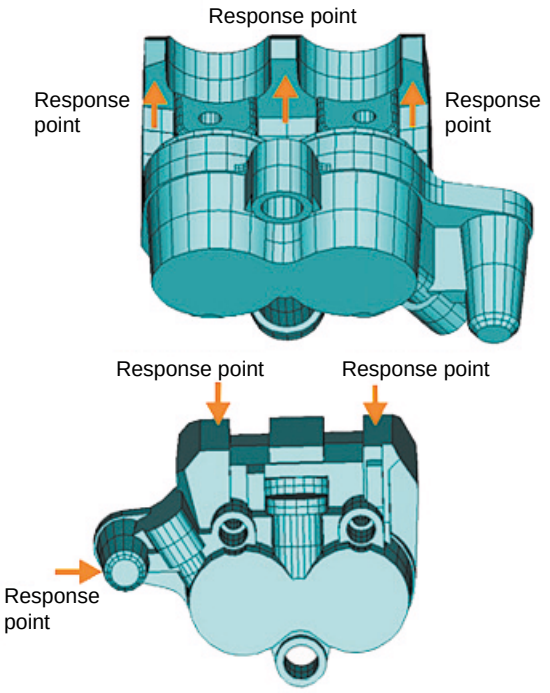


Fig. 5 FRF measurement points

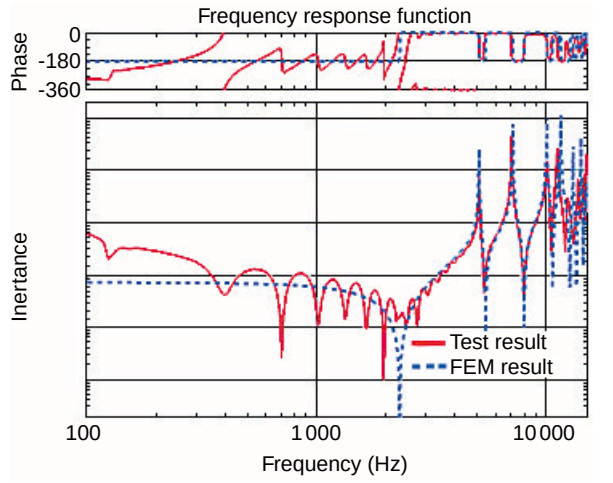


Fig. 6 Correlation sample of caliper

3.3.2. Sub-system construction and correlation

The connecting conditions of each part in the brake system defines the subsystem for every component, and the appropriate value was determined by verifying correlation.

(1) Modeling the brake disc and wheel subsystem

The brake disc is fastened to the wheel with bolts as shown in Fig. 7. The connecting conditions for the disc and wheel were determined using the correlation of the FRF in the target frequency domain. The correlation of the wheel and disc subsystem is shown in Fig. 8.

(2) Modeling the caliper and front fork subsystem

In the actual motorcycles, the calipers are fastened to the front fork with bolts through the support.

The connecting conditions between the support and the front fork, and the connecting conditions for the caliper and support were determined similarly.

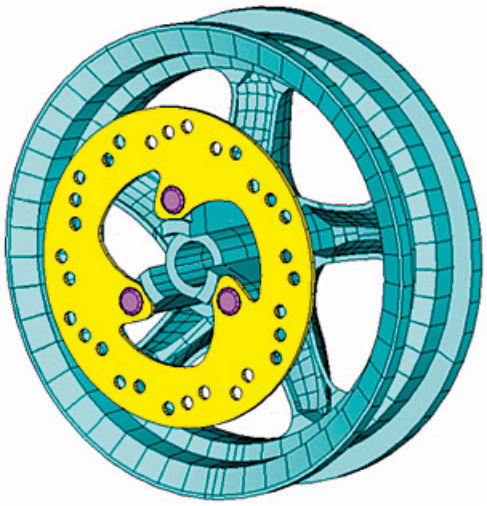


Fig. 7 Sub-system of wheel and brake disc

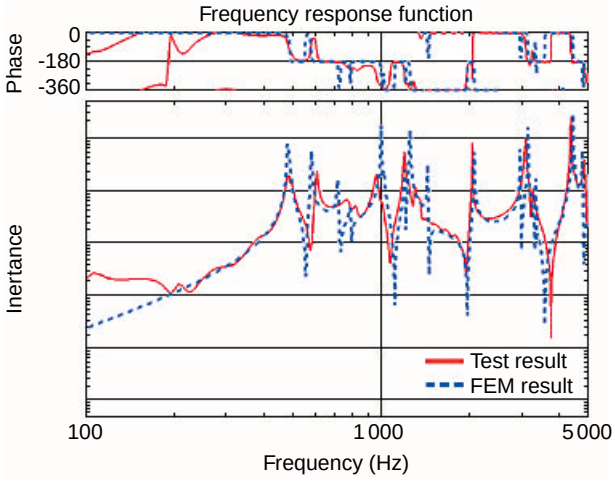


Fig. 8 Correlation of sub-system of wheel and brake disc

3.3.3. System model construction and correlation

The brake system model combined each subsystem, and the boundary conditions for the piston, the sliding section, the friction areas, etc. are also set to create a system model.

Correlation between the FRF calculation results for the various boundary conditions are modified. In this way, a brake system model with the FRF characteristics of real motorcycle conditions was obtained. A system model is shown in Fig. 9. The correlation is shown in Fig. 10. There is correlation of the frequency domain in which squeal occurs between the characteristics of the analytic model and a real motorcycle. Thus, the validity of the boundary conditions was verified.

Differences in conditions under which squeal occurs can be responded to by adjusting the boundary conditions.

4. Results and Mode Identification

4.1. Analysis Results

The parameters required for the equation of motion in the modal domain were determined by normal mode analysis of the system model. The root locus plots (Fig. 11, left) and coupling strength (Fig. 11, center) were computed by inputting them into the numerical value analysis solver together with different coefficients of friction.

This result expresses well the squeal noise phenomenon found near 1.2 kHz in actual real motorcycle measurements (Fig. 11, right). This indicates that this approach is effective.

4.2. Instability Mode Identification

The two coupling instability modes (1,220 Hz and 1,260 Hz) can be easily identified by the new stability metric (*CS*). The mode shape of the two instability modes was observed. The coupling pair mode shape is shown in Fig. 12.

The 1,220 Hz mode is the disc's '2.5 diameter node' mode. The 1,260 Hz mode is the wheel hub's torsion mode. The modes attributable to squeal were identified using this approach.

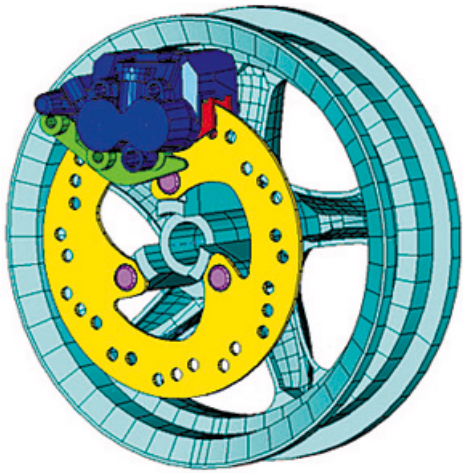


Fig. 9 Brake system model

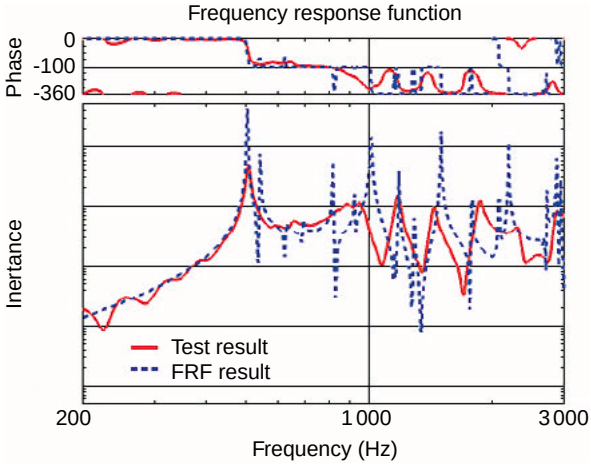


Fig. 10 Correlation in brake system model

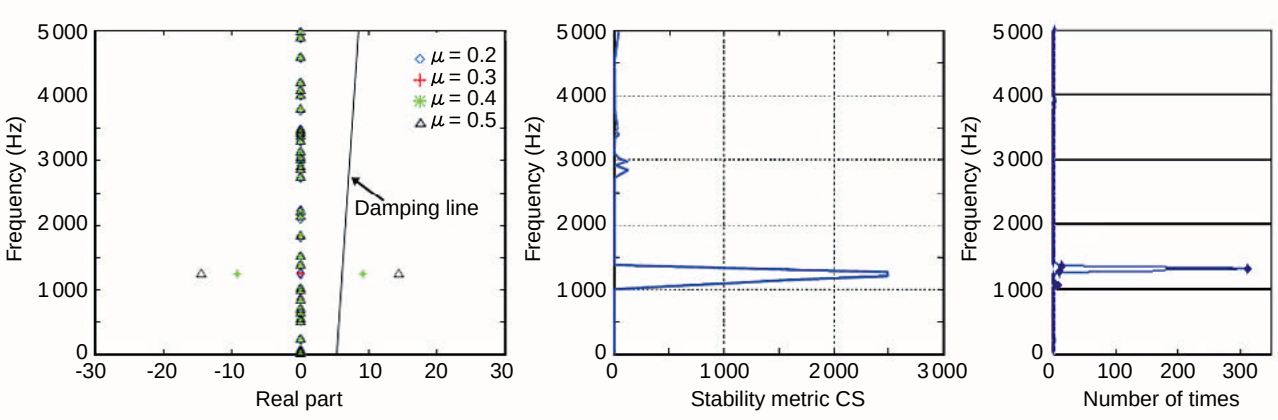


Fig. 11 Correlation between root locus plots, squeal noises and stability metric

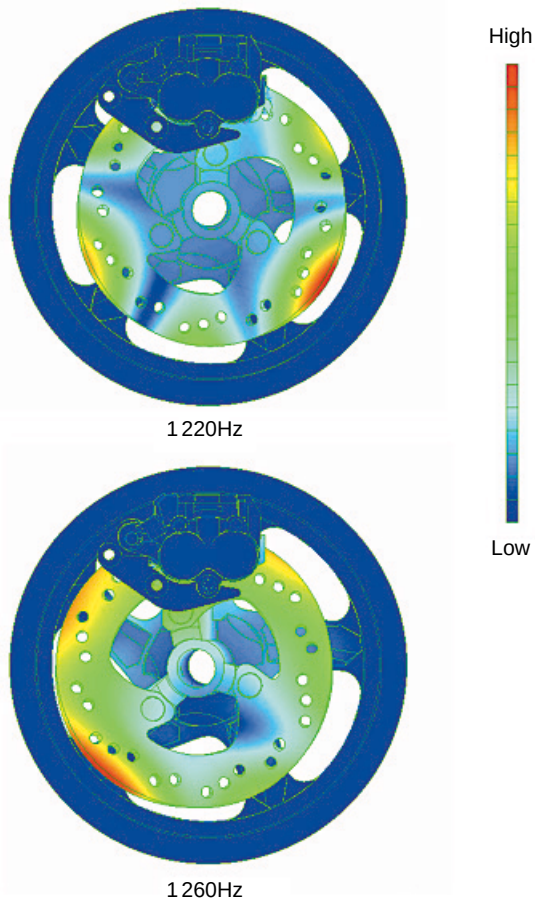


Fig. 12 Mode shape, pair modes

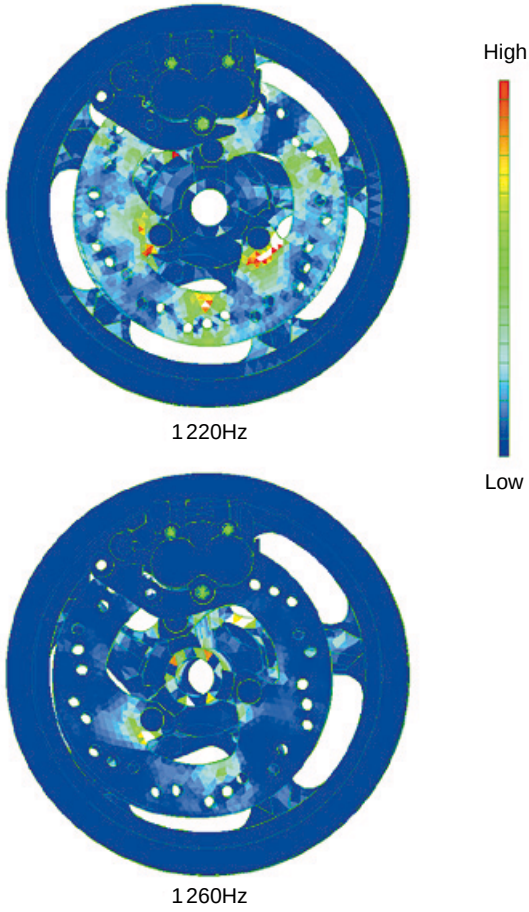


Fig. 13 Strain energy, pair modes

5. Examination of Countermeasure Specifications

5.1. Countermeasure Specification Concept

The strong coupling mode of the system converges and splits as the coefficients of friction increase. This indicates that there are two methods for addressing the issue of squeal noise. The first method is to separate the instability mode. That is, separating the eigenvalues of the two coupling modes so there is no high and positive damping even if affected by the coefficient of friction. The second method is to reduce the coupling strength of the instability mode. The examination of shape from these two viewpoints will provide countermeasures against brake squeal noises.

5.2. Examination of Countermeasure Specifications

This paper examined the separation in the two coupling pair mode. This approach is effective if attention is focused on the areas with high strain energy.

The strain energy of the coupling pair mode is shown in Fig. 13. The rate of distorted strain energy contribution for each part of the coupling pair mode is shown in Table 1. The 1,220 Hz mode has high strain energy in the disc attachment area. The 1,260 Hz mode has high strain energy in the wheel hub. Here, we changed the shape of the disc attachment area and the mode eigenvalue mode. This enabled us to determine design specifications for the disc which will increase the connecting mode separation by 3.3%.

Table 1 Contribution rate of strain energy

	Mode number 14 Frequency 1 220(Hz)	Mode number 15 Frequency 1 260(Hz)
Parts group	Strain energy (%)	
Pad A	0.37	0.6
Pad B	0.5	0.52
Bolt	0.37	0.3
Support	0	0.04
Caliper	0.64	2.44
Backplate A	0.49	0.14
Backplate B	0.06	0.1
Disc	57.1	17.08
Spring Ks	10.7	34.95
Beam	0.03	0.12
Wheel	30.2	43.71

6. Evaluation of Design Change Specifications

6.1. Stability Analysis

The root locus plots and coupling strength of the base specifications and the specifications of design change are shown in Fig. 14. The change in design specifications reduced positive damping and coupling strength. Brake specifications whereby squeal noises were not easily generated were predicted.

6.2. Prototype Evaluation

The predicted FRF and the FRF in the experiments are correlated, and it was verified that the characteristics of the design change specifications and the prototype corresponded, as shown in Fig. 15. It was confirmed that the prototype part was made according to the specifications.

6.3. Verification of Brake Squeal in Actual Motorcycles

The squeal noise was verified in a brake-noise tester using a motorcycle. The characteristics of squeal noise were judged in a matrix mode simulating the conditions of users applying the brake with speed, extent of deceleration, temperature and applied pressure as parameters.

The brake squeal occurrence frequency for the base specifications and the countermeasure specifications is shown in Fig. 16. Brake squeal disappeared in the vicinity of 1.2 kHz, our target problem area, confirming the effectiveness of the countermeasure. The charts on the left show the occurrence frequency of the noise. The charts on the right show the occurrence frequency for each condition.

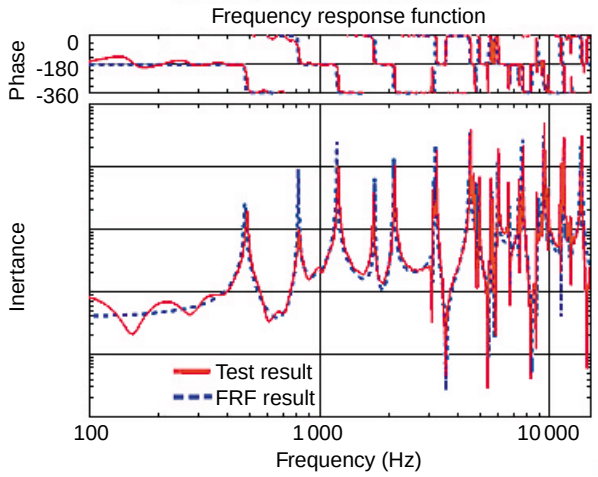


Fig. 15 Correlation between experiments and predicted values

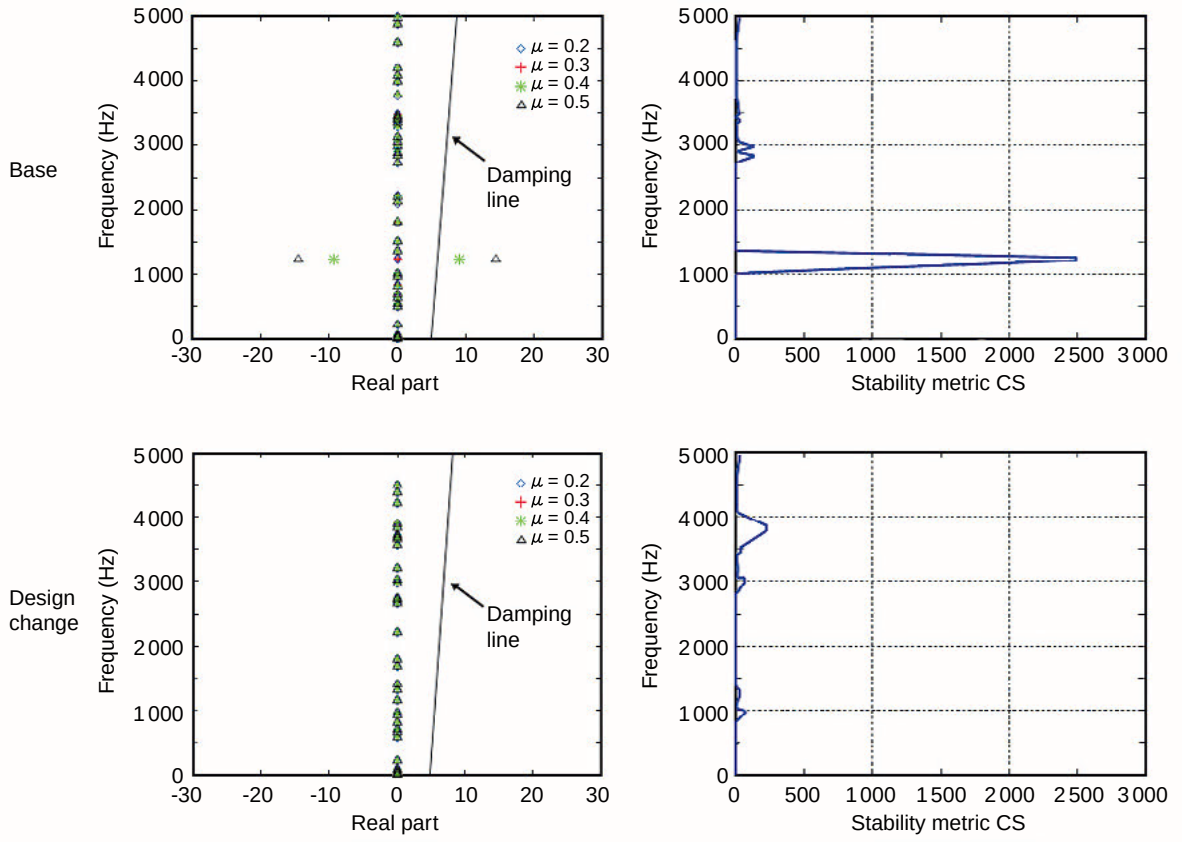


Fig. 14 Stability analysis of base specifications and specifications of design change

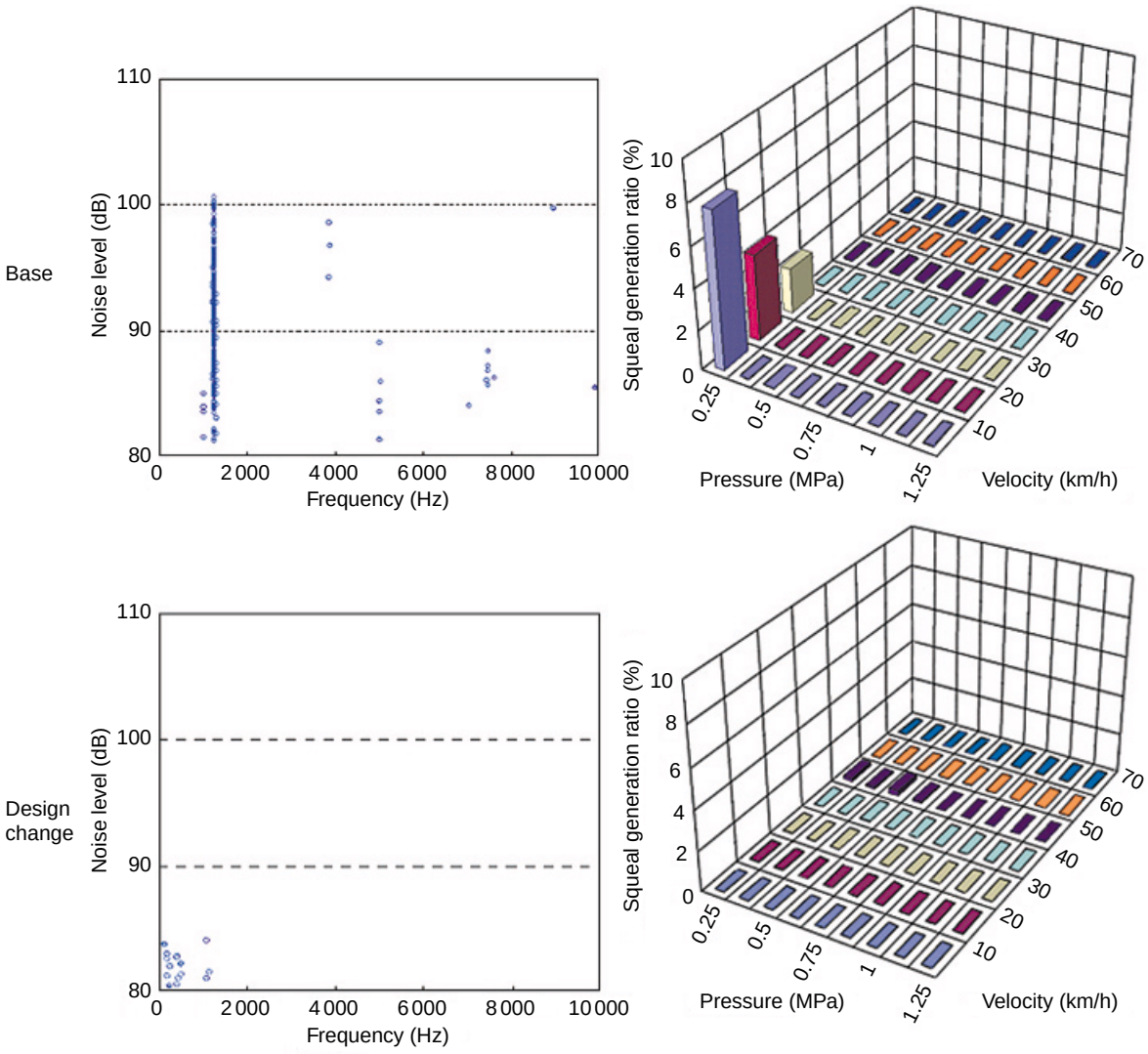


Fig. 16 Result of brake squeal noise tester matrix mode in base specifications and specifications of design change

7. Conclusion

A method to address the phenomenon of low frequency brake squeal noises in motorcycles easily and in a short period of time has been developed:

(1) The equation was made simple by converting the complicated equation of motion for the system from a physical domain to a modal domain. The method of calculating a complex eigenvalue analysis based on the normal mode analysis results in a short period of time was established.

(2) A new evaluation scale was defined for the instability mode wherein brake squeal occurs due to the coupling of two vibration modes in the brake system. This scale uses coupling strength as the basis for evaluation.

(3) A method for setting the boundary conditions, which expresses the squeal noise occurrence state of a brake system, was established.

(4) By revising the configuration of areas with high rates of strain energy contribution in the brake squeal generating mode, the countermeasures for the issue could be effectively applied.

Based on the above, we have identified the modes affecting squeal and clarified the countermeasure methods. Further, we verified the effectiveness of this approach in predicting squeal noise in the design stage.

References

(1) A New Analysis Method for Brake Squeal Part 1: Theory for Model Domain Formulation and Stability Analysis, SAE 01 nvc 103

■ Authors ■


Hiroyuki NAKATA


Kiyoshi KOBAYASHI


Masashi KAJITA

Connector Modeling in Vibration Prediction for Motorcycles

Hiroyuki KUWAHARA* Youji FUKUI*

ABSTRACT

Conventionally, when predicting motorcycle vibration using the data from drawings, connector characteristics for the components were uncertain. Therefore, using test pieces, we tested bolt fastening connector characteristics in order to investigate a potential analysis method. Further, a detailed FEM model was created, and the contact domain of connectors was calculated using the nonlinear-GAP static analysis of MSC/NASTRAN. Normal mode analysis was performed by converting the domain into a high rigidity spring element, and it was verified that the resonance frequencies for each mode were generally the same. By applying this method to an actual motorcycle and by also applying NASTRAN's RESVEC calculation to connectors of a component, the FEM model was improved.

1. Introduction

In motorcycles the frame is the key component that connects the engine, drive train, steering, suspension and other components. The frame must be strong enough to support the weight of these components and have appropriate stiffness in terms of vehicle performance. At the same time vibration characteristics acceptable to the rider must also be taken into account. These elements are interrelated, and a well-balanced structure is required. There are various types of engines and frames, and the element balance changes according to the vehicle performance and use. In addition, the nature of motorcycles is such that light weight and compact size are also vital issues, and the engine is often utilized as a part of the frame stiffness or rigidly connected to the frame due to limitations of the chain-drive drive train. Under these conditions, vibration analysis was performed in conjunction with other departments for strength, steering stability and other characteristics, and a finite element model was created to serve as a basis for analysis on the assumption of sharing with other applications.

* Asaka R&D Center

2. Creating the Component Model

Recent advances in digital technology have promoted more detailed finite element models of the frame, muffler and other components, and major advances have also been made in terms of accuracy. Conventionally modeling required enormous amounts of manpower, but the recent adoption of 3D drawings has facilitated modeling and made it possible to create finite element models of components almost in parallel with drawing creation. The modeling technology of each component affects the completed vehicle vibration prediction accuracy, and it is extremely important that continued efforts be made to improve the accuracy of modeling technology through experimental modal analysis in undetermined elements such as welding and press fitting.

In addition, at an engine speed of up to approximately 10,000 rpm and taking into account second order vibration, a frequency range of up to 330 Hz is necessary for the completed vehicle vibration prediction of motorcycles. The component model accuracy was improved using experimental modal analysis and the point impedance at the connection points.

2.1 Improving Modal Model Accuracy

It has been said that in order to obtain a correct modal model for the completed vehicle model, component modal models are necessary in the frequency band approximately 2.5 times that required for the completed vehicle model. This means that to predict completed vehicle vibration for motorcycles up to 330 Hz, the components must be expressed accurately up to 800 Hz, and extremely advanced measurement technology is needed to extract good modal data in this frequency range. Most causes of calculation and test MAC (Model Assurance Criterion) matrix deterioration are rooted in insufficient measurement, and if the initial MAC matrix is inaccurate, then correct modal model updating becomes difficult. The procedure for efficiently improving model accuracy consists of dividing component models into individual groups for which the mode shape or the modal frequency sensitivity can be calculated. Applying this procedure clarifies the model deficiencies, such as problems with modeling, welding, contact, plate thickness and so on. Fig. 1 shows an example motorcycle frame FEM model and the calculations and test MAC values obtained using an updated model.

2.2 Utilizing Local Stiffness

Correct connector characteristics depend on the vibration prediction accuracy of the component connection points, so it is extremely important to focus on the connection points. Thus, these were verified using the point impedance. The point impedance is the frequency response function (FRF) of the local vibratory response (generally, acceleration) according to the local force input at that same point. In MSC-NASTRAN, the local modes that produce rigid behavior can be calculated from V70.0. These modes supply the residual stiffness that is missing from normal mode analysis, and are thus called residual modes (RESVEC: Residual Vector)[1]. An extremely accurate frequency response function can be easily obtained by taking into account the rigid body modes, flexible modes and residual modes. Fig. 2 shows example frequency response functions when taking into account RESVEC and when synthesized from only the flexible modes up to 500 Hz. The point impedance can be divided into the four states of (1) rigid body behavior, (2) resonance behavior, (3) stiffness behavior and (4) local resonance behavior.

Connection points are usually domains that induce some weak point, so the stiffness behavior significantly affects the component connection. Stiffness behavior is generally local mode pre-resonance behavior at high frequencies. In order to correctly express the connector characteristics, it is important to obtain a modal model which includes the local mode that generates this stiffness behavior. If the local stiffness of the connector can be taken into account, then

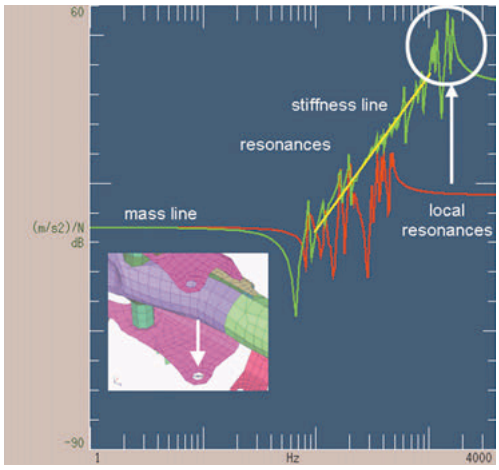


Fig. 2 Frequency bands for driving point FRF

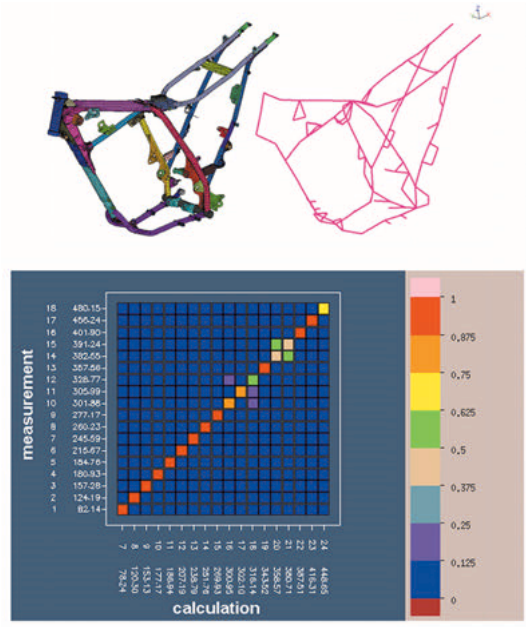


Fig. 1 Model and modal updating results of a motorcycle frame

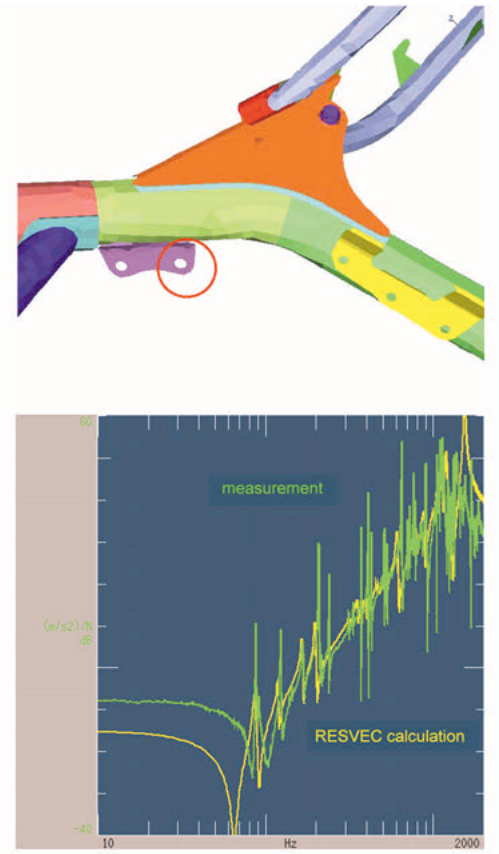


Fig. 3 Local model and driving point FRF updating procedure

there is no need to update the model expressing resonance behavior up to a sufficiently high frequency as previously mentioned. Therefore, the component modal models should be updated up to 1.5 times the frequency required by the completed vehicle model (approximately 500 Hz), and point impedance measurement should be utilized to correctly express the effects of local stiffness. The accuracy of local modeling (welding, press fitting, etc.), such as that shown in Fig. 3, can be improved by comparing the frequency response function calculated using RESVEC and the point impedance.

3. Component Connections

Elements of motorcycle component connectors include bolt fastenings, bearings, bushings and so on, and understanding the connector characteristics of these elements is an extremely important factor in vibration prediction and various other analyses. There are a number of methods for predicting system vibration such as the partial structure synthesis method, but connections between components are generally represented by a spring with six degrees of freedom as shown in Fig. 4.

However, these springs were obtained experimentally, and a database comprising a large number of tests was required[2]. In addition, when the structure changed significantly, these changes sometimes could not be supported or, occasionally, similar connectors were used, thus naturally lowering the prediction accuracy. To solve these problems, attempts were made to more analytically understand bolt fastening which is a typical connection method for motorcycles. Therefore, analysis was carried out using a test piece forming a simple connector and a simple model created by cutting out a portion of the frame in order to understand connector phenomena in detail. Finally, an example of an actual motorcycle engine-frame connection is presented.

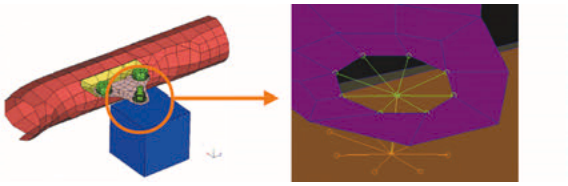


Fig. 4 Conventional connector modeling

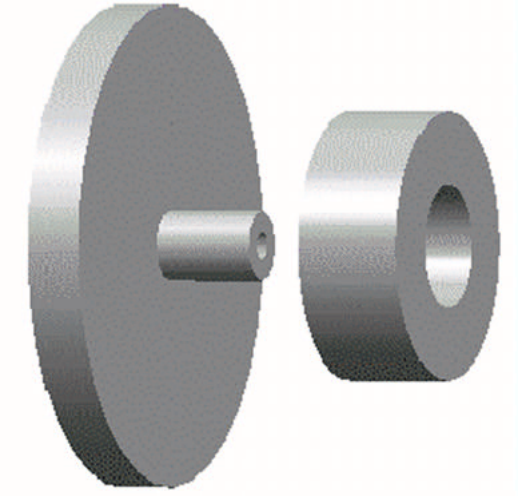


Fig. 5 Structure of test piece

3.1 Test Piece

The test piece hypothesized a motorcycle engine mount, and consisted of a two-piece component connected with an M10 bolt as shown in Fig. 5. The bolt axial force was controlled by affixing two strain gauges on the sides of the bolt. The surface roughness was at the same machining level as the frame and engine connectors. Tests varying the bolt axial force, attached plate thickness and other factors were conducted to investigate the relationship with the natural frequency, and the results showed that changes in the attached plate thickness had a significant effect.

Therefore, a detailed partial analysis model for the above test piece was created as shown in Fig. 6, and NASTRAN nonlinear-GAP analysis was performed to investigate deformation of the contact domain[3]. A 1/4-scale model was used to reduce the analysis time. For modeling conditions, peeling was thought not to occur between the bolt flange and the thin plate, so GAP elements were set only in the collar and thin plate contact portions, and the bolt flange and thin plate were connected by high stiffness springs. Fig. 7 shows the deformation drawing analyzed at an axial force of 1000 N. This figure shows that when axial force is applied, the thin plate portion peels from the collar. The same analysis was performed with varying plate thicknesses, and Fig. 8 shows the graph of the GAP element reaction force and the distance in the radial direction.

Portions with a positive reaction force are thought to be where the collar and thin plate are in firm contact, and the figure shows that the contact domain increases with the

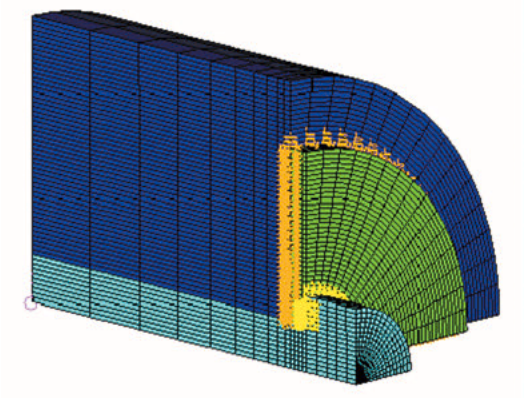


Fig. 6 Fine mesh model for GAP analysis

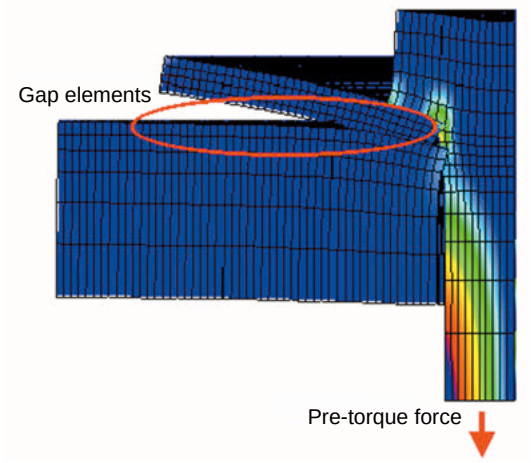


Fig. 7 Deformation result

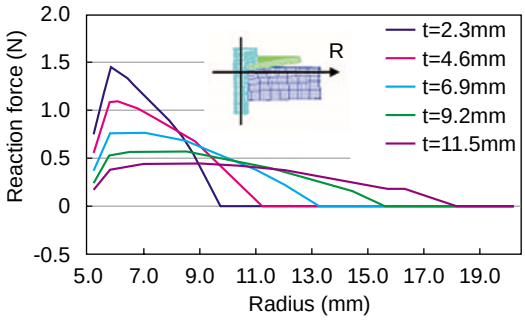


Fig. 8 Determination of contact area radius by reaction force of GAP elements

thickness of the attached thin plate. Once the contact domain was known, only this contact domain was connected with high stiffness springs (1e4N to 1e5N/mm). Modeling was then performed again, followed by normal mode analysis, and the results were compared with the measurement values for verification. Fig. 9 shows the calculation flow, and Figs. 10, 11 and 12 show the calculation and test results for each plate thickness and the resonance frequencies of an integrated body (referred to as "1 body" in the figures) which are provided as reference. The resonance frequencies matched closely regardless of the thin plate thickness, thus confirming the validity of the developed modeling method.

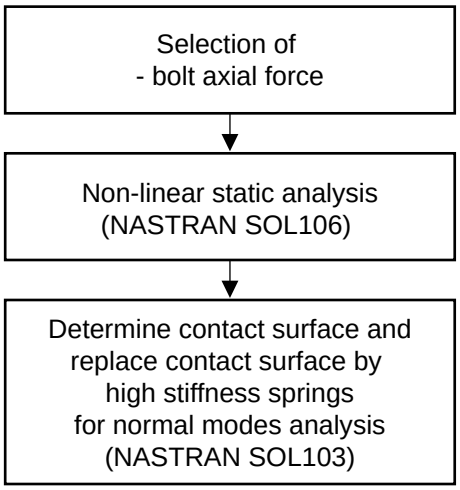


Fig. 9 Analysis flow

3.2 Frame Cut-out Model

Next, analysis was performed on a connector often applied to motorcycle engines and frames. The frame portion of the analysis model consisted of a cut-out part of an actual frame that was restrained at both cut ends, and the engine portion was a cubed block model. Fig. 13 shows

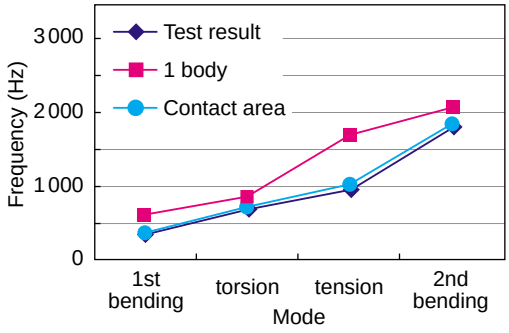


Fig. 10 Natural frequency of test-piece (t = 2.3 mm)

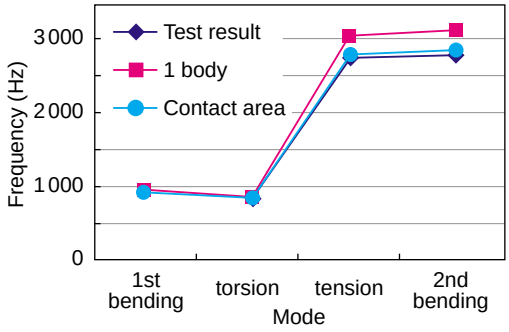


Fig. 11 Natural frequency of test-piece (t = 4.6 mm)

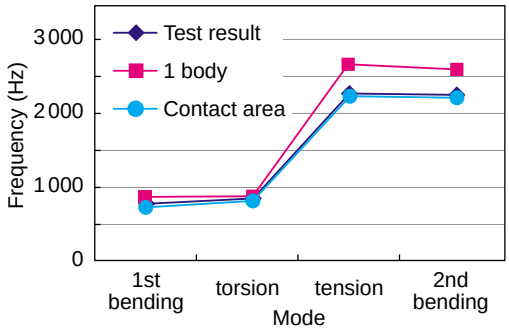


Fig. 12 Natural frequency of test-piece (t = 11.5 mm)

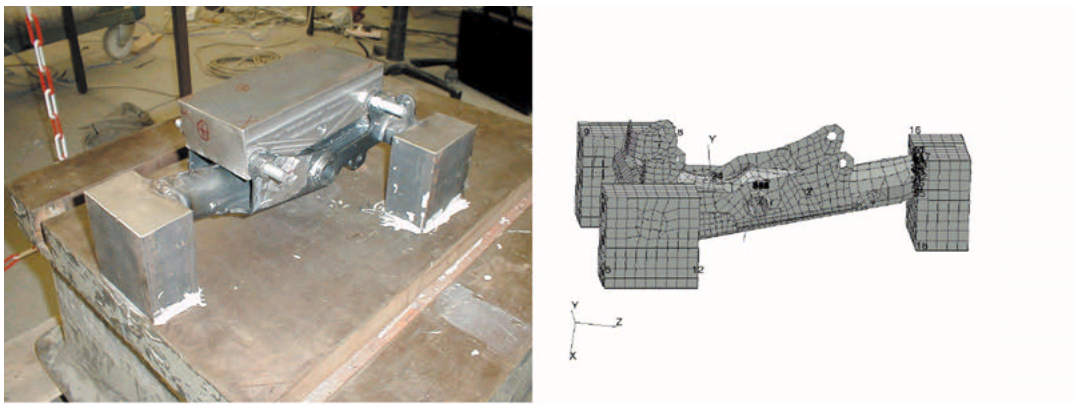


Fig. 13 Simplified model of engine frame connection and FEM model

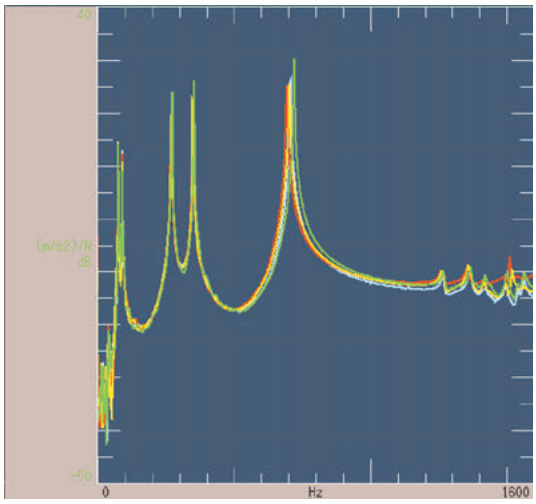


Fig. 14 Impact test result for reciprocity

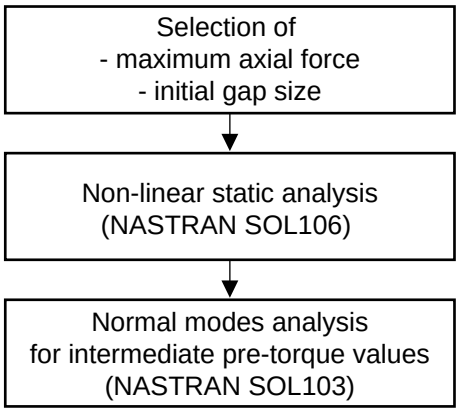


Fig. 16 Analysis flow

the actual model used in the test and the FEM model. There are some faint mode resonance frequencies that can be confirmed by simplifying the model in this manner, and the excitation test results are shown in Fig. 14. This excitation test was performed to confirm reproducibility, and the bolt axial force was controlled according to the tightening torque. The modes near 800 Hz show significant variance due to repetition, and this is thought to be mainly due to the bolt tightening torque control. In contrast, the test piece described in the previous section did not experience significant variance up to 3.2 kHz.

In addition, there is an approximately 0.5 to 1.0 mm tolerance between the engine and frame mounts due to production related reasons. When creating a bolt fastening model, GAP elements are thought to exist in four domains as shown in Fig. 15. However, as shown in this same figure, depending on the mounting configuration it is also possible to reduce this number to two GAP elements without lowering the accuracy.

The bolt axial force can be expressed by adding the opposite force in the axial direction between the bolt and

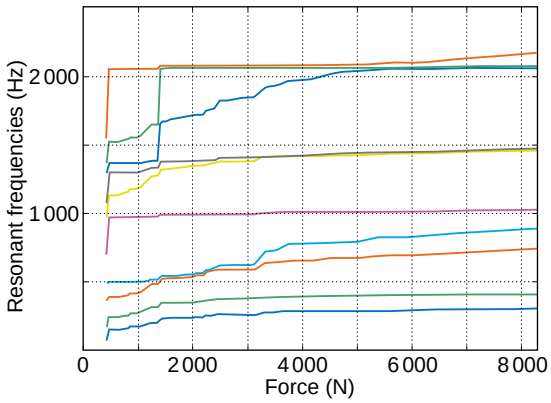


Fig. 17 Effect of bolt force on resonant frequencies

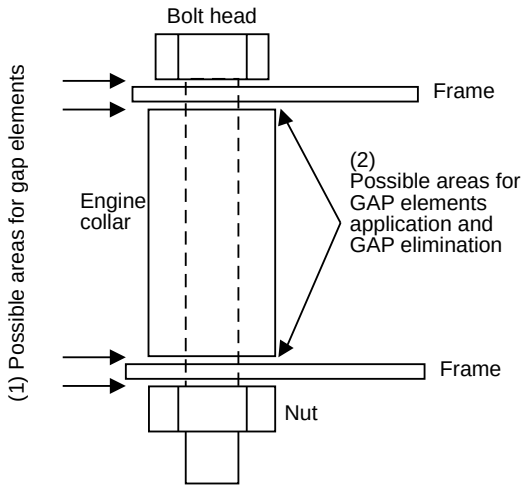


Fig. 15 Possible areas for using GAP-elements, Reduced number of GAP-areas

the nut. The effects of initial tolerance and axial force on the resonance frequency of each mode can be understood by specifying the maximum axial force, performing nonlinear static analysis using MSC-NASTRAN GAL elements, and then restarting normal mode analysis immediately thereafter. Fig. 16 shows this analysis flow, and Fig. 17 shows the analysis results. The horizontal axis is the bolt axial force, and the vertical axis is the resonance frequency. These results show that the gap closes gradually as the axial force is increased, and the resonance frequency of each mode increases together with the axial force. In addition, the rate of increase depends on the mode.

This same figure also shows that within the practical frequency range (0 to 330 Hz) for motorcycles, changes in the axial force around the normal bolt axial force of 8,000 N have little effect on the resonance frequency. Therefore, the GAP areas can also be replaced by high stiffness springs in those domains. However, if the frequency range is expanded to include higher frequencies, the effects of GAP analysis begin to appear. In this analysis it is extremely important to use highly detailed models near the bolt contact domains. Furthermore, though this method aids in the understanding of overall behavior, it is necessary to use an even finer mesh size in order to increase connector model accuracy. Applying this method for completed vehicles also achieves a balance with calculation resources.

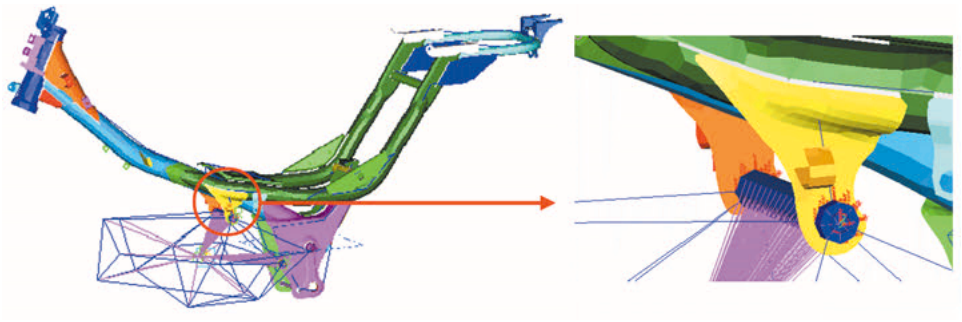
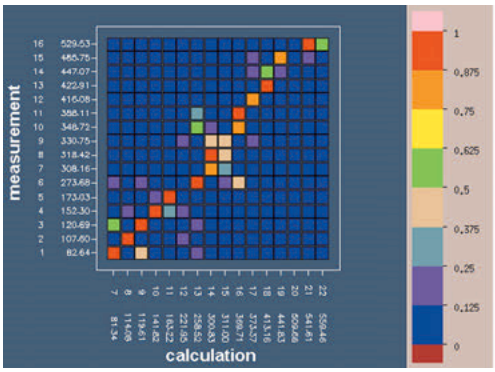


Fig. 18 Engine-frame FEM model (by new model)



Ref. ID	Ref. Freq.	Ver. ID	Ver. Freq.	Diff.	Diff. (%)	MAC
1	82.64	7	81.34	-1.31	-1.58	0.99
2	107.60	8	114.08	6.49	6.03	0.94
3	120.69	9	119.61	-1.08	-0.89	0.95
4	152.30	10	141.82	-10.48	-6.88	0.89
5	173.03	11	163.22	-9.82	-5.67	0.98
6	273.68	13	258.52	-15.16	-5.54	0.94
8	318.42	14	300.83	-17.59	-5.52	0.91
7	308.16	14	300.83	-7.33	-2.38	0.82
11	388.11	16	369.71	-18.40	-4.74	0.94
10	348.72	16	369.71	20.99	6.02	0.87
12	416.08	17	373.37	-42.71	-10.26	0.81
13	422.91	18	413.16	-9.75	-2.31	0.91
14	447.07	18	413.16	-33.91	-7.59	0.53
15	485.75	19	441.83	-43.92	-9.04	0.79
16	529.53	21	541.61	12.08	2.28	0.90

Fig. 19 MAC value of calculation and measurement results (by new model)

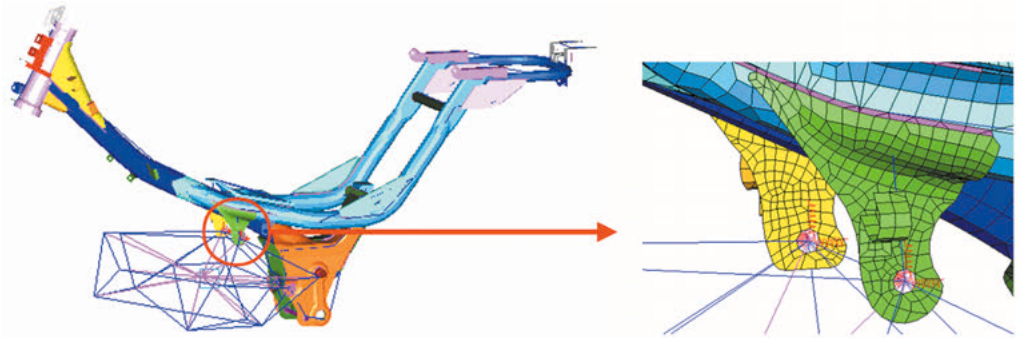
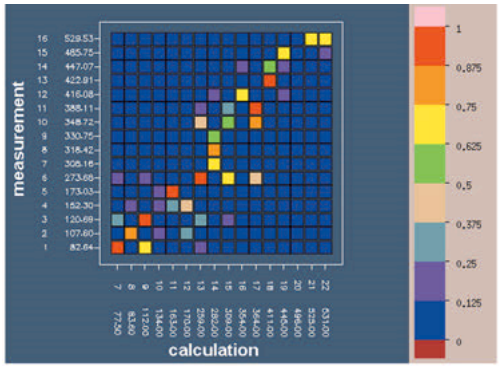


Fig. 20 Engine-frame FEM model (by conventional method)



Ref. ID	Ref. Freq.	Ver. ID	Ver. Freq.	Diff.	Diff. (%)	MAC
1	82.64	7	77.50	-5.14	-6.22	0.93
2	107.60	8	83.60	-24.00	-22.30	0.80
3	120.69	9	112.00	-8.69	-7.20	0.94
4	152.30	12	170.00	17.70	11.62	0.41
5	173.03	11	163.00	-10.03	-5.80	0.97
6	273.68	13	259.00	-14.68	-5.36	0.89
6	273.68	15	309.00	35.32	12.91	0.70
7	308.16	14	282.00	-26.16	-8.49	0.69
8	318.42	14	282.00	-36.42	-11.44	0.80
9	330.75	14	282.00	-48.75	-14.74	0.49
10	348.72	17	364.00	15.28	4.38	0.85
10	348.72	15	309.00	-39.72	-11.39	0.57
11	388.11	17	364.00	-24.11	-6.21	0.93
12	416.08	16	354.00	-62.08	-14.92	0.70

Fig. 21 MAC value of calculation and measurement results (by conventional method)

3.3 Engine-Frame Connection Model

Next, an actual engine-frame connection was investigated. Fig. 18 shows an FEM model of the engine-frame connection. In the practical frequency domain of 0 to 330 Hz, the engine is treated as a rigid body model, and the model was created using rigid body elements for all portions except for the collar portions of the connected engine. The engine collar portions and frame hanger portions were created in detail, then modeling was performed so that these portions contacted each other at the surfaces in the same manner as in the test piece, and they were connected by high stiffness springs. Fig. 19 shows the calculation and test MAC values for this engine-frame connection model. The MAC values are extremely high, and the frequency error is also within 5% for the most part, indicating the validity of this modeling method.

The model created using the conventional method and the corresponding calculation and test MAC values are shown in Figs. 20 and 21 for reference. However, the connector spring constant must be identified through tests. In addition, the rigid body connection points of the hangers which are non-connected as shown in Fig. 4 are vague, which causes the spring constant of the identified connector characteristics to change, so there are many undetermined elements. Furthermore, it was found that performing identification approximately five times such as in this study did not yield sufficient MAC values.

In the conventional method, connector characteristics were selected by experienced staff after thoroughly understanding the shape. However, this method provided highly accurate results simply by creating a detailed model of the connectors.

4. Conclusion

This paper presented the contents of connector characteristics that are important for the vibration prediction of motorcycles. The conclusions reached are as follows.

(1) The connector characteristics between components that were formerly obtained though tests can be obtained analytically by utilizing GAP analysis.
(2) The accuracy of local stiffness models for connectors can be improved by using RESVEC calculation. In addition, the number of flexible modes used can be reduced without causing a loss in accuracy.

References

(1) Yamazaki, Takagi and Yamamoto, The development of a method for modeling ADAMS flexible body using residual vectors, Proceedings of MSC. Software Solution Forum 2000

(2) Tanaka and Saegusa, Vibration models and simulation, Ouyou Gijyutsu Shuppan, 1984, P. 281 – 289

(3) Kiku, Sekine and Ryoukata, Prediction Technique for Gear Vibration Transfer in Engine Mounting Systems, Honda R&D Technical Review, vol. 13 No. 1, p. 145 – 150 (2001)

■ Authors ■



Hiroyuki KUWAHARA



Youji FUKUI

Constructing n-sided G1 Patches with the Energy Integral Minimization

Kentaro MATSUMOTO * Hongjun XIE *

ABSTRACT

A technique to create n-sided patches from n closed boundary curves with G1 continuity to the bounding surfaces has been developed. By using the data points on the boundary curves and the normal vectors of the bounding surfaces as the constraints, least squares patches are constructed with G1 continuity based on squares error minimization. Furthermore, the energy integral of the B-spline basis functions is calculated and the least squares patches are smoothed with energy integral minimization. Two coefficients, β (stretching term) and γ (bending term), are introduced as the elements used to adjust the smoothing. Consequently, the quality of the n-sided patches is improved. By using this technique the quality of the n-sided patches required for high quality styling design is improved and the time used to keep G1 continuity to the bounding surfaces is reduced.

1. Introduction

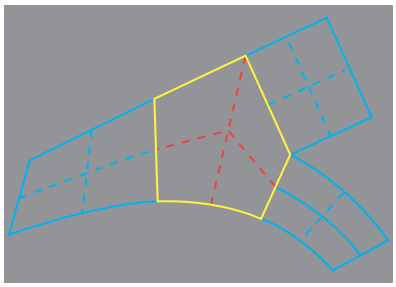
The problem of interpolating n-sided patches other than 4-sided patches is one of the central problems for CAGD (Computer Aided Geometric Design), and this is also one of the necessary functions for the development of CAD (Computer Aided Design) applications. Particularly when bounding surfaces exist, interpolating n-sided patches with G1 continuity to their bounding surfaces is important for creating high quality design data.

There are two typical approaches for interpolating n-sided patches. In the first method, an n-gon is divided into several quadrangles and then 4-sided patches are created for each quadrangle so that these 4-sided patches have G1 continuity with each other[1, 2]. The key in this method is how to determine the internal curves used to divide the n-gon as the quality of the n-sided patches is influenced by these internal curves. However, there is no simple method to determine satisfactory internal curves, which causes problems in many cases. Fig. 1, Fig. 2 and Fig. 3 show the wire frame and zebra displays of 5-sided and 6-sided patches created with commercially available CAD application using this method. It should be noted that the n-sided patches in these three cases are obviously unusable as styling surfaces.

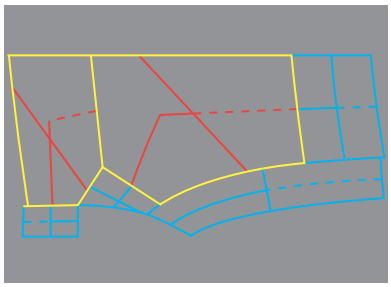
In the second approach, the least squares method is used to interpolate n-sided patches[3]–[5]. In this method, the data points are acquired from the n-gon boundary curves and a base surface that covers the n-gon region is created by solving the least squares equations. The n-sided patch to be interpolated is then completed by trimming the base surface along these boundary curves. Compared to the first approach, this method provides us with a single, distinct solution by directly solving equations and thus the arbitrariness involved in determining the internal curves is removed. This paper adopts the least squares method.

However, the quality of n-sided patches created using the least squares method depends on the data points, that is, the boundary curves, so in many cases surface smoothing must be considered. There are many methods developed for surface smoothing[6]–[10]. In this paper surface smoothing is achieved by calculating and minimizing the energy integral of the surface. Consequently, the quality of the n-sided patches is greatly improved.

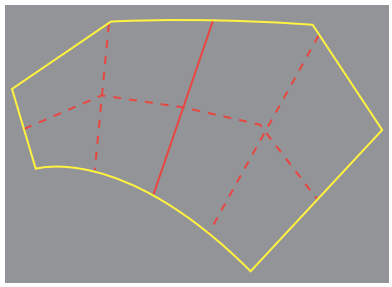
* Wako R&D Center



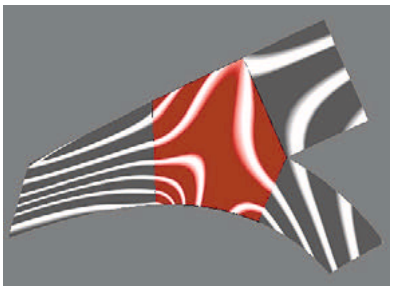
1-1 face



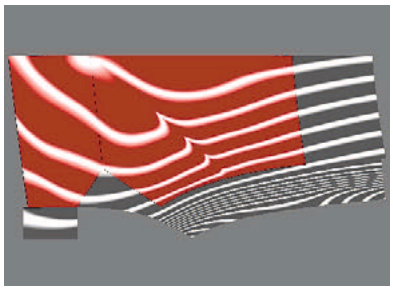
2-1 face



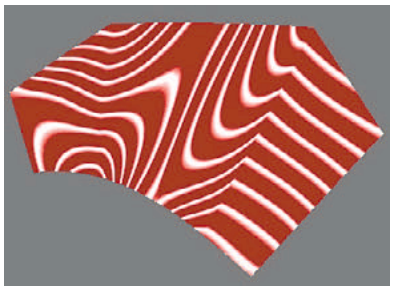
3-1 face



1-2 zebra



2-2 zebra



3-2 zebra

Fig. 1 Case 1: A 5-sided patch filled by CATIA

Fig. 2 Case 2: Two 5-sided patches filled by CATIA

Fig. 3 Case 3: A 6-sided patch filled by CATIA

2. Interpolation of the n-sided Patches by the Least Squares Method

2.1. Acquiring Data Points and Normal Vectors

When n closed boundary curves *curve*[*k*] are given, the data points $\vec{Q}_a$ for applying the least squares method can be obtained from the boundary curves. If *len*[*k*] is the length of curves respectively, l_0 is the maximum value of the lengths *len*[*k*] and m_0 is the number of points taken from the longest curve, then the number of points *m*[*k*] taken from each curve and the total number of points N_p are as follows:

$$N_p = \sum m[k] = \sum m_0 \cdot len[k]/l_0 \qquad (1)$$

Here, m_0 should be determined according to the tolerance and calculation efficiency. (In this paper m_0 is set as 200. Thus, for a 5-sided patch the total number of points is 1,000 or less and for a 6-sided patch it is 1,200 or less). The data points $\vec{Q}_a$ ($0 \le a < N_p$) taken from the boundary curves in this way should lie on the base surface $\vec{S}(u, v)$ that will be created by the data points, and they should satisfy the following equations.

$$\vec{S}(u_a, v_a) = \sum_{i=0}^{p_1-1} \sum_{j=0}^{p_2-1} N_i(u_a) M_j(v_a) \vec{P}_{ij} = \vec{Q}_a \qquad (2)$$

Here, $N_i(u_a)$ and $M_j(v_a)$ are the B-spline basis functions in the parameter u and v directions, respectively. p_1 and p_2, which represent the number of control points in the u and v directions of the base surface, can be defined as the sum of degrees and number of spans in the u and v directions, respectively. Further, $\vec{P}_{ij}$ are the unknown control points of the base surface $\vec{S}(u, v)$, and their total number is $q = p_1 \cdot p_2$.

When bounding surfaces do not exist, denoting the tangent vectors at the intersection O_k of boundary curves *curve*[*k*] and *curve*[*k*+1] as $\vec{V}_k$, $\vec{V}_{k+1}$, and if the normal vector of plane composed from $\vec{V}_k$, $\vec{V}_{k+1}$ is $\vec{n}_k = \vec{V}_k \times \vec{V}_{k+1}$, then, as constraints for equation (2), the normal vector at

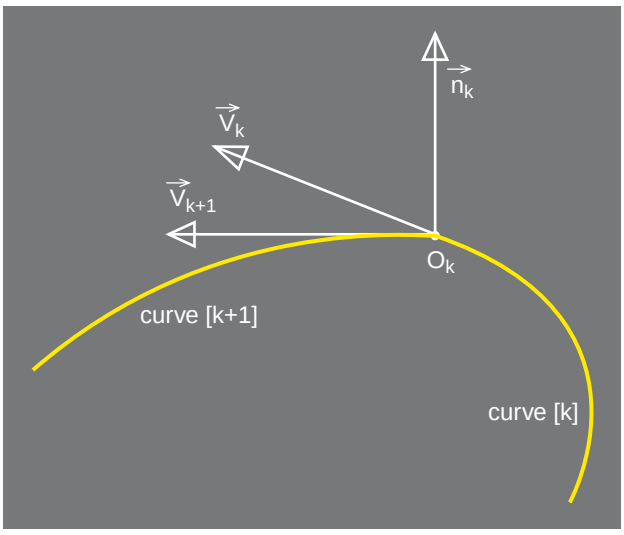


Fig. 4 A normal vector of the filling surface at the intersection of two boundary curves

the point O_k of the created n-sided patch must coincide with $\vec{n}_k$.

On the other hand, when bounding surfaces exist, the normal vectors $\vec{n}_a$ of the bounding surfaces at the related

data points $\vec{Q}_a$ lying on the boundary curves must be set as constraints for equation (2) in order to ensure G1 continuity between the created n-sided patches and the bounding surfaces. Assuming that the number of normal vectors $\vec{n}_a$ acquired from the bounding surfaces is N_n, the n-sided patches as well as the base surface satisfy the $2N_n$ constraint equations as follows:

$$\vec{n}_b \cdot \vec{S}_u(u_b, v_b) = \sum_{ij} N_i'(u_b) M_j(v_b) \vec{n}_b \cdot \vec{P}_{ij} = 0 \qquad (3)$$

$$\vec{n}_b \cdot \vec{S}_v(u_b, v_b) = \sum_{ij} N_i(u_b) M_j'(v_b) \vec{n}_b \cdot \vec{P}_{ij} = 0 \qquad (4)$$

Here, $\vec{S}_u(u, v)$ and $\vec{S}_v(u, v)$ represent the partial derivative of the base surface $\vec{S}(u, v)$ with respect to parameters u and v, respectively. $N_i'(u)$ is the derivative of $N_i(u)$, and $M_j'(v)$ is the derivative of $M_j(v)$.

2.2. Creating the Least Squares Plane

In order to calculate the B-spline basis functions and their derivatives in equation (2), (3) and (4), the location parameters (u_a, v_a) of the data points $\vec{Q}_a$ and the normal vectors $\vec{n}_a$ are required. The location parameters (u_a, v_a) for each point can be obtained from the point group $\{\vec{Q}_a\}$ as follows. First, the center of gravity G_0 of the point group $\{\vec{Q}_a\}$and its squares error are calculated. Then, the principal axis of inertia and the principal moment of inertia of the point group $\{\vec{Q}_a\}$ are obtained. If the principal axis direction of the largest and second principal moments of inertia are $\vec{X}_p$ and $\vec{Y}_p$, respectively, then the vectors $\vec{X}_p$ and $\vec{Y}_p$ compose the least squares plane. Each data point $\vec{Q}_a$ is projected onto this least squares plane, and the projection coordinates on the coordinate system having the center of gravity $\vec{G}_0$ as the origin are denoted as (x_a, y_a). Subtracting the minimum projection coordinate $(x_{\min}, y_{\min})$ from (x_a, y_a), the coordinate values $(x_a - x_{\min}, y_a - y_{\min})$ can be regarded as the location parameters (u_a, v_a) of the data points $\vec{Q}_a$. Fig. 5 shows an image of the creation of the least squares

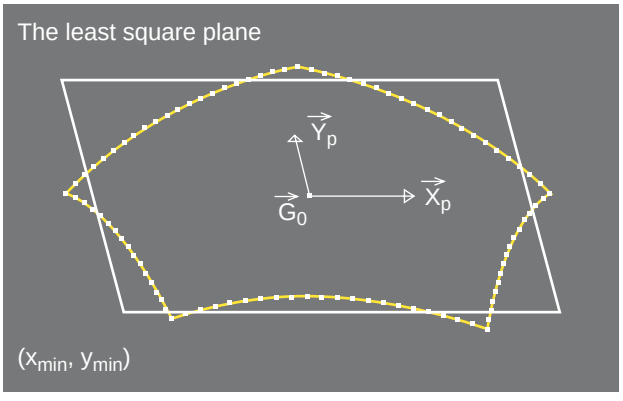


Fig.5 A least square plane obtained from a set of points on boundary curves

plane from the data points on boundary curves.

2.3. Creating n-sided Patches with G1 Continuity to the Bounding Surfaces

The B-spline basis functions $N_i(u_a)$ and $M_j(v_a)$ at points $\vec{Q}_a$ and their derivatives can be calculated using the parameters (u_a, v_a) obtained by projecting the data points $\vec{Q}_a$ onto the least squares plane. By rewriting vector equations (2), (3) and (4) into coordinate component equations and formulating $3N_p+2N_n$ simultaneous equations that include $3q$ unknowns x_i (coordinate components of unknown control points $\vec{P}_{ij}$), this can be expressed in matrix form as follows:

$$\begin{bmatrix} F \\ G \end{bmatrix} X = \begin{bmatrix} C \\ 0 \end{bmatrix} \qquad (5)$$

Here, $F = [f_{ij}]_{3N_p \times 3q}$ is the coefficient matrix of the coordinate components in equation (2) and $G = [g_{ij}]_{2N_n \times 3q}$ is the coefficient matrix of the coordinate components in equations (3) and (4), and their elements are defined as follows:

$$\begin{aligned} f_{3a,\ 3(j \cdot p_1 + i)} &= N_i(u_a) M_j(v_a) \\ f_{3a+1,\ 3(j \cdot p_1 + i)+1} &= N_i(u_a) M_j(v_a) \\ f_{3a+2,\ 3(j \cdot p_1 + i)+2} &= N_i(u_a) M_j(v_a) \\ others &= 0 \end{aligned}$$

and

$$\begin{aligned} g_{2b,\ 3(j \cdot p_1 + i)} &= N_i'(u_b) M_j(v_b) \cdot n_{bx} \\ g_{2b,\ 3(j \cdot p_1 + i)+1} &= N_i'(u_b) M_j(v_b) \cdot n_{by} \\ g_{2b,\ 3(j \cdot p_1 + i)+2} &= N_i'(u_b) M_j(v_b) \cdot n_{bz} \\ g_{2b+1,\ 3(j \cdot p_1 + i)} &= N_i(u_b) M_j'(v_b) \cdot n_{bx} \\ g_{2b+1,\ 3(j \cdot p_1 + i)+1} &= N_i(u_b) M_j'(v_b) \cdot n_{by} \\ g_{2b+1,\ 3(j \cdot p_1 + i)+2} &= N_i(u_b) M_j'(v_b) \cdot n_{bz} \end{aligned}$$

Furthermore, the matrices $X = [x_i]_{3q}$ and $C = [c_i]_{3N_p}$ of the coordinate components of the unknown control points $\vec{P}_{ij}$ and the given data points $\vec{Q}_a$ are respectively defined as follows:

$$\begin{aligned} x_{3(j \cdot p_1 + i)} &= P_{ij,x} \\ x_{3(j \cdot p_1 + i)+1} &= P_{ij,y} \\ x_{3(j \cdot p_1 + i)+2} &= P_{ij,z} \\ c_{3a} = Q_{ax},\ & c_{3a+1} = Q_{ay},\ c_{3a+2} = Q_{az} \end{aligned}$$

In the case of surface fitting, usually the number $3N_p+2N_n$ in equation (5) is much larger than the number $3q$ of the unknowns x_i, so the problem is over-specified and only some average solution can be obtained. Indeed, by approximately solving the equation (5), a fair surface with few undulations can be created.

Equation (5) is solved below using the least squares method. The squares error sum of the point group $\{\vec{Q}_a\}$ and the squares error sum of the constraints due to the normal vectors $\vec{n}_a$ are respectively written as follows:

$$\begin{aligned} E_p &= \sum_{a=0}^{N_p-1} \left| \vec{S}(u_a, v_a) - \vec{Q}_a \right|^2 \\ &= (FX - C)^t (FX - C) \end{aligned} \qquad (6)$$

$$E_n = \sum_{b=0}^{N_n-1} \left(\left| \vec{n}_b \cdot \vec{S}_u(u_b, v_b) \right|^2 + \left| \vec{n}_b \cdot \vec{S}_v(u_b, v_b) \right|^2 \right) = (GX)^t (GX) \quad (7)$$

Here, $(FX–C)^t$ and $(GX)^t$ express the transposed matrices of $(FX–C)$ and (GX), respectively. By minimizing the sum of the squares error sums (6) and (7),

$$E_{p+n} = E_p + E_n \quad (8)$$

the least squares equation for the unknowns X can be obtained as follows:

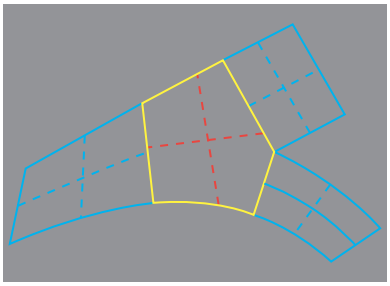
$$(F^tF + G^tG)X = F^tC \quad (9)$$

By using the solution of the equation (9), i.e. the control point coordinates of the surface, a base surface with G1 continuity to the bounding surfaces is created. Moreover, if the base surface is trimmed at the boundary curve, then the n-sided patches, which interpolate the n-gon region, can be completed.

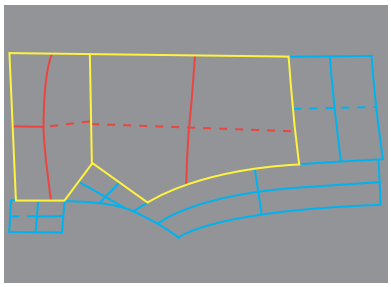
Next, the three cases shown in Fig. 1, Fig. 2 and Fig. 3 have been reconstructed by using the least squares method, and the following results have been obtained.

Comparing the results shown in Fig. 6 to Fig. 8 with Fig. 1 to Fig. 3, it is clear that the least squares fitting is superior for improving zebra continuity. Of the three cases, cases 1 and 3 have been greatly improved, and the 5-sided patch on the right side of case 2 has been also improved. However, there are also problems. Undesirable shapes such as spiral patterns are generated in the 5-sided patch on the left side of case 2.

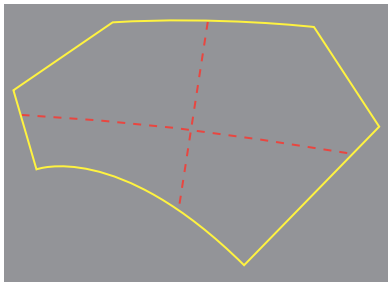
Using the least squares method, various cases of the n-sided patches have been examined, and the results show the following. (a) For a nearly flat n-sided patch such as shown in case 1, fine results can be obtained. (b) For other cases, the shortcomings that data points are not evenly distributed (they only exist on the boundary curves) becomes conspicuous, which causes two problems. The first is that the spiral patterns occur in the created n-sided patch as shown in case 2, and the second is that the base surface



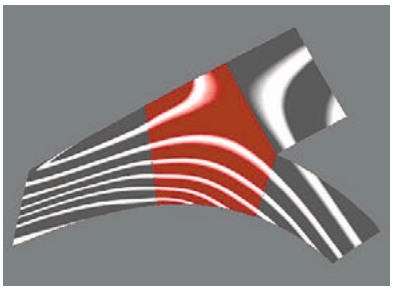
1-3 face



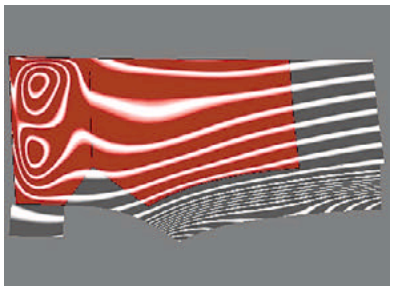
2-3 face



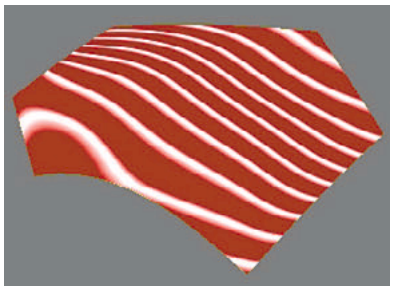
3-3 face



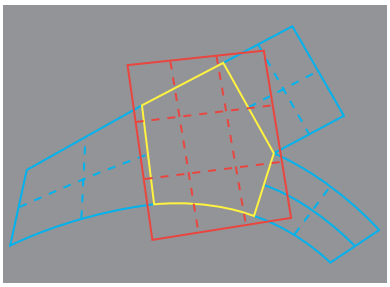
1-4 zebra



2-4 zebra

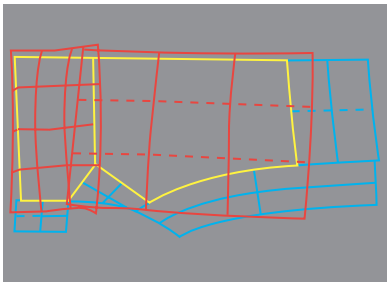


3-4 zebra



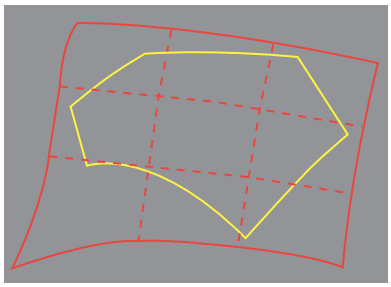
1-5 surface without trimming
maximum error = 0.00024mm

Fig. 6 Case 1: A 5-sided patch filled by the least square method



2-5 surface without trimming
maximum error of the right pentagon = 0.0017mm
maximum error of the left pentagon = 0.00067mm

Fig. 7 Case 2: Two 5-sided patches filled by the least square method



3-5 surface without trimming
maximum error = 0.0016mm

Fig. 8 Case 3: A 6-sided patch filled by the least square method

before trimming tend to diverge at the corners as shown in case 3. Satisfactory results cannot be obtained in most cases unless these two problems are solved. Therefore, surface smoothing by minimization of the surface energy integral will be considered as a solution to the above problems.

3. Smoothing by the Energy Integral Minimization

Surface smoothing is an important subject for CAGD, and various smoothing methods have been researched thus far. The main method is smoothing by minimization of the surface energy integral. In this paper, the square integrals of the first- and second-order derivatives of the B-spline basis functions with optional knot vectors are calculated. Surface smoothing is achieved by adding these integrals to the least squares equations and minimizing the energy integrals.

3.1. Square Integrals of the First-order derivatives

The square integrals of the first-order partial derivatives in the u and v directions of the surface $\vec{S}(u, v)$ are expressed as follows:

$$\iint \left| \vec{S}_u \right|^2 dudv = \sum \int N_i' N_k' du \int M_j M_l dv \vec{P}_{ij} \cdot \vec{P}_{kl}$$
$$\iint \left| \vec{S}_v \right|^2 dudv = \sum \int N_i N_k du \int M_j' M_l' dv \vec{P}_{ij} \cdot \vec{P}_{kl}$$

If the subscripts are arranged as $a = j \cdot p_1 + i$ and $b = l \cdot p_1 + k$, and the integral portions for u and v are defined as follows:

$$Au_{ab} = Au_{j \cdot p_1+i,\, l \cdot p_1+k} = \int N_i' N_k' du \int M_j M_l dv$$
$$Av_{ab} = Av_{j \cdot p_1+i,\, l \cdot p_1+k} = \int N_i N_k du \int M_j' M_l' dv$$

then the square integrals of the first-order partial derivatives are as follows:

$$\iint \left(\left| \vec{S}_u \right|^2 + \left| \vec{S}_v \right|^2 \right) dudv = \sum \vec{P}_a \cdot (Au_{ab} + Av_{ab}) \vec{P}_b$$

Furthermore, if the elements of the matrix $K_1 = [h_{ij}]_{3q \times 3q}$ are defined as follows:

$$h_{3a,\,3b} = h_{3a+1,\,3b+1} = h_{3a+2,\,3b+2} = Au_{ab} + Av_{ab}$$

$$others = 0$$

the square integrals of the first-order partial derivatives that should be minimized can be expressed as follows:

$$E_a = \iint \left(\left| \vec{S}_u \right|^2 + \left| \vec{S}_v \right|^2 \right) dudv = X^t K_1 X \qquad (10)$$

X in the above equation is the unknown control points, and the elements of the matrix K_1 can be calculated using the given knot vectors.

3.2. Square Integrals of the Second-order derivatives

The square integrals of the second-order partial derivatives in the u and v directions of the surface $\vec{S}(u, v)$ are expressed as follows:

$$\iint \left| \vec{S}_{uu} \right|^2 dudv = \sum \int N_i'' N_k'' du \int M_j M_l dv \vec{P}_{ij} \cdot \vec{P}_{kl}$$
$$\iint \left| \vec{S}_{uv} \right|^2 dudv = \sum \int N_i' N_k' du \int M_j' M_l' dv \vec{P}_{ij} \cdot \vec{P}_{kl}$$
$$\iint \left| \vec{S}_{vv} \right|^2 dudv = \sum \int N_i N_k du \int M_j'' M_l'' dv \vec{P}_{ij} \cdot \vec{P}_{kl}$$

If the subscripts are arranged in the same manner as in 3.1. and the integral portions for u and v are defined as follows:

$$Buu_{ab} = Buu_{j \cdot p_1+i,\, l \cdot p_1+k} = \int N_i'' N_k'' du \int M_j M_l dv$$
$$Buv_{ab} = Buv_{j \cdot p_1+i,\, l \cdot p_1+k} = \int N_i' N_k' du \int M_j' M_l' dv$$
$$Bvv_{ab} = Bvv_{j \cdot p_1+i,\, l \cdot p_1+k} = \int N_i N_k du \int M_j'' M_l'' dv$$

then the square integrals of the second-order partial derivatives are as follows:

$$\iint \left(\left| \vec{S}_{uu} \right|^2 + 2 \left| \vec{S}_{uv} \right|^2 + \left| \vec{S}_{vv} \right|^2 \right) dudv$$
$$= \sum \vec{P}_a \cdot (Buu_{ab} + 2Buv_{ab} + Bvv_{ab}) \vec{P}_b$$

Furthermore, if the elements of the matrix $K_2 = [k_{ij}]_{3q \times 3q}$ are defined as follows:

$$k_{3a,\,3b} = k_{3a+1,\,3b+1} = k_{3a+2,\,3b+2}$$
$$= Buu_{ab} + 2Buv_{ab} + Bvv_{ab}$$

$$others = 0$$

the square integrals of the second-order partial derivatives that should be minimized can be written as follows:

$$E_e = \iint \left(\left| \vec{S}_{uu} \right|^2 + 2 \left| \vec{S}_{uv} \right|^2 + \left| \vec{S}_{vv} \right|^2 \right) dudv$$
$$= X^t K_2 X \qquad (11)$$

E_e on the left side of the above equation represents the surface energy, and K_2 on the right side is the stiffness matrix. The elements of the matrix K_2 can be calculated using the given knot vectors.

3.3. Surface Smoothing

In regard to smoothing, adding the first-order derivatives term E_a and the second-order derivatives term E_e to the equation of the squares error sum (8), the total term that should be minimized is then written as follows:

$$E_{p+n+a+e} = \alpha E_{p+n} + \beta E_a + \gamma E_e \qquad (12)$$

Here, the subscripts p, n, a, e of $E_{p+n+a+e}$ mean point, normal, area and energy, respectively, and the non-negative fitting coefficients α, β and γ are introduced in order to enable adjustment of surface smoothing. Defining K_0 as follows:

$K_0 = F^tF + G^tG$

yields the new least squares equation.

$$(\alpha K_0 + \beta K_1 + \gamma K_2)X = \alpha F^tC \qquad (13)$$

The first term on the left side of the above equation is the least squares method term derived from the data points and the normal vectors. The second term is derived from the first-order derivatives and the third term is derived from the second-order derivatives. Here, the second term is the stretching term for minimizing the surface area, and the third term is the bending term for minimizing the surface energy.

By giving appropriate values to the fitting coefficients α, β and γ and solving the equation (13), a smoothing base surface can be created as the underlying surface of the n-sided patches.

However, the important thing when solving the equation (13) is the relative values and not the absolute values of the coefficients α, β and γ. Therefore, it is sufficient to fix one of the three coefficients and then give appropriate values to the remaining two coefficients. These coefficients are set as follows in our program in this paper.

$\alpha = 1$

β (key in) (Recommended value: $0 \leq \beta \leq 0.0001$)

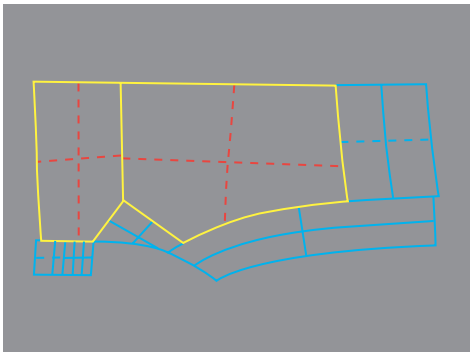
γ (key in) (Recommended value: $0 \leq \gamma \leq 0.1$)

Of course, if $\beta = \gamma = 0$ is input, the least squares equation (13) returns to the equation (9). However, the surface smoothing can be achieved by inputting $\beta \neq 0$ or $\gamma \neq 0$.

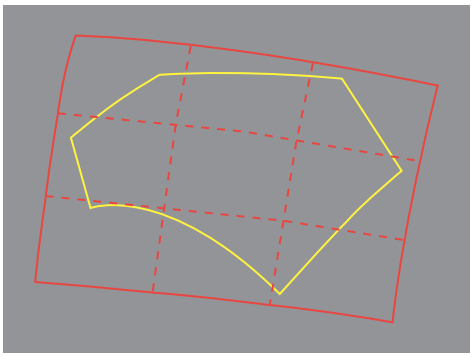
Next, we will discuss a method to improve the problems indicated in the section 2 above, i.e. the problem of the spiral patterns occurring and the problem of the divergence of the base surface at the corners.

Fig. 9 and Fig. 10 illustrate examples reconstructing cases 2 and 3 as shown in Fig. 7 and Fig. 8 by using the method of minimizing energy integrals. The maximum error, i.e. the maximum distance from the given boundary curves to the created n-sided patches slightly increases, while the quality of the n-sided patches is greatly improved. Hence the problems indicated in the section 2 are almost completely resolved.

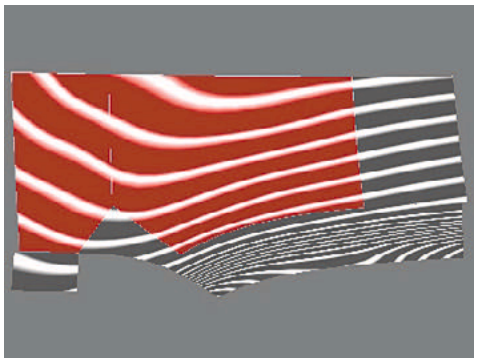
Let us look at the concrete effects of the stretching fitting coefficients β and the bending fitting coefficients γ in the equation (13) on the surface smoothing by examining



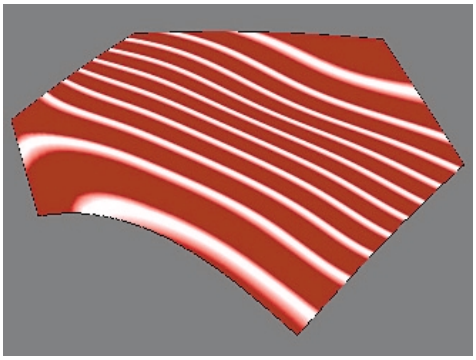
2-6 face



3-6 surface without trimming



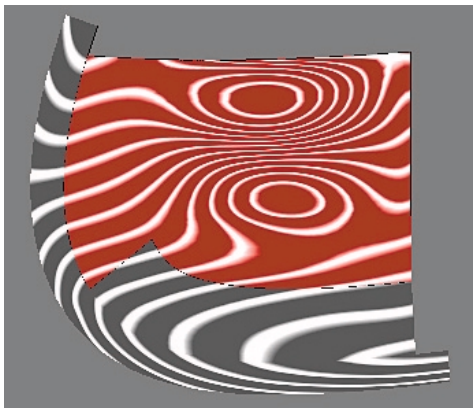
2-7 zebra
maximum error of the right pentagon = 0.0032mm
maximum error of the left pentagon =0.00067mm



3-7 zebra
maximum error = 0.0023mm

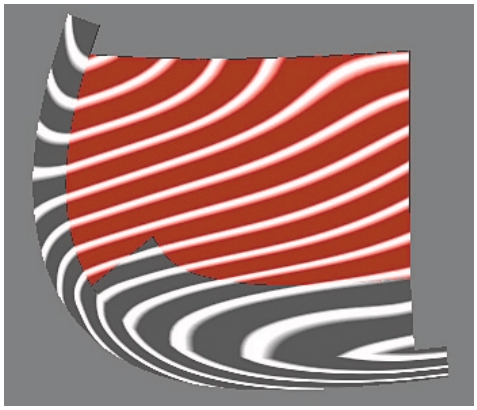
Fig. 9 Case 2: Two 5-sided patches filled by the minimal energy method with parameters β=0, γ=0.01

Fig. 10 Case 3: A 6-sided patch filled by the minimal energy method with parameters β=0, γ=0.0001



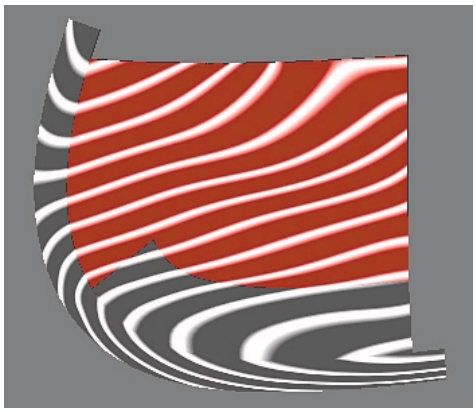
maximum error = 0.00087mm

Fig. 11 Case 4: A 5-sided concave patch filled by the minimal energy method with parameters β=0, γ=0



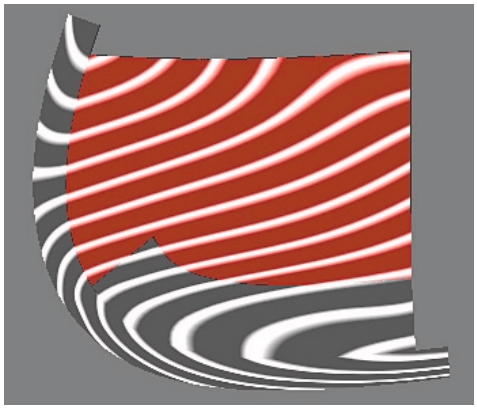
maximum error = 0.0012mm

Fig. 13 Case 4: A 5-sided concave patch filled by the minimal energy method with parameters β=0, γ=0.01



maximum error = 0.00099mm

Fig. 12 Case 4: A 5-sided concave patch filled by the minimal energy method with parameters β=0.00001, γ=0



maximum error = 0.0012mm

Fig. 14 Case 4: A 5-sided concave patch filled by the minimal energy method with parameters β=0.00001, γ=0.01

the case of a 5-sided concave patch.

The examples in Fig. 11 to Fig. 14 illustrate that the quality of the created 5-sided patch is gradually improved by adjusting the values of the fitting coefficients β and γ. As a result of studying various cases, it was concluded that β and γ value ranges of $0 \leq \beta \leq 0.0001$, $0 \leq \gamma \leq 0.1$ are appropriate.

4. Conclusion

As the fitting algorithm to create n-sided patches from n closed boundary curves with G1 continuity to the bounding surfaces, the method to interpolate a base surface to the boundary curves applying the least squares method and the surface smoothing method to minimize the energy integrals are presented. The quality of the n-sided patches in various cases has been then verified, and the following two conclusions have been reached.

1) The least squares fitting method has better results for the zebra continuity, improving upon the method of dividing an n-gon into several quadrangles and then creating 4-sided patches for each quadrangle. However, problems such as unwanted spiral patterns and the divergence of the base surface at the corners are generated.
2) Surface smoothing by minimizing the energy integrals of the B-spline basis functions has been effective at improving surface quality. Attaching the fitting coefficients to the first-order and second-order derivatives terms in the least squares equation and adjusting the two coefficients β (stretching term) and γ (bending term), the problems of the spiral patterns and the corner divergence have been almost completely resolved.

By implementing this method in the Honda in-house CAD application as one of the functions to create surfaces, the quality of design data has been greatly improved. Concurrently, the time used to ensure G1 continuity between the n-sided patches and the bounding surfaces has been greatly reduced .

References

(1) Hiroshi, T. and Hiroaki, T.: The foundation and application of 3 dimension CAD, Kyoritsu Shuppan, p. 82–88 (1991)

(2) Gregory, J.A. and Zhou, J.: Filling polygonal holes with bicubic patches, Computer Aided Geometric Design 11, p. 391–410 (1994)

(3) Rogers, D. F. and Adams, J. A.: Mathematical Elements for Computer Graphics, 2nd ed., McGraw-Hill, New York (1990)

(4) Sarkar, B. and Menq, CH.: Smooth-surface approximation and reverse engineering, Computer-Aided Design 23 (9), p. 623–628 (1991)

(5) Ma, W. and He, P.: B-spline surface local updating with unorganized points, Computer-Aided Design 30 (11), p. 853–862 (1998)

(6) Celniker, G. and Gossard, D.: Deformable Curve and Surface Finite-Elements for Free-Form Shape Design, Computer Graphics 25 (4), p. 257–266 (1991)

(7) Fasshauer, G.E. and Schumaker, L.L.: Minimal energy surfaces using parametric splines, Computer Aided Geometric Design 13, p. 45–79 (1996)

(8) Vassilev, TI.: Fair interpolation and approximation of B-splines by energy minimization and points insertion, Computer-Aided Design 28 (9), p. 753–760 (1996)

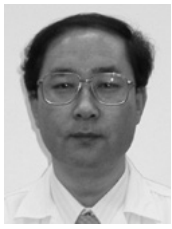
(9) Park, H., Kim, K. and Lee, SC.: A method for approximate NURBS curve compatibility based on multiple curve refitting, Computer-Aided Design 32 (4), p. 237–252 (2000)

(10) Chui, C. K. and Lai, M.J.: Filling polygonal holes using C^1 cubic triangular spline patches, Computer Aided Geometric Design 17, p. 297–307 (2000)

■Authors■



Kentaro MATSUMOTO



Hongjun XIE

Establishment of a Method for Predicting Powertrain Vibration at Engine Mounting Points under Running Conditions

Yasuhiko SEKI* Toshibumi SUZUKI*
Naoki KAMIMURA* Yukitaka TAKAHASHI*

ABSTRACT

It is well known that powertrain vibration characteristics are a critical factor influencing booming and other cabin noises. As vibration at the engine mounting points is one of the most influential of all the vibrations a precise analytical method for the prediction of vibration at the engine mounting points under running conditions was developed. This method uses simulation models that take into consideration the nonlinear characteristics of both main bearing's oil film and the engine mounts. This makes it possible to predict the vibration level at engine mounting points while preserving a practical level of accuracy. Application of this design method during the initial stages of basic powerplant structural investigations for powertrain design will enable the efficient evaluation of powertrain vibration characteristics.

1. Introduction

Consumers are looking for high quality with respect to automobile vibration and noise, and measures to reduce external noise are also required from an environmental viewpoint. As a result, there is an increased demand for quieter automobiles that feature both low vibration and low noise. This means that reducing powertrain vibration, which influences cabin noise, is becoming a requirement not just for luxury vehicles but for automobiles in all categories. Therefore, more accurate prediction technology must be established to respond quickly to market trends and to perform development within the limited automobile development period. Eigenvalue analysis using FE (Finite Element) models is currently the main tool for investigating powertrain structures. However, while eigenvalue analysis can predict the natural frequency of the overall powertrain, predicting powertrain vibration levels under running conditions is difficult. Therefore, this paper reports the establishment of a method for predicting vibration at engine mounting points under running conditions, and introduces cases where this method was applied to the evaluation of powertrain vibration characteristics.

* Tochigi R&D Center

2. Outline of Prediction Method

2.1 Analysis Procedure

Fig. 1 shows the analysis flow for this prediction method. Analysis was performed according to the procedure below.

(1) Step 1: Calculation of powertrain vibration transfer characteristics
- Creation of an FE model of the complete powertrain

(2) Step 2: Calculation of cranktrain excitation force
- Calculation of the excitation force through a FEM model of the cranktrain

(3) Step 3: Calculation of engine mounting point vibration
- Calculation of the vibration at engine mounting points under running conditions

2.2 Calculation of Powertrain Vibration Transfer Characteristics (Step 1)

2.2.1 Finite element model of the powertrain

The prediction accuracy of vibration at engine mounting points in the running condition depends greatly on the frequency response function (FRF) of each engine mounting

bracket. Therefore, the accuracy of powertrain vibration transfer characteristics is an extremely important point. The FE model of the complete powertrain consists of all equipment , and is comprised of the cylinder block, cylinder head, gear box, transmission case, intake manifold, exhaust manifold, auxiliary devices, and engine mounting brackets. Fig. 2 shows the FE model of the complete powertrain.

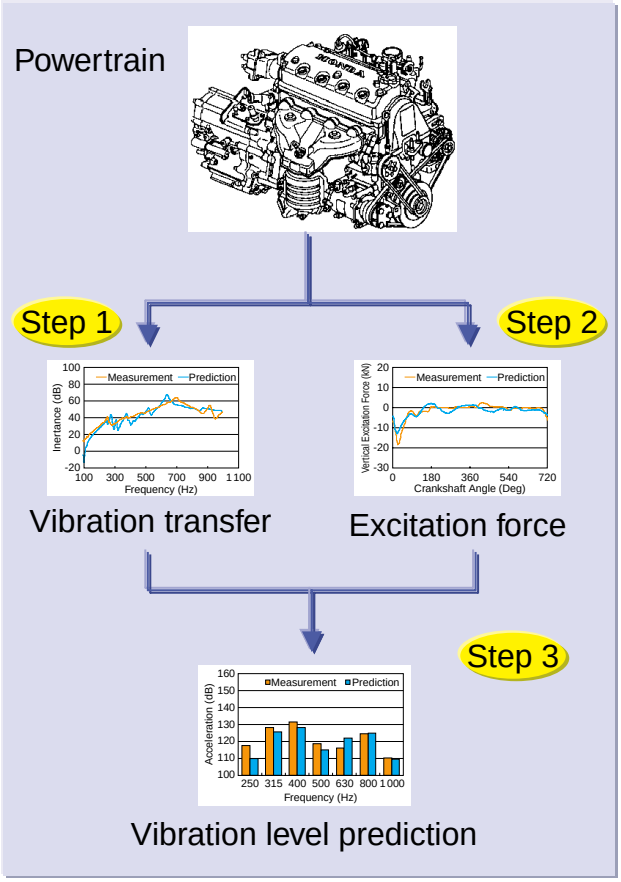


Fig. 1 Analysis procedure

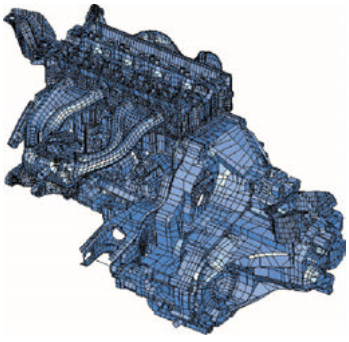


Fig. 2 FE model of powertrain

2.2.2 Calculation of Vibration Transfer Characteristics

As the correlation between the FRF of the initially created FE model of the complete powertrain and the measurement results was low, the FE model was updated. When updating the FE model, the local resonance frequency and FRF of the engine mounting brackets were used as the target functions. As shown in Fig. 3, the calculated FRF exhibited excellent correlation with the measurement results, indicating that the FE model of the powertrain had more than sufficient accuracy for practical application.

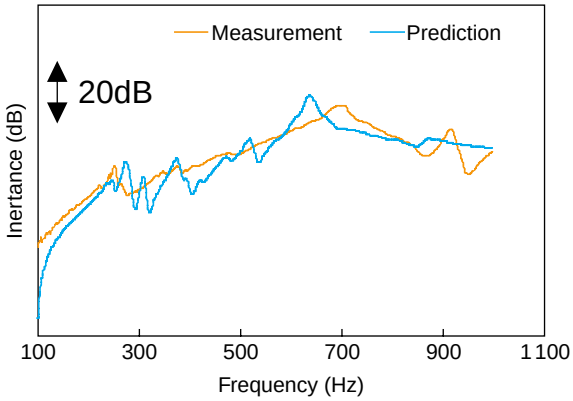


Fig. 3 Comparison of powertrain FRF

2.3 Calculation of Cranktrain Excitation Force (Step 2)

2.3.1 Finite element model of the cranktrain

The crankshaft behavior has a large effect on the cranktrain excitation force, so a highly accurate FE model is necessary. Fig. 4 shows the FE model of the cranktrain. This model is comprised of the crankshaft, pulleys, flywheel and clutch disc cover. An even more accurate FE model of the cranktrain was thought to be necessary, so the FE model of the cranktrain was updated with the natural frequency, FRF and modal assurance criterion (MAC) as target functions. Fig. 5 and Fig. 6 show a comparison of the calculated FRF and the MAC test results. The natural frequency shows an error of within ±3dB, and the MAC has an extremely high correlation of 0.7 or more, indicating that an excellent FE model was constructed.

2.3.2 Calculation of cranktrain excitation force

The gas force acting inside each combustion chamber is transmitted through the pistons and connecting rods to the crankshaft. The combined force of the piston side force generated between the pistons and cylinder liners and the inertia force acting on the pistons passes through the connecting rods as the excitation force to the powertrain, and acts on each crank pin in each firing order. The cranktrain excitation force is calculated using dynamic behavior analysis which takes into consideration the nonlinear oil film characteristics. Fig. 7 shows the calculated cranktrain excitation force on the 2nd main bearing. The conditions were an engine speed of 1600 rpm and wide open throttle (WOT). The calculated excitation force shows an excellent correlation with the measurement results.

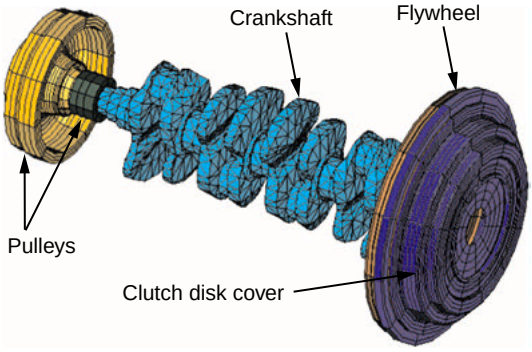


Fig. 4 FE model of cranktrain

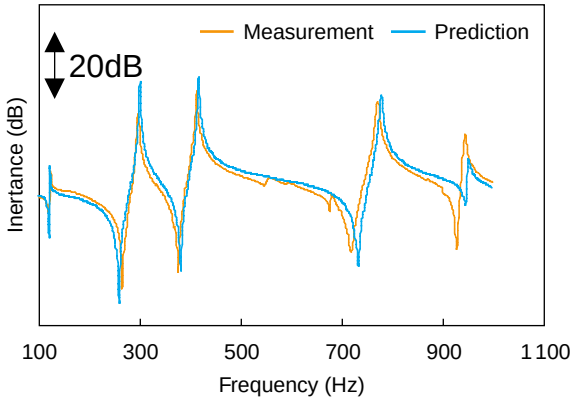


Fig. 5 FRF verification results for the cranktrain

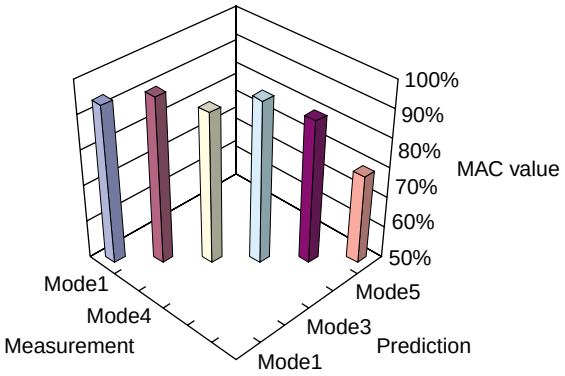


Fig. 6 MAC verification results for the cranktrain

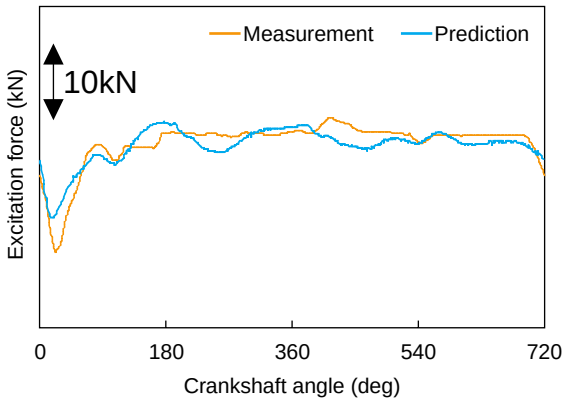


Fig. 7 Verification results for excitation force

2.4 Calculation of Engine Mounting Point Vibration (Step 3)

2.4.1 Engine mount model

Both rubber and sealed liquid type mounts are generally applied as engine mounts. However, the dynamic stiffness and attenuation, which depend on frequency and displacement, differ greatly for each mount type, so these become extremely important accuracy factors when modeling the powertrain under running conditions. Therefore, when modeling the engine mounts in this study, the accuracy was improved by changing from the conventional Kelvin-Voigt model to a mini oscillator model (MOM) that can express the nonlinear characteristics mentioned above. Fig. 8 shows both engine mount models. Parameter identification was performed to enable the strictest possible representation of measured mount characteristics, and the final engine mount characteristics used the same conditions as the set test bench conditions.

2.4.2 Calculation of engine mounting point vibration

The vibration level at the engine mounting points under running conditions was calculated in Step 1 and 2. Fig. 9 shows the vibration prediction results at engine mounting points under running conditions when the two engine mount model types mentioned above are applied. The conditions were an engine speed of 3200 rpm and wide open throttle (WOT). Changing from the Kelvin-Voigt model to MOM improved the vibration prediction accuracy at the mounting points by up to 15 dB for all frequencies up to 1 kHz. In addition, the error from the measurements was approximately ±3 to 5dB ,which shows that the method presented in this paper of applying MOM to predict vibration at engine mounting points ensures more than sufficient accuracy for practical application.

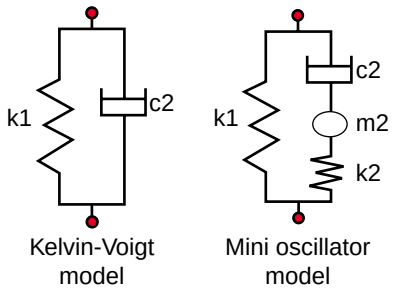


Fig. 8 Engine mount models

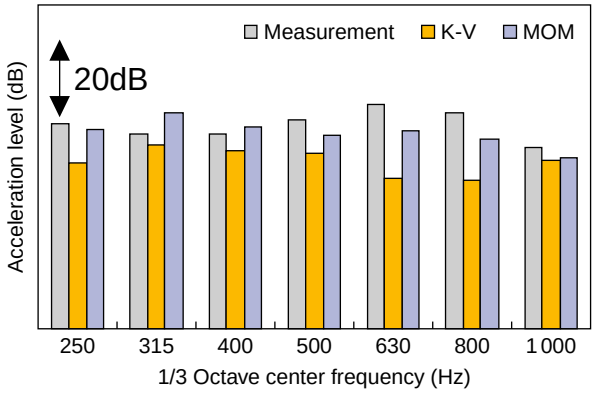


Fig. 9 Verification results for each mount model

3. Verification of Applicability to Actual Vehicles

The developed prediction method was applied to a transversally mounted in-line four cylinder engine in a front wheel drive layout and investigations were conducted to verify the feasibility of application to engine design.

3.1 Oil Pan Specification Changes

The prediction accuracy of the amount of the effects when the structure is changed was verified by changing the oil pan specifications. The test oil pan materials were steel and aluminum. Fig. 10 shows FE models of the aluminum and steel oil pans used for the investigations.



Fig. 10 FE model of the two oil pan specifications

Fig. 11 shows the prediction results for each aluminum oil pan specification, and Fig. 12 shows a comparison with the measurement results for each aluminum oil pan specification. In addition, Fig. 13 shows a comparison with measurements of the degree of the effects on vibration at engine mounting points by changing from steel to aluminum

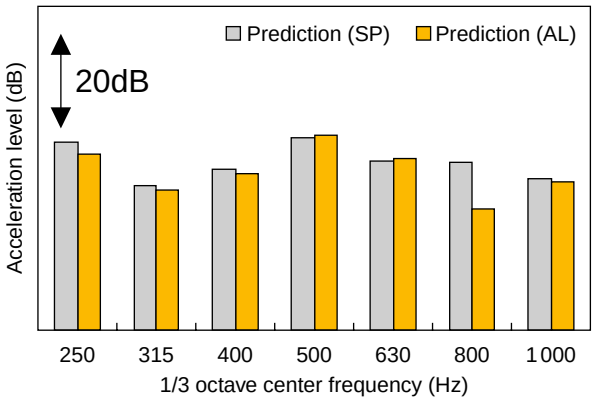


Fig. 11 Comparison of the oil pan specifications

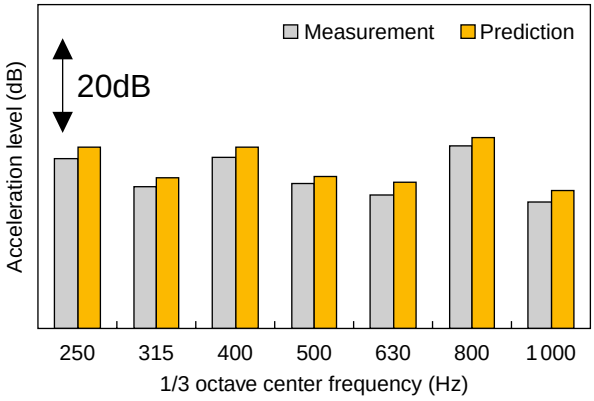


Fig. 12 Verification results for aluminum oil sump pan

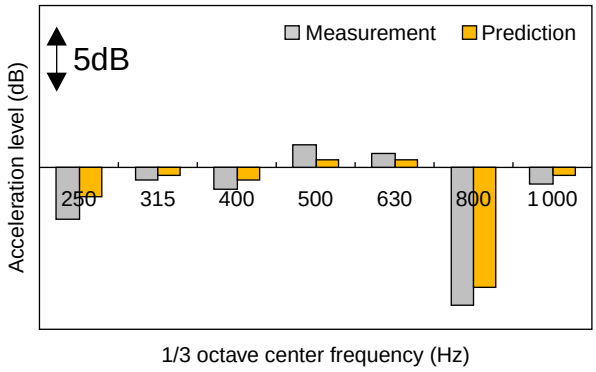


Fig. 13 Verification results for the degree of effects on vibration

oil pan specifications. The conditions were an engine speed of 4000 rpm and a load of 40 Nm. The developed method showed an error from the measurement results of approximately ±3dB, thus confirming prediction accuracy sufficient for practical application of both the vibration at the engine mounting points and the degree of the effects when the specifications are changed.

3.2 Cranktrain Specification Changes

Next, the prediction accuracy of the degree of the effects when the cranktrain specifications are changed was verified by changing the crankshaft specifications. The test crankshaft specifications were full-eight weight and semi-eight weight specifications. Fig. 14 shows the two crankshaft specifications used for the investigations.

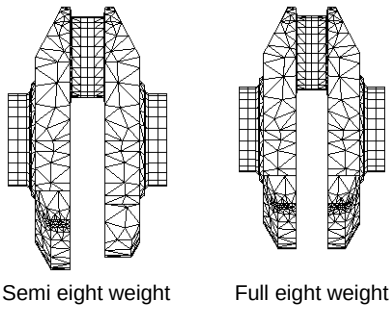


Fig. 14 Crankshaft specifications

Fig. 15 shows the results for full-eight weight specifications, and Fig. 16 shows the results for the degree of the effects on the vibration at the engine mounting points by changing from semi-eight weight to full-eight weight specifications. The conditions were an engine speed of 4000 rpm and a load of 40 Nm. The error from the measurement was approximately ±3dB, thus confirming that, like the changes to the oil pan specifications, the developed method is also accurate enough for practical application and which is capable of following changes to crankshaft specifications.

The results of investigating the feasibility of application in the above two examples confirmed that the developed method for predicting vibration at engine mounting points ensures a prediction accuracy appropriate for practical application. Therefore, the method was applied to actual engine design.

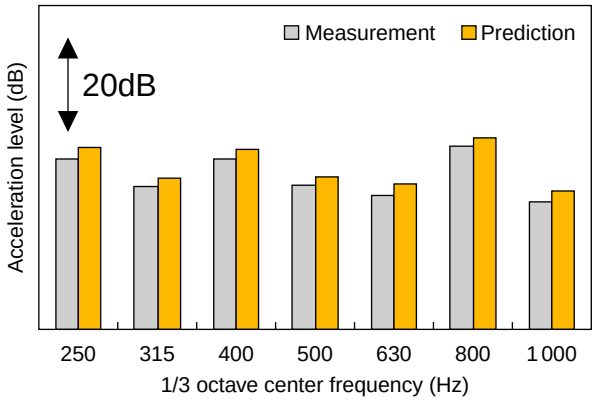


Fig. 15 Verification results for the two crankshaft specifications

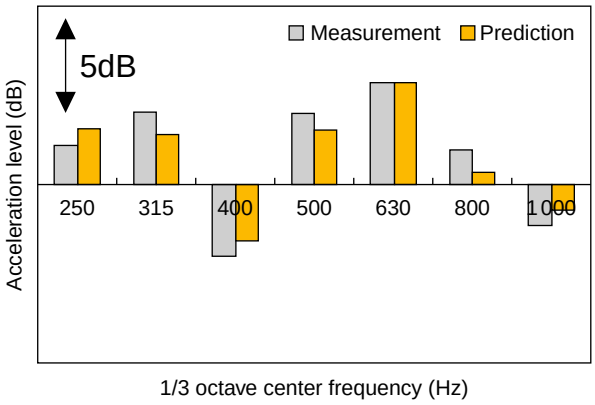


Fig. 16 Verification results for the degree of effects on vibration

4. Example of Application to an Actual Engine

An example of application of the developed method to investigations of the basic structure of an actual engine is introduced below using the example of structural modifications aimed at reducing the powertrain vibration of a transversally mounted in-line four cylinder engine in a front wheel drive layout.

4.1 Structural Modification of Cylinder Block

Ensuring cylinder block stiffness is important for reducing powertrain vibration. Of the various measures applied to ensure this stiffness, the vibration reducing effect depends largely on the position at which the ribs are attached, so the developed method was applied to investigate the rib positions. Fig. 17 shows the FE models of the cylinder block for each investigated specification. Investigations were carried out on a total of four types of specifications: SPEC-A, SPEC-B, SPEC-C and SPEC-D.

Fig. 18 shows the prediction results for each specification for the total within each frequency band (600 to 800 Hz) of the vibration at the engine mounting points. The conditions were an engine speed of 3000 rpm and wide open throttle (WOT). Based on these prediction results, SPEC-C was adopted as the most effective specification for reducing the total vibration within each frequency band of the vibration at the engine mounting points.

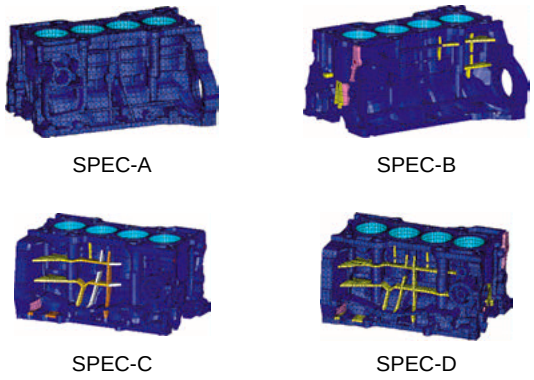


Fig. 17 Structural modification of the cylinder blocks

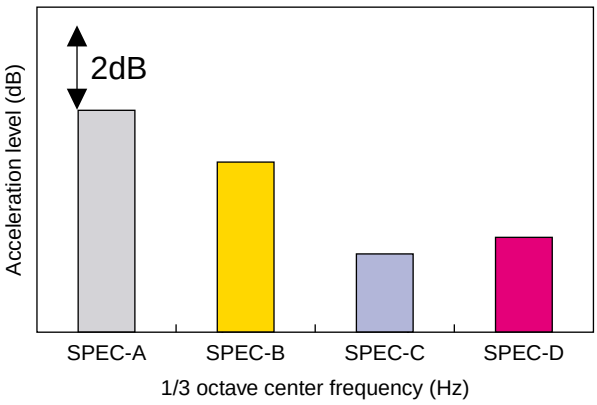


Fig. 18 Comparison of the total vibration level for each specification

4.2 Gusset Stiffener Effects

In addition to the cylinder block stiffness, the stiffness of the powertrain couplings is also extremely important in reducing powertrain vibration. Therefore, the improvement of powertrain stiffness by gusset stiffeners was investigated by predicting the vibration at the engine mounting points. Fig. 19 shows the FE model of the gusset stiffener used in the investigation.



Fig. 19 FE model of a gusset stiffener

Fig. 20 shows the prediction results for the vibration at engine mounting points with gusset stiffeners added. The conditions were an engine speed of 3000 rpm and a load of 40 Nm. The effect of adding gusset stiffeners on reducing the vibration at the engine mounting points in the middle frequency range of engine acceleration noise was correctly predicted and subsequently investigations were promoted in design.

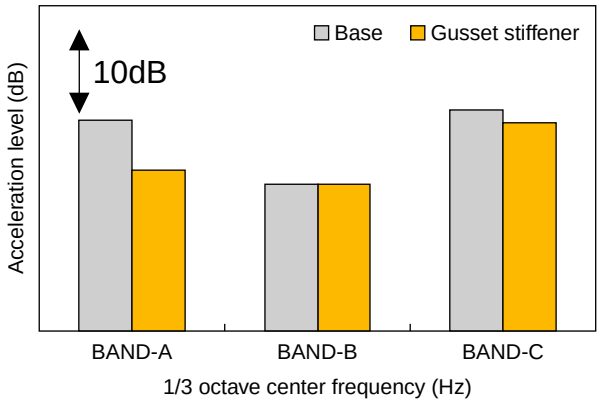


Fig. 20 Comparison of vibration level of a powerplant with and without a gusset stiffener

The above example shows that by applying the developed method to actual engine design, design guidelines can be obtained for efficiently reducing vibration and effective specification investigations can be carried out .

5. Conclusion

(1) A method was established for predicting vibration at the engine mounting points under running conditions with accuracy appropriate for practical application. This was made possible by taking into account cranktrain behavior, oil film characteristics and nonlinear engine mount characteristics.
(2) The developed prediction method was applied to a transversally mounted in-line four cylinder engine in a front wheel drive layout and investigated. The results confirmed that the developed method allows efficient evaluation of powertrain vibration characteristics, and is an effective method for investigating basic powertrain structures.

6. References

(1) Takahashi, Y., Suzuki, T., Tsukahara, M. et al.: A Method For Identification of Powerplant Joint Properties Using FRF Data and FEM Model, ASME Paper DETC97VIB4247 (1997)
(2) Heiner, Storck., Hartono, Sumali.: Characterization of a Vibration Damping Mount, SAE Paper 99012816
(3) Mctavish, D.J., Hughes, P.C.: FE modeling of Linear Viscoelastic Structures the GHM Method, AIAA Paper No. 92-2380.
(4) Suzuki, T., Takahashi, Y. et al.: How to Measure the Internal Forces of a Combustion Engine, NCA-VOL.26, p.61-65 (1999)
(5) Taylor, C.: The Internal-Combustion Engine in Theory and Practice Volume 2, Combustion, Fuels, Materials, Design Revised Edition' MIT Press, p.240-305 (1985)
(6) Mctavish, D.J., Hughes,P,C.: Modeling of Linear Viscoelastic Space Structures, Journal of Vibration & Acoustics-Transactions of the ASME, Vol. 115, p.103-110(1993)
(7) Raub, Jonathan D., Jones, Jeffrey: Analytical Investigation of Crankshaft Dynamics as a Virtual Engine Module SAE Paper 99011750
(8) Takahashi. M, Takahashi. Y, Senjyo. K.: Utilizing Large Computational Devices for Powertrain Vibration Analysis, JASE Proceedings, No.901, p.65-68 (1990)
(9) Nehl, J., Wilhelm, M., Gauch, P., Travert, M.: Evaluation of Crankshaft Clearance Influence on Specific Roughness Noise Concern SAE Paper 1999-01-1771
(10) Takahashi, Y., Suzuki, T., Tsukahara, M.: Prediction of Powerplant Vibration Using FRF Data of FE Model' SAE Paper 971959
(11) Seki, Y., Suzuki. T, Tsukahara, M., Takahashi, Y.: How to Predict Powertrain Vibration at the Engine Mounting Points Under Running Conditions SAE Paper 2001-01-1592

■ Authors ■


Yasuhiko SEKI


Toshibumi SUZUKI


Naoki KAMIMURA


Yukitaka TAKAHASH

Development of a Virtual Road Simulator for Motorcycles

Makoto HASEGAWA* Kenji NAKANISHI*
Shokichi HARASHIMA* Hideki YAMAGUCHI*

ABSTRACT

Virtual road simulator technology for motorcycles was established as a method to help predict motorcycle fatigue strength due to loading during running. This technology helped enable the prediction of dynamic behaviors and stresses during the road simulator durability test. The technology consists of the Finite Element Method, Multi Body Simulation, Road Simulator control, and fatigue analysis. The study helped enable the reproduction of the behavior of motorcycles using a simplified model of motorcycles and test rigs, including component Finite Element models. As a result, prediction of fatigue life, damage distribution, and stress waveforms of the high-stress regions in a Road Simulator durability test was achieved.

1. Introduction

Linear static analysis using the Finite Element Method is available as a method of predicting strength when establishing specifications at the drawing stage of motorcycle design. Applications of this method during design have been increasing, given its effectiveness when boundary conditions and load conditions are clear, and as relatively little manpower is required for analysis. However, prediction using linear static analysis is a challenge for parts on which multiple loads are applied at different times, and for parts having local vibration modes.

As a method to address this issue, we have developed a Virtual Road Simulator (VRS below) system that uses Multi Body Simulation to dynamically reproduce the behavior of the Road Simulator (RS below) durability test[(1)].

2. RS Durability Test

Fig. 1 shows the appearance of the RS. To shorten development time, this test can be used to confirm fatigue strength against the load received from the road surface on the bench, rather than conducting a durability test using an actual motorcycle on a track. The RS reproduces the behavior of the motorcycle using three hydraulic actuators. The drive signals input to the actuators are calculated using in-house RS control software to reproduce the loads on a motorcycle during actual running, according to the following procedures:

(1) Target signals are measured during actual running.
(2) Transfer functions are measured in a bench test.
(3) The first drive signals are calculated using the target signals and transfer functions.
(4) The motorcycle on the bench is activated using the calculated drive signals, and response signals are measured.
(5) New drive signals are calculated after correction of errors between the target signals and the response signals.
(6) Steps 4 and 5 are repeated until errors are brought within a tolerable range.

This procedure of trial activation and corrective calculation is called iteration. The target signals are front axle vertical acceleration, rear axle vertical acceleration, and front fork bending stress.

* Asaka R&D Center

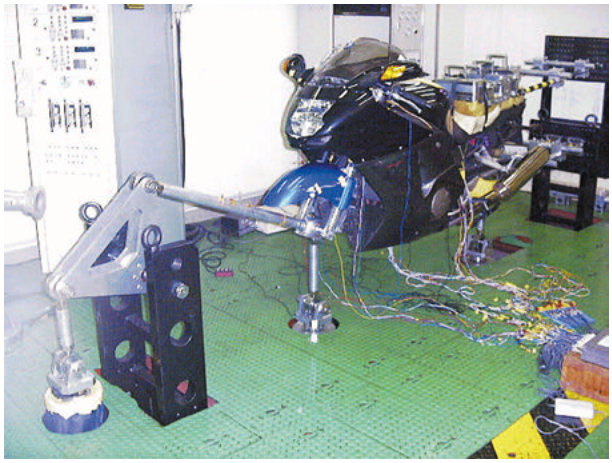


Fig. 1 Appearance of the Road Simulator (RS)

3. Outline of the VRS System

Fig. 2 shows the system flow of the VRS system. The system consists of the following four technologies:

(1) Finite Element Method (FEM) technology: Conducts analysis of mass properties and modal parameters necessary to include the Finite Element model (FE model below) in the MBS model.
(2) Multi Body Simulation (MBS) technology: Conducts motion simulation of the MBS model consisting of rigid body and flexible body components.
(3) RS control technology: Measures transfer functions of the MBS model and calculates drive signals by conducting iteration.
(4) Fatigue Analysis technology: Calculates the fatigue life and the stress waveform of the FE model using the results of the MBS.

The use of different analytic tools in the technologies described above makes data formats and their transfer complex. We therefore developed a Graphical User Interface (GUI below) to make the system easy to operate by automating the procedure and simplifying the operation.

3.1 Simulation Models

Fig. 3 shows the entire simulation model of the VRS. The VRS simulation model consists of a test rig model and a motorcycle model. Simplified models mainly using rigid body elements are used to reduce the number of man-hours involved in model preparation and computation time.

3.2 Test Rig Model

The test rig model consists of actuators, a transmission mechanism and a datum face. Although geometry is included for appearance, the models are made up of constraints without mass properties, enabling a lower computation time over models composed of flexible parts. Because this is a computational model, drives can be applied which are impossible to achieve in a RS test due to the limitations of the hydraulic actuators.

3.3 Motorcycle Model

A motorcycle model is first built up using rigid body elements for simplicity. Later, the required components are replaced with FE models to obtain the desired behavior in the part being focused on. In the model discussed here, the main frame body, engine crankcase and rear sub-frame were replaced with FE models to predict the fatigue strength of the main frame, and a flexible front fork was used.

The FE model is defined using mode characteristics calculated using the Craig-Bampton method.

The rigid body elements are defined using mass properties (mass, inertia, the moment of inertia), and three-dimensional CAD data are used for their appearance.

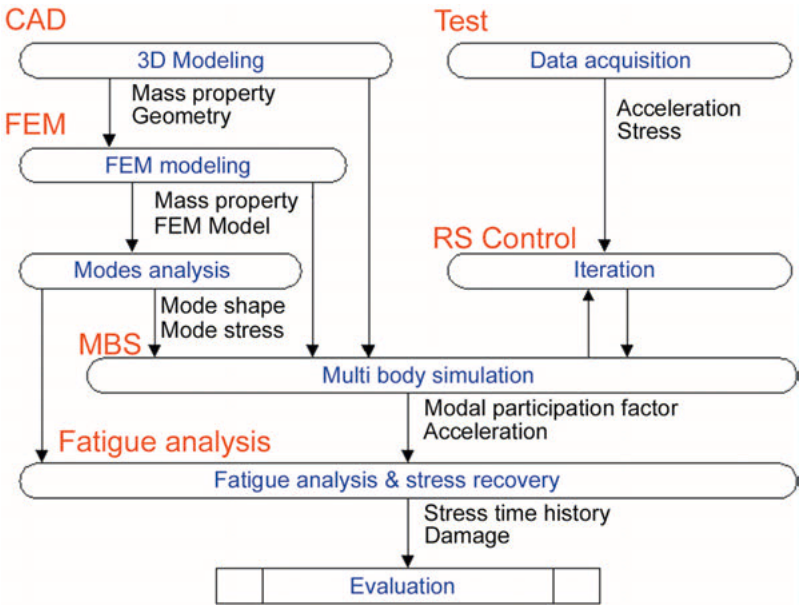


Fig. 2 System flow of virtual road simulator

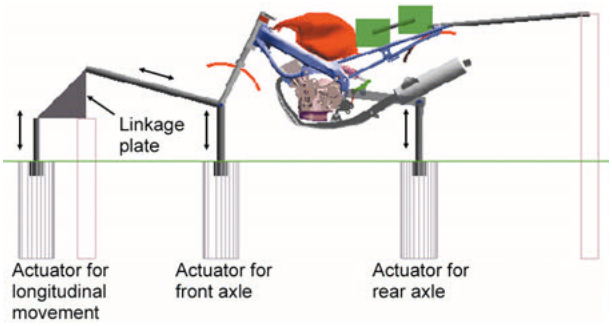


Fig. 3 Construction of virtual road simulator

3.4 Filtering

A data recorder with a built-in anti-alias filter is used for measurement of the target signals during actual running and measurement of response signals in the RS. The individual frequency characteristics of the anti-alias filter causes amplitude attenuation or phase shift in the waveform passing through it. Therefore, correct evaluation is impossible when comparing calculated results and measurement results if no filter or a filter with different characteristics has been used for calculated results. For this reason, an anti-alias filter with the same characteristics as the data recorder is used to process calculated results in the VRS.

3.5 Iteration

In this system, iteration is conducted on the VRS using target signals obtained from actual running, and drive signals are calculated. To prevent differences between the iteration on the VRS and RS caused by differences in software, the same in-house RS control software as used in RS durability tests was used.

3.6 Prediction of Fatigue Life and Calculation of Stress

In this system, the following data were analyzed to predict the fatigue life in the FE model:

(1) Stress amplitude distribution on target part surfaces
(2) Damage distribution on target part surfaces
(3) Hot spot (high-damage area) distribution
(4) Stress waveforms at hot spots.

Hot spots were specified by evaluating two-dimensional stress changes on the surface of target parts. Stress $\sigma x(t)$ at time t on hot spot position x is calculated using the following equation:

$$\sigma x(t) = \Sigma \sigma xi \xi i(t) \qquad (1)$$

where σxi is the mode stress at position x of the 'i'th mode (including constraint modes and normal modes) and ξi (t) is the modal participation factor (displacement) of the 'i'th mode at time t.

4. Verification of Simulation Accuracy

This section discusses an example of verification of simulation accuracy using an in-line 4-cylinder road sports model.

4.1 Verification Criteria

The measured results of the RS were adopted as the criteria for verification of the simulation accuracy of the VRS. In the case of measurements conducted during actual running, the number of channels that can be measured during one test is limited by the capacity of the measurement instruments, and if further measurements are conducted to increase the number of channels, consistency of data cannot be guaranteed. The reproducibility of the RS allows repeated measurements to be conducted under the same conditions. The correlation of the RS with actual running has already been verified[2]. Figs. 4a and 4b show comparisons between target signals obtained from measurements during actual running and results from VRS and RS simulations respectively.

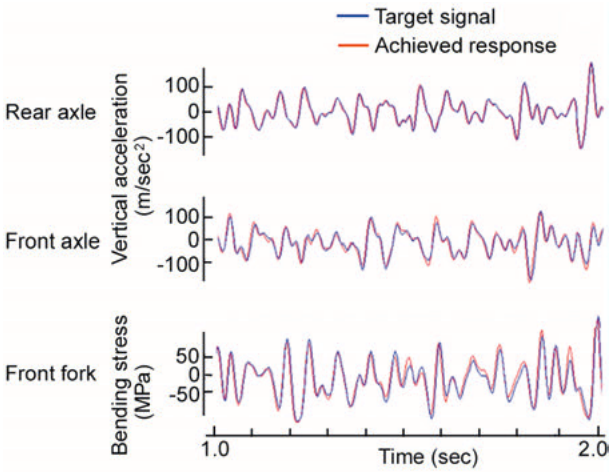


Fig. 4a Comparison between target signals (Actual running) and achieved responses on VRS

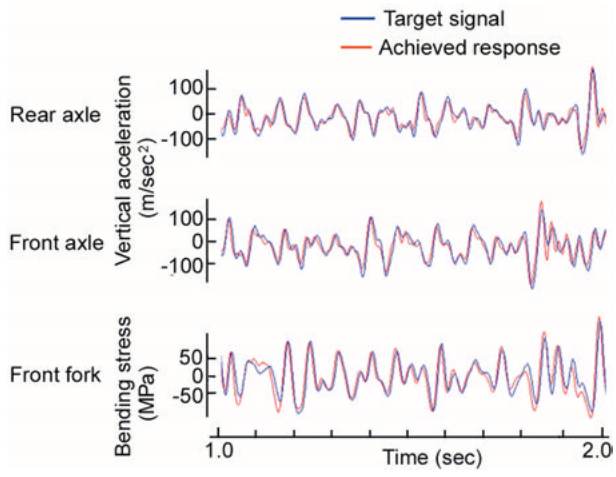


Fig. 4b Comparison between target signals (Actual running) and achieved responses on RS

4.2 Acceleration Waveforms

Fig. 5 shows acceleration measurement points and Fig. 6 shows the acceleration waveform comparison at each location. Calculation results show a strong correlation with measurement results for both vertical and longitudinal acceleration at the front and center of the body, and reproduction of movement was determined to be very high for the entire body. Using this system it will be possible to input predictions for parts with local vibration modes.

4.3 Stress Waveforms

Locations in the frame body for stress measurement and comparisons of time history stress waveforms for each location are shown in Figs. 7 and 8 respectively. At points A and B around the front of the frame, time history stress waveforms obtained by calculation show a very high correlation with measurement results. A high correlation can also be observed at point C at the rear of the frame, despite differences in absolute values. It is theoretically possible to reduce this difference by using FE model forms and increasing the accuracy of plate thickness at point C.

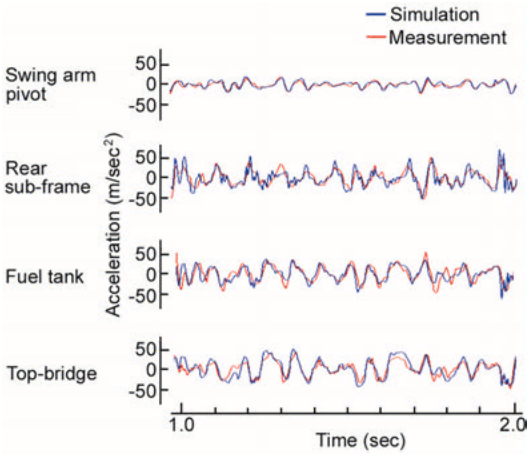


Fig. 6 Acceleration comparison between simulation and measurement

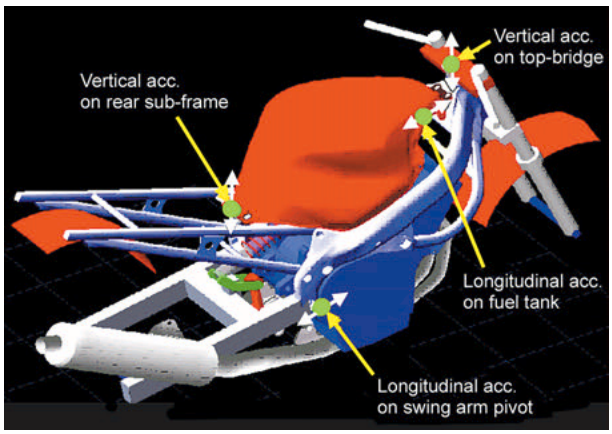


Fig. 5 Locations of acceleration measurement

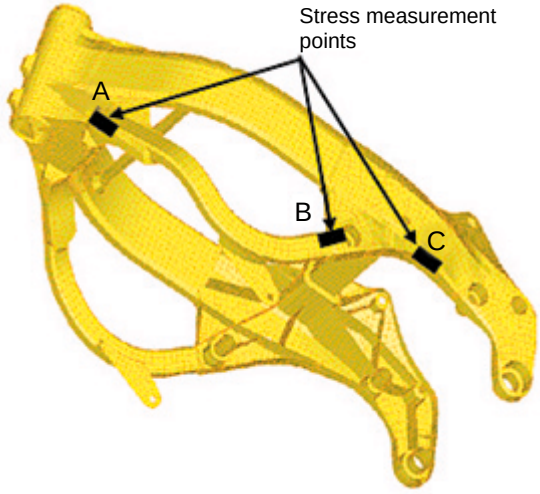


Fig. 7 Locations for stress measurement

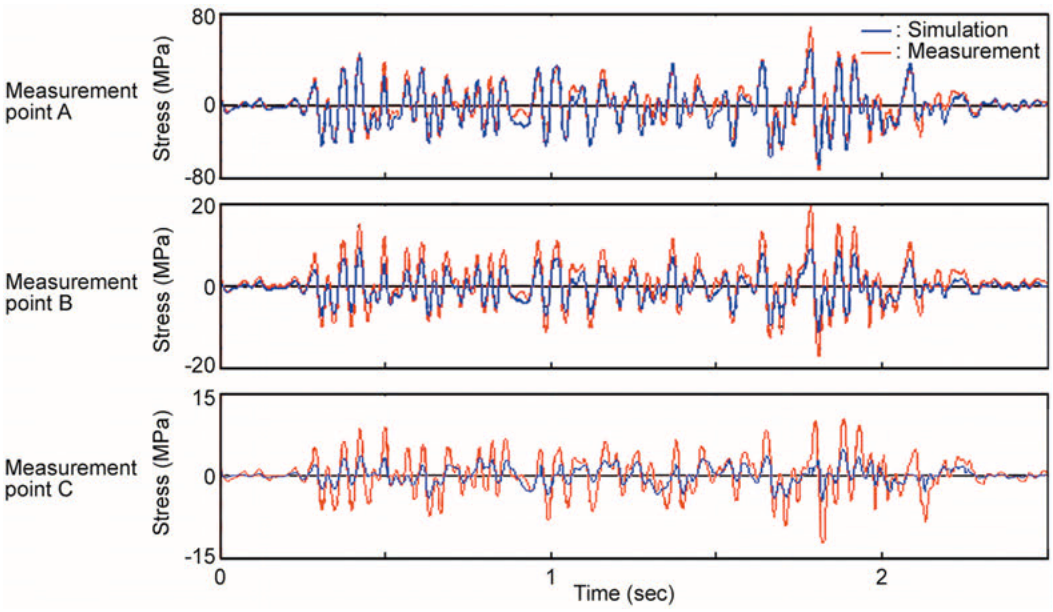


Fig. 8 Stress comparison between simulation and measurement

4.4 Damage Distribution

VRS technology makes it possible to observe damage distribution in specified parts. Fig. 9 shows an example of the result of a fatigue analysis. In the future, it will be possible to identify and respond to hot spots in the early stages of the design process, and to use the VRS to help predict the effectiveness of design changes.

5. Development of the GUI

A graphical user interface (GUI) has been developed to make VRS technology easy to use. Fig. 10 shows an example. The GUI has the following features:

(1) Simplification of model preparation procedure
The motorcycle has been divided into major parts for modeling, and templates for each part have been prepared. Users can input parameters and combinations of templates to prepare models.

(2) Automation of analytic procedure
Transfer of files between software applications, change of file format and calculation procedures have been automated.

(3) Simplification of result output
Result output has been simplified so that calculation results can be easily recognized on the GUI.



Fig. 9 Fatigue analysis result

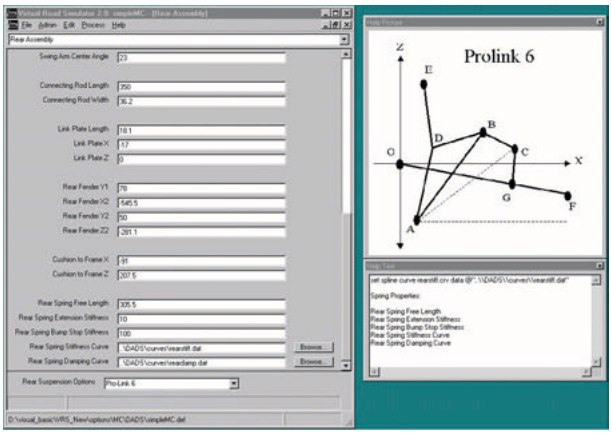


Fig. 10 GUI (Graphical User Interface)

6. Conclusion

The following results have been obtained by combining FEM, RS control, MBS and fatigue analysis technologies in the development of a VRS system:

(1) The behavior of a motorcycle in a RS durability test has been accurately reproduced.

(2) Damage distribution and stress waveforms at hot spots have been calculated from motorcycle behavior in a simulation.

(3) Automation of model preparation and procedures has been achieved using a GUI.

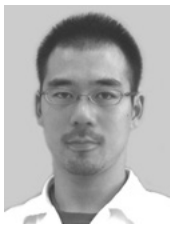
These results have helped enable prediction of fatigue durability of the whole motorcycle, including multiple loads applied to parts at different times and local vibration modes that were not possible to predict using linear static analysis.

References

(1) Harashima, S., et al., Development of Multi-use Road Simulator, SAE Paper 931912

(2) Harashima, S., Evaluation Method of Motorcycle Fatigue Strength Using Road Simulator, SAE Paper 951817

■ Authors ■


Makoto HASEGAWA


Kenji NAKANISHI


Shokichi HARASHIMA


Hideki YAMAGUCHI

Development of a Procedure for Interior Noise Estimation by Virtual Vehicle Analysis

Tatsuhide SAKAI* Masahiro TERADA*
Shuichi ONO* Naoki KAMIMURA*

ABSTRACT

This paper summarizes the development of a predictive vibro-acoustic full vehicle model of a mid-size sedan and focuses on the engineering analysis procedures used to evaluate the design performance related to engine-induced noise and vibration during the drawing stage of development. The vehicle model is comprised of a mixture of test-based and finite element component models. FRF-based substructuring is used to join these models. The virtual car model is loaded with engine forces resulting from indirect force identification. This force-set includes combustion, inertia, piston slap and crank bearing forces for engine harmonics from the 0.5 to 10th order. Analysis of this model yields predictions of vibration levels for every component and every interface between components, and of interior noise. The objective is to provide the vehicle NVH engineer with the capability to identify major causes for peak noise levels, to set targets and to develop action plans for every component design team. Having such information at any design stage will effectively reduce both the design cycle duration and the number of physical prototypes.

1. Introduction

A long time has passed since demands began for reductions in product development time. Recently, there has also been a desire to increase the speed of automobile development at every stage, from product concept to styling design, and from prototype fabrication to volume production. The most urgent issue for development engineers, in particular, is producing a satisfying match of performance to the product concept while reducing the number of prototype vehicles and prototype lots.

Meanwhile, one of the technical features of the vibro-acoustic performance of a finished vehicle is that this performance is determined by the interrelation of various systems, including the engine, subframe, and body. Therefore, when altering vibro-acoustic performance, it is crucial to clarify which systems will produce the most effective results. The investigation of methods for achieving vibro-acoustic performance objectives also requires consideration of handling, ride comfort, acceleration performance, collision characteristics, cost, weight, and other such performance objectives that are often in opposition to vibro-acoustic performance. Consequently, it becomes necessary to create many prototype vehicles that have various specifications applied to confirm all of these competing objectives.

A full vehicle model for prediction of interior noise was created to facilitate the management of the various vehicle system characteristics as they relate to vibro-acoustic performance within a shortened development time (Fig. 1).

* Tochigi R&D Center

This model was constructed from finite element component models combined with component models based on actual measurement data. The validity of this model construction and its prediction accuracy are verified in the first prototype lot. As a result, it was verified that this full vehicle model has the following features:

- The capability to define a vehicle system's contribution to cabin noise
- The capability to predict cabin noise resulting from a component design change

Use of this predictive system enables quantitative study of corrective actions taken on each vehicle system as required to control cabin noise from the initial stage of product development. This makes it possible to formulate action plans that are based on the most efficient direction regarding corrective measures to be taken by the designers of each component. Furthermore, the model enables immediate understanding of the effect outside change requests will have on cabin noise.

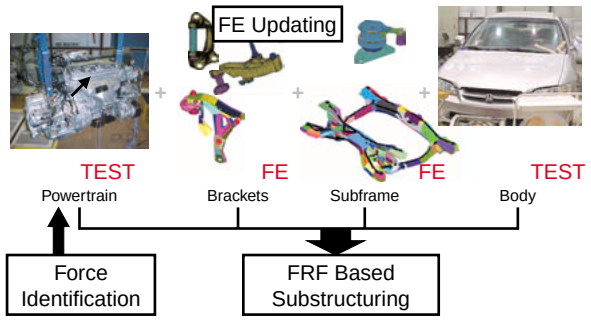


Fig. 1 Virtual vehicle model for estimation of interior noise

This paper describes the virtual vehicle model that was built from the combination of experimental and numerical models, and the verification of the resulting model. It will also show the superiority of this method.

2. Testing and CAE Modeling of Each Component and Construction of the Virtual Vehicle

The following will provide an overview of the modeling techniques used with this method.

The various components are represented by an FRF matrix defined by the degrees of freedom of the inputs, connections, and responses. They are then assembled using FRF-based substructuring.

The relationship of the response vector {Xi} to the excitation vector {Fj} for the model defined by the FRF matrix [Hij] is defined by the following:

$$\{X_i\}=[H_{ij}]\{F_j\} \quad (1)$$

Substructuring yields the FRF matrix composed of the input force degrees of freedom excited during actual operation and the response degrees of freedom, which are arbitrarily selected. Component combinations are not limited to rigid connections, but can also have connections with an intermediate elastic element that is represented by the commonly used stiffness matrix [Ks]. Thus, the structured transfer function will be in a state that balances force and linearity with respect to displacement.

The experimental model is generated using actual measurement data and is represented by an FRF matrix. Likewise, the FE model is represented by the thus generated FRF matrix. This presupposes that FE mode accuracy was improved by updating the FE model from an experimental modal analysis conducted on the first prototype product.

In addition to the inertia force component calculated from the engine specifications and the combustion force component calculated from the actual measured combustion pressure, the input force is also composed of a residual component that is identified by the inverse matrix method from the actual measured engine vibration.

Fig. 2 presents an overview of the individual components. The vehicle model described in this paper is composed of the powertrain (engine plus transmission), the engine mounting brackets, the engine mountings, the subframe, and the body, for a total of five elements and eleven parts. The powertrain and body are represented by an FRF matrix based on actual measurements. The engine mounting brackets and subframe are defined by an FE model, and the engine mountings are defined by complex stiffness curves that describe the engine mount characteristics.

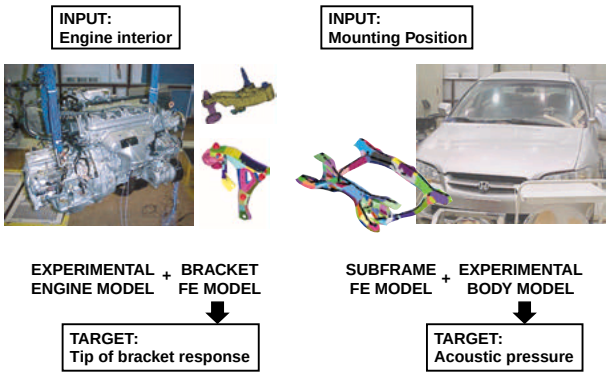


Fig. 2 Individual components of the virtual vehicle model

2.1 Experimental Engine Model

The FRF matrix for the engine model is made up of input forces with 24 degrees of freedom and responses with approximately 150 degrees of freedom. Assuming combustion pressure, piston guidance, and piston slap, the input force directions were set perpendicular to (axial) the cylinder wall and head and perpendicular (axial) to the crank bearing. In order to obtain the transfer function, the pistons, connecting rods, and crankshaft, which are the operational parts inside the engine, were removed and the engine was excited using a minishaker. Fig. 3 shows the position of two minishakers within the cylinder liners.

2.2 Finite Element Model of the Engine Mounting Bracket

The powertrain is attached to the vehicle body by four mounting brackets. The target region for this analysis is the

high frequency band of the second-order to tenth-order components of engine revolution, where there is concern that engine mounting bracket resonance will have a negative effect on the vibro-acoustic performance. For the spot welded stamped shell type bracket, an FE model was generated with shell elements, including a spot weld model. The bracket FE model was tuned using the experimental transfer function and modal parameters obtained from the initial prototype part, increasing the accuracy of the model. This method is also applied to other FE models.

Fig. 4 shows the mode correlation of the final rear bracket FE model with the experimental model. A close correlation was obtained, with MAC values of 0.70–0.95 in at least ten modes.

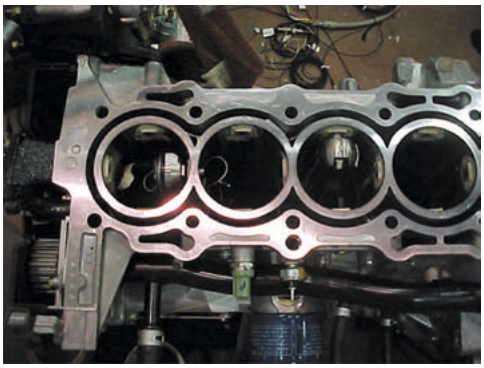
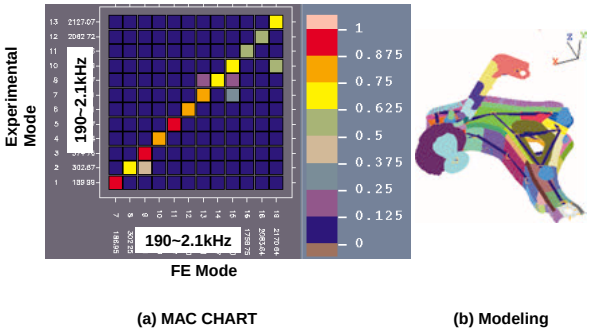


Fig. 3 Minishaker positioning in cylinder liner



(a) MAC CHART (b) Modeling

Fig. 4 Final rear bracket FEM and MAC correlation with test model

2.3 Finite Element Model of the Front Subframe

The front subframe supports two of the four mounting brackets and is fastened to the vehicle body by six bolts. The mode correlation for this component model was improved by focusing on the behavior at locations where panels are touching each other between the spot welds.

Fig. 5 shows the mode correlation between the experimental model and the final FE model through 800Hz and above. A close correlation was obtained, with MAC values of about 0.75 or more.

2.4 Test Body Model

The body was defined by a noise transfer function matrix for cabin noise and point mobility corresponding to the degrees of freedom of subframe attachment bolts (six points) and engine mounting (two points).

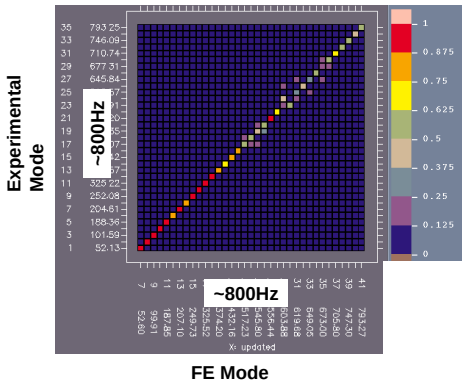


Fig. 5 Correlation chart and final FE mesh of subframe

3. Substructure Model

Two sub-assemblies are made from the various component models. The first assembly is the union of the powertrain and four mounting brackets. The next is the union of the subframe and body. Fig. 6 shows the assembly process and FRF matrix required in the case of connection between the subframe and body.

The point mobility matrices Hss (s: connection degree of freedom) for the various components are connected through the connection stiffness matrix K. The body matrix His (i: output degree of freedom, s: connection degree of freedom) is the body noise transfer function for the subframe connection degrees of freedom, and the subframe matrix Hsj (s: connection degrees of freedom, j: input force degree of freedom) is the transfer function for the responses to body connection degrees of freedom with respect to the input force from front and rear bracket attachment points. The subframe matrix Hks (k: other degrees of freedom) and Hkj are the vibration response of points representing the component structure. These are added to the matrices in order to visualize operational deflection shapes following assembly. Similar matrices are also defined for the powerplant and mounting brackets.

The substructure model thus subassembled is verified by actual measurement transfer function. Fig. 7 shows a comparison of the actual measurement and calculated transfer functions for the bracket tip response level with respect to vertical excitation of the crank bearing. The various sharp peaks result from bracket resonance. Fig. 8 shows a comparison of the body noise transfer function from the engine mounting point on the subframe to the driver's left ear as verification of the subassembly of the

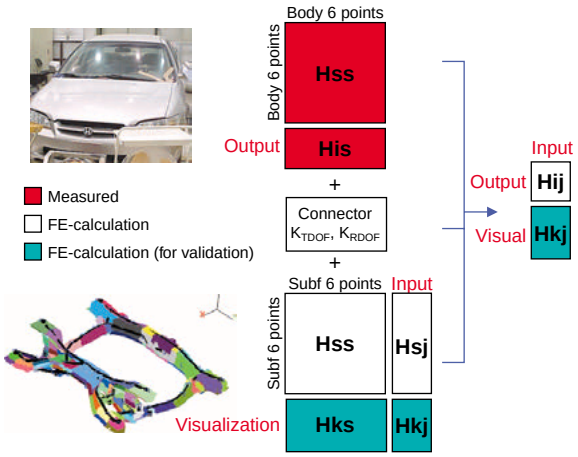


Fig. 6 Substructuring component and assembly matrix for subframe to body model

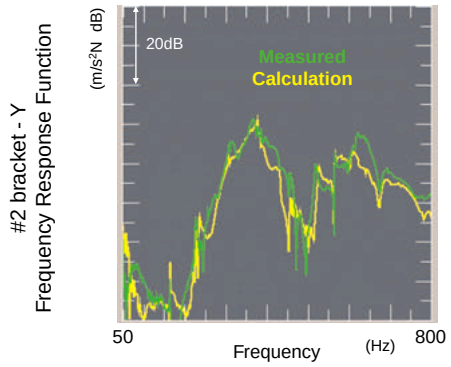


Fig. 7 Measured and predicted FRF between crankbearing force and engine bracket vibration

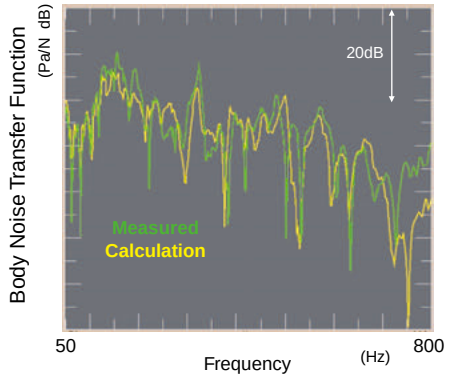


Fig. 8 Measured and predicted body noise transfer function at the engine mounting points on the subframe for the driver's left ear

subframe and the body.

It is also possible to analyze the importance of a single unit mode, in terms of the post-assembly mode, by correlation of the unit mode with the post-assembly mode.

In this paper, the steering system and suspension arms attached to the subframe are not modeled. After analysis of their respective effects during the initial test, the model also made combined use of the FRF matrix with the components that have recognized impact connected to the subframe and the body.

4. Identification of Engine Input

The forces generated inside the engine are calculated by the indirect force identification method [ref2]. This becomes an input condition for the vehicle model assembled by substructuring.

4.1 Direct Identification of Known Forces

First, the inertia force is calculated from the engine specifications (pistons, connecting rods, crankshaft) after synchronizing with the actual measured speed of the engine in operation. Next, the combustion force is derived from actual measurement of the combustion pressure signal. Phase accuracy is assured during analysis of high-order regions by using the camshaft trigger and flywheel timing pulse to convert all measurement signals from time units in order to make them compatible with crankshaft-angle units.

The inertia force and combustion force are calculated in advance. Then the transfer from the crank pin to the crank bearing is defined using the crankshaft FE model, and the force generated by the crank bearing is predicted. The inertia force and combustion force are then joined as the force generated in the crank bearing to create the known force vector. In the present analysis, known force vectors were created for the 0.5 to 10th order components of engine harmonics in 0.5-order increments.

4.2 Identification of Residual Force

Residual force was determined by using equations (2) to (7).

The powertrain vibration response generated by the known force $\{F_{known}\}$ can be derived by calculating the FRF matrix [Hij] from the input force degrees of freedom to the engine and bracket vibrations in the virtual vehicle (Equation 2).

All of the forces generated during operation are not known. Therefore, the vibration $\{X_{known}\}$ calculated from the known force above is subtracted from the total vibration generated during actual operation $\{X_{measured}\}$. The resultant $\{X_{residual}\}$ is estimated to be the outcome of the remaining residual force $\{F_{residual}\}$. The components of the known force are removed from the vibration caused during operation (Equation 3). The vibration during operation, which now contains only the components resulting from residual force, and the FRF matrix of the full vehicle model are used in a matrix inversion equation to calculate the residual force (Equation 4). This residual force $\{F_{residual}\}$ is added to the known force $\{F_{known}\}$ that was initially estimated, thus yielding the force vector $\{F_{predict}\}$ of all forces generated for each harmonic component (Equation 5). In order to verify the validity of this predictive process, it is necessary to calculate the engine and bracket vibration $\{X_{predict}\}$ resulting from all forces generated (Equation 6) and compare this with measured vibration (Equation 7).

$$\{X_{known}\}=[H_{ij}]\{F_{known}\} \quad (2)$$

$$\{X_{residual}\}=\{X_{masured}\}-\{X_{known}\} \quad (3)$$

$$\{F_{residual}\}=[H_{ij}]^{-1}\{X_{residual}\} \quad (4)$$

$$\{F_{predict}\}=\{F_{known}\}+\{F_{residual}\} \quad (5)$$

$$\{X_{predict}\}=[H_{ij}]\{F_{predict}\} \quad (6)$$

$$\{X_{error}\}=\{X_{predict}\}-\{X_{measured}\} \quad (7)$$

4.3 Effects of Matrix Size on the Prediction of Generated Force

The prediction accuracy for force generated during operation is determined by the FRF matrix used when identifying known force and residual force. In order to stabilize the matrix inversion equation, the basic degrees of freedom were set to 90 degrees of freedom for the crank bearing side on the powertrain frame and the cylinder head, while extended degrees of freedom were set for the bracket attachment points (48 degrees of freedom) and for the bracket tips (18 degrees of freedom) as these areas were considered important points for the assembly. Fig. 9 shows the differences in generated force estimates resulting from matrix models of different sizes determined by the basic and extended degrees of freedom. It is apparent that both basic and extended degrees of freedom are necessary in order to stabilize the generated force prediction calculations.

The initial prediction calculation used matrix inversion for the main body of the powertrain alone, excluding brackets. However, comparison of the calculation results for the powertrain with the four brackets attached confirmed that this matrix provided insufficient accuracy. When carrying out force identification prediction calculations in this way, it is essential to have predetermined the FRF matrix required for force identification using the powertrain model that includes the bracket FE.

Fig. 10 shows a comparison of values for 5th order vibration in the bracket tips as measured and as predicted by identification matrices of different types and sizes. During actual operation, damping due to the engine mounts occurs so the prediction results from the model with only the engine and brackets attached formed sharp peaks that were not damped and thus were different from actual measurements. There is a close match with measurement data under the other matrix conditions, which suggested that calculation of residual force using the full vehicle model FRF matrix is necessary to achieve optimum accuracy in prediction calculations.

A simple approximate modeling method for representing the body characteristics of the full vehicle model is to replace the actual measured point mobility with a fixed rigid connection to the ground. The validity of this method for the present analysis has already been verified by the prediction results shown in Fig. 10. This method is suitable for evaluation of engine mounting transfer force or vibration when there is no body model.

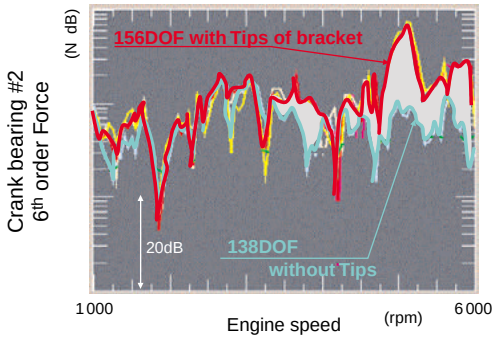


Fig. 9 Crankbearing #2 6th order force estimate for different matrix models

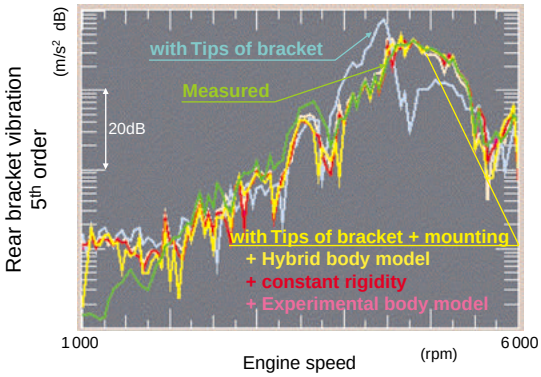


Fig. 10 Measured and predicted 5th order bracket #2 axial vibration for different matrix models

5. Verification of the Virtual Vehicle Model

Application of the identified force to the virtual vehicle yields predictions of vibration from all components and all connections between components, and prediction of cabin noise, and enables evaluation of force transmissibility. Essential matters related to vibro-acoustic performance are vibration levels on the engine side and the body and subframe side, the force transmitted through the mount as a result of internal engine forces, and the noise level in each area of the interior. The accuracy achieved by the present virtual model is described below.

5.1 Vibration in the Engine Side Bracket

Fig. 11 shows a comparison of the actual measured and predicted levels of 6th order vibration in an engine bracket. It was decided to set the FRF matrix used in force identification to specify 156 degrees of freedom in response to the input force with 24 degrees of freedom, making the matrix ratio of the matrix inversion equation 7 or higher. A close correlation was obtained, and similar prediction accuracy was also achieved with other orders of harmonics and other brackets.

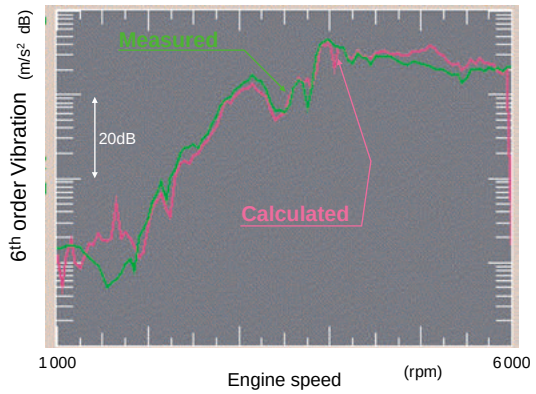


Fig. 11 Measured and predicted vibrations for 6th order bracket #2 axial vibration

5.2 Prediction of Cabin Noise

The ultimate objectives of the virtual vehicle are to predict cabin noise during actual operation and to predict the extent of the changes that will result from structural changes in component levels. Fig. 12 shows a comparison of the calculation results from the virtual model and the actual measurements of 6th order cabin noise. The calculation results show two sets of specifications. The difference is in the range settings for the experimental model and the FE model. Conducting simulations with models defined differently in this way demonstrates the importance of the following parameters to prediction accuracy:

1. Quality and accuracy of the FE component model
2. Range of the FRF matrix used for force identification
3. Reliability of the complex stiffness constant for the engine mounts

The quality of the FE model is increased when the model is constructed using the criteria from the initial prototype part. This can also be revised whenever there are subsequent opportunities to build prototypes. Any FRF matrix that is constructed from test data requires considerable effort in measurement of the previous models of the vehicle body, as well as in the engine bench tests.

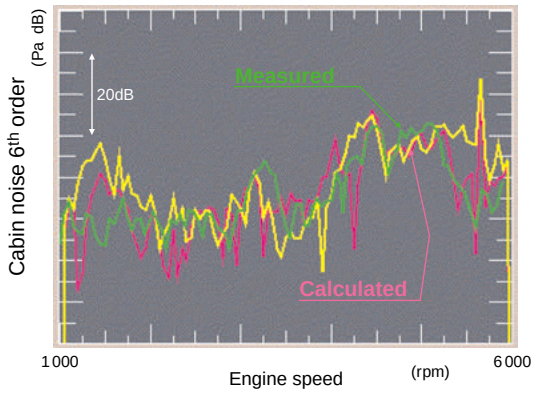


Fig. 12 Measured and predicted 6th order interior noise for 2 virtual car models

6. Application to Product Development

The present method was applied as a development tool in the initial stage of design on the basis of the above verification results.

6.1 Application of New Parts in the Virtual Model

Prototype components (hereafter referred to as A spec) were modeled by FE and incorporated into the component model (prototype engine and body) used as a test base. The resulting full vehicle model was then used for prediction. Fig.13 shows the FE model for the A spec engine mounting brackets and subframe. It was determined in the initial prediction that high noise levels resulted from component characteristics at various engine speeds. Countermeasures were applied in the form of modifications to the FE component model, and the effects were predicted in advance by the virtual vehicle model.

Verification was carried out using actual prototypes after the model predictions were made. Fig. 14 shows a comparison of predicted and measured 6th order vibration

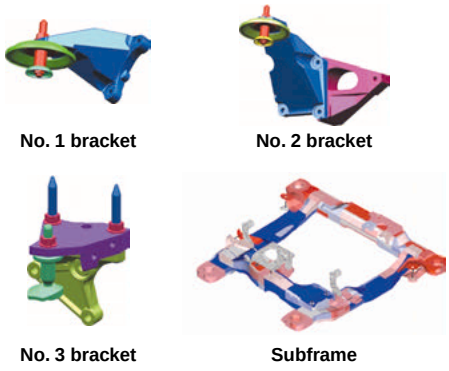


Fig. 13 A-spec parts: engine mounting brackets and front subframe

in the No. 3 engine mounting bracket. It is apparent that the model prediction accuracy is valid. Fig. 15 shows a comparison of predicted and measured body noise transfer function in the subframe. It is clear that the subframe modeling and its assembly in the virtual vehicle, with the exception of one frequency range, were valid. Points that fail to agree with the measurement resulted from structural

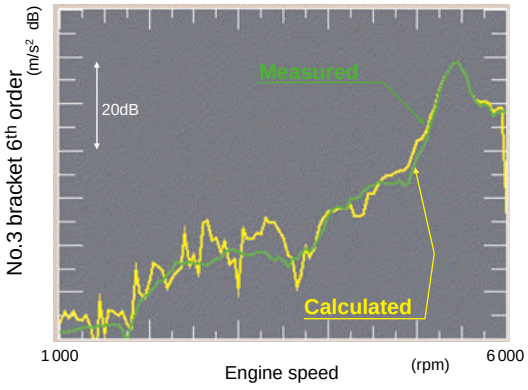


Fig. 14 6th order vibration of the No.3 engine mounting bracket on a 2nd stage prototype vehicle

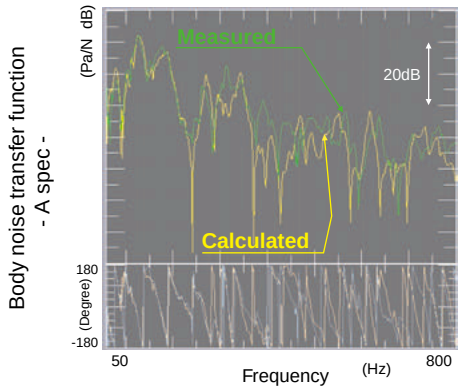


Fig. 15 Measured and predicted body noise transfer function, using improved A-spec subframe in the virtual car model

aspects that were specific to the prototype specifications, and these made up a small proportion of total predicted cabin noise.

6.2 Analysis of the Noise Transfer Path

The contribution of each ultimate transfer path for cabin noise was analyzed in detail.

6.2.1 Force transmissibility

Force transmissibility can be evaluated directly in terms of the frequency response characteristics of unit force inputs by their respective paths. It is possible to calculate the force transmitted through the engine mount during actual operation by using matrix calculation with the identified forces generated inside the engine.

Fig. 16 presents a comparison of the 6th order components of transmitted force. This shows clearly how the force transmitted through the No. 3 engine mount changed due to the change from the base specifications, which were the initial specifications, to the A spec. The transmitted force is shown to be reduced by the new design in nearly all ranges, but a new transmitted force can be seen to peak in the vicinity of 5500 rpm.

In this way it is possible to identify the force, including the effects of structural connections and the total effect from the dynamic actions of the connections between components. Consequently, it is also possible to apply this force as input to the FE model prior to substructuring. Since construction of the substructuring model can be limited to the degrees of freedom of the connection points, the forces at the connection points can be derived from a virtual model that is limited only to the necessary degrees of freedom. Those forces can be applied to the full-size FE model, so that evaluation of all of the degrees of freedom of the FE model can be carried out as a detailed analysis of the model, while at the same time decreasing the time required to construct the model.

6.2.2 Transfer path analysis of the engine mounting

The contribution of the transfer path through each engine mount to cabin noise is analyzed using ordinary path analysis.

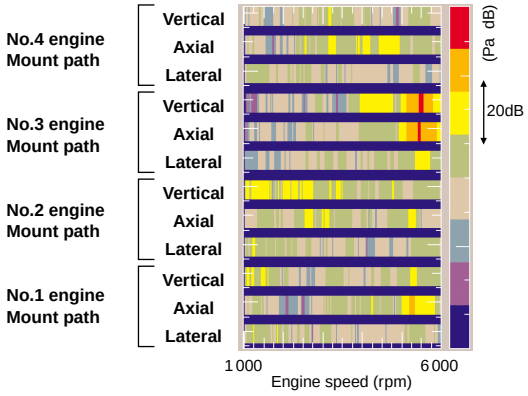


Fig. 17 Engine mount path contribution to interior noise simulation on A-spec parts vehicle

Fig. 17 is a color bar graph that shows these contributions according to engine speed. This graph shows that of the four engine mounts, the No. 3 bracket has a significantly high contribution rate in the 5500 rpm region.

Fig. 18 shows the contribution vector for cabin noise at 5500 rpm. The No. 3 engine mount is the vector that has the highest contribution. This is followed by the contribution from the No. 1 engine mount, which has generally the same phase as the total cabin noise.

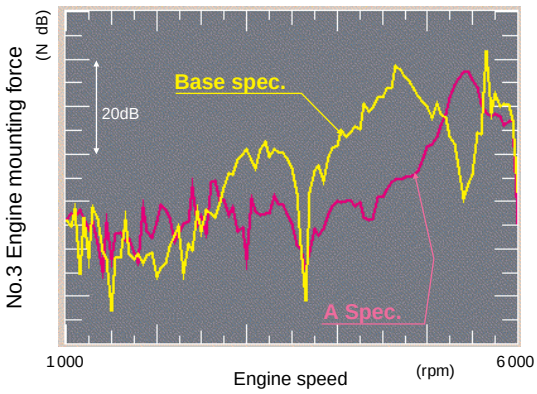


Fig. 16 Calculated force transmitted through #3 engine mounting : virtual vehicle vs. base specification

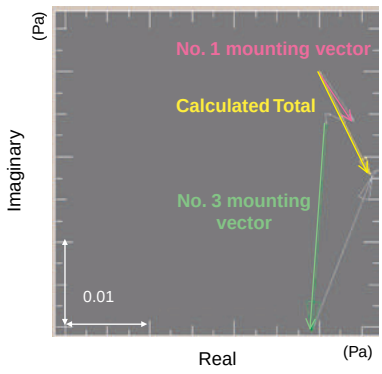


Fig. 18 6th order vector plot of interior noise contributions at 5 500rpm on A-spec parts vehicle

6.2.3 Detailed analysis of the transfer path

The force transmitted through each mount is determined by the force generated inside the engine and the transfer characteristics of the engine structure. Conducting analysis of the kind described in the previous section will clarify the contribution of the various independent paths inside the engine. Fig. 19 shows a color map of the contribution from forces inside the engine to the force transmitted through No. 3 engine mount. The interior engine forces follow 24 paths that are axial, lateral, and vertical to the crank bearing and cylinder head.

It was made clear that the predominant contributions are from forces vertical to the crank bearing and to the cylinder

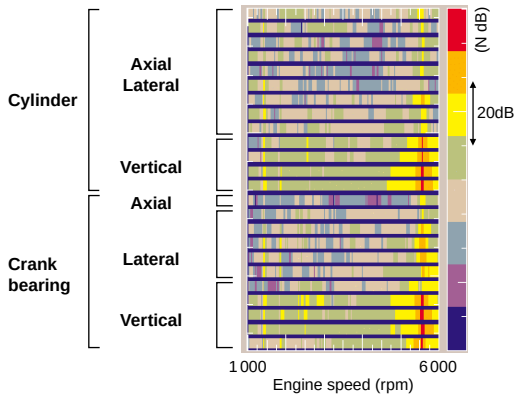


Fig. 19 6th order path contribution from interior engine forces to #3 engine mount force on A-spec parts vehicle

head. However, in the 6th order component, these counteract each other because their phases do not coincide. It is evident that the crank bearing axial force becomes significant at 5500 rpm.

The virtual vehicle model deals with the interactions of all component elements from the engine interior to the cabin interior. Consequently, it also makes it possible to analyze how the various independent paths inside the engine contribute to interior noise.

Fig. 20 shows the contribution of interior engine forces to cabin noise in the form of color bars. The same path definitions as in Fig. 19 are used, but the result includes all component elements of interior noise. It is possible to examine this in detail by using engine mount transfer path analysis to complement the force transmissibility analysis. It is apparent that the largest contributions to 6th order interior noise at 5500 rpm are from the vertical input path through the crank bearing and the vertical input path through the cylinder head, while the next largest contribution is from the axial path through the crank bearing. This shows a similar tendency to that in the contribution analysis of the force transmitted through the No. 3 engine mount. That is, the contribution of interior engine forces to cabin noise (Fig. 20) correlates closely with the contribution of force transmitted through the No. 3 mount (Fig. 19), and it becomes clear that the predominant contribution to cabin noise is from the force transmitted through the No. 3 mount (Fig. 17).

Fig. 21 shows the vector contribution of interior forces to 6th order cabin noise when the engine is operating at

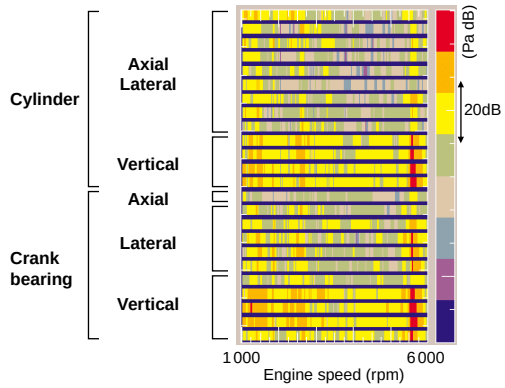


Fig. 20 6th order path contribution from interior engine forces to interior noise on A-spec parts vehicle

5500 rpm. The greatest contributions are from the vertical force through the crank bearing and the vertical force through the cylinder head. These both have generally the same magnitude but opposite phases. It is evident, therefore, that the two paths with the largest contributions are in opposite directions, so that they actually cancel each other out. The next largest contribution is from the axial crank bearing force, and since this is generally in phase with the vector sum, it clearly has a significant effect. The total vector sum also agrees very closely with the actual measured noise vector, verifying the high reliability of the model of the internal engine force transfer path.

This virtual vehicle can be applied to evaluation and analysis of vibro-acoustic design performance at every stage in the design cycle. The force transmitted from the engine to the connections between components, the force

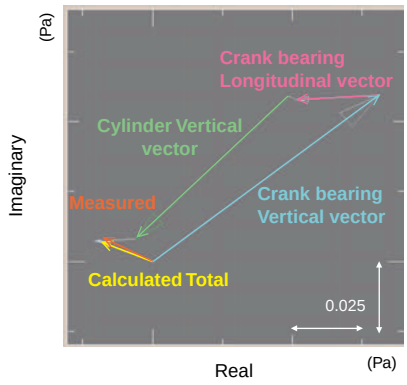


Fig. 21 Vector contribution of interior engine forces to 6th order interior noise at 5500rpm on A-spec parts vehicle

transmitted through the engine mount during operation, the vibration at the mounting bracket tips, the body vibration, and the body noise transfer function are evaluated respectively as system performance elements. Further, the ultimate target of evaluating their respective contribution to cabin noise can be achieved. The effect of the design of individual components on vibro-acoustic phenomena in an actual vehicle can be simulated with ease. Consequently, by continuously expanding and developing this model and synchronizing its use with design changes and prototype lots, it becomes possible to carry out quantitative management of vibro-acoustic objectives, system performance, and component drawings.

7. Conclusion

A method of virtual vehicle model analysis was developed that is suitable for use in decreasing the time required for the vibro-acoustic development process.

- This method makes it possible to evaluate cabin noise targets at every stage of automobile development. Since it allows effects on cabin noise to be taken into consideration at the initial stage of design, it also enables decisions to be made so that design specifications at the product planning stage will comply with cabin noise targets.
- It allows timely feedback to be provided to the component design team on how the deformation shape of subject components during operation, their transfer functions, their path contributions, their forces, and their vibration levels are positioned with regard to the targets.
- It enables path contribution analysis of cabin noise using both the interior engine forces and the forces transmitted through the engine mounts as references.
- When design changes to components are made, use of the virtual vehicle model allows rapid assessment of the changes regardless of whether the change requests are vibro-acoustic related or otherwise.

This method enables verification of contributions to cabin noise and clarification of the underlying factors in failure to meet targets. Consequently, this analysis procedure is effective in facilitating collaboration with component designers in the course of conducting vibro-acoustic management. Use of the procedure makes it possible to give quantitative consideration to product factors such as cost, weight, and strength in conjunction with vibro-acoustic product quality targets, as well as providing an effective means for continuous monitoring of cabin noise objectives.

References

(1) Sakai, T.: Development Procedure for Interior Noise Performance by Virtual Vehicle Refinement, Proceedings of the SAE Noise & Vibration Conference, 2001-01-1538 (2001)

(2) Sumi, K.: Development of a Hybrid Model for Powerplant Vibration, Proceedings of the SAE Noise & Vibration Conference, 1999-01-1656 (1999)

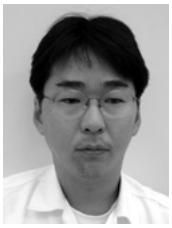
(3) Wyckaert, K.: Flexible Substructuring Based on Mixed Finite Element and Experimental Models — A Step Ahead of Transfer Path Analysis, Proceedings of the 14th International Modal Analysis Conference (1996)

(4) Wyckaert, K.: Hybrid Substructuring for Vibro-acoustical Optimisation — Application to Suspension-Car Body Interaction, Proceedings of the International Noise & Vibration Conference (1997)

■ Authors ■



Tatsuhide SAKAI



Masahiro TERADA



Shuichi ONO



Naoki KAMIMURA

Construction of an Acoustic FE Model for the Purpose of Engine Noise Reduction

Kazufumi KAWABATA* Tatsuhide SAKAI* Nobuaki HASHIMOTO*

ABSTRACT

A study was conducted in the construction of an acoustic finite element model with the velocity of vibration of the trimmed body as a boundary condition. An experimental model using velocity as the boundary condition was created by measuring the vibrational acceleration of each panel of a trimmed body by excitation measurement. The trim panel impedance was also set as a boundary condition for the acoustic FE model. It was decided that the setting values for the acoustic FE model, which provides a simple representation of multilayered trim panels, should be made approximately equivalent to actual measurement values. This hybridization of a structural experimental model and an acoustic FE model made it possible to represent the acoustic characteristics of the trimmed body up to 350Hz. It also enabled analysis of methods for efficiently minimizing the vibration level of vehicle body panel parts that contribute significantly to engine noise and for reducing the vibro-acoustic transfer function from the engine mount to passenger ear locations.

1. Introduction

To further reduce development time and number of prototypes and to achieve cost reductions in automotive development, it is essential to clarify performance requirements at the beginning of development and to predict performance during the drawing stage. With respect to the body frame in particular, high level styling, collision safety, comfort, reduction of noise and vibration and weight savings must all be achieved simultaneously. Large-scale finite element (FE) models are used to investigate body structure in development to reduce noise and vibration originating from powerplant input. However, predicting effects on noise in the cabin after modifications are made to the structure is difficult with the present technology. Furthermore, because cabin noise is also greatly affected by cabin shape, the reduction of this noise requires greater control of body vibration and acoustic characteristics rather than a simple reduction of body vibration. Therefore, high-accuracy cabin acoustic calculation models are necessary. Past research in the development of such models includes the following examples:a method for efficiently reducing acoustic sensitivity using a hybrid model composed of experimental modal body and cabin acoustic FE models [1]; and, for booming noises in heavy-duty truck cabs, an acoustic FE model using the results of an experimental modal analysis of cab structure as boundary conditions [2, 3]. In addition, trimmed body FE models have been used as structural models, instead of experimental models, to predict cabin noise up to 200Hz [4]. However, these models are not sufficiently accurate for analysis up to the frequencies of interest for cabin noise caused by engine vibration input.

The research described in this paper concerns creation of a hybrid acoustic calculation model capable of determining the vibro-acoustic transfer functions from the engine mounts to passenger ear positions at frequencies up

* Tochigi R&D Center

to 350Hz. This hybrid model uses an acoustic FE model and an experimental model formulated from trimmed body vibration tests. This technique was used as a developmental tool for the reduction of cabin noise.

2. Method for Creating the Experimental and Acoustic FE Models

2.1 Experimental Model

Body panel vibration, obtained from vibration measurements in an actual vehicle, was used as the velocity boundary conditions necessary for cabin noise calculations in the acoustic FE model. The rear engine mount, which has a high level of contribution to engine noise, was subjected to burst random vibrations in a trimmed body without an engine, transmission or suspension, and the vibrational acceleration of each panel was measured. Using this data, an experimental model was formulated (Fig. 1). In determining the number of measurement points, it was necessary to consider the upper frequency limits for acoustic calculations. To increase the accuracy of acoustic calculation results it is necessary to increase measurement points in the experiment and the number of elements in the FE model. However, this in turn increases the manpower required for the experiment and the time required for calculation. Therefore, the antinodal and nodal points of the sound waves were represented by establishing six points per wave length. The frequency f_{max} up to which the FE model is capable of analysis was found using the following equation.

$$f_{max} \leqq c/(6 \cdot l_{max}) \quad (1)$$

where c is the speed of sound, and l_{max} is the maximum distance between nodal points in the FE model. Because the upper frequency limit in this project was 350Hz, the pitch for measurement points was established at 100mm using Equation (1). Vibrational acceleration was measured at approximately 1100 points on the entire body. Sound pressure at the passenger ear position for each seat was measured at the same time as the vibrational acceleration, and used as verification for the acoustic calculation results described below.

2.2 Acoustic FE Model

The acoustic FE model used is shown in Fig. 2. Body panels and surface shapes of interior fittings were extracted from a large-scale structural FE model, and a solid model for acoustic calculation was formulated (approximately 74,000 elements). In addition to trim components such as seats and an instrument panel, acoustic speakers were modeled in the cabin to accurately represent measurement conditions in the actual vehicle. Modeling of interior fittings is important for higher-accuracy cabin sound pressure calculations. Representation of these was possible by establishing impedance or admittance as boundary conditions for the acoustic FE model. Admittance was established for the areas shown in Fig. 3. Admittance values were obtained with the following equation, using measurements of vibrational acceleration and surface sound pressure levels of trim components obtained in acoustic vibration experiments in an actual vehicle.

$$A = 1/Z = v/p \quad (2)$$

where A is admittance, Z is impedance, v is trim vibrational velocity, and p is trim surface sound pressure level. A simple model of interior fittings was formulated on the basis of measurement results for each panel. This was accomplished by using acoustic calculation software to determine boundary conditions with almost the same impedance characteristics as the measurement results (Fig. 4). When applying velocity boundary conditions to the nodal points on the FE model using panel vibration data from the experimental model, linear interpolation was used for nodes with spatial coordinates between the vibration

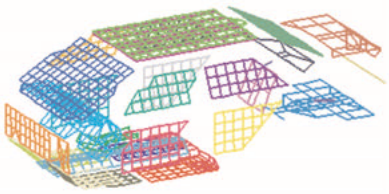


Fig. 1 Structural experimental model

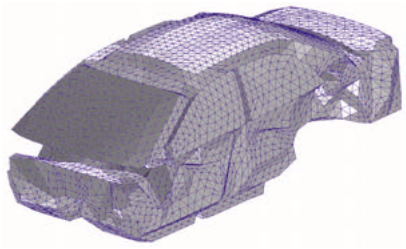


Fig. 2 Acoustic FE model

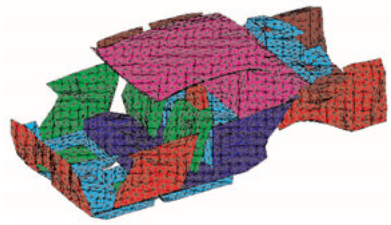


Fig. 3 Established admittance areas

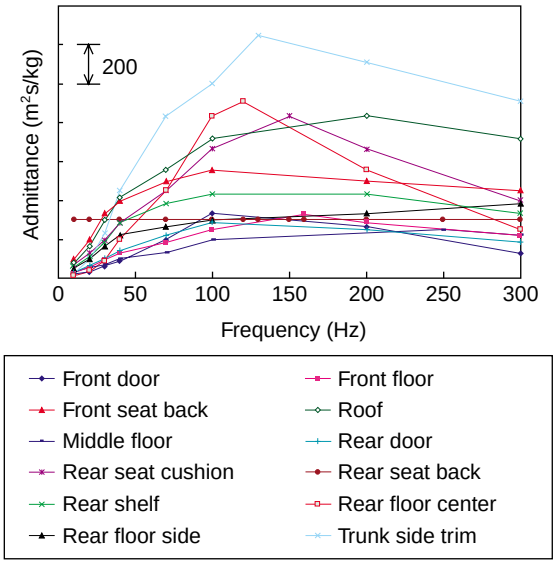


Fig. 4 Admittance values defined as boundary conditions

data points. Finally, evaluation points for cabin sound pressure level were established at passenger ear positions in each seat corresponding to the actual vehicle measurements.

3. Verification of Calculation Accuracy of the Hybrid Acoustic Model

3.1 Verification of Velocity Boundary Conditions

3.1.1 Comparison of application of body panel vibration and trim vibration to velocity boundary conditions

Following the formulation of the experimental model, the relationship between body panel and trim vibration characteristics was analyzed. Figs. 5 and 6 compare vibration responses of trim and body panels in the floor and roof. Significant differences in vibration characteristics between trim and body panels were observed (Figs. 5 and 6). Looking at the vehicle body as a whole, there is a general tendency for trim vibration levels to become high at 300Hz or less, and for the same effect to occur in body panels in a higher frequency range.

These experimental model vibration data were then input into the acoustic FE model as a boundary condition, and the acoustic transfer function from the rear engine mount to the front seat passenger's ear positions was calculated. Individual acoustic measurements were taken for instances of panel application and for trim application in those areas where both the panel and trim data were measured, and the

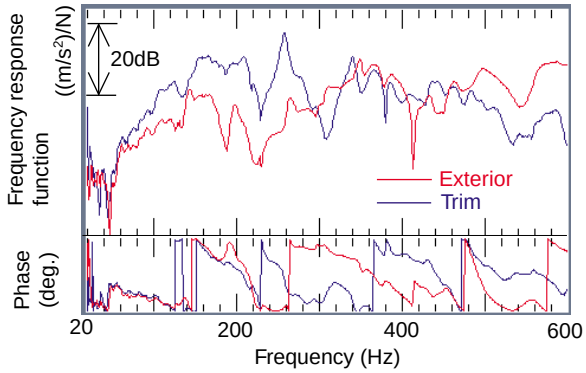


Fig. 5 Comparison of frequency response function (FRF) for the front floor upon rear engine mount excitation

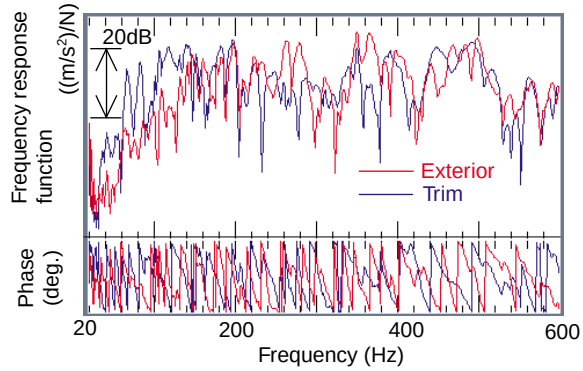


Fig. 6 Comparison of FRF for the roof upon rear engine mount excitation

effects on the acoustic transfer function to passenger ear positions was verified. Fig. 7 shows a comparison between calculated and measured vibro-acoustic transfer function values at these ear positions. It further shows that by selecting trim data as a boundary condition, the transfer function increases by 5 dB or more, particularly in the area above 200Hz, while calculated values more closely approach the actual measured values. However, despite the fact that a correlation can be observed between acoustic transfer function bottom and peak frequencies, there is a 5-10 dB difference between 120 and 240 Hz, and therefore the acoustic characteristics of actual vehicles are not accurately represented. Thus, an attempt was made to examine the disparity by calculating the effect of vibration in each panel on sound pressure levels at passenger ear positions in the acoustic FE model.

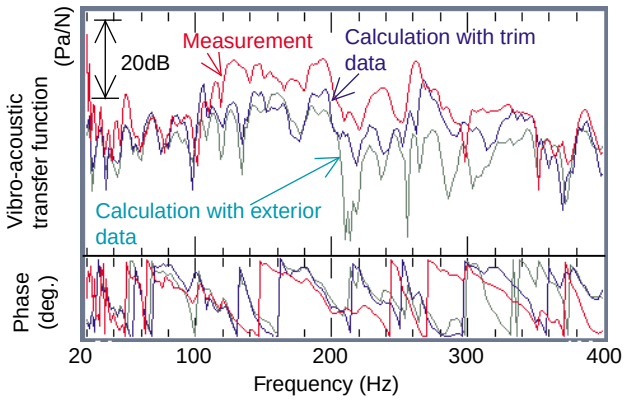


Fig. 7 Comparison of vibro-acoustic transfer function for the front/left seat upon rear engine mount excitation

3.1.2 Effect of vibration in each panel on cabin noise

A boundary element (BE) model of the same form was formulated from the FE model shown in Fig. 2, and the velocity contribution from each panel to the cabin noise was calculated, with a focus on the range between 100 and 250Hz, for which calculation accuracy was insufficient. Fig. 8 shows the acoustic transfer vector for sound pressure at passenger ear positions at 124Hz. Contribution is especially high for the dashboard lower panel, and is in reverse phase with the front window-side (instrument panel-side). Fig. 9 shows a high contribution for other frequencies at the front of the body, with the dashboard-side in reverse phase with the instrument panel-side, as was shown in Fig. 8.

Next, a method of calculating the contribution of panel vibrations to passenger ear position sound pressure in the FE model was examined. First, the boundary velocity, which up to this point had been applied to all points simultaneously, was divided for individual panels, as shown in Fig. 10, and vibro-acoustic transfer functions from the engine mount to passenger ear positions were calculated for each of the panels (Fig. 11). By recombining these individual transfer functions, vibro-acoustic transfer functions for the entire body were obtained. These functions were then compared with calculation results obtained when the boundary velocity was used for all points simultaneously (Fig.12). Fig. 11 shows a high contribution from the front of the body in the 120-200Hz range, the range for which accuracy for vibro-acoustic transfer functions at passenger

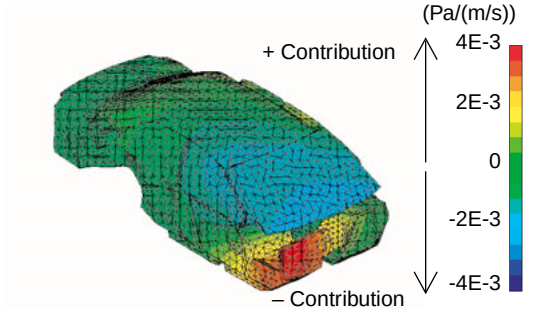


Fig. 8 Acoustic transfer vector at 124Hz

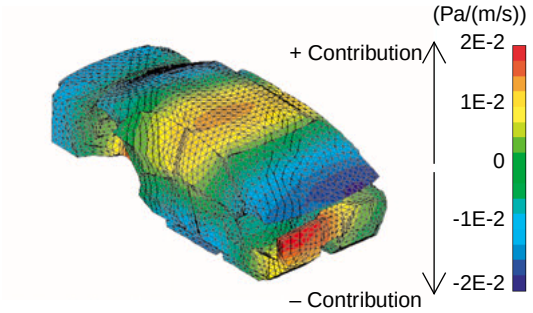


Fig. 9 Acoustic transfer vector at 182Hz

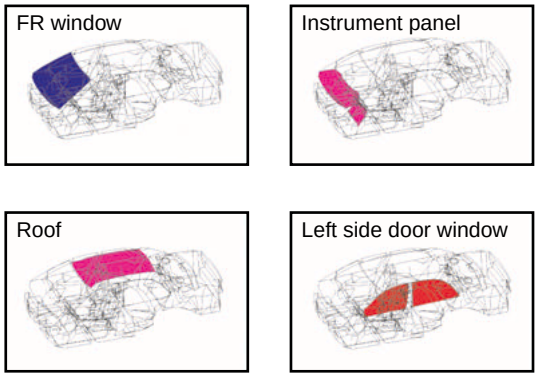
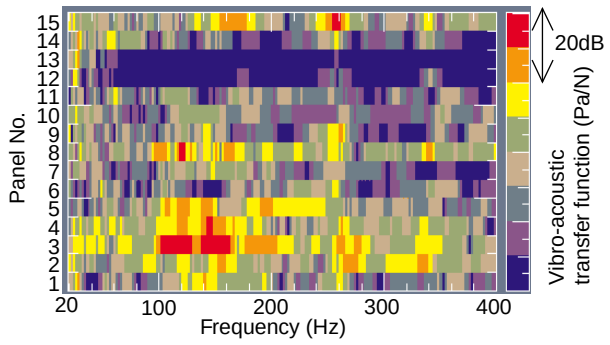


Fig. 10 Examples of set divided panels



1. Front doors
2. Front floor
3. Front window
4. Instrument panel
5. Left side door window
6. Rear shelf
7. Right side door window
8. Roof
9. Rear doors
10. Middle floor
11. Rear window
12. Rear floor
13. Trunk lid
14. Rear seat back panel
15. Middle floor carpet

Fig. 11 Panel contribution to interior engine noise level

ear level was insufficient in calculations. This is the same tendency as demonstrated by the acoustic transfer vectors in the BE model. Fig. 12 shows that when vibro-acoustic transfer functions are calculated from the engine mount to passenger ear positions, combining individual acoustic calculation results for each panel produces better results than performing a single acoustic calculation using a single velocity boundary condition for all points.

3.1.3 Panel vibration mode phase effect

Next, the vibro-acoustic transfer function at passenger ear positions was considered, with a focus on the 120 and 190Hz peaks for which there was insufficient correlation between measured and calculated values. In particular, the boundary velocity data was re-verified for the front of the body, which has a high level of contribution to cabin noise. Front floor vibration data was calculated separately for the trim and panels, and the effect on cabin noise was verified (Fig. 13). Results demonstrate that, as shown in Fig. 5, between 100 and 200Hz the trim vibration level exceeds that of the panels, but looking at the vibro-acoustic transfer function to passenger ear positions, there is a high contribution from panels between 100 and 150Hz. Therefore, the vibration modes in this frequency band were focused on using the experimental model, and as Fig. 14

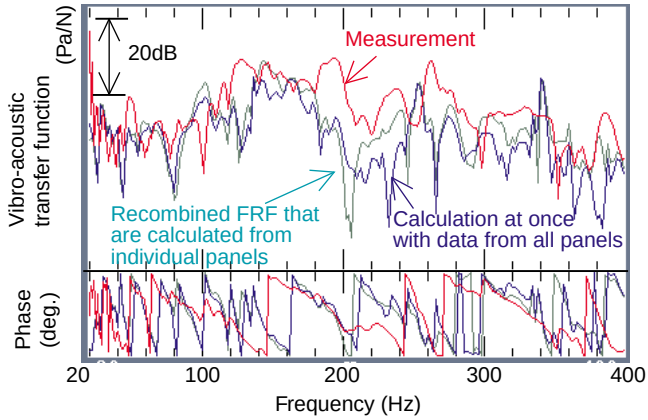


Fig. 12 Comparison of vibro-acoustic transfer function for the front/left seat upon rear engine mount excitation

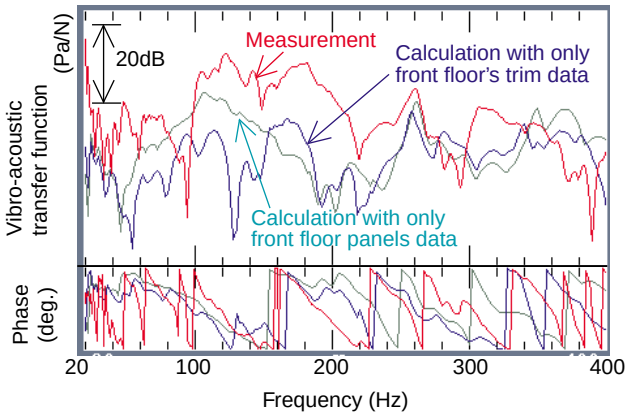


Fig. 13 Contribution of front floor vibration to vibro-acoustic transfer function for the front/right seat upon rear engine mount excitation

shows, it is clear that the front door trim did not exhibit a low order membrane vibration mode similar to the floor panels. Also, phase was unstable at each measurement point for the trim. It is believed that poor adhesion between trim materials and panels, and measurement accuracy of trim cover vibration are the cause for this difference in mode shapes. Other areas, including the middle floor, roof, trunk, etc., were also analyzed, but no major discrepancies were observed similar to the front floor situation.

Panel data for the front floor alone were then used in recalculating the vibro-acoustic transfer function to passenger ear positions. Results are shown in Fig. 15. The method applied to calculate these transfer functions was to individually apply velocity boundary conditions to each panel, and then to recombine the individually calculated transfer functions. Using front floor panel data enabled correlation between calculated and measured values to be improved between 100 and 160Hz and 220 and 240Hz. By this means it was possible to construct a structural-acoustic hybrid model representing the acoustic characteristics of an actual vehicle up to 350Hz, with the exception of the 180Hz peak.

3.2 Verification of Accuracy of the Acoustic FE Model

3.2.1 The acoustic transfer vector for cabin noise

The lack of correlation between measurements and calculations in the peak at 180Hz shown in Fig. 15 is considered from the perspectives of acoustic modes and acoustic transfer vectors calculated in the acoustic FE model. Fig. 16 shows calculation results for acoustic transfer vectors at 182Hz. It can be seen that the contributions of the dashboard lower panel and the front border of the front window, in particular, are both high (almost the same level), and are in reverse phase. Fig. 17 shows the acoustic mode at 183Hz calculated in the acoustic

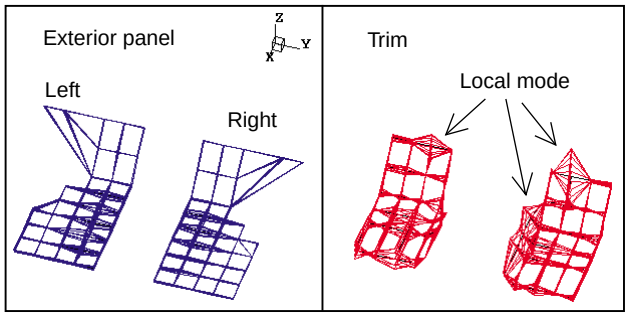


Fig.14 Running mode of front floor at 142Hz

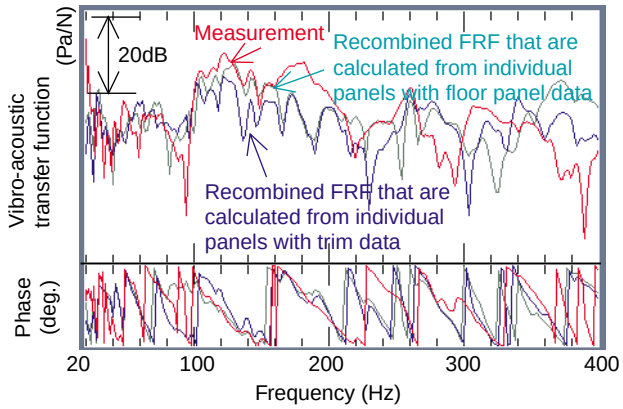


Fig. 15 Effect of using the floor panel data on vibro-acoustic transfer function for the front/right seat upon rear engine mount excitation

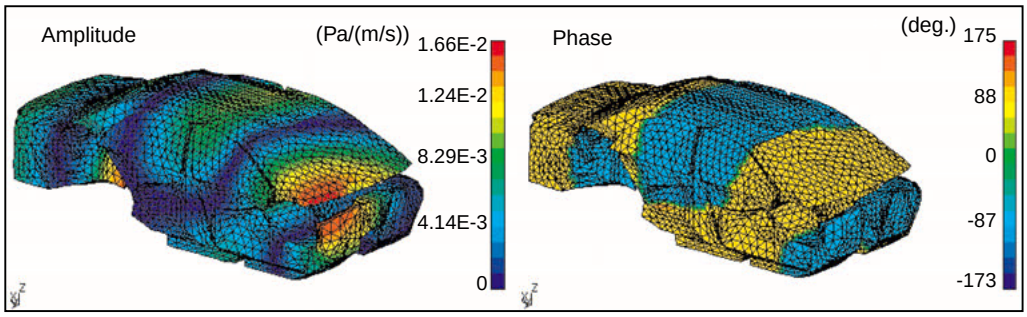


Fig. 16 Acoustic transfer vector to front/right seat at 182Hz

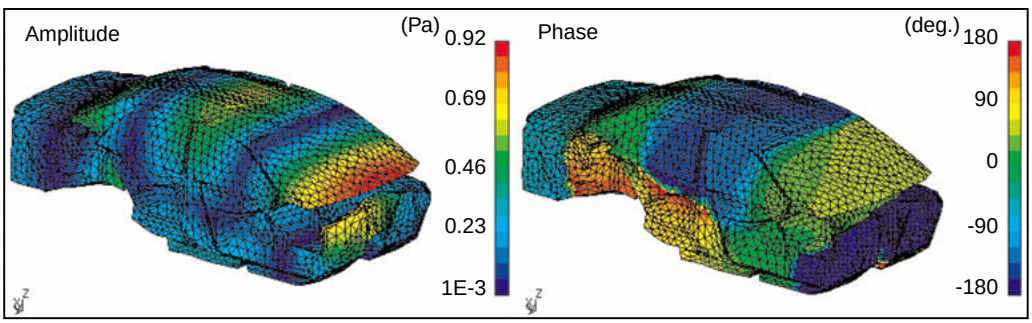


Fig. 17 Calculated acoustic mode (183Hz)

FE model. Figs. 16 and 17 show the same tendencies in amplitude level patterns. This is thought to be because acoustic modes exert a strong influence on acoustic transfer vectors.

3.2.2 Comparison of measured acoustic-acoustic transfer functions with calculated values

This stage was to verify whether acoustic characteristics calculated in the acoustic FE model accurately represent the acoustic characteristics of a real vehicle. Comparison and verification were conducted using the acoustic-acoustic transfer function H from passenger ear position sound pressure level to cabin boundary surface sound pressure level. As shown in Fig. 18, acoustic speakers were placed at passenger ear positions in a real vehicle, and the cabin boundary surface sound pressure level was measured. Using these measurements, H is derived with the following equation

$$H = P/\dot{Q} \tag{3}$$

where P is cabin boundary surface sound pressure and Q is volume acceleration produced by acoustic speakers. Sound pressure measurement points were kept to one or two per panel, with 35 in total in the cabin. The boundary velocity v as determined by equation (4) should be established for the speaker section in the acoustic FE model.

$$P/\dot{Q} = P/i\omega Sv$$
$$v = \dot{Q}/i\omega S \tag{4}$$

where ω is angular frequency and S is the area of the speaker opening.

Fig. 19 shows measurement results for acoustic-acoustic transfer function H. It can be seen that the level is high at the front of the body for the 160-200Hz range in which correlation was poor between calculated and measured values for passenger ear positions, as shown in Fig. 15. This corresponds to the areas with a high contribution to

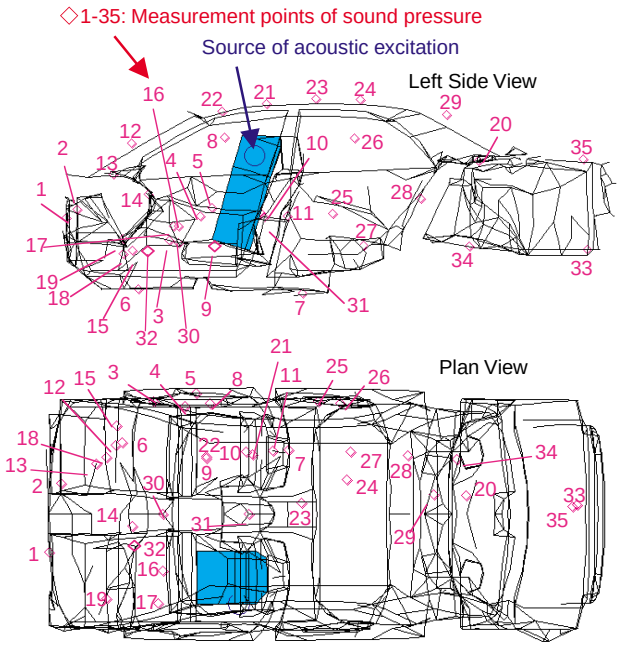
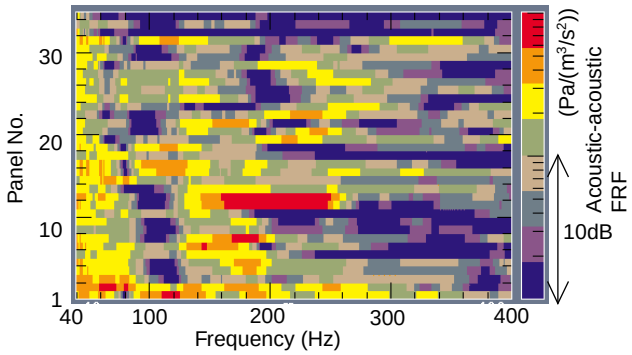


Fig. 18 Source of acoustic excitation and measurement points of sound pressure



1-2 Dashboard panel
3-5 Front door
6-7 Front floor
8 Front door window
9-11 Front seat
12 Front window
13-19 Instrument panel
20 Rear shelf
21-24 Roof
25 Rear door
26 Rear door window
27-28 Rear seat
29 Rear window
30-32 Center console
33-35 Trunk

Fig. 19 Experimental acoustic-acoustic FRF

sound pressure shown in Fig. 16. Comparisons between calculated and measured values for acoustic-acoustic transfer function H with a focus on the front of the body are shown in Figs. 20 and 21. These figures show that correlation between calculated and measured values is poor, and in particular the calculation model is incapable of representing the 180Hz peak at the dashboard panel. These results demonstrate that there are some inaccuracies in the

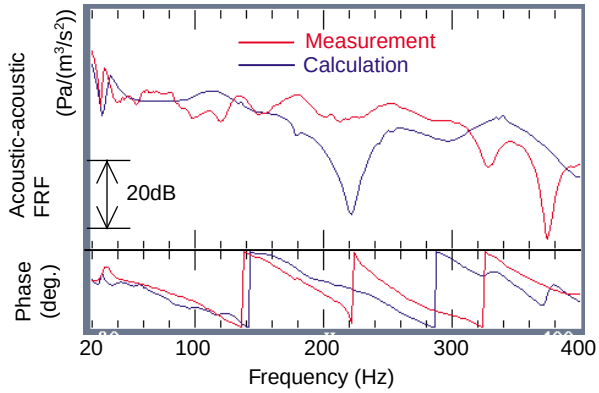


Fig. 20 Comparison of acoustic-acoustic FRF for the dashboard lower panel

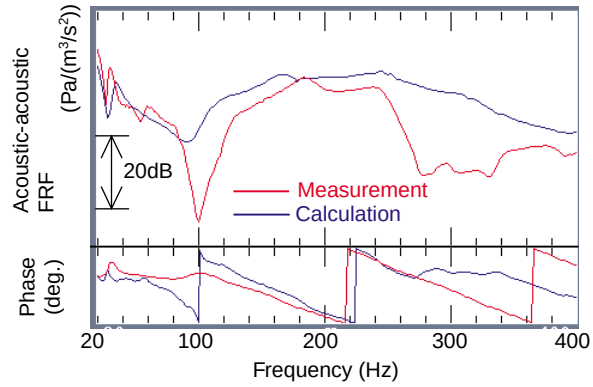


Fig. 21 Comparison of acoustic-acoustic FRF for the front window

acoustic FE model for the front of the body, specifically, the area between the front window, instrument panel and dashboard panel. Because the steering column ,hanger, pedals, air-conditioning and heating units and ducts functioning as ventilation channels are fitted in this area, it is difficult to adequately represent the form of the cabin in the FE model. However, unlike the BE model, complex fluid material characteristics can be established by section in the FE model. Therefore, it was examined whether this modeling feature could be used to establish fluid material characteristics different from air characteristics and so achieve a representation of the acoustic characteristics within the dashboard of an actual vehicle.

3.2.3 Improvements in acoustic model calculation accuracy by changing volume densities

Volume densities different to air were established in the areas shown in Fig. 22, in an attempt to improve the accuracy of the acoustic FE model. Fig. 23 shows a comparison of acoustic-acoustic transfer function H in the area around the lower part of the instrument panel before and after the volume density changes. It can be seen that changes to the volume density reduced differences in level between calculated and measured results, particularly in the area above 250Hz, and increased the accuracy of the acoustic FE model. However, no improvement in H between 160 and 200Hz was observed. This range presented difficulties for the calculation of the vibro-acoustic transfer function from engine mounts to passenger ear positions. It is clear that an improvement in accuracy cannot be expected from a change in volume density in only one area.

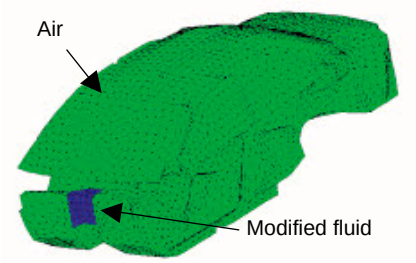


Fig. 22 Area of modified fluid properties on the FE model

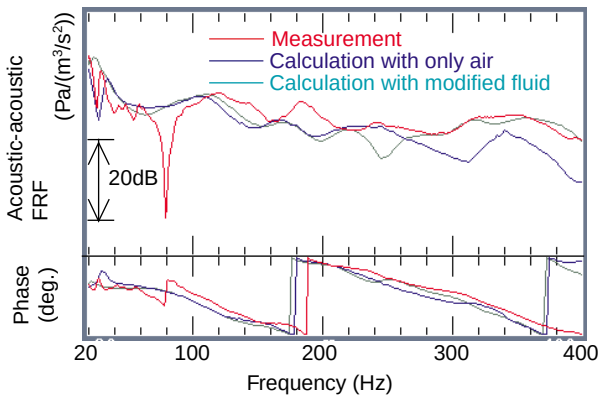


Fig. 23 Effect of fluid properties modification on acoustic-acoustic FRF under the instrument panel

4. Conclusion

An experimental model formulated from vibrational acceleration measurements in an actual vehicle and an acoustic FE model were used in the construction of a hybrid acoustic calculation model capable of analyzing vibro-acoustic transfer functions from engine mounts to passenger ear positions up to 350Hz. This model can be used as a developmental tool to reduce cabin noise due to engine vibration input. As a result, technological difficulties and methods necessary to improve the accuracy of the model have been clarified.

(1) As a result of examining the use of experimental data as velocity boundary conditions in the acoustic FE model, it is clear that trim vibration data should be used rather than panel vibration data.

(2) To prevent boundary velocity interpolation errors in the acoustic FE model, a method was examined in which boundary velocity was divided into individual panels and the vibro-acoustic transfer functions obtained for each by acoustic calculations were recombined. Correlation between calculated and measured values was improved in comparison with the method in which a single boundary velocity is used for all points simultaneously and transfer functions are calculated once. This method enabled the construction of a hybrid model capable of representing the acoustic characteristics of an actual vehicle up to 350 Hz, with the exception of the 180 Hz peak.

(3) To improve representation of the front of the body, which contributes greatly to cabin noise, a method for establishing a volume density different to air was attempted for a portion of the FE model. As a result, there was an improvement in the discrepancies between calculated and measured values of acoustic-acoustic transfer functions from passenger ear positions to the cabin boundary surface. It was demonstrated that the accuracy of the acoustic FE model could be improved.

However, to achieve further improvements in model accuracy, it will be necessary to reduce discrepancies in level between calculated and measured values for the acoustic-acoustic transfer functions throughout the cabin. To achieve this, sound pressure measurement points for actual vehicle acoustic excitation should not be limited to representative points on each panel. Rather, a more detailed experimental acoustic modal model must be formulated, and volume density settings optimized across the entire acoustic FE model through correlation between experimental modes and those calculated in the acoustic FE model.

Acknowledgements

The authors wish to express their sincere gratitude to Mr. Ludo Gielen of LMS International for his generous assistance in this research.

References

(1) Kimura, Keisuke: Technical Development Using the Structural and Acoustic Hybrid Model for Reducing Vibro-acoustic Transfer Function, Society of Automotive Engineers of Japan, Inc., 1998 Fall Conference, Technical Lecture Preprint Collection, No.78-98, p.1-4(1998)

(2) Kurokawa, Isamu: Reduction of Booming Noise in Heavy Duty Truck Cab – Part 1 Contribution Analysis of Floor Panel Vibration, Society of Automotive Engineers of Japan, Inc., 1998 Fall Conference, Technical Lecture Preprint Collection, No.78-98, p.5-8 (1998)

(3) Kurokawa, Isamu: Reduction of Booming Noise in Heavy-duty Truck Cab – Part 2 Reduction of Booming Noise by Floor Structure Modifications, Society of Automotive Engineers of Japan, Inc., 1998 Fall Conference, Technical Lecture Preprint Collection, No.78-98, p.9-12 (1998)

(4) Sung, Shung H., et al.:Development and Experimental Evaluation of a Vehicle Structural Trimmed-Body Model, Proceeding of the 1999 Noise & Vibration Conference, P-342, Vol.2, p.1135-1140 (1999)

■ Authors ■



Kazufumi KAWABATA



Tatsuhide SAKAI



Nobuaki HASHIMOTO

Establishment of an Aero-Dynamic Simulation System for Motorcycles and Its Application

Takashi WATANABE* Takefumi OKUBO*
Mutsumi IWASA* Hiroyuki AOKI*

ABSTRACT

A numerical simulation system for motorcycles was constructed aiming at predicting aerodynamic-characteristics of the bodies at the early stage of development. In order to shorten the time for constructing a complete model of a motorcycle, which have fairly complicated shapes, and to generate meshes on the model as quickly as possible, an orthogonal mesh with porosity for each cell was adopted. An evaluation of this system regarding accuracy and time needed for analysis was carried out by applying the system to some motorcycles actually under development. As a result, we found that a sufficient level of accuracy was obtained in predicting aero resistance forces and wind protection performances.

1. Introduction

Amidst increasing demands for shorter development periods, various computer simulations (CAE) have been introduced to development in recent years as a means of meeting these needs. Fluid analysis has conventionally required significant time for the creation of calculation models, and the enormous calculation time has lowered its practicality compared to the field of structural analysis. In the automotive field, aerodynamic simulations came to be frequently used for automobiles from around 1990[1]. This is thought to be because the spread of super-computers first made these types of calculations possible. However, the calculations at that time took up to 150 hours of computation time using these expensive super-computers[1], and appear to have been done more for the purpose of demonstrating that such aerodynamic calculations were possible. Since that time computer performance and software have improved, and aerodynamic calculations have become fairly well established in the automotive field.

On the other hand, there are extremely few reports thus far of these calculations in the field of motorcycles, and although there are some cases of calculations for part units such as the flow around the wheels[2], there are as yet no reports of overall calculations for the completed vehicle.

The reasons for this are as follows.

(1) Motorcycles generally have a more complicated body shape compared to automobiles, and the human body must also be modeled, which makes it quite difficult to create 3D CAD data.

* Asaka R&D Center

(2) A mesh of some type must be generated to perform fluid calculations, but it is technically difficult to generate a mesh that allows calculations for a complicated body shape such as a motorcycle.
(3) Motorcycles have a short development period compared to automobiles, so it is difficult to create a model and conduct simulations within the development period.

Therefore, in light of its position as a development tool, establishment of a simulation system for motorcycles requires a different perspective from that of automobiles.

2. Development Aim

Motorcycle design items related to air flow span a wide range, including for example even the hot exhaust wind produced by the engine and wind noise. However, this study narrowed the focus to the following two items.

- Reducing aero resistance force
- Optimizing the way the wind strikes the rider (wind protection performance)

Conventionally, these items were evaluated by manufacturing a test vehicle and then conducting wind tunnel tests. This study aimed to create aerodynamic simulation tools capable of evaluating the above two items in the initial development stage prior to completion of a test vehicle. Simulation prediction accuracy for the evaluations items is of course important, but emphasis was also placed on allowing simulations that do not take too much time.

3. Technical Investigations

3.1 Two Issues for Decreasing the Process Time

In order to shorten the simulation modeling process as much as possible, the first point to be considered is that the data must flow smoothly between each system on which 3D shapes are created or modified. To achieve this, the following points should be taken into account.

- The 3D data created by the Design Department should be usable as upstream data.
- The data should be linked with CATIA.
- Mesh generation should not take much time.

In order to create 3D shapes of completed motorcycles and allow simulations amidst this data flow, the following two issues must be considered.

- Motorcycle models are comprised of 20 to 40 components, and interference between components must be eliminated to achieve a single volume.
- A mesh for calculation must be created for complicated shapes.

These issues were handled by the methods described below to reduce the process time.

3.2 Issues for Achieving a Single Volume

Normally, large amounts of upstream data are created for each component as surface data. In order to perform simulations, the intersecting parts of these surfaces must be completely eliminated to achieve a single volume. Normally the unnecessary parts of surfaces must be removed manually on a CATIA or CAD system, or the shape must be converted to a solid and Boolean operations performed.

Therefore, the method actually used achieved a single volume in the later stage when the mesh for the calculation area was created without any merging of intersecting portions by CATIA. This is made possible by using the mesh for calculation area types described below. This reduced the overall modeling process time.

3.3 Selection of a Mesh for Calculation

Meshes used for fluid calculations are classified into the following three types.

(1) Body Fitted Coordinates (BFC) (curvilinear mesh that follows the shape)[2, 3]
(2) Unstructured mesh[4]
(3) Orthogonal and straight line mesh + porosity

Type (1) is the method conventionally used for aerodynamic simulations of automobiles, but application to motorcycles which have a complex shape is difficult.

Type (2) can also support complex shapes, and recently this method is being used with increasing frequency in various areas. This method has the potential to become an effective method for aerodynamic simulations of motorcycles, but it assumes that the data for motorcycle bodies that are comprised from multiple objects are converted to a single volume by solid Boolean operations. However, this work requires an enormous amount of process time.

The authors adopted method (3). This mesh uses straight lines, so object shapes cannot be expressed by the mesh. Therefore, object shapes are expressed by the concept of the porosity of each constituent element (cell) according to the mesh. The porosity in each cell method first determines whether each cell is empty or filled with matter. Furthermore, when a part of a cell is empty, the shape is approximated by the area ratio of the empty and matter portions at the three surfaces (two surfaces for two dimensions) that enclose the cell. Fig. 1 (a) shows the approach toward porosity for two dimensions. Here, Px and Py are porosity values, and these values are defined for all the cells. Fig. 1 (b) shows an entire motorcycle body shape expressed in terms of porosity. Each element is expressed by a color according to the Px and Py values. Cells that are completely occupied by matter are indicated in red, and cells partially occupied by matter are indicated with varying colors according to the degree.

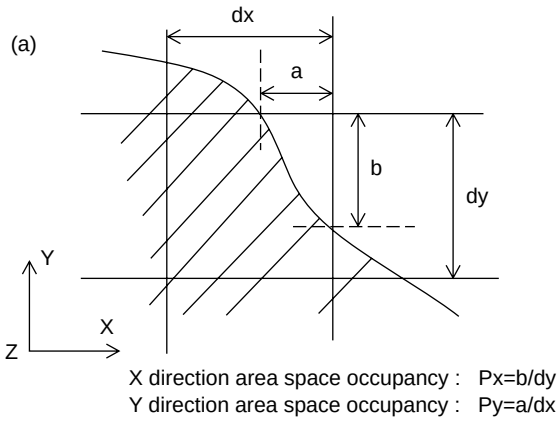


Fig. 1 (a) Concept of porosity; (b) Representation of an entire motorcycle model by porosity

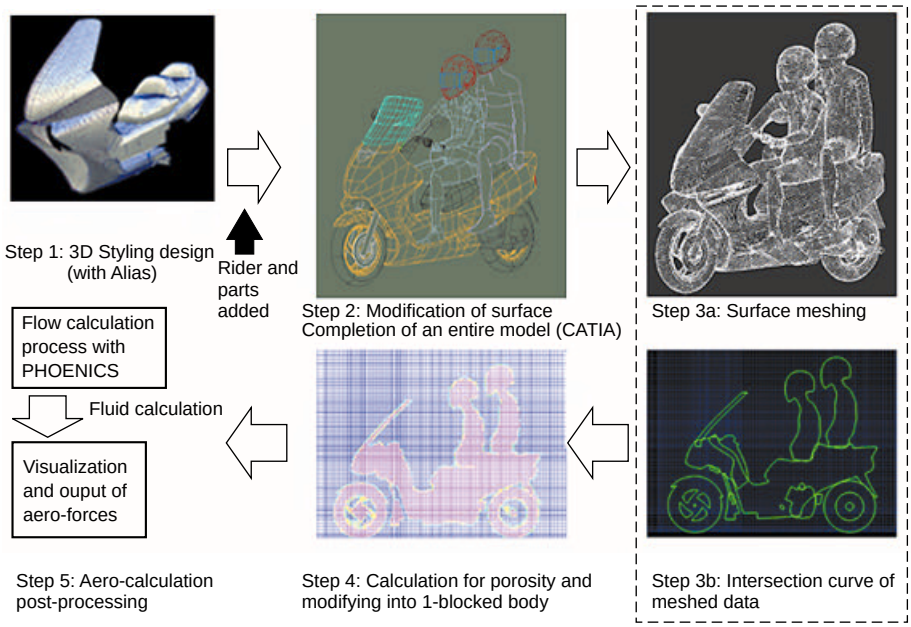


Fig. 2 Outline of system flow

3.4 Selection of a Solver

Selection of a solver was based on the premise that method (3) described in section 3.3 could be used. The solver actually used was PHOENICS developed by CHAM Inc. (England). This code is not equipped with functions for method (2), but is appropriate for using method (3). Note that the following calculation options were used.

Turbulence model : Standard k-ε model
Convection term : Hybrid method
Numerical scheme: Simplest method

4. System Outline

When constructing the system, commercially available software and in-house programs were combined as appropriate. Fig. 2 shows an outline of the system flow. Each step is described below.

Step 1: 3D design data is created using Alias.

Step 2: The step 1 data is transferred to CATIA and 3D surface data for small components is added.

Step 3: Mesh models for each component are created by the in-house mesh generator incorporated into CATIA. Then, the individual mesh models are combined into a completed vehicle condition as shown in step 3a. At this time, intersecting portions between components may still remain such as shown in the sectional drawing in step 3b.

Step 4: Porosity data corresponding to the orthogonal mesh for calculation data and shape data are created, and the intersecting portions between components are merged to achieve a single volume.

Step 5: Calculations are performed using PHOENICS with the step 4 data as the input data. The calculation results file is read and calculations for the six components of aero-force are performed. To visualize the results, the file format is converted and then the data is displayed on a commercially available post-processor FIELDVIEW.

5. Application to Development Models

The developed system was applied to models for mass-production to verify the calculation accuracy. The accuracy was verified by comparing aero resistance force, streamline, pressure distribution and other factors with wind tunnel test results using the actual vehicles. Two types of test vehicles were used: (a) sports type motorcycle and (b) large-size scooter.

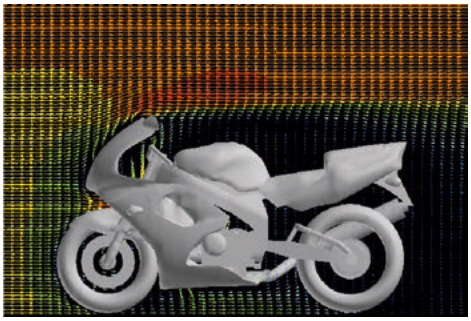


Fig. 3 Calculation results without rider

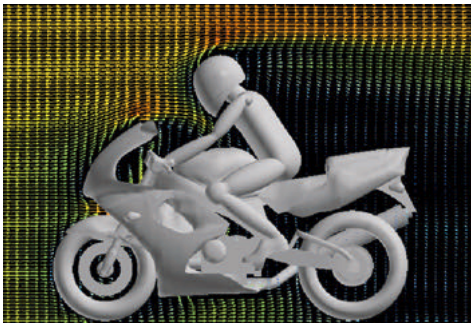


Fig. 4 Calculation results with rider

(a) Sports type motorcycle

The simulation results and wind tunnel test results for the aero resistance force and the forces acting at the front tire and rear tire contact points were compared for the cases of the motorcycle alone and the motorcycle with a rider. Fig. 3 and Fig. 4 show the simulation results for air flow speed using vectors. Fig. 5 and Fig. 6 compare the aero resistance force and the forces acting at the front tire and rear tire contact points, and show that each of these values match closely. Note that this model used 980,000 meshes for calculation and the calculation time was approximately 72 hours on an sgi ORIGIN2000 (180 MHz *8 CPU).

(b) Large-size scooter

Fig. 7 shows the 3D simulation model for calculation, Fig. 8 shows the wind tunnel test conditions, and Fig. 9 shows a comparison of calculated and actually measured aero resistance force. Here as well an excellent correlation was obtained for aero resistance force.

Fig. 10 shows the calculation results for surface pressure distribution and an image of the pressure measurement condition in the wind tunnel. Fig. 11 shows

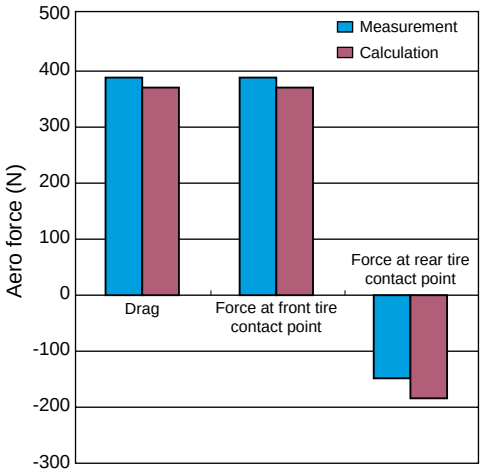


Fig. 5 Comparison of aero-dynamic forces between calculation and measurement (without rider)

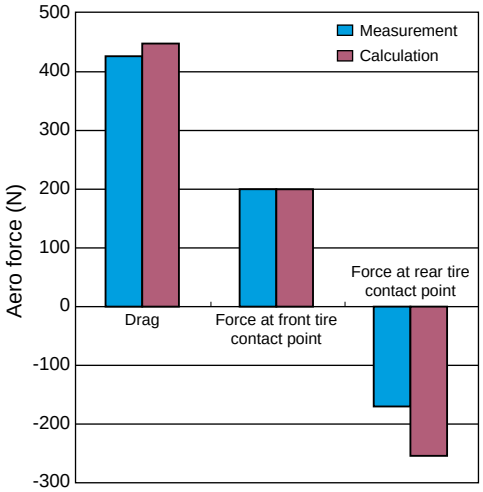


Fig. 6 Comparison of aero-dynamic forces between calculation and measurement (with rider)



Fig. 7 Calculation model of a scooter



Fig. 8 Wind tunnel test

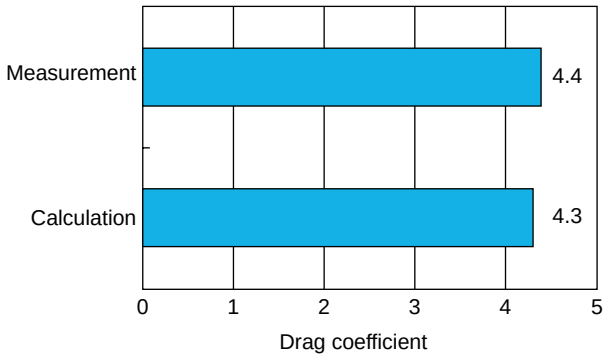


Fig. 9 Comparison of drag coefficients between calculation and measurement results

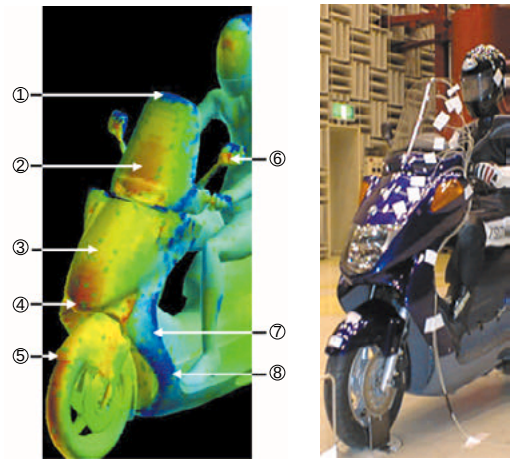


Fig. 10 Pressure distribution from the calculation results and a measurement scene in a wind tunnel

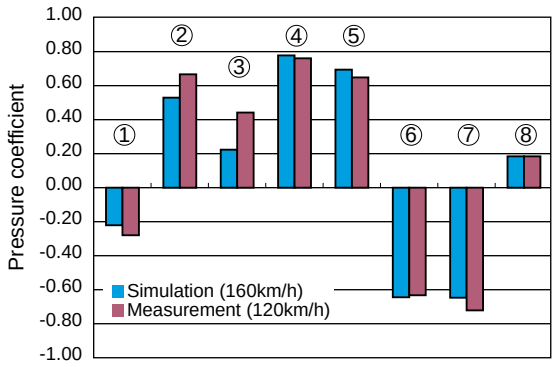


Fig. 11 Comparison of a calculation and measurement results of pressure on specified points

a comparison of these calculated and measured values. In this figure, the quantitative values matched closely except for case (3), and the overall distribution trend also matched closely.

Fig. 12 shows the calculated streamline, and Fig. 13 shows the streamline in the wind tunnel test. These results match fairly closely.

The remaining figures show a comparison of calculation results when the motorcycle body specifications are changed. Fig. 14 and Fig. 15 show the surface pressure distribution calculation results for two types of motorcycle bodies with different lower fairing outer edge shapes. Red indicates higher pressure, and means a stronger wind force. Focusing on the lower limb (from the knee downward) portion of the rear riders, Fig. 15 shows that the wind force is weaker and the wind protection performance has been improved compared to Fig. 14. Fig. 16 and Fig. 17

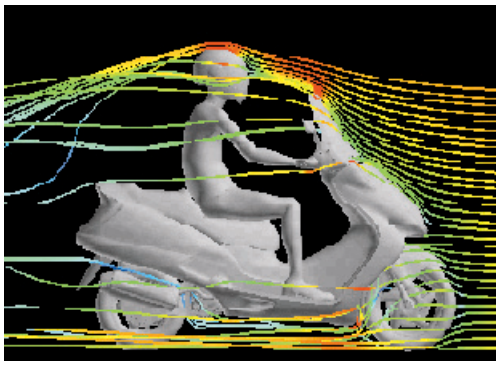


Fig. 12 Calculated stream line of a scooter model



Fig. 13 Stream line measured for an actual scooter

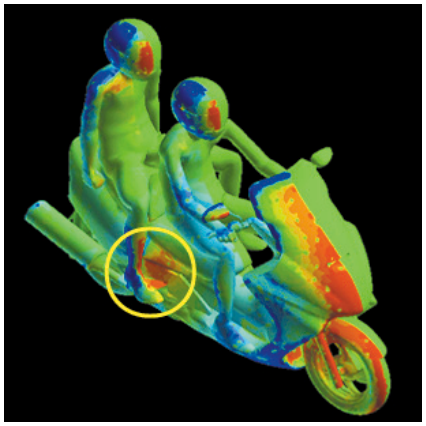


Fig. 14 Pressure distribution (Original fairing)

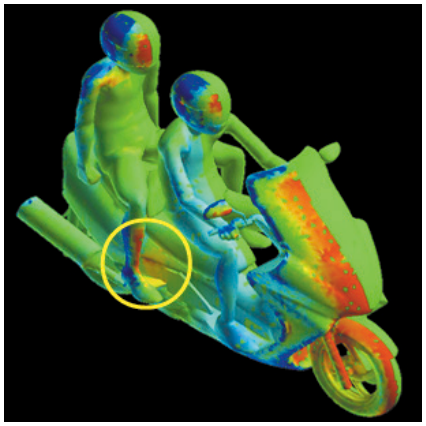


Fig. 15 Pressure distribution (Improved fairing)

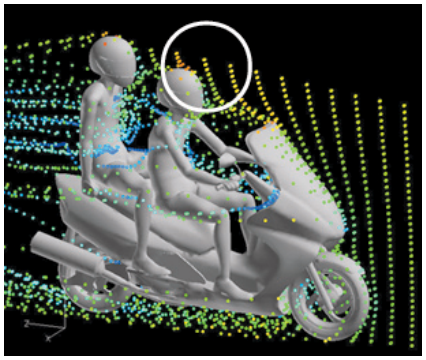


Fig. 16 Air flow pattern with riders (low windscreen)

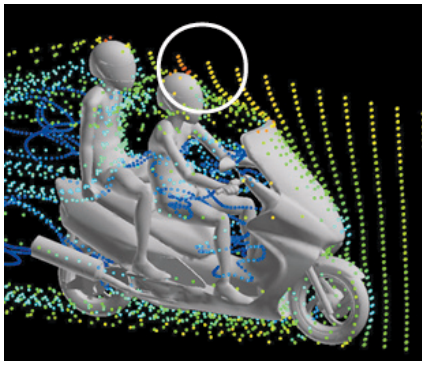


Fig. 17 Air flow pattern with riders (high windscreen)

compare the calculation results of the flow around a motorcycle body for two different windscreen specifications. The windscreen shape in Fig. 17 has a slightly longer top edge and also flares to the outside compared to the Fig. 16 windscreen shape. Fig. 17 shows that the wind force to the rider's head has been reduced.

These results showed that the developed system can be utilized for investigating the wind force to riders, that is to say the wind protection performance.

6. Reduction of Overall Simulation Process Time

In order to utilize aerodynamic simulations in the motorcycle development process, the time from modeling until the calculation results are obtained must be shortened as much as possible. Fig. 18 shows a breakdown of work process time for two years ago and at present. Modeling took approximately 45 days two years ago, but can currently be done in approximately 20 days when it is done by one person. The work item accounting for the largest percentage is model creation. This portion has been shortened from 40 days to 17 days due to improved staff modeling skills, and also because a greater percentage of the upstream data needed for modeling is 3D now compared to two years ago, which reduces the man-hours required to convert data to 3D. Thus, an environment where 3D data is available in advance is extremely important for promoting aerodynamic simulations.

The item accounting for the second largest percentage is computation time. Two years ago 900,000 meshes for calculation took approximately 3 days, but computer upgrades have presently made it possible to calculate 1.8 million meshes in 1.5 days. Tool advances have shortened the pre-processing (excluding model creation) from two days to one day, but post-processing remains almost unchanged at approximately one day. However, this accounts for a small percentage of the overall process time, so it is not a major problem.

7. Conclusion

A porosity-based aerodynamic simulation system was established and applied to development models, and the following results were obtained.

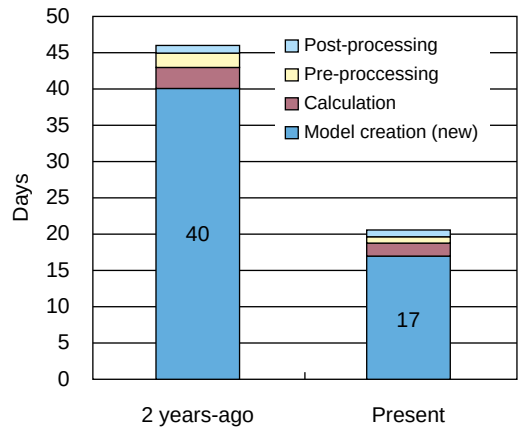


Fig. 18 Days required for an aero-dynamic simulation of a motorcycle 2 years ago and at present

(1) It was confirmed that aerodynamic simulations using this method could be performed within a practical process time even for complex shapes such as completed motorcycle bodies.
(2) The calculation accuracy was confirmed for the overall aero resistance force and air flow pattern of completed motorcycle bodies, and found to be adequate for practical application.

In addition, further approaches are required for the following issues.

(1) Porosity is used to express shapes, so the air flow accuracy near walls is insufficient.
(2) When local shapes must be accurately expressed such as when checking the effects of small holes for example, the number of meshes required by the current method increases significantly, and it becomes difficult to obtain accurate calculations using a practical number of meshes.

References

(1) Fukushima, T., Miyajima, T., Takamura, A., Developing a Computational Fluid Dynamics (CFD) System, HONDA R&D Technical Review Vol. 3, p.182 – 192, 1991
(2) Carlo Fabio, Numerical Investigation on the Fender of a Motorcycle, SAE 970412
(3) Himeno, R., Fujitani, F., Tanaka, H., A Study of Aerodynamic Characteristics of a Production Car Using a Finite Difference Analysis of Flows, JSAE Proceedings 901, 1990
(4) Takeuchi, T., Kohri, I., Development of Truck and Bus Aerodynamics Using Computational Fluid Dynamics, JSAE Proceedings 964 p.49 – 52, 1996

■ Authors ■


Takashi WATANABE


Takefumi OKUBO


Mutsumi IWASA


Hiroyuki AOKI

A Method for Evaluation of Low-frequency Noise and Vibration in Powertrain Mount Layouts using Degree of Coupling and Physical Matrices

Masafumi KYUSE* Satoshi WATANABE* Tatsuhide SAKAI*

ABSTRACT

Ride comfort and idling performance are conflicting low-frequency noise and vibration issues in vehicle development. A convenient index for evaluation of these two phenomena at the design stage was formulated by defining the degree of coupling in a simple numerical expression representing the characteristic matrix based on a physical coordinate system. The degree of coupling was used for performance evaluations of idling and ride comfort in CAE impulse forced response simulation and in an actual vehicle, with good correlation. It was ascertained that this method could be used effectively as a design tool for performance evaluations of powertrain mount layouts in designing total vehicle performance.

1. Introduction

Design methods for the vibro-isolating support of automobile engines have focused on the coupling term of characteristics matrices obtained from equations of motion. Non-coupled support methods have been advocated for some time as a means of simultaneously damping the powertrain mount resonance area and preventing vibration in the vibro-isolating range.(1) Issues for powertrain mount design in automotive development include satisfying performance relative to various phenomena such as ride comfort relative to suspension input, vehicle longitudinal vibration relative to drive train torque input, and idling noise and vibration relative to engine torque fluctuation input. However, the powertrain mount resonance and the idling noise and vibration (vibro-isolating area) frequency bands are close. Additionally, the damping performance relative to suspension input and vibro-isolating performance relative to idling noise and vibration often have a mutually interacting relationship. When creating the actual design, it is often difficult to place the powertrain mounts in the ideal locations to achieve non-coupled support inside the engine room of FF (front engine, front drive) vehicles, so a certain degree of coupled support is unavoidable.

With the construction of the CAE environment, which is representative of the improved computer performance and lower prices achieved over the past ten years, it is becoming possible to predict performance by response calculations using CAE software. This is generally done by processing large numbers of simulation proposals individually. In addition, design staff often merely evaluate the frequency response levels produced by calculation staff, and there are cases where discussion of physical issues is forgotten.

Therefore, this paper attempts to specify the degree of coupling using an index based on a simple physical coordinate system when setting the powertrain mount layout (geometry and spring value). In addition, ride comfort and idling, which are low frequency phenomena, were analyzed in regards to the following three items for a 2 liter displacement class FF transversally mounted engine passenger car, with good correlation.

*Tochigi R&D Center

(1) Degree of coupling obtained by arithmetically processing the characteristics matrices (mass, stiffness)
(2) Frequency response analysis using structural analysis software
(3) Actual vehicle tests

As a result, a degree of coupling guidelines was obtained for the FF transversally mounted engine powertrain mount layout.

2. Degree of Coupling in the Characteristics Matrices

In eigenvalue analysis, evaluation is performed according to a diagonal matrix on the inertial and elastic main axes. However, in degree of coupling analysis, evaluation is performed according to the relationship between non-diagonal terms, which are coupled, and diagonal terms, which are non-coupled. The mass matrix $[M_{gr}]$ (equation (1)) and stiffness matrix $[K_{gr}]$ (equation (2)) are analyzed from the discrete engine characteristics and the spring characteristics, respectively, with both matrices located on the grand coordinate axis. Here, 1 to 6 of subscripts I and j indicate in order the longitudinal, lateral, vertical, pitch, roll and yaw components. The mass and stiffness matrices generally contain not only diagonal terms, which are the inertial and elastic main axes on the grand coordinate axis, but also non-diagonal terms which are inertial and elastic products, indicating that the six characteristic modes are coupled.

$$[M_{gr}] = \begin{bmatrix} m & & & & & \\ & m & & & & \\ & & m & & & \\ & & & I_{xx} & -I_{xy} & -I_{xz} \\ & & & -I_{yx} & I_{yy} & -I_{yz} \\ & & & -I_{zx} & -I_{zy} & I_{zz} \end{bmatrix} \quad (1)$$

$$[K_{gr}] = \begin{bmatrix} k_{11} & & & & k_{15} & k_{16} \\ & k_{22} & & & & k_{26} \\ & & k_{33} & k_{34} & k_{35} & \\ & k_{42} & k_{43} & k_{44} & k_{11} & k_{11} \\ k_{51} & & k_{53} & k_{11} & k_{55} & k_{11} \\ k_{61} & k_{62} & & k_{11} & k_{11} & k_{66} \end{bmatrix} \quad (2)$$

To evaluate this mode coupling, [D0] is derived as the coupling matrix. The coupling matrix [D0] is calculated from the mass and stiffness matrices, which are characteristic matrices, and expressed as shown in equation (3). Here, ω is the angular speed [rad/s], and a value that matches the phenomena to be evaluated is set.

$$[D_0] = [K_{gr}] + \omega^2[M_{gr}] \quad (3)$$

$$[D_0] = \begin{bmatrix} d_{11} & & & & d_{15} & d_{16} \\ & d_{22} & & d_{24} & & d_{26} \\ & & d_{33} & d_{34} & d_{35} & \\ & & & d_{44} & d_{45} & d_{46} \\ & & sym & & d_{55} & d_{56} \\ & & & & & d_{66} \end{bmatrix} \quad (4)$$

Degree of coupling is defined from the coupling matrix [D0] as the ratio of the diagonal and non-diagonal terms that are the main components of the phenomena. For example, in the case of idling noise and vibration, the y-axis mode that is the main input direction and the coupled z-axis are calculated as shown in equation (5).

$$[D_{idle}] = d_{56} / d_{55} \quad (5)$$

Here, d_{55} is the y-axis diagonal term, and d_{56} is the z-axis non-diagonal term that is coupled to d_{55}.

The degree of coupling was set for both idling and ride comfort based on the features of each phenomenon.

3. Correlation between CAE Calculations and Actual Vehicle Tests

Three types of actual prototype powertrain mount layouts (Type A, Type B and Type C (conventional layout)) were manufactured and compared. Each layout was investigated using structural analysis software prior to confirmation in an actual vehicle. The results of investigating the degree of coupling are described below.

3.1 Idling Noise and Vibration

When this phenomenon occurs, the drive torque fluctuation is acting on the engine y-axis (hereafter "roll axis"), with the roll axis vibration mode as the main mode. The roll mode in the input direction is the main mode, and vibration is aggravated by coupling with the engine z-axis (hereafter "yaw axis") mode. The degree of coupling in idling performance evaluation is given by equation (5), and is shown in Fig. 1 using Type C as the standard.

The Type A value is approximately 1.4 times, and the Type B value is approximately 4 times the value of the conventional layout Type C.

Next, the idling vibration mode of an actual vehicle was simulated using the CAE model shown in Fig. 2. This

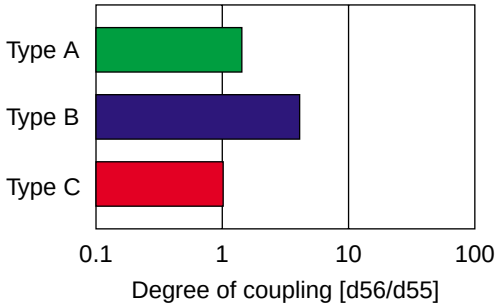


Fig. 1 Degree of coupling for idling noise and vibration

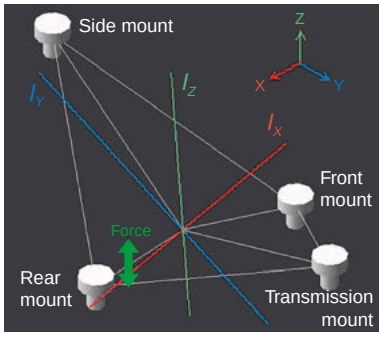


Fig. 2 CAE model for idling noise and vibration

model gives mass and inertia terms as the engine specifications, and the idling frequency characteristics as the mount spring characteristics. The response force and acceleration on the mounts are evaluated by applying the engine impulse force as shown in Fig. 3.

Fig. 3 shows that Type B has a high degree of coupling with the 20 Hz yaw rate, and this causes the vibration to increase in the idling noise and vibration range. Fig. 4 shows the test results using an actual vehicle, and the results are approximately the same as for CAE. Vibration clearly increases for Type B, and although vibration increases slightly for Type A, it is not enough to significantly affect idling noise and vibration in actual vehicle tests.

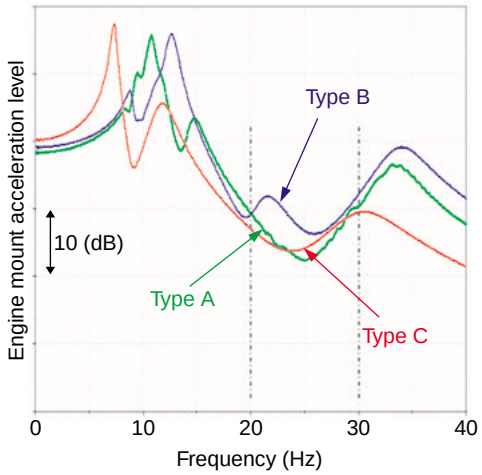


Fig. 3 Amount of engine mount vibration according to CAE

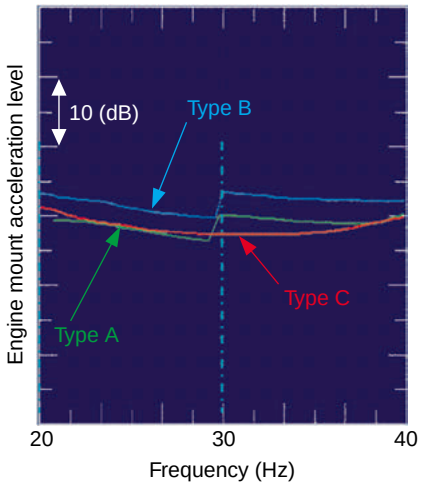


Fig. 4 Experimental level of engine mount vibration

According to the degree of coupling standard set by this study, coupling of approximately 1 to 1.4 does not adversely affect vibration at the powertrain mounting points while idling. However, Fig. 4 shows that the influence increases at 6, indicating that 1.4 is an index that should be observed.

3.2 Ride Comfort Relative to Longitudinal Input

Over the past ten years the application of sealed liquid mounts has become the general method of dealing with the phenomenon of ride comfort relative to powertrain mount vertical input. This paper tackles the longitudinal and lateral input response that is difficult to damp with the vertical damping characteristics of sealed liquid mounts.

In the case of longitudinal and lateral input, it is already known that the vibration level can be reduced by coupling the rotational component to the main translation component[(2) – (4)].

The degree of coupling for longitudinal input ride comfort is as follows, and is shown in Fig. 5 using Type C as the standard.

$$|D_{logi}| = {}^{d_{51}}\!/_{d_{11}} \qquad (6)$$

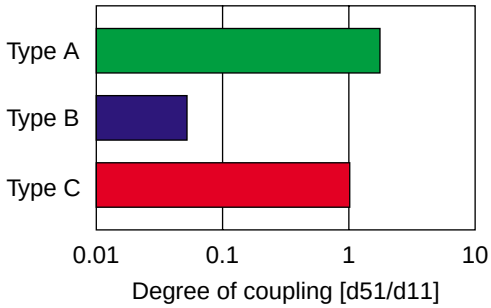


Fig. 5 Degree of coupling for ride comfort

The Type A value is approximately 1.1 times, and the Type B value is approximately 0.07 times the value of Type C.

Next, the ride comfort longitudinal vibration mode of an actual vehicle was simulated using a model such as that shown in Fig. 6 as the CAE model. Here, the engine specifications and mount characteristics were modeled in the same manner as the idling model, and the body, tires and a shaker were further modeled to evaluate ride comfort. The resulting body response force and acceleration were evaluated by exciting the shaker in the longitudinal or lateral direction. In addition, an actual vehicle was also evaluated using excitation equipment having this same structure. The simulation results are shown in Fig. 7.

Fig. 5 shows that Type B has a low degree of coupling between longitudinal characteristic vibration and the rotational component at 10 Hz, so the vibration level is higher than the other two types. In contrast to this, Types A and C have a high degree of coupling between the longitudinal and rotational components, and low vibration levels. In addition, Type A exhibits a high longitudinal

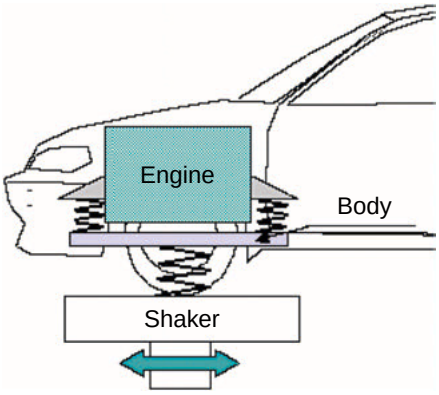


Fig. 6 CAE model for ride comfort

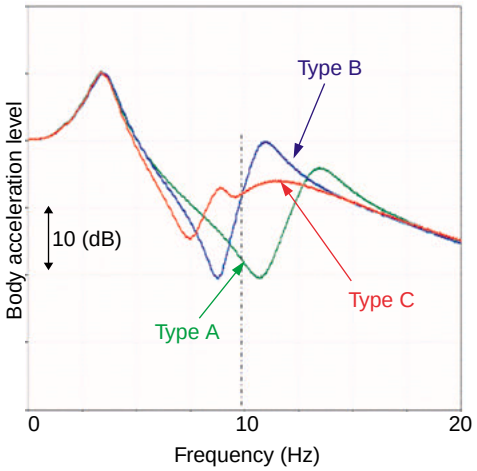


Fig. 7 Level of body vibration with CAE

characteristic value, with vibration around 10 Hz being lower than for Type C.

According to the degree of coupling standard set by this study, coupling of approximately 1 to 2 does not adversely affect body longitudinal vibration for ride comfort. However, Fig. 8 shows that the vibration level increases at 0.07, indicating that 1 is an index that should be observed.

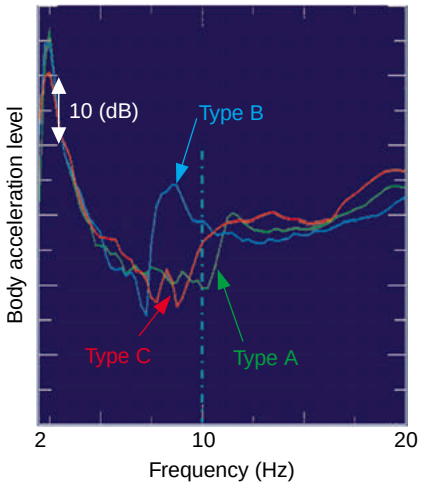


Fig. 8 Experimental level of body vibration

3.3 Ride Comfort Relative to Lateral Input

In the case of lateral input, the degree of coupling is expressed in the same manner as the longitudinal component as follows and is shown in Fig. 9 using Type C as the standard.

$$[D_{horizo}] = d_{42} / d_{22} \qquad (7)$$

The Type A value is approximately 1.3 times, and the Type B value is approximately 0.3 times the value of Type C. As shown in Fig. 10, Type B has a low degree of coupling between lateral characteristic vibration and the rotational component at 10 Hz, with vibration levels higher than the other two types. In contrast, Types A and C have

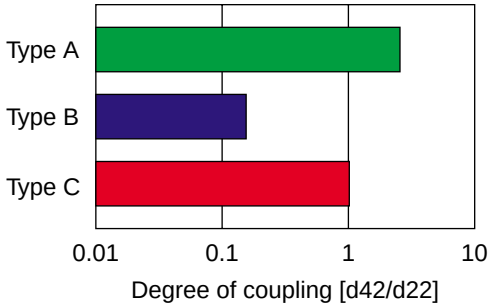


Fig. 9 Degree of coupling for ride comfort

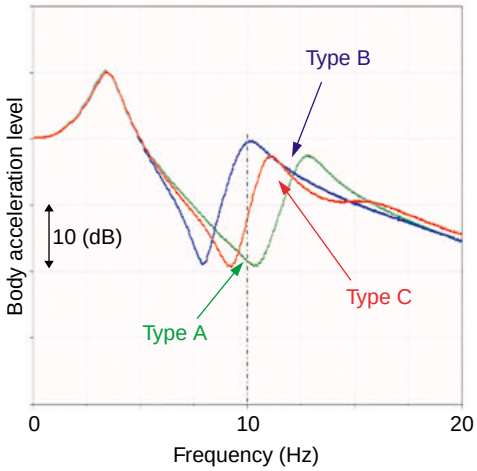


Fig. 10 Level of body vibration with CAE

a high degree of coupling between the lateral and rotational components, and low vibration levels. In addition, Type A exhibits a high lateral characteristic value, with vibration around 10 Hz being lower than for Type C.

According to the degree of coupling standard set by this study, coupling of approximately 1 to 3 does not adversely affect body lateral vibration for ride comfort. However, Fig. 11 shows that the vibration level increases at 0.2, indicating that 1 is an index that should be observed.

Viewed in terms of the overall completed vehicle, Type A can be considered the superior package.

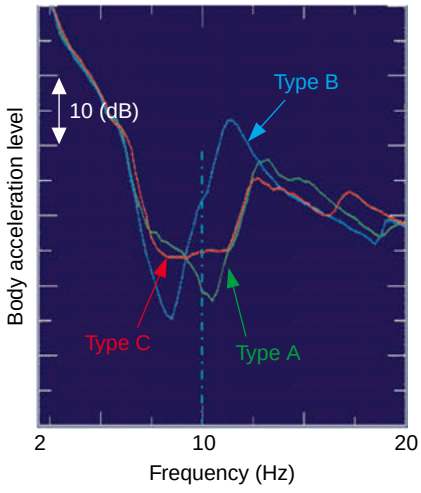


Fig. 11 Experimental level of body vibration

4. Conclusion

CAE investigations and actual vehicle tests of powertrain mount layouts verified that there is a high correlation between the degree of coupling advocated in this study and completed vehicle performance. The degree of coupling set in this study can be obtained by simple arithmetic calculations from characteristics matrices, making it easy for designers to understand ride comfort and idling noise and vibration performances relative to low-frequency phenomena in the layout stage. The non-diagonal terms in the matrix obtained by adding the mass and stiffness matrices are expressed by dividing the main mode by the related mode terms. Therefore, the meaning of the indices is also easy for designers to understand. Performance can be evaluated, even by designers without CAE calculation skills, and the indices can also be used for optimization in the stage before starting full-scale CAE investigations.

References

(1) Tohara, H.: Rubber Vibration Isolators, JARI, p.72 – 94 (1975)

(2) Sakai, T., et al.: Performance Evaluation of Engine Mount Layouts Using Impulse Forced Response Simulation, JSAE Proceedings Vol. 47, No. 6, p. 65 – 70 (1993)

(3) Sakai, T., et al.: CAE Processing in System Development for Powertrain Mount Layouts, JMAC8 (1994)

(4) Sakai, T., et al.: The Application of 3-dimensional General-purpose Structure Analysis Software to Drive Train Vibration Analysis, Honda Technical Review Vol. 2, p. 171 – 178 (1990)

(5) Sakai, T., Gielen, Ludo: Development Procedure for Interior Noise Performance by Virtual Refinement, SAE Noise and Vibration Conference, Traverse City, Michigan, USA (2001)

(6) Sakai, T., et al.: A Theoretical Study Concerning the Engine Mount Layout, Isuzu Technical Journal No. 102, p. 40 – 52 (1999)

■ Authors ■


Masafumi KYUSE


Satoshi WATANABE


Tatsuhide SAKAI

Strength Evaluation Method for Nd-Fe-B Rare Earth Sintered Magnets

Takaaki NAGI* Teruyoshi KITA*

ABSTRACT

Application of the Weibull theory to an Nd-Fe-B rare earth sintered magnet was studied for use in evaluating the specific strength characteristics arising from the structure of this magnet. The validity of the Weibull theory was verified by the correlation with the Weibull distribution and by the existence of the size effect, whereby strength decreases with increases in size. The correlation with the Weibull distribution was verified by the close correlation shown by the resistance strength Weibull plot approximation line. While the existence of the size effect was verified due to the existence of the fixed relationship between effective volume, determined by the stress distribution, and fracture stress. Consequently, it was judged that the Weibull theory is valid for evaluation of the strength of this magnet. The strength of the magnet when incorporated into the rotor of a motor was also verified, thereby demonstrating the applicability of this theory to this type of magnet.

Introduction

Advances in magnet materials in recent years have made Nd-Fe-B rare earth sintered magnets (Nd-Fe-B magnets below), which have superior magnetic characteristics, available at a low cost. At present, permanent magnet motors utilizing these magnets make up the bulk of the drive motors used in electric vehicles (EV) and hybrid electric vehicles (HEV).

In addition to low cost, critical issues for these drive motors include achieving high efficiency, high revolution speeds and a lightweight construction. The interior permanent magnet (IPM) rotor structure shown in Fig. 1, in which the magnet is embedded in the yoke, is effective in these respects.

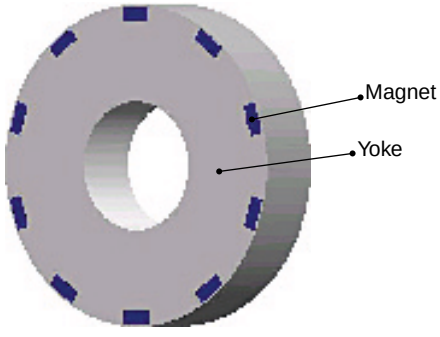


Fig. 1 IPM rotor

* Tochigi R&D Center

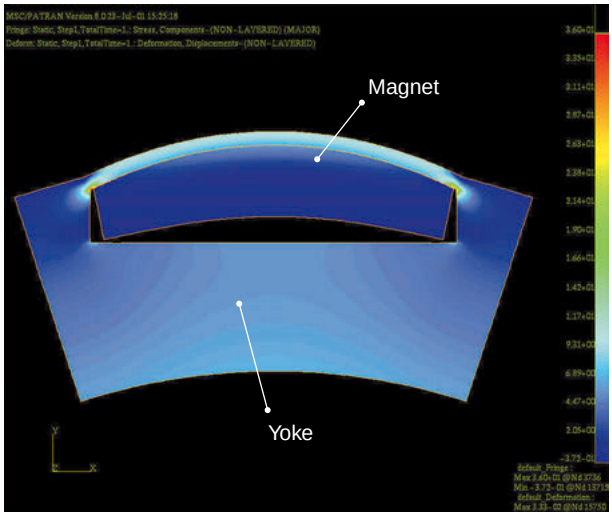


Fig. 2 Stress distribution of IPM rotor

In this type of motor, centrifugal force generates stresses on the magnet and electrical steel sheet when the motor is rotating, and thus it is very important to understand strength of these materials (Fig. 2). However, there are almost no examples of analysis of the strength of Nd-Fe-B magnets.

The tests described in this paper applied Weibull theory to the evaluation of the strength of Nd-Fe-B magnets and verified its suitability.

1. Characteristics of Nd-Fe-B Magnets

Fig. 3 shows a structural model of an Nd-Fe-B magnet. The magnet chiefly consists of an $Nd_2Fe_{14}B$ main phase and an Nd-rich grain boundary phase, which play important roles in producing magnetic characteristics. In addition to these, the structure contains traces of impurities (oxides, carbides, etc.) and pores, which are difficult to prevent in the sintering process. Fig. 4 shows an example of a graph of the load-strain relationship for Nd-Fe-B magnets. The magnet breaks (brittle fracture) without plastic deformation;

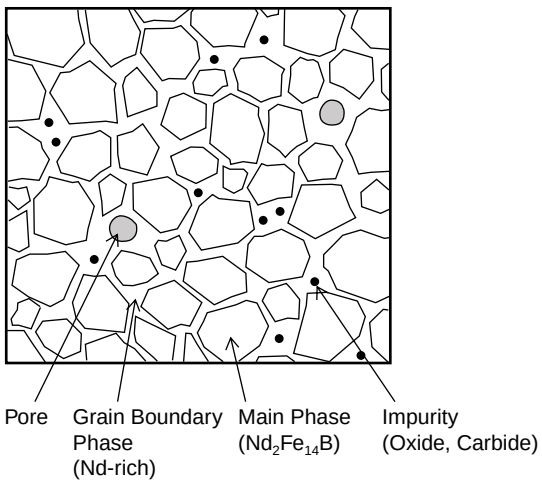


Fig. 3 Nd-Fe-B model

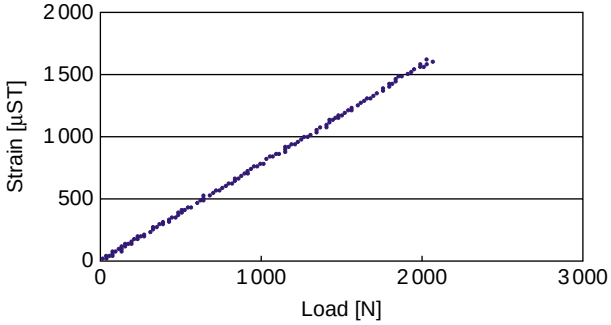


Fig. 4 Relationship between load and strain

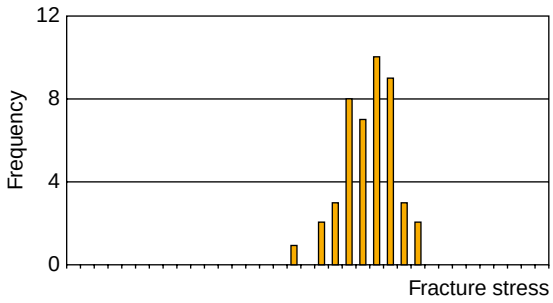


Fig. 5 Fracture test result

this is believed to occur because the main phase is composed of a hard, brittle intermetallic compound. Fig. 5 shows a histogram of the fracture stress values. The graph shows a large and broad variation in fracture stress on the low stress side, which is believed to be an effect of the impurities and pores. As demonstrated above, the unique structure of Nd-Fe-B magnets gives them different strength characteristics than those of ordinary steel. For this reason, methods of evaluation and design appropriate to these characteristics are necessary.

2. Weibull Theory

Statistical probability theory is effective in quantifying the strength of Nd-Fe-B magnets. Listed below are the elements that form the basis of this approach.

2.1 Weakest Link Theory

Nd-Fe-B magnets show great variations in strength. It is likely that this is caused by the presence of numerous tiny defects in the materials from which cracks are propagated to eventually become fractures. For this reason, fracture strength is not dependent on stresses occurring on the materials alone, but on the size and number of defects in the materials.

Because the size of the defects is several μm, it is impossible to detect them with present measurement technology without causing fracturing. For this reason, it is impossible to predict individual fracture characteristics.

Weakest link theory is effective in modeling materials with these characteristics. The following three items are necessary conditions for establishing weakest link theory:
(1) The fractures are brittle fractures.
(2) The cracks are independent of each other.
(3) The defects are constant per unit volume.

If the above conditions are satisfied, it is possible to model the strength of materials containing "N" number of defects by modeling the breaking strength of a chain comprised of a certain number, "N", of links, as shown in Fig. 6. As the chain is steadily pulled more and more strongly, the weakest links break, and thus the chain is broken even though the other links remain intact. That is, the strength of the chain is determined by the strength of the weakest link. This is the weakest link theory.

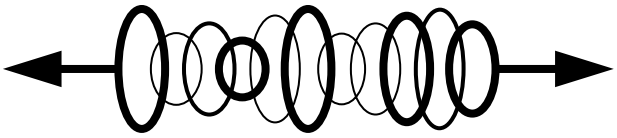


Fig. 6 Weakest link model

2.2 Weibull Theory[1] [2]

The probability of the existence of "N" number of individual connected links S_N, is shown by the following equation, where F_N is the probability of breaking:

$$S_N = 1 - F_N = (1 - F(\sigma))^N \fallingdotseq \exp(-N \cdot F(\sigma)) \quad (1)$$

$F(\sigma)$: The probability of breaking for a link receiving stress σ.

When the risk of rupture, Ra, is used, equation (1) is converted to the following, because Ra is also a stress function:

$$F(\sigma, v) = 1 - \exp\left(-\int_v Ra \cdot dV\right) = 1 - \exp\left(-\int_v f(\sigma) \cdot dV\right) \quad (2)$$

where v and V are variable volumes.

At this point, based on experimental results, Weibull hypothesized a power function as expressed by the following equation.

$$f(\sigma) = \left(\frac{\sigma - \sigma_\omega}{\sigma_o}\right)^m \quad (3)$$

where m, σ_ω and σ_o are material constants.

Accordingly, equation (2) is transformed as follows:

$$F(\sigma, v) = 1 - \exp\left\{-\int_v \left(\frac{\sigma - \sigma_\omega}{\sigma_o}\right)^m dV\right\} \quad (4)$$

In equation (4), σ_ω, known as the Weibull distribution function, is normally taken as $\sigma_\omega = 0$ to avoid excess evaluation.

$$\therefore F(\sigma, v) = 1 - \exp\left\{-\int_v \left(\frac{\sigma}{\sigma_o}\right)^m dV\right\} \quad (5)$$

If the effective volume, VE, as defined by equation (6) is applied, equation (5) can be simplified to equation (7).

$$VE = \int_v \left(\frac{\sigma}{\sigma_R}\right)^m dV \quad (6)$$

$$F(\sigma, v) = 1 - \exp\left\{-\left(\frac{\sigma_R}{\sigma_o}\right)^m VE\right\} \quad (7)$$

Using this equation with a fixed probability of breaking, the strength, σ_{R2}, of a target object of volume VE_2, can be found from the strength, σ_{R1}, of a test piece of volume VE_1.

$$\therefore \frac{\sigma_{R2}}{\sigma_{R1}} = \left(\frac{VE_1}{VE_2}\right)^{1/m} \quad (8)$$

3. Application of Weibull Theory to Magnets

3.1 Test Method

The test method for fine ceramics (JIS R1601) was used as a reference to establish a test method for Nd-Fe-B magnets according to the following criteria (Fig. 7):

- Test piece shape: L40 × W10 × T5 mm (Direction of magnetization)
- Distance between support points: 30 mm (L_1)
- Distance between load points: 10 mm (L_2)
- Cross head speed: 0.5 mm/min

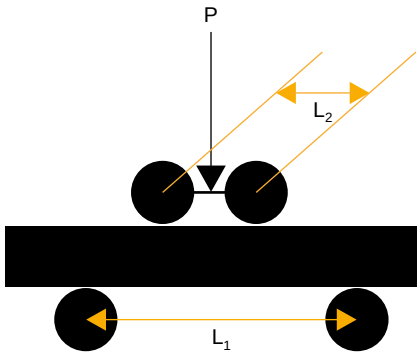


Fig. 7 Fracture test

The following equation was used to calculate stress σ from transverse load P:

$$\sigma = \frac{3P(L_1 - L_2)}{2WT^2} \quad (9)$$

3.2 Applicability of Weibull Theory

The applicability of Weibull Theory was judged according to the two items below. Results have demonstrated that Weibull Theory is applicable to the strength of Nd-Fe-B magnets. Details of the two verification items are as follows.

3.2.1 Correlation with weibull distribution

Fig. 8 shows an example of a Weibull plot for the breaking strength of an Nd-Fe-B magnet. The plotted points approach a straight line, and demonstrate a coefficient of correlation of above 0.9. Therefore, it was verified that these strength characteristics satisfy the relationships in equation (5), and the strength characteristics of Nd-Fe-B magnets were judged to follow a Weibull distribution.

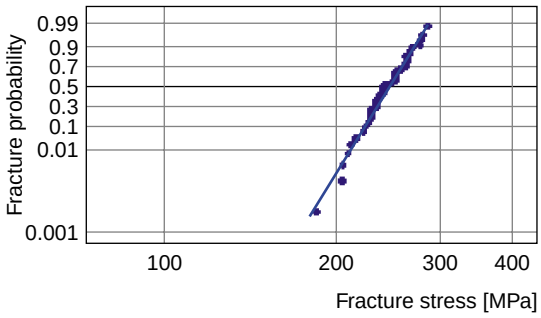


Fig. 8 Weibull plot for magnet strength

3.2.2 Size effect

Fig. 9 shows a plot of fracture stress for different widths as an example of strength when width is varied. Fig. 10 shows this as a Weibull plot.

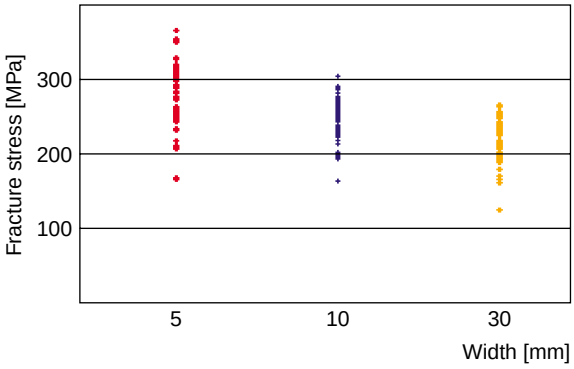


Fig. 9 Fracture stress for each width

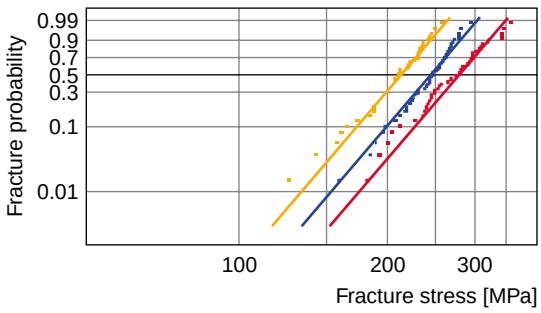


Fig. 10 Weibull plot for each width

These graphs demonstrate that while the average strength (fracture stress) varies for different widths, the Weibull number, which expresses variation conditions, is almost exactly the same. To clarify the relationship between test piece size and average strength, the relationship between effective volumes and average fracture strengths was plotted. The slope of the approximated straight line is the opposite of the negative of the Weibull number, m, and it was verified that the relationships in equation (8) were satisfied (Fig. 11).

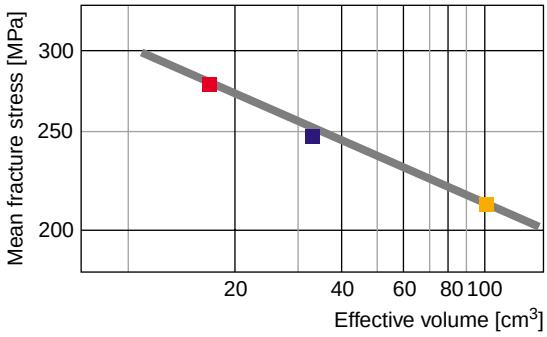


Fig. 11 Size effect

4. Verification in Actual Applications

The foregoing discussion has been concerned with the applicability of the Weibull Theory to the evaluation of the strength of Nd-Fe-B magnets. The authors also verified that this method was effective with actual magnets. Specifically, first, a rotor spin test was conducted to fracture the magnet, and the motor speed at the time the magnet fractured was measured. Next, CAE analysis was used to calculate stress values from these results, which were then Weibull plotted (Fig. 12). As the graph shows, it was possible to verify the applicability of Weibull distribution even when the magnet is in its actual form within the rotor.

Moreover, strength was predicted on the basis of Weibull Theory, using the results of four-point bending tests as the material constants.

Fig. 13 shows a graph of the results of both the calculation predictions and the actual measurement results from Fig. 12.

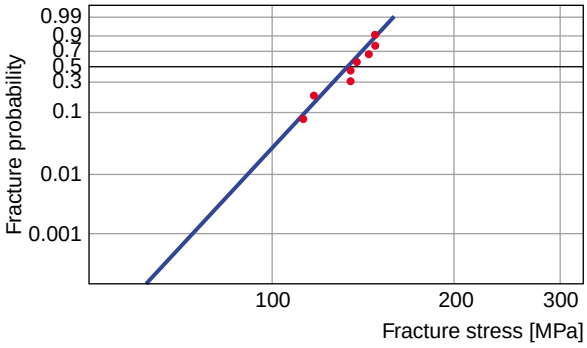


Fig. 12 Weibull plot of magnet strength of rotor (spin test result)

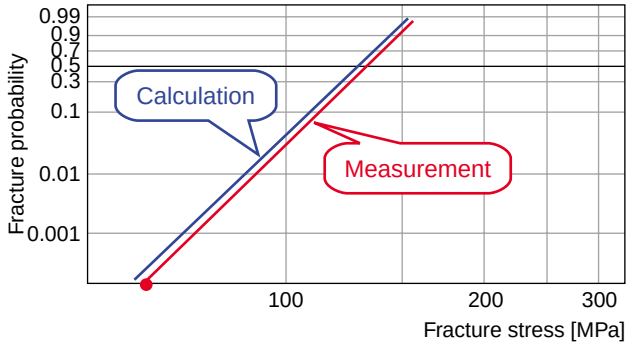


Fig. 13 Comparison of the measurement and calculation results

Results of the predictions and measurements correlate well in this graph, thus verifying the validity of the method. It is believed that in the future the application of this method will enable the prediction of the strength of the magnets from material constants during the motor design stage.

5. Conclusion

The applicability of Weibull Theory to Nd-Fe-B rare earth sintered magnets was tested, and the following results were obtained:

(1) As a result of verifying the size effect and the applicability of four-point bending test results to the Weibull distribution for a basic test piece shape, the validity of applying Weibull Theory to strength evaluations of Nd-Fe-B magnets was demonstrated.

(2) The applicability of the Weibull distribution to magnets in their actual application shape was also verified. A shape effect (size effect) was also verified from four-point bending test results for a basic test piece shape and from spin test results for actual magnets. As a result of the above verifications, it was found that this method enables the prediction of the strength characteristics for the actual shapes through the application of the Weibull Theory constants as the material constants.

The foregoing demonstrates the effectiveness of this evaluation method for strength design of magnets for motor applications.

References

(1) Matsuo, Y., The Life and Destruction of Ceramics, Tokyo, Uchidaroukakuho, 1992, p. 120

(2) Abe, H., et al., Engineering Ceramics, Tokyo, Gihoudou, 1998, p. 164

■ Authors ■



Takaaki NAGI



Teruyoshi KITA

Technical Papers Submitted to Out-of-company : (January, 2001 to June,2001)

(English Papers Only)

Date	Conference	Title	Author	Organization
2001/1/1	JSAE/JSAE Review/Vol.22 No.1	The development of joint parts for automobile body by thixocasting	Nobuhiro Saito	Tochigi R&D Center
			Takeyoshi Nakamura	Tochigi R&D Center
			Ohtani Teruyuki	Tochigi R&D Center
			Morio Kuroki	Tochigi R&D Center
			Eiji Masuda	Honda Engineering Co.,Ltd.
			Takashi Idegomori	Honda Engineering Co.,Ltd.
		Numerical Simulation Method to Predict the Thermal Environment Inside a Car Cabin	Akihiro Fujita	Tochigi R&D Center
			Hiroshi Nakagawa	Tochigi R&D Center
			Junichi Kanemaru	Honda R&D Americas
			Yoshiichi Ozeki	Asahi Glass Company
		Development of the ultra-low-fuel-consumption hybrid car - INSIGHT	Koichi Fukuo	Tochigi R&D Center
			Masaaki Saito	Tochigi R&D Center
			Kazuhiko Tsunoda	Tochigi R&D Center
			Shiro Takiguchi	Tochigi R&D Center
2001/2/1	TEXT-COM/Auto Technology	Optimum description of Interior Sound of Sports Cars	Yasuo Ishii	Tochigi R&D Center
			F.K.Brandl	AVL List GmbH
2001/2/5～8	AABC/Advanced Automotive Battery Conference/ (Las Vegas, USA)	Advanced battery performances and development issues for electric and hybrid vehicles	Noboru Sato	Tochigi R&D Center
2001/3/5～8	SAE/2001International Congress and Exposition/(Detroit,USA)	Secondary O2 Feedback Using Prediction and Identification Sliding Mode Control -Second Report-	Yuji Yasui	Tochigi R&D Center
			Shusuke Akazaki	Tochigi R&D Center
			Masaki Ueno	Tochigi R&D Center
			Yoshihisa Iwaki	Tochigi R&D Center
		Air/Fuel Distribution Simulation in a Port Injected Gasoline Lean-burn Engine	Naohiro Ishikawa	Tochigi R&D Center
			Toru Takabayashi	Tochigi R&D Center
			Atsushi Hiraide	Tochigi R&D Center
		Development of a Novel Parallel Hybrid Transmission	Gregory A. Schultz	U.S.Army Aberdeen Test Center
			Lung-Wen Tsai	University of California
			Naritomo Higuchi	Tochigi R&D Center
			Ivan C. Tong	University of Maryland College Park
		Advanced Hydro-Mechanical Transmission with High Durability for Small Utility Vehicles	Tsutomu Hayashi	Asaka R&D Center
			Mitsuru Saito	Asaka R&D Center
			Yoshihiro Yoshida	Asaka R&D Center
			Takehiko Nanri	Asaka R&D Center
		Intake and Exhaust Systems Equipped with a Variable Valve Control Device for Enhancing of Engine Power	Tetsuya Nakayasu	Asaka R&D Center
			Hajime Yamada	Asaka R&D Center
			Toshihiko Suda	Asaka R&D Center
			Noritoshi Iwase	Asaka R&D Center
			Kyo Takahashi	Asaka R&D Center
2001/3/7-9	First International Conference on Evolutionary Multi-criterion Optimization/ (Zurich, Switzerland)	Adapting weighed aggregation for multi-objective evolution strategies	Yaochu Jin	Honda R&D Europe
			Tatsuya Okabe	Honda R&D Europe
			Bernhard Sendhoff	Honda R&D Europe
2001/3/26～ 2001/3/28	Coordinating Research Council/11th CRC On-Road Vehicle Emissions Workshop/(San Diego, USA)	Real World Emissions Characteristics from the Low-Emission Natural Gas Vehicle	Toshiyuki Suga	Tochigi R&D Center
			Tadashi Muraishi	Tochigi R&D Center
			Takushi Toda	Tochigi R&D Center
			Dave Dewitt	Honda R&D Americas
2001/4/1	JSAE Review Vol.22 No.2	Development of a Closed Crankcase System Engine for Motorcycles	Osamu Kudo	Asaka R&D Center
			Yasuo Shimura	Asaka R&D Center
			Koji Terada	Asaka R&D Center
			Nobuaki Inumaru	Asaka R&D Center
2001/4/1～5	CATIA Operators Exchange/The 2001 COE Spring Conference & Techni.	Examples of CATIA FEM analysis on 3D detailed models	Takanao Uchida	Tochigi R&D Center
			Shigeru Nagai	Tochigi R&D Center
		Improvement of CATIA 3D auto-mesher	Shigeru Nagai	Tochigi R&D Center
			Takanao Uchida	Tochigi R&D Center
2001/4/3	Haus der Technik e.V., D-45117/PKW-Lenkungssysteme/(Essen,Germany)	Improvement in Driver-Vehicle system performance by VGS	Toshitake Kawai	Tochigi R&D Center
			Yasuo Shimizu	Tochigi R&D Center
			Yasuji Shibahata	Tochigi R&D Center
			Fumio Kawano	Tochigi R&D Center
			Shoichi Sano	Tokyo Denki Univ.

Technical Papers Submitted to Out-of-company：(January, 2001 to June,2001)

Date	Conference	Title	Author	Organization
2001/4/18	Material Research Society (MRS)/2001 Spring Meeting/ (San Francisco, USA)	Atomistic Simulation of Carbon Nanotube Ropes: Structure , Strength, and Thermal Transport	Yoshiya Fujiwara	Wako Research Center
			Ju Li, Sidney Yip	Massachusetts Institute of Technology
2001/4/30～ 2001/5/3	SAE/2001SAE Noise&Vibration Conference/(MI,USA)	Development procedure for interior noise performance by virtual vehicle refinement, combining experimental and numerical component models	Tatsuhide Sakai	Tochigi R&D Center
			Masahiro Terada	Tochigi R&D Center
			Shuichi Ono	Tochigi R&D Center
			Naoki Kamimura	Tochigi R&D Center
		How to Predict the Powertrain Vibration at Engine Mounting Points under Running	Yasuhiko Seki	Tochigi R&D Center
			Yukitaka Takahashi	Tochigi R&D Center
			Masayoshi Tsukahara	PSG CO.,LTD.
			Toshibumi Suzuki	Tochigi R&D Center
		A New Analysis Method for Brake Squeal	Chih-Hung Chung	MTS Systems Corporation
			William Steed	MTS Systems Corporation
			Kiyoshi Kobayashi	Tochigi R&D Center
			Hiroyuki Nakata	Tochigi R&D Center
2001/5/1	John&Sons,Inc/Journal of Polymer Science part B:Polymer Physics	Electrostriction Behavior of Nitrile-butadiene Rubber and Hydrogenated Nitrile-butafiene Rubber	Tatsuya Hattori	Wako Research Center
			Hiroshi Okamoto	Aichi Institute of Technology
2001/5/13～17	IEEE/IV 2001 IEEE Intelligent Vehicles Symposium, Proceedings./(Tokyo)	Development of Night Vision System	Takayuki Tsuji	Tochigi R&D Center
			Hiroshi Hatsutori	Tochigi R&D Center
			Masahito Watanabe	Tochigi R&D Center
			Nobuharu Nagaoka	Tochigi R&D Center
2001/5/14～ 2001/5/17	IEEE/National Institute of Informatics/ Intelligent Vehicles Symposium 2001/(Tokyo)	AMI-C Demo Car for Convergence 2000	Hideo Furukawa	Tochigi R&D Center
2001/5/27-30	2001 Congress of Evolutionary Computation/ (Seoul, Korea)	Managing Approximate Models in Evolutionary Optimization	Yaochu Jin	Honda R&D Europe
			Markus Olhofer	Honda R&D Europe
			Bernhard Sendhoff	Honda R&D Europe
		Dynamic Encoding for Shape Optimisation Using Evolution Strategies	Markus Olhofer	Honda R&D Europe
			Bernhard Sendhoff	Honda R&D Europe
2001/5/30～6/1	HIBBITT, KARLSSON & SORENSEN, INC./2001 ABAQUS Users' Conference/(Maastricht, The	Development of Metal Pushing V-Belt Stress Simulation for Continuously Variable Transmission	Toshihiro Saito	Tochigi R&D Center
			Takemasa Okano	Tochigi R&D Center
2001/5/31-6/2	International Conference on Congnitive and Neural System 2001 (Boston, USA)	Information processing in networks of spiking neurons with an external clocking signal	Tobias Rodemann	Honda R&D Europe
			Edgar Koerner	Honda R&D Europe
2001/6/4～7	17th International Technical Conference on the Enhanced Safety of Vehicles(ESV-17)/(Amsterdam, Nederland)	A Study of the Upper Leg Component Tests Compared with Pedestrian Dummy Tests	Yutaka Okamoto	Tochigi R&D Center
			Akihiko Akiyama	Tochigi R&D Center
			Yuji Kikuchi	Tochigi R&D Center
			Masayoshi Okamoto	Tochigi R&D Center
		Improvement of visibility for vulnerable parties in traffic accidents	Akio Takahashi	Tochigi R&D Center
			Nobuyoshi Asanuma	Tochigi R&D Center
		Biofidelity of test devices and validity of injury criteria for evaluating knee injuries to	Yuukou Takahashi	Tochigi R&D Center
			Yuji Kikuchi	Tochigi R&D Center
		Development of whiplash injury reducing seat system using BioRID II Dummy	Koji Sano	Tochigi R&D Center
			Yasuhiro Dokko	Tochigi R&D Center
		Study of Airbag Interference with Out of Position Occupant by the Computer Simulation	Koichi Kamiji	Tochigi R&D Center
			Nobuyuki Kawamura	Tochigi R&D Center
		Study on car to car side inpact	Tomiji Sugimoto	Tochigi R&D Center
			Shoji Yamazaki	Tochigi R&D Center
		Influence of body intrusion and deceleration on occupant injuries in front collisions between passenger cars	Hideki Suzuki	Tochigi R&D Center
			Tomiji Sugimoto	Tochigi R&D Center
			Yoshiji Kadotani	Honda R&D Americas
		Exploratory Study of an Airbag Concept for a Large Touring Motorcycle: Further Study	Takeshi Yamazaki	Asaka R&D Center
			Satoshi Iijima	Asaka R&D Center
			Takenori Yamamoto	Asaka R&D Center
2001/6/6～8	RIETER Automotive Systems/RIETER Automotive Conference/ (Switzerland)	Statistical Energy Analysis Using the Simulation of the Acoustic Property of Automotive Trim	Kazuhito Misaji	Tochigi R&D Center
			Yuji Kuruhara	Tochigi R&D Center
			Yoshihiro Noguchi	Tochigi R&D Center
			Tsuyoshi Yamashita	Tochigi R&D Center
			Maurizio Mantovani	RIETER Automotive Systems

Technical Papers Submitted to Out-of-company：(January, 2001 to June,2001)

Date	Conference	Title	Author	Organization
2001/6/7-10	28th Gottingen Neuroscience Meeting / 4th Meeting of the German Neuroscience Society (Gottingen, Germany)	The Brain Like System Simulator BLISS	Mark-Oliver Gewaltig Andreas Richter Rudiger Kupper	Honda R&D Europe Honda R&D Europe Philipps-Universitat, Marburg
2001/6/12～13	Uni of Wisconsin Engine Research Center/Exhaust Aftertreatment Racts and Fiction/The 2nd symposium of the University of Wisconsin Engine Research Center(Wiaconsin/USA)	Ultimate Low Emission S.I.	Tadayoshi Hayashi	Tochigi R&D Center
2001/6/17-22	OPTIMIZATION IN INDUSTRY III (Tuscany, Italy)	Aerodynamic Optimization for a Transonic Compressor Stator Blade Using MOGA	Yoshihiro Yamaguchi Toshiyuki Arima	Wako Research Center Wako Research Center
2001/6/17-22	OPTIMIZATION IN INDUSTRY III (Tuscany, Italy)	Aerodynamic Shape Optimisations using Evolutionary Strategies	Markus Olhofer Toshiyuki Arima Toyotaka Sonoda Bernhard Sendhoff	Honda R&D Europe Wako Research Center Wako Research Center Honda R&D Europe

Editor’s Notes

Sometimes when looking at the Internet screen I forget just where I am. Newspapers each day carry articles about the innovative technologies of space development, nuclear fusion, and genetic manipulation, making us feel that things that were once mere dreams are now within our reach. The changes that have occurred in the world over the past half-century are said to be occurring at a rate not only greater than ever before in human history, but greater than ever before in the history of life's evolution itself. We certainly seem to be living in the "third age of scientific revolution."

It is said that the status of science in medieval Europe was as one part of a theology that sought to understand nature as God's creation, and was thus hemmed in by the ethical concepts of Christianity. Science was freed from these ethical shackles when Darwin declared that apes were progenitors of man. As a result of becoming ethically neutral, physics became a systematic science its application lead to the further development of chemistry. We owe our current materially abundant lifestyle to these advances. It is now predicted that physics and chemistry will further fuse themselves with the biological sciences, proceeding into life design itself.

How will Honda's ASIMO robot evolve? Will it become a mechanical servant performing dangerous jobs in place of human beings? Or will it become more of a sensate humanoid along the lines of Osamu Tezuka's Tetsuwan Atom ("Astro Boy")? Science and technology present us with options for achieving goals, but the question of what goals to pursue is an ethical question. Aside from the search for some kind of virtual "pure" science, the development of science and technology used in the real world should not be ethically neutral or unrestricted.

What to create, and to what degree will it be useful to society? For the engineer, such ethical questions as these "software" type questions are even more difficult than those related to "hardware", and these questions will become increasingly prevalent in coming years. As we stand at the crossroads, we believe that Honda's "DNA"—as expressed in the motto "action without ideals is a dangerous weapon, and ideals without action are without meaning," will continue to light our path. It is our earnest desire that harmony exist between scientific technology and ethical concepts, and that the successes of our continued research be published in this Technical Review to thus allow each successive generation to "share the joy."

(Yasuhiro Sugimoto, Asaka Higashi R&D Center)

Honda R&D Technical Review English Version Vol. 13 No. 2

The following associates provided us with their cooperation and expertise:

Karen	Arneson	American Honda Motor Co., Inc.
Bill	Bezilla	Honda R&D Americas, Inc. Ohio Center
Marci	Bird	Honda R&D Americas, Inc. Ohio Center
Jeff	Brown	Honda R&D Americas, Inc. Ohio Center
Mary	Christopherson	American Honda Motor Co., Inc.
Jared	Cox	Honda R&D Americas, Inc. Ohio Center
Chris	Cymbal	Honda R&D Americas, Inc. Ohio Center
Ben	Davis	Honda R&D Americas, Inc. Ohio Center
Jim	Dykeman	Honda R&D Americas, Inc. Ohio Center
Jack	Frieders	Honda R&D Americas, Inc. Ohio Center
Lee M.	Goldring	American Honda Motor Co., Inc.
Hiroshi	Inutsuka	Honda R&D Americas, Inc. Ohio Center
Ken	Lantz	Honda R&D Americas, Inc. Ohio Center
Doug	Longhitano	Honda R&D Americas, Inc. Ohio Center
Raj	Manakkal	Honda R&D Americas, Inc. Ohio Center
Curt	Nice	Honda R&D Americas, Inc. Ohio Center
Ashley	Nichols	Honda R&D Americas, Inc. Ohio Center
Brian	Nutwell	Honda R&D Americas, Inc. Ohio Center
Bill	Post	Honda R&D Americas, Inc. Ohio Center
Kurt	Risic	Honda R&D Americas, Inc. Ohio Center
Hiroshi	Shinagawa	Honda R&D Americas, Inc. Ohio Center
John	Shutway	Honda R&D Americas, Inc. Ohio Center
Josh	Sigmund	Honda R&D Americas, Inc. Ohio Center
Max	Suzumoto	Honda R&D Americas, Inc. Ohio Center
Chris	Thomas	Honda R&D Americas, Inc. Ohio Center
Chuck	Thomas	Honda R&D Americas, Inc. Ohio Center
Fumiko	Uno	Honda R&D Americas, Inc. Ohio Center
Mark	Wenden	Honda R&D Americas, Inc. Ohio Center
Willam	Willen	American Honda Motor Co., Inc.
Yoshio	Yamamoto	Honda R&D Americas, Inc. Ohio Center
Terumi	Young	Tochigi R&D Center

